

Andreas Momber

Blast Cleaning Technology

 Springer

Blast Cleaning Technology

A. Momber

Blast Cleaning Technology

With 385 Figures and 169 Tables

 Springer

Andreas Momber
Privatdozent Dr.-Ing. habil.
Hamburg
Germany

ISBN: 978-3-540-73644-8

e-ISBN: 978-3-540-73645-5

Library of Congress Control Number: 2007931617

© 2008 Springer-Verlag Berlin Heidelberg

This work is subject to copyright. All rights are reserved, whether the whole or part of the material is concerned, specifically the rights of translation, reprinting, reuse of illustrations, recitation, broadcasting, reproduction on microfilm or in any other way, and storage in data banks. Duplication of this publication or parts thereof is permitted only under the provisions of the German Copyright Law of September 9, 1965, in its current version, and permission for use must always be obtained from Springer. Violations are liable to prosecution under the German Copyright Law.

The use of general descriptive names, registered names, trademarks, etc. in this publication does not imply, even in the absence of a specific statement, that such names are exempt from the relevant protective laws and regulations and therefore free for general use.

Cover design: eStudio Calamar, Girona, Spain

Printed on acid-free paper

9 8 7 6 5 4 3 2 1

springer.com

Contents

1	Introduction	1
1.1	Motivation	1
1.2	Introductory Remarks	1
1.3	Blast Cleaning Methods and Applications	3
2	Abrasive Materials	7
2.1	Classification and Properties of Abrasive Materials	7
2.2	Abrasive Material Structure and Hardness	7
2.2.1	Structural Aspects of Abrasive Materials	7
2.2.2	Hardness of Abrasive Materials	13
2.3	Abrasive Particle Shape Parameters	17
2.3.1	Basic Shape Definitions	17
2.3.2	Relative Proportions of Particles	17
2.3.3	Geometrical Forms of Particles	18
2.4	Abrasive Particle Size Distribution and Abrasive Particle Diameter	24
2.4.1	Particle Size Distribution	24
2.4.1.1	General Definitions	24
2.4.1.2	Sieve Analysis	24
2.4.1.3	Particle Size Distribution Models	25
2.4.2	Particle Diameter	27
2.4.3	Alternative Abrasive Particle Size Assessment Methods	27
2.5	Density of Abrasive Materials	30
2.6	Number and Kinetic Energy of Abrasive Particles	30
2.6.1	Abrasive Particle Number and Frequency	30
2.6.2	Kinetic Energy of Abrasive Particles	31
2.6.3	Power Availability	32
2.7	Impurities	34
2.8	Global Abrasive Evaluation Parameter	36
2.9	Process Behaviour of Abrasive Particles	37
2.9.1	Fracture Zones	37
2.9.2	Fracture Probability of Abrasive Particles	41
2.9.3	Effects of Abrasive Material Structure	45
2.9.4	Debris Size	46

2.9.5	Disintegration Numbers	47
2.9.6	Particle Shape Modification During Abrasive Fragmentation	49
2.9.7	Energy Absorption During Abrasive Fragmentation	51
2.9.8	Chemical Degradation	53
3	Air and Abrasive Acceleration	55
3.1	Properties of Compressed Air	55
3.2	Air Flow in Nozzles	59
3.2.1	Air Mass Flow Rate Through Nozzles	59
3.2.2	Volumetric Air Flow Rate	61
3.2.3	Air Exit Flow Velocity in Nozzles	66
3.2.4	Air Flow in Laval Nozzles	68
3.2.5	Power, Impulse Flow and Temperature	70
3.3	Abrasive Particle Acceleration in Nozzles	72
3.3.1	General Aspects	72
3.3.2	Simplified Solution	75
3.3.3	Abrasive Flux Rate	75
3.3.4	Abrasive Particle Spacing	76
3.4	Jet Structure	77
3.4.1	Structure of High-speed Air Jets	77
3.4.2	Structure of Air-particle Jets	78
3.4.3	Design Nozzle Pressure	80
3.5	Composition of Particle Jets	85
3.5.1	Radial Abrasive Particle Distribution	85
3.5.2	Particle Velocity Distribution Function	85
3.5.3	Radial Abrasive Particle Velocity Distribution	89
3.5.4	Area Coverage	90
3.5.5	Stream Density	90
3.6	Parameter Effects on Abrasive Particle Velocity	94
3.6.1	Effects of Air Pressure on Particle Velocity	94
3.6.2	Effects of Abrasive Mass Flow Rate on Particle Velocity	94
3.6.3	Effects of Abrasive Particle Size on Particle Velocity	97
3.6.4	Effects of Abrasive Particle Shape on Particle Velocity	100
3.6.5	Effects of Abrasive Material Density on Particle Velocity	100
3.6.6	Effects of Stand-off Distance on Particle Velocity	101
3.6.7	Effects of Nozzle Length and Nozzle Diameter on Particle Velocity	103
3.6.8	Effects of Nozzle Design on Particle Velocity	103
3.6.9	Effects of Nozzle Wall Roughness on Particle Velocity	104
3.6.10	Scaling Laws for Abrasive Particle Velocity	105
3.7	Abrasive Stream Energy Flow and Nozzle Efficiency	107
4	Blast Cleaning Equipment	109
4.1	General Structure of Blast Cleaning Systems	109
4.2	Air Compressors	109

- 4.2.1 General Aspects 109
- 4.2.2 Working Lines 111
- 4.2.3 Power Rating 112
- 4.2.4 Economic Aspects 114
- 4.2.5 Aspects of Air Quality 116
- 4.3 Blast Machine 118
 - 4.3.1 Basic Parts 118
 - 4.3.2 Abrasive Metering 119
 - 4.3.2.1 Effects of Process Parameters 119
 - 4.3.2.2 Metering Models 124
 - 4.3.2.3 Abrasive Mass Flow Adjustment 127
- 4.4 Pressure Air Hose Lines 128
 - 4.4.1 Materials and Technical Parameters 128
 - 4.4.2 Air Hose Diameter Selection 129
 - 4.4.3 Pressure Drop in Air Hose Lines 130
 - 4.4.3.1 General Approach 130
 - 4.4.3.2 Friction Numbers 132
 - 4.4.3.3 Hose Diameter Effects 136
 - 4.4.3.4 Pressure Drop in Fittings and Armatures 137
- 4.5 Abrasive Hose Lines 138
 - 4.5.1 Conveying Modes in Abrasive Hoses 138
 - 4.5.2 Critical Conveying Flow Velocities in Abrasive Hoses 140
 - 4.5.3 Optimum Flow Velocities in Abrasive Hoses 145
 - 4.5.4 Pressure Drop in Abrasive Hoses 147
- 4.6 Nozzles 154
 - 4.6.1 Nozzle Types 154
 - 4.6.2 Nozzle Wear 155
 - 4.6.2.1 Fundamentals of Nozzle Wear 155
 - 4.6.2.2 Parameter Effects on Nozzle Wear 161
 - 4.6.2.3 Wear Performance of Laminated Ceramic Nozzles .. 164
- 5 Substrate and Coating Erosion 167**
 - 5.1 Introduction 167
 - 5.2 Mechanical Properties of Oxides and Organic Coatings 167
 - 5.2.1 Relevant Mechanical Properties 167
 - 5.2.2 Mechanical Properties of Oxides 174
 - 5.2.2.1 Deformation Parameters 174
 - 5.2.2.2 Hardness 174
 - 5.2.2.3 Adhesion Parameters 174
 - 5.2.3 Mechanical Properties of Organic Coatings 175
 - 5.2.3.1 Deformation Parameters 175
 - 5.2.3.2 Hardness 177
 - 5.2.3.3 Fracture Mechanics Parameters 181

5.3	Impact Processes	182
5.3.1	Impulse and Energy Considerations	182
5.3.2	Coefficient of Restitution	182
5.3.3	Energy Absorption	185
5.3.4	Damage Number	189
5.3.5	Friction Effects	191
5.4	Material Loading Due to Solid Particle Impingement	192
5.4.1	Loading Parameters	192
5.4.2	Material Response to Particle Impingement	194
5.4.3	Formation of Radial and Lateral Cracks	196
5.5	Material Removal Models	200
5.5.1	General Aspects of Modelling	200
5.5.2	Erosion of Plastically Responding Materials	201
5.5.3	Erosion of Elastically Responding Materials	205
5.6	Erosion of Scale	206
5.6.1	Brittle Erosion Approach	206
5.6.2	Removal Mechanisms and Modelling	207
5.6.3	Removableness of Mill Scale	209
5.7	Erosion of Bulk Polymers and Elastomers	210
5.7.1	Material Removal Mechanisms for Bulk Polymers	210
5.7.2	Material Removal Mechanisms for Elastomers	213
5.7.3	Erosion Resistance of Bulk Polymers	214
5.7.4	Erosion Resistance of Elastomers	217
5.8	Erosion of Organic Coatings	221
5.8.1	Material Removal Mechanisms	221
5.8.2	Erosion Resistance	223
5.8.3	Erosion Durability	228
5.9	Debonding of Organic Coatings	229
5.9.1	Indentation Debonding	229
5.9.2	Impact Debonding	233
5.10	Coating Removal Models	236
5.10.1	Ploughing/Delamination Model	236
5.10.2	Debonding Model	237
5.10.3	Effects of a Second Phase in the Coating	239
6	Surface Preparation Process	241
6.1	Definition of Process and Target Parameters	241
6.1.1	Process Parameters	241
6.1.2	Target Parameters	242
6.2	Effects of Pneumatic Parameters	243
6.2.1	Effects of Air Pressure	243
6.2.2	Effects of Nozzle Diameter and Nozzle Length	249
6.2.3	Effects of Nozzle Design	251

- 6.3 Effects of Performance Parameters 256
 - 6.3.1 Effects of Stand-off Distance 256
 - 6.3.2 Effects of Relative Particle Distance 259
 - 6.3.3 Effects of Impact Angle 259
 - 6.3.4 Effects of Exposure Time 261
 - 6.3.5 Effects of Number of Passes 263
- 6.4 Effects of Abrasive Parameters 264
 - 6.4.1 Effects of Abrasive Mass Flow Rate 264
 - 6.4.2 Effects of Abrasive Flux Rate 268
 - 6.4.3 Effects of Abrasive Particle Diameter 270
 - 6.4.4 Effects of Abrasive Particle Shape 277
 - 6.4.5 Effects of Abrasive Material Hardness 279
- 6.5 Removal Models 281
- 6.6 Efficiency of Blast Cleaning 283
 - 6.6.1 Erosion Efficiency 283
 - 6.6.2 General Aspects of Process Efficiency 284
 - 6.6.3 Aspects of Site Management 286
 - 6.6.4 Aspects of Operators’ Fatigue 287
- 6.7 Weld Seam Cleaning 289
- 6.8 Underwater Applications 290
- 6.9 Cost Aspects 292
- 7 Health, Safety and Environment 295**
 - 7.1 Safety Features of Blast Cleaning 295
 - 7.1.1 General Safety Aspects 295
 - 7.1.2 Risk of Explosion 296
 - 7.2 Emission of Air Sound 297
 - 7.3 Emission of Body Sound 301
 - 7.4 Emission of Dust 302
 - 7.5 Emission of Airborne Metals 310
 - 7.5.1 Airborne Lead 310
 - 7.5.2 Other Airborne Metals 314
 - 7.6 Emission of Minerals and Organic Compounds 316
 - 7.6.1 Asbestos Fibres 316
 - 7.6.2 Organic Compounds 317
 - 7.7 Vibrations to the Operator 318
 - 7.8 Personal Protective Equipment 320
 - 7.9 Confined Spaces 321
 - 7.10 Soil Contamination 324
 - 7.11 Waste Disposal 325
 - 7.11.1 General Disposal Problems 325
 - 7.11.2 Abrasive Material Disposal 328
 - 7.11.3 Contamination of Abrasive Material and Leachable Metals . . . 331
 - 7.11.4 Paint Waste 332

7.12	Recycling of Abrasive Materials	333
7.12.1	Contamination with Residue	333
7.12.2	Use for Construction Materials	334
8	Surface Quality Aspects	337
8.1	Surface Quality Features	337
8.2	Visual Cleanliness	338
8.2.1	Visual Standards	338
8.2.2	Initial Conditions	339
8.2.3	Preparation Grades	341
8.2.4	Special Remarks	346
8.3	Dissolved Substances	349
8.3.1	Definitions and Measurement	349
8.3.2	Effects of Dissolved Substances on Coating Performance	351
8.3.3	Substrate Cleanliness After Blast Cleaning	357
8.4	Organic Films	362
8.4.1	Definitions and Measurement	362
8.4.2	Effects of Oil and Grease on Coating Performance	363
8.4.3	Substrate Cleanliness After Blast Cleaning	366
8.5	Dust and Embedded Abrasive Particles	367
8.5.1	Definitions and Measurement	367
8.5.2	Effects of Dust and Particle Embedment on Coating Performance	370
8.5.3	Substrate Cleanliness After Blast Cleaning	374
8.5.4	Fine Cleaning	379
8.6	Roughness and Profile of Substrates	380
8.6.1	Definitions and Measurement	380
8.6.2	Effects of Roughness on Coating Performance	384
8.6.3	Profile Parameters of Blast Cleaned Metal Substrates	394
8.6.3.1	Introduction	394
8.6.3.2	Effects of Blasting Angle	395
8.6.3.3	Effects of Stand-off Distance	396
8.6.3.4	Effects of Air Pressure and Abrasive Particle Velocity	397
8.6.3.5	Effects of Abrasive Particle Size and Shape	399
8.6.3.6	Effects of Abrasive Material Hardness	404
8.6.3.7	Effects of Specific Abrasive Rate	404
8.6.3.8	Effects of Blasting Time	405
8.6.3.9	Effects of Substrate Material	406
8.6.3.10	Effects of Surface Preparation Grade	408
8.6.3.11	Effects of Accessibility	408
8.6.3.12	Statistical Assessment Models	408
8.6.4	Height Distribution Parameters	409
8.6.5	Profiles of “Overblasted” Steel Substrates	409

- 8.7 Surface Integrity 413
 - 8.7.1 Introduction 413
 - 8.7.2 Substrate Hardness 414
 - 8.7.3 Residual Stresses 417
 - 8.7.4 Substrate Fatigue Strength 420
 - 8.7.5 Substrate Deformation Behaviour 423
 - 8.7.6 Substrate Deflection 423
 - 8.7.7 Tribological Parameters 423
 - 8.7.8 Weld Seam Morphology 425
 - 8.7.9 Near-surface Layer Chemical Composition 425
 - 8.7.10 Corrosion Resistance 429
- 8.8 Surface Energy and Work of Adhesion 434
 - 8.8.1 Definitions and Measurement 434
 - 8.8.2 Effects of Substrate Surface Energy on Corrosion and Coating Performance 437
 - 8.8.3 Surface Energies of Blast Cleaned Substrates 438
- 8.9 Wettability of Metal Substrates 441
 - 8.9.1 Definitions and Measurement 441
 - 8.9.2 Effects of Wettability on Coating Performance 445
 - 8.9.3 Wettability of Blast Cleaned Metal Substrates 447
- 8.10 Electron Transport Properties 451
- 9 Coating Performance 453**
 - 9.1 Corrosion Protection Performance of Organic Coatings 453
 - 9.1.1 Definitions and Methods 453
 - 9.1.2 Coating Performance After Blast Cleaning 456
 - 9.1.2.1 Introduction 456
 - 9.1.2.2 Coating Delamination 458
 - 9.1.2.3 Degree of Rusting 462
 - 9.1.2.4 Degree of Blistering 463
 - 9.2 Adhesion and Adhesion Strength 464
 - 9.2.1 Definitions and Measurement 464
 - 9.2.1.1 Definitions 464
 - 9.2.1.2 Adhesion Measurement 465
 - 9.2.2 Adhesion of Coatings and Adhesives to Metal Substrates 468
 - 9.2.3 Blast Cleaning Parameters Effects on Adhesion 483
 - 9.2.3.1 Effects of Blasting Angle 483
 - 9.2.3.2 Effects of Abrasive Type, Size and Shape 483
 - 9.2.3.3 Effects of Air Pressure 488
 - 9.2.3.4 Effects of Stand-off Distance 488
 - 9.2.3.5 Statistical Assessment Models 488
 - 9.3 Mechanical Behaviour of Coatings 489
 - 9.4 Corrosion Protection Performance of Coatings 492
 - 9.5 Deposition and Transport Phenomena 494
 - 9.6 Wire Embedment in Polymer Matrices 495

- 9.7 Coating Formation Processes 496
 - 9.7.1 Spreading and Splashing 496
 - 9.7.2 Powder Solidification 498
 - 9.7.3 Nucleation Processes 499
- References** 501
- List of Symbols** 529
- Index** 537

Chapter 1

Introduction

1.1 Motivation

Reams (1939), in his book *Modern Blast Cleaning and Ventilation*, and Rosenberger (1939), in his book *Impact Cleaning*, probably delivered the first serious state-of-the-art reviews about the industrial fundamentals of blast cleaning. They were followed by Plaster (1972) with his two-volume compendium on ‘*Blast Cleaning and Allied Processes*’. In Germany, Horowitz’ (1982) book about *Oberflächenbehandlung mittels Strahlmitteln (Surface Treatment with Blasting Media)* became very popular and is still a widely used reference. Since then, 25 years of intense progress in both industrial applications and scientific research have passed. The aim of this book is to provide an extensive up-to-date engineering-based review about the fundamental principles of blast cleaning.

This book is concerned with the blast cleaning of metallic substrates prior to the application of protective coatings or adhesives.

1.2 Introductory Remarks

From the point of view of the material removal mechanism, blast cleaning can be considered to be an erosion process. “Erosion”, as a tribological term, is the removal of materials due to the action of impinging solid particles. Erosion is a natural phenomenon [the correct designation in terms of geology is *corrasion* (Bates and Jackson, 1980)] and there exist a number of impressive examples about the material removal capability of natural erosion. One example, the erosion of rock columns, is illustrated in Fig. 1.1.

Blast cleaning is one of the most frequently utilised treatment methods in modern industry. The starting point of the utilisation of blast cleaning for industrial purposes was Tilghman’s patent on “*Improvement in cutting and engraving stone, metal, glass, etc.*” (Tilghman, 1870). Benjamin Chew Tilghman (1821–1901), an American scientist, invented the “*cutting, boring, grinding, dressing pulverizing, and engraving stone, metal, glass, wood, and other hard or solid substances, by means of a stream of sand or grains of quartz, or of other suitable materials, artificially driven*



Fig. 1.1 The natural erosion (corrasion) of rock columns in Palmyra (Photograph: University of Tokyo)

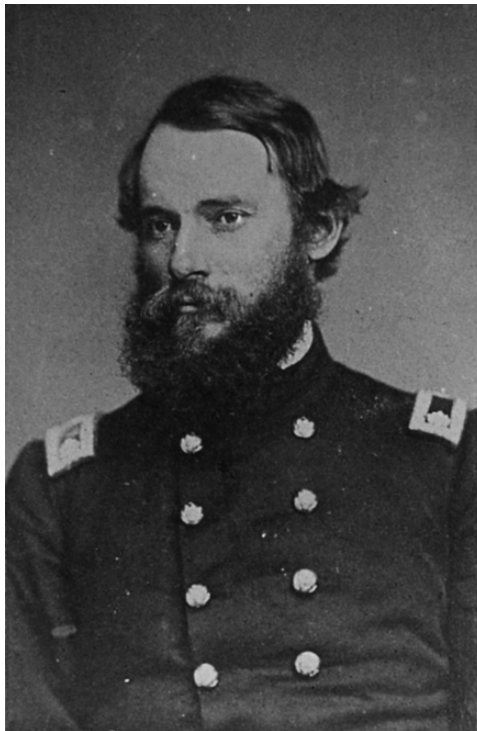


Fig. 1.2 Benjamin C. Tilghman (Copyright: ATT-Net)

as projectiles rapidly against them by any suitable method of propulsion” (Patent No. 108,408, October 18, 1870). It is not only the general idea of what we today call blast cleaning, or grit blasting, covered by this invention, Tilghman also mentioned a number of methods how to propel the solid particles against the material surface. He wrote: “The means of propelling the sand . . . is by a rapid jet or current of steam, air, water, or other suitable gaseous or liquid medium; but any direct propelling force may be used, as, for example, the blows of the blades of a rapidly-revolving fan, or the centrifugal force of a revolving drum or tube, or any other suitable machine” (Patent No. 108, 408, October 18, 1870). Benjamin Tilghman is portrayed in Fig. 1.2.

The industrial applications mentioned by Tilghman included the following: “Articles of cast or wrought metal may have their surfaces smoothed and cleaned from slag, scale, or other incrustations.” Reviews about the early developments in industrial blast cleaning were provided by Plaster (1972, 1993). Early applications included applications in the foundry industry, steel industry and corrosion protection industry. Today’s applications include the use for micro-machining, polishing, maintenance and surface preparation for coating applications. A recent advanced application in the machining industry is grit blast assisted laser milling (Li et al., 2005).

1.3 Blast Cleaning Methods and Applications

Blast cleaning methods, according to corrosion protection applications, can be subdivided as listed in Table 1.1. Blast cleaning is by definition a method “where blasting media (as tools) are accelerated in blasting devices of different blasting systems, and where they are forced to impinge the surface of a target (substrate) to be treated” (ISO 12944-4, 1998). To define a blast cleaning method completely, the following information is required:

Table 1.1 Blast cleaning methods according to ISO 12944-4 (1998)

Blast cleaning methods	Dry abrasive blast cleaning	<ul style="list-style-type: none"> – Centrifugal abrasive blast cleaning – Compressed-air abrasive blast cleaning – Vacuum or suction-head abrasive blast cleaning
	Moisture-injection abrasive blast cleaning	(No further subdivision)
	Wet abrasive blast cleaning	<ul style="list-style-type: none"> – Compressed-air wet abrasive blast cleaning – Slurry blast cleaning – Pressurised-liquid blast cleaning
	Particular applications of blast cleaning	<ul style="list-style-type: none"> – Sweep blast cleaning – Spot blast cleaning

- purpose of blasting;
- blasting system;
- blasting medium type.

A blast cleaning system is designated according to the method, and respectively the medium, that accelerates the abrasive particles up to the required velocity. From that point of view, blast cleaning systems can be subdivided into compressed-air blast cleaning, centrifugal blast cleaning and vacuum or suction-head blast cleaning.

The book deals with the application of compressed-air blast cleaning for the treatment of metallic substrates. This includes the two following applications:

- removal of mill scales, slags and coatings;
- substrate preparation for the subsequent application of coating systems or adhesive systems.

An application example is shown in Fig. 1.3. Coating systems to be applied to blast cleaned substrates include basically corrosion protective coatings and wear resistant coatings. The examples provided in Table 1.2 and in Figs. 1.4 and 1.5 very well illustrate the effects of surface preparation methods on the performance of coating systems.

Figure 1.4 shows the effects of different surface preparation methods on the degree of rusting for a variety of coating materials. It can clearly be seen that blast cleaning to a high surface preparation standard (Sa 2^{1/2}) could notably improve



Fig. 1.3 Application of blast cleaning for the surface preparation of steel (Photograph: Muehlhan AG, Hamburg)

Table 1.2 Effect of pipe surface cleanliness on cathodic disbonding; conditions: 30 days/38°C (Neal, 1999)

Coating	Cathodic disbonding in mm		
	Surface cleanliness		
	Blast cleaning (white metal) ^a	Blast cleaning (near-white blast) ^a	Power wire brush
Epoxy polymer concrete	–	5.0	17.1
Fusion bonded epoxy (FBE)	6.1	8.9	>40
Heat shrink sleeve	12.7	18.0	27.3
Tape	14.9	31.8	28.5
Coal tar urethane	13.6	16.5	26.9

^aSee Sect. 8.2.3 for surface preparation grades

the resistance of the coatings against rusting compared to the coatings applied over untreated substrate (mill scale) and over power tool cleaned (St 2 and St 3) substrates. The situation in Fig. 1.5 is more complex. It can be seen that a light blast cleaning (sweep blasting) did not succeed for all coating materials. If a PVC-based coating system was applied to the substrate, washing was more effective than blast cleaning. For the alky-based coatings, however, a preparation performed by blast cleaning substantially improved the resistance of the coating material against flaking.

Results of cathodic disbonding tests on coating materials for pipelines are listed in Table 1.2. It can be recognised that a thorough blast cleaning could notably reduce the delamination widths for all applied coating systems.

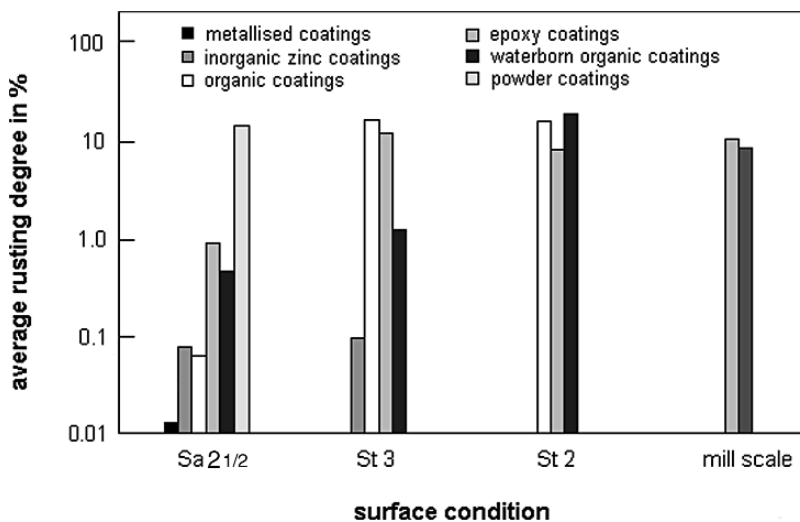


Fig. 1.4 Effects of steel substrate quality on the performance of corrosion protective coatings (Kogler et al., 1995)

Fig. 1.5 Effects of surface preparation methods on the performance of a duplex coating system (Foghelin, 1990)

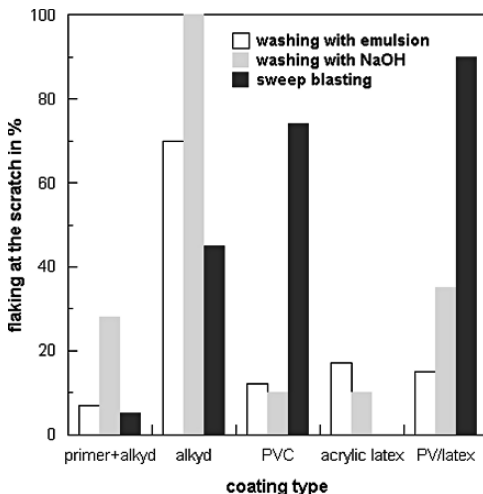


Table 1.3 Effects of surface preparation methods on the performance of a zinc-dust-based protective coating system (Brauns et al., 1964)

Surface preparation	Time to complete rusting in months		
	Splash zone	Transition zone	Underwater zone
Mill scale	5	16	10
Acid pickling	8	8	>24
Flame cleaning	8	8	>24
Blast cleaning ^a	24	>24	>24

^aAbrasive: steel cut wire

Experimental results plotted in Table 1.3 illustrate the effects of different surface preparation methods on the rusting of steel samples coated with a zinc-dust-containing paint. The time of rusting was estimated in three corrosive maritime zones, which are typical for the corrosive loading of offshore constructions. These zones included, in particular, splash zone, water exchange zone and permanent underwater exposure. It can be seen that blast cleaning with steel cut wire notably improved the performance of the corrosion protection system. The time till complete rusting of the paint film occurred could notably be extended if the substrates have been blast cleaned irrespectively of the loading zone.

Chapter 2

Abrasive Materials

2.1 Classification and Properties of Abrasive Materials

A large number of different types of abrasive materials is available for blast cleaning applications. Most frequently applied abrasive materials are listed in Table 2.1. Table 2.2 lists numerous physical, chemical and technical properties of commercial abrasive materials. Basically, there can be distinguished between *metallic* abrasive materials and *non-metallic* abrasive materials.

The evaluation of an abrasive material for blast cleaning applications includes the following important parameters:

- material structure;
- material hardness;
- material density;
- mechanical behaviour;
- particle shape;
- particle size distribution;
- average grain size.

2.2 Abrasive Material Structure and Hardness

2.2.1 Structural Aspects of Abrasive Materials

Structural aspects of abrasive materials include the following features:

- lattice parameters;
- crystallographical group and symmetry;
- chemical composition;
- crystallochemical formula;
- cleavage;
- inclusions (water–gas inclusion and mineral inclusion).

Table 2.1 Annual abrasive consumption in the USA for blast cleaning processes (Hansink, 2000)

Abrasive type	Consumption in Mio. of tonnes
Coal boiler slag	0.65
Copper slag	0.1–0.12
Garnet	0.06
Hematite	0.03
Iron slag	0.005
Nickel slag	0.05
Olivine	0.03
Silica sand	1.6
Staurolite/zirconium	0.08–0.09
Steel grit and steel shot	0.35

Table 2.3 lists typical values for some abrasive materials. Table 2.4 displays a commercial technical data and physical characteristics sheet for a typical blast cleaning abrasive material.

Abrasive particles contain structural defects, such as microcracks, interfaces, inclusions or voids. Very often, these defects are the result of the manufacturing process. Strength and fracture parameters of materials can be characterised through certain distribution types. A widely applied distribution is the Weibull distribution, and it was shown by Huang et al. (1995) that this distribution type can be applied to abrasive materials. The authors derived the following relationship between fracture probability, particle strength and particle volume:

$$F(\sigma_F) = 1 - \exp \left[-V_P \cdot \left(\frac{\sigma_F}{\sigma^*} \right)^{m_W} \right] \quad (2.1)$$

The strength parameter σ^* is a constant, which is related to the defects distribution. The power exponent m_W is the so-called Weibull modulus; it can be read from a graphical representation of (2.1). Low values for m indicate a large intrinsic variability in particle strength. A Weibull plot for aluminium oxide abrasive particles, based on the results of compressive crushing tests, is displayed in Fig. 2.1. Values for the Weibull modulus estimated for different abrasive materials are listed in Table 2.5. There is a notable trend in the values that both fracture strength and Weibull modulus drop with increasing particle size. Therefore, scatter in strength of abrasive particles can be assumed to be wider for larger particles. The relationship between abrasive particle size and fracture strength of the particles is shown in Fig. 2.2. This phenomenon can be explained through the higher absolute number of defects in larger particles. The probability that a defect with a critical dimension (for example, a critical crack length in a fracture mechanics approach) exists increases with an increasing number of defects.

This effect was also observed by Larssen-Basse (1993). This author found also that the Weibull modulus of abrasive particles depended on the atmospheric humidity. Larssen-Basse (1993) performed crushing tests with SiC-particles, and he found that, if humidity increased, the Weibull modulus and the number of fragments both

Table 2.2 Selected abrasive properties (References: manufacturer data)

Brand name	Bulk density ^a in t/m ³	Apparent density in t/m ³	Hardness ^{b,e}	Melting point in °C	Grain size min-max in mm	Major composite in %	Technical name
Abrablast	-	4.3	9 ^b	1,900	-	Al ₂ O ₃ (71.9)	Zirconium corundum
Abramax	1.0-2.0	3.95	2,200 ^c	2,000	-	Al ₂ O ₃ (99.6)	Corundum
Abrasit	1.1-2.3	3.96	2,100 ^c	2,000	-	Al ₂ O ₃ (96.4)	Corundum
Afesikos	1.4	2.6	8 ^b	-	0.04-1.4	SiO ₂ (53)	Aluminium silica
Afesikos HS	2.83	4.1	8 ^b	-	0.04-1.4	SiO ₂ (36)	Garnet
Afesikos SK	1.8	3.96	9 ^b	-	0.06-2.8	Al ₂ O ₃ (99.3)	Corundum
Asilikos	1.3	2.5-2.6	7-8 ^b	-	0.06-2.8	SiO ₂ (51)	Aluminium silica
Cast steel	-	-	60 ^d	-	0.12-3.36	-	-
Garnet	-	3.9-4.1	8-9 ^b	1,315	-	SiO ₂ (41.3)	Garnet
Glass beads	1.5	2.45	6 ^b	-	0.07-0.4	SiO ₂ (73)	-
GSR	3.7-4.3	7.4	44-58 ^d	-	0.1-2.24	-	Cast steel
Cast iron	2.7-4.3	7.4	56-64 ^d	-	up to 3.15	-	-
Ceramic spheres	2.3	3.8	60-65 ^d	-	0.07-0.25	ZrO ₂ (67)	Ceramics
MIKE	1.75	3.92	1,800-2,200 ^e	-	0.001-2.8	Al ₂ O ₃ (99.6)	Corundum
Olivine	1.7-1.9	5.3	6.5-7 ^b	1,760	0.09-1.0	MgO (50)	-
Scorex	1.35	-	-	-	0.5-2.8	SiO ₂ (40)	Refinery slag
Steel grit	-	7.5	48-66 ^d	-	0.2-1.7	-	-
Steel shot	-	7.3	46-51 ^d	-	0.2-2.0	-	-
Testra	1.2-1.4	2.5-2.7	7 ^b	-	0.09-2.0	SiO ₂ (54)	Melting chamber slag

^aDepends on grain sizeHardness parameter: ^bMohs; ^cVickers; ^dRockwell; ^eKnoop

Table 2.3 Structural properties of abrasive materials (Vasek et al., 1993)

Material	Damaged grains (%)	Lattice constant (Å)	Cell volume (Å ³)
Almandine	5–60	11.522 (0.006)	1,529.62
Spessartine	–	11.613 (0.005)	1,566.15
Pyrope	–	11.457 (0.005)	1,503.88
Grossular	30	11.867 (0.005)	1,671.18
Andradite	80–90	12.091 (0.009)	1,767.61

increased. This feature can be attributed to moisture-assisted sharpening of the tips of surface defects present in the particles.

The presence of defects, such as cracks and voids, affects the cleaning and degradation performance of abrasive materials. Number and size of defects are,

Table 2.4 Data sheet for a garnet blast cleaning abrasive material (Reference: GMA Garnet)

Parameter	Value
Average chemical composition	
SiO ₂ ^a	36%
Al ₂ O ₃	20%
FeO	30%
Fe ₂ O ₃	2%
TiO ₂	1%
MnO	1%
CaO	2%
MgO	6%
Physical characteristics	
Bulk density	2,300 kg/m ³
Specific gravity	4.1
Hardness (Mohs)	7.5–8
Melting point	1,250°C
Grain shape	Sub-angular
Other characteristics	
Conductivity	10–15 mS/m
Moisture absorption	Non-hygroscopic
Total chlorides	10–15 ppm
Ferrite (free iron)	<0.01%
Lead	<0.002%
Copper	<0.005%
Other heavy metals	<0.01%
Sulphur	<0.01%
Mineral composition	
Garnet (Almandine)	97–98%
Ilmenite	1–2%
Zircon	0.2%
Quartz (free silica)	<0.5%
Others	0.25%

^aRefers to SiO₂ bound within the lattice of the homogeneous garnet crystal (no free silica)

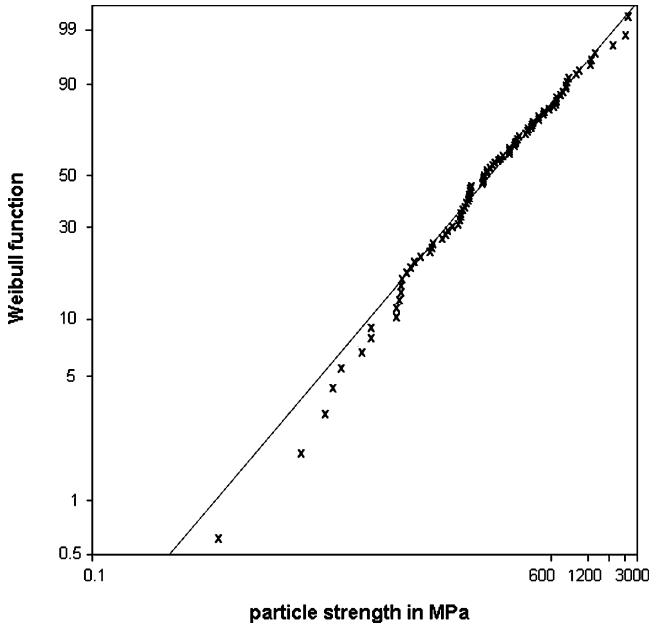


Fig. 2.1 Weibull plot for the strength of aluminium oxide particles (Verspui et al., 1997). Abrasive particle size: 10–500 μm

therefore, important assessment criteria. Cast steel shot, for example, should not contain cracked particles, as illustrated in Fig. 2.3, in excess of 15%. Cast steel grit should not contain cracked particles, as shown in Fig. 2.4, in excess of 40% (SFSA, 1980). Requirements for the defects of particles of metallic abrasive materials are listed in Table 2.6.

Table 2.5 Strength parameters for abrasive materials (Yashima et al., 1987; Huang et al., 1995)

Abrasive material	Grain size in mm	Fracture strength in MPa	Weibull modulus	* ^a in MPa/mm ³
Brown corundum	2.58	67.5	1.98	228.8
	1.85	78.6	2.47	142.8
	1.29	115.4	2.88	135.1
	0.78	200.5	3.47	149.0
Rounded corundum	1.85	96.1	3.41	160.8
White corundum	1.29	79.5	2.57	127.3
Sintered corundum	1.85	110.8	3.85	174.9
Green silicon carbide	1.85	62.2	1.92	155.5
Quartz	0.1–2.0	–	21.0	–
Glass beads	–	–	5.90	–

^aDefect distribution parameter

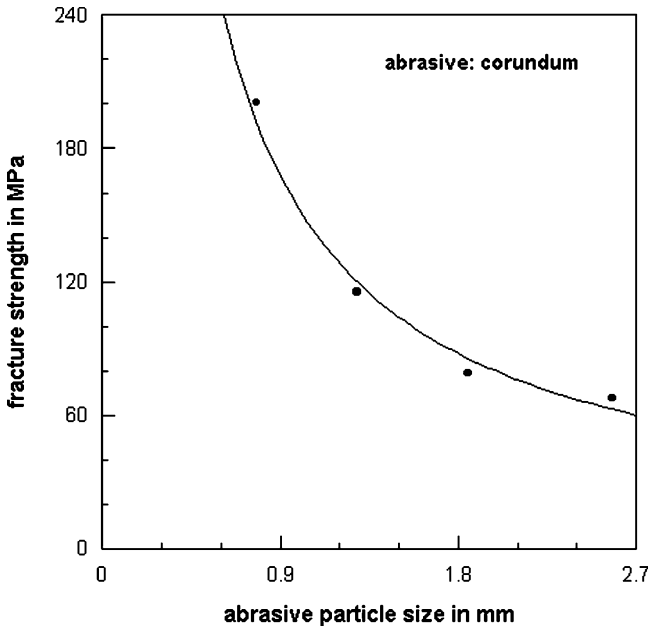


Fig. 2.2 Relationship between abrasive particle size and particle fracture strength (values from Huang et al., 1995)

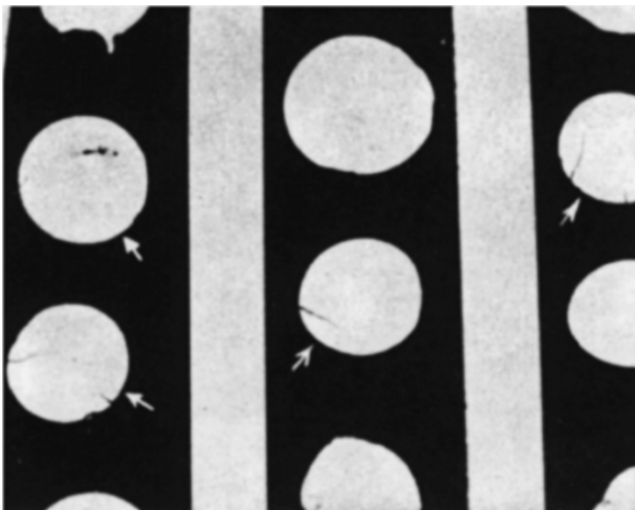


Fig. 2.3 Cracks in cast steel shot particles; magnification: 10× (SFSA, 1980)

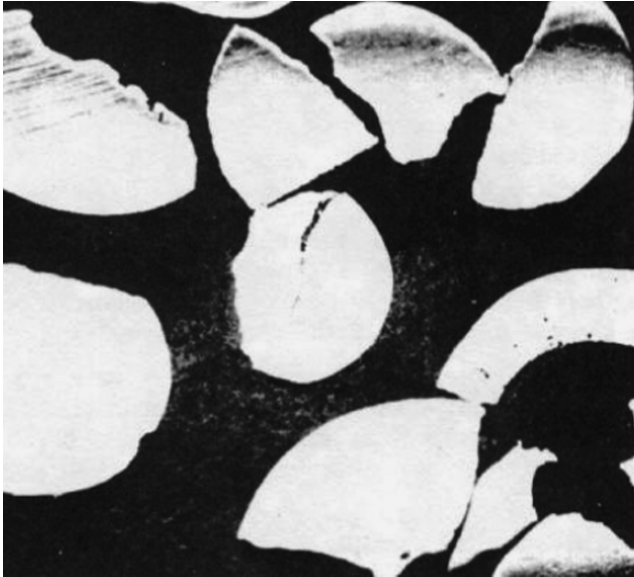


Fig. 2.4 Cracks in cast steel grit particles; magnification: 10× (SFSA, 1980)

2.2.2 Hardness of Abrasive Materials

The hardness of abrasive materials is usually estimated by two types of tests: a scratching test for non-metallic abrasive materials, which delivers the *Mohs hardness*, and indentation tests for metallic materials, which deliver either the *Knoop hardness* or the *Vickers hardness*. Respective values for commercial abrasive materials are listed in Table 2.2.

Mohs hardness is based on a scale of ten minerals, which is provided in Table 2.7. The hardness of a material is measured against the scale by finding the hardest

Table 2.6 Particle defect requirements for metallic abrasive materials (ISO 11124/2-4)

Property	Chilled iron grit	High-carbon cast steel shot	High-carbon cast steel grit	Low-carbon cast steel shot
Particle shape	Max. 10% shot or more than half-round	Max. 5% non-round	Max. 10% shot or more than half-round for grit up to 700 HV; max. 5% for grit above 700 HV	Max. 5% non-round
Voids	Max. 10%	Max. 10%	Max. 10%	Max. 15%
Shrinkage defects	Max. 10%	Max. 10%	Max. 10%	Max. 5%
Cracks	Max. 40%	Max. 15%	Max. 40%	None
Total defects	Max. 40%	Max. 20%	Max. 40%	Max. 20%

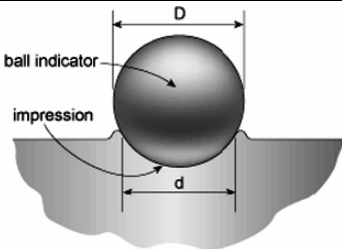
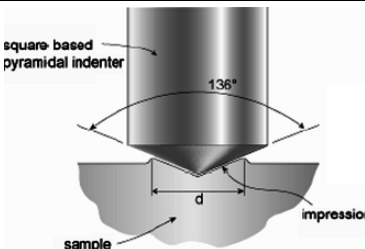
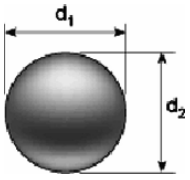
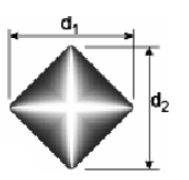
Table 2.7 Mohs scale (Tabor, 1951)

Material	Mohs hardness
Talc	1
Gypsum	2
Calcite	3
Fluorite	4
Apatite	5
Orthoclase (Feldspar)	6
Quartz	7
Topaz	8
Corundum	9
Diamond	10

material that the given material can scratch, and/or the softest material that can scratch the given material. For example, if some material is scratched by quartz but not by feldspar, its hardness on Mohs scale is 6.5. In abrasive standardisation, abrasive particles are being rubbed against a glass plate having a Mohs hardness corresponding to 7. If the particles can scratch the plate, their hardness is >Mohs 7. If they do not scratch the plate, their hardness is <Mohs 7. It is because of this procedure that data sheets for mineral abrasive materials often list the Mohs hardness as >7 only.

The principles of two frequently applied indentation hardness tests are illustrated in Table 2.8. In laboratory practice, an abrasive particle is embedded in a special resin matrix, and it is then being polished in order to obtain an even

Table 2.8 Indentation hardness measurement methods (Images: TWI, Cambridge, UK)

Method	Brinell	Vickers
Principle		
Measurement		
Calculation ^a	$H_B = \frac{F}{\frac{\pi}{2} \cdot D \cdot [D - (D^2 - d^2)^{1/2}]}$	$H_V = \frac{2 \cdot F \cdot \sin(136^\circ/2)}{d^2}$

^aF= indentation load

$$d = \text{indentation size} = \frac{d_1 + d_2}{2}$$

D = indenter size

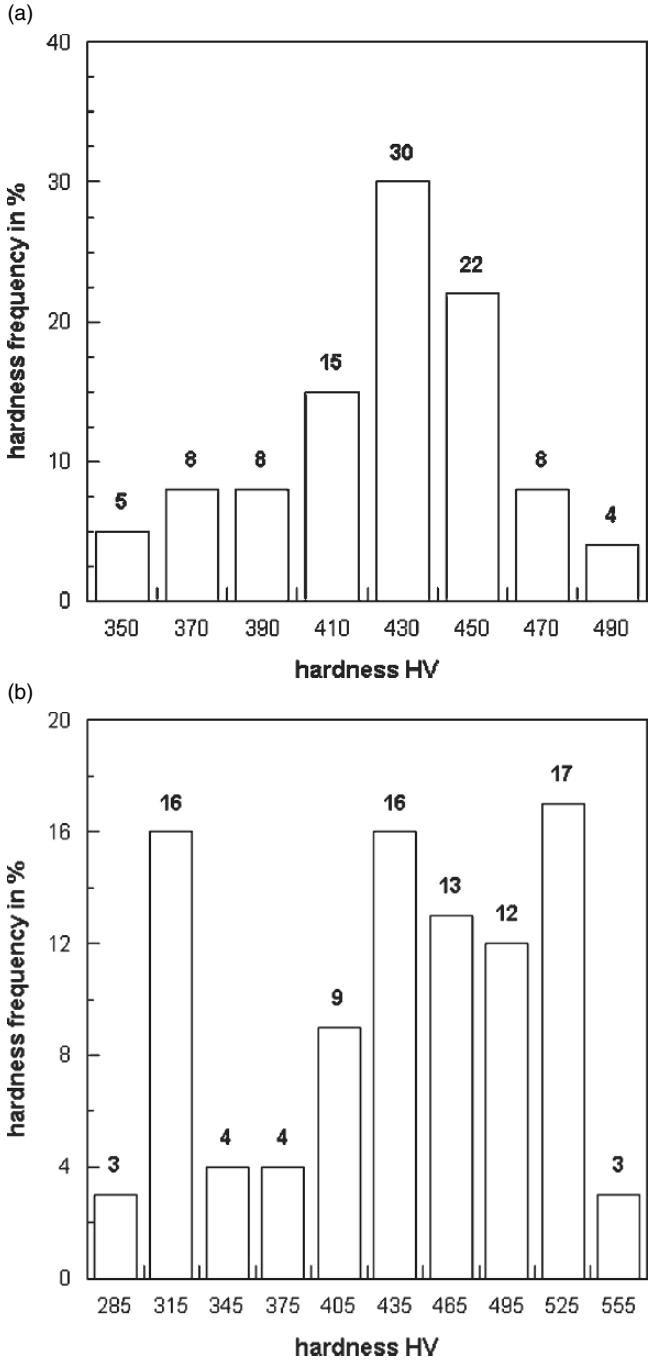


Fig. 2.5 Vickers hardness distributions of two cut wire samples (Gesell, 1979). (a) Laboratory sample; (b) Work sample

smooth cross-section where the actual indentation test is being performed. Indentation hardness values are always dependent on indentation load, and care should be taken to provide the certain applied indentation load in data sheets. Values from indentation hardness tests and from Mohs hardness tests can be related to each other; exceptions are diamond and corundum (Bowden and Tabor, 1964).

The hardness of metallic abrasive particles is a probabilistic parameter, and the hardness values mentioned in data sheets are mainly mean values only. Two typical abrasive hardness distribution diagrams of cut wire samples are provided in Fig. 2.5. Figure 2.5a shows the distribution of a laboratory sample, whereas Fig. 2.5b illustrates the distribution of a working sample. Although both materials had equal hardness designations of 420 HV, the distributions differed widely. The laboratory sample had a unimodal distribution with a maximum at a Vickers hardness of about 430 HV, whereas the working sample featured a multimodal distribution. The hardness distribution of the laboratory sample can be expressed through a Normal distribution – this is shown in Fig. 2.6. This result points to a rather homogeneous response of the wire material to the indentation with the Vickers pyramid, which is not always the case (Lange and Schimmöller, 1967). Such a distribution was also reported by Flavenot and Lu (1990) for steel wire shot.

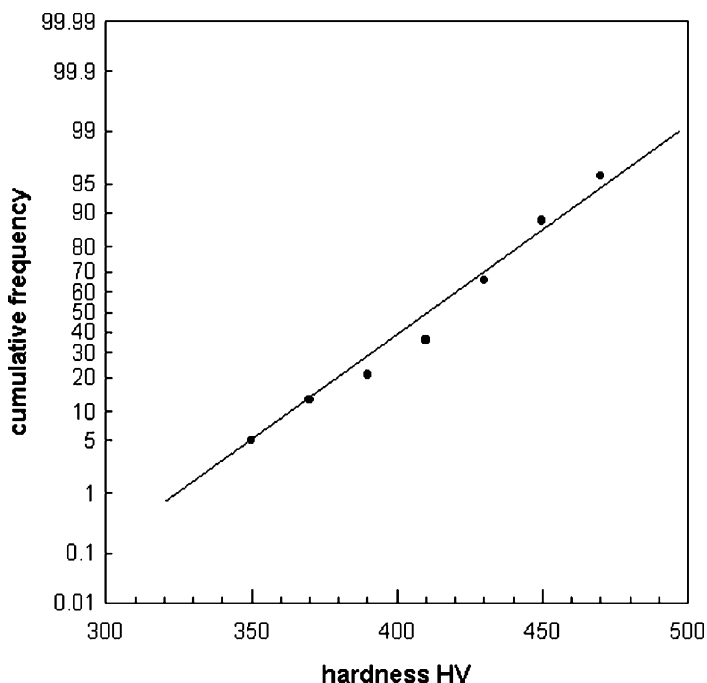


Fig. 2.6 Normal distribution function for the laboratory cut wire sample plotted in Fig. 2.5a

2.3 Abrasive Particle Shape Parameters

2.3.1 Basic Shape Definitions

The following three basic shape definitions are provided for abrasive particles used for blast cleaning applications:

- shot;
- grit;
- cylindrical.

The corresponding designations are listed in Table 2.9. Examples for two shape definition are displayed in Fig. 2.7. The term *shot* characterises grains with a predominantly spherical shape. Their length-to-diameter ratio is <2 , and they do not exhibit sharp edges or broken sections. The term *grit* characterises grains with a predominantly angular shape. These grains exhibit sharp edges and broken sections. The term *cylindrical* denotes grains that are manufactured by a cutting process. Their length-to-diameter ratio is ~ 1 . This shape can only be found with cut steel wire pellets.

2.3.2 Relative Proportions of Particles

Shape parameters characterise the shape of individual particles. Wadell (1933) and Heywood (1933) were probably the first who gave rigorous analyses of shape parameters. Heywood (1933) considered the shape of a particle to have the following two distinct characteristics:

- the relative proportions of length, breadth and thickness;
- the geometrical form.

The relative proportion includes two parameters: (1) the *elongation ratio* (r_E) and (2) the *flatness ratio* (r_F). Both parameters are defined and illustrated in Table 2.10. Bahadur and Badruddin (1990) applied the elongation ratio to investigate the influence of the abrasive particle shape on particle impact erosion processes. They found notable relationships between abrasive type, abrasive particle diameter and abrasive particle shape. Some results of their study are provided in Fig. 2.8. Silica carbide particles became more elongated and less circular with an increase in the particle size, while the opposite was the case with aluminium oxide particles. The general variation of silica oxide was similar to that of silica carbide particles, though not as systematic. The elongation ratios for the silica carbide particles and for the

Table 2.9 Grain shape designations

Designation	Grain shape	Symbol
Shot	Spherical, round	S
Grit	Angular, irregular	G
Cylindrical	Sharp-edged	C

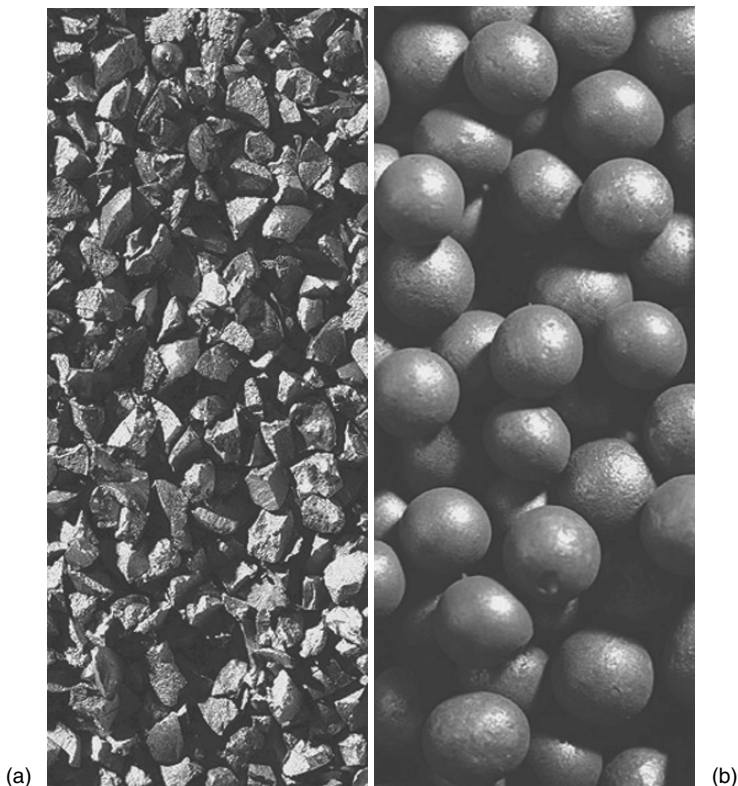


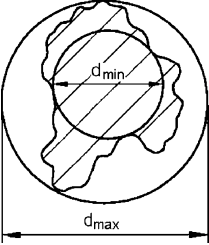
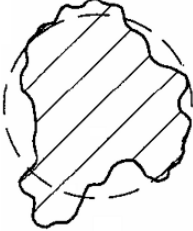
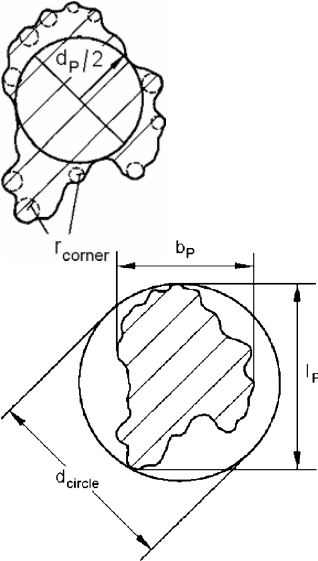
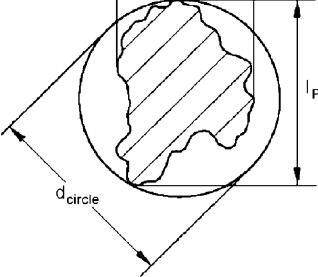
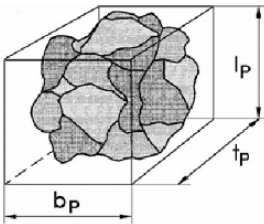
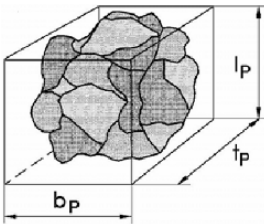
Fig. 2.7 Basic shape designations for abrasive particles (Photographs: Kuhmichel GmbH). (a) Grit; (b) Shot

aluminium oxide were very sensitive to the particle size in the range of small particles. For equal grain sizes, silica oxide particles featured much higher elongation ratios than silica carbide particles. For a particle diameter of $d_p = 300\ \mu\text{m}$, as an example, the elongation ratio was $r_E = 0.53$ for silica carbide, and $r_E = 0.7$ for silica oxide. A relationship between particle abrasive size and shape was also noted by Djurovic et al. (1999). For starch media, these authors found that smaller particles were less elongated than larger particles. These results clearly show that particle shape may be considered an abrasive material characteristic.

2.3.3 Geometrical Forms of Particles

The geometrical form is a volumetric shape factor, representing the degree to which a particle approximates an ideal geometric form (cube, sphere or tetrahedron). The following two parameters can describe the geometrical form of particles: (1) the *sphericity* (S_P) and (2) the *roundness* (S_R).

Table 2.10 Shape parameters for abrasive particles

Parameter and definition	Graphical expression
Shape factor	
$F_{\text{shape}} = \frac{d_{\text{min}}}{d_{\text{max}}}$	 <p>A diagram showing an irregularly shaped particle inside a circle. A horizontal line segment across the narrowest part of the particle is labeled d_{min}. A horizontal line segment across the widest part of the particle is labeled d_{max}.</p>
Circularity factor	
$F_0 = \frac{4 \cdot \pi \cdot A_p}{\text{Perimeter}^2}$	 <p>A diagram of an irregularly shaped particle filled with diagonal hatching lines.</p>
Roundness	
$S_R = \frac{\sum \left(\frac{2 \cdot r_{\text{corner}}}{d_p} \right)}{N_{\text{corner}}}$	 <p>A diagram of a particle with several small circles at its corners, each labeled r_{corner}. A horizontal line through the center of the particle is labeled $d_p/2$. A horizontal dimension to the right is labeled b_p. A vertical dimension to the right is labeled l_p. Below this, a circle is shown with a diameter dimension labeled d_{circle}.</p>
Sphericity	
$S_p = \sqrt{\frac{4}{\pi} \cdot b_p \cdot l_p}$ d_{circle}	 <p>A diagram showing a particle inside a circle. The diameter of the circle is labeled d_{circle}. The horizontal width of the particle is labeled b_p. The vertical height of the particle is labeled l_p.</p>
Elongation ratio	
$r_E = \frac{l_p}{b_p}$	 <p>A diagram showing a particle inside a rectangular box. The vertical height of the box is labeled l_p. The horizontal width of the box is labeled b_p.</p>
Flatness ratio	
$r_F = \frac{l_p}{t_p}$	 <p>A diagram showing a particle inside a rectangular box. The horizontal width of the box is labeled b_p. The depth of the box is labeled t_p.</p>

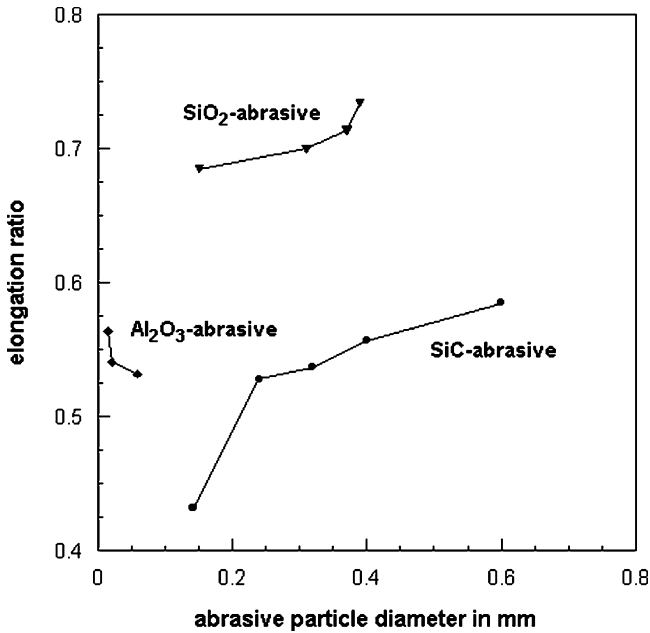


Fig. 2.8 Relationships between abrasive material, particle size and particle shape (Bahadur and Badruddin, 1990)

The sphericity, introduced by Wadell (1933), is defined and illustrated in Table 2.10. In two dimensions, the sphericity is related to the projection area of the sphere yielding the roundness, which is defined and illustrated in Table 2.10 as well. Both sphericity and roundness range from “0” for very angular particles to “1” for ideally round particles. Hansink (1998) defined an alternative roundness scale, which is illustrated in Fig. 2.9, for the assessment of the shapes of abrasive particles. This scale defines and quantifies the often used qualitative terms *angular* or *rounded*. Several references used roundness–sphericity diagrams in order to characterise the shape of abrasive particles. Such a roundness–sphericity diagram is illustrated in Fig. 2.10.

Vasek et al. (1993) and Martinec (1994) suggested a circularity factor, which was originally developed by Cox (1927), and a shape factor in order to characterise abrasive particles. The *circularity factor* (F_0) is defined and illustrated in Table 2.10. For a perfectly round particle, circularity factor will be unity. Gillespie (1996) and Gillespie and Fowler (1991) applied image analysis in order to estimate circularity factors (which they called “shape factors” in their papers) for shot peening media, and they defined any value for the circularity parameter $F_0 > 0.83$ as acceptable for shot peening applications. Some of their results, featuring circularity factors for a number of real abrasive particles, are illustrated in Fig. 2.11, and it can be seen that a notable number of particles would not meet the critical circularity factor. Figure 2.12 shows a histogram of circularity factors based on an automatic image analysing



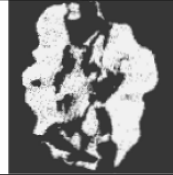


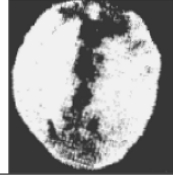
Designation	Very angular	Angular	Sub-angular
Definition	0.5	1.5	2.5
Shape image			
Designation	Sub-rounded	Rounded	Well rounded
Definition	3.5	4.5	5.5
Shape image			

Fig. 2.9 Designations for angular and rounded particle shapes (Hansink, 1998)

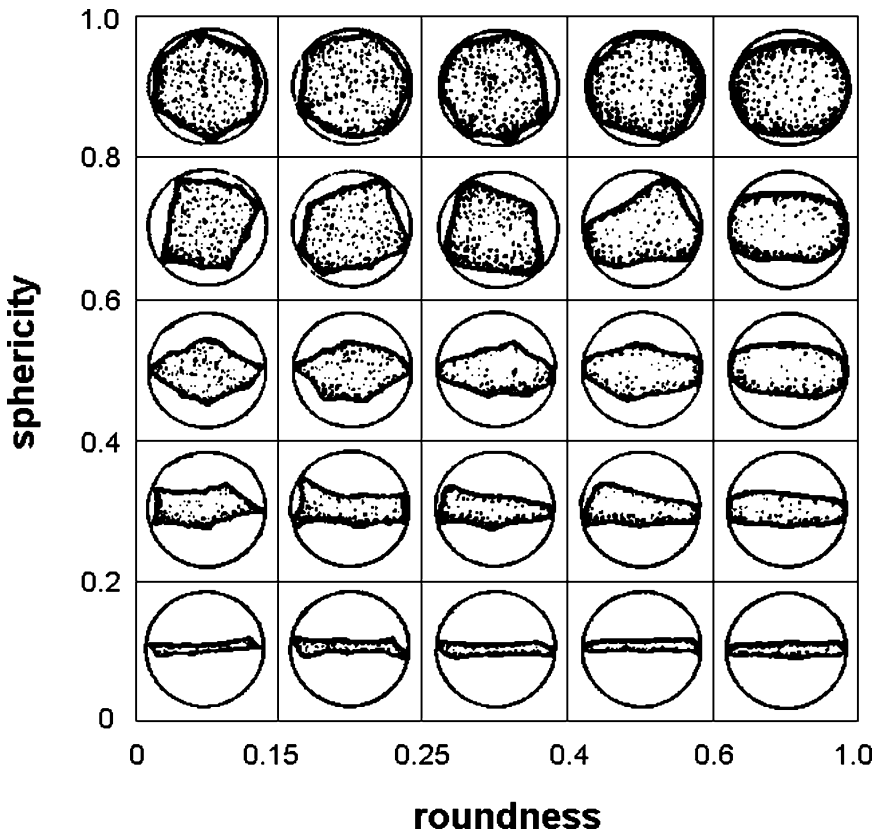


Fig. 2.10 Roundness-sphericity diagram for a garnet abrasive material (Reference: Bohemia Garnet)

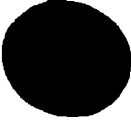










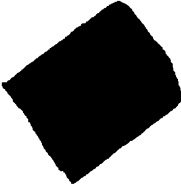
		
0.958	0.923	0.921
		
0.921	0.872	0.858
		
0.849	0.823	0.799
		
0.772	0.717	0.704

Fig. 2.11 Circularity factors of steel shot particles, assessed with image processing technique (Gillespie, 1996)

procedure. It can clearly be seen that “shape” is not a well-defined standard property for a given abrasive material. Shape parameters in general are rather characterised by distributions with certain statistical parameters. Typical statistical parameters for an assessment procedure are listed in Table 2.11; the listing very well illustrates the high number of assessment parameters delivered by an automatic image analysis procedure.

The *shape factor* (F_{shape}) is also defined and illustrated in Table 2.10. For circles, the shape factor is unity. Table 2.12 lists some typical values for circularity and shape factors for a number of different abrasive materials.

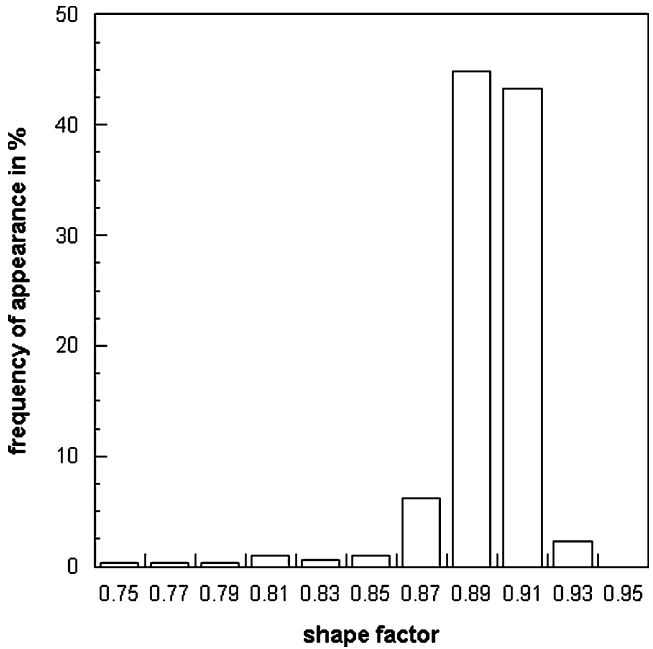


Fig. 2.12 Frequency distribution functions of shape factors (Gillespie and Fowler, 1991)

Table 2.11 Statistics of circularity factors of cast steel shot S-280, based on automatic image analysis (Gillespie and Fowler, 1991)

Parameter	Value
Minimum	0.487
Maximum	0.926
Median	0.898
25% quartile	0.890
75% quartile	0.906
Total value	577
Mean	0.894
Geometric mean	0.893
Harmonic mean	0.893
Sample variance	0.00083
Sample standard variation	0.029
Population variance	0.00083
Population standard variation	0.02
Standard deviation of the mean	0.0011
Relative standard error	0.0013
Skew	-17, 402
Kurtosis	0.000057

Table 2.12 Shape factors and shape characteristics of garnet abrasive materials (Vasek et al., 1993)

Mineral	Subtype	Shape parameter	
		F_0	F_{shape}
Almandine	B	0.66	0.65
	M	0.69	0.67
	K	0.68	0.66
	G	0.66	0.64
Grossular	–	0.71	0.70
Andradite	V–A	0.67	0.65
	V–B	0.68	0.68
	V–C	0.65	0.68

2.4 Abrasive Particle Size Distribution and Abrasive Particle Diameter

2.4.1 Particle Size Distribution

2.4.1.1 General Definitions

In general, the term “diameter” is specified for any equidimensional particle. By convention, particle sizes are expressed in different units depending on the size ranges involved. Coarse grains are measured in inches or millimetres, fine particles in terms of screen size, very fine particles are measured in micrometer or manometer. A number of “diameter” definitions are known. The diameter is defined either in terms of some real property of the particle, such as its volume or surface area, or in terms of behaviour of the particle in some specific circumstances, such as settling in water under defined conditions (Kelly and Spottiswood, 1982). In the area of blast cleaning, the particle size is usually given in mesh designation (according to the Tyler-Standard-Screen sieve series), which barely mentions the related particle size distributions or the shape of the particles. A regression study made to link the Tyler sieve series to the corresponding average particle diameter delivers the following relationship:

$$d_p = 17,479 \cdot \text{mesh}^{-1.0315} \quad (2.2)$$

with a regression coefficient of 0.998. The particle diameter is in μm in this equation. A mesh number 180 would correspond to an average particle diameter of $d_p = 82 \mu\text{m}$.

2.4.1.2 Sieve Analysis

Because it is impracticable to individually estimate each particle, size analysis is carried out by dividing the particles into a number of suitably narrow size ranges. Table 2.13 presents results of sieve analyses for abrasive particle samples used in

Table 2.13 Sieve analyses results for two abrasive mixtures (Metabrasive Ltd.)

Sieve size in μm	Weight in %	
	Alumina 700	Metagrit 65
125	–	2
150	–	5
212	–	20
300	4	28
425	26	35
600	45	10
850	22.5	–
1,180	2.5	–
Total	100	100

blast cleaning. Graphically, data are conventionally presented by plotting the particle size horizontally and the measured quantity of property vertically. Two approaches are used to present the quantity: (1) plotting the absolute amount in each size fraction (Fig. 2.13a) and (2) plotting the cumulative amount above or below a certain size (Fig. 2.13b).

2.4.1.3 Particle Size Distribution Models

A number of models were developed to mathematically describe the size distributions of fine-grained comminution products, which include abrasive particles. These models have empirical relationships, which to a greater or lesser extent were found capable of describing comminution products size distributions. Table 2.14 lists the most frequently used models. These equations are all of the general type:

$$M_0(d_p) = f \left(\frac{d_p}{d^*} \right)^{n_M} \quad (2.3)$$

The size modulus, d^* , is an indication of an average particle diameter. When the equation has an upper size limit, d^* is in fact the maximum particle size in the distribution. Equation (2.3) also includes a second parameter, n_M , that is frequently called the distribution modulus, since it is a measure of the spread of particle sizes. The higher the value for n_M , the more homogeneous is the grain size structure of the sample. For $n_M \rightarrow \infty$, the sample consists of grains with equal diameters. Figure 2.14a, b shows fits for the sieve analysis from Table 2.13 by two common particle-size distribution functions. The Rosin–Rammler–Sperling–Bennett (RRSB) distribution is of particular interest because its distribution parameters are utilised by some authors as a measure of the ageing and reusability of metallic abrasive particles (Wellinger et al., 1962).

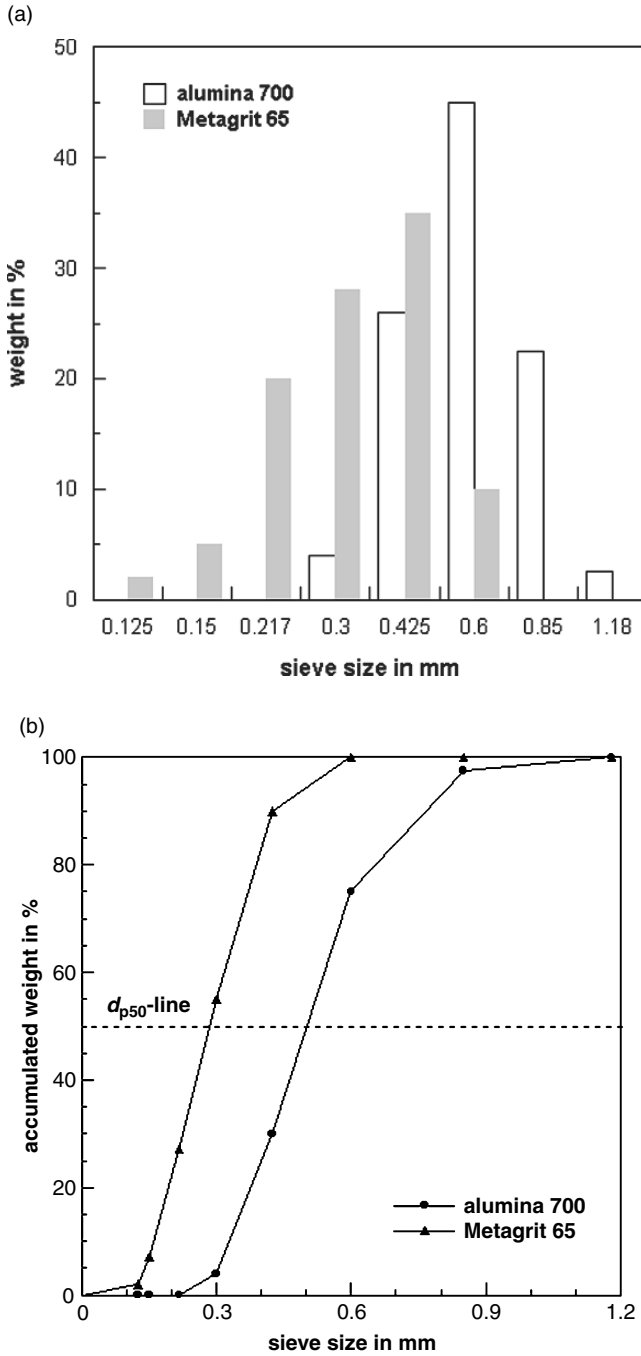


Fig. 2.13 Graphical representations of sieve analysis results (see Table 2.13). (a) Absolute distribution; (b) Cumulative distribution

Table 2.14 Particle-size distribution functions (Kelly and Spottiswood, 1982; Schubert, 1988)

Function	Formula $M_0(d_p)$	Significance of d^*	Equation
Logarithmic probability	$\text{erf} \left[\frac{\ln \frac{d_p}{d^*}}{\sigma} \right]$	Medium particle diameter	2.3a
Rosin–Rammler–Sperling–Bennett (RRSB)	$1 - \exp \left[\left(\frac{d_p}{d^*} \right)^{n_M} \right]$	Particle diameter at $M_0 = 63.2\%$	2.3b
Gates–Gaudin–Schumann (GGS)	$\left(\frac{d_p}{d^*} \right)^{n_M}$		2.3c
Gaudin–Meloy	$1 - \left[1 - \frac{d_p}{d^*} \right]^2$	Maximum particle diameter	2.3d
Broadbent–Callcott	$\frac{1 - \exp \left[-\frac{d_p}{d^*} \right]}{1 - \exp(-1)}$	–	2.3e

2.4.2 Particle Diameter

According to regulations in ISO 1117, the particle diameter is defined according to a particle “size class”. A size class of “140”, for example, means a particle diameter of 1.4 mm.

If the particle size distribution is known from the sieve analysis, several “average” diameter values of the particle sample can be estimated. The *median diameter*, d_{50} , is the 50% point on any cumulative distribution curve (Fig. 2.13b). For the examples presented in Table 2.13 and Fig. 2.13, this diameter is $d_{p50} = 510 \mu\text{m}$ (Alumina 700) and $d_{p50} = 280 \mu\text{m}$ (MG 65), respectively. The *geometric mean diameter*, d_{pG} , is based on the assumption of an even graduation in size from maximum to minimum, and it assumes an equal number of particles in each size average:

$$d_{pG} = \frac{d_{p\max} + d_{p\min}}{2} \quad (2.4)$$

In the examples given in Table 2.13 and Fig. 2.13, this diameter is $d_{pG} = 740 \mu\text{m}$ (Alumina 700) and $d_{pG} = 362 \mu\text{m}$ (MG 65), respectively. A third approach is the definition of a *statistical diameter*, d_{pSt} , which follows the equation:

$$d_{pSt} = \frac{\sum_{i=1}^n (m_i \cdot d_{pi})}{100} \quad (2.5)$$

For the examples in Table 2.13 and Fig. 2.13, the statistical diameter is $d_{pSt} = 613 \mu\text{m}$ (Alumina 700) and $d_{pSt} = 345 \mu\text{m}$ (MG 65), respectively.

2.4.3 Alternative Abrasive Particle Size Assessment Methods

Particle sizes, but also particle size distributions, can be assessed also by applying image analysis methods. This alternative approach is not a standard in

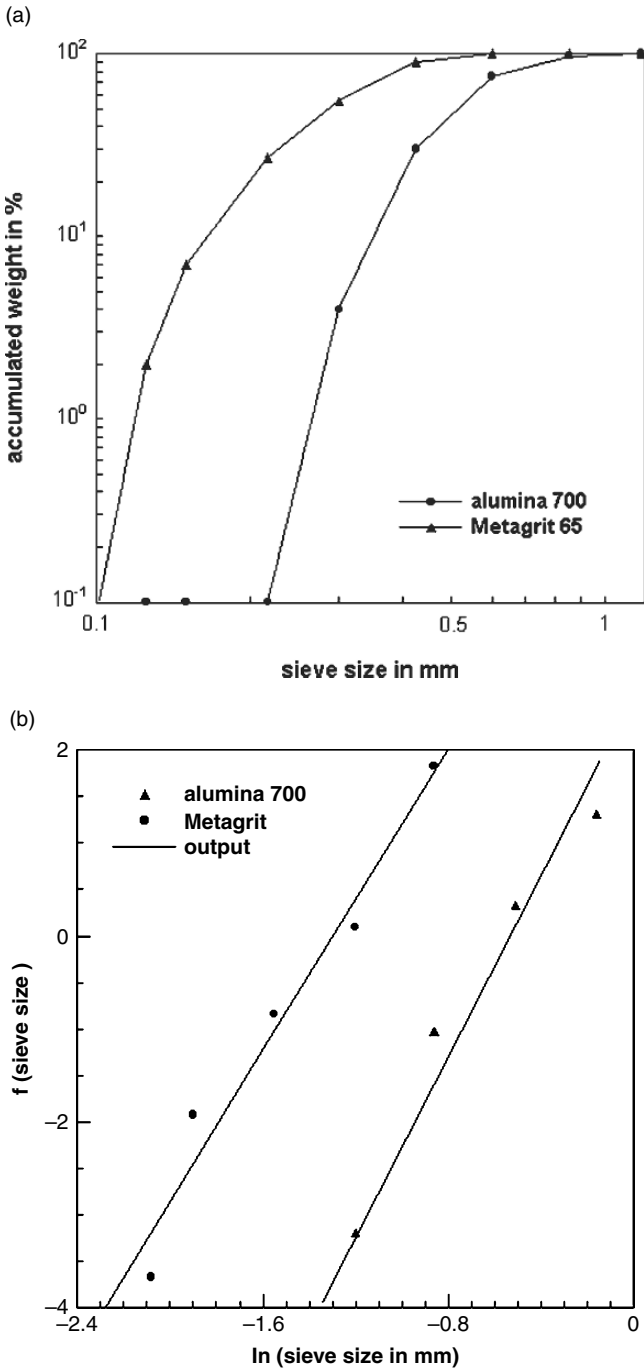


Fig. 2.14 Distribution functions for sieve analysis results (see Table 2.12). (a) Gates–Gaudin–Schumann (GGS) distribution; (b) Rosin–Rammler–Sperling–Bennett (RRSB) distribution

the blast cleaning industry, although promising results have been reported for the image analysis of shot peening media. Gillespie (1996) and Gillespie and Fowler (1991) performed comparative size measurements by using conventional sieve analysis, a digital micrometer and image analysis. Some results are displayed in Fig. 2.15. The agreement between the three methods depended on the sieve size; it was very good (less than 2 wt.%) for the smaller sieve sizes. The average difference between sieve analysis and image analysis was 2.71 wt.%. Image analysis is of definite interest because this method can deliver information on particle size as well as on particle shape. Promising experience is available on the shape assessment of particles, either of shot peening media (Gillespie and Fowler, 1991; Gillespie, 1996) or of erosion debris (Momber and Wong, 2005b), with image analysis methods. Further details on this application are provided in Sect. 2.3.

Optical methods for the assessment of particle sizes are very familiar in particle technology. Sparks and Hutchings (1993) have, however, shown that these methods must be applied with caution to broken abrasive particles. Especially glass particles show different optical properties whether they are round (e.g. glass beads) or broken (e.g. glass grit). Broken glass particles would, in a correct orientation with respect to a laser beam, diffract light in such a way so as to suggest that they were of larger diameter.

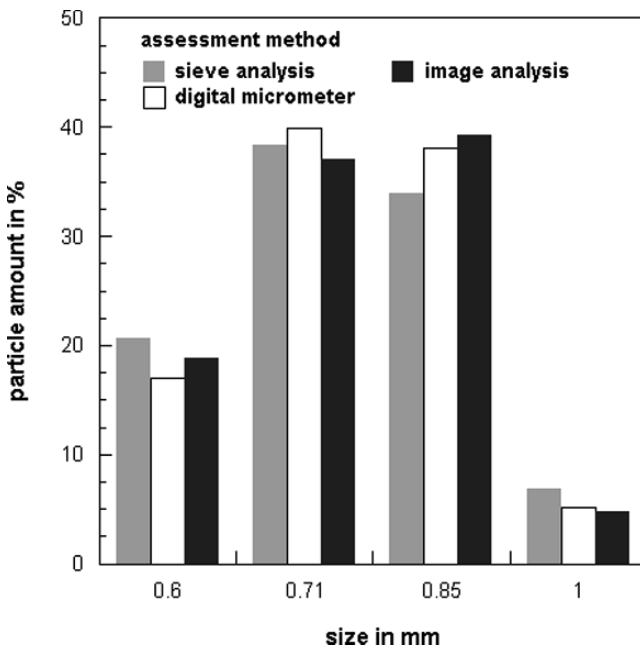


Fig. 2.15 Comparison between abrasive size assessment methods (Gillespie, 1996)

2.5 Density of Abrasive Materials

The following two density parameters are defined for abrasives:

- apparent density;
- bulk density.

The apparent density is the ratio between mass and volume of a single abrasive grain:

$$\rho_P = \frac{m_P}{V_P} = \frac{6 \cdot m_P}{\pi \cdot d_P^3} \quad (2.6)$$

It can be estimated with well-defined methods. This density parameter includes flaws, pores and cracks. Therefore, it is a physical constant of the material. The apparent density must, for example, be used if kinetic energy of an impinging grain is calculated.

The bulk density is the mass of a volume of a group of individual grains. Bulk density depends on packing density of the grain sample. It is affected, for example, by grain size and grain shape. Exactly seen, it is not a material property. However, some values for typical blasting media are listed in Table 2.2, based on standard grain samples. A typical ratio between apparent density and bulk density is ~ 2 for many abrasive materials.

2.6 Number and Kinetic Energy of Abrasive Particles

2.6.1 Abrasive Particle Number and Frequency

The number of particles involved in a blast cleaning process can be approximated as follows:

$$N_P = \frac{\dot{m}_P}{m_P} \cdot t_E \quad (2.7)$$

The mass of an individual abrasive particle is:

$$m_P = \frac{\pi}{6} \cdot d_P^3 \cdot \rho_P \quad (2.8)$$

for spherical particles. If, for example, the median particle diameter d_{P50} is utilised, the number of particles in a transversal (y -direction) moving blast cleaning jet is:

$$N_P = \frac{6 \cdot \dot{m}_P \cdot y}{\pi \cdot \rho_P \cdot d_{P50}^3 \cdot v_T} \quad (2.9)$$

For a given traverse distance, the higher the abrasive mass flow rate, the higher the number of abrasive particles. The higher the abrasive material density and average abrasive particle diameter, the lower the number of abrasive particles. The abrasive particle impact frequency is simply:

$$\dot{N}_P = \frac{N_P}{t_E} = \frac{\dot{m}_P}{m_P} \quad (2.10)$$

For a given exposure time, the impact frequency increases with an increase in abrasive mass flow rate and with a decrease in average particle diameter. If abrasive material density increases, the impact frequency decreases. Henning and Brauer (1986) introduced a particle frequency number:

$$\dot{n}_P = \frac{\dot{N}_P}{A_C} \quad (2.11)$$

which considers geometrical effects. The unit of this parameter is $1/(s \cdot m^2)$. Glatzel and Brauer (1978) defined a dimensionless collision number, which characterised the collision between reflected and incident abrasive particles:

$$c_K = \frac{c_R \cdot d_N}{d_P \cdot \cos \varphi} \quad (2.12)$$

The variable c_R is the particle concentration in the impinging stream. This variable can be calculated as follows:

$$c_R = \frac{4}{\pi} \cdot \frac{\dot{m}_P}{v_P \cdot \rho_P \cdot d_N^2} \quad (2.13)$$

The collision number is high for a high particle concentration, for a small nozzle diameter, for small abrasive particles, and for high angles of impingement.

2.6.2 Kinetic Energy of Abrasive Particles

The kinetic energy of a spherical abrasive particle is simply:

$$E_P = \frac{\pi}{12} \cdot d_P^3 \cdot \rho_P \cdot v_P^2 \quad (2.14)$$

Data plotted in Fig. 2.16 illustrate typical values for kinetic energies. The kinetic energy of a glass bead with a density $\rho_P = 2,450 \text{ kg/m}^3$, a diameter $d_P = 1.5 \text{ mm}$ and an impingement velocity $v_P = 100 \text{ m/s}$ reads $E_P = 0.022 \text{ J}$ as marked in the graph. It may, however, be noted that abrasive particle size and abrasive particle velocity cannot be varied independently on each other in most blast cleaning devices. This special topic is discussed in Sect. 3.6.3. The power delivered to the cleaning site by

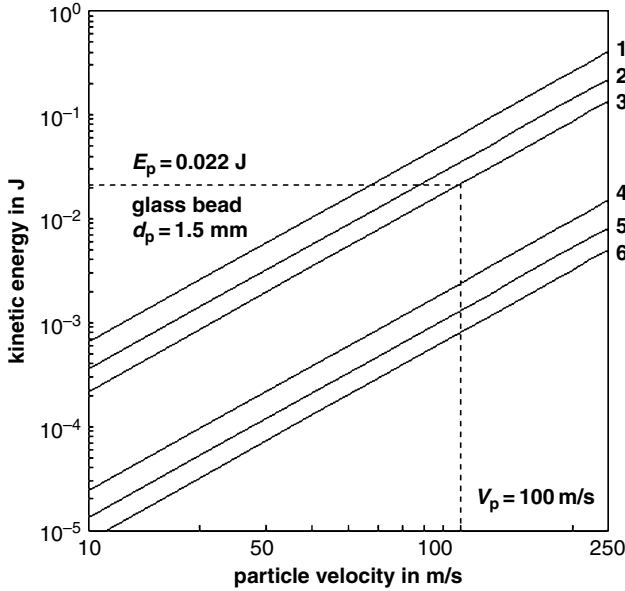


Fig. 2.16 Kinetic energies of abrasive particles; calculated with (2.14). 1 to 3: particle diameter $d_p = 1.5$ mm; 4 to 6: particle diameter $d_p = 0.5$ mm; 1+4: steel ball ($\rho_p = 7,300$ kg/m³); 3 + 6: glass bead ($\rho_p = 2,450$ kg/m³); 2 + 5: garnet ($\rho_p = 4,000$ kg/m³)

an abrasive particle stream is given through the following relationship:

$$P_p = \frac{\dot{m}_p}{2} \cdot v_p^2 = E_p \cdot \dot{N}_p \quad (2.15)$$

This is a simplified relationship, which assumes abrasive particles of equal sizes. The situation for such a case is illustrated in Fig. 2.17. If a certain power is available, it can be divided between individual abrasive particle energy and abrasive particle number (frequency). If a power of $P_p = 1.25$ kW is available, it can be seen from Fig. 2.17 that this power can either be spread over 765,000 particles per second, each with a kinetic energy of $E_p = 0.002$ J; or it can be spread over 19,400 particles per second, each with a kinetic energy of $E_p = 0.06$ J. Therefore, *loading intensity* (kinetic energy) and *loading frequency* (particle number) can be controlled. This control is mainly due to variations in abrasive particle size and abrasive particle material density.

2.6.3 Power Availability

Equation (2.15) characterises the power available at the nozzle exit. This amount of power is not available at the impact site. In order to consider this difference, Ciampini et al. (2003b) introduced the *power availability* for a target impinged by a

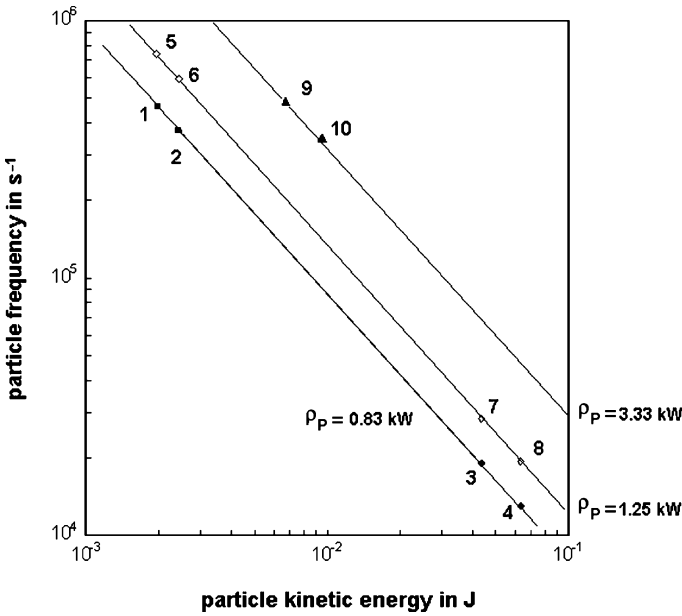


Fig. 2.17 Relationship between loading intensity (particle kinetic energy) and loading frequency (particle frequency) for three power values 1: $\dot{m}_p = 10 \text{ kg/min}$, $v_p = 100 \text{ m/s}$; 2: $\dot{m}_p = 10 \text{ kg/min}$, $v_p = 100 \text{ m/s}$; 3: $\dot{m}_p = 10 \text{ kg/min}$, $v_p = 100 \text{ m/s}$; 4: $\dot{m}_p = 10 \text{ kg/min}$, $v_p = 100 \text{ m/s}$; 5: $\dot{m}_p = 15 \text{ kg/min}$, $v_p = 100 \text{ m/s}$; 6: $\dot{m}_p = 15 \text{ kg/min}$, $v_p = 100 \text{ m/s}$; 7: $\dot{m}_p = 15 \text{ kg/min}$, $v_p = 100 \text{ m/s}$; 8: $\dot{m}_p = 15 \text{ kg/min}$, $v_p = 100 \text{ m/s}$; 9: $\dot{m}_p = 10 \text{ kg/min}$, $v_p = 200 \text{ m/s}$; 10: $\dot{m}_p = 10 \text{ kg/min}$, $v_p = 200 \text{ m/s}$

stream of abrasive particles. This parameter can be calculated as follows:

$$P^* = \frac{2 \cdot P_T}{m_p \cdot v_p^2 \cdot \dot{N}_p} \tag{2.16}$$

The numerator is equal to (2.15). The denominator is the power of the abrasive particle stream available at the impinged surface, including the effect of interference between incident and rebound streams:

$$P_T = f(\dot{N}_p; d_N; d_p; m_p; v_p; x; \epsilon_R; f_C) \tag{2.17}$$

The variables listed in the brackets can be replaced by dimensionless values as shown in Sect. 3.5.5. The value for P^* is a measure of the degree to which incident particles are scattered by rebounding ones. A high value of P^* is a necessary (but not sufficient) condition for an effective blast cleaning process. Figure 2.18 shows the dependence of the dimensionless power availability on the ratio between nozzle radius and abrasive particle radius for a range of stream densities (see Sect. 3.5.5) and impact angles. At low stream densities, the dependence on r_N/r_p is rather weak; but at higher stream densities, the dependence becomes weak only when $r_N/r_p > 15$,

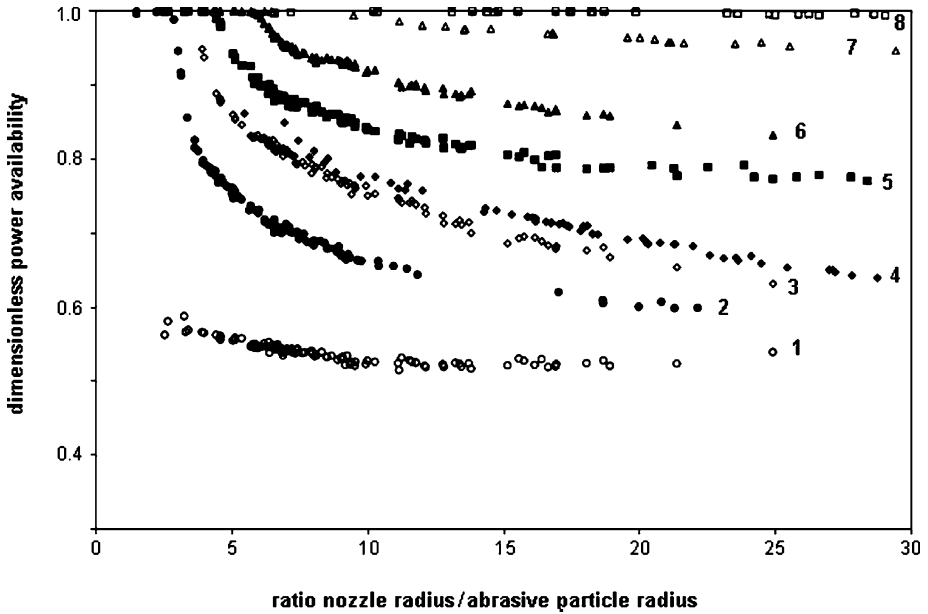


Fig. 2.18 Effects of nozzle diameter, particle diameter and particle stream density on power availability (Ciampini et al., 2003b). Ratio ρ_S/φ : 1 – 0.01/90°; 2 – 0.03/45°; 3 – 0.01/60°; 4 – 0.001/90°; 5 – 0.01/45°; 6 – 0.001/15°; 7 – 0.001/45°; 8 – 0.0001/45°

regardless of the impact angle. A more detailed discussion of these effects is provided by Ciampini et al. (2003b). The authors found, among others, that power availability decreased at higher impact angles and with larger relative distances between individual abrasive particles. There was, however, a certain value for the relative distance between individual particles at about $L^* = 20$, where the power availability reached unity.

2.7 Impurities

Impurities can deteriorate quality and efficiency of blast cleaning particles; they are in particular of importance if recycled abrasive material is being used. Impurities to be considered include non-abrasive residue, lead, water soluble contaminants and

Table 2.15 Requirements for recycled abrasives (SSPC-AB 2, 2004)

Matter	Limitation
Non-abrasive residue	1% by weight
Lead content	0.1% by weight
Water soluble contaminants	1,000 $\mu\Omega/\text{cm}$ (electric conductivity)
Oil content	No presence, either on the surface of the water or as an emulsion in the water after 10 min

Table 2.16 Maximum permissible content of hazardous substrates (BGV D26)

Substrate	Permissible content (wt.%)
Total content	
Antimony, arsen, beryllium, lead, cadmium, chromate, cobalt, nickel, tin	2%
Arsen, beryllium, chromate, cobalt, nickel	0.2%
Individual contents	
Beryllium	0.1%
Cadmium	0.1%
Chromate	0.1%
Cobalt	0.1%
Free crystalline silica	
Cristobalit	2%
Quartz	2%
Tridymit	2%

oil. Some limits are listed in Table 2.15. Data sheets very often present impurities in mass percentage. Foreign solid matter can easily be estimated for metallic particles by use of magnets. Soluble foreign matter, however, such as salts, are more difficult to estimate. Basically, conductivity measurements or chemical analyses are required to quantify these parameters.

Table 2.16 lists critical amounts of hazardous substances that should not be exceeded. The limits being listed must be undershoot as far as possible. Blast cleaning abrasives must not contain more than 2 wt.% of free crystalline silica. Free silica includes the modifications listed in Table 2.16.

Contamination of abrasive particles is a critical issue if the abrasive material is being recycled. Table 2.17 gives results of measurements performed on six different recycled abrasive materials. It can be seen that the values for lead content and the values for electric conductivity exceeded critical regulatory limits. Further results are published by Johnson (1990).

Jopp (1995) measured the pH-values of numerous abrasive materials. He mixed 100 g abrasive material into 100 ml demineralised water and stored the suspension for 4 weeks at room temperature. Results of these measurements are provided in Fig. 2.19. Glass beads and glass powder caused a high alkalinity which may increase the probability of corrosion of the blast cleaned steel substrate at elevated

Table 2.17 Contamination of recycled abrasive field work mixes (Boocock, 1994)

Sample No.	Lead in ppm ^a	Electric conductivity in $\mu\text{S}/\text{cm}^b$
1	8,200	480
2	220	480
3	8,400	540
4	<50	120
5	1,100	400
6	2,600	700

^aLimit: 200 ppm

^bLimit: 1,000 $\mu\text{S}/\text{cm}$

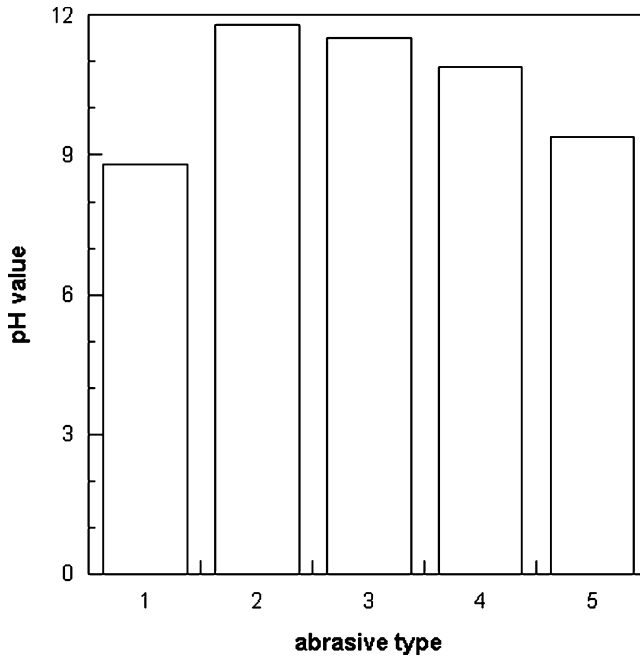


Fig. 2.19 pH-values for different abrasive materials (Jopp, 1995). Abrasive material: 1 – corundum; 2 – glass beads; 3 – glass powder; 4 – steel shot; 5 – steel grit

temperatures. It was shown that the pH-values of abrasive materials had a direct relationship to the durability of epoxy-based adhesive joints. Joints prepared with an abrasive material having a high pH-value exhibited the lowest durability values, and vice versa (Jopp, 1995).

2.8 Global Abrasive Evaluation Parameter

A global abrasive assessment parameter does not exist for blast cleaning processes. For a similar machining process – hydro-abrasive machining – Agus et al. (1995) introduced the following global assessment parameter to evaluate abrasive materials:

$$\chi_P = H_P^{a_1} \cdot S_P^{a_2} \cdot \rho_P^{a_3} \cdot d_P^{a_4} \cdot \dot{m}_P^{a_5} \quad (2.18)$$

This equation includes the following variables:

- abrasive material hardness;
- abrasive particle shape;
- abrasive material density;
- abrasive particle diameter;
- abrasive mass flow rate.

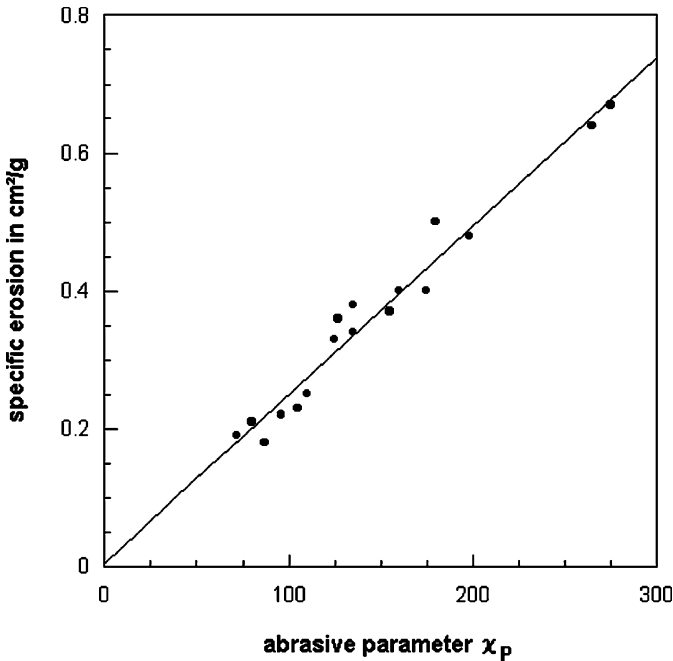


Fig. 2.20 Relationship between erosion rate and global abrasive assessment parameter for hydro-abrasive machining (Agus et al., 1995)

In (2.18), H_P is the Knoop hardness, and S_P is a particle shape factor. The evaluation parameter χ_P can be directly related to the specific erosion capability of hydro-abrasive jets (Agus et al., 1995). Some results are displayed in Fig. 2.20. For this special erosion case, abrasive material hardness and abrasive particle shape showed the most remarkable effects on the erosion process. For harder substrate materials, abrasive material hardness was predominant; whereas particle shape was most important for softer materials. Although corresponding relationships are not known for blast cleaning processes, the approach may form some basics for further research.

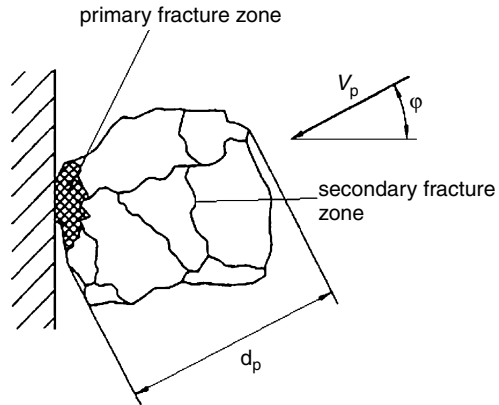
2.9 Process Behaviour of Abrasive Particles

2.9.1 Fracture Zones

Abrasive particles fracture during the blast cleaning process. This fracture process modifies certain properties of the particles, namely size and shape. These changes affect the reusability of the materials.

Figure 2.21 shows a simplification of the fracture structure in a non-regular particle subjected to impact. In the figure, two fracture zones can be distinguished. The *primary zone* is a result of high-velocity stress waves generated during the

Fig. 2.21 Geometric situation and fracture structure of a particle subjected to impact (adapted from Buhlmann, 1970)

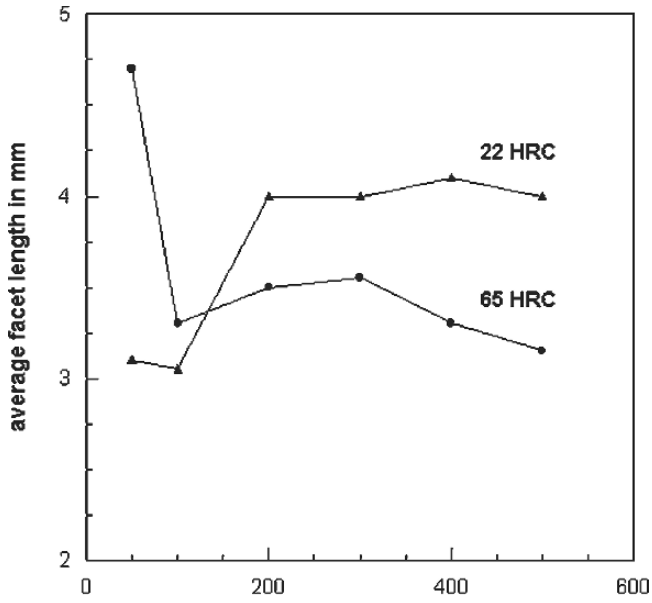


impact. On their way through the particle, the waves decelerated and reflected on the rear side of the particle. The reflected waves hit the fracture front. When the reflected waves partially stopped the fracture front, coarser fragments formed on the rear side of the particles which is defined as the *secondary zone*. Among others, Reiners (1960) documented these processes by using a high-speed photography technique. Salman and Gorham (2000) rationalised the appearance of damage and fracture features for impinging glass beads. The authors found that fracture appearance depended on impact velocity. For lower impact velocities ($v_p = 25$ m/s), only crack figures (Hertzian crack systems) could be observed; whereas fragment formation and powder formation took part at higher velocities ($v_p = 50$ m/s). Sparks and Hutchings (1993) reported that the initial fracture of impinging glass spheres ($v_p = 98$ m/s) occurred in two ways: by the detachment of a small cap, and by splitting across the whole sphere, forming almost hemispherical fragments. Many smaller fragments, with flat faces and sharp angular corners, were also observed.

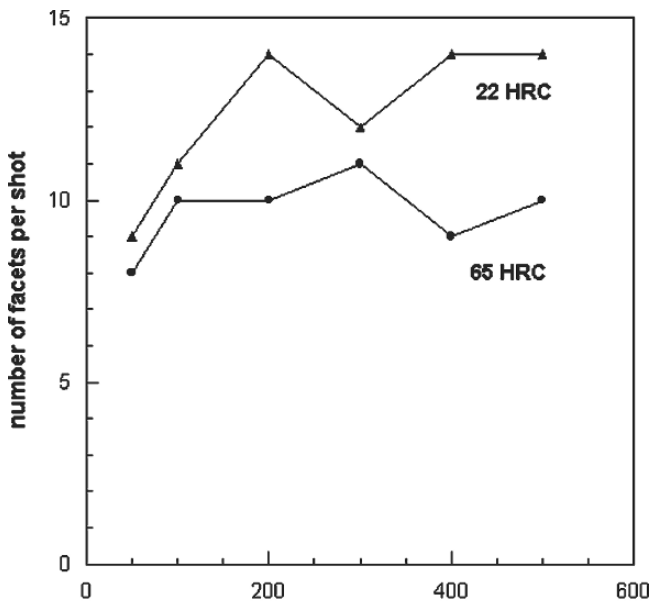
Calboreanu (1991) found notable differences in the behaviour of steel shot whether it was impinged against a hard target surface (65 HRC) or against a soft target surface (22 HRC). In case of the hard target surface, he observed well-developed deformation bands on the shot particles, and the main breakdown mechanism was accomplished by internal crack extension. Shot impacted against the soft target surface presented small peripheral radial cracks (50–100 μm in length). The author also found that steel shot impacted against a softer surface had a higher amount of facets and a longer average size of the facets than the shot propelled against a harder surface. Results of these investigations are shown in Fig. 2.22.

Figure 2.23 illustrates the change in hardness of cut steel shot after a number of impact cycles. A significant increase in hardness can be seen for the first cycles, which probably corresponded to work hardening of the metal during the initial plastic deformation cycles. The hardness then stabilised, but finally started to drop at about 1,000 cycles, probably because the metal was softened after a high number of deformation cycles.

Wellinger and Gommel (1967) also performed deformation studies on cut steel wire abrasives. They measured the changes in hardness in the rim region as well



(a)



(b)

Fig. 2.22 Effects of target plate hardness and number of cycles on facet parameters for steel shot (Calboreanu, 1991); impact velocity: 61 m/s; shot designation: S 460. (a) Average facet length; (b) Average number of facets

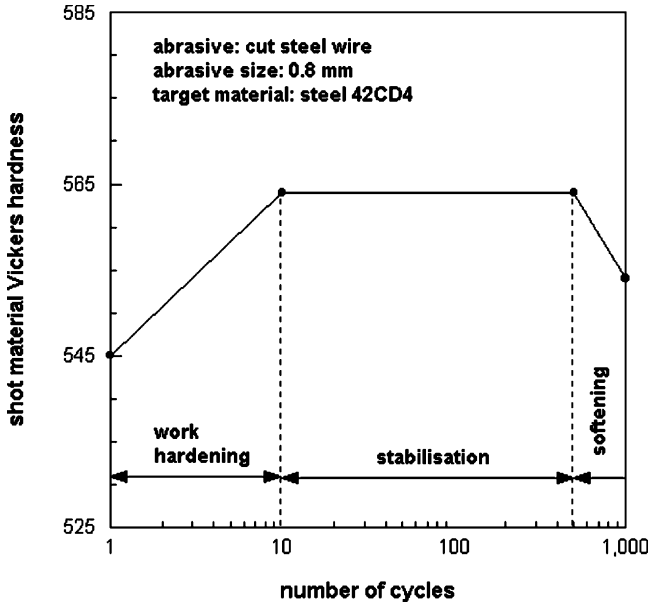


Fig. 2.23 Hardness modification of cut steel wire during shot peening (Flavenot and Lu, 1990)

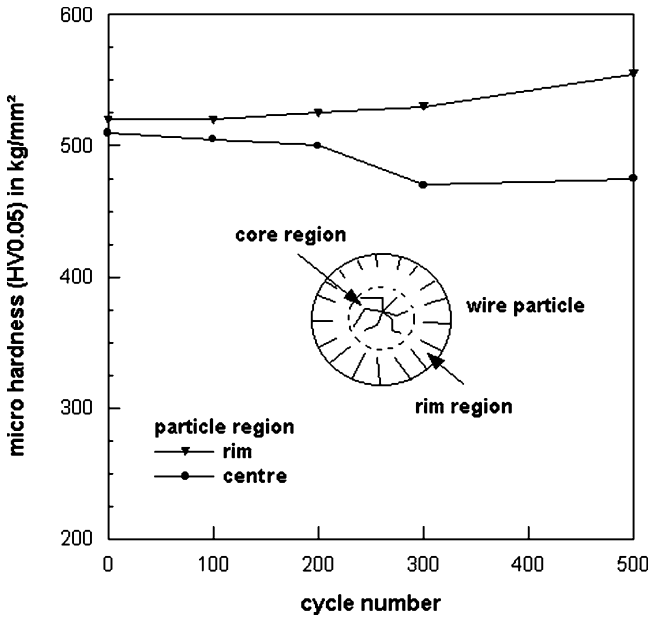


Fig. 2.24 Hardness modification of cut steel wire during the impingement on a steel plate (Wellinger and Gommel, 1967); abrasive size: 900 μm ; impact speed: 70 m/s; wire strength: 170 kg/mm^2 ; substrate hardness: 750 kg/mm^2 (VH10)

as in the core region of the particles as a function of the number of impact cycles. Results of this study are displayed in Fig. 2.24. It can be seen that the hardness increased in the rim region with an increasing number of impact cycles, whereas the hardness in the core region decreased. The hardness decrease in the core region is assumed to be a measure of material fatigue. The difference in the hardness values between rim and core first increased with an increase in the number of cycles, but it reached a saturation level at about 500 cycles. At this cycle number, the authors observed the first fragmentation of abrasive particles. Obviously, the deformation capability of the material was exhausted at this cycle level.

2.9.2 Fracture Probability of Abrasive Particles

The major kinematic parameter in impact comminution is the impact velocity which is equal to the velocity of the impinging abrasive particle. The particle hits the solid surface whereby stresses are generated not only on the target surface, but also in the particle. Figure 2.21 illustrates the geometrical situation. A certain probability exists that an impinging grain fractures during the impact. This fracture probability strongly depends on impact velocity, impact angle and particle diameter. Experimental results are reported by Rumpf (1965) and Ruppel and Brauer (1990). Figure 2.25 shows the effects of impact velocity and impact angle on the fracture probability of non-regular quartz particles. The fracture probability increased with an increase in the impact velocity and an increase in the impact angle. Two critical velocity values can be distinguished in this graph.

The first value is a *threshold velocity*. In the graph, it is about $v_p = 40$ m/s for the glass sphere impinging the target at an angle of $\varphi = 89^\circ$. This velocity must be exceeded in order to introduce fracture of individual particles. The threshold velocity is rather constant for most artificial abrasive materials, say glass beads; but it shows some scatter for natural abrasive materials, say quartz. The reason is the irregular uncontrolled distribution of flaws in the natural materials. Yashima et al. (1987) have shown that the threshold velocity depended on the particle size, and they derived the following relationship:

$$\frac{m_p}{2} \cdot v_p^2 \propto d_p^{\frac{3 \cdot m_F - 5}{m_F}} \quad (2.19)$$

This relationship delivers:

$$v_{pt} \propto d_p^{\frac{1}{2} \cdot \left(\frac{3 \cdot m_F - 5}{m_F} - 3 \right)} \quad (2.20)$$

Here, m_F is a flaw size distribution parameter of the abrasive material. Typical values are $m_F = 5.9$ for glass beads and $m_F = 21$ for quartz particles (with particle sizes between $d_p = 100$ and $2,000 \mu\text{m}$). With these m_F -values, (2.20) delivers $v_{pt} \propto d_p^{-0.42}$ for glass beads and $v_{pt} \propto d_p^{-0.12}$ for quartz.

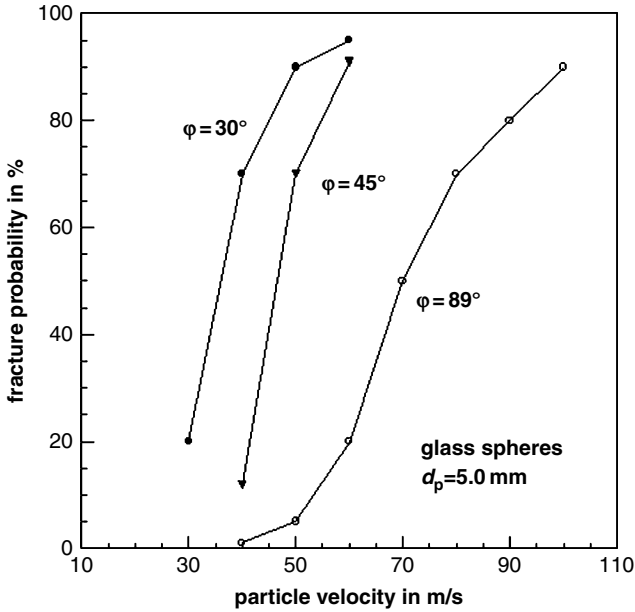


Fig. 2.25 Relationships between fracture probability, impact velocity and impact angle (Ruppel and Brauer, 1990)

The threshold velocity also depends on a large amount of the target material properties. Shipway and Hutchings (1993b) investigated the effects of substrate hardness and found a notable influence of the hardness on the threshold velocities for glass beads. Results of their study are summarised in Table 2.18. It can be seen that the threshold velocity was rather low for target materials featuring a high hardness.

The second critical value, which is illustrated in Fig. 2.25, is a *saturation velocity*. If this velocity is being exceeded, any impinging abrasive particle will be fractured; the fracture probability is unity. This saturation velocity is not being reached in any of the conditions considered in Fig. 2.25.

Relationships between impact velocity, particle size and fragmentation behaviour of impinging particles were in detail investigated by Andrews and Kim (1998, 1999)

Table 2.18 Effect of target material hardness on threshold velocity of 700- μm glass beads (Shipway and Hutchings, 1993b)

Target material	Vickers hardness in GPa	Threshold velocity in m/s
Aluminium alloy	1.75	216–240
Brass	1.22	216–289
Copper	0.89	250–288
Glass	6.14	175–200
Mild steel	1.98	201–218
Zirconia	14.0	41–48
Silicone carbide	30.5	47–82
Titanium alloy	3.25	174–203

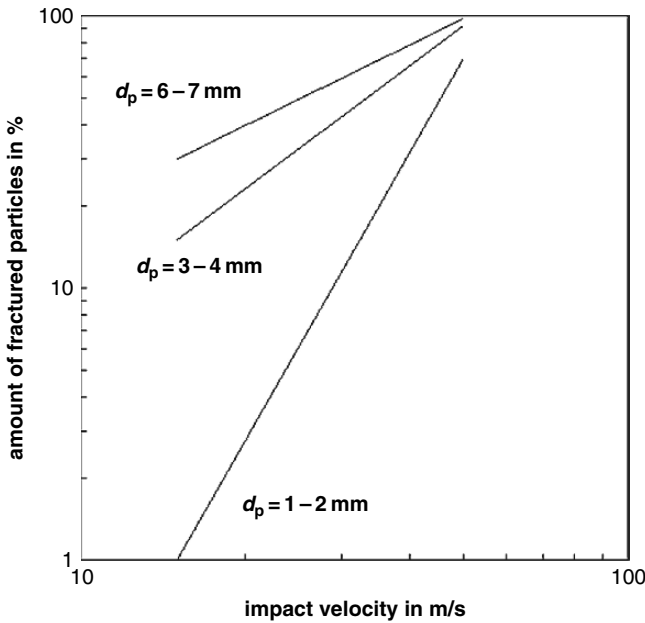


Fig. 2.26 Effects of impact velocity and particle diameter on the fracture probability of quartz particles (Rumpf, 1965)

and Rumpf (1965). Figure 2.26 illustrates relationships between fracture probability, particle velocity and particle diameter. As the figure shows, fracture probability is very sensitive to particle size. Because the curves are plotted in a bi-logarithmic mode in Fig. 2.26, straight lines can be drawn through the experimental points. It is evident that the ascent of these lines decreased with an increase in particle size. The ascent of the lines may be considered to describe the homogeneity of grain fragmentation. Whenever the particles contain a rather high number of cracks with different length, or of other flaws, the probability function will exhibit a low progress in a log-log-net.

Hutchings (1992) suggested that beyond a critical particle size and a critical particle velocity, the fragmentation of the particle is introduced. Particles smaller than a threshold size cannot be fractured, but will deform plastically; this threshold diameter is:

$$d_{Ppl} = 30 \cdot \left(\frac{K_{Ic/P}}{H_P} \right)^2 \tag{2.21}$$

The following expressions for the critical particle size above which fracture will occur on impact at a given velocity can be derived for three cases (Hutchings, 1992):

- (1) For $H_P > H_M$ and for an angular particle:

$$d_{Pf} \propto \left(\frac{K_{Ic/P}}{H_P} \right)^2 \cdot \frac{H_P^{1/2}}{H_M^{1/6}} \cdot \rho_P^{-1/3} \cdot v_P^{-2/3} \quad (2.22)$$

(2) For $H_P > H_M$ and for a rounded particle:

$$d_{Pf} \propto \left(\frac{K_{Ic/P}}{H_P} \right)^2 \cdot \frac{H_P^{1/2}}{H_M^{1/4}} \cdot \rho_P^{-1/4} \cdot v_P^{-1/2} \quad (2.23)$$

This relationship corresponds well with (2.20) for $m_F = 5.9$ for glass beads.

(3) For $H_P < H_M$ and for any geometry of the particle:

$$d_{Pf} \propto \left(\frac{K_{Ic/P}}{H_P} \right)^2 \cdot H_P^{1/4} \cdot \rho_P^{-1/4} \cdot v_P^{-1/2} \quad (2.24)$$

These conditions for abrasive particle fracture can be represented graphically. The case (1) for hard angular particles, shown in Fig. 2.27, illustrates three regimes of behaviour. The sloping line between the regimes III and II represents the condition for particle fracture given by (2.23). Within regime III, particle fracture will occur. Slikkerveer (1999) investigated the fragmentation behaviour of fused alumina powder ($d_p = 29\text{--}44 \mu\text{m}$), and he found a rather high threshold velocity for powder particle fragmentation of about $v_p = 125 \text{ m/s}$.

Bandaru (2004) considered the volume loss of abrasive particles as a fragmentation criterion, and he investigated the effects of numerous process parameters on the

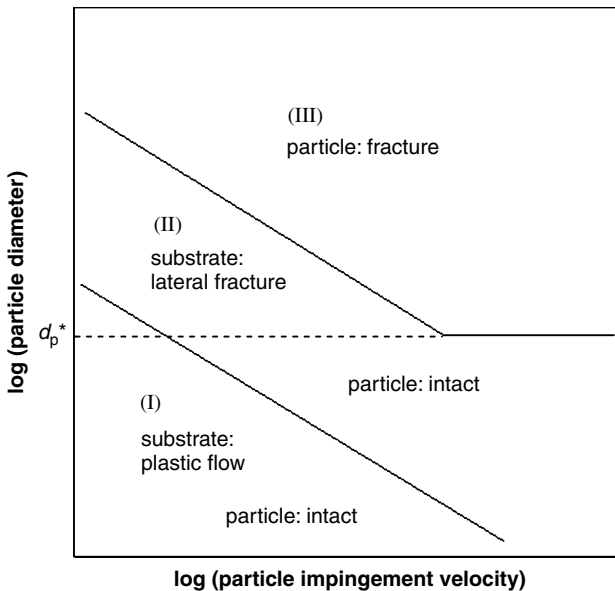


Fig. 2.27 Graphical representation of (2.24) for hard angular abrasive particles

volume loss. He found that volume loss increased linearly with increases in impact velocity, impact angle and abrasive particle size.

2.9.3 Effects of Abrasive Material Structure

The fracture probability of abrasive particles also strongly depends on their structure, in particular on the number and distribution of non-regularities, such as micro-cracks, grain boundaries and dislocations. Figure 2.28 illustrates how particle threshold velocity depends on the particle size and on abrasive material. A quartz particle with a diameter of $d_p = 500 \mu\text{m}$ requires a critical velocity of $v_p = 25 \text{ m/s}$, whereas a quartz glass particle of equal size requires a critical velocity of $v_p = 50 \text{ m/s}$. It is known that the number of flaws in an abrasive grain depends on the volume of the abrasive particle (Huang et al., 1995). Equation (2.1) is an expression to this relationship. Experimental results by Martinec (1994) showed the validity of this concept for the fragmentation of abrasive particles. The author found that garnet particles with very small diameters were extremely homogeneous, and thus they showed good stability in size and shape during the acceleration process in mixing nozzles.

Cleaver and Ghadiri (1993) suggested a reduced impact fragmentation for particles with lower hardness, lower density, larger fracture toughness and lower

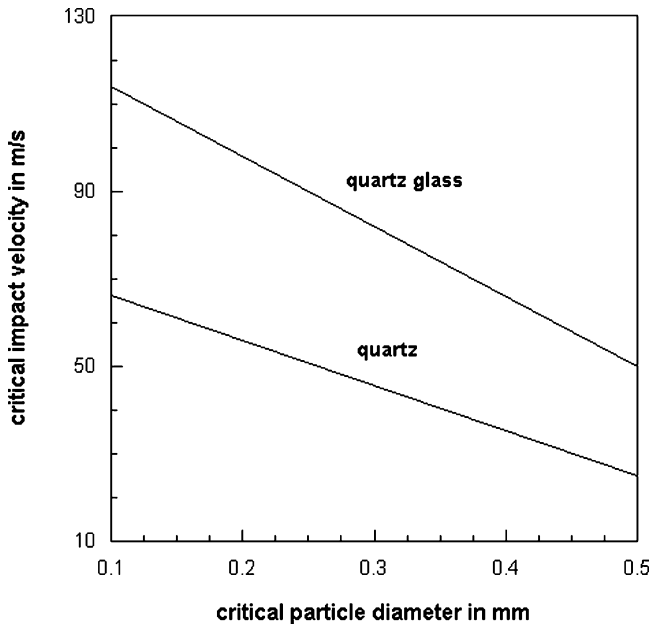


Fig. 2.28 Effects of abrasive material on threshold conditions for impact fragmentation (Yashima et al., 1987)

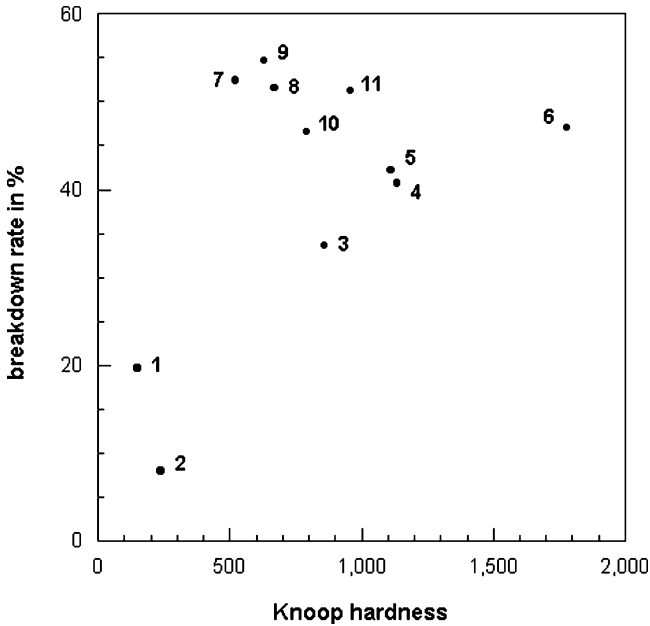


Fig. 2.29 Relationship between breakage ratio and abrasive material hardness (Fairfull and Weldon, 2001). Abrasive type; 1 – staurolite; 2 – steel grit; 3 – olivine; 4 – iron oxide; 5 – garnet. (A); 6 – garnet (B); 7 – copper slag; 8 – coal slag (A); 9 – coal slag (B); 10 – silica sand; 11 – nickel slag

particle diameter. Murugesu et al. (1991) reported similar relationships. Kiesskalt and Dahlhoff (1965) and Dahlhoff (1967) found significant relationships between the wave velocity in minerals and their resistance against impact comminution. The higher the wave velocity, the higher was the resistance against fragmentation. Figure 2.29 shows results for breakdown experiments performed by Fairfull and Weldon (2001) on a number of abrasive materials. It can be seen that the breakdown rate was low for abrasives having a low Knoop hardness. No trend could be recognised in the area of moderate and high hardness values. In that range, the effects of structural properties probably covered those of the hardness.

2.9.4 Debris Size

Reiners (1960) analysed debris generated during the impact of glass spheres. For not very high impact velocities ($v_p = 100$ m/s), this author found large portions of sharp-shaped particles in all grain-size classes. At higher impact velocities ($v_p = 650$ m/s), the debris consisted mainly of cubic and rectangular grains. Debris size decreased according to a power function if impact velocity increased. Reiners (1960) also found that the target material and geometry affected the average debris size. Debris size was largest for a copper substrate compared with a steel substrate.

2.9.5 Disintegration Numbers

Gommel (1967a) introduced a so-called *shatterability*, a parameter which quantifies the particle fragmentation during the impingement on a substrate. It was shown that shatterability depended on substrate hardness and impact velocity. If substrate hardness and impact velocity increased, shatterability increased. However, particle fragmentation was independent of impact velocity if the substrate hardness approached the hardness of the abrasive particle material (Gommel, 1967a).

Ohlsen (1997) introduced a *disintegration number* as follows:

$$\phi_D = 1 = \frac{\bar{d}_{Pout}}{\bar{d}_{Pin}} \tag{2.25}$$

$$0 < \phi_D < 1$$

If $\phi_D = 0$, no disintegration of the particles occurs. The particle size parameter can be substituted by the particle parameters discussed in Sect. 2.4, for example, by d_{P50} . Results, based on steel shot tests, are displayed in Fig. 2.30. The disintegration numbers are rather low, pointing to a high size stability of the particles. It can also be noted that the disintegration number depended on the number of impact cycles, but also on the hardness of the target material. For the soft target material, the disintegration number was almost one order of magnitude larger than for the

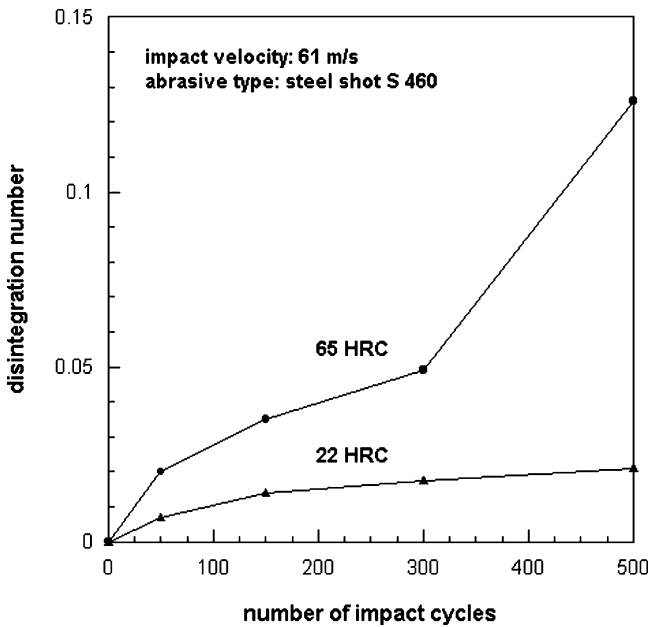


Fig. 2.30 Effects of number of impacts and target material hardness on the disintegration number (based on the sieve curves displayed in Fig. 2.33)

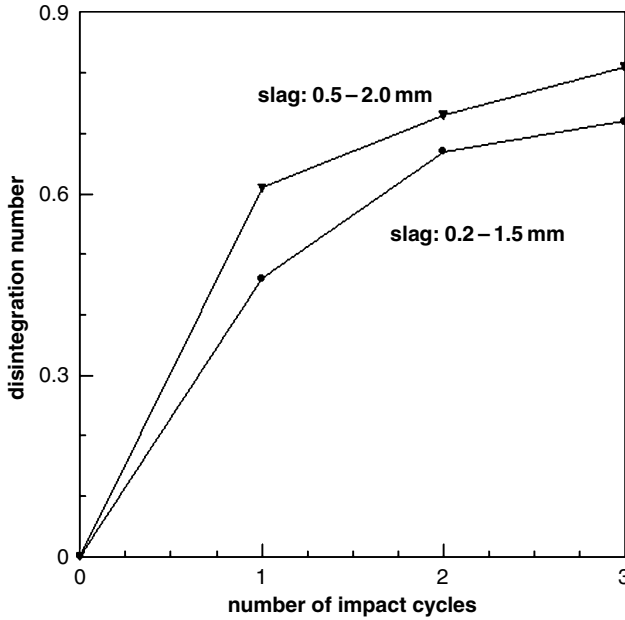


Fig. 2.31 Effects of number of impacts and abrasive particle size on the disintegration number (calculation is based on results reported by Hareux and Riac, 1986)

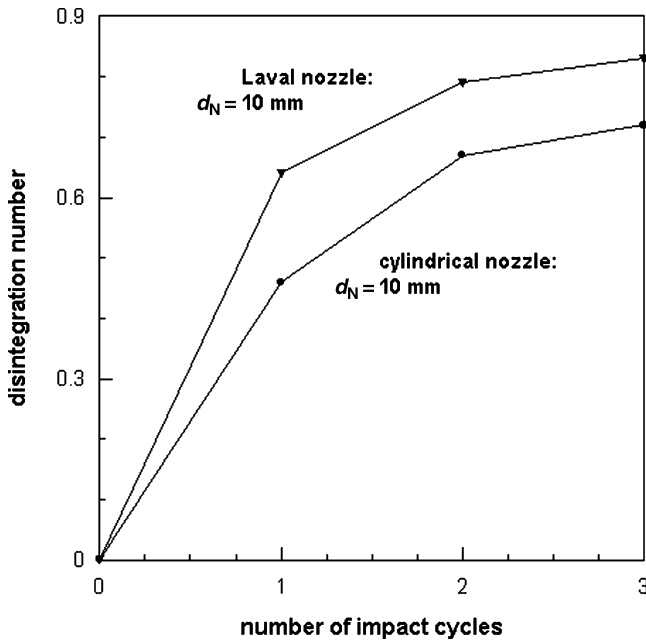


Fig. 2.32 Effects of number of impacts and nozzle type on the disintegration number (calculation is based on results reported by Hareux and Riac, 1986)

hard target material. Figure 2.31 illustrates the effect of the particle size of a slag material on its disintegration number. As could be expected from the results of the previous sections, disintegration number increased with an increase in the particle size. Another aspect is illustrated in Fig. 2.32 which shows the effect of nozzle type on the disintegration number. The disintegration of the abrasive material was more severe if the acceleration took part in a Laval nozzle. Laval-type nozzles can accelerate abrasive particles to higher speeds compared with cylindrical nozzles (see Sect. 3.3), and this results in a higher impingement speed and in a more severe fragmentation of the particles.

Repeated impingement of abrasive particles also affects the entire size distribution function of abrasive samples. An example is shown in Fig. 2.33. The amount of fine particles (left part of the graph) notably increased with an increase in number of impingement cycles. In recycling units, these rather fine particles are being removed from the sample if a certain amount is exceeded.

2.9.6 Particle Shape Modification During Abrasive Fragmentation

Another important aspect of the abrasive fragmentation is the *change in the shape* of the individual grains that may significantly influence the mechanism for material removal.

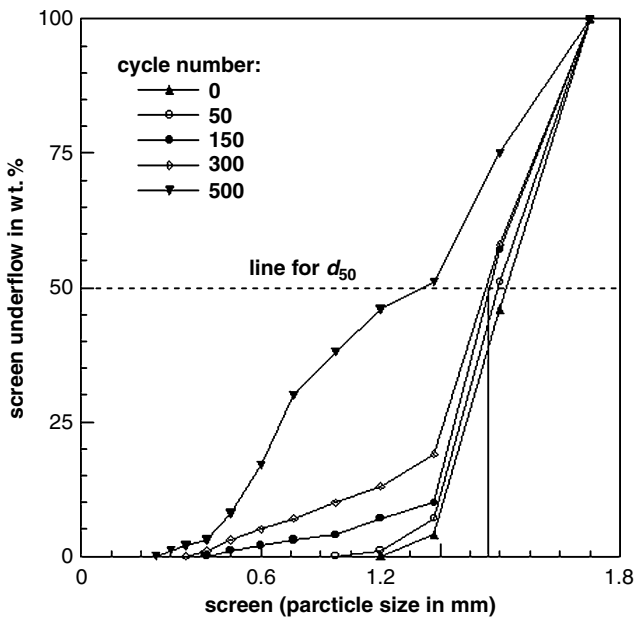


Fig. 2.33 Effect of number of impact cycles on the particle size distribution functions

Calboreanu (1991) who utilised round steel shot (S 460) for the impingement on cast iron samples noted a change of the shot contour from round to polygonal after 50 impact cycles ($v_p = 61$ m/s). A representative SEM-image of a polygonal shot contour is provided in Fig. 2.34.

Beitelman (2003) propelled very angular crushed steel grit (G 50) particles against carbon steel plates. He observed the following limiting cycle numbers: initial (zero cycles): very angular; after six cycles: angular; after 11 cycles: sub-angular; after 30 cycles: sub-rounded; after 200 cycles: rounded (see Fig. 2.9 for the particle shape designations). The author also investigated the effects of shape modifications on substrate profile and on the adhesion of coating systems; see Sects. 8.6.4 and 9.2.3 for the results. Wellinger and Gommel (1967) investigated the fragmentation behaviour of cut steel wires with a size of $d_p = 900 \mu\text{m}$ at a moderate impact speed

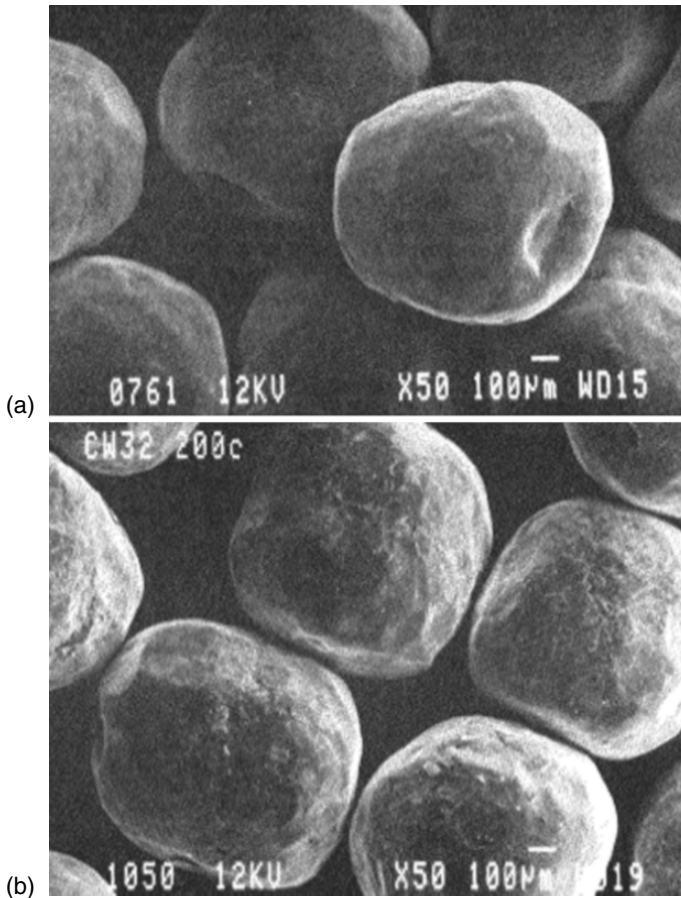


Fig. 2.34 SEM-images of shot particles (Flavenot and Lu, 1990); shot designation: S 460. (a) New, conditioned shot; (b) After 50 impact cycles (impact velocity: $v_p = 61$ m/s) on a cast iron target

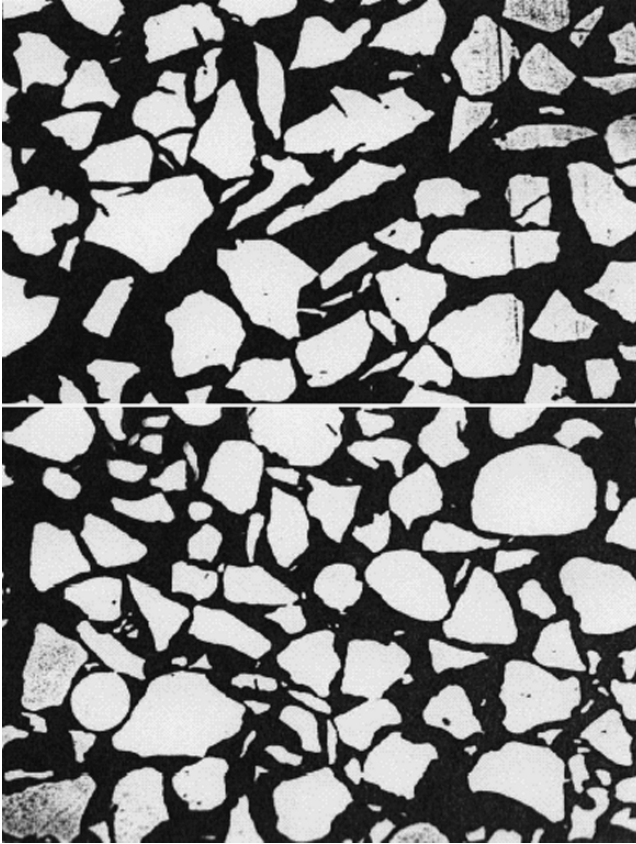


Fig. 2.35 SEM-images of stainless steel grit particles (Reference: Vulkan Inox GmbH, Hattingen); upper image: new particles; lower image: particles after one year of operation

of $v_p = 70$ m/s, and they found that the original wire shape changed into an almost spherical shape after about 150 impact cycles. Figure 2.35 illustrates the change in grain shape of stainless steel particles after one year in operation. A rounding of the originally irregular particles can be recognised in the lower image.

2.9.7 Energy Absorption During Abrasive Fragmentation

The process of abrasive fragmentation absorbs a certain amount of the kinetic energy of the particles. If the original grain-size distribution of the particle mixture and that of the mixture after the blast cleaning process are known, Bond's (1953, 1961) comminution formula can be applied to approximate the energy involved in this fragmentation process. The specific absorbed energy is then given by:

Table 2.19 Workability indices of minerals (Bond, 1953)

Material	Workability index in kWh/t
Ferrochromite	7.64
Ferromagnesite	8.30
Glass	12.31
Gravel	16.06
Quartzite	13.57
Slag	9.39
Silica carbide	25.87
Silica sand	14.10

$$E_F = w_i \cdot \frac{\sqrt{d_{p80in}} - \sqrt{d_{p80out}}}{\sqrt{d_{p80in}}} \cdot \sqrt{\frac{100}{d_{p80out}}} \quad (2.26)$$

The particle diameters must be given in μm . The power absorbed by the fragmentation process is finally as follows:

$$P_F = E_F \cdot \dot{m}_p \quad (2.27)$$

In (2.26), w_i is the index of workability which must be estimated with a standard comminution tests. Table 2.19 lists values for some materials. Figure 2.36 displays

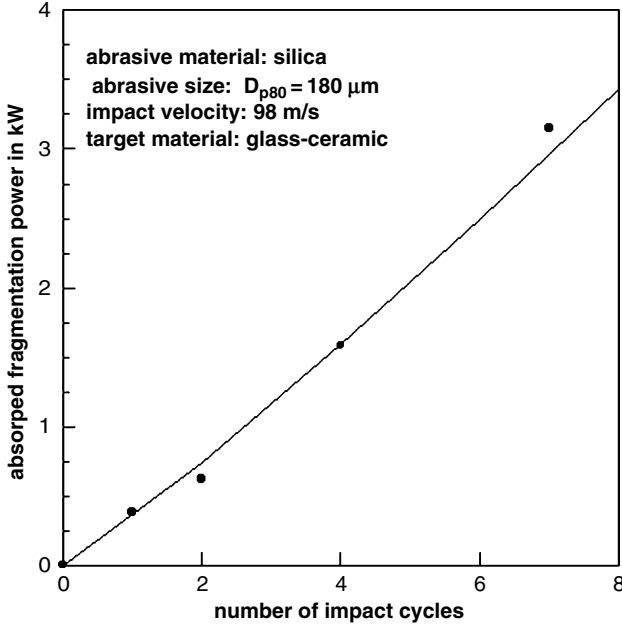


Fig. 2.36 Absorbed abrasive particle fragmentation power (calculation based on results reported by Sparks and Hutchings, 1993)

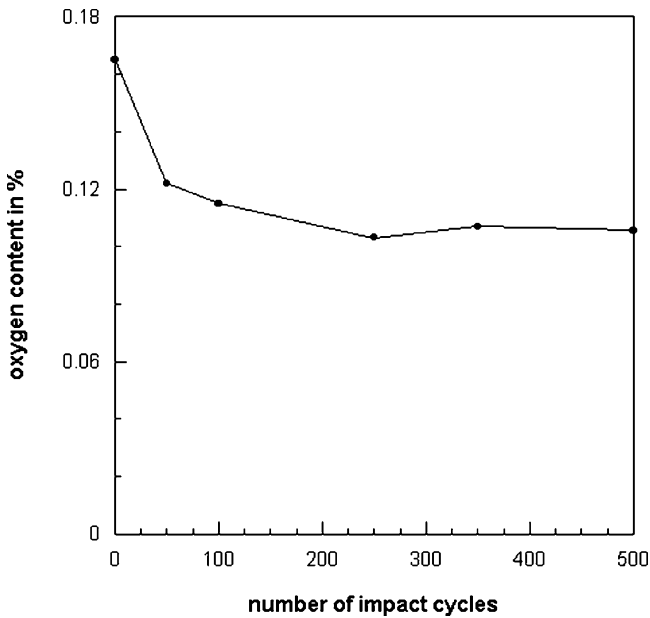


Fig. 2.37 Variation of oxygen content in steel shot after the impingement on cast iron (Calboreanu, 1991). Impact velocity: 61 m/s; shot designation: S 460

results of calculations performed with (2.27). The particle size parameters d_{P80in} and d_{P80out} for silica particles were taken from a detailed repeated impact study performed by Sparks and Hutchings (1993). The impact speed of the particles was $v_p = 98$ m/s, and the abrasive mass flow rate was assumed to be 10 kg/min. A Bond index of $w_i = 14.1$ kWh/t for silica sand was applied (see Table 2.19). For one impact cycle, the calculation delivers $P_F = 0.38$ kW. The power of the impinging abrasive particles can be calculated with (2.15), which delivers $P_P = 0.8$ kW. Therefore, almost 50% of the power delivered to the erosion site is dissipated into particle fragmentation. This rather high value is, however, caused by the high hardness of the target material, and it cannot be applied to other applications.

2.9.8 Chemical Degradation

Calboreanu (1991) investigated the behaviour of steel shot, impacted against cast iron, and found that the shot did not show chemical degradation after 500 cycles, except for a diminishment of the oxygen content due to the removal of the surface oxide layer. Results of this study are displayed in Fig. 2.37.

Chapter 3

Air and Abrasive Acceleration

3.1 Properties of Compressed Air

Air is a colourless, odourless and tasteless gas mixture. It consists of many gases, but primarily of oxygen (21%) and nitrogen (78%). Air is always more or less contaminated with solid particles, for example, dust, sand, soot and salt crystals. Typical properties of air are listed in Table 3.1. If air is considered to be an ideal gas, its behaviour can be described based on the general law of state:

$$p \cdot v_s = R_i \cdot T \tag{3.1}$$

where p is the static air pressure, v_s is the specific volume of the gas, R_i is the individual gas constant and T is the absolute temperature. It can be distinguished between three pressure levels, which are illustrated in Fig. 3.1. The relationships between these pressure levels are as follows:

$$p = p_0 + p_G \tag{3.2}$$

The parameter p is the absolute pressure, the parameter p_G is the gauge pressure usually read by the pressure gages in the blast cleaning pressure systems, and the parameter p_0 is the atmospheric pressure. The atmospheric pressure is a function of altitude. It is important not to confuse the absolute pressure and the gauge pressure. For theoretical calculations, the absolute pressure must be used.

The parameter R_i in (3.1) is the individual gas constant, which is the energy delivered by a mass of 1 kg of air if its temperature is increased by $+1^\circ\text{C}$ (K) at constant pressure. Its value for air is provided in Table 3.1. The individual gas constant is the difference between isobaric heat capacity and isochoric heat capacity of the gas:

$$R_i = c_p - c_v \tag{3.3}$$

The ratio between isobaric heat capacity and isochoric heat capacity is the isentropic exponent of the gas:

$$\kappa = \frac{c_p}{c_v} \tag{3.4}$$

Table 3.1 Properties of air

Parameter	Symbol	Unit	Value
Density ^a	ρ_A	kg/m ³	1.225
Dynamic viscosity ^a	η_0	Ns/m ²	1.72×10^{-5}
Isobaric specific heat capacity ^b	c_P	Nm/(kg K)	1,004
Isochoric specific heat capacity ^b	c_V	Nm/(kg K)	717
Gas constant	R_i	Nm/(kg K)	287
Adiabatic exponent	κ	–	1.4
Critical pressure ratio	β	–	0.528
Kinematic viscosity	ν_A	m ² /s	1.82×10^{-5}
Specific evaporation heat	q_V	Nm/kg	1.97×10^{-5}
Speed of sound ^a	c	m/s	331
Sutherland parameter	C_S	K	113

^aThermodynamic standard (Table 3.2: $\vartheta = 0^\circ\text{C}$, $p = 0.101325\text{ MPa}$)

^bFor $T = 273\text{ K}$

Values for the heat capacities and for the isentropic exponent of air can be found in Table 3.1. The absolute temperature is given as follows:

$$T = \vartheta + 273.2 \tag{3.5}$$

Its physical unit is K. The parameter ϑ is the temperature at the Celsius scale ($^\circ\text{C}$). With $\nu_S = 1/\rho_A$, (3.1) reads as follows:

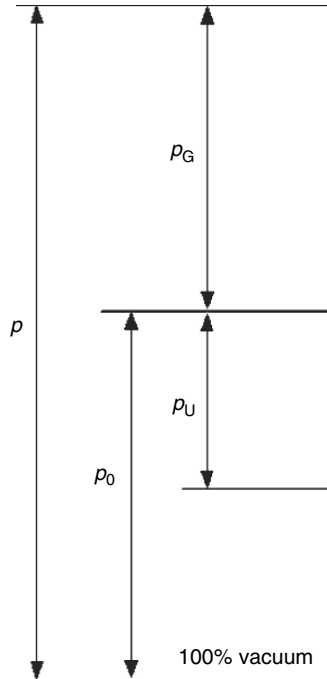


Fig. 3.1 Pressure levels

$$\frac{p}{\rho_A} = R_i \cdot T \tag{3.6}$$

This equation suggests that air density depends on pressure and temperature. These relationships are displayed in Fig. 3.2. For $T = 288.2 \text{ K}$ ($\vartheta = 15^\circ\text{C}$) and $p = p_0 = 0.101325 \text{ MPa}$, the density of air is $\rho_A = 1.225 \text{ kg/m}^3$ according to (3.6).

The volume of air depends on its state. The following four standards can be distinguished for the state of air:

- physical normal condition (DIN 1343, 1990);
- industry standard condition (ISO 1217, 1996);
- environmental condition;
- operating condition.

These standards are defined in Table 3.2. It can be seen that the physical normal condition and the industry standard condition both apply to dry air only with a relative humidity of 0%. For wet air, corrective factors must be considered (see DIN 1945-1).

The dynamic viscosity of air is independent of pressure for most technical applications, but it depends on temperature according to the following relationship (Albring, 1970):

$$\eta_A = \eta_0 \cdot \left(\frac{T}{T_0}\right)^{1/2} \cdot \frac{1 + (C_S/T_0)}{1 + (C_S/T)} \tag{3.7}$$

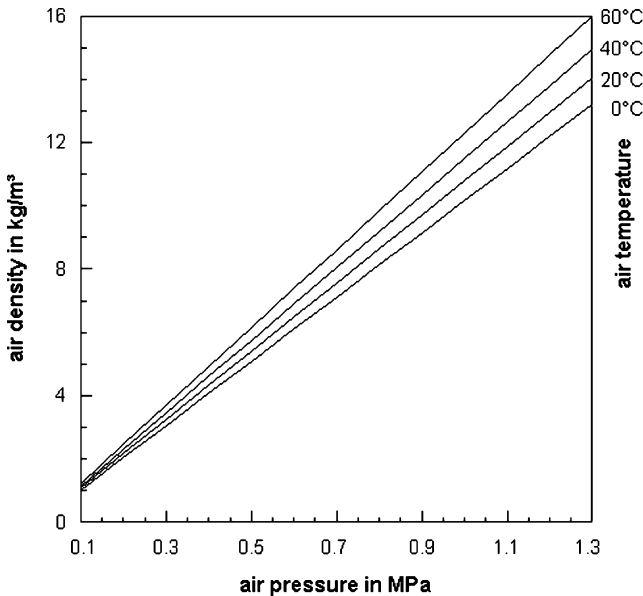


Fig. 3.2 Relationship between air pressure, air temperature and air density

Table 3.2 Conditions of state for air (DIN 1343, ISO 1217)

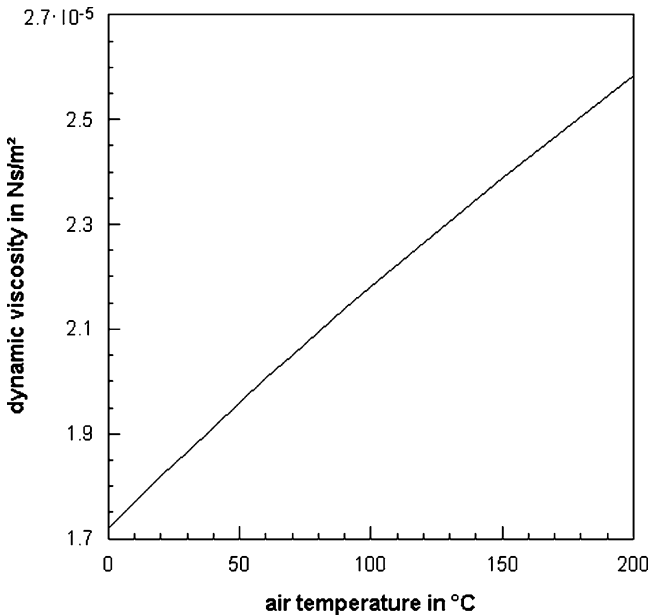
State	Temperature	Air pressure	Relative humidity	Air density
Physical standard (Normative standard)	0°C = 273.15 K	1.01325 bar = 0.101325 MPa	0%	1.294 kg/m ³
Industry standard	20°C = 293.15 K	1.0 bar = 0.1 MPa	0%	–
Environmental condition	Environmental temperature	Environmental pressure	Environmental humidity	Variable
Operating condition	Operating temperature	Operating pressure	Variable	Variable

The Sutherland parameter C_S for air is listed in Table 3.1. Results of (3.7) are plotted in Fig. 3.3, and it can be seen that dynamic viscosity rises almost linearly with an increase in temperature (in contrast to water, where dynamic viscosity decreases with an increase in temperature). The kinematic viscosity of air depends on pressure, and the relationship is as follows:

$$\nu_A = \frac{\eta_A}{\rho_A} \quad (3.8)$$

with $\rho_A = f(p, T)$.

The speed of sound in air is a function of the gas properties and absolute temperature:

**Fig. 3.3** Relationship between air temperature and dynamic viscosity of air

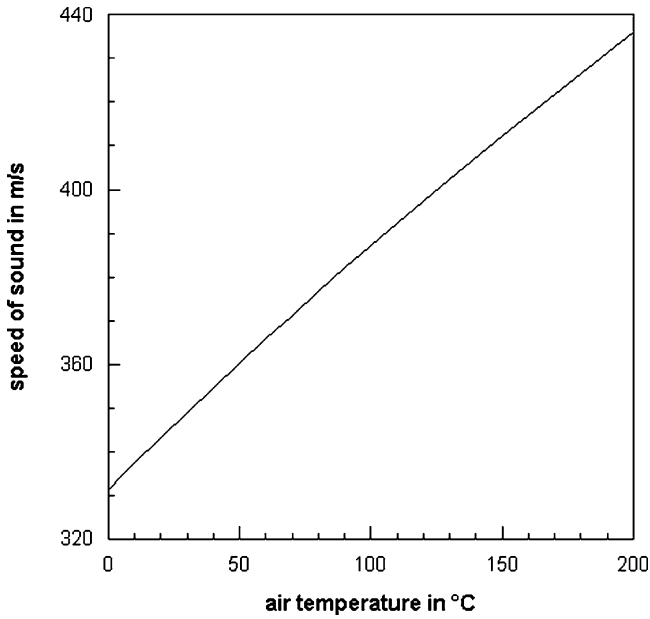


Fig. 3.4 Relationship between air temperature and speed of sound in air

$$c = (\kappa \cdot R_i \cdot T)^{1/2} \tag{3.9}$$

Results of (3.9) for different air temperatures are plotted in Fig. 3.4. The ratio between the actual local flow velocity and the speed of sound is the Mach number, which is defined as follows:

$$Ma = \frac{v_F}{c} \tag{3.10}$$

For $Ma < 1$, the flow is subsonic, and for $Ma > 1$, the flow is supersonic. For $Ma = 1$, the flow is sonic.

3.2 Air Flow in Nozzles

3.2.1 Air Mass Flow Rate Through Nozzles

Because air is a compressible medium, volumetric flow rate is not a constant value, and mass flow rate conversion counts for any calculation. The theoretical mass flow rate of air through a nozzle is given by the following equation (Bohl, 1989):

$$\dot{m}_{Ath} = \frac{\pi}{4} \cdot d_N^2 \cdot (2 \cdot \rho_A \cdot p)^{1/2} \cdot \underbrace{\left\{ \frac{\kappa}{\kappa - 1} \cdot \left[\left(\frac{p_0}{p} \right)^{\frac{2}{\kappa}} - \left(\frac{p_0}{p} \right)^{\frac{\kappa+1}{\kappa}} \right] \right\}^{1/2}}_{\text{outflow function } \Psi} \tag{3.11}$$

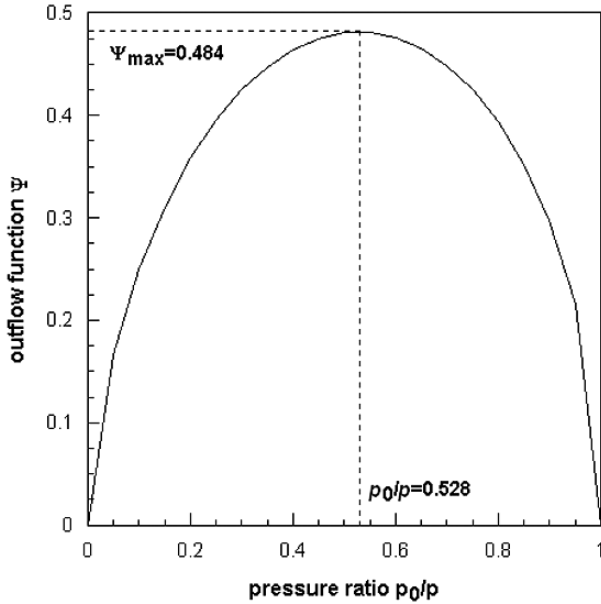


Fig. 3.5 Outflow function $\Psi = f(p_0/p)$ for air

The outflow function $\Psi = f(p_0/p)$ is plotted in Fig. 3.5. It is a parabolic function with a typical maximum value at a critical pressure ratio p_0/p . This critical pressure ratio is often referred to as *Laval pressure ratio*. It can be estimated as follows:

$$\left(\frac{p_0}{p}\right)_{\text{crit}} = \left(\frac{2}{\kappa + 1}\right)^{\frac{\kappa}{\kappa - 1}} \quad (3.12a)$$

With $\kappa = 1.4$ for air, (3.12a) delivers the following value for the Laval pressure ratio:

$$\left(\frac{p_0}{p}\right)_{\text{crit}} = 0.528 \quad (3.12b)$$

The corresponding value for the outflow function is $\psi_{\max}(0.528) = 0.484$. The graph plotted in Fig. 3.5 does not describe reality. In reality, air mass flow rate does not drop for pressure ratios < 0.528 . The air mass flow rate rather follows the horizontal dotted line for $\psi_{\max} = 0.484$. Equation (3.11) can, therefore, be simplified for the condition $p_0/p < 0.528$ (respectively $p > 0.19$ MPa for $p_0 = 0.1$ MPa):

$$\dot{m}_{\text{Ath}} = \frac{\pi}{4} \cdot d_N^2 \cdot (2 \cdot \rho_A \cdot p)^{1/2} \cdot 0.484 \quad (3.13)$$

Equation (3.13) delivers the theoretical mass flow rate. The real mass flow rate includes a nozzle exit parameter:

Table 3.3 Nozzle exit coefficient α_N (Schwate, 1986)

Nozzle geometry	α_N -value
Sharp-edged opening	0.6
Opening with $l_N = 1.5 \cdot d_N$	0.8
Conical entry opening with rounded edges	0.9
Very smooth surface; rounded edges with radius = $0.5 \cdot d_N$	0.95

$$\dot{m}_A = \alpha_N \cdot \frac{\pi \cdot 0.484}{4} \cdot d_N^2 \cdot (2 \cdot \rho_A \cdot p)^{1/2} \tag{3.14}$$

The values for the nozzle exit coefficient α_N depend on nozzle geometry. Some values are listed in Table 3.3. Calculated theoretical air mass flow rates are plotted in Fig. 3.6. It can be seen that the mass flow rate linearly increases with an increase in nozzle pressure.

3.2.2 Volumetric Air Flow Rate

The volumetric air flow rate can be calculated as follows:

$$\dot{Q}_A = \frac{\dot{m}_A}{\rho_A} \tag{3.15}$$

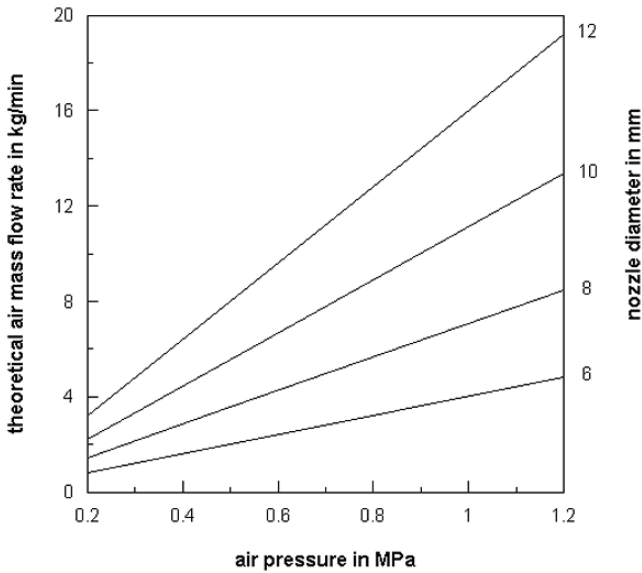


Fig. 3.6 Theoretical mass flow rates for a blast cleaning nozzle as functions of pressure and nozzle diameter (air temperature: 20 °C)

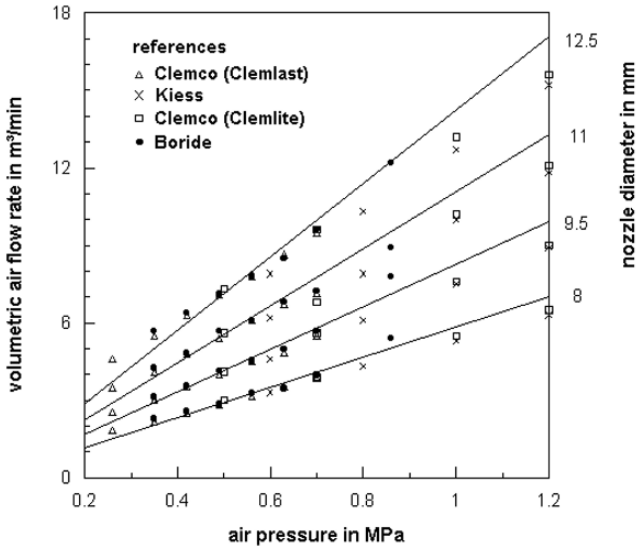


Fig. 3.7 Theoretical volumetric flow rates for a compressor (for an ambient air temperature of $\vartheta = 20^\circ\text{C}$) and recommended values from equipment manufacturers

The density is given through (3.6). If the volumetric flow rate, which must be delivered by a compressor, is requested, the density ρ_A for the environmental conditions (see Table 3.2) must be inserted in (3.15). Because air density depends on temperature, the ambient air temperature in the vicinity of a compressor may affect the volumetric air rate. A change in ambient air temperature of $\Delta T = 10\text{ K}$ ($\Delta\vartheta = 10^\circ\text{C}$), however, leads to a 3%-change in the volumetric air flow rate.

Results of (3.14) and (3.15) for typical parameter configurations are plotted in Fig. 3.7 together with recommendations issued by equipment manufacturers. The deviations between calculation and recommendation cannot be neglected for nozzle pressures higher than $p = 0.9\text{ MPa}$. Results obtained with (3.14) and (3.15) correspond very well with results of measurements reported by Nettmann (1936). For $p = 0.5\text{ MPa}$ (gauge pressure) and $d_N = 10\text{ mm}$, this author reported a value of $\dot{Q}_A = 5.65\text{ m}^3/\text{min}$. The calculation (based on industry standard, $\vartheta = 20^\circ\text{C}$) delivers $\dot{Q}_A = 5.63\text{ m}^3/\text{min}$. Nettmann (1936) was probably the first who published engineering nomograms for the assessment of compressor volumetric air flow rate and of compressor power rating for varying gauge pressures and nozzle diameters. Equations (3.14) and (3.15) can be utilised to calculate nozzle working lines. Working lines for three different nozzles are plotted in Fig. 4.3.

If abrasive material is added to the air flow, it occupies part of the nozzle volume and displaces part of the air. This issue was in detail investigated experimentally by Adlassing (1960), Bae et al. (2007), Lukschandel (1973), Uferer (1992) and Plaster (1973); and theoretically by Fokke (1999). Fokke (1999) found that the abrasive particle volume fraction in the nozzle flow depended on abrasive mass flow rate, and it had values between $F_p = 0.01$ (1 vol.%) and 0.04 (4 vol.%).

Uferer (1992) derived a critical abrasive volume fraction for blast cleaning processes, and he suggested that the value of $F_P = 0.12$ (12 vol.%) should not be exceeded in order to guarantee a stable blast cleaning process.

Due to the dislocation effect, the air flow rate through a nozzle reduces if abrasive material is added to the flow, and a modified relationship reads as follows:

$$\dot{Q}_{A(P)} = \Phi_P \cdot \dot{Q}_A \quad (3.16)$$

The reduction parameter has typical values between $\Phi_P = 0.7$ and 0.9 ; it depends mainly on abrasive mass flow rate (Adlassing, 1960; Lukschandel, 1973; Plaster, 1973; Uferer, 1992; Bae et al., 2007). Fokke (1999) found that particle size had a very small influence on the air mass flow rate if rather high air pressures were applied.

Uferer (1992) recommended the following relationship for the estimation of the reduction parameter:

$$\Phi_P = \frac{1}{\left(1 + \frac{v_P}{v_A} \cdot \frac{\dot{m}_P}{\dot{m}_A}\right)^{1/2}} \quad (3.17)$$

For typical blast cleaning parameters ($\dot{m}_P/\dot{m}_A = 2$, $v_P/v_A = 0.3$), this equation delivers $\Phi_P = 0.79$, which is in agreement with the reported experimental results. Values estimated by Uferer (1992) are listed in Table 3.4. It can be seen that the value of the reduction parameter depended on abrasive type, nozzle geometry and mass flow ratio abrasive/air. For the range $R_m = 1.5$ to 3 , which is recommended for blast cleaning processes, the values for the reduction parameter were between $\Phi_P = 0.75$ and 0.85 .

Bae et al. (2007) and Remmelts (1968) performed measurements of volumetric air flow rates as a function of abrasive mass flow rate. Their results, partly plotted in Fig. 3.11, can be fitted with the following exponential regression:

$$\Phi_{P(Laval)} = \frac{\dot{Q}_{A(P)}}{\dot{Q}_A} = 0.98^{\dot{m}_P} \quad (3.18a)$$

Table 3.4 Reduction parameter values for different blast cleaning conditions (Uferer, 1992)

Abrasive type	Nozzle geometry	Mass flow ratio abrasive/air	Φ_P
Slag and quartz sand	Cylindrical	< 1.5	0.8
		1.5–3	0.75
	Convergent-divergent (Laval)	< 1.5	0.9
		1.5–3	0.85
Cut steel wire	Cylindrical	< 1.5	0.8
		1.5–3.5	0.75
		3.5–5.5	0.7
		> 5.5	0.6

The abrasive mass flow rate must be inserted in kg/min. The coefficient of regression is as high as 0.95 for all fits. It can be seen that $\Phi_p = 1$ for $\dot{m}_p = 0$. For a typical abrasive mass flow rate of $\dot{m}_p = 10$ kg/min, the equation delivers $\Phi_p = 0.82$, which corresponds well with the values cited earlier. The regression is valid for Laval nozzles fed with steel grit. The basic number 0.98 in (3.18a) is independent of the dimensions of the nozzles (d_N , l_N), and it can be assumed to be typical for Laval nozzles. However, the basic number may change if other abrasive materials than steel grit are utilised.

Results of measurements of volumetric flow rates performed by some authors are presented in Figs. 3.8 and Fig. 3.9. The results provided in Fig. 3.8 demonstrate the effects of different abrasive types on the volumetric air flow rate. The addition of chilled iron was more critical to the volumetric air flow rate compared with the addition of the non-ferrous abrasive material. The results plotted in Fig. 3.9 showed that air volumetric flow rate depended on abrasive type, nozzle type and air pressure, if abrasive material was added. Interestingly, the effect of the abrasive material type was only marginal for small nozzle diameters. This effect was also reported by Adlassing (1960). The reduction in air flow rate was more severe if a Laval nozzle was utilised instead of a standard nozzle. Laval nozzles consumed approximately 10% more air volume than conventional cylindrical nozzles, if abrasives (quartz, SiC, corundum and steel grit) were added (Lukschandel, 1973). This result agrees with measurements provided in Table 3.4. Based on these results, the following very preliminary approach can be made:

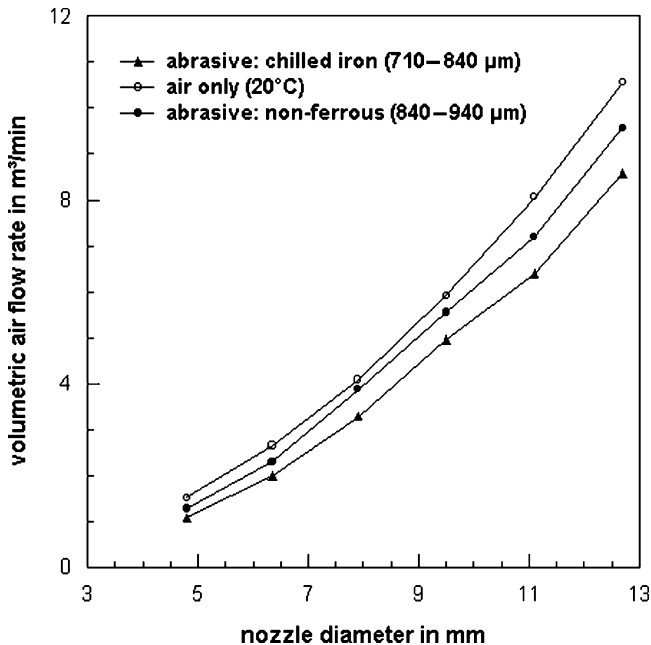


Fig. 3.8 Effect of abrasive type on volumetric air flow rate (Plaster, 1973)

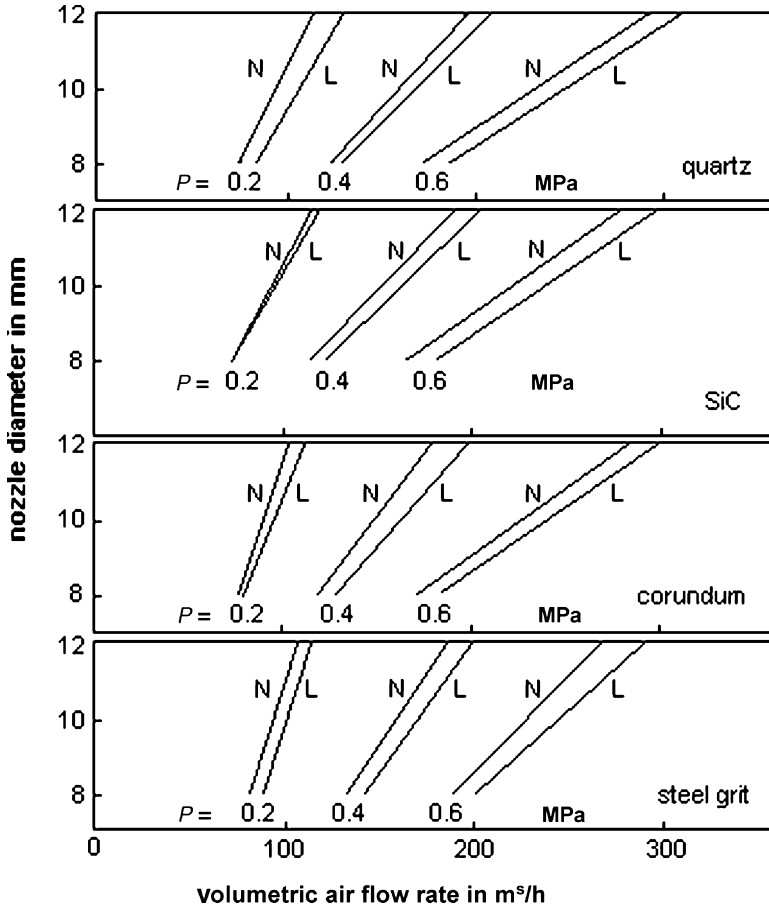


Fig. 3.9 Effects of air pressure, nozzle diameter, nozzle geometry and abrasive type on volumetric air flow rate (Lukschandel, 1973). “N” – cylindrical nozzle; “L” – convergent–divergent (Laval) nozzle

$$\Phi_{P(\text{cylinder})} = 0.9 \cdot \Phi_{P(\text{Laval})} \tag{3.18b}$$

More experimental evidence is provided in Figs. 3.10 and 3.11. Figure 3.10 illustrates the effect of nozzle layout on the air volume flow, if abrasive material (crushed cast iron) was added. The deviation in air volume flow rate was about 10%. The effects of varying nozzle geometries on the volumetric air flow rates were further investigated by Bae et al. (2007). Some of their results are displayed in Fig. 3.11. The effect of nozzle geometry parameters is much more pronounced compared with the results plotted in Fig. 3.10. The graphs also illustrate the effects of abrasive mass flow rate on the volumetric air flow rate. The more the abrasive material added, the lesser the air volume flow through the nozzle. The curves ran parallel to each

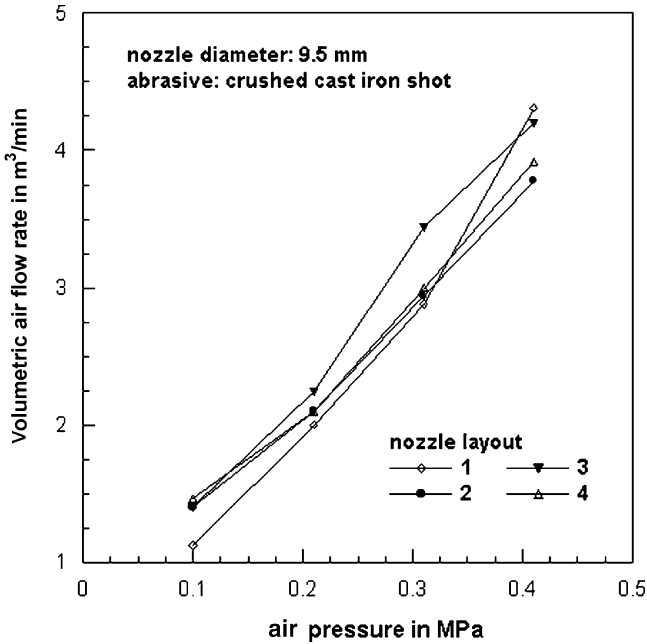


Fig. 3.10 Effects of nozzle geometry on volumetric air flow rate (Plaster, 1973); abrasive type: crushed chilled cast iron shot; $d_N = 9.5$ mm. Nozzle layout: “1” – convergent–divergent; “2” – bell-mouthed + convergent; “3” – bell-mouthed + divergent; “4”: bell-mouthed + convergent–divergent

other; thus, the general trend was almost independent of the nozzle geometry. These relationships are expressed through (3.18a).

3.2.3 Air Exit Flow Velocity in Nozzles

For an isotropic flow (no heat is added or taken and no friction), the velocity of an air jet exiting a pressurised air reservoir through a small opening can be expressed as the enthalpy difference between vessel and environment as follows:

$$v_A = (2 \cdot \Delta h_A)^{1/2} \quad (3.19)$$

After some treatment, the velocity of air flow at the exit of a nozzle can be calculated with the following relationship (Kalide, 1990):

$$v_A = \left(2 \cdot \frac{\kappa}{\kappa - 1} \cdot \frac{p}{\rho_A} \cdot \left[1 - \left(\frac{p_0}{p} \right)^{\frac{\kappa - 1}{\kappa}} \right] \right)^{1/2} \quad (3.20)$$

As an example, if compressed air at a temperature of $\vartheta = 27^\circ\text{C}$ ($T = 300\text{ K}$) and at a pressure of $p = 0.6\text{ MPa}$ flows through a nozzle, its theoretical exit velocity is about $v_A = 491\text{ m/s}$.

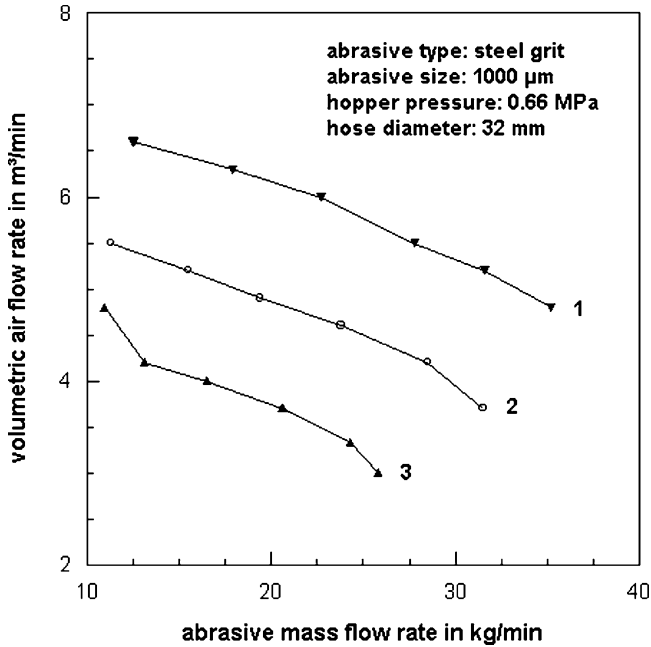


Fig. 3.11 Effects of abrasive mass flow rate and nozzle geometry on the air volume flow rate in convergent–divergent nozzles (Bae et al., 2007). Nozzle “1” – nozzle length: 150 mm, throat (nozzle) diameter: 11.5 mm, divergent angle: 2.1°, convergent angle: 9.3°; Nozzle “2” – nozzle length: 216 mm, throat (nozzle) diameter: 11.0 mm, divergent angle: 1.3°, convergent angle: 7.9°; Nozzle “3” – nozzle length: 125 mm, throat (nozzle) diameter: 12.5 mm, divergent angle: 7.6°, convergent angle: 3.9°

The maximum exit velocity, however, occurs at the point of maximum mass flow rate, which happens under the following conditions: Ψ_{max} and $(p_0/p)_{crit}$ (see Fig. 3.5). If the Laval pressure ratio $(p_0/p)_{crit}$ is introduced into (3.20), the following maximum limit for the air velocity in parallel cylindrical nozzles results:

$$v_{A\ max} = \left(2 \cdot \frac{\kappa}{\kappa + 1} \cdot \frac{p}{\rho_A} \right)^{1/2} \tag{3.21}$$

After further treatment, the final equation reads as follows:

$$v_{A\ max} = v_L = (\kappa \cdot R_i \cdot T)^{1/2} \tag{3.22}$$

The equation is equal to (3.9). This critical air velocity is frequently referred to as *Laval velocity* (v_L). It cannot be exceeded in a cylindrical nozzle. It depends not on pressure, but on gas parameters and gas temperature. Figure 3.4 presents results for calculated Laval velocities. For the example mentioned in relationship with (3.20), the critical air flow velocity is $v_L = 347$ m/s, which is much lower than the velocity of $v_A = 491$ m/s calculated with (3.20).

If the exit air velocity needs to be increased further in order to exceed the Laval velocity given by (3.22), the nozzle exit region must be designed in a divergent shape. Nozzles which operate according to this design were independently developed by the German engineer Ernst K rting (1842–1921) and the Swedish engineer Gustav de Laval (1845–1913). In honour of the latter inventor, they are called Laval nozzles.

3.2.4 Air Flow in Laval Nozzles

If air velocities higher than the Laval velocity ($v_A > v_L$) are to be achieved, the cross-section of the nozzle must be extended in a way that smooth adiabatic expansion of the air is possible. Such a nozzle geometry is called convergent–divergent (Laval) nozzle. An example is shown in Fig. 3.12. The figure shows an image that was taken with X-ray photography. The flow direction is from right to left. The nozzle consists of a convergent section (right), a throat (centre) and a divergent section (left). The diameter of the throat, which has the smallest cross-section in the system, is considered the nozzle diameter (d_N). For this type of nozzle, (3.20) can be applied without a restriction. For practical cases, a nozzle coefficient φ_L should be added, which delivers the following equation for the calculation of the exit velocity of the air flow:

$$v_A = \varphi_L \cdot \left(2 \cdot \frac{\kappa}{\kappa - 1} \cdot \frac{p}{\rho_A} \cdot \left[1 - \left(\frac{p_0}{p} \right)^{\frac{\kappa-1}{\kappa}} \right] \right)^{1/2} \quad (3.23)$$

The Laval nozzle coefficient φ_L is a function of a dimensionless parameter ω . Relationships for two nozzle qualities are exhibited in Fig. 3.13. The parameter ω depends on the pressure ratio p_0/p (Kalide, 1990). Examples for certain pressure levels are plotted in Fig. 3.14. It can be seen that the dimensionless parameter takes values between $\omega = 0.5$ and 1.0 for typical blast cleaning applications. The parameter ω decreases if air pressure increases. A general trend is that nozzle efficiency decreases for higher air pressures. Results of (3.23) are displayed in the left graph in Fig. 3.15. The right graph displays results of (3.22). One result is that air flowing through a cylindrical nozzle at a high temperature of $\vartheta = 200^\circ\text{C}$ and at a rather low pressure of $p = 0.2$ MPa obtains an exit velocity which is equal to that of air which

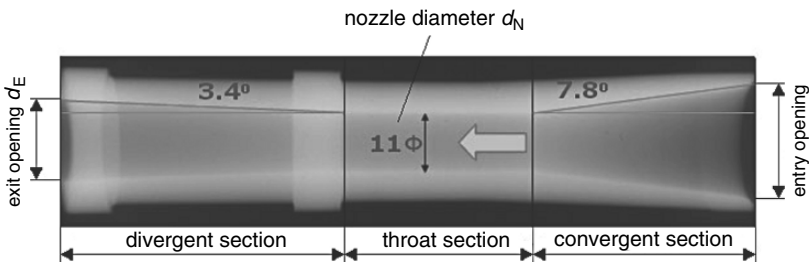


Fig. 3.12 X-ray image of a convergent–divergent (Laval) nozzle design (Bae et al., 2007)

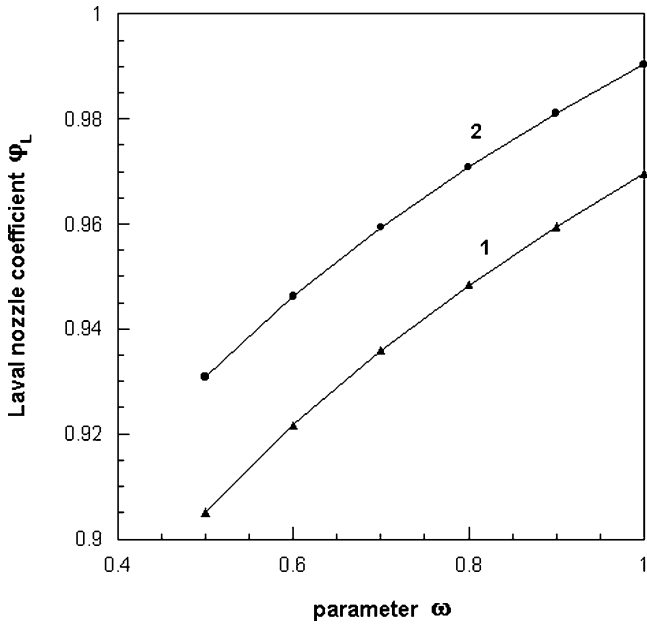


Fig. 3.13 Relationship between ϕ_L and ω (Kalide, 1990). “1” – Straight nozzle with smooth wall; “2” – curved nozzle with rough wall

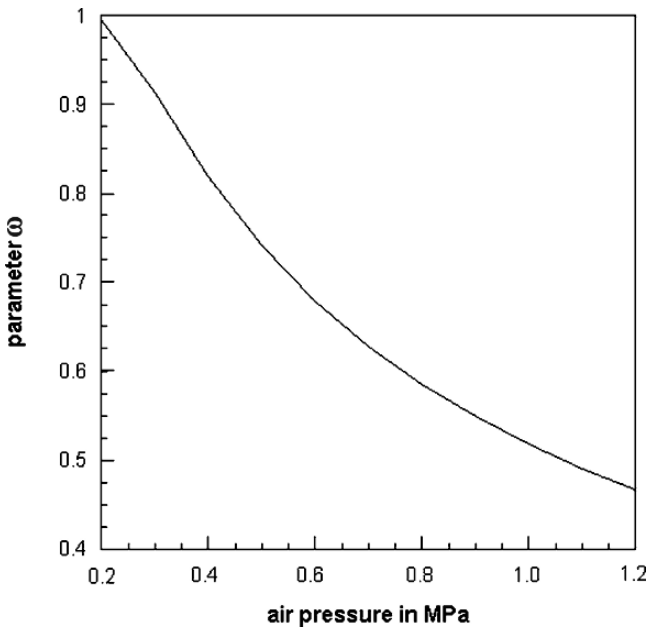


Fig. 3.14 Function $\omega = f(p)$ for $p_0 = 0.1$ MPa; according to a relationship provided by Kalide (1990)

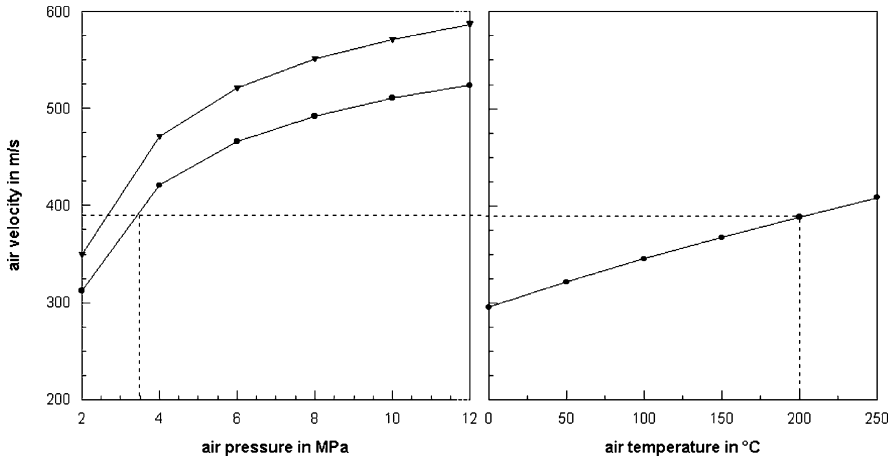


Fig. 3.15 Theoretical air exit velocities in Laval nozzles. Left: air temperature effect; upper curve: $\vartheta = 100^\circ\text{C}$; lower curve: $\vartheta = 20^\circ\text{C}$; Right: air pressure effect; $p = 0.2\text{ MPa}$

is flowing through a Laval nozzle at a temperature of $\vartheta = 20^\circ\text{C}$ and at a much higher pressure of $p = 0.35\text{ MPa}$.

The air mass flow rate through a Laval nozzle can be calculated with (3.14), whereby d_N is the diameter of the narrowest cross-section (throat) in the nozzle. For air at a pressure of $p = 0.6\text{ MPa}$ and a temperature of $\vartheta = 27^\circ\text{C}$ ($T = 300\text{ K}$) flowing through a Laval nozzle with $d_N = 11\text{ mm}$ and $\alpha_N = 0.95$, (3.14) delivers a mass flow rate of about $\dot{m}_A = 0.133\text{ kg/s}$.

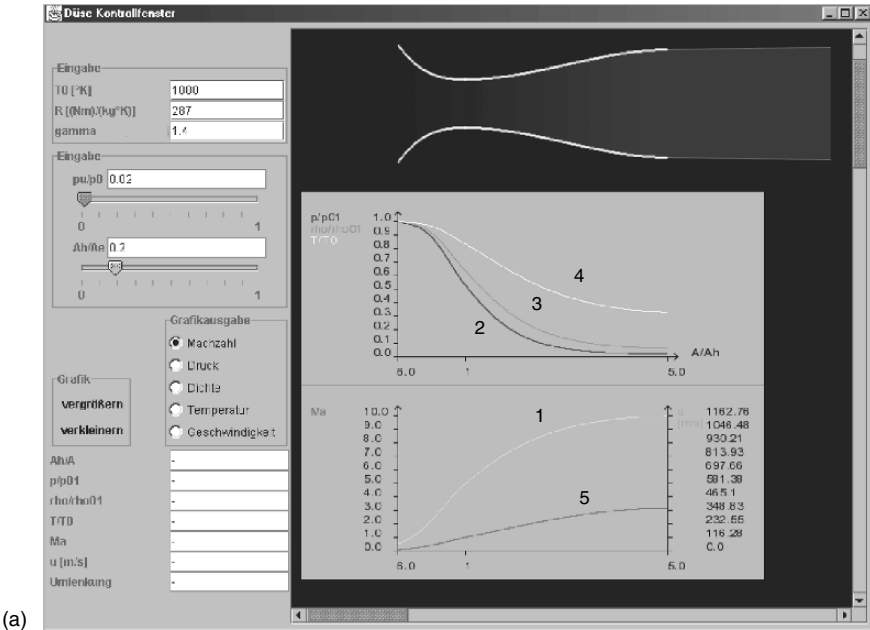
The flow and thermodynamics either in cylindrical nozzles or in Laval nozzles can be completely described with commercially available numerical simulation programs, which an example of is presented in Fig. 3.16a. In that example, the progresses of Mach number, air density, air pressure and air temperature along the nozzle length are completely documented. It can be seen that pressure, density and temperature of the air are all reduced during the flow of the air through the nozzle.

The flow regimes that are set up in a convergent–divergent nozzle are best illustrated by considering the pressure decay in a given nozzle as the ambient (back) pressure is reduced from rather high to very low values. All the operating modes from wholly subsonic to underexpanded supersonic are shown in sequences “1” to “5” in Fig. 3.26, which will be discussed later in Sect. 3.4.3.

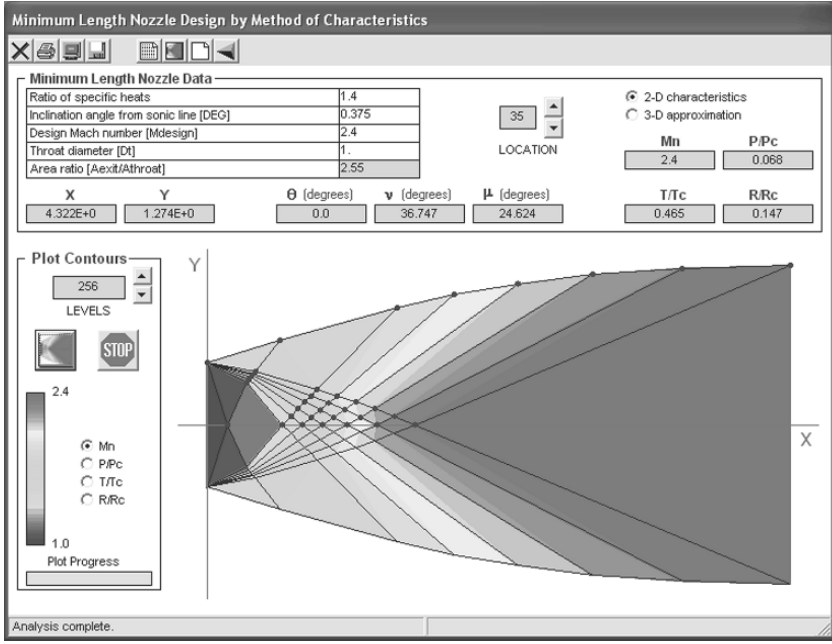
3.2.5 Power, Impulse Flow and Temperature

The power of the air stream exiting a nozzle is simply given as follows:

$$P_A = \frac{\dot{m}_A}{2} \cdot v_A^2 \quad (3.24)$$



(a)



(b)

Fig. 3.16 Results of numerical simulations of the air flow in convergent–divergent nozzles (Laval nozzles). (a) Gradients for Mach number (1), pressure (2), density (3), temperature (4) and air velocity (5); image: RWTH Aachen, Aachen, (Germany); (b) Complete numerical nozzle design including shock front computation (Aerorocket Inc., Citrus Springs, USA)

For the above-mentioned example, the air stream power is about $P_A = 16 \text{ kW}$. The impulse flow of an air stream exiting a nozzle can be calculated as follows:

$$\dot{I}_A = \dot{m}_A \cdot v_A \quad (3.25)$$

For the parameter combination mentioned above, the impulse flow is about $\dot{I}_A = 65 \text{ N}$.

Because of the air expansion, air temperature drops over the nozzle length (see Fig. 3.16a). The temperature of the air at the nozzle exit can be calculated based on (3.19). A manipulation of this equation delivers the following relationship (Bohl, 1989):

$$T_E = T_N - \frac{v_A^2}{2 \cdot c_p} \quad (3.26)$$

In that equation, T_N is the entry temperature of the air. The value for the isobaric heat capacity of air is listed in Table 3.1. For the above-mentioned example, (3.26) delivers an air exit temperature of $T_E = 180 \text{ K}$ ($\theta_E = -93^\circ\text{C}$).

3.3 Abrasive Particle Acceleration in Nozzles

3.3.1 General Aspects

Solid abrasives particles hit by an air stream do accelerate because of the drag force imposed by the air stream. The situation is illustrated in Fig. 3.17 where results of a numerical simulation of pressure contours and air streamlines around a sphere are shown. The acceleration of the sphere is governed by Newton's second law of motion:

$$m_p \cdot \frac{dv_p}{dt} = F_D = c_D \cdot A_p \cdot \frac{\rho_A}{2} \cdot |v_A - v_{p0}|^2 \quad (3.27)$$

The drag force F_D depends on the particle drag coefficient, the average cross-sectional area of the particle, the density of the air and on the relative velocity between air and particle. The term $|v_A - v_{p0}| = v_{\text{rel}}$ is the relative velocity between gas flow and particle flow. For very low particles flow velocities, for example, in the entry section of a nozzle, $v_{\text{rel}} = v_A$. The term $1/2 \cdot \rho_A \cdot v_{\text{rel}}^2$ is equal to the dynamic pressure of the air flow.

The drag coefficient is usually unknown and should be measured. It depends on Reynolds number and Mach number of the flow: $c_D = f(Re, Ma)$, whereby the Mach number is important if the air flow is compressible. Settles and Geppert (1997) provided some results of measurements performed on particles at supersonic speeds.

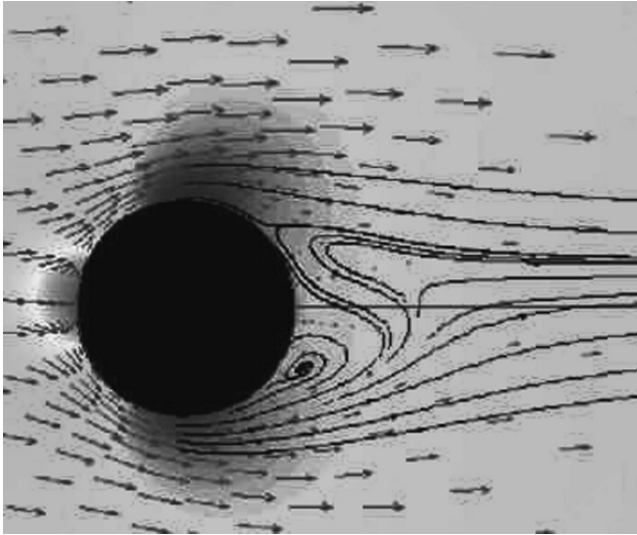


Fig. 3.17 Numerically simulated pressure contours and flow streamlines on a solid particle in a high-speed air flow (image: H.A. Dwyer, University of California, Davis)

Their results, plotted in Fig. 3.18, suggest that the drag coefficient only weakly depends on Reynolds number, but is very sensitive to changes in the Mach number. The c_D -value is rather low at low Mach number values, but it dramatically increases after a value of $Ma = 1$. It finally levels off around a value of unity for Mach numbers greater than $Ma = 1.4$. More information on this issue is delivered by Bailey and Hiatt (1972), who published c_D - Ma - Re data for different nozzle geometries, and by Fokke (1999). Other notable effects on the drag coefficient are basically those

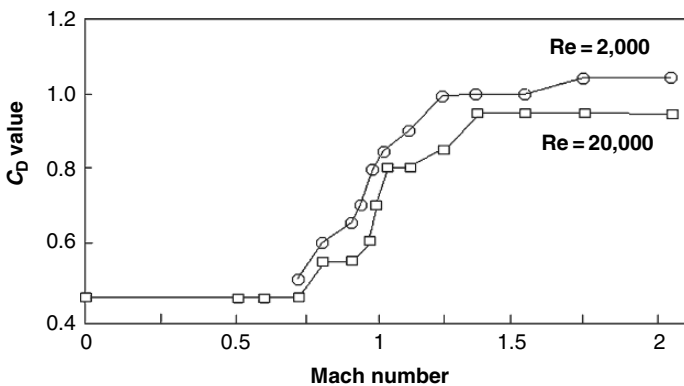


Fig. 3.18 Effects of Mach number and Reynolds number on friction parameter (Settles and Geppert, 1997)

of acceleration, of particle shape and of particle shielding, which are discussed in Brauer's (1971) book.

The air density is, in the first place, a function of pressure and temperature as expressed by (3.6). This is an interesting point because both parameters notably vary over the nozzle length as witnessed by the results of numerical simulations provided in Fig. 3.16a. Both air pressure and air temperature drop if they approach the exit. The relative velocity can, for practical purposes, be replaced by the velocity of the air flow ($v_A \gg v_{p0}$), if the acceleration process starts. In cylindrical nozzles, this velocity cannot exceed the speed of sound (see Sect. 3.2). However, because speed of sound depends on gas temperature (3.9), a theoretical possibility for an increase in drag force due to gas temperature increase exists.

The acceleration acting on a particle during the particle–air interaction can be approximated as follows:

$$a_P = \dot{v}_P = \frac{F_D}{m_P} \quad (3.28)$$

This condition delivers the following relationship:

$$\dot{v}_P \propto \frac{c_D \cdot \rho_A \cdot v_A^2}{d_P \cdot \rho_P} \quad (3.29)$$

Acceleration values for convergent–divergent nozzles were calculated by Achtsnick (2005), who estimated values as high as $a_P = 10^7 \text{ m/s}^2$. This author could also verify the trend expressed in (3.29) for the particle diameter. The particle acceleration increased extraordinarily when the abrasive particle diameter was reduced below $d_P = 10 \text{ }\mu\text{m}$. If particles get smaller, they start to follow the trajectories of air flow they are suspended, and the slip between particles and air flow reduces. The acceleration period required to realise a given final particle speed can be approximated as follows:

$$t_a \propto \frac{v_P \cdot d_P \cdot \rho_P}{c_D \cdot \rho_A \cdot v_A^2} \quad (3.30)$$

Acceleration is, of course, not a constant value over the nozzle length, but (3.29) depicts that acceleration effects are, in general, less severe if particles with larger diameter and larger density are entrained into the air flow. For a desired particle speed, acceleration period (nozzle length) must be increased if heavy (ρ_P), respectively large (d_P), abrasive particles are injected. Acceleration period (nozzle length) can be reduced if air flow density (ρ_A), air flow velocity (v_A) and drag coefficient (c_D) feature high values.

Equation (3.27) must be solved by numerical methods, and numerous authors (Kamzolov et al., 1971; Ninham and Hutchings, 1983; Settles and Garg, 1995; Settles and Geppert, 1997; Johnston, 1998; Fokke, 1999; Achtsnick et al., 2005) utilised such methods and delivered appropriate solutions. Results of such calculation procedures are provided in the following sections.

3.3.2 Simplified Solution

Iida (1996) and Kirk (2007) provided an approximation for the velocity of particles accelerated in a cylindrical blast cleaning nozzle. The solution of Iida (1996) neglects effects of friction parameter and air density. Kirk's (2007) approximation reads as follows:

$$\left(\frac{v_P}{v_A - v_P} \right)^2 = \frac{c_D \cdot L_N}{d_P} \cdot \frac{\rho_A}{\rho_P} \quad (3.31)$$

Due to certain simplifications, this equation can only serve for the assessment of trends, but cannot deliver suitable quantitative results. A solution to (3.31) delivers the following trends:

$$v_P \propto p^{0.68} \quad (3.32a)$$

$$v_P \propto d_P^{-0.36} \quad (3.32b)$$

$$v_P \propto \rho_P^{-0.38} \quad (3.32c)$$

Uferer (1992) applied a simplified numerical procedure for the calculation of abrasive particles accelerated in blast cleaning nozzles. Some results of these calculations for two nozzle layouts are provided in Fig. 3.19. The graphs demonstrate that the utilisation of a Laval nozzle increases the velocities of air and abrasive particles, but the gain is much higher for the air acceleration. The reason is the drop in air density in the divergent section of the Laval nozzle (see Fig. 3.16a). According to (3.27), this causes a reduction in the drag force acting at the particles to be accelerated. Thus, although Laval nozzles are very efficient in air acceleration, they do not increase the abrasive exit speed at an equally high ratio.

3.3.3 Abrasive Flux Rate

The abrasive flux rate through a nozzle (in kg/s per unit nozzle area passing through the nozzle) can be approximated as follows (Ciampini et al., 2003b):

$$\dot{m}_N = \rho_P \cdot v_P \cdot \rho_S^* \quad (3.33)$$

Thus, for a given abrasive material and incident abrasive velocity, interference effects resulting from changes in flux are described by the dimensionless stream density (see Sect. 3.5.5).

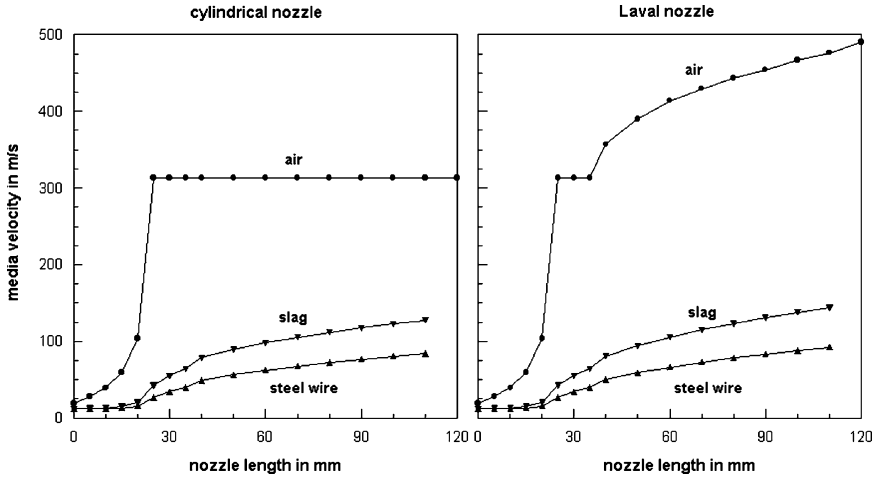


Fig. 3.19 Effects of nozzle layout on calculated air and abrasive velocities (Uferer, 1993)

3.3.4 Abrasive Particle Spacing

The average distance between individual abrasive particles in a blast cleaning nozzle can be approximated as follows (Shipway and Hutchings, 1994):

$$L_p = \left(\frac{m_p \cdot v_p \cdot \pi \cdot r_N^2}{\dot{m}_p} \right)^{1/3} \tag{3.34}$$

Results obtained by Shipway and Hutchings (1994) are listed in Table 3.5. The ratio between spacing distance and abrasive particle diameter had a typical value of about $L_p/d_p = 15$. For a low abrasive mass flow rate, this value increased up to $L_p/d_p = 23$.

Table 3.5 Average distances between abrasive particles in a blast cleaning nozzle (Shipway and Hutchings, 1994)

Particle diameter in μm	Particle velocity in m/s	Abrasive mass flow rate in g/min	Average distance in μm	L_p/d_p
63–75	70	50	900	~ 13
125–150	52	6	3,200	~ 23
212–250	45	31	4,000	~ 17
650–750	29	37	7,900	~ 13

3.4 Jet Structure

3.4.1 Structure of High-speed Air Jets

A schematic sketch of a free air jet is shown in Fig. 3.20. The term “free jet” designates systems where a fluid issues from a nozzle into a stagnant medium, which consists of the same medium as the jet. Two main regions can be distinguished in the jet: an initial region and a main region. The *initial region* is characterised by a potential core, which has an almost uniform mean velocity equal to the exit velocity. The velocity profile is smooth in that region. Due to the velocity difference between the jet and the ambient air, a thin shear layer forms. This layer is unstable and is subjected to flow instabilities that eventually lead to the formation of vertical structures. Because of the spreading of the shear layer, the potential core disappears at a certain stand-off distance. Ambient air entrains the jet, and entrainment and mixing processes continue beyond the end of the potential core. In the *main region*, the radial velocity distribution in the jet finally changes to a pronounced bell-shaped velocity profile as illustrated in Fig. 3.20. The angle θ_J is the expansion angle of the jet. In order to calculate this angle, the border between air jet and surrounding air flow must be defined. One definition is the half-width of the jet defined as the distance between the jet axis and the location where the local velocity $[v_J(x,r)]$ is equal to the half of the local maximum velocity situated on the centreline $[v_J(x,r=0)]$. Achtsnick (2005) who applied this definition estimated typical expansion angles between $\theta_J = 12.5^\circ$ and 15° .

Shipway and Hutchings (1993a) took schlieren images from acetone-air plumes exiting cylindrical steel nozzles at rather low air pressures up to $p = 0.09$ MPa, and they could prove that the plume shape differed just insignificantly if the gas exited either from a nozzle with a low internal roughness ($R_a = 0.25 \mu\text{m}$) or from a nozzle with a rough wall structure ($R_a = 0.94 \mu\text{m}$). This situation changed if abrasive particles were added to the air flow.

The structure of an abrasive jet is disturbed due to rebounding abrasive particles if the nozzle is being brought very close to the specimen surface. This was

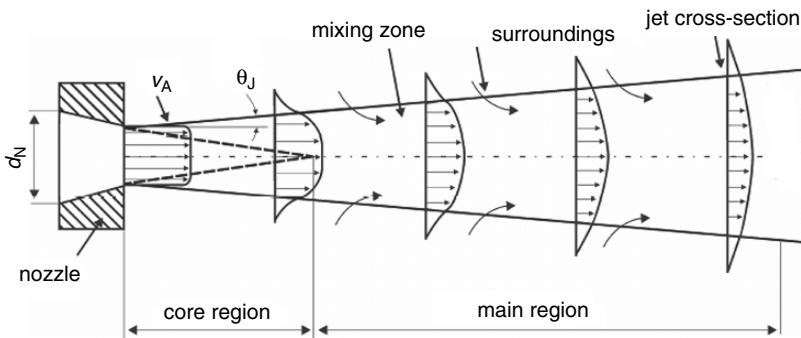


Fig. 3.20 Structure of an air jet issued from a nozzle into stagnant air (adapted from Achtsnick, 2005)

verified by Shipway and Hutchings (1994) who took long-exposure photographs of the trajectories of glass spheres in an air jet and observed many particle trajectories, which deviated strongly from the nozzle axis. It was supposed that these are particles rebounding from the target.

3.4.2 Structure of Air-particle Jets

Plaster (1972) was probably the first who advised the blast cleaning industry into the effect of nozzle configuration on the structure of air-particle jets. The images shown in Fig. 3.21 clearly illustrate the influence of nozzle design on jet stability. Figure 3.21a shows a jet exiting from a badly designed nozzle, which results in a shock wave at the tip (central image) and in an erratic projection of abrasives (right image). A correctly designed nozzle is shown in Fig. 3.21b. This nozzle produces a smooth flow as can be seen by the configuration of the air stream (central image) and by the even projection of the abrasives (right image).

The width (radius) of high-speed air-particle jets at different jet lengths was measured by Fokke (1999) and Slikkerveer (1999). Kirk and Abyaneh (1994) and Slikkerveer (1999) provided an empirical relationship as follows:

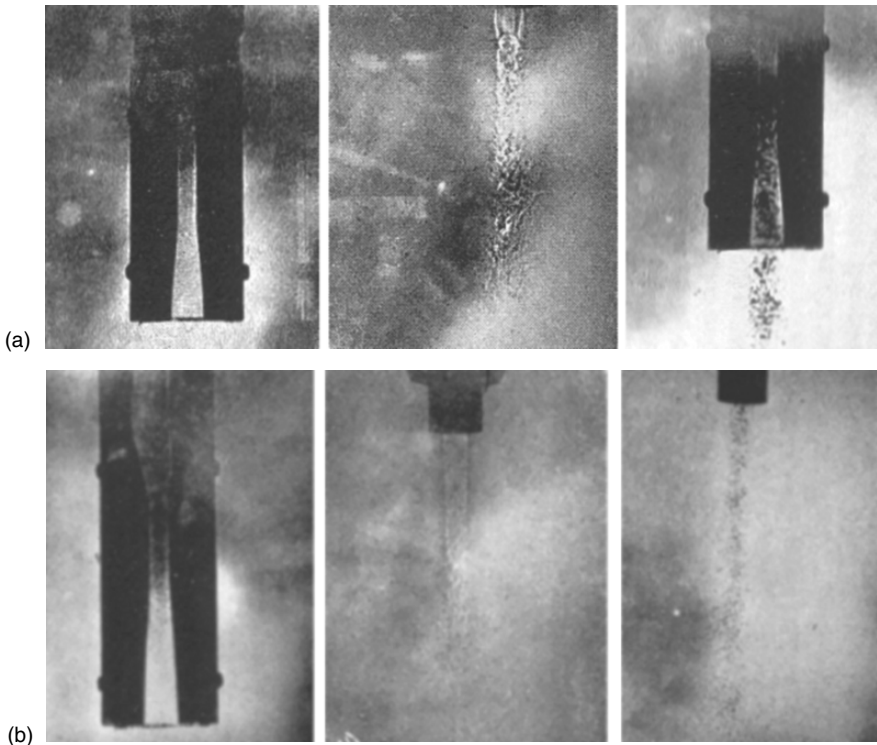


Fig. 3.21 Effect of nozzle design on jet structure and abrasive acceleration (Plaster, 1972). (a) Badly designed nozzle; (b) Correctly designed nozzle

$$d_J = d_N + 2 \cdot x \cdot \tan \theta_J \tag{3.35}$$

The expansion angle can be considered to be between $\theta_J = 3^\circ$ and 7° (Slikkerveer, 1999; Achtsnick et al., 2005). Therefore, it is smaller than for a plain air jet. Results of calculations based on (3.35) for $\theta_J = 5^\circ$ are displayed in Fig. 3.22.

Fokke (1999) found an almost linear relationship between jet half width and jet length. The air mass flow rate showed marginal effects on the half width at longer jet lengths: with an increase in air mass flow rate, half width slightly decreased. Some relationships are illustrated in Fig. 3.23. These results corresponded to that of Mellali et al. (1994) who found a linear relationship between stand-off distance and the area of the cross-section hit by a blast cleaning jet.

Shipway and Hutchings (1993a) took schlieren images from glass bead plumes exiting cylindrical steel nozzles at air pressures up to $p = 0.09$ MPa. They noted a distinct effect of the nozzle wall roughness on the plume shape as a result of the differences in the interaction of the particles with the nozzle wall. Variations in the rebound behaviour of the glass beads on impact with the nozzle wall caused the particles to leave the nozzle exit with different angular distributions. These authors also defined a “plume spread parameter”, respectively a “focus coefficient”:

$$\beta_P = \alpha_P \cdot x \tag{3.36}$$

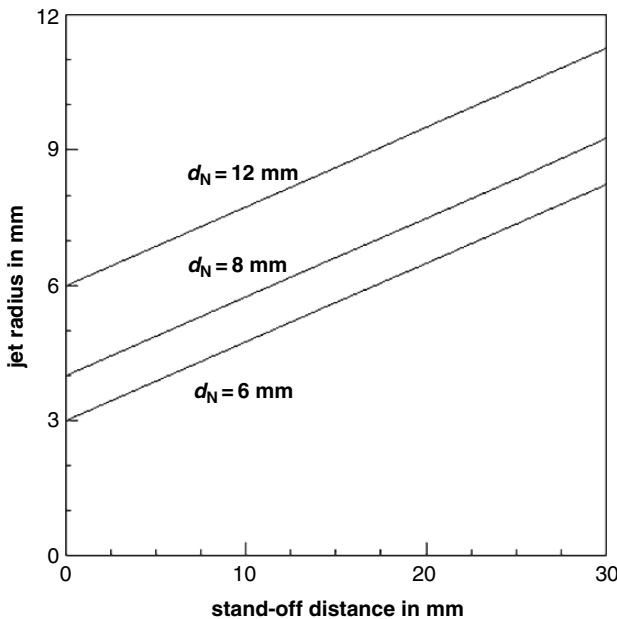


Fig. 3.22 Radius of a particle-air jet according to (3.35)

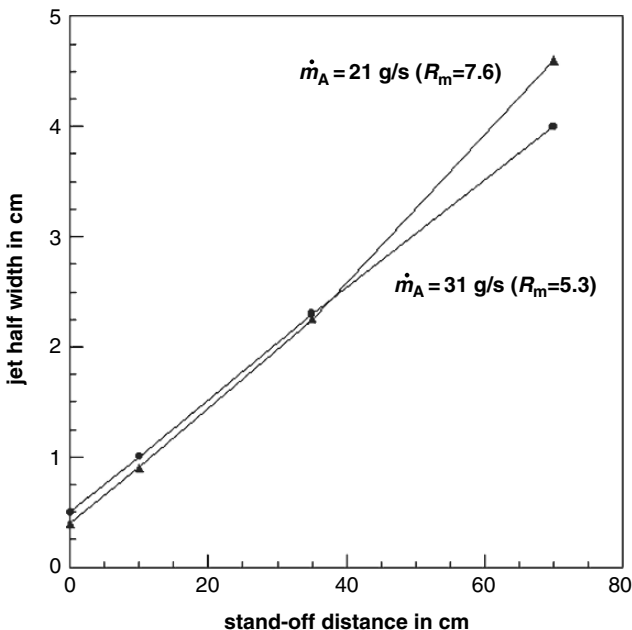


Fig. 3.23 Effects of stand-off distance and air mass flow rate (respectively mass flow ratio abrasive/air) on jet radius (Fokke, 1999)

Here, α_p is a constant that depends on the nozzle configuration. Lower values for α_p mean less spread and vice versa. Shipway and Hutchings (1993a) provided a method for the estimation of the dimensionless *focus coefficient*. It could be shown experimentally that the focus coefficient depended on the roughness of the nozzle wall surface. Results of this investigation are listed in Table 3.6. It was also shown by Stevenson and Hutchings (1995b) that the focus coefficient depended on nozzle length and abrasive particle velocity. It exhibited maximum values at moderate nozzle lengths. If abrasive particle velocity increased, the focus coefficient decreased notably.

3.4.3 Design Nozzle Pressure

Each Laval nozzle (convergent–divergent nozzle) has a so-called *design nozzle pressure* that enables it to produce a supersonic jet of air into the atmosphere with

Table 3.6 Relationships between nozzle wall roughness, abrasive particle type and *focus coefficient* (Shipway and Hutchings, 1993a)

Wall roughness in μm	Focus coefficient	
	Silica	Glass beads
0.94	14	8.7
0.25	22.3	15.2

minimum disturbance. The design criterion is the air pressure at the nozzle exit (P_E). The value for this pressure should be equal to the pressure of the surrounding air (called *back pressure* in the flow dynamics literature). The situation is characterised by the curve “1” in Fig. 3.26. For blast cleaning applications, the back pressure is usually the atmospheric pressure. The design criterion can be written as follows [modified from Bohl’s (1989) book]:

$$\left(\frac{d_E}{d_N}\right)^2 = \left(\frac{\kappa + 1}{2}\right)^{\frac{1}{\kappa-1}} \cdot \left(\frac{P_E}{p}\right)^{\frac{1}{\kappa}} \cdot \left\{ \frac{\kappa + 1}{\kappa - 1} \cdot \left[1 - \left(\frac{P_E}{p}\right)^{\frac{\kappa-1}{\kappa}} \right] \right\}^{1/2} \quad (3.37)$$

For $p_E = p_0$, this equation delivers a ratio between exit diameter and nozzle (throat) diameter, which must be maintained in order to allow an undisturbed air flow at the given nozzle inlet pressure. A graphical solution to (3.37) is provided in Fig. 3.24. If the nozzle dimensions (d_N, d_E) are known, the corresponding *design pressure* can be read from this graph. Only data points located at the solid line correspond to the expansion condition characterised by Fig. 3.25d and by line “1” in Fig. 3.26.

It must be noted, however, that these relationships apply to the flow of plain air only. If solid particles are added, the effects of the particle flow must be considered. Fokke (1999) performed numerical simulations of the nozzle flow, and he could show that the addition of abrasive particles (steel balls, $d_P = 50\text{--}1,000 \mu\text{m}$;

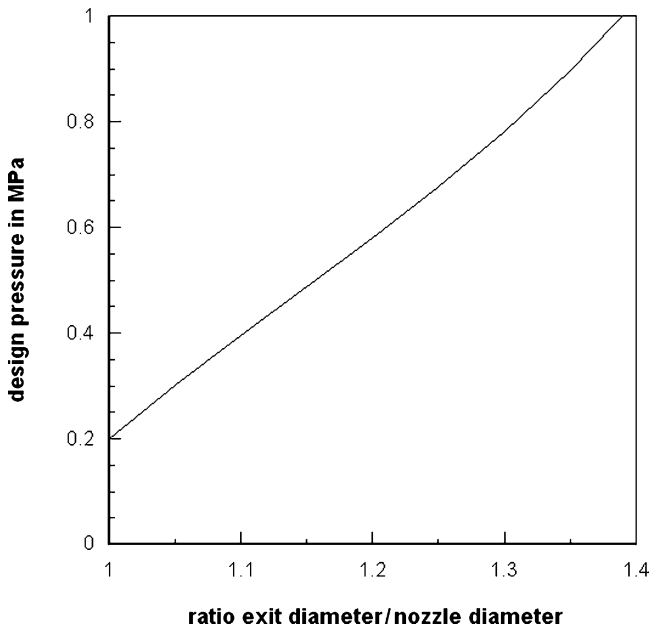


Fig. 3.24 Relationship between nozzle geometry and design pressure for convergent–divergent nozzles. Based on (3.37)

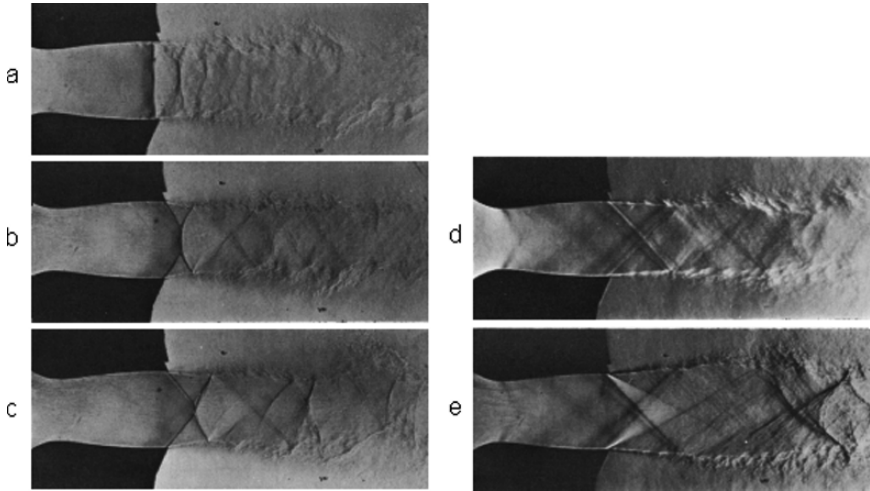


Fig. 3.25 Flow situation near the exit of a convergent–divergent nozzle (Oosthuizen and Carscallen, 1997) **(a)** Overexpanded flow with shock front leaving the nozzle exit; **(b)** Overexpanded flow with disappearing normal central shock front outside the nozzle; **(c)** Overexpanded with oblique shocks outside the nozzle; **(d)** Almost isentropic nozzle flow; **(e)** Underexpanded flow with severe expansion waves outside the nozzle

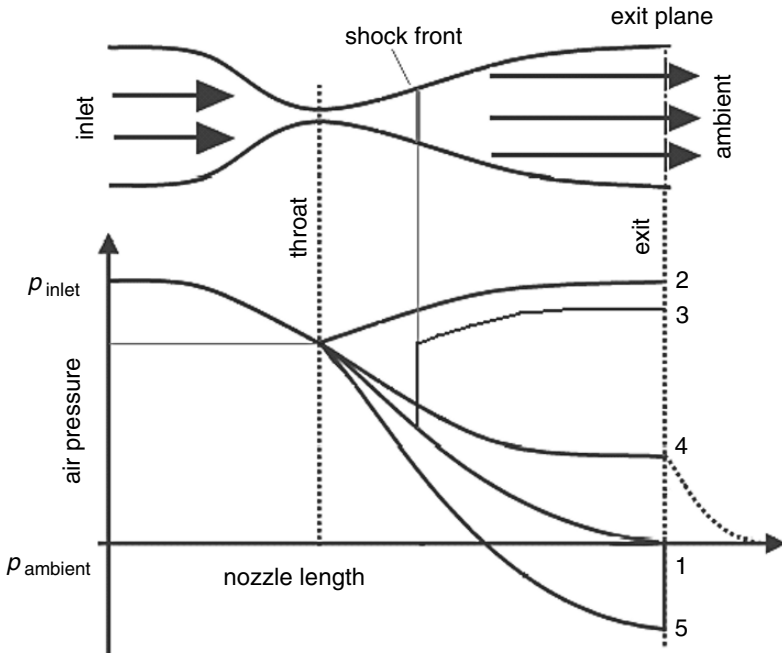


Fig. 3.26 Operating conditions of a convergent–divergent nozzle; see text for “1” to “5” (adapted from Oertel, 2001)

$R_m = 0.1-6$) was sensitive to the nozzle exit pressure. For all loading ratios, exit pressure increased with decreasing particle size. Exit pressure also increased with an increase in the mass flow ratio abrasive/air. Although the nozzle in Fokke's (1999) work was designed in a way that the air exit pressure would meet the atmospheric pressure, the exit pressures were all well below the atmospheric pressure as the abrasive particles were added. Effects of abrasive particle on the gas flow properties in the nozzle vanished for small mass flow rates abrasive/air ($R_m \ll 1$).

It is recommended to run a Laval nozzle at least at the design pressure for the nozzle being used, and at higher pressure if possible. When the nozzle is operated below the design pressure, the flow forms shock waves that slow down air flow as well as abrasive particles. Schlieren optics has been utilised by several authors to reveal such shock wave structures (Settles and Garg, 1995; Mohamed et al., 2003; Kendall et al., 2004). Some images are provided in Figs. 3.25 and 3.27.

Figure 3.26 summarises possible pressure decay modes along a convergent-divergent nozzle operating between nozzle inlet pressure and ambient pressure. Up to the throat, in the divergent section, the nozzle pressure decreases for all flow conditions. If the nozzle is being designed in a way that the nozzle exit pressure meets the atmospheric (back) pressure, the gas exits the nozzle as an undisturbed flow with parallel flow patterns. The flow is isentropic and shock-free. This situation is illustrated through the curve "1" in Fig. 3.26 and the image in Fig. 3.25d. In the situation characterised by the line "2" in Fig. 3.26, the back pressure is higher than the nozzle exit pressure (and also higher than the Laval pressure), but is reduced sufficiently to make the flow reach sonic conditions at the throat ($Ma = 1$). The flow in the divergent section is still subsonic because the back pressure is still high. Under ideal flow conditions (no friction), the exit nozzle pressure is equal to the

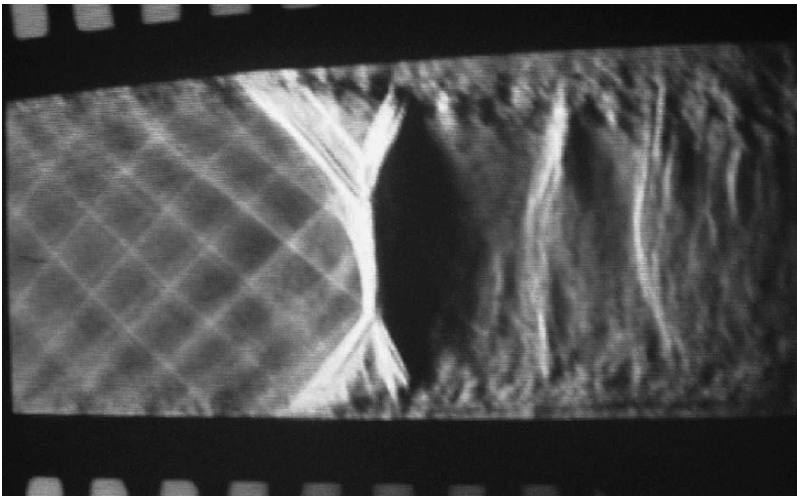


Fig. 3.27 Shock wave in the divergent section of a nozzle, followed by flow separation (image: Mechanical and Aerospace Engineering, University of California, Irvine)

nozzle entry pressure. The line “3” illustrates the situation if the back pressure is further reduced. In that case, a compression shock occurs in the flow in the divergent section of the nozzle. An example for such a shock front is provided in Fig. 3.27. This compression shock front in the divergent part of the nozzle develops normal to the flow, and it generates a “pressure jump”, which is illustrated by the vertical line between line “1” and line “3” in Fig. 3.26. In front of this shock front, the flow is supersonic, whereas the flow behind the shock front moves at subsonic speed. Precise location and strength of the shock front depend on the back pressure. Decreasing the back pressure moves the shock wave downstream, and it finally reaches the nozzle exit plane (see image in Fig. 3.25a). If the back pressure is further reduced, the shock wave moves outside the nozzle, and the “pressure jump” takes place through a series of oblique shock waves. This type of nozzle flow is termed *over-expanded*. Line “4” in Fig. 3.26 and the images in Fig. 3.25b and c illustrate this case. The central shock wave head is at an almost normal position as shown in Fig. 3.25b, but the shock trajectories start to incline as in Fig. 3.25c for the lower back pressure. If the back pressure is further reduced and becomes less than the nozzle exit pressure, the flow expands, and the expansion takes place through a series of expansion waves outside the nozzle. This case is expressed through the line “5” in Fig. 3.26. Such a nozzle flow is termed *under-expanded*. Figure 3.25e provides an example. The system of expansion waves can clearly be distinguished in front of the nozzle exit. More illustrative photographs for the different types of pressure distribution can be found in Oertel (2001), where some very early schlieren images, taken by Ludwig Prandtl in 1907, are presented.

It was found, however, by some investigators that air expansion regime and shock location depended on abrasive parameters as well, namely on abrasive mass flow rate and abrasive particle size and density (Komov 1966; Myshakov and Shirokov, 1981; Fokke, 1999; Achtsnick et al., 2005). Komov (1966) found that the degree of air expansion was less for a particle-laden flow compared with the plain gas flow. This difference increased as the mass flow ratio abrasive/air increased. The authors also took images from shock fronts in a flow of air as well as in a particle-laden air flow, and they found that the shock front in the particle-laden air flow was located further upstream. They noted that this effect was most pronounced for high mass flow rates abrasive/air and smaller particles.

The operating characteristics of convergent nozzles and convergent–divergent nozzles are in detail described and discussed by Oosthuizen and Carscallen (1997). Schlieren images of shock waves formed in nozzles and in the exiting air jets under certain operating conditions can be found in Oertel’s (2001) book. Examples of air jets formed under different operating conditions are shown in Fig. 3.25. Sakamura et al. (2005) have shown that pressure-sensitive paint technique can very well capture pressure maps for the two-dimensional flow in a convergent–divergent nozzle, and these results offer the opportunity for adding more knowledge to this issue. The shock characteristics in blast cleaning nozzles can be modelled with commercially available software programmes. An example is provided in Fig. 3.16b.

3.5 Composition of Particle Jets

3.5.1 Radial Abrasive Particle Distribution

Adlassing (1960) designed a special device for the assessment of the radial distribution of abrasive particles in an air jet exiting from blast cleaning nozzles. Interestingly, no distinguished effects of nozzle geometry (e.g. nozzle length) could be noted. General results were as follows: the inner core (24 cm² cross-section) consumed between 20 and 25 wt.% of all particles; the medium section (76 cm² cross-section) consumed between 45 and 45 wt.% of all abrasives; the external section (2,150 cm² cross-section) consumed between 25 and 30 wt.% of all abrasives. A curvature of the entry section of the nozzle did not change the distribution. The width of the particle-occupied section of a jet decreased if air pressure rose.

Particle density distribution over the nozzle exit cross-section is difficult to measure directly, and no systematic experimental study is known dealing with this issue. Achtsnick (2005) has subjected a polished glass plate to an abrasive particle flow formed in a blast cleaning nozzle. The visible impacts were microscopically detected and counted regardless their sizes. The results are presented in Fig. 3.28, and they demonstrated that the particles were essentially centred near the nozzle axis. Outside the centre, the number of impacts decreased sensitively towards the borders of the flow. The resulting particle concentration inside a cylindrical nozzle exit was of a bell-shape type. Outside the circle, drawn in Fig. 3.28, particle impacts occurred only incidentally. The same test was repeated for the perpendicular scanning direction and delivered equal results.

In order to get further information on the particle distribution, numerical simulations have been performed for different nozzle configurations by Achtsnick et al. (2005) and McPhee (2001). Results of these simulations are provided in Figs. 3.29 and 3.30. It can be seen that abrasive particle density distribution notably depended on nozzle layout and abrasive particle size. Effects of nozzle layout are illustrated in Fig. 3.29. According to these images, a Laval nozzle with a modified abrasive entry channel and a rectangular nozzle exit cross-section provided a more even distribution of the particles over the cross-section, whereas the conventional cylindrical nozzle design resulted in a concentration of abrasive particles in the central area of the nozzle cross-section. Some comparative measurements verified these trends (Achtsnick et al., 2005). The images in Fig. 3.30 characterise the effects of abrasive diameter on the particle density distribution in conventional round nozzles. In both cases, particles were concentrated in the centre of the nozzle cross-section, but the particle distribution was more favourable for the smaller abrasives.

3.5.2 Particle Velocity Distribution Function

Achtsnick (2005), Hamed and Mohamed (2001), Linnemann (1997), Linnemann et al. (1996), Slikkerveer (1999), Stevenson and Hutchings (1995) and Zinn et al.

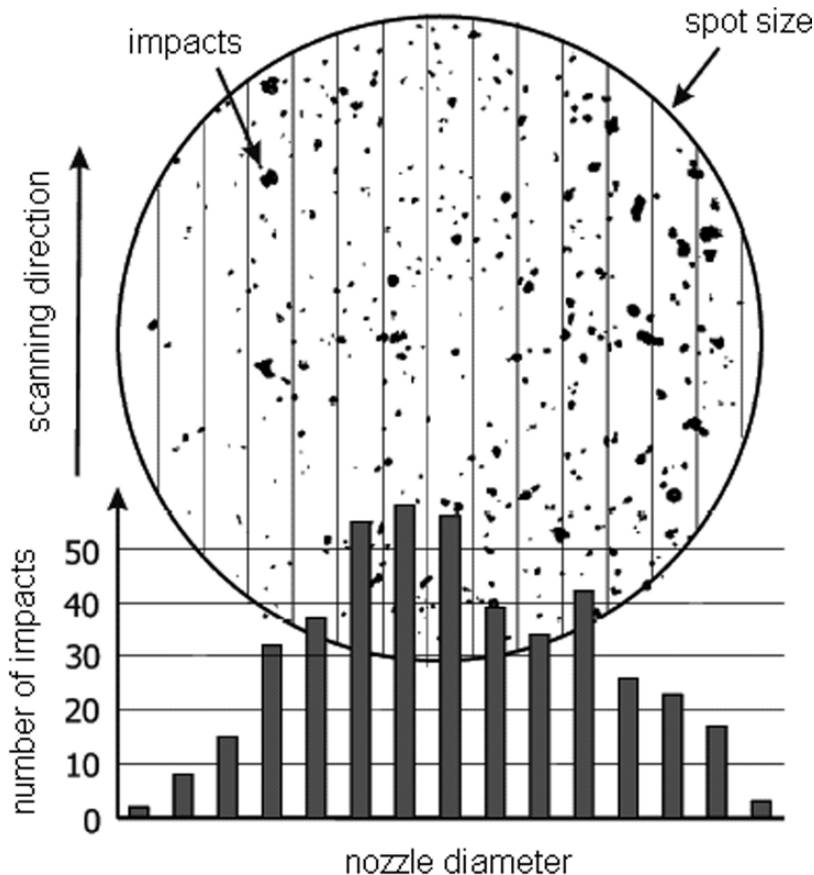


Fig. 3.28 Suggested abrasive particle distribution in the exit plane of a blast cleaning nozzle, based on impact spot inspections (Achtsnick, 2005)

(2002) experimentally investigated the statistical distribution of abrasive particle velocities in air-abrasive jets. The authors found velocity distributions as shown in Figs. 3.31 and 3.32. Figure 3.31 displays results of measurements of the velocities of aluminium oxide powder particles (mesh 360) accelerated in a convergent–divergent nozzle at two different air pressures. As expected, the average particle velocity increased with an increase in air pressure. Similar is the situation for the two graphs plotted in Fig. 3.32. In that case, silica sand particles were accelerated in a convergent-parallel nozzle. A Gaussian normal distribution could be applied to mathematically characterise the distribution of the axial particle velocity:

$$f(v_P) = \frac{1}{\sqrt{2 \cdot \pi} \cdot \sigma_{v_P}} \cdot \exp \left[\frac{-(v_P - \bar{v}_P)^2}{2 \cdot \sigma_{v_P}^2} \right] \tag{3.38}$$

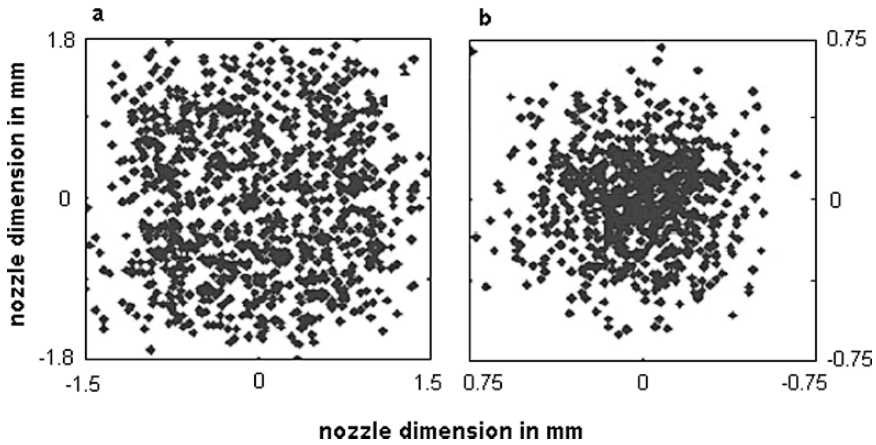


Fig. 3.29 Abrasive particle distributions in the exit planes of blast cleaning nozzles (Achtsnick et al., 2005). (a) Square convergent–divergent nozzle; (b) Conventional cylindrical nozzle

Typical values were $\bar{v}_p = 75$ m/s for the average axial particle velocity and $\sigma_{VP} = \pm 10$ m/s for the standard deviation of the axial abrasive particle velocity (Stevenson and Hutchings, 1995); and $\bar{v}_p = 15$ m/s for the average axial particle velocity and $\sigma_{VP} = \pm 5$ m/s for the standard deviation of the axial abrasive particle velocity (Linnemann, 1997). Lecoffre et al. (1993) found that the spreading of axial velocity distribution decreased as the nozzle diameter increased. Fokke (1999) has shown that particle velocity standard deviation slightly increased if air pressure rose, and he also found that the standard deviation did not change notably when the mass flow ratio abrasive/air ($R_m = 1.0\text{--}4.5$) or the stand-off distance (up to $x = 80$ mm) was varied.

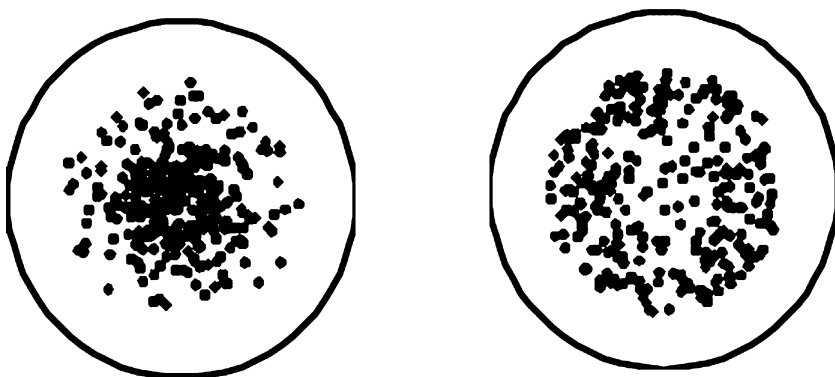


Fig. 3.30 Abrasive particle distributions in the exit plane of a round blast cleaning nozzle (McPhee, 2001). Abrasive material: steel grit; left: $d_p = 820$ μm ; right: $d_p = 300$ μm

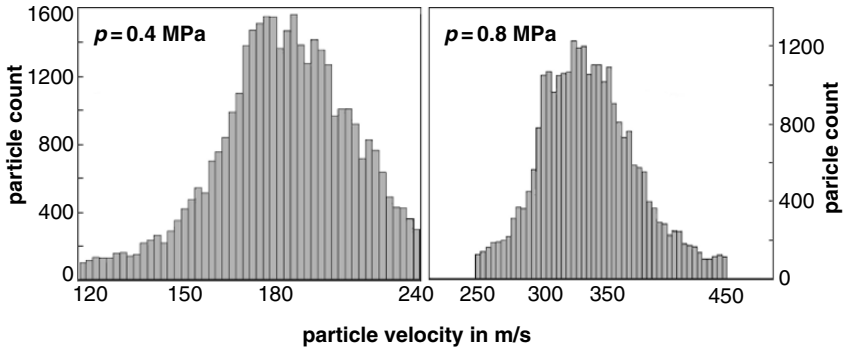


Fig. 3.31 Abrasive particle distributions in abrasive air jets; measurements with aluminium oxide powder (mesh 360) for two pressure levels in a convergent–divergent nozzle (Achtsnick, 2005)

Average particle velocity and abrasive particle velocity standard deviation are not independent on each other; this was shown by Zinn et al. (2002) based on experimental results with rounded-off wire shot. Typical values for the standard deviation were between $\sigma_{VP} = 1.2$ and 2.7 m/s for average abrasive velocities between $\bar{v}_p = 20$ and 47 m/s. The relationships were complex, and parameters which affected these relationships included nozzle type, abrasive particle size and abrasive mass flow rate.

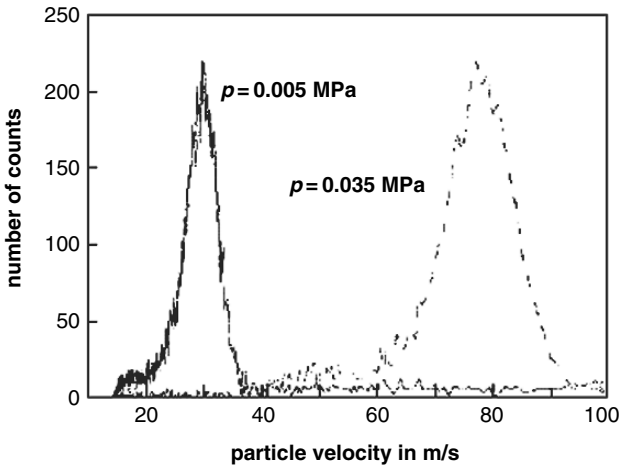


Fig. 3.32 Abrasive particle distributions in abrasive air jets; measurements with silica particles ($d_p = 125\text{--}150\ \mu\text{m}$) for two low pressure levels in a cylindrical nozzle (Stevenson and Hutchings, 1995). Pressure is gauge pressure

3.5.3 Radial Abrasive Particle Velocity Distribution

Results of measurements of abrasive particle velocities over the cross-sections of two nozzles are plotted in Fig. 3.33. Radial abrasive velocity depended notably on nozzle design and air pressure. It can be seen that the cylindrical nozzle (left graph) featured a typical bell-shaped velocity profile. Such profiles are typical for standard Laval nozzles as well (Johnston, 1998). The modified Laval nozzle with a rectangular cross-section (right graph), however, approached a more favourable rectangular velocity distribution. It can also be seen that high air pressure deteriorated the particle velocity profile. The bell-shape was most pronounced for the highest air pressure.

Figure 3.34 shows results of erosion spot topography measurements performed by Johnston (1998). The term “erosion potential” is equal to the local material

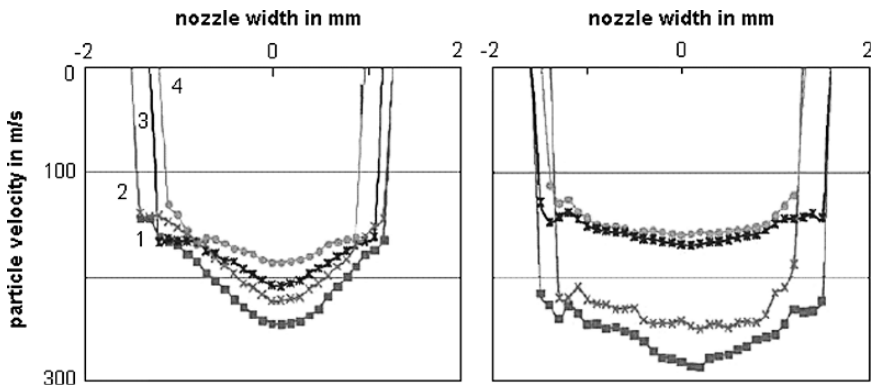


Fig. 3.33 Radial abrasive particle velocity distributions in blast cleaning nozzles (Achtsnick et al., 2005). Left: conventional nozzle; right: square Laval nozzle; Pressure levels: “1” – $p = 0.8$ MPa; “2” – $p = 0.6$ MPa; “3” – $p = 0.5$ MPa; “4” – $p = 0.4$ MPa

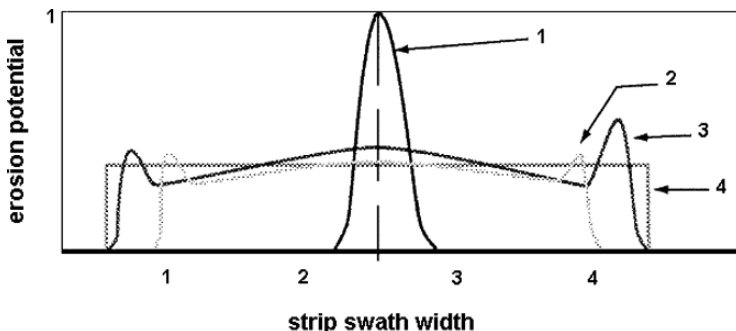


Fig. 3.34 Erosion potential for different nozzle geometries (Johnston, 1998); $p = 0.28$ MPa, $\dot{m}_p = 5.4$ kg/min, $\varphi = 45^\circ$, $x = 51$ mm; “1” – Laval design; “2” and “3”: modified nozzles; “4” – ideal distribution

removal depth in a special model material. The standard Laval nozzle (designated “1”) generated a small but deep spot formed due to a highly uneven localised erosion potential. The erosion potential was very high at the centre, but was restricted to this central range only. The two “modified” nozzles generated a much more even distribution. The erosion potential was equally distributed over almost the entire width. Only at the rim, there was an increase in the erosion potential. The curve “4” illustrates the erosion potential of an “ideal” blast cleaning nozzle. Here, the erosion potential was equally distributed over the entire strip swath width.

3.5.4 Area Coverage

Aspects of area coverage are illustrated in Figs. 3.35 and 3.36. Figure 3.35 shows images of two dent distributions, whereby the dents are the impressions formed on the target surface due to abrasive particle impingement. Measurements performed by Tosha and Iida (2001) have shown that dent distribution density [dent number/(s · m²)] decreased if abrasive particle diameter increased. Figure 3.36 is a typical area coverage graph, where the area coverage is plotted against the exposure time. The area coverage can be calculated as follows (Kirk and Abyaneh, 1994; Karuppanam et al., 2002):

$$C_A(t_E) = 100 \cdot \left[1 - \exp \left(- \frac{3 \cdot r_1^2 \cdot \dot{m}_p \cdot t_E}{4 \cdot A_G \cdot r_p^3 \cdot \rho_p} \right) \right] \quad (3.39)$$

The trend between area coverage and abrasive mass flow rate was experimentally verified by Hornauer (1982). The author also found that values for the area coverage decreased if the traverse rate of the blast cleaning nozzle increased. Because of $t_E \propto v_T^{-1}$, this result also supports the validity of (3.39).

A typical area coverage function can be subdivided into two sections: (1) initial area coverage and (2) full area coverage. This is illustrated in Fig. 3.36. It was experimentally verified (Tosha and Iida, 2001) that the initial area coverage depended, among others, on abrasive particle diameter (initial area coverage dropped if abrasive diameter increased) and abrasive particle velocity (initial area coverage increased if abrasive particle velocity increased). The critical exposure time, where full area coverage started, depended on process parameters as follows (Tosha and Iida, 2001):

$$t_F \propto \frac{d_p^{1/2} \cdot H_M^{1/2}}{v_p} \quad (3.40)$$

3.5.5 Stream Density

Ciampini et al. (2003a) introduced a dimensionless stream density, the geometric basis of which is illustrated in Fig. 3.37a, and derived the following expression:

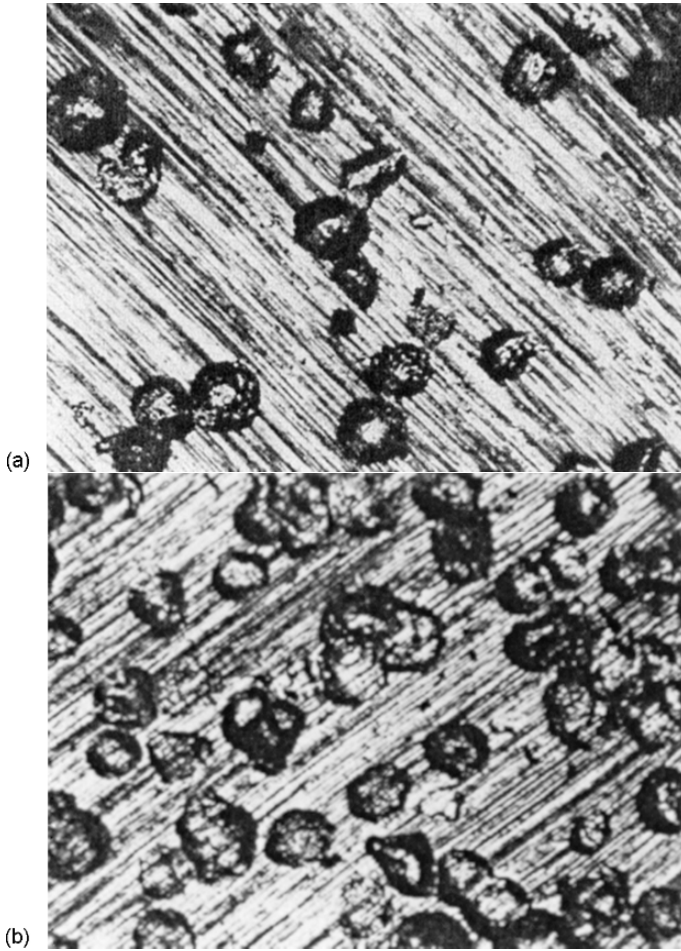


Fig. 3.35 Aspects of area coverage (Meguid and Rabie, 1986). **(a)** Coverage: 16%; **(b)** Coverage: 52%

$$\rho_s^* = \frac{4 \cdot r_p^{*3}}{3 \cdot r_N^{*2} + 3 \cdot r_N^* \cdot x^* \cdot \tan \theta_j + x^{*2} \cdot \tan^2 \theta_j} \quad (3.41)$$

The dimensionless numbers in (3.41) read as follows. The dimensionless nozzle radius is defined as follows:

$$r_N^* = \frac{\dot{N}_p \cdot r_N}{v_p} \quad (3.42)$$

It is the number of particles launched in the time taken for a particle of average velocity to travel a distance equal to the nozzle radius. The dimensionless particle radius is defined as follows:

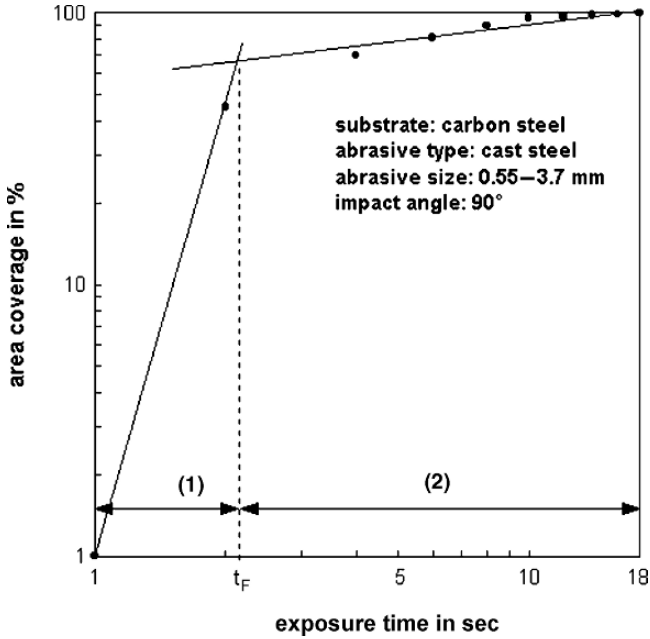


Fig. 3.36 Relationship between exposure time and area coverage (Tosha and Iida, 2001)

$$\Gamma_P^* = \frac{\dot{N}_P \cdot \Gamma_P}{v_P} \tag{3.43}$$

It is the number of particles launched in the time taken for a particle of average velocity to travel a distance equal to the particle radius. The dimensionless stand-off distance is defined as follows:

$$x^* = \frac{\dot{N}_P \cdot x}{v_P} \tag{3.44}$$

It is the number of particles launched in the time taken for a particle of average velocity to travel a distance equal to the stand-off distance between nozzle exit and target surface. The stream density can be applied to the calculation of a relative distance between abrasive particles as follows:

$$L_P^* = \frac{L_P}{d_P} = \left(\frac{\pi}{6 \cdot \rho_S^*} \right)^{1/3} \tag{3.45}$$

This parameter characterises the ratio between the average distance of two incident particles and the particle diameters.

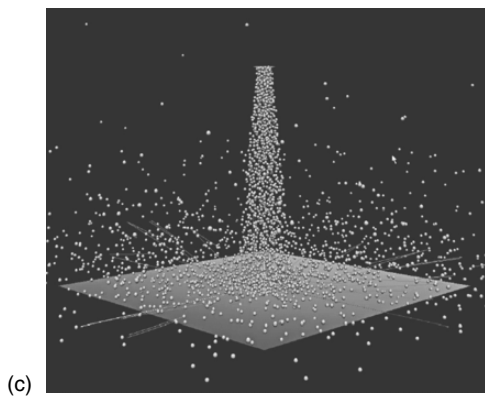
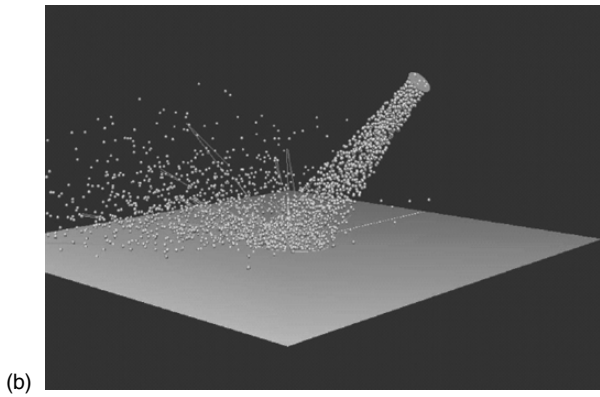
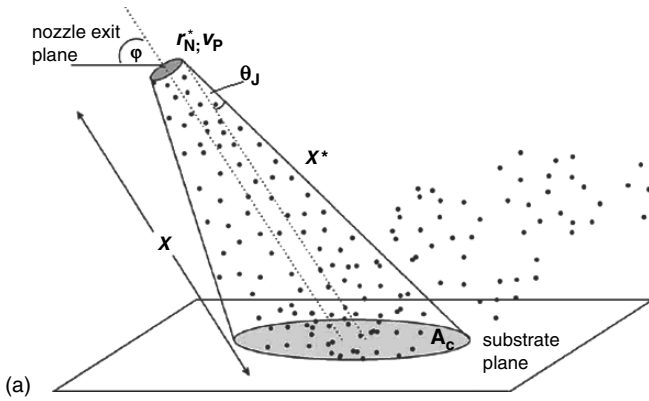


Fig. 3.37 Stream density (Ciampini et al., 2003a). (a) Geometric condition; (b) Simulation for oblique impact; (c) Simulation for normal impact

3.6 Parameter Effects on Abrasive Particle Velocity

3.6.1 Effects of Air Pressure on Particle Velocity

Tilghman (1870), in his original patent, wrote: “*The greater the pressure of the jet the bigger will be the velocity imparted to the grains of sand.*” Generally, the relationship between air pressure and particle velocity can be described as follows:

$$v_p \propto p^{n_v} \quad (3.46)$$

The power exponent n_v seemed to depend on numerous process parameters, among them the abrasive mass flow rate. Some authors (Green et al., 1981; Lecoffre et al., 1993; Linnemann, 1997; Remmelts, 1969; Ruff and Ives, 1975) found a linear relationship between air pressure and abrasive particle velocity ($n_v = 1$). Remmelts (1969) reported that the coefficient of proportionality depended on abrasive type. It was high for slag material (low material density) and low for cut steel wire (high material density). Results delivered by Belloy et al. (2000), Clausen and Stangenberg (2002), Linnemann et al. (1996), Ninham and Hutchings (1983), Stevenson and Hutchings (1995) and Zinn et al. (2002), however, suggest a power exponent $n_v < 1$ for numerous abrasive materials (e.g. glass beads, steel shot and ceramic abrasives). A solution to (3.31) delivers $n_v = 0.68$. Achtsnick (2005) performed a regression of experimentally estimated aluminium oxide particle (mesh 360) velocities in a cylindrical nozzle, and he estimated a power exponent of $n_v = 0.52$. Results of numerical simulations and of measurements performed by Fokke (1999) are displayed in Figs. 3.38 and 3.39. The results plotted in Fig. 3.39 suggest a power exponent of $n_v = 0.6$. These rather large deviations in the values could be attributed to the effects of other process parameters, namely abrasive mass flow rate and nozzle design, but also to assumptions made for the calculation procedures. Figure 3.39 illustrates the effect of the abrasive particle size on the power exponent. There is only a marginal effect of the particle diameter on the power exponent.

A rise in air pressure increases air density as well as air flow velocity; both effects contribute to an increase in the drag force according to (3.27). Measurements performed by Bothen (2000) have shown the following (particle diameter between $d_p = 23$ and $53 \mu\text{m}$): abrasive particle velocity increased by +35% if the air pressure rose from $p = 0.2$ to 0.4 MPa; if air pressure rose from $p = 0.4$ to 0.6 MPa, abrasive particle velocity increased by +25%.

3.6.2 Effects of Abrasive Mass Flow Rate on Particle Velocity

Experimental results have shown that abrasive particle velocity dropped with an increase in the abrasive mass flow rate (Pashatskii et al., 1970; Green et al., 1981;

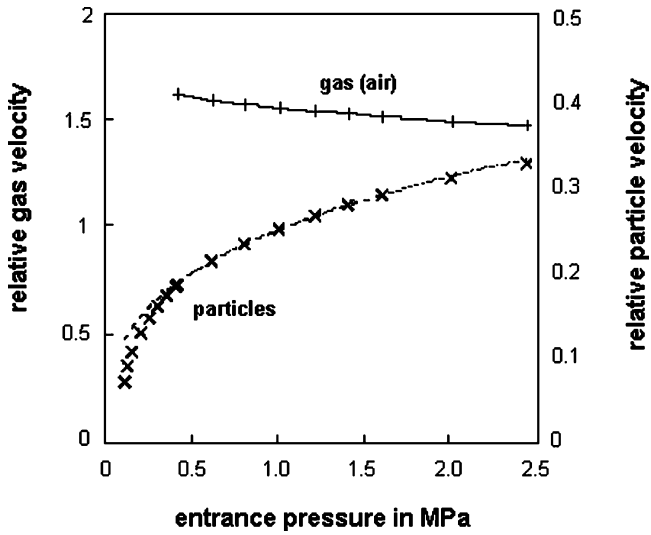


Fig. 3.38 Effect of air pressure on relative air velocity and relative particle velocity (Fokke, 1999). (Relative velocity is the ratio between actual velocity and velocity of sound.)

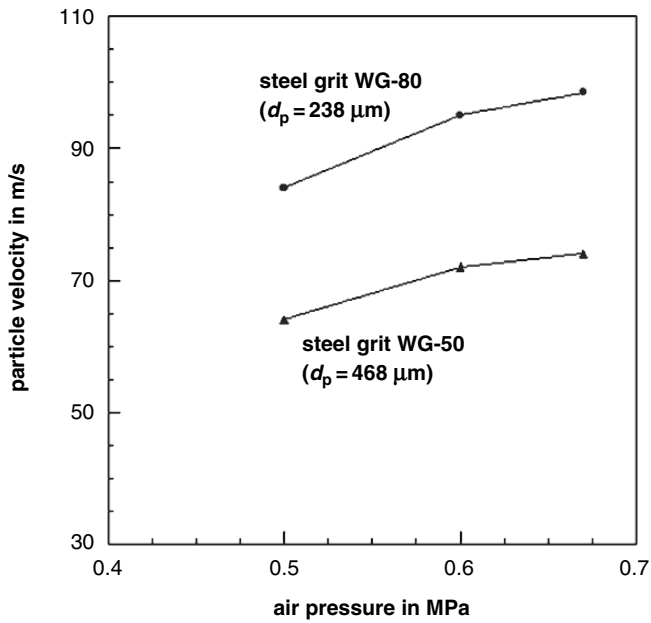


Fig. 3.39 Effects of air pressure and abrasive particle size on particle velocity (Fokke, 1999)

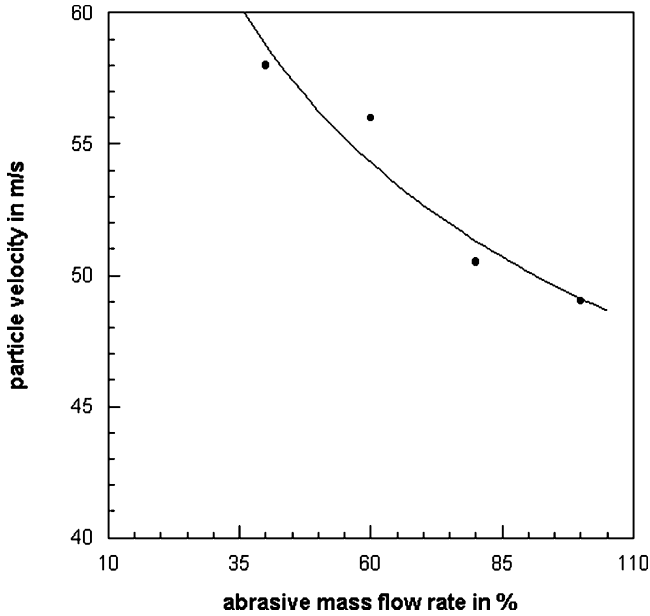


Fig. 3.40 Effect of relative abrasive mass flow rate on particle velocity (Lecoffre et al., 1993)

Lecoffre et al., 1993; Linnemann et al., 1996; Zinn et al., 2002). An example is shown in Fig. 3.40. The general trend is as follows:

$$v_P \propto \dot{m}_P^{-n_m} \quad (3.47)$$

The power exponent has values of $0 < n_m \leq 1$. If the impulse flow (respectively force) of the air flow according to (3.25) is considered, a value for the power exponent of $n_m = 1$ could be derived as a preliminary number.

Figure 3.41 shows the effects of changes in the mass flow ratio abrasive/air on the particle velocity. It can be seen that the particle velocity dropped if the mass flow ratio abrasive/air increased. This trend was observed by Hauke (1982), Pashatskii et al. (1970) and Wolak et al. (1977). The trend seemed to depend on the nozzle diameter for rather small R_m -values, and the influence of the nozzle diameter seemed to vanish for high values of R_m . Wolak et al. (1977) derived the following empirical relationship:

$$v_P \propto \exp(-k_R \cdot R_m) \quad (3.48)$$

Numerical simulations performed by Fokke (1999) for mass flow ratios up to $R_m = 6$ verified this trend: particle velocity dropped if mass flow ratio was increased. The author could also show that the effect of the mass flow ratio abrasive/air on particle velocity was largest for ratios between $R_m = 0.1$ and 3.0.

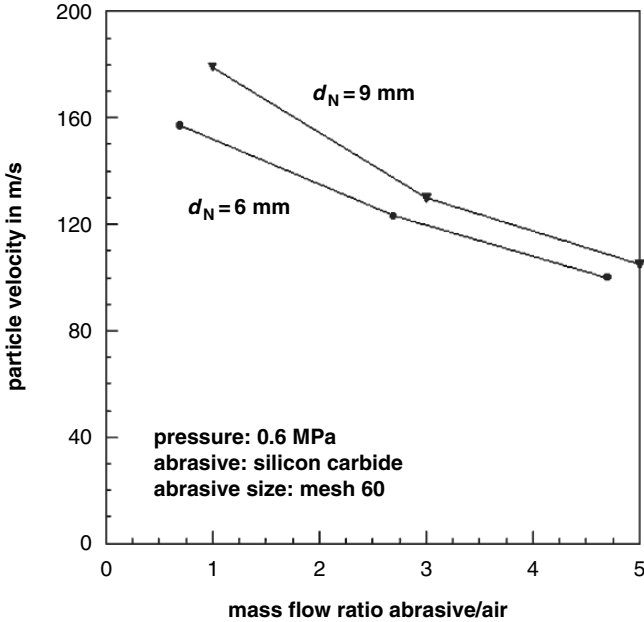


Fig. 3.41 Effects of mass flow ratio abrasive/air and nozzle diameter on particle velocity (Wolak et al., 1977)

3.6.3 Effects of Abrasive Particle Size on Particle Velocity

Measurements performed by several authors have shown that abrasive particle velocity dropped with an increase in the abrasive particle size. This trend was verified through experimental results provided by Achtsnick (2005), Fokke (1999), McPhee (2001), McPhee and Ebadian (1999), Neilson and Gilchrist (1968), Pashatskii et al. (1970), Stevenson and Hutchings (1995) and Zinn et al. (2002). Examples are shown in Fig. 3.39 and in Figs. 3.42–3.44. Achtsnick (2005) and Stevenson and Hutchings (1995) applied different nozzle types, and they measured particle velocities of particles in the diameter range between $d_p = 63$ and 500 μm . They derived the following regression function:

$$v_p \propto d_p^{-n_d} \quad (3.49)$$

The power exponent took a value of $n_d = 0.29$ for a cylindrical nozzle (Stevenson and Hutchings, 1995), and it took a value of $n_d = 0.36$ for a Laval nozzle with a square cross-section (Achtsnick, 2005). A solution to (3.31) delivers $n_d = 0.36$. Larger particles offer a larger projection area, which, according to (3.27), allows higher friction forces. However, due to their higher weight, larger particles need a longer acceleration distance to achieve a demanded final velocity according to (3.29). Fokke (1999) as well as Settles and Garg (1995) performed numerical

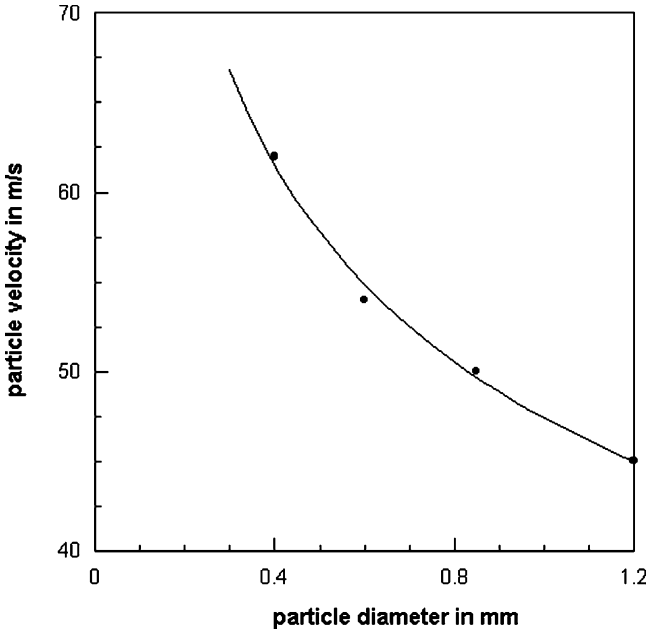


Fig. 3.42 Effect of abrasive particle diameter on particle velocity (Lecoffre et al., 1993)

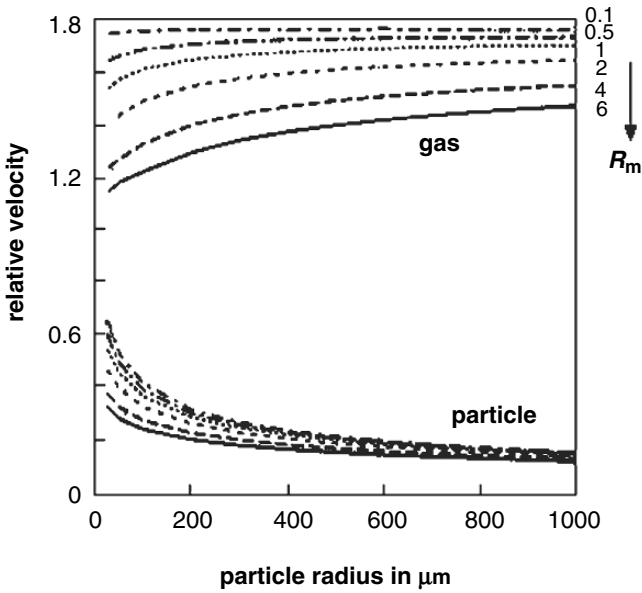


Fig. 3.43 Effects of abrasive particle diameter and mass flow ratio abrasive/air on relative particle velocity and relative air velocity (Fokke, 1999). (Relative velocity is the ratio between actual velocity and velocity of sound.)

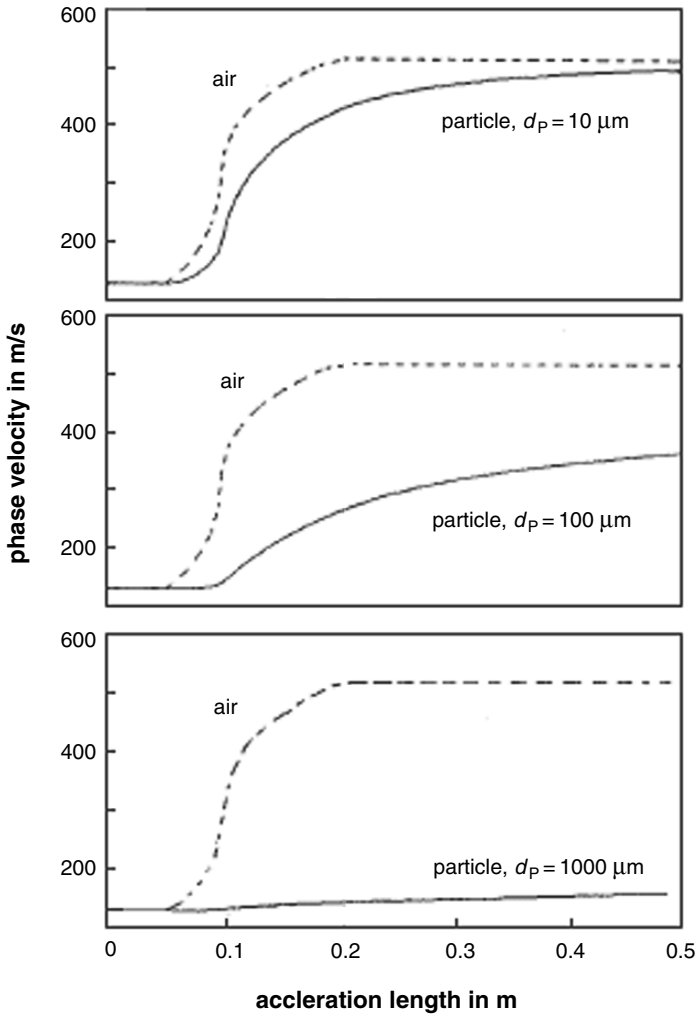


Fig. 3.44 Effect of abrasive particle diameter on particle velocity gradient in a convergent-divergent nozzle (Settles and Garg, 1995)

simulations for Laval-type nozzles, and they could prove that smaller abrasive particles could achieve higher velocities. Results of investigations are shown in Fig. 3.44. A particle with $d_p = 10 \mu\text{m}$ reached a nozzle exit velocity of about $v_p = 500 \text{ m/s}$, whereas a particle with a diameter of $d_p = 1,000 \mu\text{m}$ reached a velocity of about $v_p = 150 \text{ m/s}$ only. The $10 \mu\text{m}$ particles lagged behind the airflow somewhat, but managed to achieve more than 80% of the air velocity at the nozzle exit. The $100 \mu\text{m}$ particles lagged more seriously and reached only about half the air velocity at the nozzle exit. The $1,000 \mu\text{m}$ particles were barely accelerated at all by the air flow in the nozzle. Settles and Garg (1995) performed measurements of the velocities

of steel particles ($d_p = 50\text{--}70\ \mu\text{m}$) and aluminium particles ($d_p = 50\text{--}70\ \mu\text{m}$) accelerated in convergent–divergent nozzles, and they found excellent agreement between the measured velocities and the velocities calculated with their simulation method. The gain in using smaller abrasive particles was especially evident for short nozzles. If longer nozzles were utilised, the influence of the abrasive particle diameter became less important.

3.6.4 Effects of Abrasive Particle Shape on Particle Velocity

A very early statement on the effect of the abrasive particle shape on the particle velocity, based on experimental results, was due to Rosenberger (1939): “*The shape of the abrasive particles also influences the velocity. Spherical particles travel slower than angular particles, other conditions being equal.*”

Shipway and Hutchings (1993a) found experimentally that glass spheres achieved lower final velocities than irregular silica particles for a given air pressure for many nozzle types. They attributed this effect for two reasons. Firstly, the irregularity of the silica shapes means that each particle with a given (sieve) diameter may have less mass than a sphere of this diameter, and may also have a greater drag coefficient. Secondly, the rebound behaviour of spheres and angular particles at the nozzle walls will differ. For a sphere, the rebound angle tended to be equal to or larger than the approach angle. An angular particle can rotate on impact, leading to a rebound angle which can be smaller than the approach angle. This may lead to higher acceleration along the nozzle, and therefore a greater final velocity. Fokke (1999) applied a numerical procedure developed for spherical steel particles and compared the numerical results with experimental results obtained with irregular steel grit particles. He noted a 20% difference between numerical and experimental results. This 20% increase in abrasive particle velocity for grit particles is, however, a very preliminary number, and further research is needed.

3.6.5 Effects of Abrasive Material Density on Particle Velocity

A very early statement on the effect of the abrasive material density on the particle velocity, based on experimental results, was due to Rosenberger (1939): “*The abrasive velocity bears some relation to the specific gravity of the abrasive material, being lowest when the specific gravity is high and vice versa.*”

Results from measurements performed by Stevenson and Hutchings (1995) with a cylindrical nozzle in the abrasive material density range between $\rho_p = 2,500\ \text{kg/m}^3$ (glass beads) and $5,600\ \text{kg/m}^3$ (zirconia sand), and investigations performed by Neilson and Gilchrist (1968a) and by Remmelts (1969) have shown that particle velocity dropped if particle material density increased. An empirical relationship reads as follows:

$$v_p \propto \rho_p^{-n_p} \quad (3.50)$$

Stevenson and Hutchings (1995) estimated a value of $n_p = 0.54$. A solution to (3.31) delivers $n_p = 0.39$. This inverse relationship is basically due to the larger momentum of the heavier abrasive material, which, for equal particle diameter, requires longer acceleration distances. For longer nozzles, the difference in the terminal velocity will therefore reduce. Remmelts (1969) reported a velocity ratio of 1.45 for the velocities of crushed slag ($\rho_p = 2,900 \text{ kg/m}^3$) and cut steel wire ($\rho_p = 7,800 \text{ kg/m}^3$), which agrees well with the values plotted in Fig. 3.19.

If (3.50) is combined with (3.49), an *abrasive parameter* could be defined for cylindrical nozzles, which determines the effects of abrasive material parameters on the abrasive particle velocity:

$$v_p \propto \underbrace{d_p^{-n_d} \cdot \rho_p^{-n_p}}_{\text{abrasive parameter}} \quad (3.51)$$

Heavier particles (e.g. with higher density and larger diameter) would need a longer acceleration distance compared with lighter particles; the relationship is $a_p \propto (d_p \cdot \rho_p)^{-1}$ from (3.29). For a given acceleration distance, particle speed will, therefore, be lower for a heavy particle. This simple argument can partly explain the effects of particle diameter and particle material density.

3.6.6 Effects of Stand-off Distance on Particle Velocity

Bothen (2000), Fokke (1999), Uferer (1992) and Wolak et al. (1977) performed studies into the effects of the stand-off distance on the velocity of abrasive particles. Results of these studies are displayed in Figs. 3.45–3.47. Figure 3.39 shows the effect of variations in stand-off distance on the relative abrasive particle velocity. It was evident that an optimum stand-off distance existed where abrasive particle velocity had maximum values. Because there is still a velocity slip between particles and accelerating gas if the flow exits the nozzle, the particles will be further accelerated until gas and solid medium flow at equal velocities. This effect, illustrated in Fig. 3.46 for two different nozzle types and two different abrasive materials, was experimentally verified by high-speed photograph inspections performed by Bothen (2000). A velocity balance will occur at a certain critical distance from the nozzle exit. If this stand-off distance is being exceeded, particle velocity will start to drop due to effects of air friction. The graphs in Fig. 3.47 illustrate the effect of mass flow ratio abrasive/air on the abrasive velocity. It can be seen that a stand-off distance effect was rather pronounced for the lowest mass flow ratio (the highest air mass flow value). It also seemed from these results that the optimum stand-off distances shifted to higher values for higher mass flow ratios abrasive/air (lower air mass flow rate).

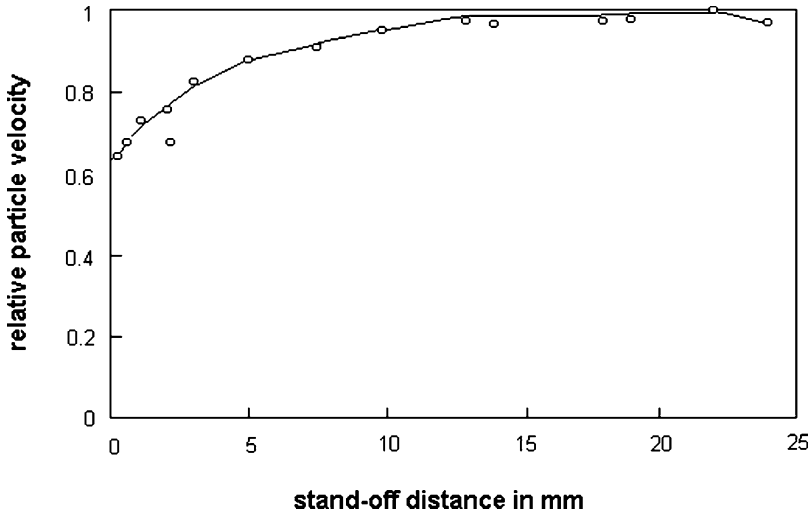


Fig. 3.45 Effect of stand-off distance on relative particle velocity (Bothen, 2000). (Relative velocity is related to the value “1”, which characterises the maximum particle velocity.)

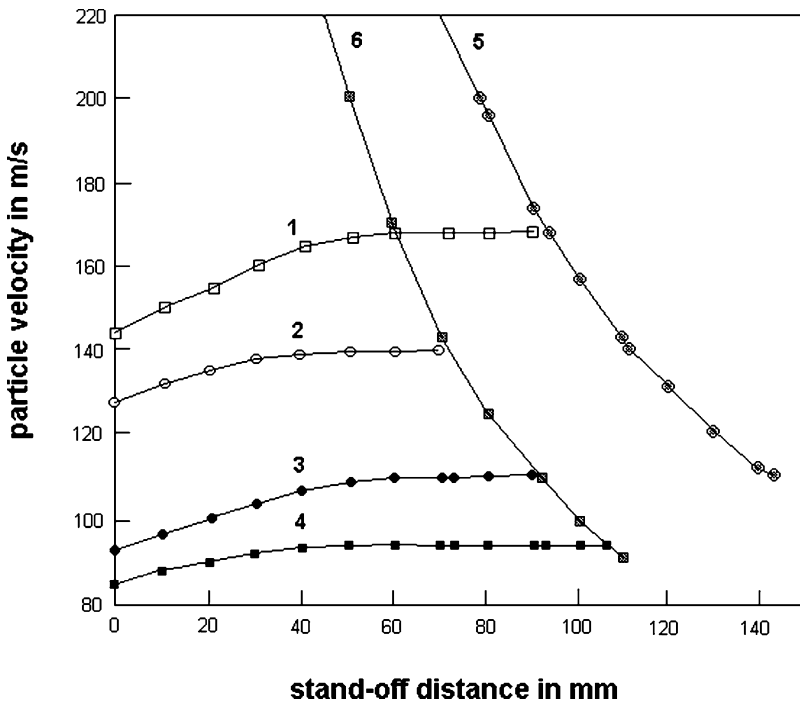


Fig. 3.46 Effect of stand-off distance on particle velocity (Uferer, 1992). “1” – convergent-divergent nozzle (slag); “2” – cylindrical nozzle (slag); “3” – convergent-divergent nozzle (steel cut wire); “4” – cylindrical nozzle (steel cut wire); “5” – convergent-divergent nozzle (air flow only); “6” – cylindrical nozzle (air flow only)

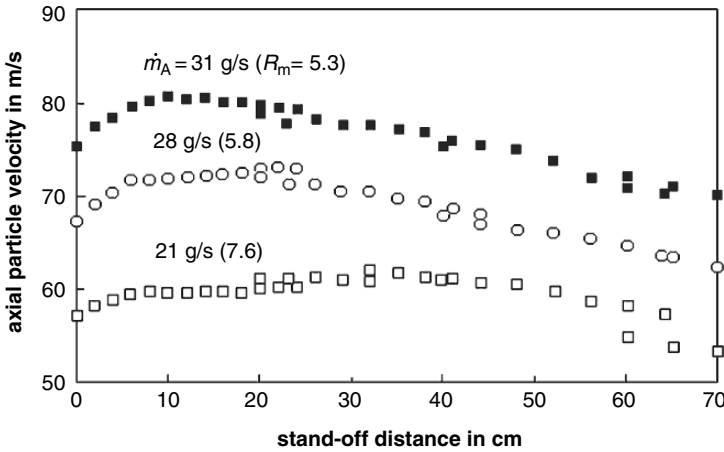


Fig. 3.47 Effects of stand-off distance and air mass flow rate (respectively mass flow ratio abrasive/air) on particle velocity (Fokke, 1999); $d_p = 468 \mu\text{m}$

3.6.7 Effects of Nozzle Length and Nozzle Diameter on Particle Velocity

Results of measurements on the effect of nozzle length on abrasive particle velocity are illustrated in Fig. 3.48. It can be seen that optimum nozzle lengths existed where velocity was highest (Wolak et al., 1977; Stevenson and Hutchings, 1995). This optimum slightly shifted to smaller nozzle length values if nozzle diameter decreased, but it did not seem to depend on the mass flow rate abrasive/air. The nozzle length to give the maximum axial particle velocity, at any given mass flow ratio, was approximately equal to 20 internal diameters of the nozzle for a cylindrical nozzle (Wolak et al., 1977). The dependence of particle velocity on nozzle length, and especially the existence of an optimum nozzle length, may be attributed to several mechanisms. Increased nozzle length increases the time during which the particles are exposed to the acceleration by the air, and consequently the particle velocities increase. However, a longer nozzle imposes proportionally higher friction effects on the air flow, and air velocity and the drag on the particle would decrease resulting in lower particle velocities. Another factor is the friction between particles and nozzle wall, evidenced through the wear of the nozzle walls. This expenditure of particle energy will also reduce particle velocities.

Abrasive particle velocity increased if nozzle diameter increased; this is shown in Figs. 3.41 and 3.48. However, it can be seen from Fig. 3.41 that this effect seemed to vanish for higher values of the mass flow ratio abrasive/air and for short nozzles.

3.6.8 Effects of Nozzle Design on Particle Velocity

Figure 3.49 displays results of abrasive particle measurements performed by Hamann (1987) on blast cleaning nozzles with different layouts. It can be seen that the highest

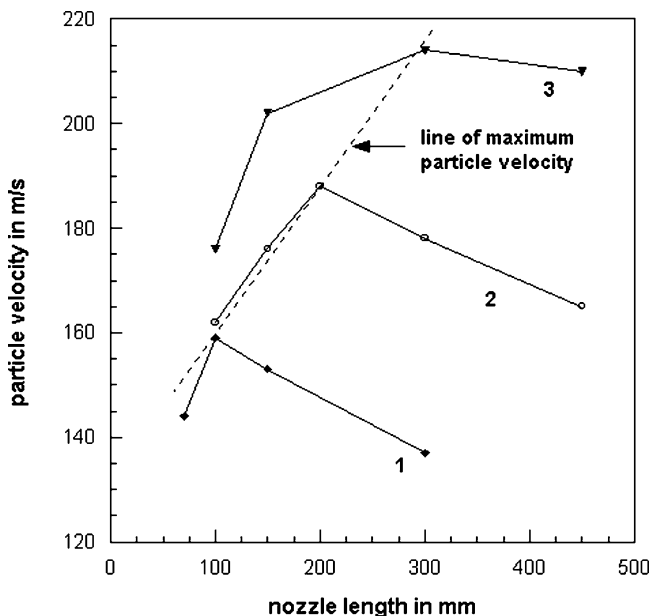


Fig. 3.48 Effects of nozzle length, nozzle diameter and mass flow ratio abrasive/air on particle velocity (Wolak et al., 1977); abrasive type: silicone carbide (mesh 60). “1” – $d_N = 6$ mm, $0.75 < R_m < 1.30$; “2” – $d_N = 9$ mm, $0.88 < R_m < 1.33$; “3” – $d_N = 12$ mm, $0.45 < R_m < 0.71$

abrasive particle velocity could be realised with a divergent–convergent nozzle with a specially designed inlet flow section (nozzle type “4”). The lowest abrasive particle velocity was delivered by a cylindrical nozzle with a bell-shaped inlet section (nozzle type “1”). The differences in abrasive particle velocities were as high as 45% among the tested nozzle layouts. Figure 3.50 shows the effects of the cross-section geometry on the velocity of abrasive particles. It can be recognised that the utilisation of a rectangular cross-section could notably increase the particle velocity compared with the use of a conventional circular cross-section. The effect of the nozzle cross-section on the abrasive particle velocity depended on the nozzle air pressure. The increase in abrasive particle velocity was +67% for a nozzle pressure of $p = 0.45$ MPa, and it was +93% for a nozzle pressure of $p = 0.57$ MPa.

3.6.9 Effects of Nozzle Wall Roughness on Particle Velocity

Shipway and Hutchings (1993a) could prove that the velocities of glass beads accelerated in cylindrical stainless steel nozzles depended on the roughness of the inner nozzle wall. The smoother the wall surface, the higher were the exit velocities of the particles. For a pressure of $p = 0.06$ MPa, for example, the theoretical particle velocity for glass beads ($d_p = 125$ – 150 μm) was $v_p = 100$ m/s; the particle velocity measured with a smooth nozzle ($R_a = 0.25$ μm) was $v_p = 85$ m/s and the particle

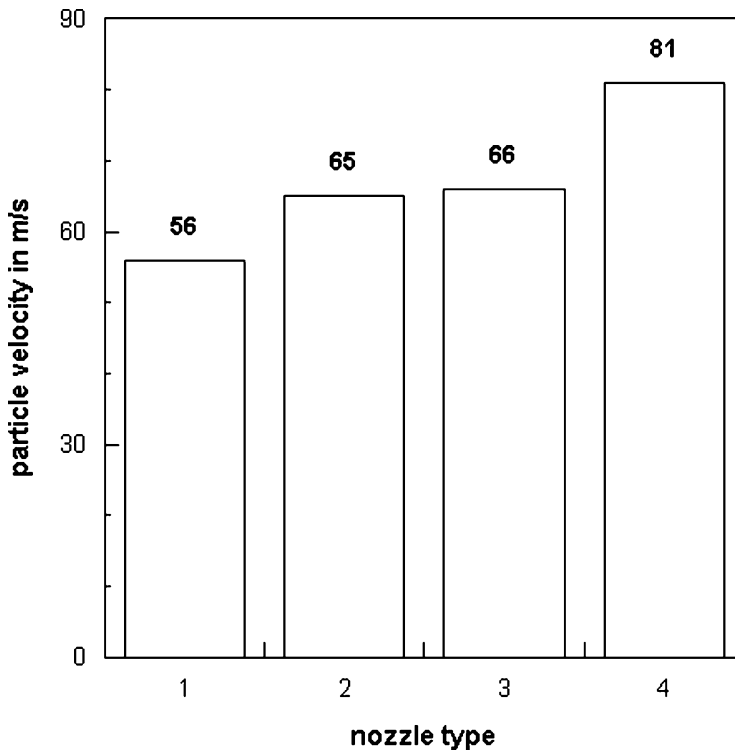


Fig. 3.49 Effects of nozzle type on abrasive particle velocity (Hamann, 1987). Nozzle type: “1” – bell-mouthed + cylinder; “2” – bell-mouthed + convergent; “3” – standard convergent–divergent; “4” – convergent–divergent with specially designed entry section

velocity measured with a rough nozzle ($R_a = 0.94 \mu\text{m}$) was $v_p = 65 \text{ m/s}$ only. It was also shown that the standard deviation for the particle exit velocity increased with an increase in wall roughness. These results were attributed to rebound effects. As the wall roughness increases, the rebound angle tended to increase, leading to a shorter distance between successive impingement points along the nozzle. The impact of abrasive particles with the nozzle wall can be assumed to be a stochastic event, with some particles impacting many times, and others rarely. There will thus be a spread of particle exit velocities, which will tend to increase with wall roughness.

3.6.10 Scaling Laws for Abrasive Particle Velocity

Shipway and Hutchings (1995) performed an extensive experimental study in order to investigate the effect of process parameters on the velocity of abrasive particles accelerated in a cylindrical nozzle. Some results of this study are already presented in Fig. 3.32. Abrasive materials considered in their study included silica sand ($d_p = 90\text{--}710 \mu\text{m}$; $\rho_p = 2,650 \text{ kg/m}^3$), soda lime glass ballotini ($d_p = 125\text{--}150 \mu\text{m}$;

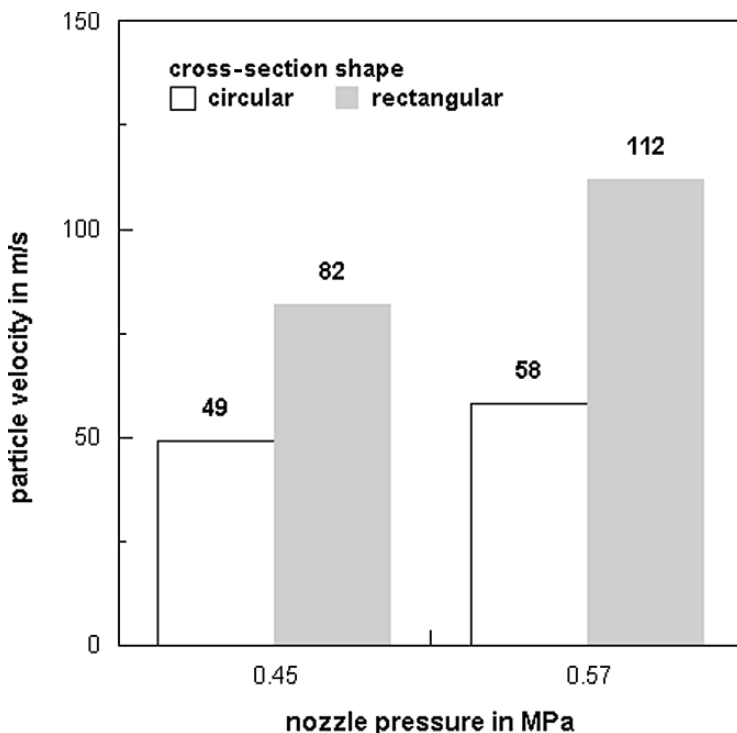


Fig. 3.50 Effects of pressure and nozzle cross-section shape on the velocity of abrasive particles (McPhee et al., 2000)

$\rho_P = 2,500 \text{ kg/m}^3$), aluminium oxide ($d_P = 63\text{--}75 \text{ }\mu\text{m}$; $\rho_P = 3,950 \text{ kg/m}^3$), silicon carbide ($d_P = 125\text{--}150 \text{ }\mu\text{m}$; $\rho_P = 3,160 \text{ kg/m}^3$), steel shot ($d_P = 212\text{--}300 \text{ }\mu\text{m}$; $\rho_P = 7,980 \text{ kg/m}^3$) and zirconia sand ($d_P = 125\text{--}500 \text{ }\mu\text{m}$; $\rho_P = 5,600 \text{ kg/m}^3$). The authors summarised their results with the following regression equation:

$$v_P \propto \left(\frac{p}{d_P^{0.57} \cdot \rho_P^{1.08}} \right)^{0.5} \quad (3.52)$$

The scaling law for the estimation of the ratio between air velocity and abrasive particle velocity had the following form:

$$\frac{v_P}{v_A} \propto d_P^{-0.285} \cdot \rho_P^{-0.54} \quad (3.53)$$

Both scaling laws are valid for parallel-sided cylindrical nozzles with a nozzle diameter of about $d_N = 5 \text{ mm}$ and for rather low nozzle pressures between $p = 0.005$ and 0.035 MPa .

3.7 Abrasive Stream Energy Flow and Nozzle Efficiency

The energy flow of an abrasive stream exiting a blast cleaning nozzle is given through the following relationship:

$$\dot{E}_P = \frac{1}{2} \cdot \dot{m}_P \cdot v_P^2 \quad (3.54)$$

This relationship is equal to (2.15). The energy flow can be estimated if abrasive particle velocity and abrasive mass flow rate can be measured. Results plotted in Fig. 3.51 illustrate that the abrasive stream energy flow (exit stream power) depended on nozzle design. A convergent–divergent nozzle with a specially designed entry flow section delivered a value of about $\dot{E}_P = 500 \text{ Nm/s}$, whereas a cylindrical nozzle with a bell-mouthed inlet section delivered a value of $\dot{E}_P = 209 \text{ Nm/s}$ only. This is a difference of about 240%. If the abrasive stream energy flow is related to the power of the compressor consumed for the compression of the air (see Sect. 4.2.2), an efficiency parameter can be derived as follows:

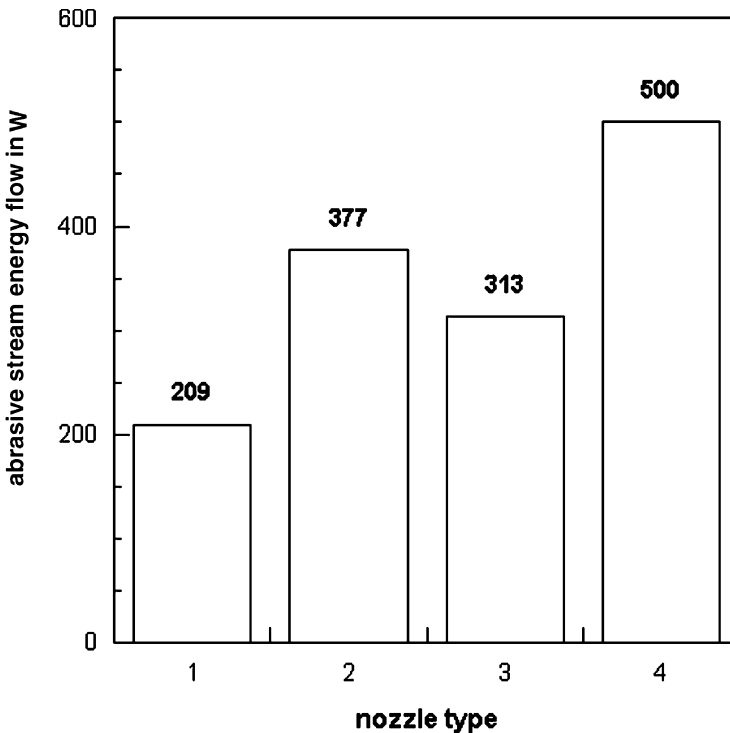


Fig. 3.51 Effects of nozzle type on abrasive stream energy flow (Hamann, 1987). Nozzle type: “1” – bell-mouthed + cylinder; “2” – bell-mouthed + convergent; “3” – standard convergent–divergent; “4” – convergent–divergent with specially designed entry section

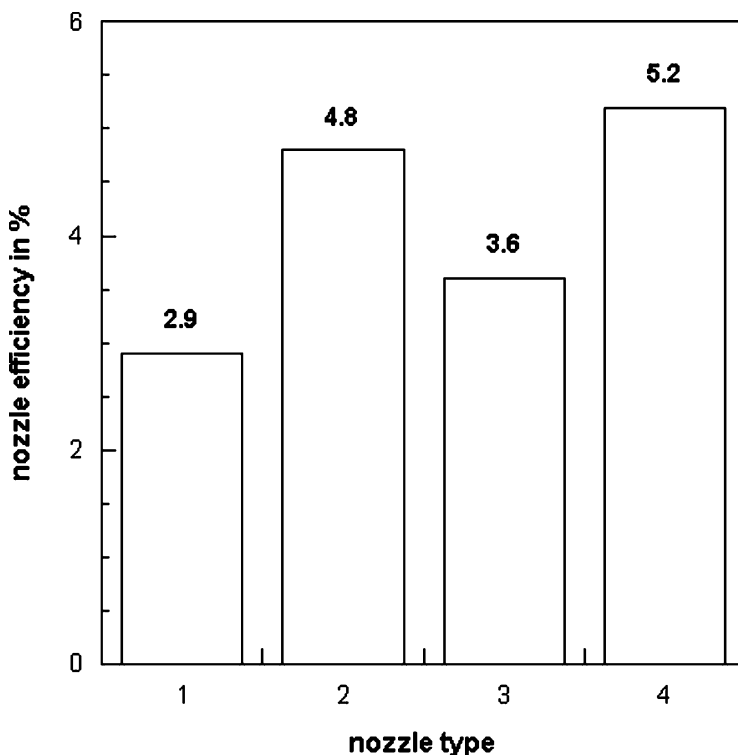


Fig. 3.52 Effects of nozzle type on efficiency (Hamann, 1987). Nozzle type: “1” – bell-mouthed + cylinder; “2” – bell-mouthed + convergent; “3” – standard convergent–divergent; “4” – convergent–divergent with specially designed entry section

$$\eta_N = \frac{\dot{m}_P \cdot v_P^2}{2 \cdot P_H} \quad (3.55)$$

This parameter describes the power transfer between compressed air and abrasive particles. The higher this efficiency parameter, the better is the power transfer. Results of measurements on the effects of varying nozzle types are displayed in Fig. 3.52. The trend is equal to that shown in Fig. 3.51. The certain values are between $\eta_N = 3$ and 5%. Similar results were reported by Uferer (1992). If the compressor power (P_H) in (3.49) is replaced by the power available at the nozzle inlet, (3.55) can characterise the quality of blast cleaning nozzles. According to this criterion, the nozzle with the best quality would be nozzle “4” in Fig. 3.52.

Chapter 4

Blast Cleaning Equipment

4.1 General Structure of Blast Cleaning Systems

The general structure of a pressure blast cleaning system is illustrated in Fig. 4.1. It basically consists of two types of equipment: air suppliers and air consumers. The prime *air supplier* is the compressor. At larger sites, storage pressure vessels accompany a compressor. These vessels serve to store a certain amount of pressurised air, and to allow an unrestricted delivery of a demanded amount of compressed air to the consumers. The prime *air consumer* is the blast cleaning nozzle. However, hoses, whether air hoses or abrasive hoses, are air consumers as well – a fact which is often not considered. Another consumer is the breathing air system. However, it is not uncommon to run separate small compressors for breathing air supply; an example is shown in Fig. 4.1. Further parts of a blast cleaning configuration are control devices, valve arrangements and safety equipment.

4.2 Air Compressors

4.2.1 General Aspects

Compressed air can be generated by several methods as illustrated in Fig. 4.2. For industrial applications, the most frequently type used is the screw compressor. Screw compressors are available in two variants: oil-lubricated and oil-free. Table 4.1 lists technical data of screw compressors routinely used for on-site blast cleaning operations. Screw compressors feature the following advantages:

- no wear because of the frictionless movements of male and female rotors;
- adjustable internal compression;
- high rotational speeds (up to 15,000/min);
- small dimensions.

The fundamental principle for screw compaction was already invented and patented in 1878. It is based on the opposite rotation of two helical rotors with aligned profiles. The two rotors are named as male and female rotors, respectively.

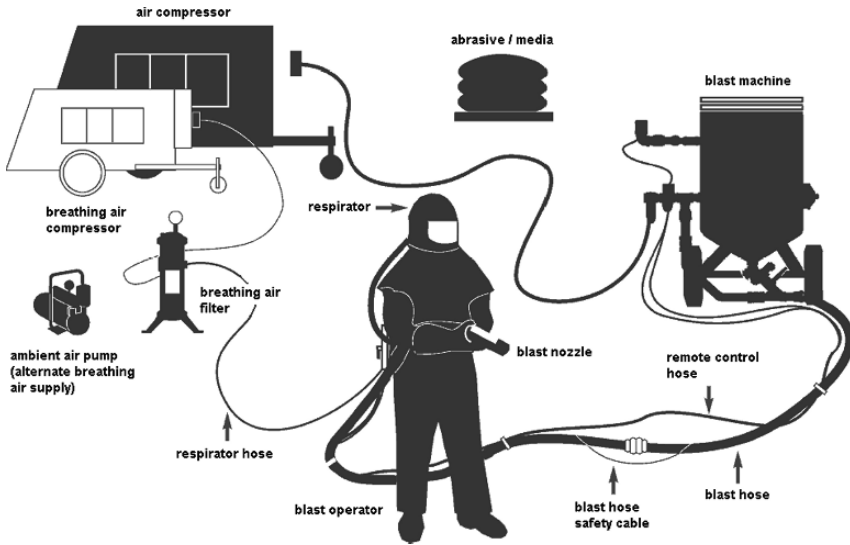


Fig. 4.1 Basic parts of a compressed air system for blast cleaning operations (Clemco Inc., Washington)

The air to be compacted will be sucked into the compressor via an air filter. The air will be compacted in the closed room generated between cylinder wall and the teeth of the two rotors. The sealing between screws and body is due to oil injection. This oil, that also lubricates the bearings and absorbs part of the process heat, will later be removed with the aid of an oil separator. Therefore, oiled screw compressors cause rather low maintenance costs.

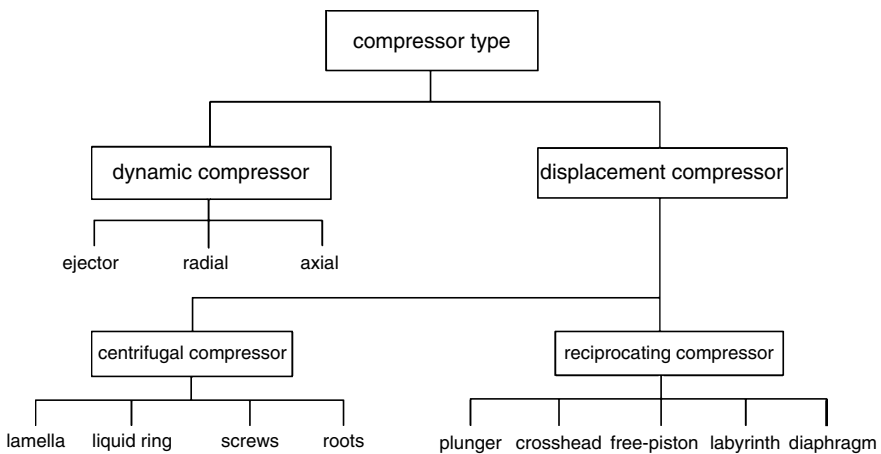


Fig. 4.2 Compressor types for air compression (Ruppelt, 2003)

Table 4.1 Technical data of mobile screw compressors (Atlas Copco GmbH, Essen)

Type	Unit	XAHS 365	XAHS 350	XAS 125
Nominal pressure	MPa	1.2	1.2	0.7
Nominal volumetric flow rate	m ³ /min	21.5	20.4	7.5
Power rating in kW	kW	206		
Length total	mm	4,210	4,650	4,177
Width total	mm	1,810	1,840	1,660
Height total	mm	2,369	2,250	1,527
Weight (empty)	kg	3,800		
Weight (ready for operation)	kg	4,300	4,500	1,430
Air exit valves	–	1 × 2" + 1 × 1"	1 × 1/4" + 1 × 3/4"	1/4" + 3 × 3/4"
Noise level	dB (A)	74	75	71

The displaced volume per revolution of the male rotor not only depends on diameter and length of the rotor but also on its profile. One revolution of the main helical rotor conveys a unit volume q_0 , and the theoretical flow rate for the compressor reads as follows:

$$\dot{Q}_0 = n_C \cdot q_0 \quad (4.1)$$

The actual flow rate, however, is lowered by lost volume; the amount of which depends on the total cross-section of clearances, air density, compression ratio, peripheral speed of rotor and built-in volume ratio. More information is available in standard textbooks (Bendler, 1983; Bloch, 1995; Groth, 1995).

4.2.2 Working Lines

A working line of a compressor is defined as follows:

$$p = f(\dot{Q}_A) \quad (4.2)$$

where p is the pressure delivered by the compressor and \dot{Q}_A is the volumetric air flow rate. The precise shape of (4.2) depends on the compressor type. A working line of a screw compressor is shown in Fig. 4.3 together with the working lines for three nozzles with different nozzle diameters. The working lines for nozzles can be established according to the procedure outlined in Sect. 3.2.1.

It can be seen in Fig. 4.3 that the working line of the compressors and the working lines of two nozzles intersect. The intersection points are called *working points* of the system. This point characterises the parameter combination for the most effective performance of the system. If a compressor type is given, the positions of the individual working points depend on the nozzle to be used. These points are designated "II" for the nozzle "2" with $d_N = 10$ mm and "III" for the nozzle "3" with $d_N = 12$ mm. The horizontal dotted line in Fig. 4.3 characterises the pressure limit for the compressor; and it is at $p = 1.3$ MPa. It can be seen that

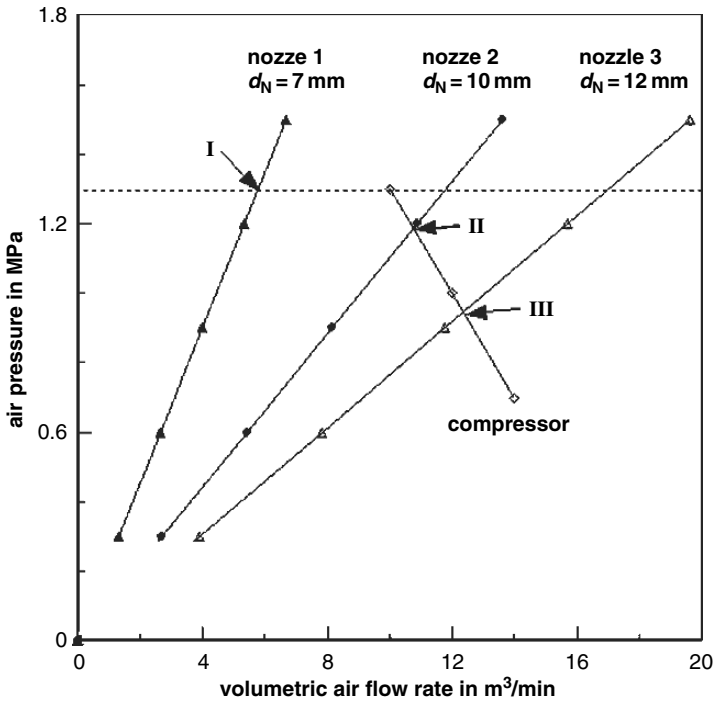


Fig. 4.3 Working lines of a screw compressor and of three blast cleaning nozzles

the working line of the nozzle “1” with $d_N = 7$ mm does not cross the working line of the compressor, but it intersects with the dotted line (point “I”). Because the cross-section of this nozzle is rather small, it requires a high pressure for the transport of a given air volumetric flow rate through the cross-section. This high pressure cannot be provided by the compressor. The dotted line also expresses the volumetric air flow rate capabilities for the other two nozzles. These values can be estimated from the points where working line and dotted line intersect. The critical volumetric flow rate is $\dot{Q}_A = 12$ m³/min for nozzle “2”, and it is $\dot{Q}_A = 17$ m³/min for nozzle “3”. The compressor cannot deliver these high values; its capacity is limited to $\dot{Q}_A = 10$ m³/min for $p = 1.3$ MPa, which can be read from the working line of the compressor. However, the calculations help to design a buffer vessel, which can deliver the required volumetric air flow rates.

4.2.3 Power Rating

If isentropic compression is assumed (entropy remains constant during the compression), the theoretical power required to lift a given air volume flow rate from a

pressure level p_1 up to a pressure level p_2 can be derived from the work done on isentropic compression. This power can be calculated as follows (Bendler, 1983):

$$P_H = \frac{\kappa}{\kappa - 1} \cdot \dot{Q}_A \cdot p_1 \cdot \left[\left(\frac{p_2}{p_1} \right)^{\frac{\kappa-1}{\kappa}} - 1 \right] \tag{4.3}$$

The ratio p_2/p_1 is the ratio between exit pressure (p_2) and inlet pressure (p_1). These pressures are absolute pressures. Results of calculations for a typical site screw compressor are displayed in Fig. 4.4. It can be seen from the plotted lines that the relationship between pressure ratio and power rating has a degressive trend. The relative power consumption is lower at the higher pressure ratios.

The theoretical power of the compressor type XAHS 365 in Table 4.1, estimated with (4.3), has a value of $P_H = 130$ kW. In practice, the theoretical power input is just a part of the actual power, transmitted through the compressor coupling. The actual power should include dynamic flow losses and mechanical losses. Therefore, the actual power of a compressor reads as follows:

$$P_K = \eta_{K_m} \cdot \eta_{K_d} \cdot P_H \tag{4.4}$$

The mechanical losses, typically amounting to 8–12% ($\eta_{K_m} = 0.08-0.12$) of the actual power, refer to viscous or frictional losses due to the bearings, the timing and step-up gears. The dynamic losses typically amount to 10–15% ($\eta_{K_d} = 0.1 - 0.15$)

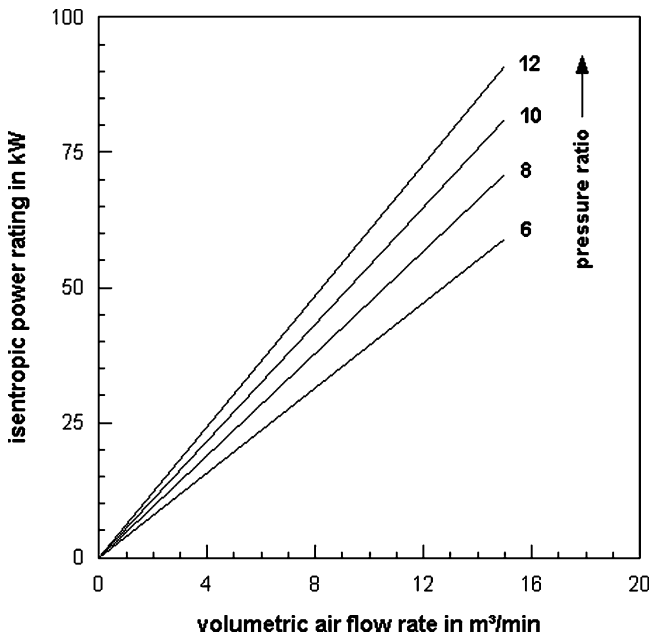


Fig. 4.4 Calculated compression power values, based on (4.3)

of the actual power. More information on these issues can be found in Bloch (1995) and Grabow (2002). The actual power rating of the compressor type XAHS 365 in Table 4.1 is $P_K = 206 \text{ kW}$. If the theoretical power of $P_H = 130 \text{ kW}$, estimated with (4.3), is related to this value, the losses cover about 36%.

Air compressors can be evaluated based on their specific power consumption, which is defined as the ratio between actual power rating and volumetric air flow rate:

$$P_S = \frac{P_K}{\dot{Q}_A} \quad (4.5)$$

For the compressor type XAHS 365 in Table 4.1, the specific power consumption is, for example, $P_S = 9.6 \text{ kW}/(\text{m}^3/\text{min})$. Different types of compressors have different specific power consumptions even if they deliver equal pressure and volumetric air flow rate values. Larger compressors have lower specific power consumption; thus, they perform more efficient. The physical unit of the specific power consumption is that of a specific volumetric energy (kWh/m^3), and it can, therefore, also characterise the energy required for the compression of a given air volume.

Part of the compression energy is consumed by the heating of the gas. Gas temperature increases during the compression process. For an adiabatic compression process, the final gas temperature can be calculated with the following equation (Bendler, 1983):

$$T_K = T_1 \cdot \left(\frac{p_2}{p_1} \right)^{\frac{\kappa-1}{\kappa}} \quad (4.6)$$

Results of calculations are displayed in Fig. 4.5. It can be seen that air temperatures as high as $\vartheta = 300^\circ\text{C}$ can be achieved. Because hot air can carry much more moisture than cold air, there is a high risk of condensation in the blast cleaning system. More detailed information on this issue is presented, among others, by Siegel (1991). This author provides a nomogram where the amount of condensation water can be read for different pressure ratios. A typical calculation example ($p_2 = 0.6 \text{ MPa}$, $\vartheta_1 = 20^\circ\text{C}$, 60% relative humidity) delivers a condensation water rate of 8 g per cubic metre of air. For a volumetric air flow rate of $\dot{Q}_A = 10 \text{ m}^3/\text{h}$, the total amount of condensation water would be about 5 l/h. Therefore, an after cooling process is recommended after the compression process.

4.2.4 Economic Aspects

The technical and economical evaluation of compressors is a complex issue. However, the key performance parameters, pressure (p) and volumetric air flow rate (\dot{Q}_A), usually allow a selection of appropriate consumers (e.g. grinders and blast cleaning nozzles). Key roles in the interaction between compressor and air consumers not only play dimension and condition of the consumers, in particular blast cleaning nozzles (see Fig. 4.3); but also the dimensions of connecting devices,

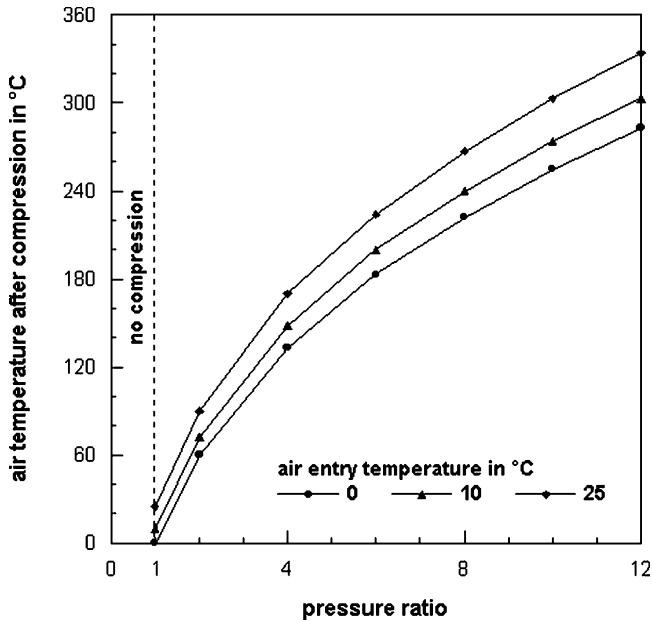


Fig. 4.5 Calculated air exit temperature after adiabatic compression; based on (4.6)

in particular hose lines, valves and fittings. If these parts are insufficiently tuned, efficiency drops and costs increase. These aspects are discussed in the following sections.

Pressure losses in hoses, fittings and armatures as well as leakages must also be taken into account if the size of a compressor needs to be estimated. This aspect is discussed in Sects. 4.4 and 4.5.

Another problem is pressure fluctuation, which affects the volumetric air flow rate. A rule says that even good maintained compressors require a correction factor of 1.05. This means a plus of +5% to the nominal volumetric flow rate requested by the consumer.

The pressure valve located at the outlet of the compressors should be adjusted to the nozzle diameter of the blast cleaning system. Some relationships are listed in Table 4.2. A general recommendation is as follows: $d_{VK} \geq 4 \cdot d_N$. For a nozzle with a diameter of $d_N = 10$ mm, the minimal internal diameter of the compressor outlet valve should be $d_{VK} = 40$ mm. Values for the sizes of air exit valves of three compressors are listed in Table 4.1.

A good maintenance programme is critical to compressor life and performance. A good maintenance programme is one that identifies the need for service based on time intervals and equipment hours. Additional items that also need to be considered when developing a programme are environmental conditions such as dust, ambient temperature and humidity, where filter changes may be required before the recommended intervals. Most equipment manufacturers have developed a preventive

Table 4.2 Adjustment between nozzle diameter and compressor outlet valve diameter (Clemco Inc., Washington)

Nozzle diameter in mm	Valve diameter in mm
5.0	19
6.5	25
8.0	32
9.5	38
11.0	50
12.5	50
16.0	64
19.0	76

maintenance schedule for their equipment, and it must be followed as a minimum. However, manufacturers cannot account for all operational conditions, and a maintenance plan may be developed by the operator of the equipment. Table 4.3 lists some recommendations.

4.2.5 Aspects of Air Quality

Basically, compressed air can be subdivided into the following four groups:

- oil-free air;
- moisture-free air;
- oil-lubricated air;
- breathing air.

Regulatory demands on the quality of pressurised air are prescribed in ISO 8573-1 (2001). The most important criteria are listed in Table 4.4. It can be seen that the standard distinguished between 10 quality classes for compressed air. Major assessment parameters include solid content (respectively dust), moisture content and oil content.

The requirement for oil-free air comes from surface quality arguments. The occupancy of blast cleaned steel surfaces by oil will reduce the adhesion of the coating systems to the substrate, and it will deteriorate the protective performance. These aspects are discussed in Sect. 8.4. In oil-injected compressors, the air usually picks up a certain amount of oil due to its way through the compaction room. This oil can appear as liquid, aerosol, or even as vapour. Even professionally maintained screw compressors ran without oil separators generate rest oil contents as high as 5 ppm (milligram of oil per cubic metre of air). Part of this oil will be intercepted together with condensation water in appropriate cooling devices. However, in order to also separate oil vapour reliably, multiple-step cleaning systems are required. A typical system consists of the following components:

- an after-cooler to cool down the compressed air;
- a high-performance fine filter to intercept aerosols;
- an activated carbon filter to absorb oil vapours.

Table 4.3 Example of a preventive air compressor maintenance programme (Placke, 2005)

	Daily	Weekly	Monthly	Quarterly	Bi-yearly	Yearly
Small size unit				250 h	500 h	1,000 h
Large size unit				500 h	1,000 h	2,000 h
Compressor oil level	C					
Engine oil level	C					
Radiator cooling level	C					
Meters/lamps	C					
Air filter service gauge	C					
Fuel tank (fill at shift end)	C				Empty	
Water/fuel separator empty	C					
Discharger of pre-cleaner of air cleaner		C				
Alternator belts		C				
Battery connections/level		C				
Tire pressure/tread		C				
Wheel bolts			C			
Hoses (oil, air, intake, etc.)			C			
Automatic shutdown system test			C			
Air purificator system, visual			C			
Compressor oil radiator, external			C	Clean		
Engine oil radiator, external			C	Clean		
Clamps				C		
Air purificator elements				W		
Fuel/water separator element					R	
Compressor element				B	A	
Compressor oil					R	
Wheels (bearings, seals, etc.)					C	C
Engine cooler tests					C	R
Shutdown switch lockout test						C
Scavenging orifice and common elements						Clean
Oil separator element						R
Hook Augen bolts		Check before towing				
Lights (drive, brakes, flasher)		Check before towing				
Engine oil change, filters, etc.		Refer to the engine operators manual				

A – Change only to the small size unit; B – Change only to the large size unit; C – Check (adjust or replace as needed); R – Replace; WI – When indicated

Moisture-free compressed air is recommended for blast cleaning operations to avoid moisturisation of abrasive particles. Moist particles tend to agglutinate which could, in turn, clog pressure air lines. Many compressors are equipped with devices that remove condensation water. These devices include the following parts:

- an after-cooler;
- a condensation water precipitator;
- a filter systems to separate water vapour;
- an air heating systems.

There are also anti-icing lubrication agents available that can absorb water and reduce the hazard of ice formation.

Table 4.4 Quality classes for compressed air (ISO 8573-1)

Class	Solids/dust				Size in μm	Content in mg/m^3	Moisture Pressure dew point in $^{\circ}\text{C}$ ($X_w = \text{water in g}/\text{m}^3$)	Total oil content in mg/m^3
	Max. number per m^3 of particles with given diameter							
	≤ 0.1	$0.1 < 0.5$	$0.5 < 1.0$	$1.0 < 5.0$				
0	According to operator							
1	–	100	1	0	–	–	≤ -70	≤ 0.01
2	–	100,000	1,000	10	–	–	≤ -40	≤ 0.1
3	–	–	10,000	500	–	–	≤ -20	≤ 1.0
4	–	–	–	1,000	–	–	$\leq +3$	≤ 5.0
5	–	–	–	20,000	–	–	$\leq +7$	–
6	–	–	–	–	≤ 5	≤ 5	$\leq +10$	–
7	–	–	–	–	≤ 40	≤ 10	$X_w \leq 0.5$	–
8	–	–	–	–	–	–	$0.5 \leq X_w \leq 5.0$	–
9	–	–	–	–	–	–	$5.0 \leq X_w \leq 10.0$	–

Table 4.5 Limits for breathing air according to DIN 3188

Medium	Limit
Carbon dioxide	$< 800 \text{ mg}/\text{m}^3$ air
Carbon monoxide	$< 30 \text{ mg}/\text{m}^3$ air
Dust	Max. $0.01 \mu\text{m}$
Oil vapour	$0.3 \text{ mg}/\text{m}^3$ (20°C and 0.7 MPa)

The supply of breathing air is especially important for all blast cleaning operations. Critical substances in breathing air include carbon dioxide, carbon monoxide, dust and oil vapour. Regulatory limits for breathing air are listed in Table 4.5. Compressed air without special treatment cannot meet these requirements. Therefore, compressed air needs to be treated in breathing air treatment devices. These devices usually perform in multiple steps, and they include fine filters to intercept water, oil and dust; activated carbon filters to adsorb oil vapour; and catalysts to strip carbon dioxide and carbon monoxide.

4.3 Blast Machine

4.3.1 Basic Parts

The blast machine is a key part of any dry blast cleaning configuration. The major task of the blast machine is the delivery and dosing of the abrasive particles into the air stream. The structure of a typical blast machine is shown in Fig. 4.6. It consists basically of an air inlet line, a pressure sealing system, the actual storage part and an abrasive metering system. Blast machines are available at numerous sizes.

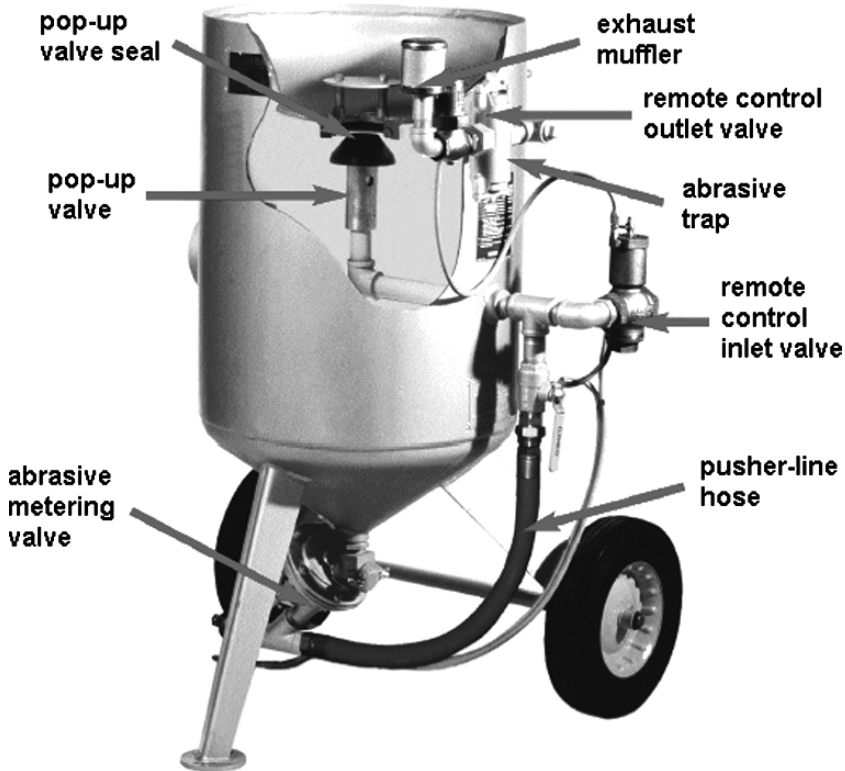


Fig. 4.6 Basic design of a blast pot (Clemco, Inc., Washington)

4.3.2 Abrasive Metering

4.3.2.1 Effects of Process Parameters

The metering of the abrasive particles is a challenging task, and the success of a blast cleaning operation depends to some amount on correct and reliable metering (see Sect. 6.4.1). The mass flow rate of abrasives is regulated simply due to changes in the size of the passage in a metering valve. Plaster's, (1972) review still gives a very good overview on typical pressure vessels and mixing valve designs. More recent information was provided by Nadkarni and Sharma (1996).

The performance of abrasive metering processes was investigated by Bae et al. (2007), Bothen (2000) and Rimmels (1968). The process of abrasive mass flow metering due to valve passage size variations is illustrated in Fig. 4.7, where the abrasive mass flow rate is plotted against the passage size for a given valve system. A power relationship with a power exponent greater unity can be noted between valve opening size and abrasive mass flow rate. The graphs also illustrate the effects of changes in nozzle diameter: the larger the nozzle, the more abrasive material was pushed through the valve passage. Changes in nozzle diameter seemed to affect the

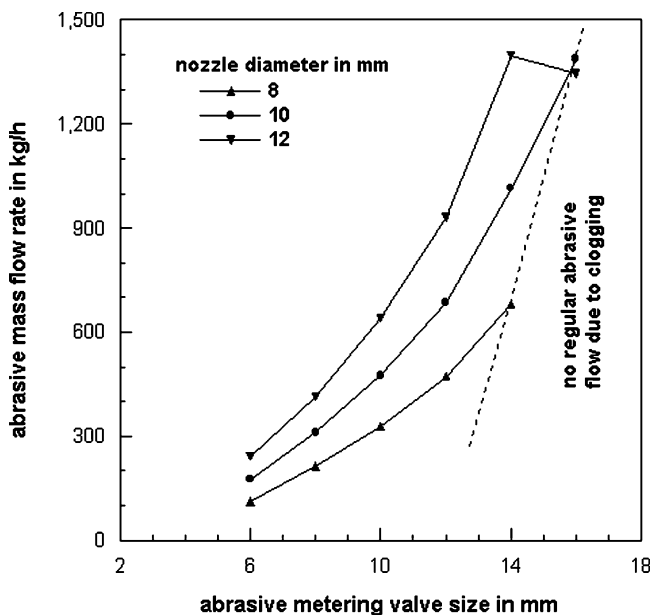


Fig. 4.7 Effects of metering valve passage and nozzle diameter on abrasive mass flow rate (Remmelts, 1968). Air pressure: $p=0.5$ MPa; abrasive type: Zirconium; abrasive size: $d_p = 100 \mu\text{m}$

abrasive mass flow rate, especially, at the large valve openings. The diameter of the blast cleaning nozzle seemed to influence the power exponents for the individual graphs. The larger the nozzle diameter, the higher was the value for the power exponent. A critical case is illustrated in Fig. 4.7 by the divergent process behaviour for the largest valve opening – here, a clogging of the abrasive material can be noted. The cross-section of the valve opening was too small to maintain the abrasive delivery process if the abrasive mass flow rate exceeded a value of about $\dot{m}_p = 24$ kg/min. Therefore, valve size and nozzle diameter must always be adjusted accordingly.

Effects of air volume flow rate on the abrasive metering process are shown in Figs. 4.8 and 4.9. There is a general trend that abrasive mass flow rate increased if air volume flow rate increased, but the detailed situation is very complex. In the case of the lower air pressure ($p = 0.4$ MPa) in Fig. 4.8, the metering process seemed to become very unstable at high air volume flow rates. It may be considered that the situation shown in Fig. 4.8 applies to micro-blasting processes, which involve very small abrasive particles as well as rather small dimensions for the metering device. A precise abrasive metering process could not be maintained under these special conditions.

Abrasive metering is also sensitive to changes in air pressure. The higher the pressure, the more abrasive material is pushed through the valve passage (Goldman et al., 1990; Mellali et al., 1994; Bothen, 2000; Remmelts, 1968). Examples are shown in Figs. 4.8 and 4.10. Mellali et al. (1994) performed measurements with

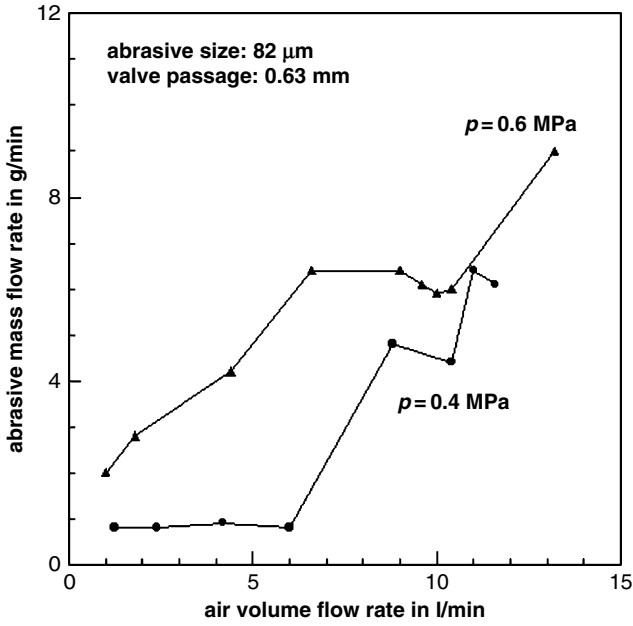


Fig. 4.8 Effects of air volumetric flow rate and pressure on abrasive mass flow rate (Bothen, 2000)

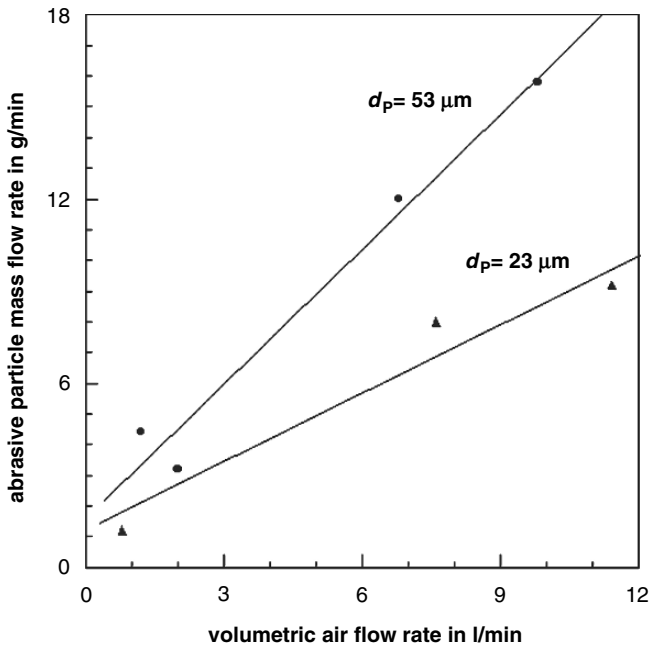


Fig. 4.9 Effects of air volumetric flow rate and abrasive particle size on abrasive mass flow rate for a micro-blasting machine (Bothen, 2000)

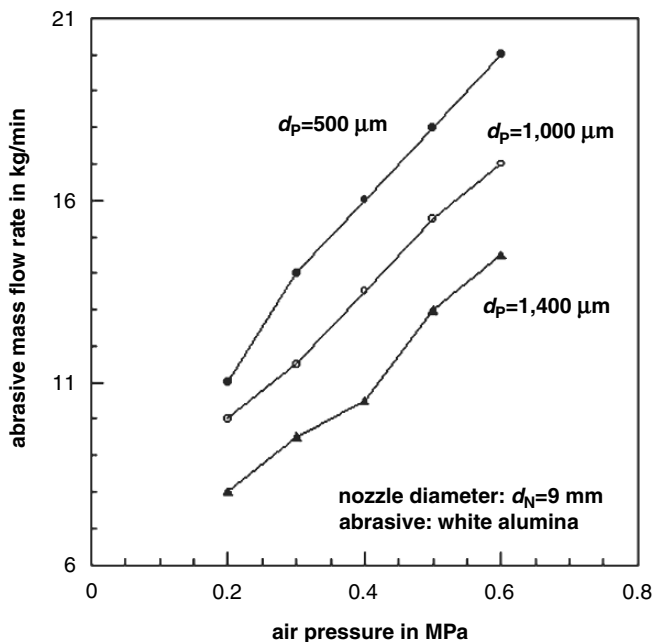


Fig. 4.10 Effects of air pressure and abrasive particle size on abrasive mass flow rate (Mellali et al., 1994)

aluminium oxide abrasives ($d_p = 500\text{--}1,400 \mu\text{m}$), and they found an almost linear relationship between air pressure and abrasive mass flow rate delivered by a laboratory blast pot. Results of their work are provided in Fig. 4.10. It can be seen that the functional relationships between both parameters followed a linear trend and that ascents of the functions depended on the abrasive particle size. The steepest ascent was estimated for the smallest abrasive particle diameter. The difference in abrasive mass flow rate in the parameter range considered in Fig. 4.10 was as high as 300%. Stallmann et al. (1988) measured the abrasive mass flow rate for two slag materials at three different compressor pressure levels, and they noted rather complex relationships as well as abrasive type effects. Whereas abrasive mass flow rate increased with an increase in the compressor pressure for copper slag, it showed maximum values at a moderate compressor pressure for melting chamber slag.

Effects of abrasive particle size variations on the performance of abrasive metering processes were investigated by Bothen (2000), Goldman et al. (1990) and Mellali et al. (1994). It was shown by Mellali et al. (1994) that abrasive mass flow rate delivered by a metering valve arrangement was very sensitive to changes in abrasive particle size. Results are provided in Fig. 4.10. It can be seen that abrasive mass flow rate increased if smaller abrasive particles were added to the system. This trend was also found for the use of glass beads by Goldman et al. (1990), whereby the effect of abrasive size seemed, however, to become insignificant at rather low pressures ($p < 0.2 \text{ MPa}$). For the highest pressure ($p = 0.6 \text{ MPa}$) in Fig. 4.10, the

difference in abrasive mass flow rate, caused by changes in the abrasive particle size, was as high as 40%. Another example for the influence of the abrasive particle size on abrasive mass flow rate is depicted in Fig. 4.9. In that particular case, the abrasive mass flow rate delivered by the metering system was larger for the larger abrasive particle diameters at a given valve passage size. This result does not agree with the results delivered by Goldman et al. (1990) and Mellali et al. (1994). A reason could be the very small dimensions for the abrasive materials ($d_p = 23\text{--}53\ \mu\text{m}$) and the valve ($d_v = 670\text{--}1,000\ \mu\text{m}$) used by Bothen (2000).

Adlassing and Jahn (1961) reported on measurements on the effects of abrasive material density and abrasive bulk density on the abrasive mass flow rate delivered by an abrasive metering device. These authors could prove that the abrasive mass flow rate increased almost linearly with an increase in the abrasive material density. The progress of the linear functions was independent of nozzle pressure ($p = 0.2\text{--}0.4\ \text{MPa}$). The lowest abrasive mass flow rate was measured for quartz sand ($\rho_p = 2,600\ \text{kg/m}^3$; $\rho_B = 1.48\ \text{kg/l}$), and the largest abrasive mass flow rate was measured for steel cut wire ($\rho_p = 7,900\ \text{kg/m}^3$; $\rho_B = 4.29\ \text{kg/l}$).

Figure 4.11 illustrates the effects of nozzle layout and number of valve turns on the abrasive metering process. It can be seen that the geometry of the nozzle affected the metering process mainly in the range of high numbers of valve turns. However, the general linear trend between number of valve turns and mass ratio abrasive/air did not seem to be affected by variations in the nozzle geometry. Changes in nozzle geometry have an influence on both air mass flow rate and abrasive mass flow rate. It can be seen that the mass flow ratio abrasive/air took very high values for all numbers of valve turns; it was basically larger than a value of $\dot{m}_p/\dot{m}_A = 2$, which is an upper limit for an efficient blast cleaning process (see Sect. 6.4.1). The increase in the mass flow ratio abrasive/air is not only attributed to a larger amount of abrasive flowing through the larger valve opening, but is also due to a reduction in the volumetric air flow rate. This aspect is illustrated in Fig. 4.12. The higher the number of valve turns, the lower is the volumetric air flow rate measured at the nozzle. Figure 3.11 clarifies the problem from the point of view of abrasive mass flow rate. The trends are equal to those shown in Fig. 4.12. The geometry of the nozzle had a pronounced effect on the absolute values for the volumetric air flow rate, but it did not affect the general trends of the curves. If (3.11) and (3.15) are applied, the volumetric air flow rate at the nozzle can be calculated. For the conditions in Fig. 4.12 (assumed air temperature $\vartheta = 25^\circ\text{C}$), the following values were calculated: nozzle "1" ($d_N = 11.5\ \text{mm}$): $\dot{Q}_A = 8.2\ \text{m}^3/\text{min}$; nozzle "2" ($d_N = 11\ \text{mm}$): $\dot{Q}_A = 7.4\ \text{m}^3/\text{min}$ and nozzle "3" ($d_N = 12.5\ \text{mm}$): $\dot{Q}_A = 9.6\ \text{m}^3/\text{min}$. The amount of displaced air volume depended on number of valve turns, respectively on abrasive mass flow rate; but it could be as high as 50% for the conditions in Fig. 4.12 (for nine valve turns). If, however, the more typical condition of four valve turns is applied, the amount of displaced air volume is between 17% and 25%. These values approve results of measurements performed by other authors (see Sect. 3.2.1).

An increase in the number of valve turns increases the abrasive mass flow rate. An increase in mass flow rate will increase pressure drop in the grit hose, thus reducing the nozzle pressure. This effect is shown in Fig. 4.13. It can be seen that the air

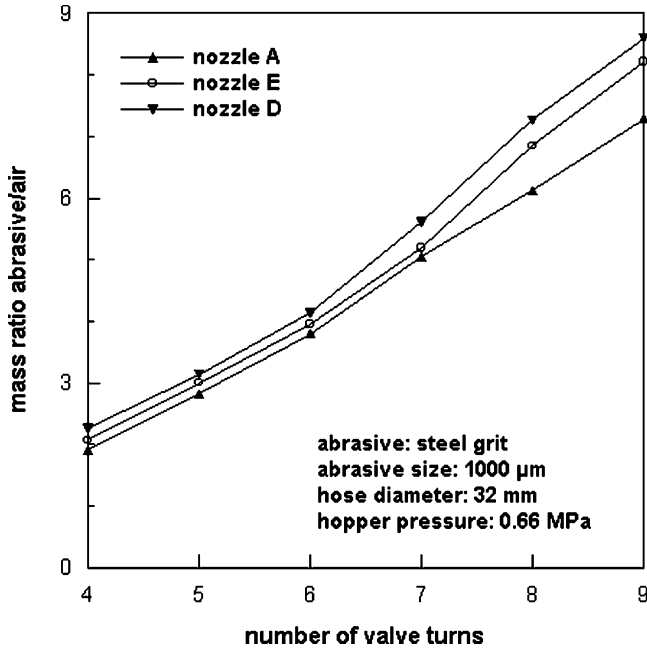


Fig. 4.11 Effects of number of valve turns and nozzle geometry on the mass flow ratio abrasive/air in convergent-divergent nozzles (Bae et al., 2007). Nozzle “A” – nozzle length: 125 mm, throat (nozzle) diameter: 12.5 mm, divergent angle: 7.6°, convergent angle: 3.9°; Nozzle “D” – nozzle length: 185.7 mm, throat (nozzle) diameter: 9.5 mm, divergent angle: 1.2°, convergent angle: 8.5°; Nozzle “E” – nozzle length: 215 mm, throat (nozzle) diameter: 11 mm, divergent angle: 1.3°, convergent angle: 7.9°

pressure at the nozzle dropped if abrasive mass flow rate increased. The pressure drop again depended on the geometry of the nozzle. It was most pronounced for the nozzle “A”. For a typical value of $\dot{m}_p = 15 \text{ kg/min}$, the air pressure dropped from $p = 0.66 \text{ MPa}$ (at the hopper) down to $p = 0.53 \text{ MPa}$ at the nozzle if a grit hose with a diameter of $d_H = 32 \text{ mm}$ was used (hose length was not given). This particular problem will be discussed in more detail in Sect. 4.5.3.

The graphs in Fig. 4.11 illustrate another permanent problem in abrasive metering. The values for the mass ratio abrasive/air were very high if the number of valve turns was high. Mass ratios of $R_m = 1.0\text{--}2.0$ are most efficient for an effective blast cleaning (see Sect. 6.4.1). This optimum range was met for the arrangement in Fig. 4.11 for four valve turns only. Any additional valve turn will deteriorate the blast cleaning process although more abrasive mass is being delivered to the cleaning point.

4.3.2.2 Metering Models

The aforementioned relationships can be summarised as follows:

$$\dot{m}_p = f(d_V; d_N; p; d_p; \rho_p; \rho_B) \quad (4.7)$$

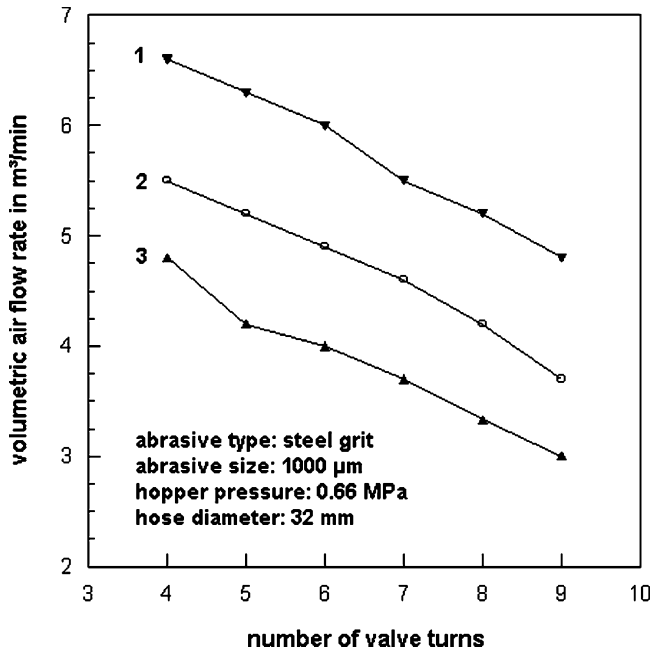


Fig. 4.12 Effects of number of valve turns and nozzle geometry on the volumetric air flow rate in convergent-divergent nozzles (Bae et al., 2007). Nozzle “1” – nozzle length: 150 mm, throat (nozzle) diameter: 9.5 mm, divergent angle: 2.1°, convergent angle: 9.3°; Nozzle “2” – nozzle length: 216 mm, throat (nozzle) diameter: 11.0 mm, divergent angle: 1.3°, convergent angle: 7.9°; Nozzle “3” – nozzle length: 125 mm, throat (nozzle) diameter: 12.5 mm, divergent angle: 7.6°, convergent angle: 3.9°

This complex relationship makes it almost impossible to reliably precalculate a certain desired abrasive mass flow rate.

Brauer (1971) reviewed the results of experimental investigations in the field of bulk material transport, and he suggested the following relationships:

$$\dot{m}_P \propto d_V^{2.5 \text{ to } 2.96} \tag{4.8a}$$

$$\dot{m}_P \propto d_P^{-0.18 \text{ to } -1.0} \tag{4.8b}$$

$$\dot{m}_P \propto \rho_P \tag{4.8c}$$

The qualitative trends between abrasive mass flow rate and valve opening size (Fig. 4.7), particle density and particle size (Fig. 4.10), which were discussed earlier, are properly reflected by these relationships.

Beverloo et al. (1961) developed a model for the approximation of the mass flow rate of particulate solids flowing through the discharge openings of hoppers. The model considers gravity-induced discharge only, and it is valid for particle sizes

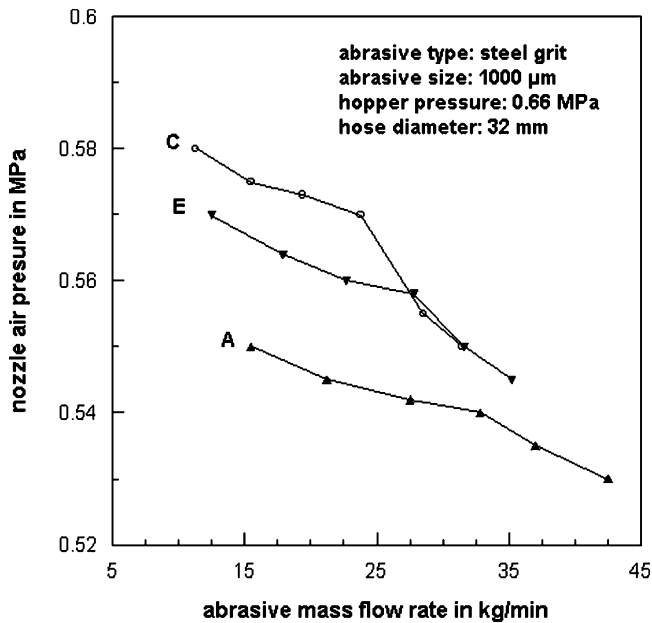


Fig. 4.13 Effects of abrasive mass flow rate and nozzle geometry on the nozzle air pressure (Bae et al., 2007). Nozzle “A” – nozzle length: 150 mm, throat (nozzle) diameter: 11.5 mm, divergent angle: 2.1°, convergent angle: 9.3°; Nozzle “C” – nozzle length: 125 mm, throat (nozzle) diameter: 12.5 mm, divergent angle: 7.6°, convergent angle: 3.9°; Nozzle “E” – nozzle length: 216 mm, throat (nozzle) diameter: 11.0 mm, divergent angle: 1.3°, convergent angle: 7.9°

larger than $d_p = 500 \mu\text{m}$. Another restriction is $d_v/d_p > 6$. The model delivers the following relationship:

$$\dot{m}_p \propto \rho_p \cdot g^{1/2} \cdot (d_v - k_Z \cdot d_p)^{5/2} \quad (4.9)$$

The parameter k_Z characterises the limit for gravity-induced flow. If pressure gradients are involved in the discharge process, a second term must be added, which leads to the following expression (Seville et al., 1997):

$$\dot{m}_p \propto \underbrace{\rho_p \cdot g^{1/2} \cdot (d_v - k_Z \cdot d_p)^{5/2}}_{\text{gravity induced}} \cdot \underbrace{\left(1 + \frac{\Delta p}{\rho_p \cdot g}\right)}_{\text{pressure gradient induced}} \quad (4.10)$$

The power relationship between mass flow rate and valve opening is clearly expressed in this relationship (see Fig. 4.7). The general trend for the effect of variations in particle size is also recorded, at least for standard dimensions of particles and valve opening (see Fig. 4.10). The proposed linear trend between abrasive material density and abrasive mass flow rate is supported by experimental results reported by Adlassing and Jahn (1961).

In practice, however, a working characteristic, similar to the graphs shown in Figs. 4.7 and 4.11, must be installed for any particular valve type for certain air pressures, nozzle diameters and abrasive materials. Such working characteristics are not available from manufacturers, and it must be estimated experimentally.

4.3.2.3 Abrasive Mass Flow Adjustment

In current industry practice, it is often the potman, who does this adjustment manually. How sensitive the entire blast cleaning procedure reacts on such a manual adjustment is illustrated in Fig. 6.20 and Table 4.6. Figure 6.20 shows that the cleaning rate was very sensitive to the number of turns for a metering valve. If the copper slag was being considered, a change from five turns to six turns led to an increase in cleaning rate from about 60 m²/h to 72 m²/h (+20%). The results listed in Table 4.6 illustrate the effects of manual fine adjustment on the blast cleaning process. If the number of turns of the metering valve was changed from 2 to 2.5 for garnet, cleaning rate almost tripled, and the specific abrasive consumption dropped up to -30%. For the steel grit, the situation was different. A change in the number of valve turns from 3 to 3.5 did not affect the cleaning rate, but increased the specific abrasive consumption by +30%. These examples highlight the economic potential of a precise abrasive metering.

Table 4.6 Metering valve adjustment test data (Hitzrot, 1997)

Abrasive material	Number of turns	Abrasive mass flow rate in kg/min	Cleaning rate in m ² /h	Specific abrasive consumption in kg/m ²
Fine coal slag	2	7.6	30.4	15.2
	3	9.5	32.4	17.7
	5	12.6	23.0	32.9
Star blast	2	5.5	24.3	13.6
	3	13.9	38.1	22.2
	5	17.5	36	29.3
Aluminium oxide	2	6.4	11.6	32.9
	3	13.0	19.4	40.0
	5	32.1	30.4	62.7
G-50 steel grit	2	5.4	11.3	28.3
	3	13.7	20.0	41.4
	3.5	17.3	19.2	54.1
	4.5	19.7	19.7	59.6
Garnet	2	2.6	6.6	23.8
	2.5	5.6	19.6	17.2
	3	10.1	20.9	28.8
	3.5	10.6	21.1	30.8
	4.5	21.3	23.7	54.1
Glass blast	2.75	7.6	19.3	23.8
	3	10.0	22.5	26.8
	3.5	11.5	29.9	22.7
	4	18.1	29.9	36.4

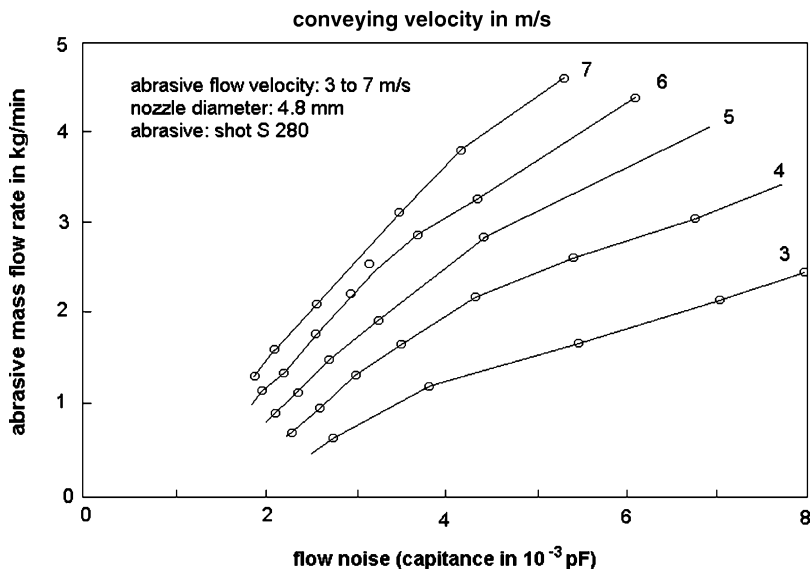


Fig. 4.14 Relationship between abrasive mass flow rate, abrasive conveying velocity in an abrasive hose, and the flow noise (Neelakantan and Green, 1982)

An experienced potman adjusts the abrasive mass flow rate according to the noise developed by the abrasive material if it flows through the hose. An optimum flow pattern causes a typical noise (see Sect. 4.5.1 for flow pattern types). Results plotted in Fig. 4.14 show that this empirical approach has a physical background. The flow noise had distinct relationships with air flow velocity in the hose and abrasive mass flow rate. These relationships offer the opportunity to control and adjust abrasive mass flow rates by acquiring and treating acoustic signals.

4.4 Pressure Air Hose Lines

4.4.1 Materials and Technical Parameters

The transport of the compressed air from the compressor to the blast machine occurs through pressure lines. For on-site applications, these are flexible hose lines. Hose lines are actually flexible hoses operationally connected by suitable hose fittings. Hose fittings are component parts or sub-assemblies of a hose line to functionally connect hoses with a line system or with each other. Pressure air hoses are flexible, tubular semi-finished product designed of one or several layers and inserts. They consist of an outer cover (polyamide, nylon), a pressure support (specially treated high-tensile steel wire) and an inner core (POM, polyamide, nylon). Technical parameters are listed in Table 4.7. It can be recognised from the listed values that the hose diameter is an important handling parameter. An increase in hose diameter is

Table 4.7 Technical parameters for blast cleaning hoses (Phoenix Fluid Handling Industry GmbH, Hamburg)

Internal diameter in mm	Wall thickness in mm	Bend radius in mm	Specific weight in kg/m
19	5.0	95	0.95
25	7.0	125	1.00
32	8.0	200	1.38
38	8.0	240	1.60
42	9.0	330	2.00

accompanied by an increase in bend radius and an increase in specific weight. Thus, larger hoses are more difficult to handle.

4.4.2 Air Hose Diameter Selection

The speed of the air flow through the hose for compressible flow can be calculated based on mass flow conservation, which delivers the following relationship:

$$v_F = \frac{4}{\pi} \cdot \frac{\dot{m}_A}{\rho_A \cdot d_H^2} \quad (4.11)$$

The air density, and therefore the flow velocity, depends on pressure and temperature [see (3.6)]. Typical hose diameters for blast cleaning operations are between $d_H = 19$ mm and 50 mm (see Table 4.7). For a volumetric flow rate of $\dot{Q}_A = 10$ m³/min, delivered at a pressure of $p = 1.0$ MPa, the velocity of the air flow for a hose diameter of $d_H = 40$ mm is $v_F = 13$ m/s. More results of calculations are provided in Fig. 4.15.

An empirical rule for selecting the proper hose diameter is: the flow velocity in the hose should not exceed the value of $v_F = 15$ m/s (Gillesen et al., 1995). Based on (4.11), the corresponding minimum hose diameter is as follows:

$$d_H = 0.29 \cdot \left(\frac{\dot{m}_A}{\rho_A(p, T)} \right)^{1/2} \quad (4.12)$$

In that equation, the air mass flow rate is given in kg/s, and the hose diameter is given in m. If no standard diameter is available for the calculated value, the next larger diameter should be selected. As an example, for an air mass flow rate of $\dot{m}_A = 10$ kg/min, delivered at a pressure of $p = 1.0$ MPa and a temperature of $\vartheta = 20^\circ\text{C}$, (4.12) delivers a value of $d_H = 34.5$ mm; the recommended internal hose diameter is $d_H = 38$ mm. The critical hose diameters for the situations displayed in Fig. 4.15 are: $d_H = 45$ mm for $p = 0.7$ MPa; $d_H = 40$ mm for $p = 0.9$ MPa and $d_H = 37$ mm for $p = 1.1$ MPa. The lower the pressure, the higher becomes the selected hose diameter. The reason is the increase in volumetric air flow rate if the air pressure drops [see (3.1)]. For a given air volumetric flow rate, the trend between air pressure and critical hose diameter follows

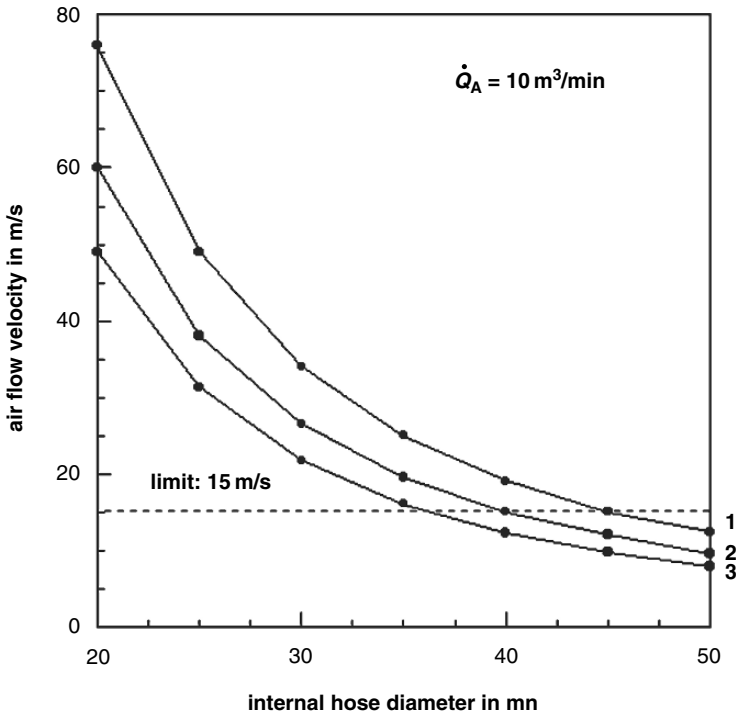


Fig. 4.15 Calculated air flow velocities in blast cleaning air hoses (air flow rate: $\dot{Q}_A = 10 \text{ m}^3/\text{min}$). Pressure levels: “1” – $p = 0.7 \text{ MPa}$; “2” – $p = 0.9 \text{ MPa}$; “3” – $p = 1.1 \text{ MPa}$

a power relationship with a negative power exponent (for the examples in Fig. 4.15, the power exponent has a value of -0.43).

4.4.3 Pressure Drop in Air Hose Lines

4.4.3.1 General Approach

A permanent problem with air hose lines is the pressure drop in the hose lines. The situation is illustrated in Fig. 4.16. The well-known general approach for estimating the pressure drop for incompressible flow is as follows (Bohl, 1989):

$$\frac{\Delta p_A}{\rho_A} = \underbrace{\sum_i \left(\lambda_{Ai} \cdot \frac{l_H}{d_H} \cdot \frac{v_F^2}{2} \right)}_{\text{straight hose}} + \underbrace{\sum_k \left(\xi_{Ak} \cdot \frac{v_F^2}{2} \right)}_{\text{knees and aramtures}} \quad (4.13)$$

$$\Delta p_A = p_1 - p_2$$

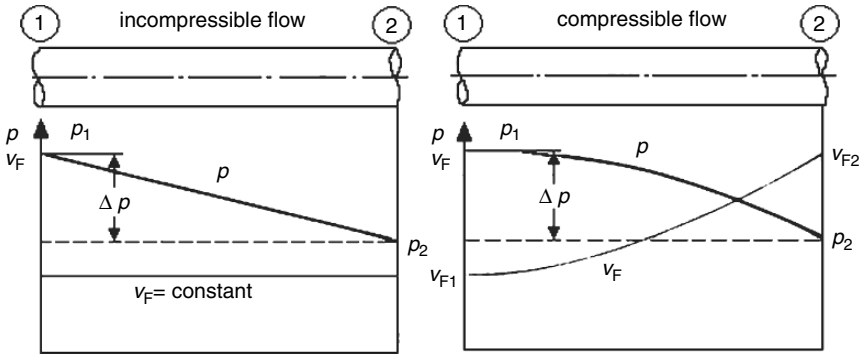


Fig. 4.16 Parameter variation along a hose line for compressible flow conditions (adapted from Wille, 2005)

where, p_1 is the static pressure at the point “1” and p_2 is the static pressure at the point “2” as shown in Fig. 4.16. The parameters λ_A and ξ_A are friction numbers, v_F is the flow velocity, l_H is the hose length, and d_H is the hose diameter.

However, for compressible flow, which should usually be considered for the air flow in blast cleaning hoses, the pressure drop is not linear, and the air flow velocity is not at a constant level over the hose length (see Fig. 4.16, right drawing). Approximations for the calculation of pressure losses for compressible flow can be found in standard monographs on technical fluid dynamics (Glück, 1988; Bohl, 1989; Sigloch, 2004). A feasible approximation is as follows (Bohl, 1989):

$$\frac{p_1^2 - p_2^2}{2 \cdot p_1} = \lambda_A \cdot \frac{l_H}{d_H} \cdot \rho_A \cdot \frac{v_F^2}{2} \cdot \frac{\bar{T}}{T_1} \tag{4.14}$$

Here, the density variation over the hose length (due to changes in pressure and temperature) must be considered. The average temperature can be assumed as follows:

$$\bar{T} \approx \frac{T_1 + T_2}{2} \tag{4.15}$$

The temperature at the end of the hose line can be approximated as follows:

$$T_2 \approx T_1 \cdot \left(\frac{p_2}{p_1} \right)^{\frac{\kappa-1}{\kappa}} \tag{4.16}$$

If the temperature does not vary notably along the hose length (isotherm flow), the term \bar{T}/T_1 in (4.14) can be neglected. For an adiabatic flow, however, the temperature term must be considered.

4.4.3.2 Friction Numbers

The friction number for wall friction depends on the Reynolds number and on the ratio between hose diameter and internal wall roughness. The general relationship is as follows (Bohl, 1989):

$$\lambda_A = f \left(Re_H; \frac{k_H}{d_H} \right) \quad (4.17)$$

The Reynolds number of the air flow through a hose is given as follows:

$$Re_H = \frac{v_F \cdot d_H \cdot \rho_A}{\eta_A} \quad (4.18)$$

It can be seen that Re_H is a function of pressure and temperature, because density and dynamic viscosity of the air are involved in the calculations. In order to consider these effects, (3.6) and (3.7) must be applied. For a pressure of $p = 1.0$ MPa, a volumetric flow rate of $\dot{Q}_A = 10$ m³/min, an air temperature of $\vartheta = 20^\circ\text{C}$ and a hose diameter of $d_H = 35$ mm, the Reynolds number is $Re_H = 4.1 \times 10^5$. More results of calculations are provided in Fig. 4.17. It can be seen that changes in temperature have only marginal effects. The Reynolds number decreases if the hose diameter increases. A combination of (4.11) and (4.18) delivers the relationship: $Re_H \propto d_H^{-1}$.

The precise solution to (4.17) is a function of the flow type in the hose and the thickness of the laminar boundary layer at the hose wall. For blast cleaning processes, a turbulent flow ($Re_H > 2,300$) is basically assumed. However, even if the flow is turbulent, a thin laminar boundary layer forms at the wall regions of the hoses (Bohl, 1989; Wille, 2005). This laminar layer is illustrated in Fig. 4.18. The thickness of this layer can be calculated as follows (Wille, 2005):

$$\delta_H = \frac{5}{Re_H^{1/2}} \cdot d_H \quad (4.19)$$

Results of (4.19) are displayed in Fig. 4.19. It can be seen that air temperature does not have a notable effect on the thickness of the boundary layer. But the effect of the hose diameter is very pronounced. Combining (4.11), (4.18) and (4.19) delivers the relationship: $\delta_H \propto d_H^{3/2}$.

For $\delta_H > k_H$, the hose surface is considered to be *hydraulically smooth*, and the so-called Blasius equation can be utilised to calculate the friction number for a Reynolds number range between $Re_H = 2.3 \times 10^3$ and 10^5 (Bohl, 1989):

$$\lambda_A = 0.3164 \cdot Re_H^{-0.25} \quad (4.20)$$

For higher Reynolds numbers between $Re_H = 10^5$ and 10^6 , the so-called Nikuradse equation for hydraulically smooth pipes can be applied (Bohl, 1989):

$$\lambda_A = 0.0032 + 0.221 \cdot Re_H^{-0.237} \quad (4.21)$$

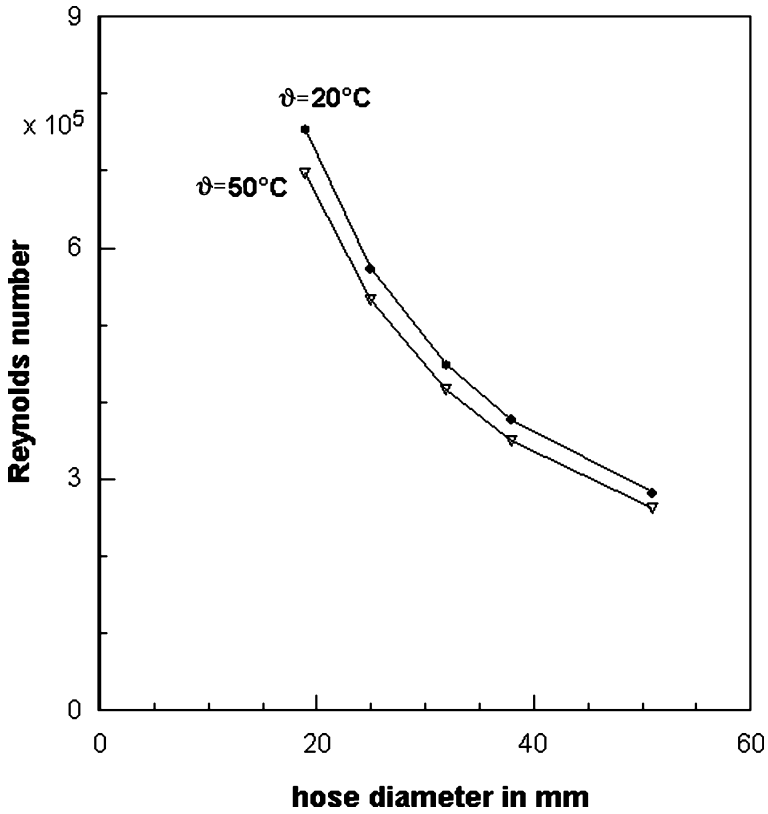


Fig. 4.17 Calculated Reynolds numbers for the flow of air in blast cleaning air hoses for two values of air temperature (air volume flow rate: $\dot{Q}_A = 10 \text{ m}^3/\text{min}$, air pressure: $p = 1.0 \text{ MPa}$)

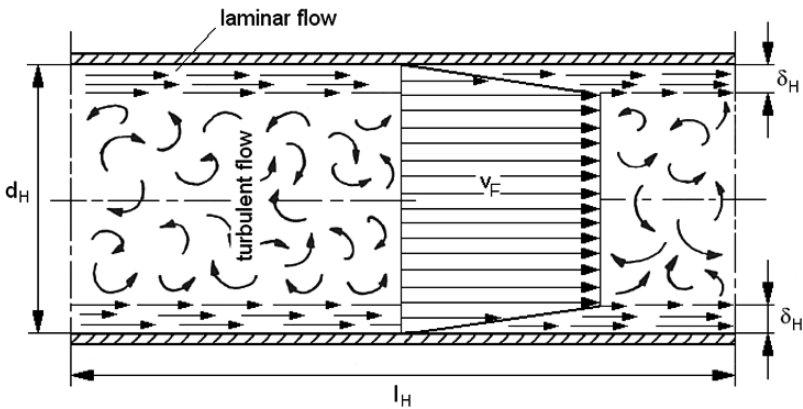


Fig. 4.18 Structure and parameters of a laminar boundary layer on a hose wall (Wagner, 1990)

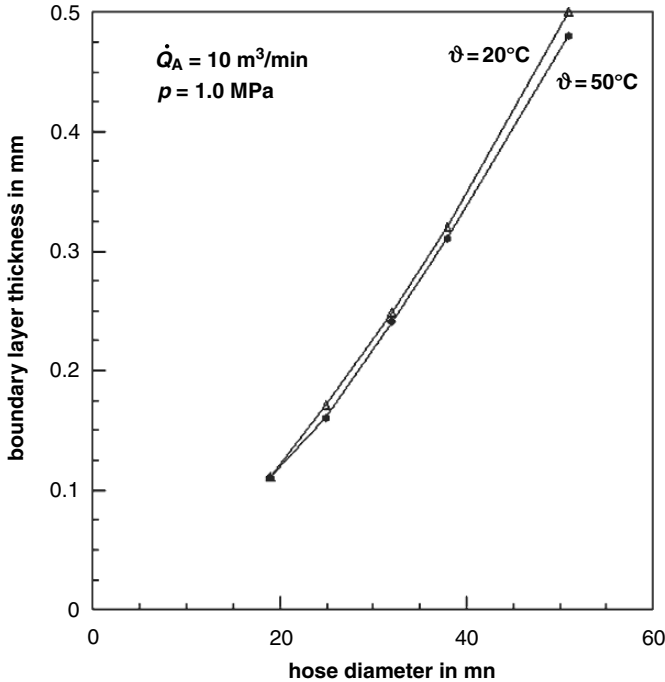


Fig. 4.19 Calculated values for the thickness of laminar boundary layers for the flow of air in blast cleaning hoses for two values of air temperature

In these cases, the friction number is independent of the wall roughness, and it is a function of the Reynolds number only. Equations (4.20) and (4.21) are graphically expressed in Figs. 4.20 and 4.21. Typical values for λ_A can be read from these two graphs.

For $\delta_H < k_H$, the hose surface is considered to be *hydraulically rough*, and the friction number can be estimated from the so-called Prandtl–Colebrook charts, which can be found in standard books on technical fluid mechanics (Oertel, 2001; Wille, 2005). A Prandtl–Colebrook chart is displayed in Fig. 4.22. If the Reynolds number and the ratio d_H/k_H are known, the corresponding value for λ_A can be read at the ordinate. The special case *hydraulically smooth* is also included in that graph. A general empirical relationship for the turbulent flow regime is the Colebrook-White equation (Wille, 2005):

$$\frac{1}{\lambda_A^{1/2}} = -2 \cdot \log \left(\frac{2.51}{\text{Re}_H \cdot \lambda_A^{1/2}} + 0.27 \cdot \frac{k_H}{d_H} \right) \quad (4.22)$$

Equations 4.20–4.22 are illustrated in Figs. 4.20–4.22. For the example mentioned above, the boundary layer thickness is $\delta_H = 0.27 \text{ mm}$. Rubber hoses, manufactured for blast cleaning applications, have a typical roughness value of about

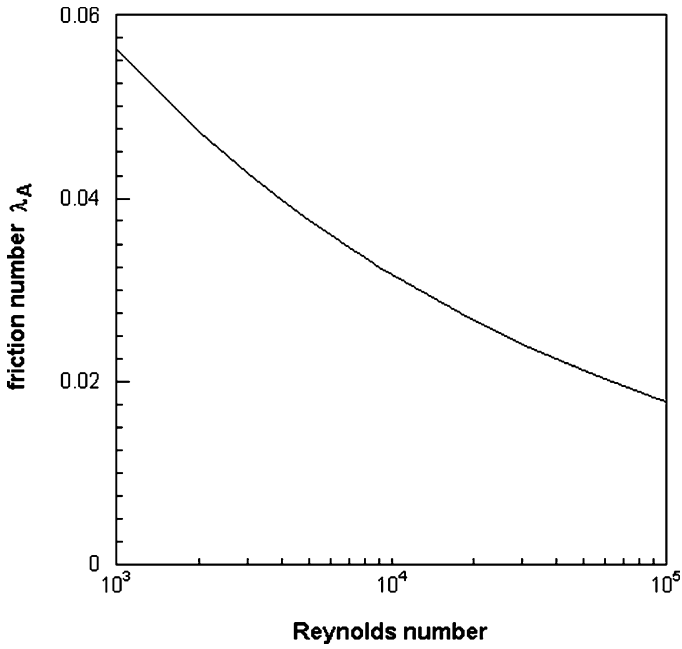


Fig. 4.20 Friction parameter for *hydraulically smooth* flow conditions at high Reynolds numbers: Blasius' solution (4.20)

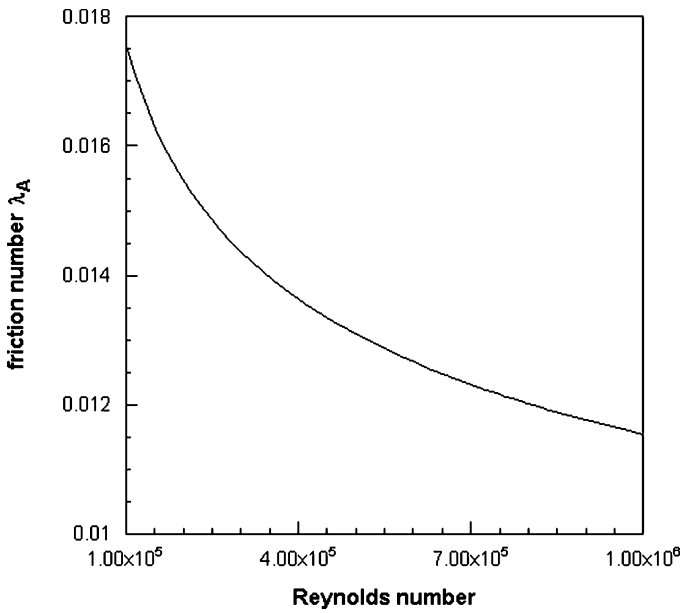


Fig. 4.21 Friction parameter for *hydraulically smooth* flow conditions at very high Reynolds numbers: Nikuradse's solution (4.21)

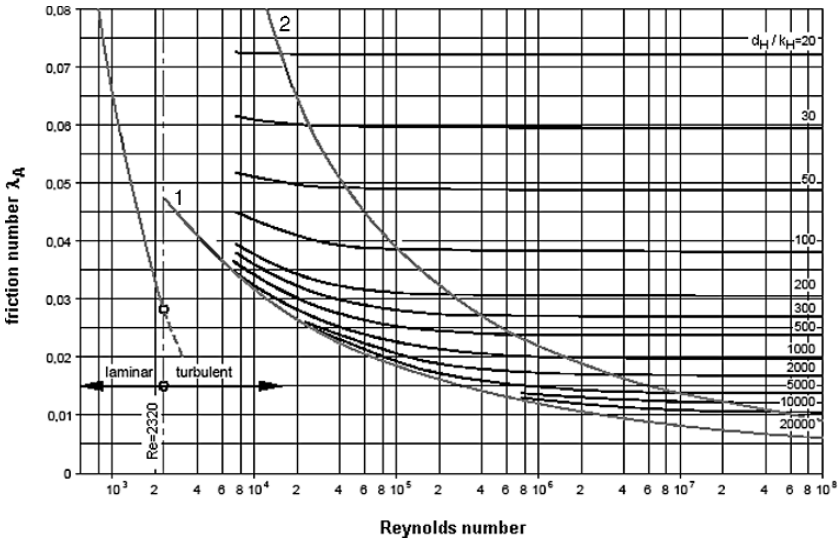


Fig. 4.22 Relationships between Reynolds number, relative roughness and friction parameter (Wille, 2005). 1-hydraulically smooth; 2-hydraulically rough (limit)

$k_H = 0.016 \text{ mm}$ (Bohl, 1989). This value is one order of magnitude lower than the typical values for the thickness of the laminar boundary layer (see Fig. 4.19). The Reynolds numbers for the flow in blast cleaning hoses usually exceed the value $Re_H = 10^5$ (see Fig. 4.17). Therefore, the rather simple (4.21) can be applied for the estimation of the friction number for most blast cleaning applications.

4.4.3.3 Hose Diameter Effects

The equations mentioned above deliver the following relationship between pressure drop and hose diameter:

$$\Delta p_A \propto d_H^{-5} \tag{4.23}$$

This equation illuminates the overwhelming influence of the hose diameter on the pressure loss. (A precise physical deviation delivers a power exponent value somewhat smaller than 5.) This influence is graphically expressed in Fig. 4.23, which shows results of measurements of the pressure drop in hoses with different diameters. The rapid pressure drop in the hose with the small diameter of $d_H = 19 \text{ mm}$ can be recognised. These experimental results agree very well with results calculated from (4.14). More values, calculated with (4.14), are plotted in Fig. 4.24. The graphs show, among others, that pressure drop reduces at higher air pressures. This phenomenon can be explained with (3.6), which suggests that the air density increases with an increase in pressure. Higher air density means lower air volume, which in turn reduces the air flow velocity in the hose. Equation 4.14 shows that lower air flow velocity leads to less pressure drop. More relationships are displayed in Fig. 4.16. The graphs show the relationship between hose length and air flow velocity in the

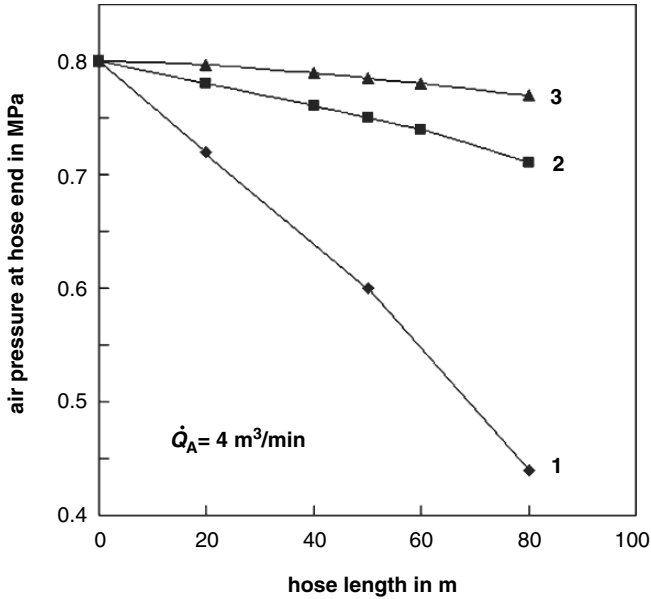


Fig. 4.23 Effect of hose diameter on experimentally estimated pressure loss in air hoses (Neumann, 1985). Air flow rate: $\dot{Q}_A = 4.0 \text{ m}^3/\text{min}$; hose diameter: “1” – $d_H = 19 \text{ mm}$; “2” – $d_H = 25 \text{ mm}$; “3” – $d_H = 32 \text{ mm}$. Pressure drop is non-linear

hose. It can be seen at the right graph in Fig. 4.16 that the air flow velocity increases with an increase in hose length. The reason is the expansion flow caused by the pressure drop in the hose line. Lower air pressure causes the air density to decrease. The reduction in air density leads to an increase in air volumetric flow rate and, thus, to an increase in flow velocity [see (4.11)]. Another important effect is that of the abrasive material. Although no abrasive material flows through the air hose, it affects the pressure drop. This effect is caused by the reduction in the air volumetric flow rate due to the addition of the abrasive particles [see (3.18) and Fig. 3.11].

4.4.3.4 Pressure Drop in Fittings and Armatures

The precise pressure drop in hose fittings and in armatures, characterised through ξ_A in (4.13), should be measured for any individual fitting. However, such values are not available for an individual accessory in most cases, but pressure loss values for certain groups and types of armatures and valves are published in the technical literature. A large collection of friction numbers for numerous armatures, valves, pipe elements, etc. can be found in Bohl’s (1989) and Wagner’s (1990) books. Two examples are shown in Figs. 4.25 and 4.26. For most valve constructions, the friction values are almost independent on pipe diameter. It can be seen that friction numbers for armatures are usually one order of magnitude larger than friction numbers for the flow in straight hoses. The valve constructions shown in Figs. 4.25 and 4.26, for example, can have friction numbers between $\xi_A = 1$ and 7.

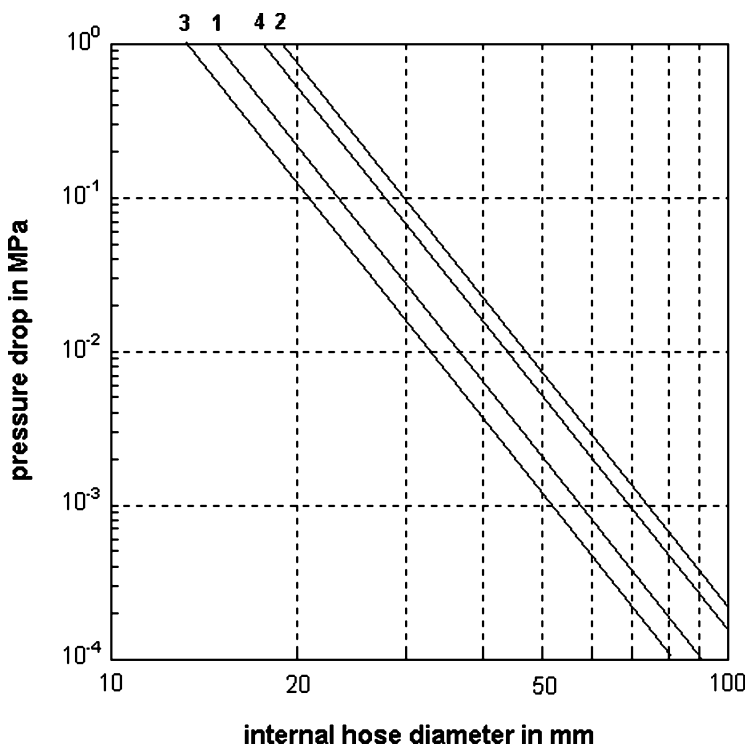


Fig. 4.24 Results of (4.14); hose length: $l_H = 40$ m. Conditions: “1” – $p = 0.7$ MPa, $\dot{Q}_A = 5.0$ m³/min; “2” – $p = 0.7$ MPa, $\dot{Q}_A = 10$ m³/min; “3” – $p = 1.0$ MPa, $\dot{Q}_A = 5.0$ m³/min; “4” – $p = 1.0$ MPa, $\dot{Q}_A = 10$ m³/min

Another principle for the assessment of pressure drops in armatures is the *equivalent length*. It is assumed that the pressure drop in a certain type of armature corresponds to the pressure drop in a pipe of a certain *equivalent length*. Examples for this procedure are provided in Table 4.8. If, for example, a seat valve with an inlet pipe diameter of 40 mm is considered, the equivalent length is 10 m. These two values must now be inserted into (4.14) in order to calculate the approximate pressure drop for this particular armature ($d_H = 40$ mm, $l_H = 10$ m). More examples can be found in Bohl (1989).

4.5 Abrasive Hose Lines

4.5.1 Conveying Modes in Abrasive Hoses

Abrasive hoses serve to convey the abrasive materials from the blast machine to the blast cleaning nozzle. This process can be considered pneumatic conveying, and

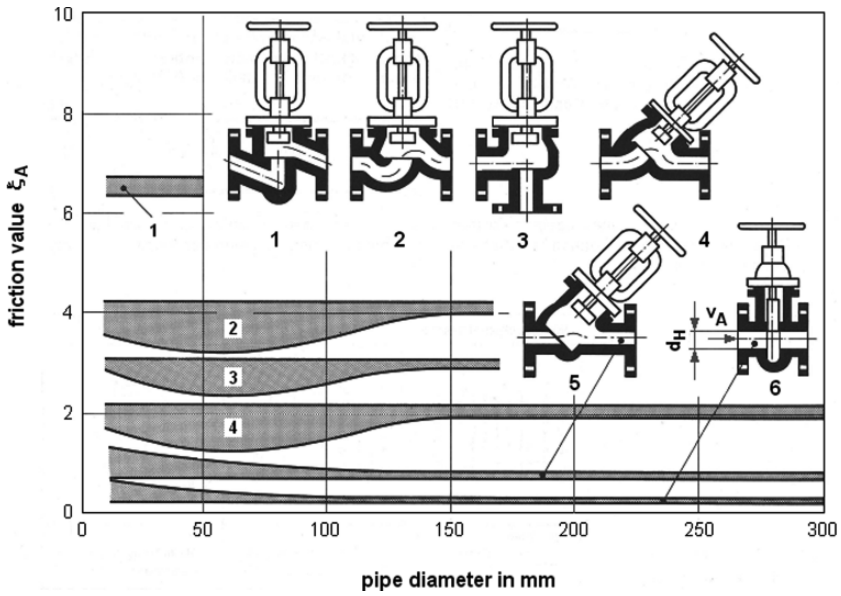


Fig. 4.25 Typical friction values for valve armatures (Wagner, 1990)

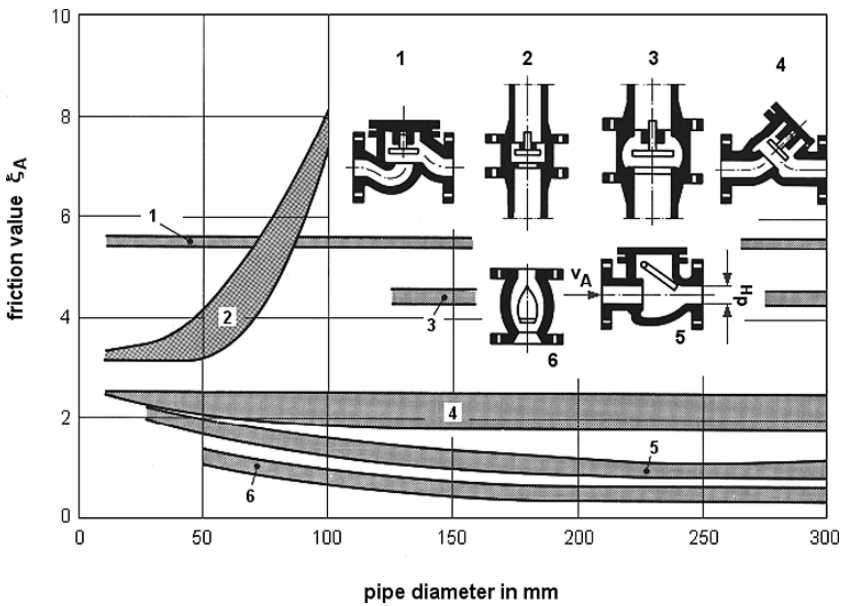


Fig. 4.26 Typical friction values for check valves (Wagner, 1990)

Table 4.8 *Equivalent lengths* for numerous air armatures (Fraenkel, 1954)

Armature	Equivalent length in m						
	Pipe diameter in mm						
	25	40	50	80	100	125	150
Seat valve	6	10	15	25	30	50	60
Streamline valve	3	5	7	10	15	20	25
Gate valve	0.3	0.5	0.7	1	1.5	2	2.5
Bend (peak corner)	1.5	2.5	3.5	5	7	10	15
Bend (smooth corner)	1	2	2.5	4	6	7.5	10
Bend ($r = D$)	0.3	0.5	0.6	1	1.5	2	2.5
Bend ($r = 2D$)	0.15	0.25	0.3	0.5	0.8	1	1.5
Hose coupling (T-shape)	2	3	4	7	10	15	20
Reducer	0.5	0.7	1	2	2.5	3.5	4

relationships known from pneumatic conveying techniques can, to a certain amount, be utilised.

Engineering treatments on pneumatic conveying processes can be found in Buhrke et al. (1989), Marcus et al. (1990), Siegel (1991) and Weber (1974). For fine particles suspended in an air stream, two basic conveying modes can occur: stable flow and unstable flow. Moreover, five different flow patterns can be observed, namely fully suspended (stable), surging (unstable), stationary bed (stable), moving bed (very unstable) and stationary bed (stable). These patterns depend on air conveying velocity and abrasive mass flow rate. Some relationships are illustrated in Figs. 4.27–4.29. Stable conveying conditions are one preposition for an efficient functioning of abrasive hose systems. The graphs plotted in Fig. 4.28 show, in particular, how changes in air flow velocity and abrasive mass flow rate affect the flow regime. An air flow velocity of $v_F = 15$ m/s and an abrasive mass flow rate of $\dot{m}_P = 4$ t/h (67 kg/min) lead to “instable region” flow. If the air flow velocity is increased up to $v_F = 20$ m/s, the process turns into a more effective “hank conveying”, whereby the pressure drop slightly increases. “Hunk conveying” can also be obtained, if the abrasive mass flow rate is reduced to $\dot{m}_P = 2$ t/h (33 kg/min). For this condition, the flow turns into “hank conveying”, whereby the original air flow velocity ($v_F = 15$ m/s) can be maintained.

4.5.2 Critical Conveying Flow Velocities in Abrasive Hoses

The graphs plotted in Figs. 4.27–4.29 show that a typical air flow velocity exists where pressure drop has minimum values. This flow velocity is denoted “critical air velocity” in Fig. 4.27. The higher the abrasive mass flow rate, the higher is the value for this optimum air flow velocity. This trend is illustrated in Fig. 4.29 by the line designated “optimum”. For a typical blast cleaning condition (e.g. $\dot{m}_P = 16$ kg/min), the optimum air flow velocity may be in the range of $v_F = 16$ m/s. If the abrasive mass flow rate is reduced to $\dot{m}_P = 4.2$ kg/min, the optimum flow velocity is about $v_F = 12$ m/s (see Fig. 4.29).

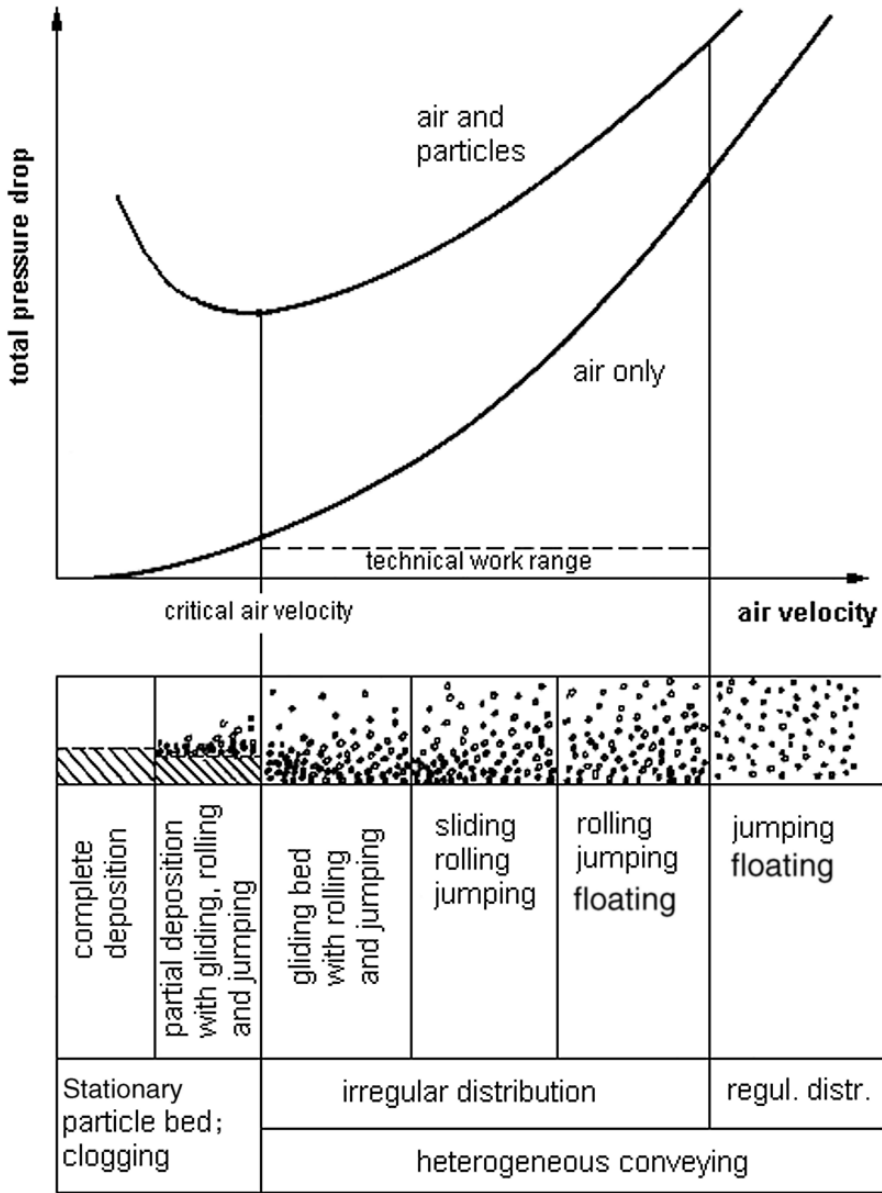


Fig. 4.27 Conveying modes in pneumatic solid particle conveying lines: general relationships (Buhrke et al., 1989)

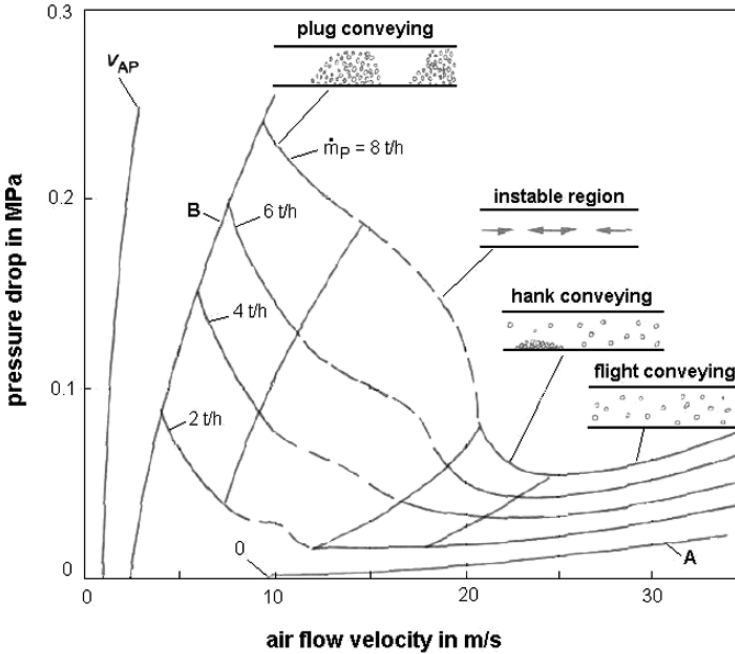


Fig. 4.28 Effect of abrasive mass flow rate on conveying modes in pneumatic solid particle conveying lines (Siegel, 1991); see text for the meanings of “A” and “B”

The line “A” in Fig. 4.28 characterises the plain air flow without any solid particles. The relationship is $\Delta p_A \propto v_F^2$. The line “B” in Fig. 4.28 marks the limits for abrasive conveying for a given abrasive mass flow rate. For $\dot{m}_p = 4 \text{ t/h}$ (67 kg/min), the limiting flow velocity is at about $v_F = 7 \text{ m/s}$. But the conveying process is still possible for the lower mass flow rate ($\dot{m}_p = 2 \text{ t/h}$).

The line “ v_{AP} ” in Fig. 4.28 characterises the general limit for any pneumatic conveying for the given solid material. This critical velocity, called “saltation velocity”, is about $v_{AP} = 3 \text{ m/s}$ for the conditions in Fig. 4.28. Each abrasive material requires a saltation velocity, which is the minimum gas flow velocity for horizontal conveying. Certain approaches are known for the analytical estimation of this parameter. A rather simple approach is due to Rizk (1973):

$$\frac{\dot{m}_p}{\dot{m}_A} = \frac{1}{10^{1.44 \cdot d_p + 1.96}} \cdot \left[\frac{v_{AP}}{(g \cdot d_H)^{1/2}} \right]^{1.1 \cdot d_p + 2.5} \tag{4.24}$$

It can be seen from (4.24) that the saltation velocity depends on the mass flow ratio abrasive/air, hose diameter (m) and abrasive particle size (mm). Uferer (1992) adapted a similar model for the use in blast cleaning hoses, and he derived the following relationship:

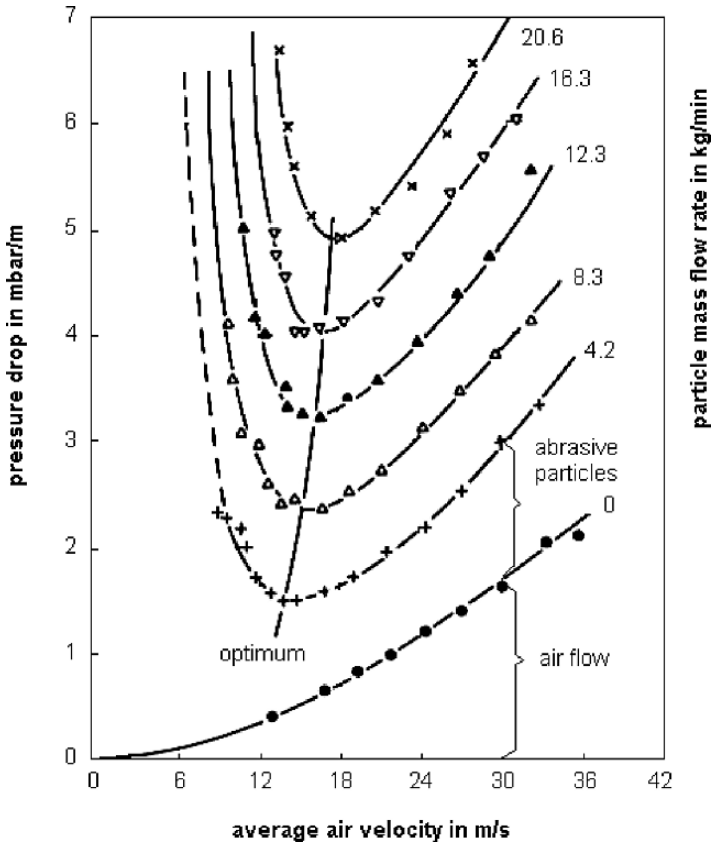


Fig. 4.29 Relationships between air velocity, abrasive mass flow rate, and pressure loss in pneumatic conveying lines (Marcus et al., 1990)

$$v_{AP} = 18.8 \cdot \left(\frac{\dot{m}_P}{\dot{m}_A} \right)^{1/3} \cdot d_H^{1/2} \cdot g^{1/2} \tag{4.25}$$

In this simplified approach, abrasive particle size is excluded. For typical conditions ($\dot{m}_P/\dot{m}_A = 1.5$, $d_H = 35$ mm), the critical air conveying velocity is about $v_{AP} = 13$ m/s. Further results are plotted in Fig. 4.30. It can be seen that saltation velocities typically between $v_{AP} = 10$ m/s and 15 m/s are required for blast cleaning applications.

The actual demanded air velocity in an abrasive hose can be adjusted through variations in the ratio between abrasive hose diameter and nozzle diameter according to the following approach suggested by Uferer (1992):

$$\left(\frac{d_H}{d_N} \right)^2 = \frac{181}{v_F} \tag{4.26a}$$

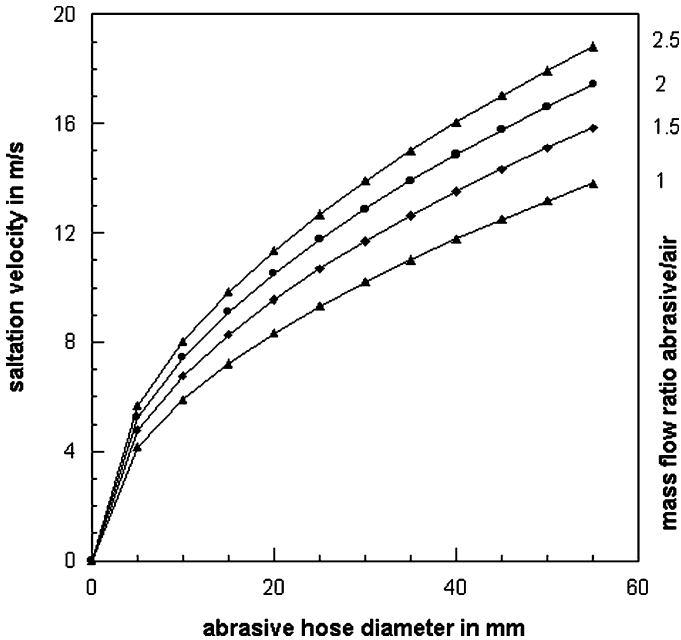


Fig. 4.30 Saltation air flow velocity for particle conveying, based on (4.25)

This relationship holds if air temperature does not vary, and if the air pressure exceeds the value of $p = 0.09$ MPa. Results of calculations are plotted in Fig. 4.31. If a value of $v_F = 15$ m/s for the air velocity is being considered (which is just above the saltation velocity), an optimum diameter ratio is at about $d_H/d_N = 3.5$. This result agrees well with recommendations issued by equipment manufacturers, and it verifies the application of methods developed for pneumatic conveying of solids to the condition in blast cleaning hoses. If, for example, a nozzle with a diameter of $d_N = 12$ mm and a mass flow ratio abrasive/air of $R_m = 1.5$ are used, the optimum abrasive hose diameter would be $d_H = 42$ mm according to (4.26a). The next larger standard hose diameter is $d_H = 50$ mm, which would deliver a diameter ratio of $50/12 = 4.2$. From (4.26a), the corresponding air flow velocity is about $v_F = 10$ m/s, which is lower than the typical saltation velocity plotted in Fig. 4.30 for $d_H = 50$ mm (which is $v_{AP} = 15$ m/s). Thus, unsteady abrasive conveying, or even clogging, may occur, which would increase pressure losses in the hose because of air flow through deposited abrasive particle conglomerates (this would apply to the region left from the line marked by “critical air velocity” in Fig. 4.27). The next smaller standard hose diameter is $d_H = 38$ mm, which leads to an increase in air flow velocity up to $v_F = 18$ m/s. Although the flow is now in the “technical working range” (see Fig. 4.27), this rather high flow velocity would notably increase pressure drop (compare also Fig. 4.29). Equation 4.26a is valid in that particular configuration only for $l_H = 0$ (pressure drop in hoses is not considered). For the case $l_H > 0$, the relationship must be modified as follows (Uferer, 1992):

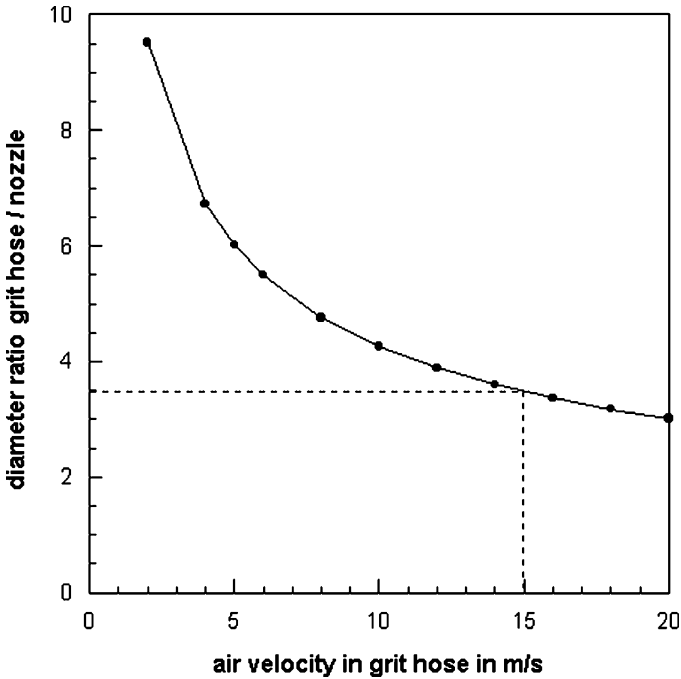


Fig. 4.31 Relationships between air velocity, abrasive hose diameter and nozzle diameter, based on (4.26a)

$$\left(\frac{d_H}{d_N}\right)^2 = \frac{181}{v_F} \cdot \left(\frac{1}{1 + (\Delta p_T/p)}\right) \tag{4.26b}$$

For $\Delta p_T = 0$, (4.26b) reduces to (4.26a). For an assumed pressure drop of 25% and an air flow velocity $v_F = 15$ m/s, (4.26b) delivers an optimum ratio $d_H/d_N = 3.1$. For the example mentioned earlier ($d_N = 12$ mm), the optimum hose diameter is $d_H = 37.2$ mm. The next commercially available hose diameter is $d_H = 38$ mm, which is very close to the requested value. Because the pressure drop is a function of the hose length, the diameter ratio d_H/d_N depends on hose length. In an optimum blast cleaning system, the parameters d_N , d_H and l_H are well balanced, and if one of the parameters changes value, the other parameters must be adjusted accordingly.

4.5.3 Optimum Flow Velocities in Abrasive Hoses

Pressure drop in abrasive hose lines is due to air flow and abrasive material conveying in these hoses. Experience with pneumatic conveying systems has shown that pressure drop depended on air conveying velocity (respectively, dynamic air pressure and air flow Froude number) and mass flow ratio abrasive/air. One example is shown in Fig. 4.29; more information can be found, among others, in Coulson and

Richardson (1968) and Marcus et al. (1990). It can be recognised from the graph in Fig. 4.29 (as well as from Figs. 4.27 and 4.28) that the pressure drop for a solid-air flow is much higher compared with that for a plain air flow. For an air conveying velocity $v_F = 15$ m/s, the pressure drop is $\Delta p_T = 0.5$ mbar/m for air only, but it is about $\Delta p_T = 2.4$ mbar/m for $\dot{m}_P = 8.3$ kg/min. It can also be noted from Fig. 4.29, that pressure loss has distinct minimum values at certain optimum air conveying velocities. This optimum air flow velocity depends on the Froude number of the particle settling flow. For vertical conveying processes, the optimum air flow velocity can be approximated as follows (Ahland, 1966):

$$v_{\text{opt}} = 4.1 \cdot g^{0.2} \cdot d_H^{0.2} \cdot v_S^{0.6} \quad (4.27)$$

This equation is valid for a range of Froude numbers (related to settling speed) between $Fr = 2.5$ and 25. The relationship is graphically expressed in Fig. 4.32 for typical blast cleaning conditions. It is important to note that the optimum air conveying velocity depends on hose diameter, although hose size effects become considerable in the range of rather high settling velocities. The settling velocities of abrasive particles in air must be estimated experimentally. Weber (1974) published an extensive number of experimental results. If particle material density and

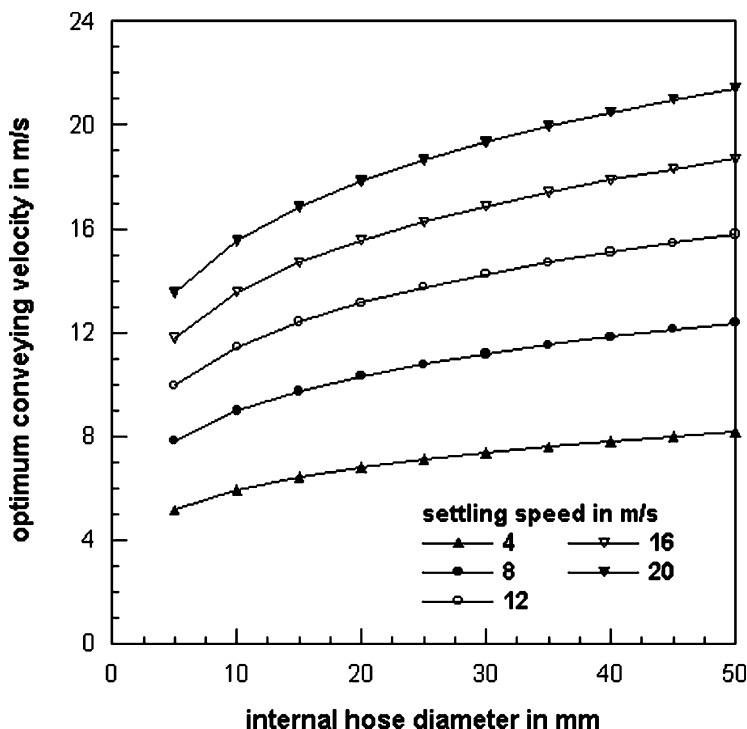


Fig. 4.32 Optimum air velocity for vertical conveying according to (4.26)

particle diameter are known, the settling velocity in air can be read from the corresponding graphs. If only particle properties are considered, and gas properties (mainly density) are excluded, settling velocity drops if particle size and particle material density decrease. A copper slag particle ($\rho_P = 3,700 \text{ kg/m}^3$) with a size of $d_P = 1,000 \text{ }\mu\text{m}$ has a settling speed of about $v_S = 9 \text{ m/s}$, whereas a steel shot particle ($\rho_P = 7,000 \text{ kg/m}^3$) of equal size has a settling velocity of about $v_S = 15 \text{ m/s}$. The graphs in Weber's (1974) book are restricted to spherical particles, but a comparison with results of other authors supports the suitability for other particle shapes. Buhrke et al. (1989) published correction factors, which consider effects of particle shape, turbulence degree and particle interactions. More importantly, the graphs plotted in Weber's (1974) book do not consider effects of air density; they apply to atmospheric conditions only, and they may deliver different results if air density variations due to higher air pressures in the hose are taken into account. Some limited measurements of settling velocities of particles in air under different air pressures are reported by Seville et al. (1997). Some of their results are plotted in Fig. 4.33. It can be seen that the air pressure notably affects the settling velocity. For the particles with a diameter of $d_P = 1,000 \text{ }\mu\text{m}$ suspended in an air temperature of $\vartheta = 27^\circ\text{C}$ ($T = 300 \text{ K}$), the settling velocity is $v_S = 7 \text{ m/s}$ for an air pressure of $p = 0.1 \text{ MPa}$, but it is $v_S = 2.5 \text{ m/s}$ only for an air pressure of $p = 1.0 \text{ MPa}$. This is a reduction of -64% . The effects of air pressure are more pronounced for the larger particle size. A typical average reduction value would be about -50% for the conditions considered in Fig. 4.33. If this reduction factor is applied to (4.27), it can be seen that the optimum air flow velocity changes by a factor of $0.5^{0.6} = 0.66$.

4.5.4 Pressure Drop in Abrasive Hoses

A general formal approach for estimating the pressure drop in an abrasive hose line is as follows:

$$\Delta p_T = \Delta p_A + \Delta p_P \quad (4.28)$$

Here, Δp_A is the pressure drop due to air flow, and Δp_P is the pressure drop caused by abrasive conveying. This relationship is illustrated in Fig. 4.29. In the figure, the lowest line (denoted "0") illustrates the pressure drop due to plain air flow, whereas the next line (denoted "4.2") characterises the total pressure drop due to air flow and abrasive conveying (in that particular case for $\dot{m}_P = 4.2 \text{ kg/min}$). The vertical distance between these two lines, designated "abrasive particles", characterises the pressure drop caused by the abrasive conveying process. The additional pressure loss Δp_P is for two reasons. First, the settling movement of the solid particles in the hose must be balanced; second, the solid particles affect the conditions of the air flow. Based on (4.13) and (4.14), a suitable approach is as follows:

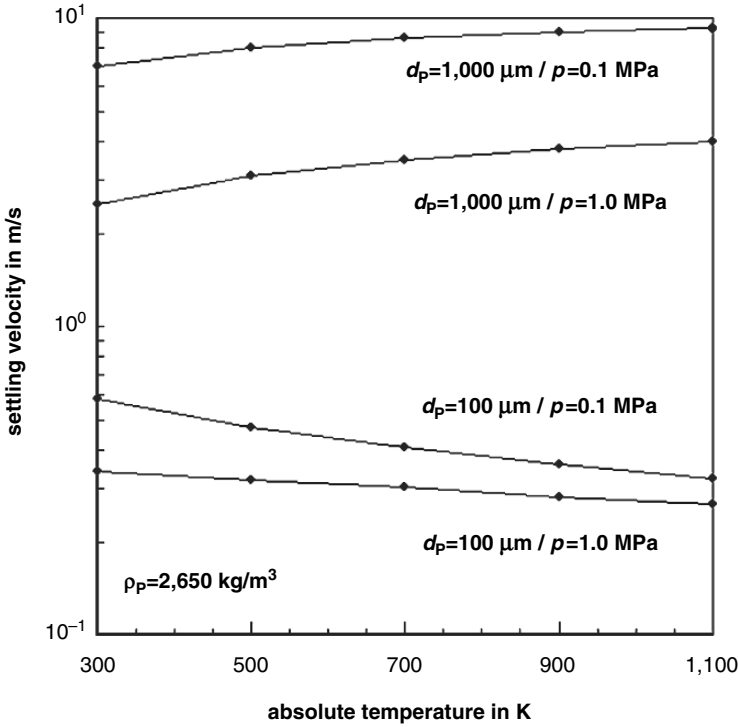


Fig. 4.33 Relationship between air density, particle size and settling velocities for grit particles in air (Seville et al., 1997)

$$\frac{\Delta p_T}{\rho_A} = \underbrace{(\lambda_A + \lambda_P) \cdot \frac{l_H}{d_H} \cdot \frac{v_F^2}{2}}_{\text{straight hose}} + \underbrace{(\xi_A + \xi_P) \cdot \frac{v_F^2}{2}}_{\text{knee or armature}} \tag{4.29}$$

The parameters λ and ξ are friction numbers. The subscript “A” stands for air flow, whereas the subscript “P” stands for abrasive conveying. The friction parameter λ_A can be calculated with (4.21). Corresponding values can be found in Fig. 4.21. The parameter λ_P can be approximated with pneumatic conveying arguments. An approach delivered by Uferer (1992) is as follows:

$$\lambda_P = \frac{C_P}{Fr_P^{\alpha_F}} \tag{4.30}$$

The constant C_P as well as the power exponent α_F depend on abrasive properties. The Froude number is given as follows:

$$Fr_P = \frac{v_F}{(d_P \cdot g)^{1/2}} \tag{4.31}$$

Uferer (1992) performed a number of experiments in order to specify (4.30) for the conditions in blast cleaning hoses. He derived the following semi-empirical relationship:

$$\lambda_P = \frac{C_{TP}}{Fr_P^{0.15}} \cdot \left(\frac{\dot{m}_P}{\dot{m}_A} \right)^{1.8} \quad (4.32)$$

The approach is valid for Froude numbers between $Fr_P = 30$ and 200 , and for mass flow ratios abrasive/air between $R_m = 0.5$ and 5.0 . The constant C_{TP} is an abrasive material parameter. Typical values for this parameter are listed in Table 4.9. A very rough approximation for slag materials and quartz is as follows (Uferer, 1992):

$$C_{TP} = 0.014 \cdot v_S \quad (4.33)$$

The graphs in Fig. 4.33 can be utilised for the approximation of v_S -values. If an average value of $v_S = 5$ m/s is taken from Fig. 4.33 for $d_P = 1,000 \mu\text{m}$ in the pressure range between $p = 0.1$ MPa and 1.0 MPa, (4.33) delivers $C_{TP} = 0.07$. This value is in the range for quartz sand and lead-thin slag (see Table 4.9). Results of measurements are compared with results based on (4.32) in Fig. 4.34. Typical values are between $\lambda_P = 0.05$ and 0.2 . In certain cases, these values are one order of magnitude larger than friction values for the flow of air only (see Fig. 4.21 for comparative values). This is shown by the dotted line in the lower section of the graph, which characterises a typical friction parameter for the air flow under the given conditions. The lines “1” to “4” in Fig. 4.34 refer to results obtained with the calculation model discussed earlier for two abrasive materials and for different mass flow ratios abrasive/air. These lines follow the relationship $\lambda_P \propto Fr_P^{-0.15}$. The lines “1” (nickel slag, $R_m = 2.0$) and “4” (quartz sand, $R_m = 1.0$) mark typical upper and lower limits for the friction numbers in abrasive hoses. Equations (4.30)–(4.33) can be applied to approximate values for λ_P under different process conditions.

The values for λ_P in Fig. 4.34 are notably higher than values for friction numbers for pneumatic conveying in rigid pipes. Typical examples for friction values for pneumatic conveying in rigid pipes are listed in Table 4.10. More examples are published in Marcus et al. (1990). The reasons for the higher values for the blast cleaning process are that flexible rubber hoses are used for blast cleaning, and that the abrasive particles act as erosive media. Results listed in Table 4.10 very effectively illustrate the effect of material parameters on the friction number. If the hardness of the pipe material drops, friction value increases by a factor of 5

Table 4.9 C_{TP} -values for some abrasive materials (Uferer, 1992)

Abrasive material	C_{TP} -value
Lead-tin slag	0.078
Phosphor slag	0.102
Iron-nickel slag	0.129
Quartz sand	0.07

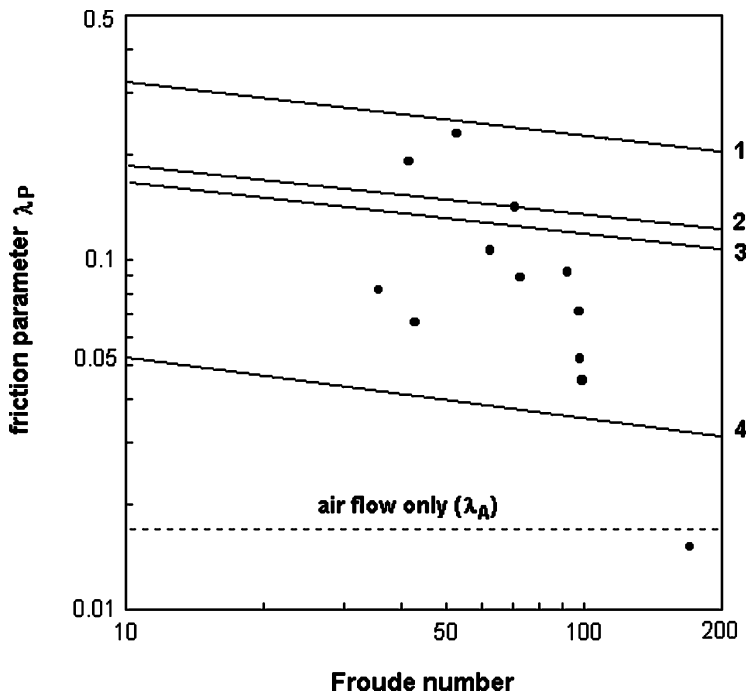


Fig. 4.34 Relationship between Froude number and friction parameter for abrasive-air flow in abrasive hoses (based on results reported by Uferer, 1992). 1 – nickel slag ($R_m = 2.0$); 2 – nickel slag ($R_m = 1.5$); 3 – quartz sand ($R_m = 2.0$); 4 – quartz sand ($R_m = 1.0$)

for quartz. If the abrasive particle material hardness increases (from Mohs 5.5 for glass beads to Mohs 7 for quartz), friction value also increases notably. This latter effect very well demonstrates that hose (with respect to pipe) material erosion has a notable influence on the friction number.

A plainly empirical approach is due to Gasterstädt (1924), who found the following relationship for pressure losses in conveying pipes based on extensive experimental work:

Table 4.10 Effects of material properties on the friction factor in rigid pipes (Weber, 1974)

Abrasive material	Pipe material	Friction factor λ_p	
		Absolute	Relative
Glass beads ($d_p = 4.0$ mm)	Steel (hardened)	0.0025	1.00
	Steel (not hardened)	0.0032	1.28
	Aluminium	0.0051	2.04
	Copper	0.0053	2.12
Quartz ($d_p = 3.0$ – 5.0 mm)	Steel (hardened)	0.0060	2.40
	Steel (not hardened)	0.0072	2.88
	Aluminium	0.0184	7.36
	Copper	0.0310	12.40

$$\frac{\Delta p_T}{\Delta p_A} = 1 + C_\lambda \cdot \frac{\dot{m}_P}{\dot{m}_A} \tag{4.34}$$

For the case $\dot{m}_P/\dot{m}_A = 0$, (4.34) delivers $\Delta p_T = \Delta p_A$. The empirical constant C_λ characterises the effects of abrasive and pipe wall material; it takes typical values for certain material combinations. Values for this parameter must be estimated by experiments. It can be concluded from the discussion in the previous section that C_λ has high values for hard, irregularly shaped solid particles. An exploitation of experimental results reported by Uferer (1992) for mass flow ratios abrasive/air between $R_m = 1.0$ and 2.0 delivers typical values of $C_\lambda = 1-4$ for slag materials as well as for quartz sand conveyed in blast cleaning hoses. An analysis of the reported results depicted that the C_λ -values showed a relationship to the hose diameter. The larger the hose diameter, the higher were the values for C_λ . Equation (4.34) is graphically expressed in Fig. 4.35 for different C_λ -values. It can be seen that the pressure drop ratio can become as high as $\Delta p_T/\Delta p_A = 10$ for typical mass flow ratios abrasive/air. Although Gasterstädt's (1924) relation helps to find pressure loss values from a restricted number of measurement, its physical relevance is controversial. This approach cannot be used for the estimation of the individual pressure drop caused by abrasive addition. Another critical issue is that \dot{m}_P and \dot{m}_A cannot be varied independently on each other if nozzle flow is considered.

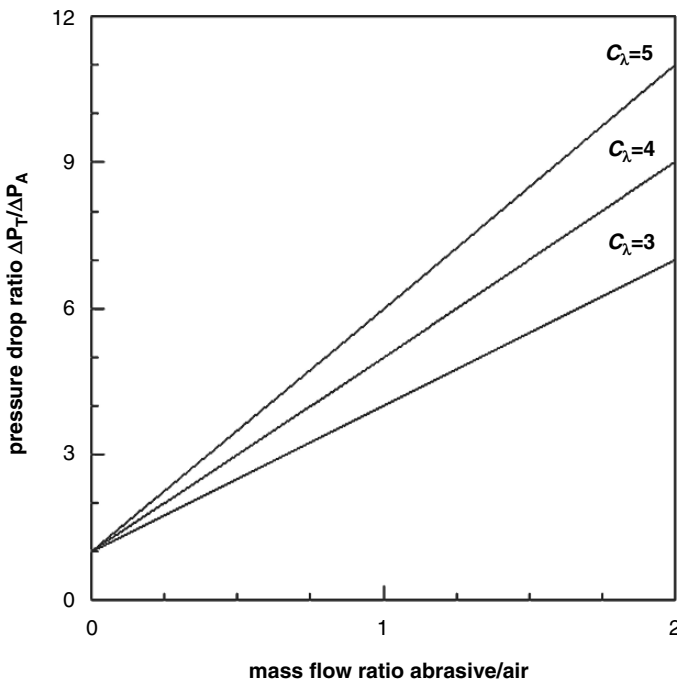


Fig. 4.35 Graphical expression of Gasterstädt's relation for different C_λ -values

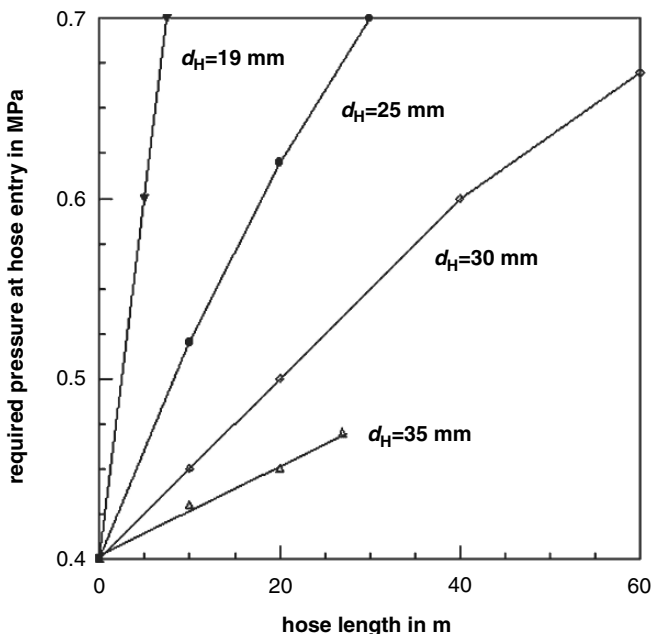


Fig. 4.36 Experimentally estimated pressure drop values in abrasive hoses (Uferer, 1992)

Uferer (1992) performed systematic measurements of pressure drops in blast cleaning abrasive hoses. Results of his work are provided in Fig. 4.36. The graphs not only illuminate the dominating effect of the hose diameter, but also verify that pressure loss is more severe in abrasive hose lines compared with plain air hose lines (compare Fig. 4.24). If a hose with a diameter of $d_H = 25$ mm is in operation, the pressure drop reaches a value of $\Delta p_T = 0.45$ MPa after a distance of $l_H = 3$ m. If the operator can choose either a long air hose line or a long abrasive hose to be utilised, abrasive hose line must be as short as possible.

Results of numerical simulations performed by Tashiro and Tomita (2004) for the calculation of pressure drops in pipes for horizontal pneumatic transport depicted notable effects of abrasive material density, air flow velocity and mass flow ratio abrasive/air on the additional pressure drop caused due to abrasive addition. The additional pressure drop caused by the addition of abrasive particle to the air flow was very pronounced for abrasive materials with rather low densities. If particles with a density of $\rho_p = 2,000$ kg/m³ were added into an air stream with a flow velocity of about $v_F = 28$ m/s, the additional pressure drop was about $\Delta p_p = 50$ Pa/m for a mass flow ratio of $R_m = 2$. If particles with a density of $\rho_p = 1,000$ kg/m³ were added, the additional pressure drop increased to a value as high as $\Delta p_p = 200$ Pa/m. If the air flow velocity was reduced down to $v_F = 19$ m/s, the values for the additional pressure drop were reduced down to $\Delta p_p = 7$ Pa/m ($\rho_p = 2,000$ kg/m³, $R_m = 2$),

respectively to $\Delta p_P = 25 \text{ Pa/m}$ ($\rho_p = 1,000 \text{ kg/m}^3$, $R_m = 2$). Distinguished effects of air compressibility on the additional pressure drop could not be estimated by Tashiro and Tomita (2004).

Results of measurements on pressure drop in grit hose performed by Bae et al. (2007) were already shown in Fig. 4.13. The lines illustrate the effects of abrasive mass flow rate and nozzle design on the pressure drop. The curves can be fitted with a simple linear law according to the following equation:

$$\Delta p_T = C_1 \cdot \dot{m}_P + C_2 \quad (4.35)$$

The pressure drop is given in MPa, and the abrasive mass flow rate is given in kg/min. The precise values for the regression parameters C_1 and C_2 depend on the geometry of the nozzle. The regression is valid for rather high abrasive mass flow rates between $\dot{m}_P = 11 \text{ kg/min}$ and 40 kg/min . It can only be applied to determine trends, because the hose length was not given in Bae et al. (2007) work. Comparative pressure drop measurements were performed by Bosshard and Fritchman (1992). The authors used steel shot (S110) and deployed moderate air pressures ($p = 0.12\text{--}0.45 \text{ MPa}$) and moderate abrasive mass flow rates ($\dot{m}_P = 0.8\text{--}5.0 \text{ kg/min}$). The ratio between hose diameter and nozzle diameter was $d_H/d_N = 2.5$. The authors found that the pressure drop in abrasive hoses increased linearly with an increase in abrasive mass flow rate. The pressure drop ratio between plain air flow ($\dot{m}_P = 0$) and flow with abrasive material was between $\Delta p_P/\Delta p_A = 1.5$ to 3 , and this ratio depended on the abrasive mass flow rate.

The graphs presented in Figs. 4.13 and 4.36 demonstrate that the working line of a nozzle, as plotted in Fig. 4.3, is a function of the pressure drop in the blast cleaning system. An ideally performing system would permanently cross-check the actual nozzle working line with the compressor working line, and it would take corrective action.

Figure 4.37 illustrates the effect of the abrasive hose dimensions on the relative cleaning rate. The graphs are based on measurements performed by Uferer (1992). If pressure drop is not considered ($l_H = 0$), the systems with the nozzle diameter $d_N = 8$ perform at a relative cleaning rate of 100%. If the nozzle diameter increases up to $d_N = 10 \text{ mm}$ (e.g. due to nozzle wear), and no buffer vessel is placed between compressor and nozzle, the efficiency notably drops down to 64%. However, the situation changes if abrasive hoses are considered. It can be seen that the efficiency notably drops for the system with the smaller hose diameter ($d_H = 25 \text{ mm}$). This effect is due to the severe pressure drop in the narrow hose. If a hose length as short as $l_H = 20 \text{ m}$ is exceeded, this system performs worse than the system with the larger nozzle diameter. At a hose length of $l_H = 50 \text{ m}$, this system delivers only 40% of the original cleaning rate. For very long hoses ($l_H > 70 \text{ m}$), the two systems with the larger hose diameter ($d_H = 32 \text{ mm}$) perform almost equally good. This discussion very well illustrates the complex relationships behind any blast cleaning optimisation procedure.

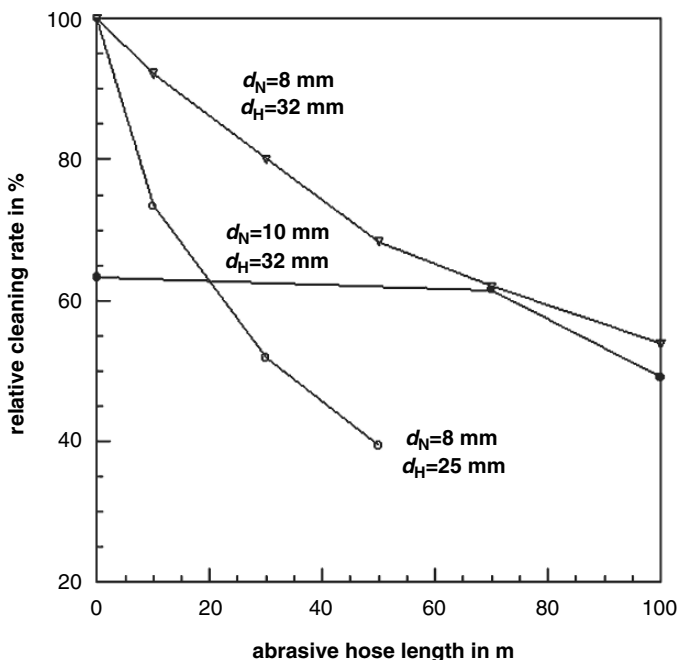


Fig. 4.37 Relationship between nozzle diameter, abrasive hose diameter, abrasive hose length and relative cleaning rate (based on measurements reported by Uferer, 1992)

4.6 Nozzles

4.6.1 Nozzle Types

For blast cleaning operations, the following two prime nozzle types can be distinguished:

- cylindrical nozzles with convergent inlet sections;
- nozzles with a convergent–divergent shape (Laval nozzles).

The performance characteristics of both nozzle types are described in Chap. 3.

For convergent–divergent nozzles, Settles and Geppert (1997) issued the following optimisation design rules:

- The convergent section should be minimised to bring the Mach number between air and abrasive particles to unity ($Ma = 1$) as soon as possible.
- The throat section should not be longer than necessary to avoid its wearing.
- The divergent nozzle section should be contoured rapidly until the Mach number between air and abrasive particles reaches a value of about $Ma = 1.4$ (see Fig. 3.18).
- The divergent contouring should be gradually maintained to maintain the relative Mach number of $Ma = 1.4$.

- The length of the divergent section should be extended as required to achieve the desired abrasive particle velocity at the nozzle exit.
- The ratio between nozzle exit area and nozzle throat area should be chosen for the given exit pressure to be near perfect expansion (see Fig. 3.24).

Each individual blast cleaning nozzle has its particular working line, which is given as follows:

$$p = f(d_N) \cdot \dot{Q}_A \quad (4.36)$$

Three examples for nozzle working lines are plotted in Fig. 4.3. The functions depict a linear relationship between the two parameters (see Sect. 3.2.1). The fundamentals of nozzle flow are discussed in Sect. 3.2.

Blast cleaning nozzles consist of a nozzle body (housing) and an inlet section. Whereas the body is usually made from steel, the inlet sections are made from different materials, including steels, tungsten carbides, ceramics and composite materials.

4.6.2 Nozzle Wear

4.6.2.1 Fundamentals of Nozzle Wear

Nozzle wear is a serious problem with any blast cleaning system. Nozzle wear deteriorates efficiency and often avoids a continuous blast cleaning operation. The basic mechanism is the erosion of the nozzle wall due to impinging abrasive particles. The processes discussed in Chaps. 2 and 5 relate on nozzle wear as well.

Ishii and Kawasaki (1982) performed numerical simulations of the particle streamlines in blast cleaning nozzles. Their results deduced an upper limiting point in the wall region where the particle could impinge, when the impingement of the particles on the nozzle wall occurred in the supersonic section of the nozzle (see Sect. 3.3). The location of this point did not depend on particle size, but on nozzle geometry.

Examples of worn blast cleaning nozzle inlet sections are shown in Fig. 4.38. The images “a” and “c” illustrate the wear of an aluminium oxide nozzle, whereas the images “b” and “d” illustrate the wear of a boron carbide nozzle. It can be seen that the wear did not occur regularly, but rather concentrated in the upper section of the nozzle inlet. Figure 4.39 provides information on the change in the internal nozzle geometry due to wear. It can be seen that the erosion was not regular over the nozzle length; the worn cross-section rather moved towards the nozzle exit over time. But the minimum cross-section, which determines air flow rate and air flow velocity (see Sect. 3.2), was already extended after 6 hours. After an exposure time of $t_B = 20$ h, this worn section had reached the nozzle exit. Similar observations were reported by Lukschandel (1973). Observations have shown that the internal geometry of cylindrical nozzles without a convergent inlet section changed over the time; their geometry approached that of convergent–divergent (Laval) nozzle. The same happened with cylindrical nozzles that already contained a convergent

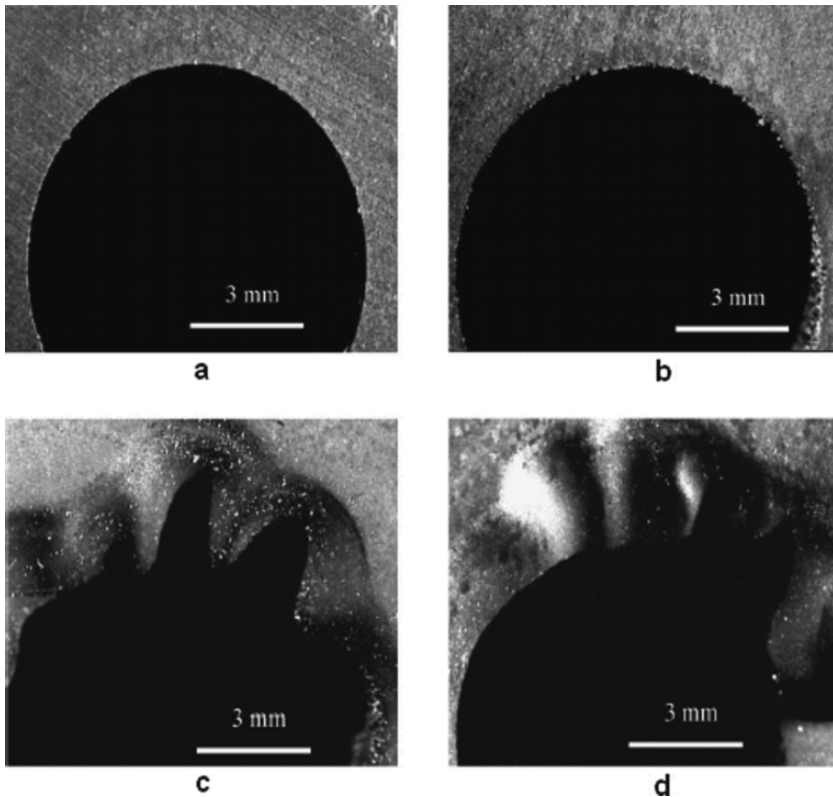


Fig. 4.38 Entry sections of ceramic blast cleaning nozzles (Deng et al., 2003b). (a) New aluminium oxide nozzle; (b) New boron carbide nozzle; (c) Worn aluminium oxide nozzle after $t_B = 4$ h; (d) worn boron carbide nozzle after $t_B = 4$ h

inlet section (Pashatskii et al., 1971; Kumar et al. 1983). An example is provided in Fig. 4.40. The dotted line expresses the shape of the worn steel nozzle after an operation period of 25 min. It seemed that the wear, in terms of diameter, increased to approach a saturation value for a given ratio between (eroded) exit diameter and bore diameter; values for this ratio were reported to be between 3 and 5 for conical nozzles (Pashatskii et al. 1971). Sheldon et al. (1977) sectioned an aluminium tube ($d_N = 5$ mm, $l_N = 305$ cm) into individual short tube sections 2.54-cm long. Each individual tube section was carefully weighed, and the tube sections were then re-assembled to form a tube of original length. This tube was eroded with hardened steel shot ($d_p = 270$ μ m; $\dot{m}_p = 1.26$ g/s, $p = 0.17$ MPa). After eroding, the tube was disassembled and each section was weighed. It was noted that the erosion rate (kg/kg) was very low at the inlet section of the tube, where the velocity of the particles was rather low, and then rose in a non-linear manner to a maximum value at the exit section of the tube. Deng (2005b) scanned the internal profile of a ceramic nozzle eroded over a period of 50 hours. Results of this study are displayed

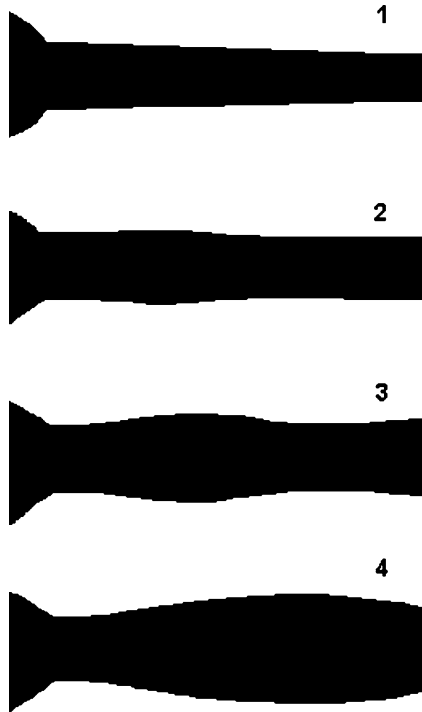


Fig. 4.39 Wear pattern in a blast cleaning nozzle (Gesell, 1969). 1 – new nozzle; 2 – after $t_B = 6$ h; 3 – after $t_B = 9$ h; 4 – after $t_B = 20$ h

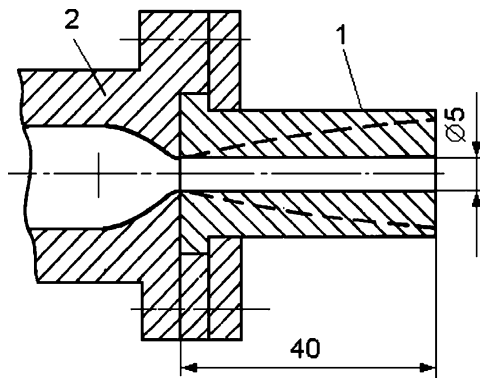


Fig. 4.40 Wear pattern in hardened steel blast cleaning nozzle with convergent entry section (Pashatskii et al., 1971). 1 – wear pattern after $t_B = 25$ min; 2 – nozzle body. Dimensions in mm

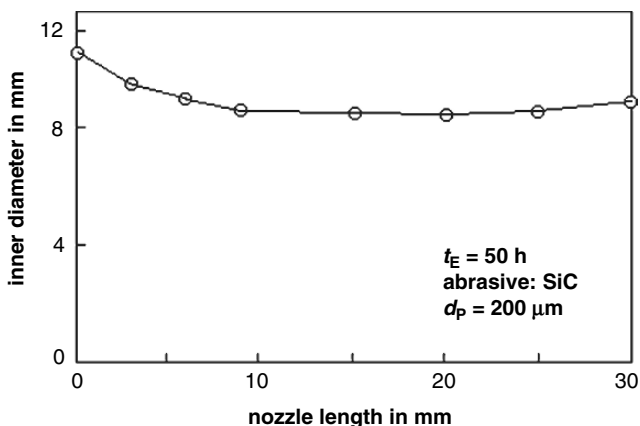


Fig. 4.41 Geometry of a ceramic blast cleaning nozzle after a performance time of 50 h (Deng, 2005b)

in Fig. 4.41. Originally, the nozzle had a cylindrical design, but it changed to a convergent–divergent shape over the time. This change in internal geometry may be one reason for the observation that used cylindrical nozzles sometimes perform better than new, unused cylindrical nozzles.

Worn nozzles should be replaced in time. It is not always easy to define a worn nozzle, but a general rule is: nozzles should be replaced if the (smallest) nozzle bore diameter is being increased between one and one-and-a-half millimetre. Results of quantitative wear measurements on a cylindrical blast cleaning nozzle are displayed in Fig. 4.42. It can be seen that both entry and exit bore diameters of the nozzle increased during the operation. After 9 h, the diameter of the exit bore was increased by about 1 mm; therefore, the value for the minimum diameter in the nozzle, which determines air mass flow rate and air velocity, had changed. The graphs also show a decrease in the wear rate (slopes of the curves) with an increase in operation time. The entry section, in particular, featured a very steep initial wear rate. These curves characterise nozzle wear as a non-stationary process. A quantitative comparison of the wear performance of different nozzles should, therefore, always be performed at operation times long enough to guarantee a stationary wear process. For the example plotted in Fig. 4.42, this critical operation time would be at about 8 h for the exit section.

Equation 3.9 illustrates that an increase in nozzle diameter is accompanied by a decrease in pressure in order to maintain the desired air flow rate. An example of how nozzle wear increased the volumetric air flow rate is shown in Fig. 4.43. The nozzle wear (in terms of diameter increase) shown in Fig. 4.43a followed a square-root relationship:

$$d_N(t_E) \propto t_E^{1/2} \quad (4.37)$$

Such a trend was also found on ceramic nozzles by Bothen (2001) and on steel nozzles by Pashatskii et al. (1971). However, the experimentally estimated increase

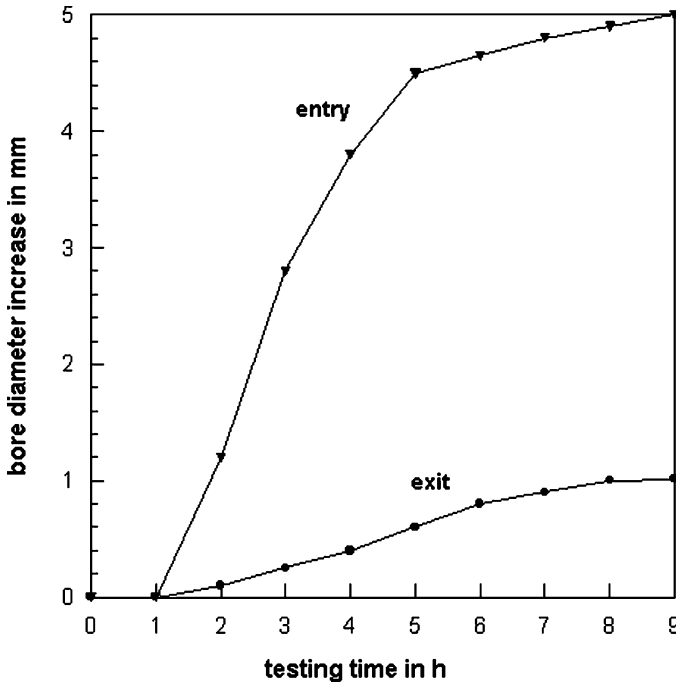


Fig. 4.42 Development of wear of blast cleaning nozzles (Deng et al., 2003a)

in volumetric air flow rate followed a linear relationship as shown in Fig. 4.43b. Because of $\dot{Q}_A \propto d_N^2$, this is not an unexpected result. If the compressor cannot deliver this demanded air flow rate, air pressure drops. According to (3.11), the relationship between nozzle diameter and nozzle air pressure is as follows:

$$d_N^2 \propto p^{-1} \tag{4.38}$$

A combination of $d_N = 12$ mm and $p = 1.0$ MPa delivers a volumetric air flow rate of $\dot{Q}_A = 13.5$ m³/min. If the nozzle diameter increases up to $d_N = 13$ mm, the reduced nozzle pressure is $p = 1.0 \text{ MPa} \cdot (12/13)^2 = 0.85$ MPa. To compensate this pressure drop, the compressor must deliver a volumetric air flow rate of $\dot{Q}_A = 15.8$ m³/min (at $\vartheta = 20^\circ\text{C}$). These calculations show that nozzle wear affects the working line of a nozzle. If the throat diameter of a nozzle is worn from originally $d_N = 10$ mm to 12 mm, the nozzle working line changes notably. This situation is illustrated in Fig. 4.3. The working point for the entire system changes from “II” to “III”, and the system must be readjusted. Therefore, wear-resistant nozzles are a basic requirement for stable blast cleaning processes. If the compressor cannot deliver the desired additional volumetric air flow rate, the pressure at the nozzle drops, and the cleaning rate will be reduced. An example is provided in Fig. 4.37. It can be seen that the relative cleaning rate drops from originally 100% for $d_N = 8$ mm down to 64% for $d_N = 10$ mm. This particular example does not consider effects of abrasive hose lines ($l_H = 0$).

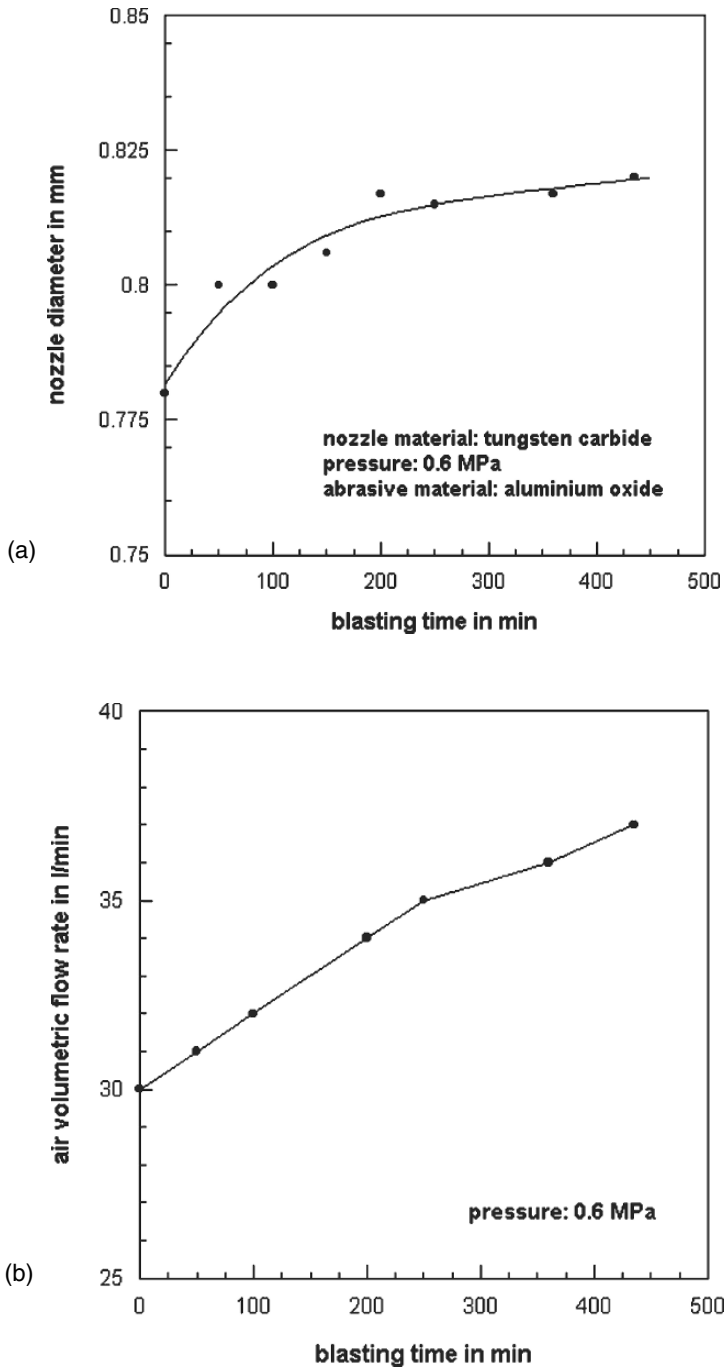


Fig. 4.43 Wear of a Laval nozzle (Bothen, 2000). (a) Increase in nozzle diameter; (b) Increase in air volume flow rate

4.6.2.2 Parameter Effects on Nozzle Wear

Nozzle wear depends on nozzle and abrasive parameters as well as on process parameters. Investigations into the effects of blast cleaning and material parameters on nozzle wear were performed by many authors.

It is known for more than 40 years (Adlassing and Jahn, 1961) that nozzles made from boron carbide featured the highest wear resistance, and that the use of aluminium oxide as an abrasive accelerated blast cleaning nozzle wear. More recent measurements verified these early results (Grearson et al., 1989). Results from site experience are listed in Table 4.11. The reason for the high wear resistance of boron carbide is its high hardness (see Table 4.12). A typical relationship between the erosion rate of tungsten carbide composites and hardness is as follows (Laugier, 1986):

$$E_R \propto H_N^{-3.5} \tag{4.39}$$

Figures 4.38, 4.44 and 4.45 illustrate the effects of nozzle material hardness. Results plotted in Fig. 4.44 show that an increase in nozzle material hardness notably improved the resistance of the nozzle to wear. It can be seen from Fig. 4.45, that the nozzle made from boron carbide experienced a much lower erosion rate compared with the nozzle made from aluminium oxide.

The influence of the abrasive type is illustrated in Table 4.11 and Fig. 4.45. From the materials listed in Table 4.11, corundum (aluminium oxide) abrasives caused the most severe erosion, which may again be due to the high hardness of this material. Figure 4.45 shows, however, that the intensity of nozzle wear is controlled by a combination of the hardness for nozzle material and abrasive material. Although the erosion increased for the alumina nozzle and for the boron carbide nozzle if the abrasive material hardness increased, the alumina nozzle was more sensitive to changes in abrasive material hardness. It will, therefore, basically be the hardness ratio between nozzle material and abrasive material, which determines wear resistance. This ratio is given as follows:

$$R_H = \frac{H_N}{H_P} \tag{4.40}$$

If the hardness ratio is high, wear rate is low and vice versa. These aspects are illustrated in Fig. 4.45, which shows that wear increased if abrasive material hardness

Table 4.11 Nozzle lifetime values (Kennametal, Inc., Charlotte)

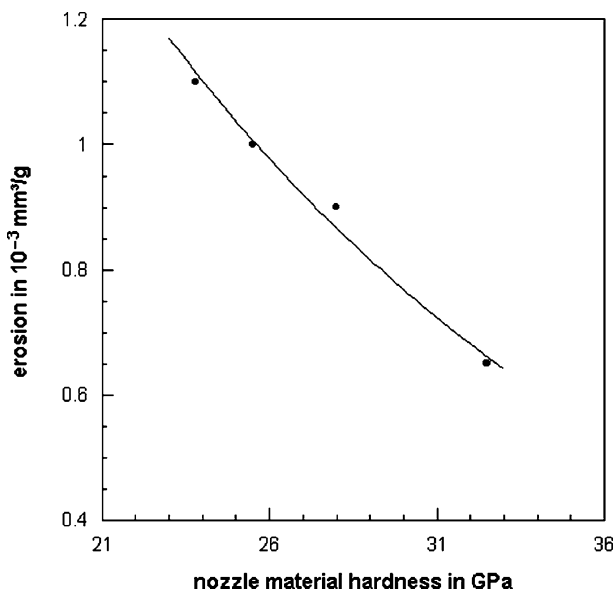
Nozzle material	Approximate lifetime in h		
	Abrasive material		
	Steel shot/grit	Quartz sand	Aluminium oxide
Aluminium oxide	20–40	10–30	1–4
Tungsten carbide	500–800	300–400	20–40
Silicon carbide composite	500–800	300–400	50–100
Boron carbide	1,500–2,500	750–1,500	200–1,000

Table 4.12 Mechanical properties nozzle of materials (Deng et al., 2003a)

Nozzle material	Flexural strength in MPa	Hardness in GPa	Fracture toughness in MPa m ^{1/2}
Boron carbide (B ₄ C)	350	32.5	2.5
Tungsten carbide (WC/8Co)	1,500	14.8	14.5
Alumina carbide (Al ₂ O ₃ /45C)	850	21.5	4.9

increased; but the absolute wear was always less for the boron carbide nozzle. The effect of the nozzle material hardness on nozzle wear is illustrated in Fig. 4.44. Erosion rate notably dropped if a nozzle material with a high hardness was utilised. The performance in terms of reduced wear could be almost doubled if a nozzle material with a hardness of $H_N = 23.8$ GPa [boron carbide composite, B₄C/50 wt.% (W, Ti) C] was replaced by a nozzle material with a hardness of $H_N = 32.5$ GPa (boron carbide, B₄C). Table 4.12 lists mechanical properties of some typical blast cleaning nozzle materials.

Nozzle geometry parameters, namely nozzle diameter and nozzle length, affect the wear performance as well (Adlassing, 1960; Kumar et al., 1983). Results of respective measurements are provided in Fig. 4.46. Nozzle mass loss, which expresses wear, increased if longer and wider nozzles were used. The relationship between bore diameter and nozzle mass loss was of a parabolic shape (Adlassing, 1960). An opposite trend was reported by Kumar et al. (1983) for the wear of very small steel nozzles ($d_N = 0.8$ – 1.6 mm). These authors found a decrease in wear for larger nozzle diameters. The effects of varying angles of the nozzle entry section on the wear

**Fig. 4.44** Effect of nozzle material hardness on nozzle wear (Deng, 2005a)

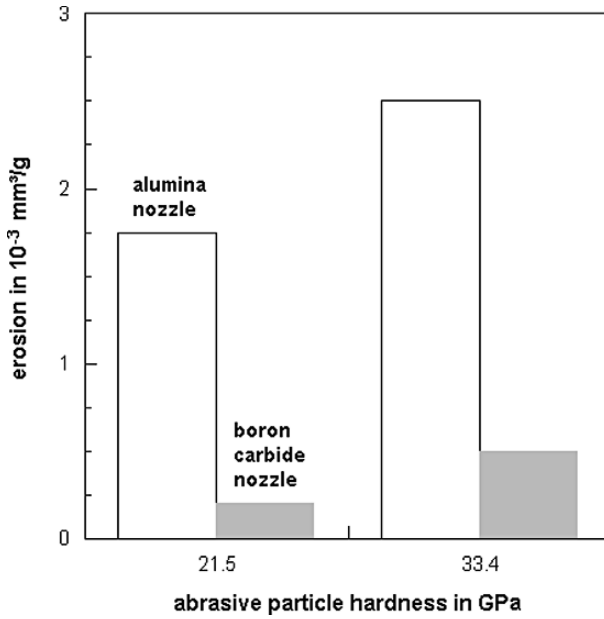


Fig. 4.45 Effect of abrasive material hardness on nozzle wear (Deng et al., 2003b)

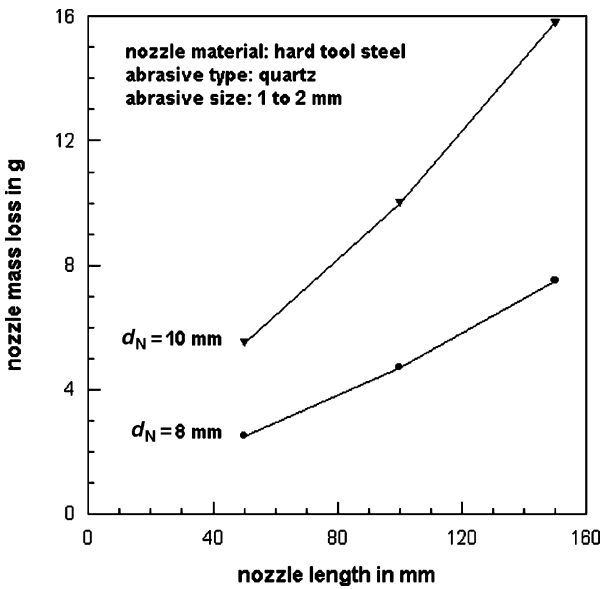


Fig. 4.46 Effects of nozzle length and nozzle diameter on nozzle wear (Adlassing, 1960)

of convergent-cylindrical steel nozzles was also investigated by Kumar et al. (1983), and they could prove that the wear increased for smaller entry angles. This result was contributed to an increase in the length of the convergent section of the nozzle.

Process parameters also affect nozzle wear. It was found by several authors that nozzle wear increased if air pressure rose (Adlassing, 1960; Pashatskii et al., 1971). Nozzle wear was also found to increase linearly if the abrasive particle concentration (Pashatskii et al., 1971) or the mass flow ratio abrasive/air (Kumar et al., 1983) was increased. Kumar et al. (1983) investigated the influence of the abrasive particle size on the wear of steel nozzles. They utilised small aluminium oxide particles ($d_p = 30$ and $38 \mu\text{m}$), and they could show that the nozzle wear was more severe for the larger abrasive particles. However, a notable difference between the effects of the two different particle sizes was obvious at rather long exposure times only.

4.6.2.3 Wear Performance of Laminated Ceramic Nozzles

A new approach to increase nozzle lifetime is the utilisation of laminated ceramic nozzles (Deng et al., 2007). Due to the different thermal expansion coefficients and due to shrinkage of the individual layer materials, residual compressive stresses are generated in the laminated sections of the nozzle (entry and exit sections). These compressive stresses may partly balance tensile stresses which form during the erosion process in the nozzle. Figure 4.47 exhibits results of comparative wear tests.

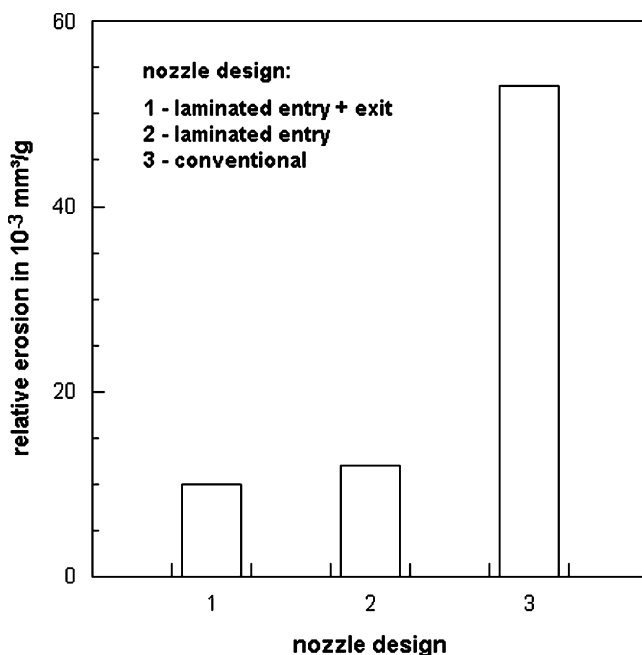


Fig. 4.47 Results of comparative wear measurements on conventional ceramic nozzles and laminated ceramic nozzles (Deng et al., 2007)

The standard nozzle exhibited the most severe wear. The nozzle with a laminated entry section performed better, but the best performance was delivered by the nozzle with laminated entry and exit section. Long-term (540 min) measurements of the entry bore diameter of different nozzles were also made. The entry bore diameter of a conventional nozzle increased up to $\Delta d_N = 7$ mm, whereas the entry bore diameter of a laminated nozzle increased up to $\Delta d_N = 1$ mm only (Deng et al., 2007).

Chapter 5

Substrate and Coating Erosion

5.1 Introduction

The basic process of blast cleaning is the impingement of individual abrasive particles under different conditions on the target material. In the reference literature, this process is often referred to as *solid particle* erosion. The system “coating – interfacial layer – substrate” is illustrated in Fig. 5.1. This complete system responds by the following two mechanisms to the impingement of solid particles:

- erosion of the coating material (cohesive mode);
- debonding of the coating material (adhesive mode).

These mechanisms are illustrated in Fig. 5.2, and they will be discussed in detail in the subsequent sections.

Erosion occurs usually either if the coating is rather thick or if the adhesion of the coating to the substrate is very good. The erosive response of *bulk (coating) materials* can be subdivided into elastic response (brittle) and elastic–plastic response (ductile). These modes of response are illustrated in Fig. 5.3 in terms of scratching images of organic coatings.

Debonding and delamination in the interface between substrate and coating are alternative coating removal mechanisms, and they occur at rather small coating thickness, or if the adhesion is low.

5.2 Mechanical Properties of Oxides and Organic Coatings

5.2.1 Relevant Mechanical Properties

The material to be considered for blast cleaning is rather a material system composed of the three following parts:

- substrate;
- interfacial layer;
- layer (coating, oxide).

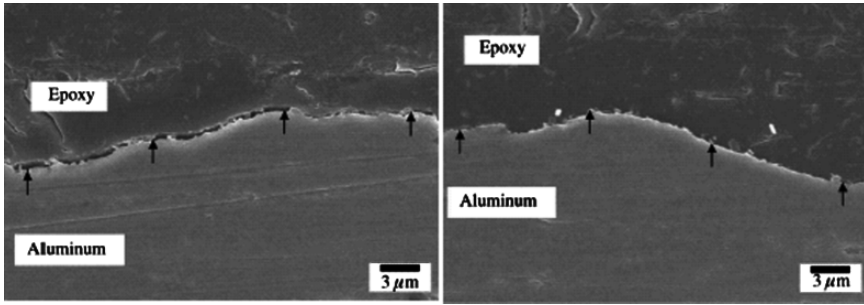


Fig. 5.1 System: substrate (aluminium) – interface – coating (epoxy). Photographs: Zhang et al., (2003). Left: deteriorated adhesion: Right: good adhesion

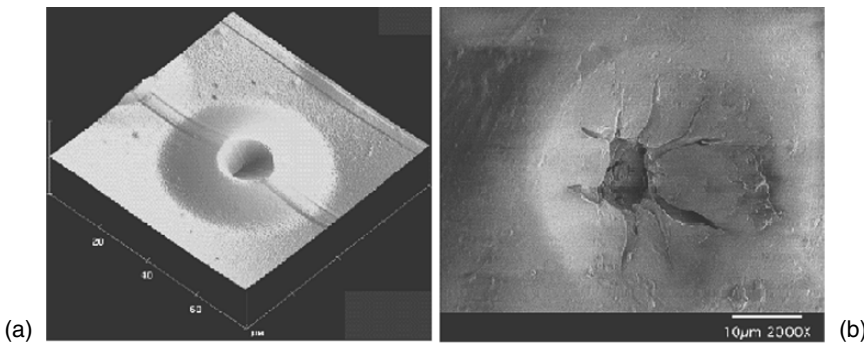


Fig. 5.2 Basic types of coating response to solid particle impingement (Strojny et al., 2000). (a) Buckling and debonding; (b) Brittle response with bulk material erosion

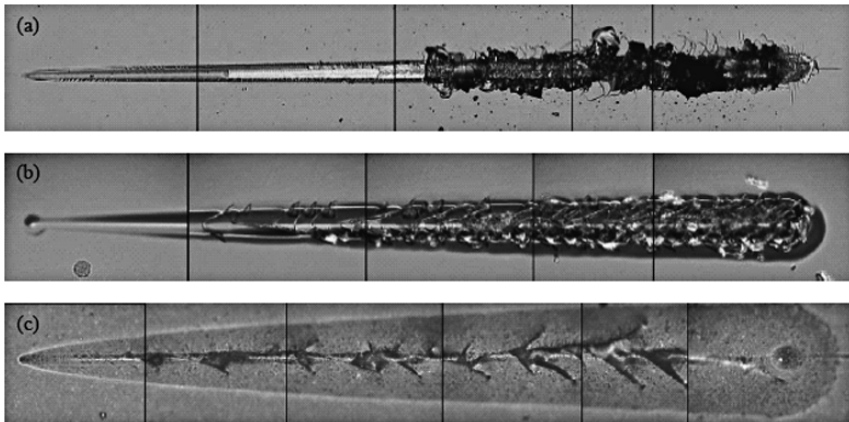


Fig. 5.3 Basic types of organic coating response to scratching (Randall, 2006). (a) PVC-based hardcoat finish: elastic response with cracking; (b) Silicone finish: elastic-plastic response with permanent deformations; (c) Automotive varnish coat: plastic response with some ruptures

Such a system is shown in Fig. 5.1. Whether cohesive mode or adhesive mode dominates depends on the adhesion between coating and substrate and on coating thickness. If both adhesion strength and coating thickness are low, adhesive delamination occurs. For the cohesive mode, the bulk properties are of importance, but it is known that, for coating materials, cohesive properties, e.g. indentation properties, depend on the distance to the substrate (Roche et al., 2003).

Over the years, many erosion studies have been performed on a variation of materials. It was shown that no single material property can determine the resistance of a material against the erosion by impinging solid particles. However, there are some properties which were observed to notably affect the erosion resistance of materials. These *cohesive material properties* include the following:

- hardness;
- Young's modulus;
- strain energy density;
- tensile strength;
- fracture mechanics parameters.

Adhesive system properties, say adhesion strength between substrate and adhering layer (oxide, glue and coating), also affect the behaviour of the system.

An extensive review about parameters and measurements methods for coating materials is provided by Papini and Spelt (2002).

The cohesive properties can be exhibited in a stress–strain diagram of a stressed material volume. Typical stress–strain diagrams for three types of material response are shown in Fig. 5.4. The plot in Fig. 5.4a illustrates the linear-elastic response of a material. This response is characterised by the damage features shown in Fig. 5.3a. The plot in Fig. 5.4b illustrates the elastic–plastic response of a material. This response relates to the damage features shown in Fig. 5.3b. The shapes of stress–strain curves are not general material properties, but depend on the loading conditions. Stress–strain curves of paint materials are, for example, sensitive to the loading rate. This aspect was in detail investigated by Dioh and Williams (1994). The Hardness and Young's modulus represent the deformation response of a material. Hardness is

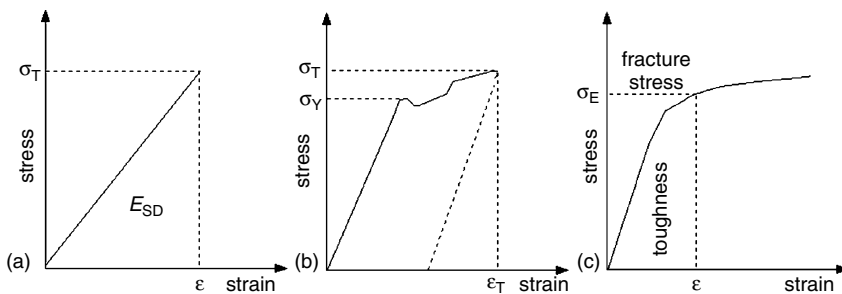


Fig. 5.4 Stress–strain diagrams and deformation parameters. (a) Linear-elastic response; (b) Elastic-plastic response; (c) Dynamic compressive diagram (Levin et al., 1999)

for many materials coupled with the yield strength (Tabor, 1951), and for elastomers it is linearly related to Young's modulus (Li and Hutchings, 1990). *Strain energy density* is the area under the stress–strain curve of a material:

$$E_{SD} = \int_0^{\epsilon_T} \sigma(\epsilon) d\epsilon \quad (5.1)$$

It has the unit kJ/m^3 which is that of a specific volumetric energy. For elastically responding materials, elastic strain energy density can be approximated as follows:

$$E_{SD} = \frac{\sigma_T^2}{2 \cdot Y_M} \quad (5.2)$$

The variables are illustrated in Fig. 5.4a. The elastic strain energy density has been applied by several authors as a parameter which can characterise the resistance of a material against solid particle erosion (Bitter, 1963; Kriegel, 1968). The detailed shape of a stress–strain curve can already deliver a rough estimate of the behaviour of the material in question. Some examples are provided in Fig. 5.5. The term “hard” in this graph corresponds to elastic response, whereas the term “soft” points to a rather plastic material response. Levin et al. (1999) extended the stress–strain approach and developed an idea to apply a dynamic (high strain rate) compression stress–

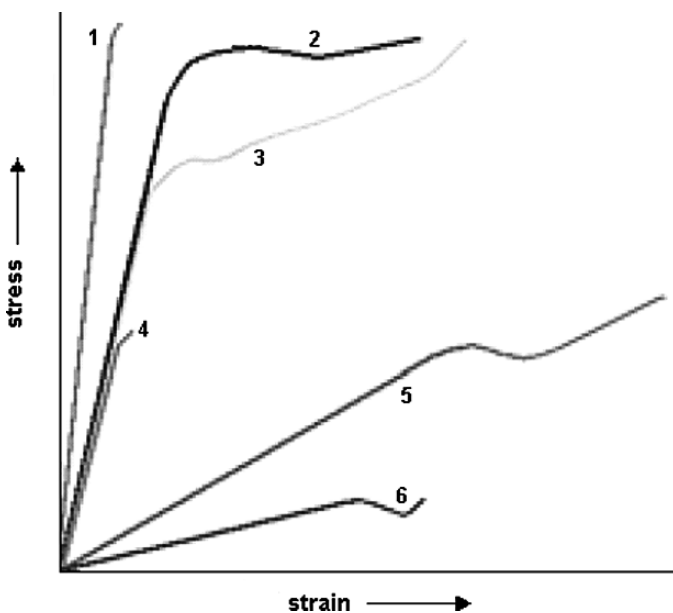


Fig. 5.5 Stress–strain diagrams for different response characteristics (Hare, 1996). Material characteristics: 1 – hard and brittle; 2 – hard and strong; 3 – hard and tough; 4 – weak and brittle; 5 – soft and tough; 6 – soft and weak

strain curve for the assessment of the response of ductile metals to solid particle erosion. This approach is illustrated in Fig. 5.4c. The area under the modified stress–strain curve, denoted “tensile toughness” by the authors, characterises the energy absorbed during the erosion process. The failure stress estimated from such a dynamic stress–strain curve is related to the hardness of the eroded surface as follows:

$$\sigma_E = A_D \cdot H_M \quad (5.3)$$

The constant had values between $A_D = 3.4$ and 4.0 for many metal alloys (Levin et al., 1999).

Mechanical properties depend on a number of physical effects, namely strain rate sensitivity and temperature sensitivity. Solid particle impingement, the basic mechanism for blast cleaning, is associated with high strain rates (see Sect. 5.4.1). Values as high as 10^6 per second can be assumed (Hutchings, 1977a). The response of metals and organic coatings to loading depends on deformation velocity and strain rate. An increase in strain rate may, for example, change the response of organic coatings from plastic deformation to intense chipping, and may cause a two-fold increase in yield stress (Dioh and Williams, 1994). An increase in deformation rate rises tensile strength of organic lacquers (Skowronnek et al., 1991). An increase in strain rate also modifies material properties as shown in Fig. 5.6 for the yield stresses of organic materials (see Fig. 5.4b for the definition of the yield stress). Siviour et al. (2005) found for polymer materials a change in the structures of stress–strain curves if temperature and strain rate were varied.

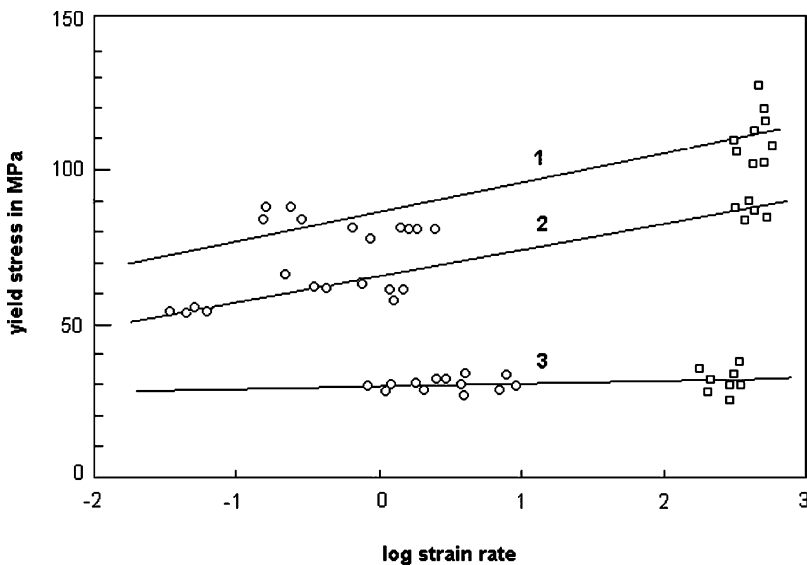


Fig. 5.6 Strain rate effects on yield strength of polymeric materials (Kukoreka and Hutchings, 1984). Materials: 1- polyethersulphone; 2- polycarbonate; 3- high-density polyethylene

Table 5.1 Dynamic hardness values of steel blades and deposits (Raykowski et al., 2001)

Material	Dynamic hardness in GPa
Compressor blade deposit	0.22–0.26
Compressor substrate	0.3–0.43
Turbine blade deposit	6.3

Based on a balance between the kinetic energy of an impinging particle and the work done in plastically deforming the impinged coating material, Tangestanian et al. (2001) derived a *dynamic hardness*:

$$H_d = \frac{m_p \cdot v_p^2}{2 \cdot \pi \cdot \left[(d_p^2 - a_{C_{\max}}^2)^{1/2} \cdot \left(\frac{1}{3} \cdot a_{C_{\max}}^2 + \frac{2}{3} \cdot d_p^2 \right) - \frac{2}{3} \cdot d_p^3 \right]} \quad (5.4)$$

This parameter is defined as the instantaneous force resisting indentation during a collision divided by the instantaneous contact area. The dynamic hardness is an important property in determining the impact behaviour at high strain rates. Values for this material parameter are listed in Table 5.1.

Temperature variations can be responsible for ductile–brittle (plastic–elastic) transition of coatings under impact conditions (Moore, 2001). At low temperature, brittle fracture will occur with a comparatively low amount of absorbed impact energy. A ductile–brittle transition will occur at some fixed temperature. Other coating properties, namely deformation properties and fracture properties, also depend on temperature; examples are provided in Fig. 5.7 for the variations in fracture toughness and yield strength. Figure 5.8 illustrates the general effect of temperature variations on the behaviour of organic materials.

Fracture mechanics parameters include mainly fracture toughness and energy release rate. Both parameters can be applied to individual materials, but also to

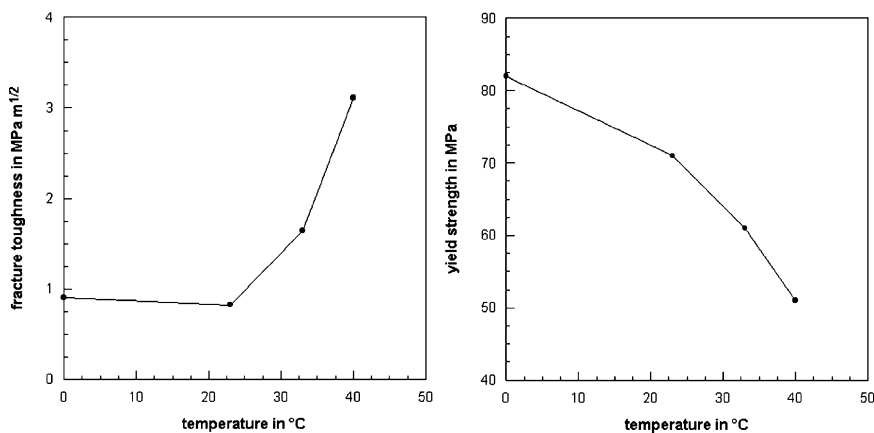


Fig. 5.7 Effect of temperature on mechanical properties of organic coating materials (Moore, 2001). Left: effect on fracture toughness; right: effect on yield strength

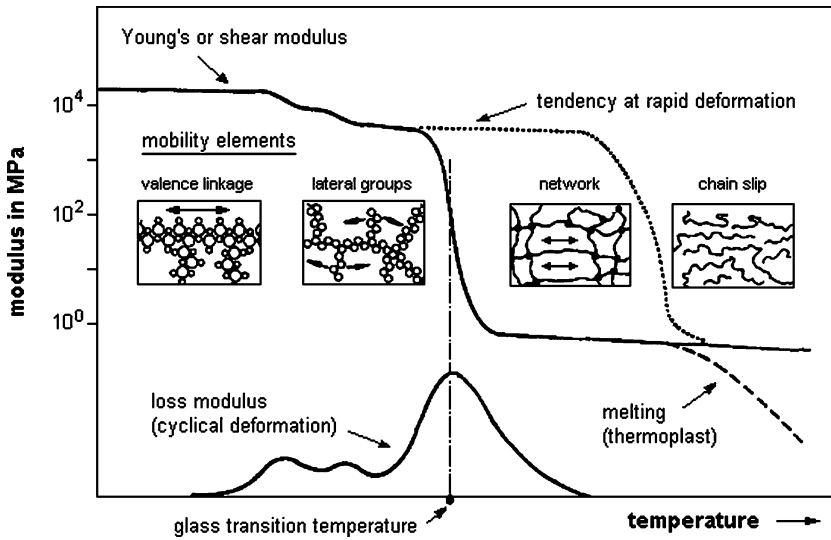


Fig. 5.8 Effects of temperature on the behaviour of organic coating materials (Zorll, 1984)

interfaces between two materials, say coating and substrate, as well as to joints. Principles of fracture mechanics with respect to contact mechanics and erosion are described in Lawn's (1993) book. The fracture toughness characterises a critical value for the stress intensity at the tip of a crack required to extend the crack. It is defined as follows:

$$K_{Ic} = \alpha_C \cdot \sigma_T \cdot (\pi \cdot l_C)^{1/2} \tag{5.5}$$

In that equation, l_C is the crack length, σ_T is the failure tensile stress and α_C is a shape factor. The fracture toughness must be estimated experimentally. Its physical unit is MN/m^{3/2}. The critical energy release rate is defined as follows:

$$G_{Ic} = \frac{K_{Ic}^2}{Y_M} \tag{5.6}$$

The critical energy release rate characterises the specific energy required to extend a crack. Its physical unit is J/m². The subscript "I" in (5.5) and (5.6) shows that both relationships are valid for a tensile loading mode (mode I) only. A method for the estimation of critical energy release rate for the interfacial zone between steel substrates and adhesives under impact load was developed by Faiji et al. (1990). A typical value for combination steel-epoxy was $G_{Ic} = 0.15 \text{ kJ/m}^2$. State-of-the-art measurement methods for the assessment of fracture mechanics parameters for organic coatings as well as for interfaces between organic coatings and substrate materials are described in detail by Papini and Spelt (2002).

5.2.2 Mechanical Properties of Oxides

5.2.2.1 Deformation Parameters

Oxides are basically formed either due to atmospheric effects (corrosion) or due to thermal effects (mill scale). The composition of oxides is complex, and they usually consist of numerous layers with different chemical compositions. Detailed descriptions of mill scale compositions are provided by Wirtz (1962). The mechanical properties of mill scale depend mainly on the formation temperature. The effect of temperature on the Young's modulus of growing mill scale layers was investigated for different metals by Hurst and Hancock (1972) and Tangirala (1998). For high temperatures, Young's modulus reduced. Typical values for Young's modulus of scales were: $Y_M = 2 \times 10^5$ MPa for iron, $Y_M = 3 \times 10^5$ MPa for nickel, and $Y_M = 2.2 \times 10^5$ MPa for an alloyed steel. Table 5.2 lists further elastic parameters for iron oxides at different formation temperatures. For comparison, the elastic parameters of the plain iron are also listed in the table.

5.2.2.2 Hardness

Results of microhardness measurements on oxides of numerous metals were reported by Lepand (1963), Wood and Hodgkiess (1972) and Zieler and Lepand (1964); some results are listed in Table 5.3. It was found that microhardness can basically be related to the crystal structure of the oxides. Oxides with a rhombohedral structure (e.g. Cr_2O_3) featured very high hardness values. When layered structures were formed on pure metals, e.g. FeO , Fe_3O_4 and Fe_2O_3 on iron, the hardness increased from the metal towards the oxide.

5.2.2.3 Adhesion Parameters

Spangenberg (1972) and Engell (1960) performed investigations into the adhesion strength of mill scale to metal substrates. Spangenberg (1972) utilised three steel types as listed in Table 5.4. He derived an empirical relation of the general form:

$$\sigma_M = C_1 + C_2 \cdot h_Z + C_3 \cdot \vartheta_R + C_4 \cdot \varepsilon_M \quad (5.7)$$

Table 5.2 Mechanical properties of iron and iron oxide (Tangirala, 1998)

Parameter	Material	Formation temperature in °C			
		570	674	743	800
Young's modulus in GPa	Iron oxide	182	168	158	151
	Iron	155	150	135	125
Poisson's ratio	Iron oxide	0.34	0.34	0.34	0.34
	Iron	0.34	0.34	0.34	0.34
Fracture stress in MPa	Iron oxide	38	2.4	1.9	4.9

Table 5.3 Microhardness values of metal oxides (Zieler and Lepand, 1964; Wood and Hodgkiess, 1972)

Oxide	Hardness in kg/mm ²
ZnO	184
NiO	600
TiO ₂	624
Cu ₂ O	232
Cr ₂ O ₃	1,820–3,270
FeO	270–390
Fe ₂ O ₃	690
α-Fe ₂ O ₃	986–1,219
Fe ₃ O ₄	420–500
α-Al ₂ O ₃	2,160

Here, σ_M is the adhesion strength of the mill scale to the substrate (N/cm²), h_Z is the mill scale layer thickness (μm), ϑ_R is the rolling temperature (°C) and ε_D is the deformation degree (%). The deformation degree is a function of the steel plate thickness before and after the rolling process. Typical values for the adhesion strength as well as the constants C_1 to C_4 are listed in Table 5.4. The effect of the mill scale layer thickness is most important. The effect of the oxidation temperature was investigated in more detail by Engell (1960). This author found that adhesion of oxides to iron is best at moderate temperatures; an example is provided in Fig. 5.9.

5.2.3 Mechanical Properties of Organic Coatings

5.2.3.1 Deformation Parameters

Paul et al. (2004) have shown that numerous organic coating materials (e.g. oxide primer, polyurethane-based enamel) feature a linear stress–strain behaviour according to Fig. 5.4a. The progress of the stress–strain function, thus Young’s modulus, depended on coating composition. Figure 5.10 shows the effects of hardener concentration and film thickness on the Young’s modulus of organic coatings. It can be noted in the figure that coating dry film thickness affects the mechanical parameter; the higher the film thickness, the higher the values for Young’s modulus. Values for

Table 5.4 Adhesion strength values for mill scale (Spangenberg, 1972)

Parameter σ_M in N/cm ²	Steel type		
	Armco iron	St 42	St 70
	200–1,600	100–1,800	200–1,600
C_1	531	1,649	2,019
C_2	11.2	3.5	5.4
C_3	–0.8	–1.8	–1.8
C_4	5.6	9.0	0

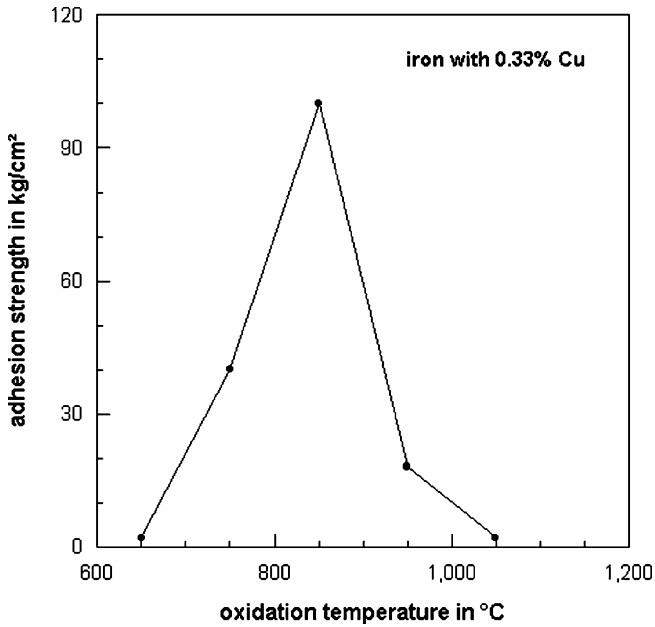


Fig. 5.9 Effect of oxidation temperature on the adhesion of oxides to the metal substrate (Engell, 1960)

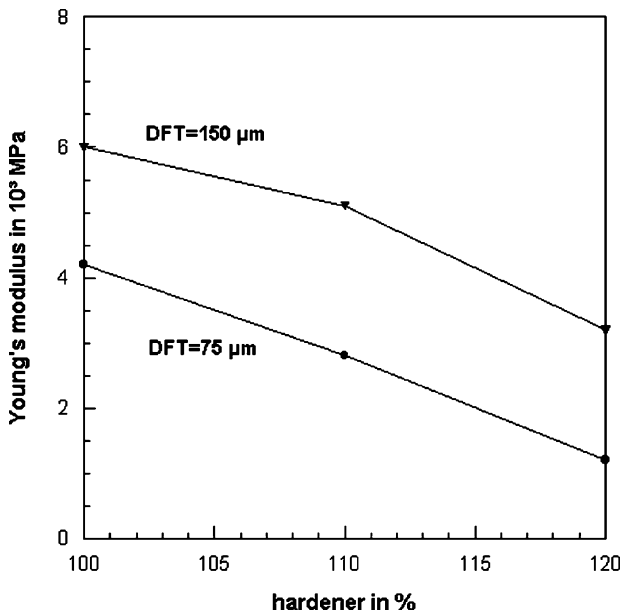


Fig. 5.10 Effects of hardener concentration and coating thickness on Young's modulus (Fokke, 1999)

the strain (relative elongation) of more than 30 epoxy-based organic coatings are listed by Askheim et al. (2001).

Values for fracture toughness and yield strength of an epoxy coating are shown in Fig. 5.7 as functions of temperature.

Impact resistance of coatings is often described in terms of an energy required to penetrate a coating layer of defined thickness. A ranking of different coating materials for a drop weight test is as follows: polyethylene: 30 Nm; polyurethane: 20 Nm; tar epoxy: 5 Nm (Sato et al., 2003). Erosion processes are associated with high strain rates (Hutchings, 1992), which affect materials properties as well as the deformation response of the coating materials. An example is provided in Fig. 5.6 showing a notable increase in yield stress for three polymers for high strain rates. A review on the affects of strain rate variations on mechanical properties of polymer materials was provided by Siviour et al. (2005). The authors also noted significant effects of the temperature on mechanical properties. Storage modulus and peak stress, measured during high strain rate loading, decreased with an increase in temperature. Values for a number of mechanical properties of organic coatings are listed in Tables 5.5 and 5.6.

5.2.3.2 Hardness

Hardness values measured on organic coatings were provided by Fokke (1999), Gnyp et al. (2004), Kotnarowska (1999), Neumaier (1993), Pickles and Hutchings (1997), Rehacek (1982) and Tangestanian et al. (2001). Some results are provided in Tables 5.7 to 5.9. It can be seen that hardness depended on temperature – it usually increased with an increase in temperature. For comparison, a hardness value for steel as a typical substrate material is provided. Vickers hardness of organic coatings is also sensitive to coating material composition and to film thickness. Examples are provided in Figs. 5.11 and 5.12. Vickers hardness increased if volumetric pigment volume and hardener concentration increased, and it dropped if film thickness increased. The latter relationship is of special importance for blast cleaning processes. Neumaier (1993) noted a strong relationship between hardness of organic paint materials and their degree of cross-linkage.

Rehacek (1982) investigated the response of organic coatings to Vickers indentation. He developed a method for the estimation of elastic (reversible) and plastic components of hardness. Results are provided in Table 5.8 and Fig. 5.11. The capability of plastic deformation depended mainly on the resin. It can be seen in

Table 5.5 Mechanical data for polymeric coatings (Rutherford et al., 1997)

Coating	Peak stress in MPa	Strain to break in %	Energy to break in kJ/m ²	Tensile modulus in MPa
R1	29.6	2.1	8.5	1,740
R2	24.4	1.7	5.5	1,680
F1	17.6	22.8	69.9	297
F2	17.5	15.7	50.0	423
L1	26.8	30.7	161.0	1,160
L2	51.6	4.7	39.7	1,870

Table 5.6 Mechanical data for polymeric coatings (Trezona et al., 1997)

Coating	Polymer type	Peak stress in MPa	Failure strain in %	Tensile modulus in MPa	Tensile failure energy in MJ/m ³
F1	Acrylic	17.6	22.8	297	3.04
F2	Acrylic	25.8	35.1	855	5.25
F3	Acrylic	49.1	14.3	1,375	5.10
F4	2C PU	57.7	29.0	1,418	9.19
R1	Acrylic	24.4	1.7	1,680	0.17
R2	Acrylic	29.6	2.1	1,740	0.24
R3	Acrylic	47.1	2.9	1,802	0.65
R4	Acrylic	77.0	4.1	2,617	1.87
R5	2C PU	77.0	5.9	1,990	2.27
R6	2C PU	61.6	8.4	1,614	3.60
L1	2C PU	26.8	30.7	1,160	4.02
H1	2C PU	51.6	4.7	1,870	0.87

Table 5.7 Brinell hardness values for certain organic coatings (Gnyp et al., 2004)

Coating name and composition	Thickness in μm	Treatment temperature in $^{\circ}\text{C}$	Brinell hardness in MPa
KO-FMI-5	400–450	20	303
		150	277
		170	509
		250	391
Laquer + coal ash + close packing with ultrasound	400–450	20	258
		150	303
		170	407
		250	375
Pompur 804	–	–	143
Ambercoat 2000	–	–	213
Steel substrate	–	–	1,310

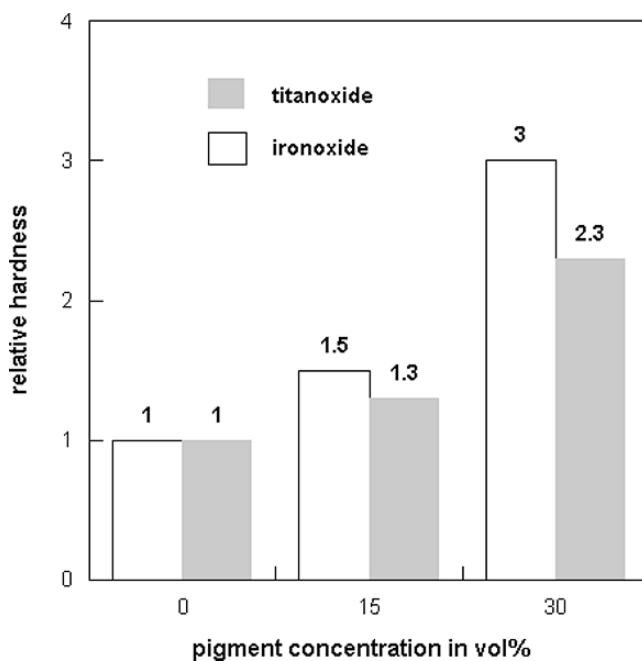
Table 5.8 Vickers hardness values for organic coatings (Rehacek, 1982)

Alkyd resin	Vickers hardness in MPa	Amount of plastic deformation in %
Alkyd	82	34 \pm 4
Alkyd with low soy bean oil content	66	47 \pm 5
Alkyd with moderate linseed oil content	58	42 \pm 1
Alkyd with moderate soy bean oil content	17	53 \pm 2
Alkyd with high soy bean oil content	5.7	25 \pm 8

Table 5.9 Results of deformation measurements on organic paint materials (Neumaier, 1993)

Material	Deformation energy in %		Young's modulus in GPa
	Elastic	Plastic	
Coil coating	19.4	80.6	7.8
Clear lacquer	42.4	57.6	3.2
Filler	29.2	70.8	7.1

Fig. 5.11 that an increase in volumetric pigment concentration led to an increase in hardness. The relative increase in hardness depended on the type of pigment (the addition of iron oxide delivered higher hardness values than the addition of titanium oxide), but not on resin type. The addition of a hardener to the coating material reduced hardness, especially at a higher film thickness. This is verified by the experimental results plotted in Fig. 5.12. Neumaier (1993) found due to comparative hardness measurements on organic paint systems that a spherical indenter promoted an elastic response much more than a pyramid indenter. The energy consumed for permanent deformation in a paint film was about 58% for a pyramid indenter, whereas it was about 10% only for a spherical indenter. Typical elastic and plastic deformation parameters of paint materials, estimated due to indentation tests, are provided in Table 5.9. Therefore, spherical indenters were more suitable for the assessment of the elastic properties of paint films.

**Fig. 5.11** Effects of volumetric pigment concentration and pigment type on Vickers hardness (Rehacek, 1982)

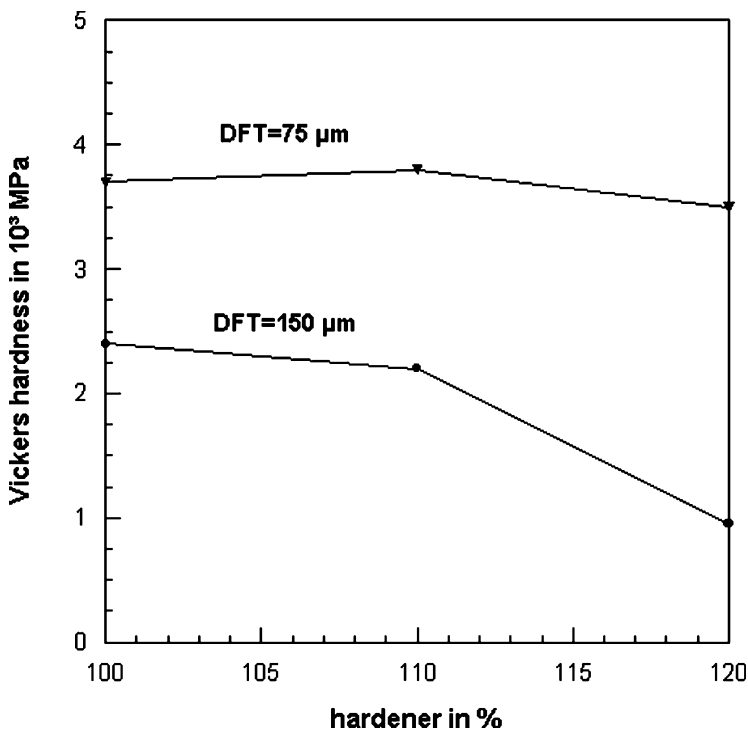


Fig. 5.12 Effects of hardener concentration and coating thickness on Vickers hardness (Fokke, 1999)

The effects of ageing on the hardness of organic coatings are not completely clear. Tangestanian et al. (2001) found a decrease in Vickers hardness of a polyurethane coating if the coating was thermally aged. However, hardness most probably depends on the type of ageing. This was shown through experimental results delivered by Kotnarowska (1999). Hardness (Buchholz hardness) decreased dramatically if ageing occurred due to ultraviolet radiation. Ageing due to thermal shock, on the other hand, did not affect hardness. If ageing took place in salt solutions under immersed conditions, hardness decreased for ageing times of about 600h, and it then rested on a saturation level. Hardness decrease was more pronounced in sulphate solutions than in chloride solutions. Weathering did not affect Buchholz hardness. It was shown that weathering even can notably increase Vickers hardness (Rehacek, 1982; Trezona et al., 2000b). Neumaier (1993) found that especially UV-radiation contributed to an increase in the hardness of organic paint systems. Figure 5.13 illustrates how coating ageing may affect the deformation behaviour of organic coating materials.

Typical values for the dynamic hardness as defined in (5.4) of an organic coating of different ages are listed in Table 5.10. An interesting conclusion can be made from these results: the elastic property (Young's modulus) remained almost

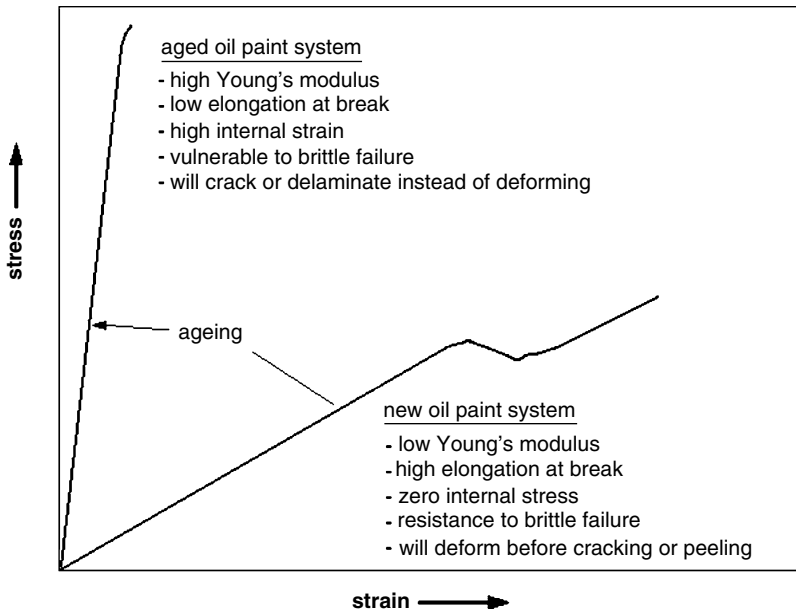


Fig. 5.13 Modification of stress–strain behaviour of coating materials due to ageing (Hare, 1996)

constant, whereas the plastic behaviour (dynamic hardness) was notably affected due to ageing.

During hardness measurements of paint films, the depth of penetration on indenters in the coating should not exceed 10% of the total film thickness in order to exclude any effects of the substrate material (Neumaier, 1993).

5.2.3.3 Fracture Mechanics Parameters

Fracture mechanics parameters include fracture toughness and critical energy release rate (work of fracture). These parameters can be estimated with standard fracture mechanics tests (Ravi-Chandar, 2004), but not much information is available for organic paint films. Some values for the fracture toughness of organic coating materials are listed in Table 5.11. The results show that fracture toughness increased with age. Singh et al. (2004) could show for epoxy resin coatings that the work of fracture depended on the pigment concentration. If pigmented with titanium oxide,

Table 5.10 Mechanical properties of an organic coating system (Tangestanian et al., 2001)

Parameter	Coating age in days				
	fresh	1	2	4	8
Dynamic hardness in GPa	1.43	–	1.64	1.61	1.91
Coefficient of restitution	0.35	–	0.46	–	0.44
Young's modulus in MPa	4,030	4,420	4,160	4,350	4,090

Table 5.11 Fracture toughness values for organic coating materials (Andrews, 2002)

Material	Fracture toughness in MN/m ^{3/2}	
	New	After 12 months
Acrylated urethane	0.61	1.48
Epoxy	0.87	0.80
Acrylic	0.51	0.73

the work of fracture exhibited maximum values at a pigment concentration of about 15%. Typical values for the work of fracture ranged between 5 and 25 kJ/m². Kim and Nairn (2000) published values for the critical energy rate of organic paint films, and they found that the critical energy release rate was a function of the baking time of the coatings. Values ranged between 30 and 200 J/m².

Values for the fracture toughness and energy release rate of numerous hybrid sol-gel coatings can be found in Ballard et al. (2001).

5.3 Impact Processes

5.3.1 Impulse and Energy Considerations

If a solid body hits another solid body at high speed, impulse and energy are transferred from the impinging body (particle) to the impinged body (target). The impulse transferred to the target material can be calculated as follows:

$$I_p = \int_0^{t_p} dt = m_p \cdot (v_p - v_{p2}) \quad (5.8)$$

The energy transferred to the target can be calculated as follows:

$$\Delta E_p = \frac{m_p}{2} \cdot (1 - e_R^2) \cdot v_p^2 \quad (5.9)$$

The parameter e_R is known as the coefficient of restitution (sometimes referred to as impact number).

5.3.2 Coefficient of Restitution

The coefficient of restitution characterises the amount of the kinetic energy of an impinging particles which is supplied to the workpiece for deformation and mass removal. Because the loss of energy is mainly due to plastic deformation, the coefficient of restitution can be considered a measure of the deformation capabilities of

target and particle. A simple definition for vertical impact, where friction between particle and target surface can be neglected, is as follows:

$$e_R = \frac{v_{P2}}{v_P} = \left(1 - \frac{E_i}{E_P}\right)^{1/2} \quad (5.10)$$

The energy E_i is the energy irreversibly stored in the workpiece. Depending on the material response, this energy will be consumed for plastic deformation, crack formation, stress wave penetration, heat generation, etc. Two limits exist for the coefficient of restitution: for $e_R = 1$ ($E_i = 0$), a completely elastic response occurs, and no energy is transferred into the workpiece; for $e_R = 0$ ($E_i = E_P$), a completely plastic response occurs, and the entire kinetic energy is dissipated into the workpiece. A simple measure for the restitution coefficient is the following, based on changes in the potential energy:

$$e_R = \left(\frac{h_2}{h_1}\right)^{1/2} \quad (5.11)$$

Here, h_1 is the height the particle is located at before the impingement and h_2 is the height of the reflected particle measured after the impingement. Illyes and Brauer (1987) performed a study into the effects of impact parameters on the coefficient of restitution. For the material pair steel–steel, they measured typical values between $e_R = 0.35$ and 0.95 . They also noted that this parameter decreased if impingement velocity increased and if impact angle increased. There seemed to exist a critical impact velocity where the coefficient of restitution was independent of impact velocity. This limit was at lower values for shallow impact angles. Tangestanian (1999) investigated the effects of impact velocity on the coefficient of restitution of organic materials. Particles were steel balls with $d_P = 1.5$ mm in diameter. The results of this study indicated a decrease in the coefficient of restitution with an increase in impact velocity. Values for the coefficient of restitution were between $e_R = 0.15$ and 0.43 . Ruppel and Brauer (1990) found an inverse power relationship between impact angle and coefficient of restitution:

$$e_R \propto \frac{1}{\phi^{n_e}} \quad (5.12)$$

The power exponent n_e depended on the target material properties. Hutchings et al. (1981) investigated the rebound behaviour of hard spheres impinging a plastically deformable target material for a wide range of impact velocities and impact angles. They found that rebound velocity was almost linearly related to the impact velocity ($v_{P2} \propto v_P$), whereby the coefficient of proportionality decreased with an increase in impact angle. The rebound angle also showed an almost linear relationship to the particle impact velocity, and the coefficient of proportionality increased if impact angle increased. Sheldon et al. (1977) impinged aluminium with steel balls ($d_P = 3.2$ mm) at velocities between $v_P = 90$ and 200 m/s and noted a

power relationship between coefficient of restitution and rebound angle. Values for the coefficient of restitution were rather low and pointed to a high degree of plastic deformation either in the steel balls or in the aluminium targets. The rebound angle was found to depend on the impingement angle in a linear fashion.

For metal alloys, Levin et al. (1999) derived the following relationship between the coefficient of restitution and material parameters:

$$e_R = \frac{1.75 \cdot H_M^{5/8} \cdot k_E^{1/2}}{\rho_P^{1/8} \cdot v_P^{1/4}} \quad (5.13)$$

The variable k_E summarises the elastic properties of the materials:

$$k_E = \frac{1 - \nu_M^2}{Y_M} + \frac{1 - \nu_P^2}{Y_P} \quad (5.14)$$

Some conclusions can be drawn from this analysis. For metals with high ratios between hardness and Young's modulus, a larger portion of the incident kinetic particle energy transforms into rebound kinetic energy. Energy used for plastic deformation is lower for hard metals than for soft metals.

Tangestanian et al. (2001) measured the coefficient of restitution for the impingement of steel spheres ($m_P = 14$ mg) on at relative low impact velocities ($v_P = 30$ – 35 m/s) on polyurethane coatings. Results of these experiments are listed in Table 5.10 as a function of coating age. It can be seen that the parameter was approximately the same for all aged samples, and that the fresh paint had a significantly lower value. This result means that the freshly applied paint would experience greater plastic (permanent) deformation upon impact.

Hutchings et al. (1981) measured rebound parameters of steel balls after the impingement on steel substrates. They found that the rebound velocity increased almost linearly with the incident impact velocity. Rebound velocity also decreased if impingement angle increased, which was also reported by Papini and Spelt (1998a) for the impingement of steel spheres on polyamide/polyurethane coatings. This trend was also observed by Slikkerveer (1999) for the impact of alumina powder particles ($d_P = 29$ μ m, $v_P = 110$ – 200 m/s) on glass substrates, but the trend held only up to an impact angle of $\varphi = 75^\circ$. If this angle was exceeded, rebound velocity increased with a further increase in impact angle. Interestingly, this author did not measure the rebound behaviour of individual particles, but the rebound characteristics of a particle flow issued from a blast cleaning nozzle ($d_N = 1.5$ mm).

Hutchings et al. (1981) reported that the rebound angle increased if incident impact velocity and impact angle increased. Slikkerveer (1999) could, however, show that the rebound angle of alumina powder particles increased with an increase in impact angle. The relationship was linear, whereby a relationship $\varphi_{\text{rebound}} = 0.5 \cdot \varphi$ could be established. This result was not confirmed for the impact of steel spheres on polyamide/polyurethane coatings, where the rebound angle was more or less independent on incident impact angle (Papini and Spelt, 1998a).

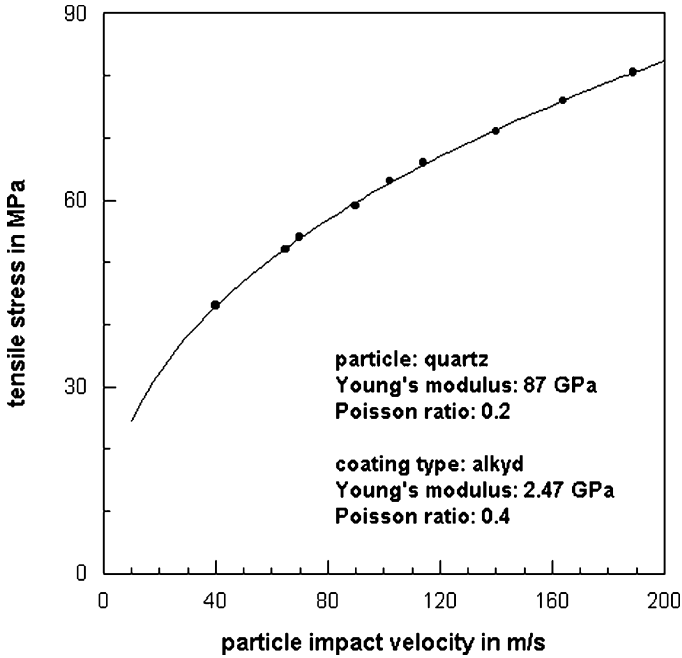


Fig. 5.14 Tensile stresses due to solid particle impingement calculated for a typical substrate-coating arrangement

5.3.3 Energy Absorption

A simple analysis delivers the following subdivision of energy terms:

$$E_p = \frac{m_p}{2} \cdot v_p^2 = \underbrace{\frac{m_p}{2} \cdot v_r^2}_{\text{restitution}} + \underbrace{E_{pp} + E_{ep}}_{\text{particle}} + \underbrace{E_{pm} + E_{em} + E_{0m}}_{\text{target}} + E^* \quad (5.15)$$

The first subscript “p” stands for plastic deformation, and the first subscript “e” stands for elastic deformation. The second subscript “p” stands for particle, and the second subscript “m” stands for target material. Energy absorption mechanisms related to E^* (surface heating, mechanical activation, light emission) are discussed later in this section.

Figure 5.15 illustrates the situation as expressed by (5.15) and provides a qualitative assessment of the energy situation. The initial kinetic energy of the particle (E_p) is absorbed by both particle (grain) and target material. The energy dissipated by the target is subdivided into elastic deformation energy, plastic deformation energy and the surface energy. The latter parameter is frequently called “fracture energy” and relates to the thermodynamic specific surface energy (see Griffith, 1923). Uetz and Föhl (1978) related this parameter to the erosion rate by assuming $E_R = k_0 \cdot E_{0m}$. It can be seen from Fig. 5.15 that the value for the parameter k_0 depends

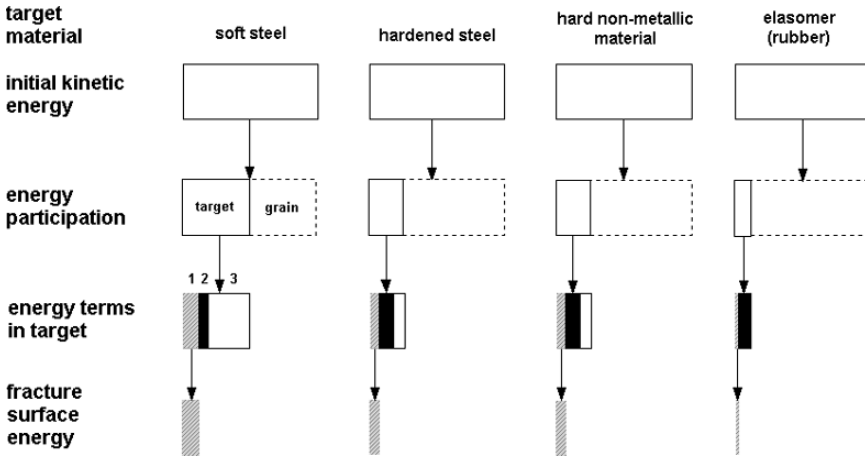


Fig. 5.15 Qualitative proportion of kinetic energy for different target materials during solid particle impinging processes (Uetz and Föhl, 1978). 1 – specific surface energy; 2 – elastic deformation energy; 3 – plastic deformation energy

on the target material. It is rather high for the metals and rather low for the rubber. Figure 5.16 illustrates the situation in a quantitative way for an impinging steel sphere. It can be seen that the concrete energy situation depended on the abrasive materials hardness. The higher this value, the more energy was transferred to the target. For lower abrasive hardness values, a higher amount of energy was transferred to the impinging particle; probably due to permanent plastic deformation of the ball. Hutchings et al. (1976, 1981), Gommel (1967), Uetz and Föhl (1978) and Wellinger and Gommel (1967) performed detailed studies into the energy absorption during abrasive particle impingement.

Hutchings et al. (1981) performed impact experiments with hard steel spheres impinging on soft metals. They found a power relationship between the loss of kinetic energy and particle impact velocity, whereby the power exponent increased if impact angle increased. A model, developed by Hutchings et al. (1976), delivered a power exponent of 2.3 for a steel sphere impinging at an angle of $\varphi = 30^\circ$ on mild steel. These authors also found that the energy loss increased for higher impact angles, whereby the intensity of energy loss was less for higher impact angles.

Gommel (1967b) could show that the energy loss increased if substrate hardness and particle velocity increased. Energy loss was higher for quartz particles compared with steel spheres, which was attributed to the fracture of the brittle pre-damaged quartz. For steel balls, Gommel (1967) found a power-law relationship between the energy loss in the target ($E_{pm} + E_{em}$) and the particle incident impact velocity; with power exponents between 2.4 and 3.3, provided the target material hardness was lower than that of the sphere material.

Illyes and Brauer (1987) defined an abrasive material parameter H_F/Y_M , which was assumed to characterise the type of material response, and found the following relationship between specific energy loss and the material parameter:

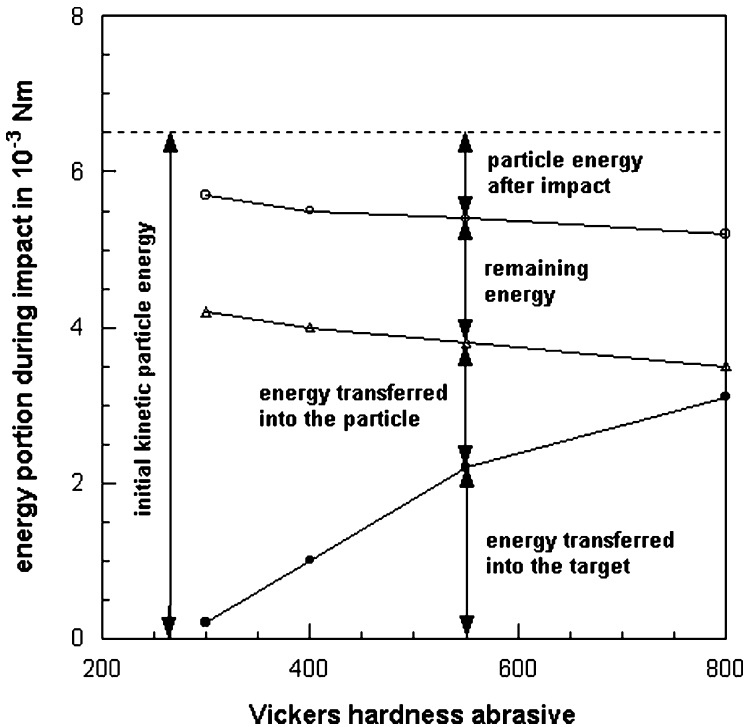


Fig. 5.16 Quantitative proportion of kinetic energy during the impingement of a steel sphere on a steel plate (Uetz and Föhl, 1978)

$$E_I = 1 - 0.125 \cdot \frac{H_P}{Y_M} \tag{5.16}$$

A very similar parameter ratio between hardness and Young’s modulus was proposed by Levin et al. (1999).

Uetz and Gommel (1966) performed a study into the temperature increase in the contact zones between steel plates and impinging steel spheres. Results of these investigations are displayed in Fig. 5.17. Temperature values as high as 380°C were measured at the substrate surface. The temperature in the contact zone increased with an increase in impact velocity and a decrease in steel ball diameter. Both heat development and temperature increase are strongly linked to localised plastic deformations in the target material. Gillström and Jarl (2004) impinged steel wires with wheel-driven steel shot ($d_p = 420\text{--}710\ \mu\text{m}$) and measured the temperature rise in the wires as a function of the shot mass flow rate. The authors measured an increase in temperature of up to 75°C, which corresponded to about 33% of the kinetic energy provided by the shot during impact.

Zehnder et al. (1993) performed investigations into the temperature rise in paints during simulated stone impact. Cold rolled steel panels, coated with automobile

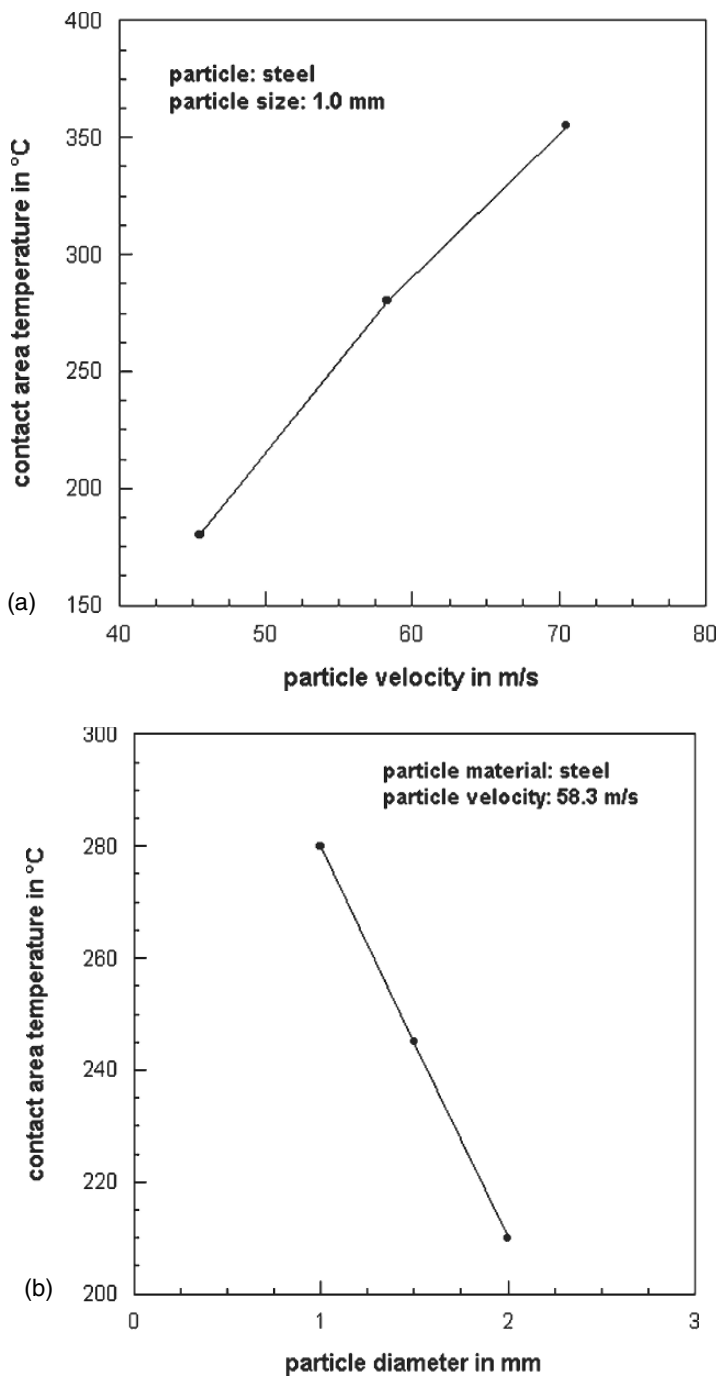


Fig. 5.17 Effects of particle impact parameters on contact temperature (Uetz and Gommel, 1966). (a) Effect of particle velocity; (b) Effect of particle size

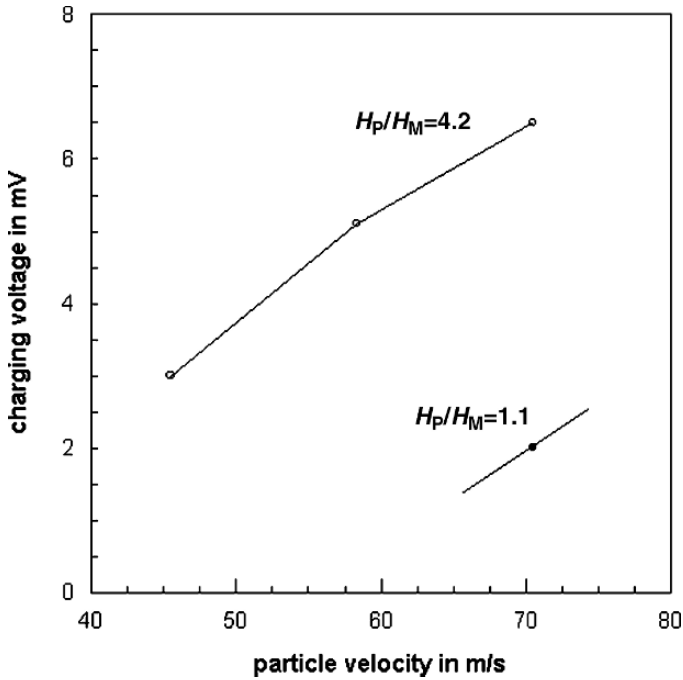


Fig. 5.18 Effects of particle velocity and hardness ratio particle/target on the charging voltage measured during the impingement (Uetz and Gommel, 1966)

paints, were impinged with granite particles at velocities between $v_p = 47$ and 78 m/s. The temperature rise was as high as 200°C , high enough to put the coatings past their glass transition temperatures.

Uetz and Gommel (1966) measured the mechanical activation of steel plate surfaces during the impingement process. As the results in Fig. 5.18 show, charging voltage increased with an increase in impact speed. The charging process was much more intense if the hardness ratio between impinging particle and impinged plate was high. Spark formation could frequently be observed on more electropositive target materials. Figure 5.19 provides a photograph of sparks produced during the impingement of small sand particles on a titanium alloy surface. The energy absorbed by this process as well as by light emission due to abrasive particle fracture during impingement could not be quantified yet.

5.3.4 Damage Number

Johnson (1972) introduced the following dimensionless number for the assessment of impact processes:

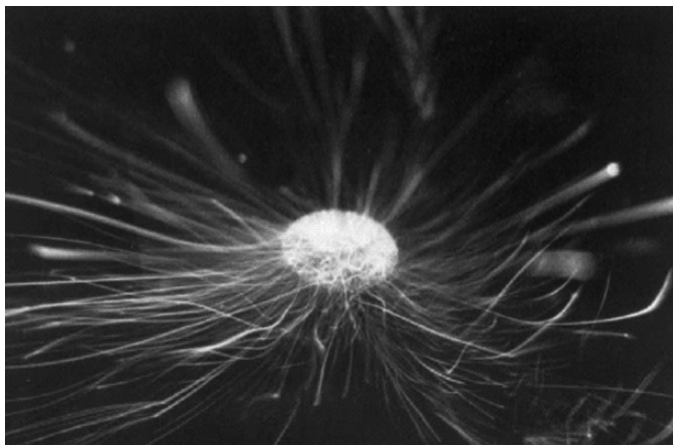


Fig. 5.19 Sparks produced in a titanium alloy impinged by sand particles (Cavendish Laboratory, Cambridge); impact speed: $v_P = 200$ m/s, sand particle diameter: $d_P = 300\text{--}600$ μm

$$N_D = \frac{\rho_P \cdot v_P^2}{\sigma_f} \quad (5.17)$$

This *damage number* N_D is a useful guide for assessing the regime of behaviour of metals in impact situations; it can be understood as a measure of the order of strain imposed in the regions where severe plastic deformation occurs. For a typical mild steel, the following regions can be identified: quasi static/elastic regime at $N_D = 10^{-5}$; plastic behaviour starts at $N_D = 10^{-3}$; extensive plastic deformation at $N_D = 10^1$. A weakness attached to the use of the damage number is that no account is taken of projectile nose shape. Walley et al. (1984, 1987) therefore modified this parameter as follows:

$$N_D = \frac{(\chi_G \cdot \rho_P) \cdot v_P^2}{\sigma_f} \quad (5.18)$$

Here, the parameter χ_G is a geometrical factor which can be estimated as follows (Walley et al., 1987):

$$\chi_G = \frac{\text{volume of whole grain}}{\text{volume of part that ploughs the surface}} \quad (5.19)$$

For an irregular quartz particle impinging a polymer surface, the geometrical factor can have a value as high as $\chi_G = 180$ (Walley et al., 1987). If applied to (5.18), this value corresponds to a velocity ratio of about 13. It was in fact noted by Walley et al. (1984, 1987) for polymer materials, that quartz created certain damage

features at much lower impact velocities compared with steel balls. This approach, therefore, allows for the scaling of different abrasive materials in terms of failure mapping diagrams (compare Fig. 5.37).

5.3.5 Friction Effects

If a notable horizontal component is involved in the impact process, friction effects between target surface and particle surface become important. The coefficient of friction is the ratio between friction force and normal force. The coefficient of friction for impact conditions can be approximated as follows (Hutchings et al., 1976):

$$\mu_F = \frac{2 \cdot r_P \cdot \omega_P}{5 \cdot (v_P \cdot \sin \varphi + v_{P2} \cdot \sin \varphi_2)} \quad (5.20)$$

This relationship considers the rotation of the impinging particle. A typical value for the pair steel–steel is $\mu_F = 0.04$ (Hutchings et al., 1976).

Ratner and Styler (1981) investigated the effects of impact angle variations on the coefficient of friction. For rather low impact velocities ($v_P = 20$ m/s), they found that the coefficient of friction decreased with an increase in impact angle for vulcanised materials. For polymers, in contrast, they found maximum values for the coefficient of friction between $\mu_F = 0.2$ and 0.35 at low impact angles ($\varphi = 30^\circ$ and 40°). The impinging particles were steel beads with a diameter of $d_P = 2$ mm.

Friction coefficients for abrasive contact situations for a number of coating materials are listed in Table 5.12. Yabuki and Matsumura (1999) published a number of friction coefficients for particle impingements at low impact velocities. Some of their results are listed in Table 5.13. The authors found that the friction coefficient decreased with an increase in impact velocity, but it rested at a saturation level for velocity values in excess of $v_P = 3$ m/s.

Table 5.12 Friction coefficients of organic coating materials (Calabrese and Murray, 1982)

Material	Friction coefficient
Bitumastic	0.03
Epoxy	0.1
Polyethylene	0.05
Polyurethane	0.06
Polyurethane (filled)	0.14
PTFE	0.11
Steel (uncoated)	0.37

Table 5.13 Friction values for particle impingement situations (Yabuki and Matsumura, 1999)

Particle	Particle diameter in μm	Particle velocity in m/s	Target material	Friction coefficient
Steel shot	3,000	0.8	Aluminium	0.22
	3,000	0.9	Brass	0.19
	600	1.4	S45C	0.18
Brass shot	3,000	1.0	Aluminium	0.26
	3,000	1.2	Brass	0.22
	3,000	1.5	S45C	0.17
Steel grit	280	3.0	S45C	0.36
	880	2.1	S45C	0.28
	1,130	1.7	S45C	0.23
Silicone carbide	270	2.7	S45C	0.39
	290	2.3	S45C	0.39
	560	2.3	S45C	0.38
Silica sand	260	2.5	S45C	0.29
	340	2.3	S45C	0.26
	400	2.1	S45C	0.25

5.4 Material Loading Due to Solid Particle Impingement

5.4.1 Loading Parameters

Tensile stresses generated in an elastically responding material by an impinging spherical particle have maximum values at the surface at the edge of contact according to Hertz's (1882) theory for elastic contact:

$$\sigma_T = \frac{(1 - 2 \cdot \nu_M) \cdot F_C}{2 \cdot \pi \cdot a_C^2} \quad (5.21)$$

Here, a_C is the contact radius, and F_C is the contact force. The contact radius is given by:

$$a_C = \left(\frac{3 \cdot k_E \cdot F_C \cdot d_P}{8} \right)^{1/3} \quad (5.22)$$

The contact force generated by an impinging spherical particle can be derived either by applying a force balance (Mintrop, 1941; Timoshenko and Goodier, 1970):

$$m_P \cdot \frac{dv_P}{dt} = -F_C \quad (5.23)$$

or by applying an energy balance (Knight et al. (1977):

$$\frac{2 \cdot \pi \cdot \rho_P \cdot r_P^3}{3} \cdot v_P^2 = \int_0^{z_{\max}} F_C(z) dz \quad (5.24)$$

A solution to (5.24) is:

$$F_C = \left(\frac{5}{3} \cdot \pi \cdot \rho_P \right)^{3/5} \cdot \left(\frac{3}{4} \cdot k_E \right)^{-2/5} \cdot v_P^{6/5} \cdot \left(\frac{d_P}{2} \right)^2 \quad (5.25)$$

[The relationship $F_C \propto v_P^{6/5}$ was already found by Hertz (1882).] The parameter k_E balances the elastic properties of particle and target material according to (5.14).

A combination of the above-mentioned equations delivers the following relationship between maximum tensile stress and particle velocity:

$$\sigma_T \propto v_P^{2/5} \quad (5.26)$$

Figure 5.14 shows tensile stresses, calculated for typical elastic properties of an organic coating material.

The contact time for an elastic contact was first derived by Hertz (1882) for two spheres with identical properties. Timoshenko and Goodier (1970) offered the following solution (written in a modified form):

$$t_P^E = 2.94 \cdot \left[\frac{5 \cdot \pi \cdot \rho_P}{4} \cdot \left(\frac{1 - v_M^2}{Y_M} + \frac{1 - v_P^2}{Y_P} \right) \right]^{2/5} \cdot \frac{d_P}{2} \cdot v_P^{-1/5} \quad (5.27)$$

Results of calculations performed with (5.27) are plotted in Fig. 5.20. In reality, however, plastic deformations and fracture processes in particle and target material must be considered. These processes can notably extend the contact time. Thus, a plastic contact time must be added to the elastic contact time. Chaudri and Walley (1978) suggested the following equation for the calculation of the plastic contact time:

$$t_P^{PL} = \frac{\pi}{2} \cdot \left(\frac{m_P}{2 \cdot \pi \cdot r_P \cdot H_{ID}} \right)^{1/2} \quad (5.28)$$

The plastic contact time mainly depends on the dynamic hardness of the target material, and it is independent of the impact velocity. The total contact time is given by:

$$t_P = t_P^E + t_P^{PL} \quad (5.29)$$

An approximation for the strain rates associated with high-speed particle impingement was provided by Hutchings (1977) who derived the following equation:

$$\dot{\epsilon}_P \cong \frac{2^{3/2}}{2 \cdot \pi} \cdot \frac{v_P^{1/2}}{r_P} \cdot \left(\frac{3 \cdot P_C}{2 \cdot \rho_P} \right)^{1/4} \quad (5.30)$$

The contact pressure in (5.30) can be replaced through the indentation hardness of the target material. The trends for the effects of impact velocity and particle size were experimentally verified by Groß (1988) for aluminium targets. This author

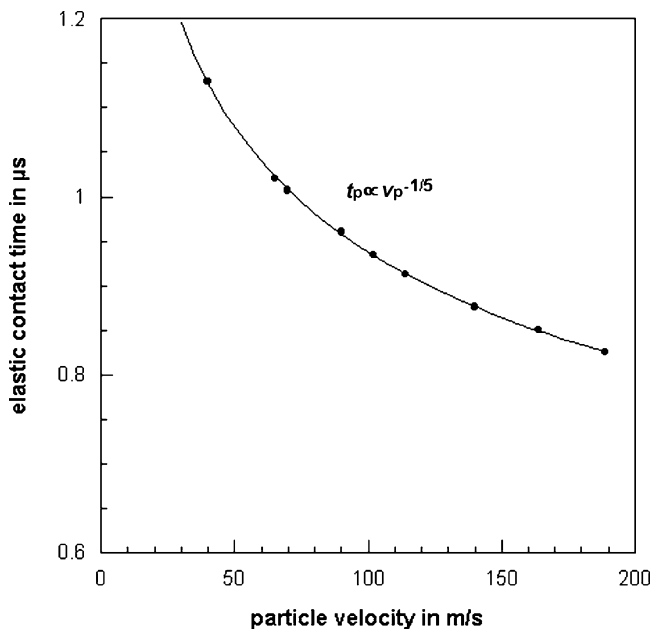


Fig. 5.20 Elastic contact time calculated for a typical substrate-coating arrangement (see Fig. 5.14 for elastic constants)

measured strain rates between $\dot{\epsilon}_p = 1 \times 10^4$ and 4×10^4 per second for impact velocities up to $v_p = 130$ m/s.

5.4.2 Material Response to Particle Impingement

Depending on the contact situation, materials respond either elastic or plastic to solid particle impingement. Examples are shown in Fig. 5.21. The critical particle velocity for plastic flow during particle impact is (Johnson, 1985):

$$v_{PL}^2 = \frac{26 \cdot (\sigma_f/Y_M)^4 \cdot \sigma_f}{\rho_p} \tag{5.31}$$

The threshold particle velocity for Hertzian crack formation can be derived from (5.24) in combination with Auerbach’s law ($P_H = A_a \cdot d_p$). This procedure delivers:

$$v_H = A_a^{5/6} \cdot \left(\frac{3}{4} \cdot k_E\right)^{1/3} \cdot \left(\frac{5}{3} \cdot \pi \cdot \rho_p\right)^{-1/2} \cdot \left(\frac{d_p}{2}\right)^{-5/6} \tag{5.32}$$

Here, A_a is the Auerbach constant. For $v_H = v_{PL}$ and $\sigma_f = H_M$, (5.31) and (5.32) deliver the following condition for elastic–plastic transition:

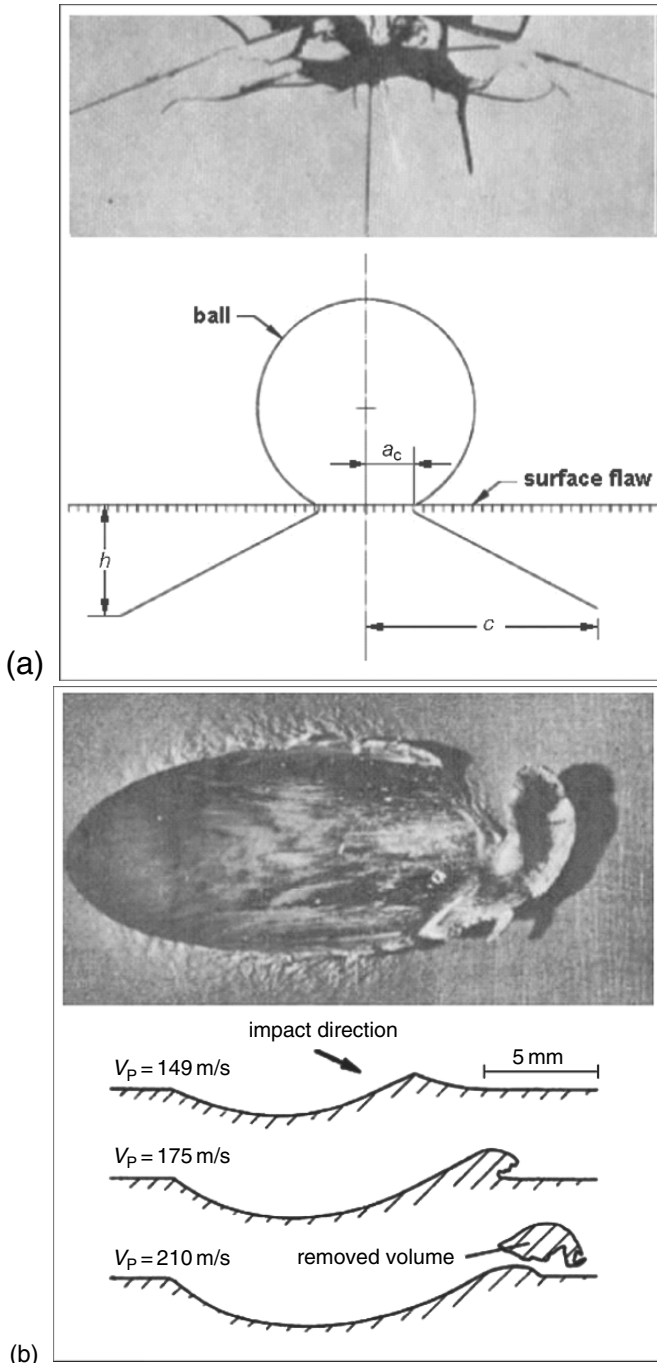


Fig. 5.21 Types of response to solid particle impingement (Aquano and Fontani, 2001). (a) Elastic response with cone crack formation; (b) Plastic-elastic response at different particle impact velocities ($\varphi = 25^\circ$); the lower drawing is adapted from Winter and Hutchings (1974).

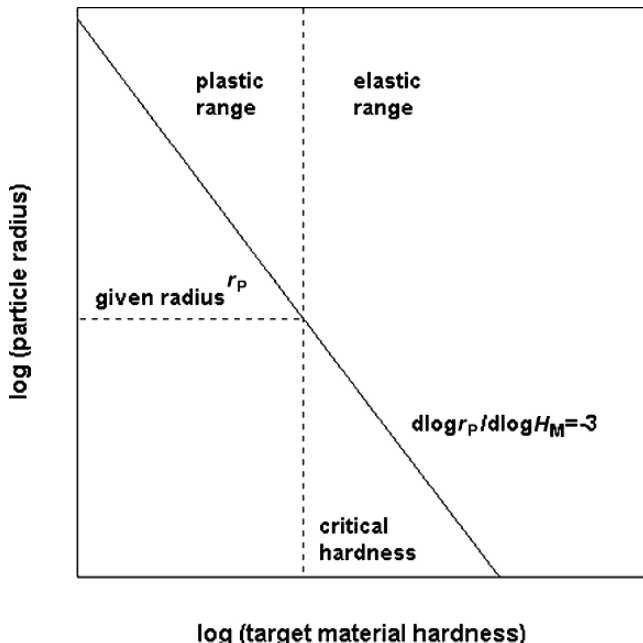


Fig. 5.22 Impact transition criterion for coating materials according to (5.33)

$$\frac{d_{PL}}{2} \propto H_M^{-3} \tag{5.33}$$

This relationship is illustrated in Fig. 5.22. This graph reveals a size and a shape effect for erosion processes. The transition from elastic to plastic response depends on the diameter of the abrasive particles; the smaller the impinging particle, the higher is the probability of plastic response. Also, the higher the curvature of the particle tip (broken, irregularly shaped abrasive particles have high curvature values), the higher is the probability of plastic response.

5.4.3 Formation of Radial and Lateral Cracks

A crack system as shown in Fig. 5.23 forms under certain contact conditions in brittle coatings. *Radial cracks* form in the intermediate surface region of brittle materials if a certain stress level (particle velocity) is exceeded. The formation of a radial crack in a brittle material is illustrated in Fig. 5.24. The figure shows high-speed photographic sequences of the normal impingement of a 1.0-mm diameter glass sphere on a block of soda lime glass. The interframe time was 1 μs. The designation “R” in frame “4” labels the cone and radial cracks formed during the loading. Radial cracks do not lead to material removal, but they reduce strength in

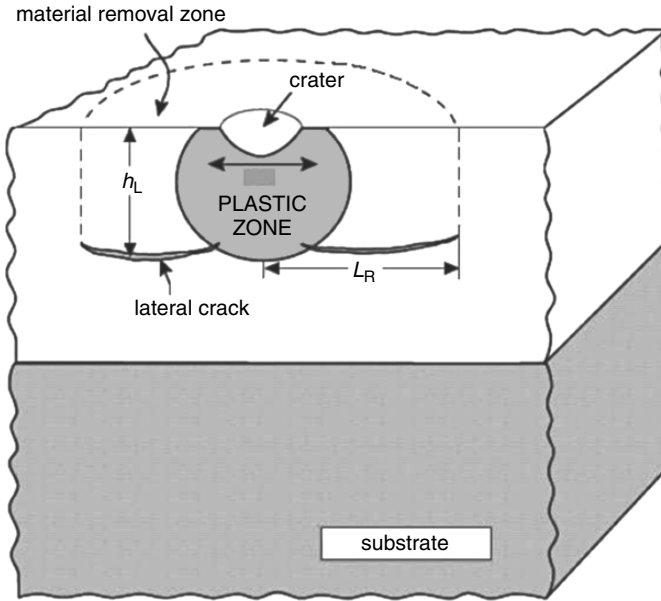


Fig. 5.23 Crack system, formed in the bulk of a brittle coating due to particle impingement (Evans et al., 2006)

the near-surface region. The lengths of these cracks depend on process parameters as follows (Anderson et al., 1993):

$$L_R \propto \frac{d_P^{4/3} \cdot v_P}{K_{Ic}^{2/3}} \tag{5.34}$$

Number and distribution of radial cracks depend on particle velocity, and the relationship between number of cracks and impact velocity is (Kirchner and Gruver, 1978):

$$N_R \propto v_P^{6/5} \tag{5.35}$$

Lateral cracks are critical to material removal processes. They grow from the bottom of the permanent depression during the unloading phase of the contact. They grow into the direction of the surface. If they meet the surface, material is removed. This process is shown in Fig. 5.25. The following two threshold criteria for the formation of lateral cracks were derived by Hutchings (1992). The first criterion reads as:

$$d_P \propto \left(\frac{K_{Ic}}{H_M} \right)^2 \cdot \frac{Y_M^{1/2}}{H_M^{1/4} \cdot \rho_M^{1/4}} \cdot v_P^{-1/2} \tag{5.36a}$$

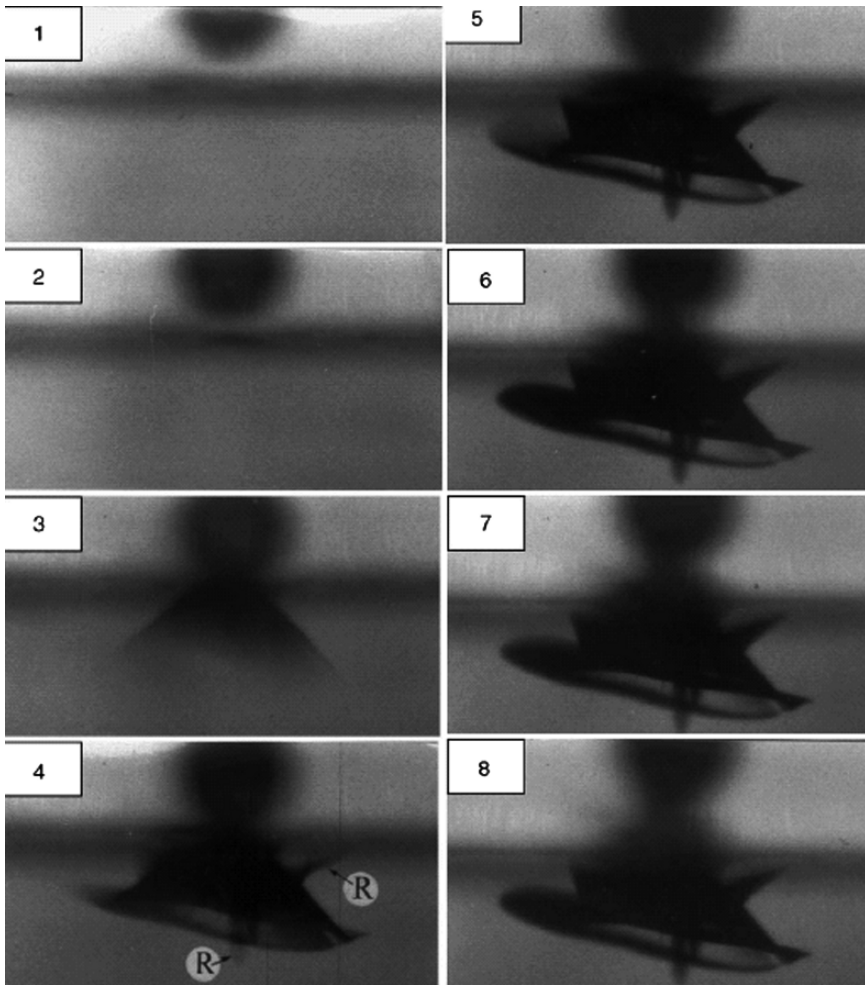


Fig. 5.24 Formation of cone and radial cracks in soda lime glass impinged by a steel sphere at $v_p = 140$ m/s (Chaudri and Walley, 1978); “R” – cracks

This criterion holds for spherical particles. The second criterion reads as:

$$d_p \propto \left(\frac{K_{Ic}}{H_M} \right)^2 \cdot \frac{Y_M^{1/2}}{H_M^{1/6} \cdot \rho_M^{1/3}} \cdot v_p^{-2/3} \tag{5.36b}$$

This criterion holds for irregular particles. The ratio K_{Ic}/H_M – sometimes referred to as “brittleness” – plays a dominating role. Graphical solutions to (5.36a) and (5.36b) are provided in Fig. 5.26. If the depth, a lateral crack is formed at, is assumed to be equal to the depth of the permanent depression, it can be approximated as follows (Lange and Evans, 1979; Evans et al., 1978):

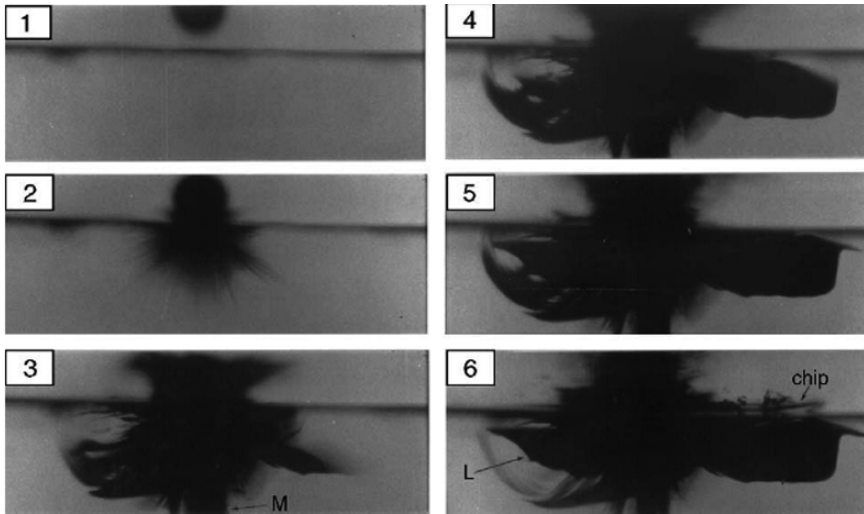


Fig. 5.25 Formation of lateral cracks in soda lime glass impinged by a steel sphere ($d_p = 800 \mu\text{m}$) at $v_p = 300 \text{ m/s}$ (Knight et al., 1977); “L” – lateral crack

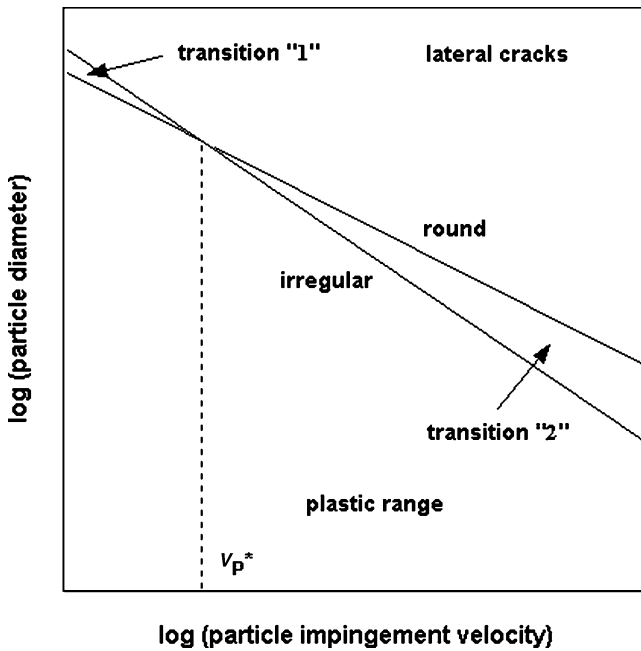


Fig. 5.26 Threshold criteria for lateral crack formation according to (5.36)

$$h_L = \frac{3.5 \cdot d_p}{2} \cdot \left(\frac{\rho_p}{H_M} \right)^{1/4} \cdot v_p^{1/2} \quad (5.37)$$

It can be seen from Fig. 5.23, that length of a radial crack (5.34) and depth of a lateral crack (5.37) can be used to approximate the volume of the coating material being removed from the surface:

$$V_M = \alpha_M \cdot \frac{\pi}{4} \cdot L_R^2 \cdot h_L \quad (5.38)$$

The geometry parameter is $0 < \alpha_M \leq 1$. Equation (5.38) is the basic approach for the modelling of material removal processes due to solid particle impingement in the elastic–plastic response range. More information is provided by Momber (2004a, b). For $h_L = h_C$, the adhesion fracture energy of the interface between substrate and coating material becomes important.

5.5 Material Removal Models

5.5.1 General Aspects of Modelling

The literature about solid-particle erosion is extensive. Adler (1979), Engel (1976) and Preece (1979) presented general reviews about earlier investigations. More recently, Ellermaa (1993) and Meng and Ludema (1995) analysed the state-of-the-art modelling of solid particle erosion. Meng and Ludema (1995) defined four sub-mechanisms by which solid particles separate material from a metal surface. These mechanisms are cutting, fatigue, melting and brittle fracture. Elastic-plastic fracture, as described in Sect. 5.4, must be added as a fifth mechanism. These mechanisms generally do not act separately, but in combination. Their importance for the particular erosion process depends on several factors, such as impact angle, particle kinetic energy, particle shape, target material properties and environmental conditions.

The solid-particle erosion process can generally be characterised by a dimensionless erosion rate:

$$E_R = \frac{m_M}{m_p} \quad (5.39)$$

Thus, the removed volume per solid particle can be defined as follows:

$$V_M = \frac{E_R \cdot m_p}{\rho_M} \quad (5.40)$$

5.5.2 Erosion of Plastically Responding Materials

The material removal process for a plastically responding material is simplified in Fig. 5.27a-c. Examples for a plastic coating response are provided in Fig. 5.3. Magnee (1995) suggested the following generalisation of solid particle erosion models for plastically responding (ductile) materials:

$$V_M \propto \frac{v_P^2 \cdot m_P}{\epsilon_C} \cdot f\left(\frac{H_P}{H_M}\right) \cdot f(\phi) \quad (5.41)$$

The effects of the considered abrasive and coating parameters are discussed in Chap. 5.8. An early and often used consideration of the material erosion by micro-cutting is due to Finnie (1958). A typical micro-cutting process is illustrated in Fig. 5.28. The figure shows high-speed photographic sequences of the impingement of a square tool steel plate on a mild steel target at high speed. The interframe time is 19 μm . The plate rotated backwards during impact. Figure 5.29 shows a chip formed during the micro-cutting of low-carbon steel during the impingement with aluminium oxide particles. Finnie (1958) discussed the process by assuming a plastic response character of the material determined by its flow stress. Figure 5.30 shows the basic geometrical and kinematic parameters of this model. After calculating the trajectory

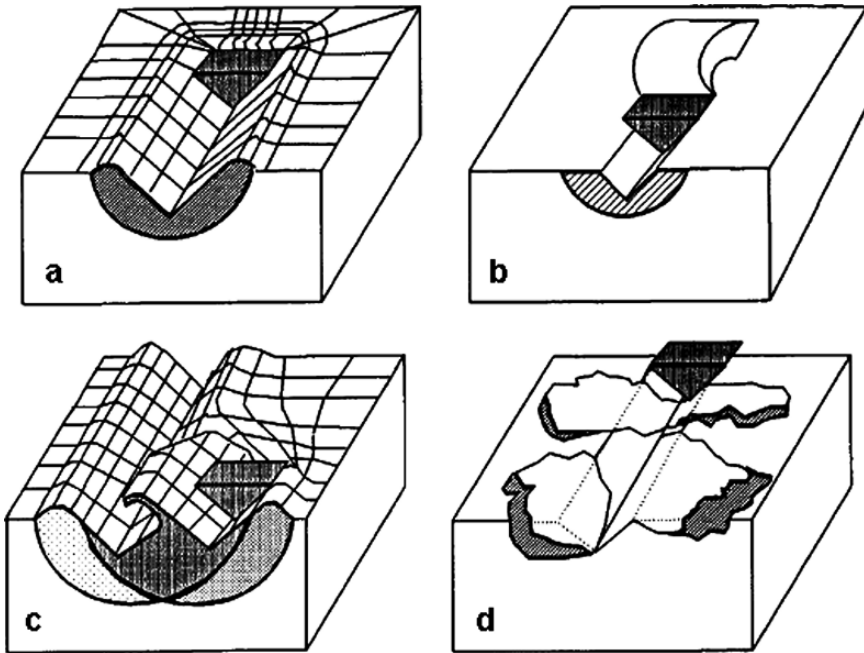
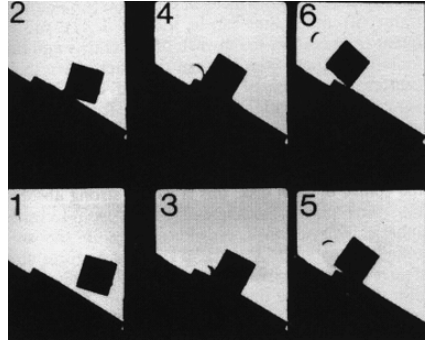


Fig. 5.27 Schematics of material removal in a coating material due to an abrasive particle (adapted from Zum Gahr, 1987). (a) Micro-ploughing; (b) Micro-cutting; (c) Micro-fatigue; (d) Micro-fracturing

Fig. 5.28 High-speed photographic images of a micro-cutting process (Hutchings, 1977); $v_p = 186 \text{ m/s}$, $\varphi = 30^\circ$.



of a single particle during the removal process, Finnie (1958) derived the following equation for the estimation of the eroded volume:

$$V_M = \frac{m_p \cdot v_p^2}{\sigma_f \cdot K_F \cdot \psi_F} \cdot f(\varphi) \quad (5.42)$$

$$f(\varphi) = \sin(2 \cdot \varphi) - \frac{6}{K_F} \cdot \sin^2 \varphi \quad \left(\text{for } \tan \varphi < \frac{K_F}{6} \right),$$

$$f(\varphi) = \frac{K_F \cdot \cos^2 \varphi}{6} \quad \left(\text{for } \tan \varphi > \frac{K_F}{6} \right),$$

$$K_F = \frac{F_Y}{F_X} \cong 2, \quad \psi_F \cong 2.$$

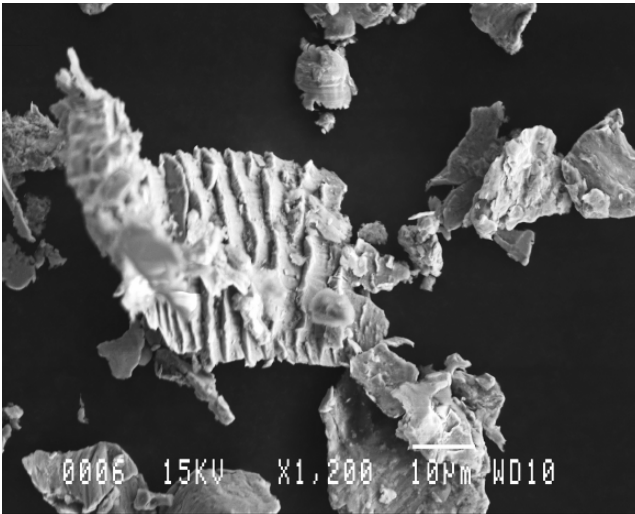
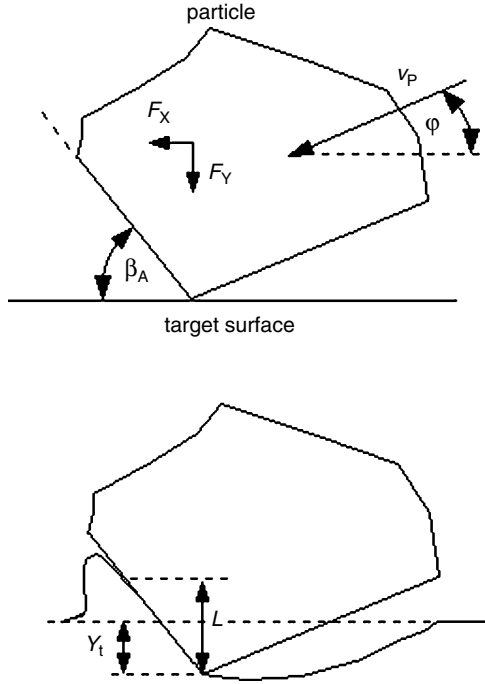


Fig. 5.29 Chip formation during the micro-cutting of low-carbon steel (Momber and Wong, 2005b)

Fig. 5.30 Finnie’s (1958) micro-cutting model



Equation (5.42) has the structure of (5.41) when the material’s flow stress is replaced by the hardness of the eroded material. The parameter K_F is the ratio of vertical to horizontal force, and $\psi_F = L/y_t$ (Fig. 5.30). Later, Finnie and McFadden (1978) improved the model leading to a particle velocity exponent of about 2.5.

Bitter (1963) developed a more general model. He divided the entire material removal process into two modes, which he called the “cutting wear”, that happened at low-impact angles, and “deformation wear”, that occurred at high-impact angles. By considering the energies involved in the erosion process, he derived two formulas for both material removal modes. For the “cutting wear” mode, the following relationship was derived:

$$V_{Mcut} = \frac{m_p \cdot [v_p^2 \cdot \cos^2 \phi - C_2 \cdot (v_p \cdot \sin \phi - v_{EL})^2]}{2 \cdot \epsilon_{Ccut}} \tag{5.43}$$

$$C_2 = f(Y_M, Y_P, \rho_M, v_M, v_P)$$

For the “deformation wear” mode, the following relationship was derived:

$$V_{Mdef} = \frac{m_p \cdot (v_p \cdot \sin \phi - v_{EL})^2}{2 \cdot \epsilon_{Cdef}} \tag{5.44}$$

The parameter v_{EL} is a threshold impact velocity which must be exceeded to introduce the material removal process. For certain conditions, (5.43) is equal to (5.41). Neilson and Gilchrist (1968b) later simplified this model.

Hutchings (1979b) introduced an alternative discussion of the micro-cutting processes during particle-induced erosion. Based on high-speed photographs and SEM observations, he defined two modes of material removal due to micro-cutting, namely “cutting-deformation” and “ploughing-deformation”. The ploughing-deformation mode dominates the material removal by spherical particles, whereas cutting-deformation is significant for sharp-edged, angular particles. Hutchings (1979b) made a further subdivision of the cutting-deformation mode into “type I cutting-deformation” and “type II cutting-deformation”, depending on the direction of the particle rotation. For forward rotating particles, “type I” is dominant, and for backward rotation, “type II” is valid (see Fig. 5.21b). Hutchings (1979b) also developed a solid-particle erosion model for normal impact that is based on low-cycle fatigue. Gane and Murray (1979) developed an approach for the transition from a ploughing mode to a cutting mode of erosion. The transition was considered to occur at a critical angle (β_A) between particle face and target surface (see Fig. 5.30). For high values of the face angle, the friction between target material and abrasive face are low, and chip formation is the dominant material removal mode.

The plastic work associated with the deformation of a material around the impact site largely degrades into heat. Hutchings and Levy (1989) gave a review about thermal effects in solid-particle erosion of ductile materials. It appeared from their discussion that thermally determined features of the solid-particle erosion process were not a necessary assumption under all impact conditions. With smaller particles at low impact velocities, for example, thermal effects were not important.

Ellermaa (1993) performed a critical review of solid-particle erosion models developed for the estimation of the materials removal in plastically responding materials. As she has shown, Finnie’s model especially exhibited a comparatively high divergence from experimentally estimated values, illustrating that a simple micro-cutting process does not cover the complexity of the material removal process. This result is in agreement with results of erosion debris morphology measurements performed by Momber and Wong (2005b). Based on erosion tests on low carbon steel, the authors found that micro-cutting played a negligible role only, and that about 60% of all acquired debris were of a platelet-type shape as suggested by Bellmann and Levy (1981).

Levin et al. (1999) derived the following relationship for the erosion response of metal alloys:

$$\dot{V}_M \propto \frac{\text{energy used for plastic deformation}}{\text{energy required to cause fracture}} \propto \frac{1 - H_M}{T_D} \quad (5.45)$$

The two material parameters must be estimated from dynamic stress–strain curves (see Fig. 5.4c). In materials with high hardness, the transformation of impact energy into the impinged material is reduced. For high toughness values, more energy is dissipated before the material fractures.

Andrews and Field (1982) discovered and described a certain material removal mode for soft materials (mild steel). Based on high-speed camera images, they

showed that single hardened steel spheres could remove material even when they stroke the targets at normal impingement. Material loss occurred by the rapid radial expansion (jetting) of material from under the spheres. This mechanism of erosion is most likely when the deformation is highly localised.

Carter et al. (1991) performed experiments into the effects of reflected abrasive particles on the erosion process for ductile materials. For impact angles larger than $\varphi = 20^\circ$, no observable signs of reflection efficient enough to cause erosion on the receiving erosion plane were detected. The authors did not observe mirror reflection, but rather reflection angles much smaller than the incident angles. The severity of the secondary erosion due to reflected abrasive particles depended on the incident impact angle. Relative to the erosion rate of direct incidence, the secondary erosion was: 50% for $\varphi = 20^\circ$; 15% for $\varphi = 15^\circ$ and 34% for $\varphi = 5-10^\circ$. These results were valid for copper targets impinged by corundum particles ($d_p = 30 \mu\text{m}$).

5.5.3 Erosion of Elastically Responding Materials

The material removal process for an elastically responding material is simplified in Fig. 5.27d. An example for the elastic response of an organic coating material is provided in Fig. 5.3a. Erosion models for elastically responding (brittle) materials are well established. The most important material parameters which control the erosion process were identified based mainly on developments in indentation fracture mechanics (Lawn, 1993). The general equation for the material removal in elastically responding materials by an impacting solid particle is given through (5.38).

The erosion model developed by Evans et al. (1978), and the elastic-plastic theory of Wiederhorn and Lawn (1979), related the volume loss to the depth of particle penetration and the maximum size of the lateral cracks which form during impact (Figs. 5.27a and 5.23), whereby it was assumed that the depth of the lateral cracks is proportional to the size of the radial cracks.

Most of the models developed for the erosion by brittle fracture follow the general relation:

$$V_M \propto \left(\frac{d_p}{2}\right)^{c_2} \cdot v_p^{c_3} \cdot H_M^{c_4} \cdot K_{Ic}^{c_5} \cdot Y_M^{c_6} \tag{5.46}$$

Table 5.14 lists the power exponents of the different models related to (5.46).

Table 5.14 Solid particle erosion models for brittle-behaving materials, (5.46)

Model	Reference	c_2	c_3	c_4	c_5	c_6
Elastic model	Sheldon and Finnie (1966)	$f(M)^a$	$f(M)^a$	–	–	–
Quasi-static lateral crack model	Wiederhorn and Lawn (1979)	3.67	2.45	0.11	–1.33	–
Dynamic lateral crack model	Evans et al. (1978)	3.67	3.17	–0.25	–1.33	–
Modified lateral crack model	Marshall et al. (1982)	3.50	2.33	–1.42	–1.00	1.25

^a Depends on material structure

5.6 Erosion of Scale

5.6.1 Brittle Erosion Approach

Scale is considered here to be a system of brittle, elastically responding layers that forms on a ductile substrate. In cases, such as for duplex nickel, scale consists of a dense outer and a porous inner layer. The removal of scale is typical of a brittle material. This is verified by Fig. 5.31 which shows partly eroded scale from a low-carbon steel substrate. The formation of crack can be recognised in the untreated scale (upper right region) as well as in the partly eroded scale (lower right region). Levy (1995) noted a mixed response of scale subjected to solid particle impingement, including plastic indentation and the formation of lateral and radial cracks in the outer scale layer, and the formation of Herzian ring cracks in the inner scale layer (see Sect. 5.4). These phenomena are illustrated in Fig. 5.32. Cone cracks form under initial plastically deformed craters. All of this action serves to divide the scale into a mosaic of small, cracked areas that can be removed from the surface by subsequent particle impingement.

From investigations of relatively thick nickel oxide scale, it was determined that scales eroded sequentially down through their thickness by a cracking and chipping mechanism rather than being knocked off the metal in pieces at the scale–metal interface. This incremental erosion process is illustrated in Fig. 5.33 for a thin ($20\ \mu\text{m}$) and thick ($100\ \mu\text{m}$) scale. It can be seen that the scale has a threshold period where the scale is being cracked, but none has been removed. At “E1” for the $100\text{-}\mu\text{m}$

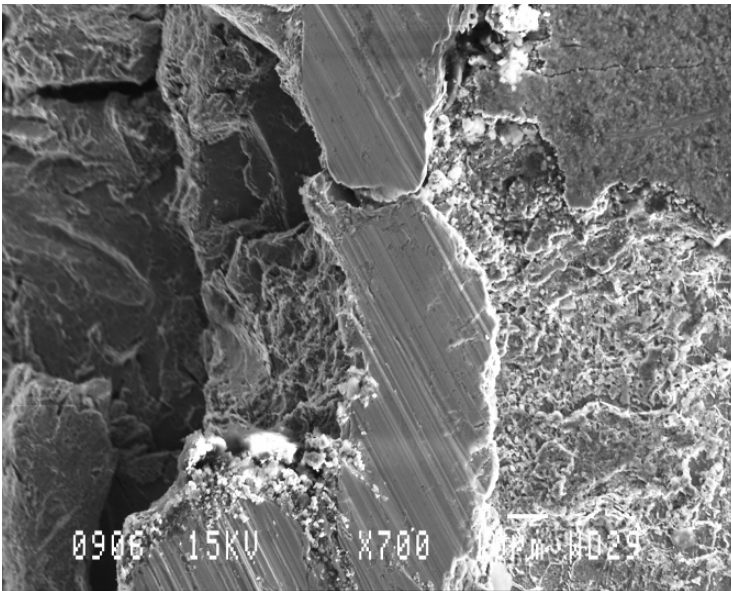


Fig. 5.31 Scale removal from low-carbon steel; crack formation visible at several locations. (Photo: author)

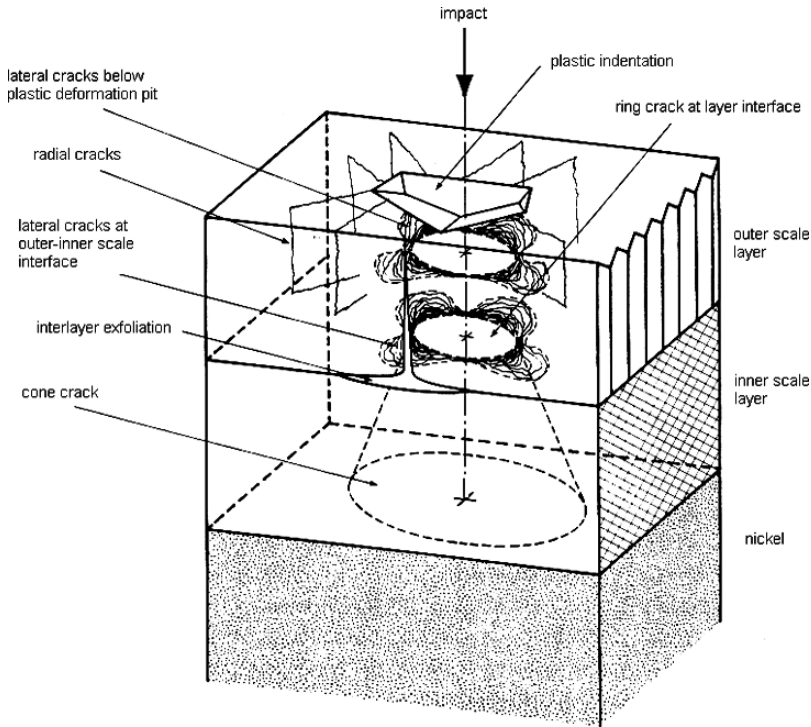


Fig. 5.32 Material removal scheme for scale (Levy, 1995)

scale, weight loss begins to occur. At “E2”, the weight loss is primarily that of the dense outer scale layer that occurs at a lower rate than at “E3”. At “E3”, the particles are eroding the porous inner scale layer, and a maximum erosion rate can be recognised. The 20- μm scale had only the dense outer scale. It reaches its relatively low peak erosion rate nearly compared to the 100- μm scale, and it then fell off rapidly.

The presence of the ductile metal substrate did not appear to have a major effect on the way the brittle scale eroded. However, the ductile substrates had a small effect. The thinner scales could transfer more of the kinetic energy of the impinging particles to the ductile nickel and, hence, they cracked and chipped and eroded at lower rates than the thicker scale. As the thicker scales were removed, their rates of erosion decreased to a rate that became nearly the same for all scale thickness values.

5.6.2 Removal Mechanisms and Modelling

Schmithals (1961) performed a systematic investigation into the removal modes of mill scale during blast cleaning. He derived the following equation for the estimation of rest scale on rolled steel panels as a function of blast cleaning time:

$$m_{SC} = (1 - K_S)^{tB} \tag{5.47}$$

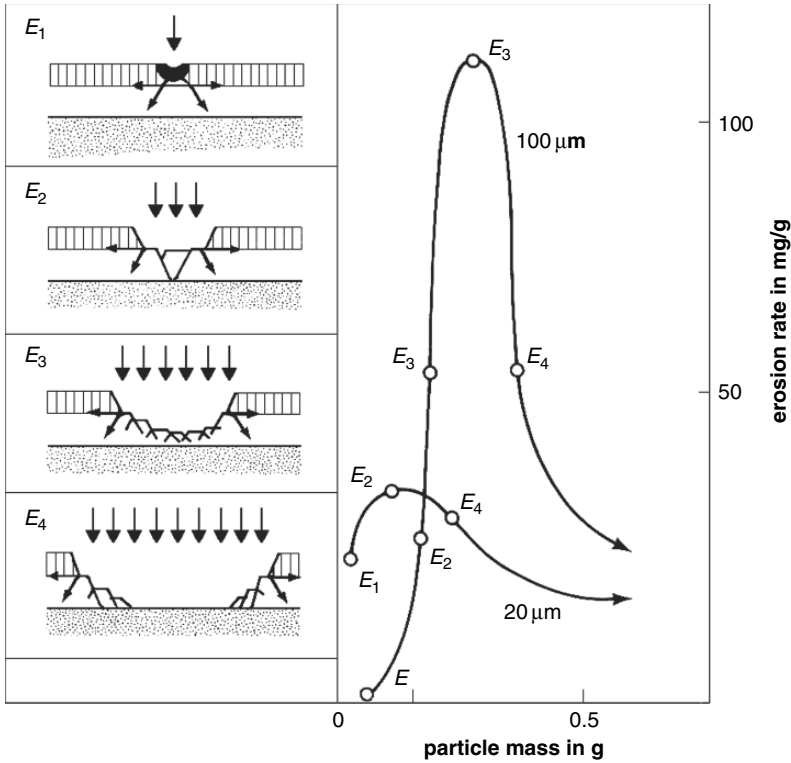


Fig. 5.33 Incremental erosion of nickel oxide scale (Levy, 1995). Impact angle: $\varphi = 90^\circ$

The parameter K_S characterises the resistance of mill scale against blast cleaning. A typical value for this parameter was $K_S = 0.48$. The mass loss of mill scale as a function of abrasive mass follows a typical relationship as shown in Fig. 5.34. The function can be subdivided into two sections: a progressively increasing branch (I) and a linear branch (II). The intersection between these two branches characterises the limit for the complete removal of the mill scale. The linear part of the function is a result of plain steel removal only. The intersection point, characterised by m_E , expresses the mass of abrasive material required to generate a completely mill scale free-steel substrate. Its value depends on the chemical composition of the mill scale. Experimentally estimated results are listed in Table 5.15. In descaling practice, the parameter m_E showed a linear relationship to the specific abrasive mass flow, and an inverse relationship to the traverse speed of the blast cleaning tool required to obtain scale free surfaces (Schmithals, 1961).

Schmithals (1961) distinguished three basic material removal mechanisms for mill scale, which are shown in Fig. 5.35. In case (I), scale is removed at the impinged area, but also on locations further away from the impacted area. In case (II), scale removal is restricted to the impinged area only. In case (III), scale is pressed into the substrate surface, and the pressurised scale band is cracked. In the latter case, the

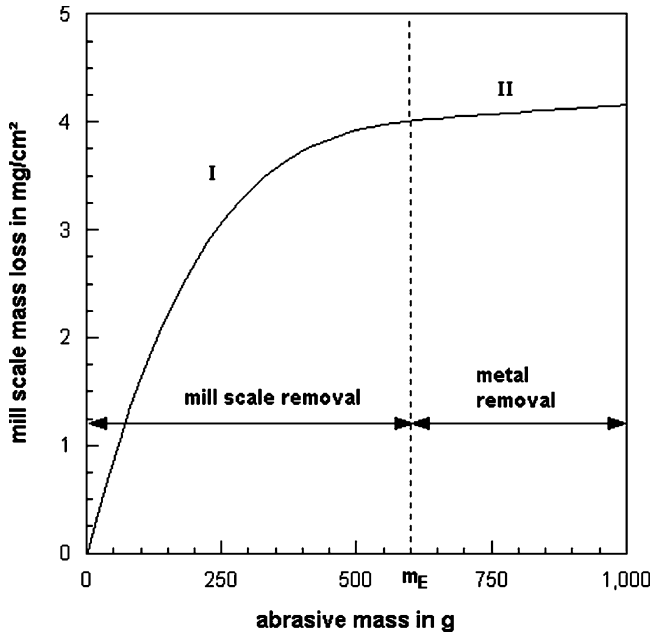


Fig. 5.34 Relation between mill scale mass loss and abrasive mass (Schmithals, 1961)

parameter m_E showed rather high values. If mill scale is being removed according to mechanism (I), the removal process can reliably be modelled with (5.47). If the two other mechanisms were applied, experimental results differed widely from the theoretical results of (5.47).

5.6.3 Removableness of Mill Scale

Rädeker and Wild (1958) performed a study into the removableness of mill scales of different steel types. Surface preparation methods considered in this study included

Table 5.15 Descaling parameter m_E and chemical composition of mill scale (Schmithals, 1961)

Chemical composition of mill scale in %					m_E in g
C	Si	Mn	P	S	
0.05	0.02	0.35	0.018	0.026	605
0.03	0.01	0.31	0.012	0.010	515
0.07	0.01	0.39	0.031	0.014	330
0.08	0.01	0.33	0.013	0.027	370
0.41	0.94	0.97	0.027	0.024	355
1.30	0.24	0.32	0.017	0.010	335
0.05	0.01	0.27	0.040	0.028	515
0.05	0.01	0.36	0.049	0.026	675

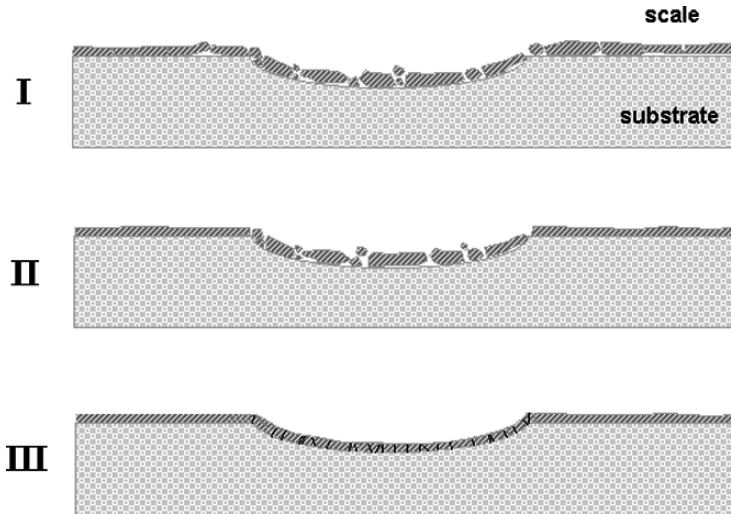


Fig. 5.35 Material removal mechanisms for mill scale during blast cleaning (Schmithals, 1961)

acid pickling, blast cleaning and flame cleaning. For the blast cleaning process, removableness was defined as the number of blast cleaning steps required to completely remove the mill scale. The authors found that the rolling temperature did not affect the removableness in a systematic way. Especially, the scale of unkilld steels did not show any relationship to the rolling temperature. A better correlation was found between the removableness and the adhesion of the mill scale to the core steel (see Fig. 5.9 for typical adhesion strength values). With the exception of some Si–Al-steel, the removableness decreased with an increase in adhesion. Adhesion is, however, not the only criterion for the removableness of mill scale. Manufacturing regime and composition of steel and mill scale affect this parameter as well.

Peltzer (1955) gave some recommendations about the particle size of metallic abrasives for effective removal of mill scale. He found that the optimum blast cleaning abrasive size depended on the plate thickness. For coarse plates (thickness between 2.8 and 6.4 mm), he recommended a particle size of about $d_p = 500 \mu\text{m}$; for moderate plates (thickness between 1.3 and 2.8 mm), he recommended a particle size smaller than $d_p = 200 \mu\text{m}$.

5.7 Erosion of Bulk Polymers and Elastomers

5.7.1 Material Removal Mechanisms for Bulk Polymers

Figure 5.36 illustrates different material removal modes in polymers impinged by solid particles. Zhang et al. (1995) investigated the response of a number of polymers to abrasive erosion and identified different material removal mechanisms,

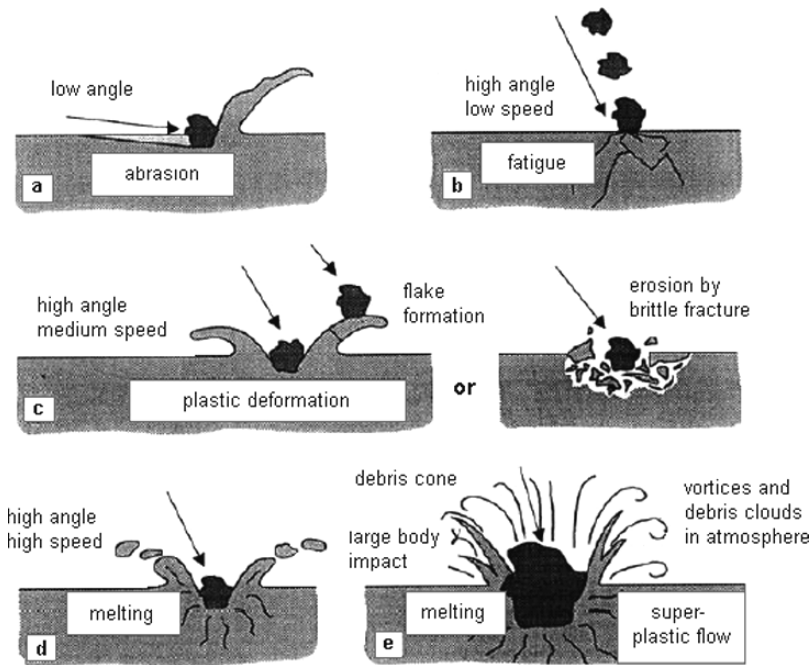


Fig. 5.36 Material removal modes in polymers, impinged by solid particles (Barkoula and Karger-Kocsis, 2002)

namely micro-cutting, micro-delamination and surface peeling. On *polyurethane* surfaces, indentations and scratches were found as results of micro-cutting. The formation of cracks was also noted which nucleated probably from the fracture of intermolecular chains. On *Nylon-6* surfaces, scratches due to micro-cutting, but also some amount of small plastically deformed areas were found. On *polytetrafluorethylene* surfaces, material removal occurred due to ploughing and scratch formation, accompanied by plastic deformation.

The erosion of bulk *polyethylene* (PE), *polypropylene* (PP) and *polyetheretherketone* (PEEK) through abrasive particles was in some detail investigated by Walley and Field (1987) and Walley et al. (1984, 1987). They found that PEEK showed less damage in single particle erosion than either PE or PP and explained this observation by the liability of the PEEK to brittle failure. Based on single impact experiment and discussions of crater morphology, the authors identified numerous material removal mechanisms, and they classified these mechanisms as functions of particle impact velocity and angle. Results for PE are illustrated in Fig. 5.37. Smooth craters, which were observed at rather low impact speeds, were defined to be those where very little surface modification has taken place. In a narrow range of shallow impact angles, a regular series of bands of displaced material was observed. As the impact angle raised, the bands became fewer, and most of the displaced material ended up at the end of the crater as a lip. At high impact angles, penetration and, respectively,

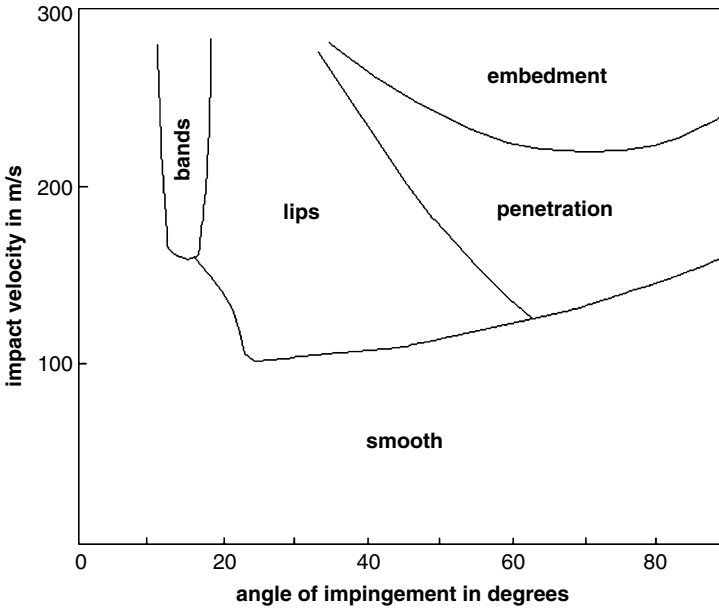


Fig. 5.37 Erosion mechanisms for polymer materials (Walley and Field, 1987)

embedment of spherical abrasives took place. The impact velocity needed to cause the latter two mechanisms to occur had a minimum at an impact angle of about $\varphi = 70^\circ$. Walley et al. (1984, 1987) applied the damage number according to (5.18) for the construction of general damage maps for polymers (see Sect. 5.3.4).

From the geometry point of view, craters could be classified into four types: smooth; ploughed; cut and sharply dented. The frequency of occurrence of the certain geometry depended mainly on impact angle as verified by the results listed in Table 5.16 for PE and PEEK.

For PE, lip volume and crater volume increased with increasing impact velocity according to a power function:

$$V_M \propto v_p^{\alpha_B} \quad (5.48)$$

The power exponent had values $\alpha_B = 2.77$ for the crater volume and $\alpha_B = 2.8$ for the lip volume (Walley and Field, 1987). The specific energy for lip formation as well as for crater formation decreased with increasing impact velocity implying that a greater fraction of the energy dissipated went into permanent material displacement as the velocity rose. For an impact velocity $v_p = 200$ m/s, the specific energy values were about 0.4 J/mm^3 for crater formation, and about 1.1 J/mm^3 for lip formation (Walley and Field, 1987). Scratch deformation maps for polymers, very similar to that shown in Fig. 5.37, are issued by Briscoe and Sinha (2003).

Aspects of thermal effects were also investigated by Walley and Field (1987). Based on a heat transfer analysis, they found that a particle impact frequency of

Table 5.16 Percentage of crater types in bulk polymers for various impact angles; see Fig. 5.37 (Walley et al., 1987; Walley and Field, 1987)

Impact angle in °	Percentage of crater type in %							
	Smooth		Ploughed		Cut		Sharply dented	
	PE ^a	PEEK ^b	PE	PEEK	PE	PEEK	PE	PEEK
10	45		30		11		14	
20	28	62	43	21	22	14	7	3
30	42	37	40	32	5	24	13	6
40	62	42	21	47	4	10	13	1
50	68	35	14	46	5	16	13	2
60	80	14	7	59	4	22	9	6
70	90	36	6	46	0	16	4	3
80	86		3		1		10	
90	90	31	5	46	0	21	5	2

^a Polyethylene^b Polyetheretherketone

about 11/s was required to build up enough heat in PE to make thermal effects become significant. This frequency corresponded to a rather high flux rate of about 180 kg/(m² s). Measurements delivered real impact frequencies between 0.4 and 1.2 per second; thus one order of magnitude is too low for thermal effects to play a significant role.

5.7.2 Material Removal Mechanisms for Elastomers

Arnold and Hutchings (1992, 1993), Besztercey et al. (1999) and Hutchings et al. (1987) investigated the behaviour of rubber materials during the erosion by impinging abrasive particles. The major mechanism identified by the authors was the propagation of fatigue cracks. The fatigue cracks propagated under the action of tensile stresses generated during particle impact. Crack nucleation could, for example, occur at the interfaces between rubber matrix and filler particles (Besztercey et al., 1999). The individual cracks formed a dense net on the surface as verified by SEM imaging studies (Arnold and Hutchings, 1992, 1993). An example is shown in Fig. 5.38. When individual cracks intersected, material was being detached. The depth of cracked layers in rubber was typically between 10 and 150 μm, and the crack separation distance was typically between 2 and 30 μm. Both parameters depended on abrasive particle diameter; if abrasive size increased, these parameters increased almost linearly (Arnold and Hutchings, 1993).

Hutchings et al. (1987) noted that the concrete material removal modes in rubber depended on the resilience of the materials. High-resilience rubbers formed distinctive surface ridges on erosion at $\varphi = 30^\circ$, similar to features seen on abraded rubber surfaces and possibly indicative of a similar cyclic crack growth mechanism caused by the tangential component of the impact force. Rounded particles of rubber, which

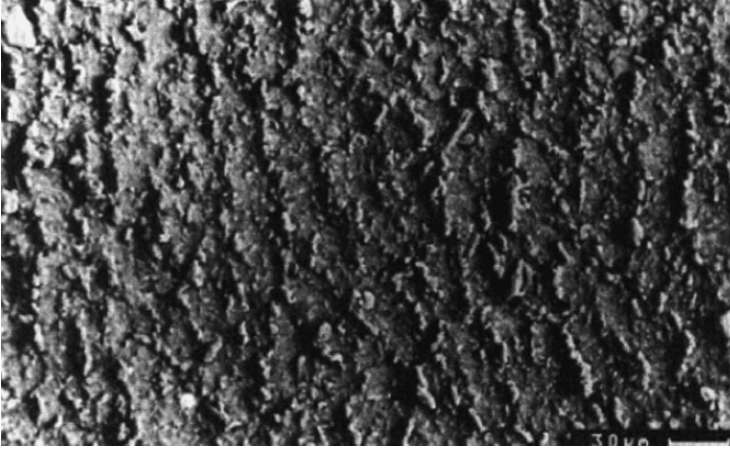


Fig. 5.38 SEM image of an eroded rubber surface, showing fatigue cracks (Arnold and Hutchings, 1992); impact direction from the left, $v_p = 100$ m/s, $d_p = 120$ μ m, $\phi = 30^\circ$, abrasive: silica

probably provided a source of material loss, formed at the peaks of these ridges. The surfaces of low-resilience rubbers eroded at the same angle, were in contrast much more uniformly roughened, showing evidence of apparently loosely attached angular rubber fragments distributed over the surface, and numerous cracks and fissures. The occurrence of these cracks, which were not seen on the high-resilience rubbers, suggested that erosion may have proceeded by a catastrophic tearing process.

Arnold and Hutchings (1989) found that the flux rate (respectively impact frequency) had strong effects on the erosion regime in rubber, especially if glass beads were used. The strain produced by a single impact was insufficient to cause material removal, and successive impacts were necessary to raise the strain to a sufficient level to cause material removal. The authors also noted an incubation period at low flux rates, within no material was removed, but a darkened area was found on the surfaces of the samples. Infrared spectra delivered evidence for environmental degradation; considerable amounts of oxygen were incorporated into the surface of the elastomers.

5.7.3 Erosion Resistance of Bulk Polymers

Kriegel (1968) derived a material resistance model, which he applied to polymeric materials. An erosion resistance parameter based on this model includes the following parameters:

$$R_E \propto \underbrace{\frac{Y_M}{\rho_P \cdot v_P^2}}_{\text{energy number}} \cdot \underbrace{\frac{v_P}{N_P \cdot d_P}}_{\text{frequency number}} \cdot \underbrace{\frac{\sigma_V}{Y_M}}_{\text{strength number}} \quad (5.49)$$

The unit of the erosion resistance is s/mm in (5.49). A similar approach was made by Urbanovich et al. (1995). The strength number in (5.49) balances “erosion strength” (σ_V) and Young’s modulus of the target material. The erosion strength is defined as follows:

$$\sigma_V = \frac{\sigma_T - \sigma_{0.1}}{Y_M} \cdot \sigma_T \quad (5.50)$$

In that equation, σ_T is the tensile strength and $\sigma_{0.1}$ is the stress at the elastic limit for a deformation of 0.1%. A combination of (5.49) with (5.50) delivers the following relationship:

$$E_R \propto Y_M^{-1} \quad (5.51)$$

Experimental results displayed in Fig. 5.39 verify this approach: erosion resistance decreased if Young’s modulus of the polymeric materials increased. It may be mentioned that this particular trend was observed by Kriegel (1968) and Brauer and Kriegel (1963) for plastics only. For many metals, and especially for brittle materials, an opposite trend was noted.

Cizmas and Slattery (2006) assumed a visco-elastic deformation behaviour and applied a dimensionless analysis to the solid particle erosion of polymers. They introduced a dimensionless modulus of elasticity [$Y_M/(\rho_M \cdot v_p^2)$] and found that this

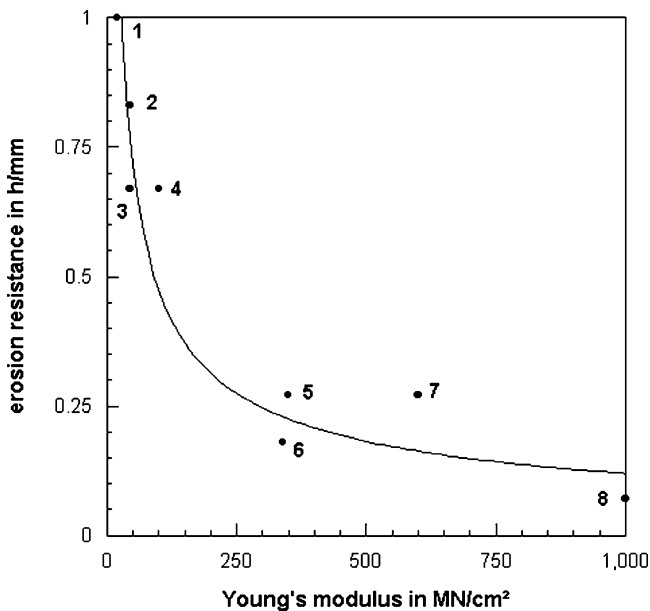


Fig. 5.39 Relationship between Young’s modulus of polymeric materials and erosion resistance (Kriegel, 1968). Materials: 1 – soft polyethylene; 2 and 3 – hard polyethylene; 4 – polyamide; 5 – PMMA; 6 – PVC; 7 – phenolic polymer; 8 – epoxy + quartz dust

parameter was proportional to the erosion resistance for a given group of polymers. This approach verifies the “energy number” derived in (5.49).

Böhm et al. (1990) found that the resistance of polymeric materials against abrasion and solid particle erosion reduced if the elongation to tensile fracture increased. Results of their investigation are displayed in Fig. 5.40.

A negative correlation between erosion resistance and hardness was found by Kriegel (1968) for PVC samples, and by Miyazaki (1996) for thermoplastic polyimide resins: erosion resistance decreased if hardness (Shore hardness; Vickers hardness) rose. Results are displayed in Fig. 5.41. Miyazaki (1996) explained this behaviour through the fact that softer polymers could absorb higher amounts of the kinetic energy of the impinging particles prior to fracture. Degree of crystallinity was also important: if the structure changed from an amorphous structure to a crystalline structure, erosion resistance dropped (see Fig. 5.41). This was because hardness increased with a rise in the degree of crystallinity (Miyazaki, 1996).

Friedrich (1986) investigated the resistance of a number of polymers against particle impingement, and he suggested that the ratio H_M/G_{Ic} (denoted “brittleness index” by the author) provides a better indication of erosion resistance than hardness alone. Results of his measurements are provided in Fig. 5.42. It can be seen that the ratio between hardness and fracture energy is a good indication of the erosion resistance of different polymer materials for a wide range of process conditions. The fracture energy of polymers is closely related to the cross-link density

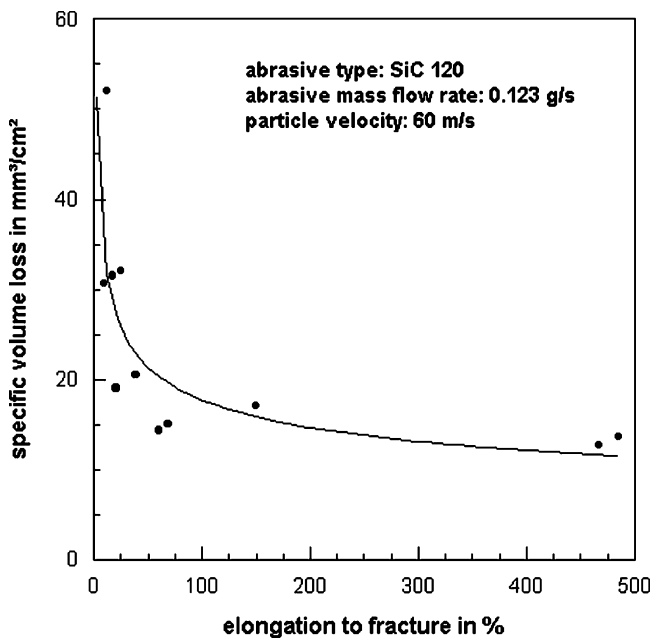
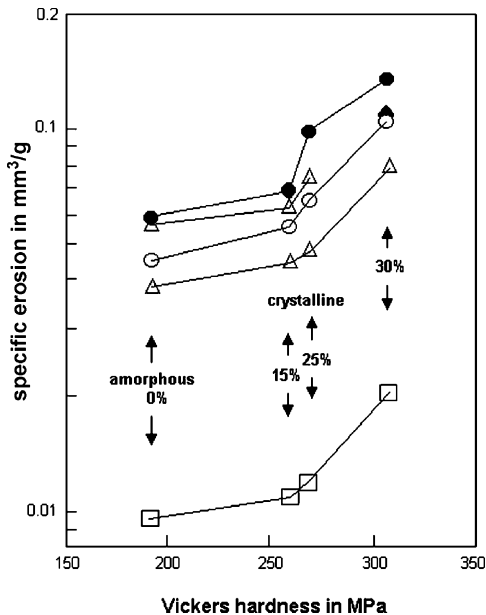


Fig. 5.40 Relationship between elongation to fracture of polymeric materials and erosion resistance (Böhm et al., 1990)

Fig. 5.41 Relationships between erosion rate, Vickers hardness and degree of crystallinity (Miyazaki, 1996).



of cross-linked thermoplastics (Barkoula, 2002). Figure 5.43 shows the effect of cross-link density of polymers on the relative erosion resistance for different impact angles. Erosion resistance initially decreased if cross-link density increased, but rested on a saturation level if cross-link density exceeded a certain threshold. The saturation threshold was lower for shallower impact angles. The resistance of fusion-bonded epoxy powder coatings against slurry erosion was also controlled by the amount of cross-linked bonds (Luo et al., 2003).

Thermal properties, that could play a role in terms of erosion, are thermal conductivity and glass transition temperature. Low thermal conductivity would lead to high temperature increase during plastic deformation. Temperature rise is lower if heat can flow away from the impact site faster than it is being generated. High temperatures may briefly soften polymers; however, as mentioned in Sect. 5.7.1, this becomes critical only at rather high flux rates.

5.7.4 Erosion Resistance of Elastomers

The erosion of rubber was modelled by Arnold and Hutchings (1992, 1993) for oblique and normal impact conditions. The model for normal impact angles delivered the following relationship between erosion rate and material parameters (Arnold and Hutchings, 1993):

$$E_R \propto \frac{\rho_M}{(1 - v_M)^{\beta_F}} \tag{5.52}$$

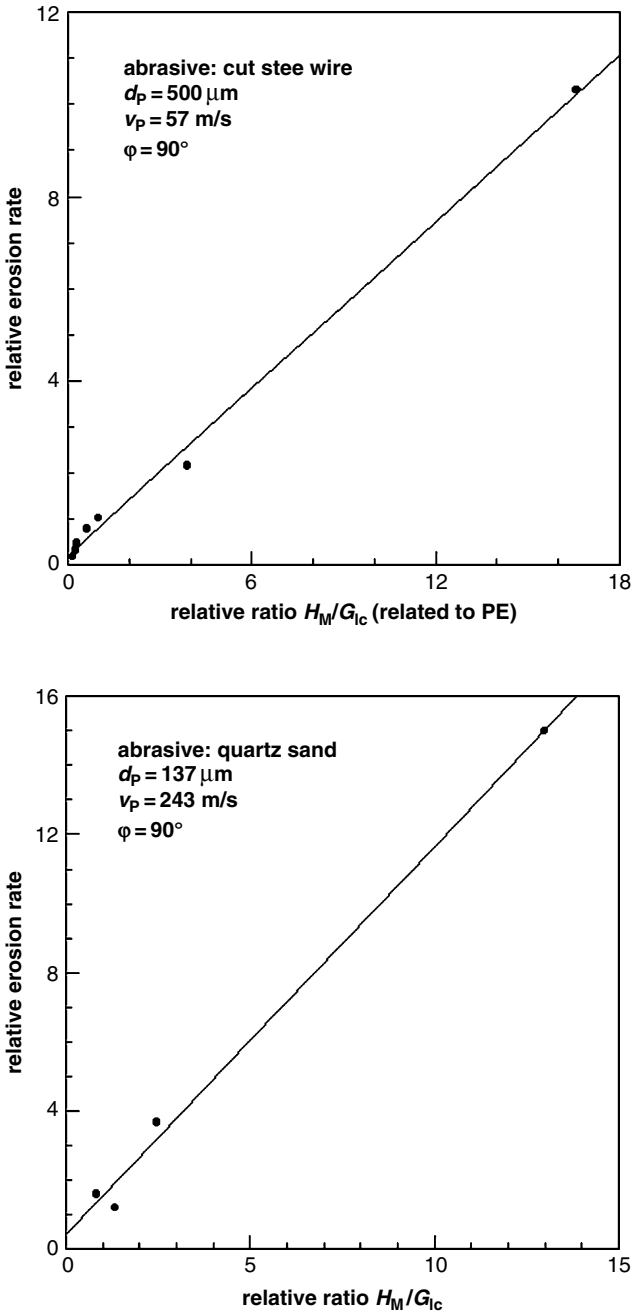


Fig. 5.42 Relationship between “brittleness index” (H_M/G_{Ic}) and erosion resistance of polymer materials (Friedrich, 1986). (a) Tests with cut steel wire at low impact velocity; (b) Tests with quartz sand at high impact velocity

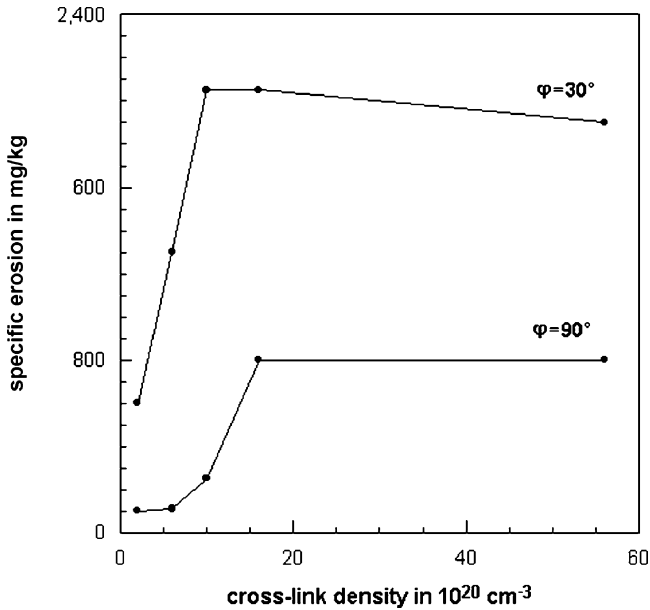


Fig. 5.43 Effect of cross-link density of polymeric materials on specific erosion resistance (Barkoula, 2002)

The model for oblique impact angles delivered the following relationship between erosion rate and material parameters (Arnold and Hutchings, 1992):

$$E_R \propto \rho_M \cdot E_M^{(\beta_F - 1)/2} \quad (5.53)$$

From these relationships, erosion resistance decreases if material density increases. Young's modulus has an effect on erosion resistance at oblique impact angles only. Such trends could in fact be observed, if Young's modulus was replaced by material hardness. [Hardness of elastomers has a linear relationship to Young's modulus; Li and Hutchings (1990).] Hardness had an effect on the erosion resistance of rubber mainly at shallow impact angles. For silica particles impinging at an angle of $\varphi = 30^\circ$ and an impact velocity of $v_p = 120 \text{ m/s}$, Arnold and Hutchings (1993) noted an increase in erosion for rubber types with higher hardness values, whereas the erosion rate was not affected by changes in rubber hardness at $\varphi = 90^\circ$. These relationships are illustrated in Fig. 5.44. A general trend between hardness and erosion resistance could neither be observed during tests performed by Hutchings et al. (1987). Samples with moderate hardness values (Shore A) showed the lowest erosion resistance, whereas the resistance was high for samples with low and high hardness values. However, if samples with comparative values for rebound resilience are considered, erosion rate can be related to the hardness of elastomers [Li and Hutchings (1990)]; this is illustrated in Fig. 5.45.

The parameter β_F contained in (5.52) and (5.53) is originally a material fatigue parameter. From tensile fatigue tests, typical values for rubber are between 2.0 and

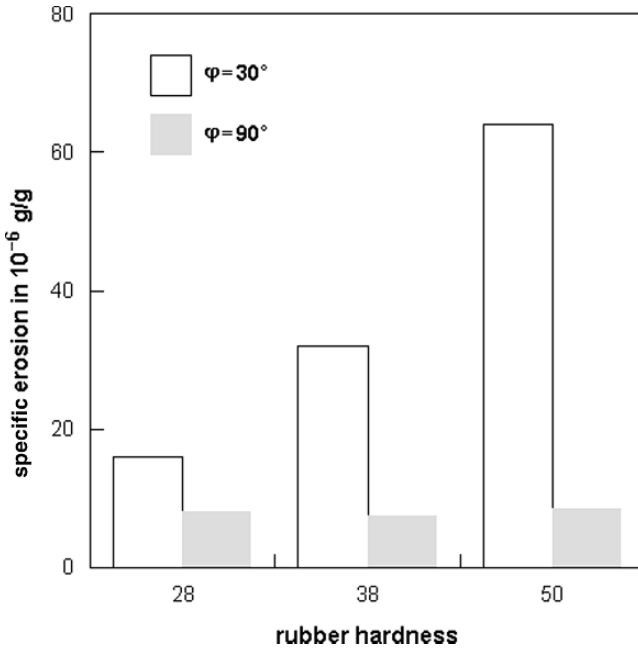


Fig. 5.44 Relationships between target hardness, impact angle and specific erosion of rubber materials (Arnold and Hutchings, 1993)

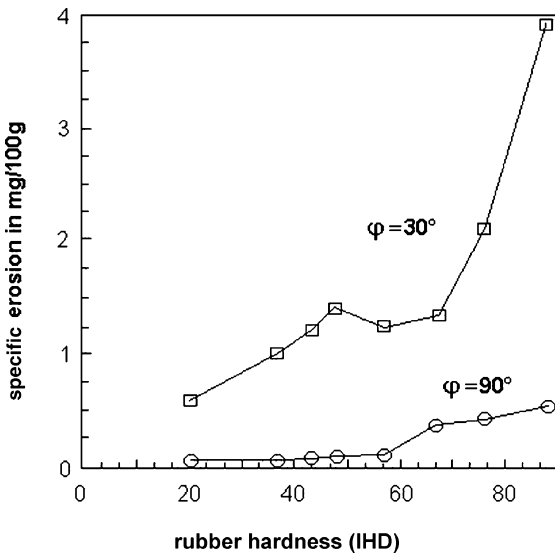


Fig. 5.45 Relationship between target hardness (ASTM D1415) and specific erosion in rubber for almost equal values for rebound resilience (Li and Hutchings, 1990)

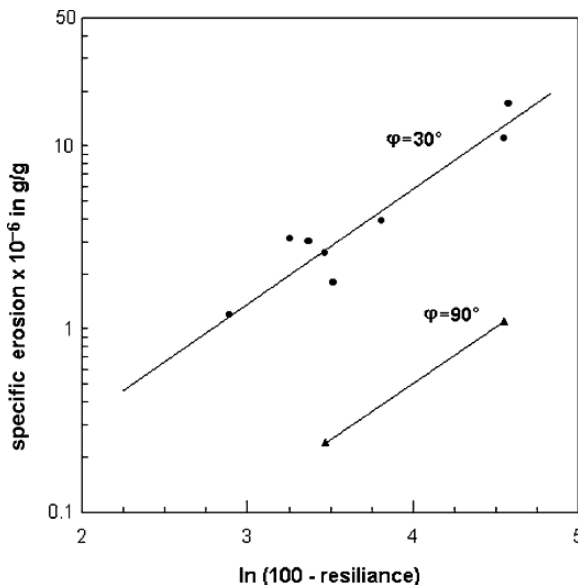


Fig. 5.46 Relationship between rebound resilience and specific erosion of unfilled elastomers (Hutchings et al., 1987)

7.9. Results of erosion tests delivered values between 1.8 and 3.2 for normal impact angles, and values between 2.1 and 4.4 for shallow impact angles (Arnold and Hutchings, 1993).

Figure 5.46 shows the effect of the rebound resilience on the erosion resistance of unfilled elastomers. The quantity “100 – resilience” represents the fraction of the initial energy of the impinging particles which is absorbed by the target material. An inverse relationship can be found in Fig. 5.46 for shallow as well as for perpendicular impact. At constant rebound resilience, a low material hardness correlated with a high erosion resistance for a range of polyurethane elastomers (Li and Hutchings, 1990).

Tensile strength is not a measure of erosion resistance; rubbers with quite different values for tensile strength exhibited similar erosion behaviour. Glass transition temperature also did not show any unique relationship to the erosion resistance of rubbers (Hutchings et al., 1987)

5.8 Erosion of Organic Coatings

5.8.1 Material Removal Mechanisms

Generally, elastic and elastic-plastic response mechanisms may act during coating erosion. The transitions between these two groups depend, among others, on temperature, strain rate and coating thickness. A transition coating thickness can, for

example, be assumed for organic coatings. Elastic response (brittle fracture) can be expected in the coating material when the coating thickness is rather large, and when the coating thickness is much larger than the size of the plastic zone around an inherent flaw. This was shown by Moore (2001) for epoxy coatings.

Microscopic inspections of impact sites in epoxy-based organic coatings revealed a large variety of crater topologies. If adhesion strength between substrate and coating was lower than the cohesion strength of the bulk coating material, the damaged surfaces were always several times larger than the area of impact. This phenomenon is described in Sect. 5.5. In organic coating materials, wedge-like craters could be observed, but also lip formation at crater edges (Fokke, 1999). Subsequent impacts near such lips removed more paint material than it would on an undamaged layer. Thus, a simple assumption that each abrasive particle removes a certain amount of paint independently from each other cannot be made. Basically, for rather young epoxy-based organic coatings, a ductile material removal regime with a maximum erosion at an impact angle of $\varphi = 40^\circ$ could be observed (Fokke, 1999). Trezona and Hutchings (2001) measured the size of damage areas in organic coatings formed due to quartz particle impact ($v_p = 58$ m/s), and identified sizes between 15 and 35 μm in diameter. These values were one order of magnitude smaller than the diameters of the corresponding quartz particles ($d_p = 125\text{--}150$ μm). Tangestanian et al. (2001) performed surface profilometry on thin organic coatings impinged by steel spheres at rather low velocities ($v_p = 30\text{--}35$ m/s), and they found that the impact caused extrusion of the plastically deformed coating into raised edges around the crater.

For enamel coatings as used for pipeline corrosion protection, spalling was identified as the important mechanism during free abrasive wear (Tong et al., 1998). During sliding of abrasive particles against the surface of the coating, circular microcracks were formed under a tangential stress which then propagated on the surface and into the surface layer. Eventually, hemispherical pits were formed. The surfaces inside the pits were rough, which shows that the cracks propagated irregularly into the subsurface layer. Examples are shown in Fig. 5.47. This particular mechanism occurred in coatings with rather low impact toughness (e.g. 2,400 Jm²).

Luo et al. (2001) proposed a selective material removal mode for the erosion of fusion-bonded epoxy powder coatings, which consist of a soft epoxy resin and a hard filler material. For rather small abrasive particles with low kinetic energies, the mass loss of the coating was determined mainly by the response of the matrix which had a rather low erosion resistance. The matrix was removed, and the filler particles were exposed. If impinged at shallow angles, the filler particle shielded the matrix from direct impacts. For larger abrasive particles with higher kinetic energies, the filler material was destroyed, and the entire material removal was accelerated.

Breinsberger and Koppelman (1982) performed experiments with impinging steel spheres and cones on organic coating systems. For low impact velocities, they could observe permanent depressions in the coating film only. If, however, a certain threshold velocity was exceeded, crack formation started. Values for this threshold velocity are plotted in Fig. 5.48 for different coating types. It was rather low for the cone-shaped erodent. Ball size did not seem to have a major effect on the threshold velocity. For normal temperatures (0–50°C), the threshold velocity increased if temperature rose,

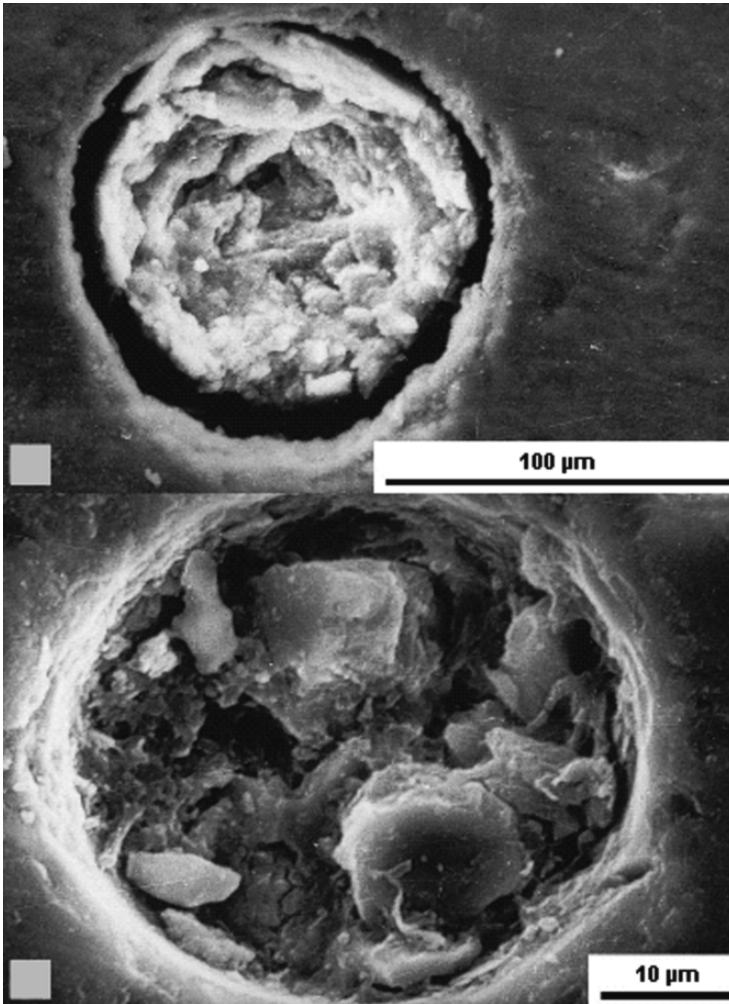


Fig. 5.47 Erosion pits in enamel coatings (Tong et al., 1998)

when steel balls were used. For the cone-shape erodent, the situation was more complex. If the velocity was further increased, the complete coating film was penetrated and the erodents reached the steel substrate surface. If this second threshold velocity was exceeded, any further increase did not lead to a notable rise in the damaged area because the substrate materials absorbed the additional kinetic energy of the erodent.

5.8.2 Erosion Resistance

Relationships to the abrasion resistance of organic automotive clearcoats were tested by Trezona et al. (1997). An example is illustrated in Fig. 5.49. It is clear that

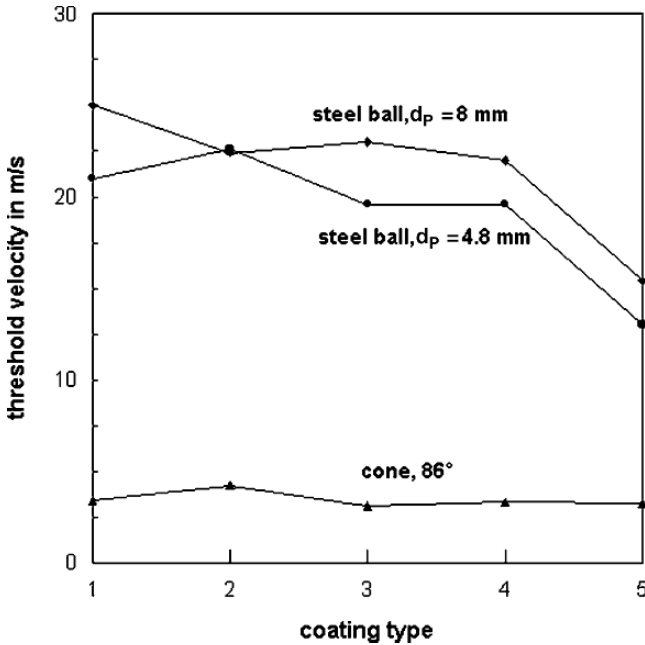


Fig. 5.48 Critical particle impact velocity for crack onset in organic coatings as a function of particle geometry (Breinsberger and Koppelman, 1982). Notations 1–5: different filler types; coating thickness: DFT = 72–80 μm

although there was a general trend for coatings with higher tensile failure energy to be more durable, there was some scatter especially in the range of moderate energy values.

The energy for failure was taken by Rutherford et al. (1997) as a measure of the resistance of organic coatings against the erosion by solid particle impact. Typical values for the energy for failure are listed in Table 5.6. Results of measurements shown in Fig. 5.50a depict a power relationship. The effect of the failure energy became less pronounced if the energy value increased, and the effect of changes in failure energy was most important for low energy values. The effect of elastic strain energy [see (5.2)], which is a frequently utilised parameter for the assessment of erosion resistance of metals (Bitter, 1963; Kriegel, 1968), on the erosion resistance is shown in Fig. 5.50b. Although there was some trend between both parameters, no valid statement could be made for higher strain energy density values. The Ratner–Lancaster parameter, which is frequently utilised to describe the mechanical response of polymers, is plotted against erosion resistance in Fig. 5.50c. There was a unique negative trend between the two parameters with a good reliability:

$$R_E \propto \frac{1}{\sigma_f \cdot \epsilon_Y} \quad (5.54)$$

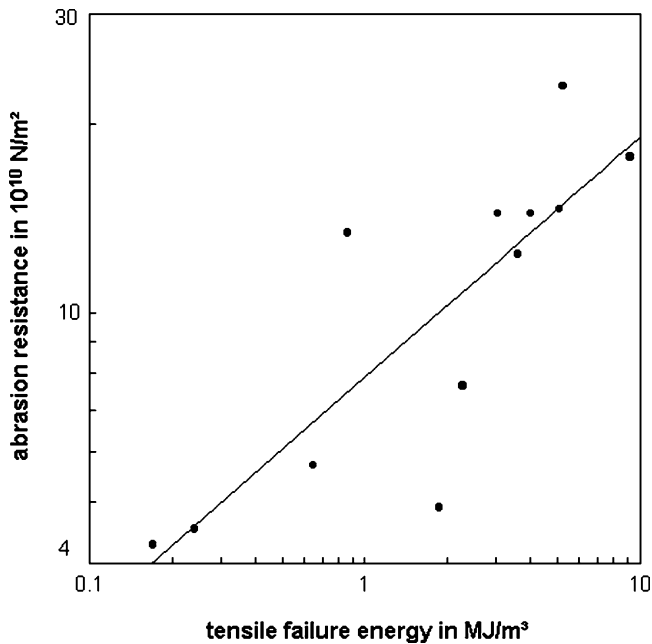


Fig. 5.49 Relationship between tensile failure energy and abrasion resistance of organic paint films (Trezona et al., 1997)

Work on weathered organic coatings indicated a negative correlation between erosion resistance and hardness for automobile clearcoats (Trezona et al., 2000b).

The erosion resistance of organic coating systems was, as experimental results in the temperature range between $\vartheta = 30$ and 65°C (Trezona et al., 2000a) suggested, better at higher temperatures. This is a surprising result because organic coatings are significantly softer at higher temperatures and should absorb more of the energy delivered by the impinging abrasive particles.

Kotnarowska (2003) found a pronounced relationship between erosion intensity (given in $\mu\text{m}/\text{kg}$ in her paper) and the dry film thickness of three-layer epoxy coatings. Results are displayed in Fig. 5.51. Erosion resistance basically increased at high film thickness values. For coatings, reinforced with glass micro-spheres, however, erosion resistance had a maximum at moderate values for film thickness (DFT = $120\text{--}160\mu\text{m}$) and started to increase for very high film thicknesses. Ramamurthy et al. (1994) referred to effects of water saturation of organic coatings subjected to stone impact. They identified a plastification effect of water in coatings, with a dry coating exhibiting larger damage when compared to one saturated with water vapour.

Luo et al. (2003) investigated the effects of filler materials in fusion-bonded epoxy powder coatings on the resistance against slurry erosion. The authors found that the erosion rate decreased if the content and the size of the filler particles increased. The erosion rate notably decreased with an increase in the fracture

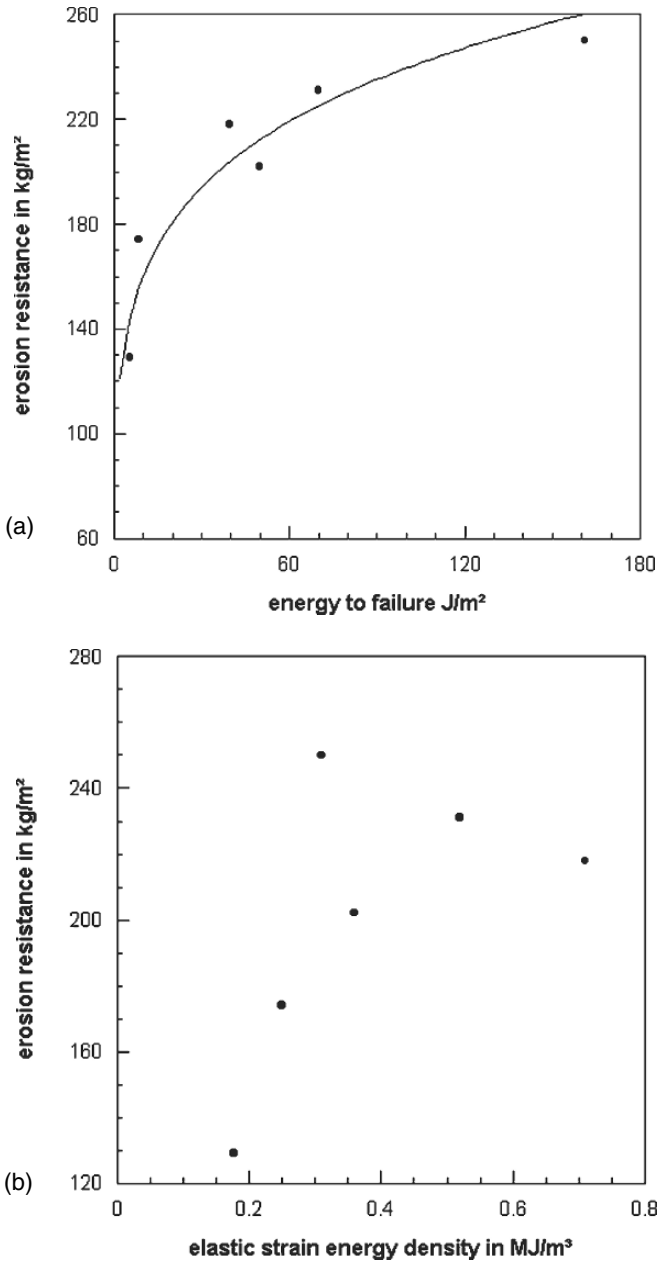


Fig. 5.50 Mechanical material property effects on erosion resistance of polymeric paint films (Rutherford et al., 1997). (a) Energy for failure; (b) Elastic strain energy density; (c) Ratner-Lancaster parameter

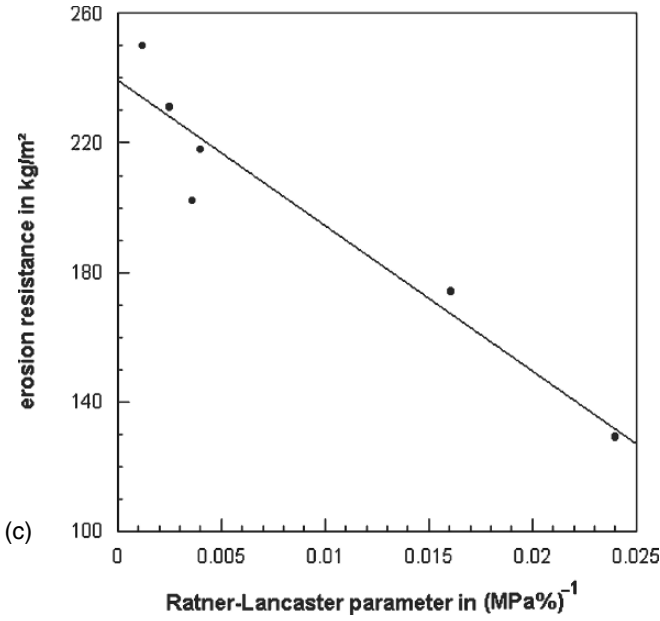


Fig. 5.50 Continued

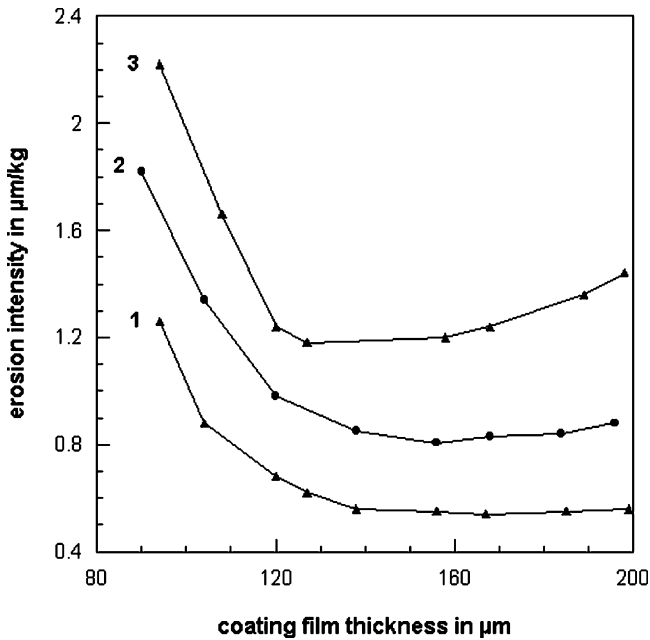


Fig. 5.51 Dry film thickness effects on erosion intensity of organic coatings (Kotnarowska, 2003). 1 – three-layer epoxy coating with composite interlayer; 2 – three-layer epoxy coating; 3 – three-layer epoxy coating modified with glass micro-spheres

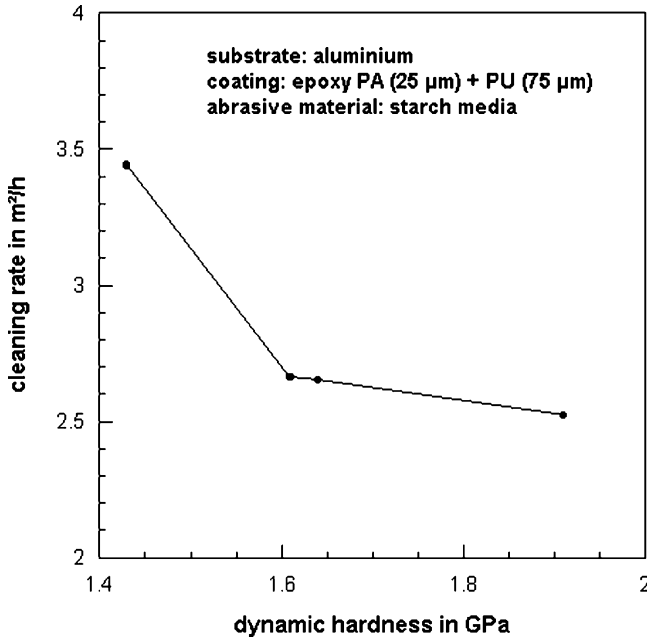


Fig. 5.52 Effect of dynamic hardness on the cleaning rate for an organic coating system (Tangestanian et al., 2001)

toughness of the filler materials. Zorll (1976) could show that the addition of talcum to organic coatings increased the resistance to particle impact.

Branco et al. (2004) performed erosion tests on sprayed ceramic coatings, and they found a significant effect of the porosity on the relative volume loss. The relative volume loss of the coatings increased with high porosity, and this particular result is very important for a sprayed ceramic or metal coating.

Figure 5.52 shows the effect of the dynamic hardness [see (5.4)] of an organic coating system on the cleaning rate. An increase in dynamic hardness notably decreased the cleaning efficiency. The values for the dynamic hardness are listed in Table 5.10.

Fokke (1999) introduced the inverse specific erosion energy with the unit (m^2/J), which could be interpreted as a coating resistance parameter. For epoxy-based organic coatings, values were between 1×10^{-5} and 3×10^{-5} m^2/J , whereas the lower value applied to high impact angles.

5.8.3 Erosion Durability

Rutherford et al. (1997) introduced the parameter *erosion durability* for the resistance of organic coatings to abrasive and erosive wear. This parameter expresses the critical abrasive mass per unit area just required for complete coating removal:

Table 5.17 Values for the erosion durability of organic coatings (Trezona and Hutchings, 2001)

Coating composition	Coating thickness in μm	Erosion durability in kg/m^2	Specific erosion resistance in $\text{kg}/\text{m}^2/\mu\text{m}$
Flexible acrylic/melamine clearcoat	48	260	5.4
	36	130	3.6
Two-component urethane clearcoat	41	240	5.8
	44	205	4.7
Rigid acrylic/melamine clearcoat	37	60	2.0
	35	50	1.4

$$Q_C = \frac{\beta_P^2 \cdot m_P}{2 \cdot \pi \cdot x^2} \cdot \exp\left(-\frac{\beta_P \cdot r_i}{x}\right) \quad (5.55)$$

Its physical unit is kg/m^2 . The parameter r_i is the radius of a scar generated at the impinging surface. Typical values for different paint systems are listed in Table 5.17. It was shown that the erosion durability depended on the deformation behaviour of the substrate material. The erosion durability of clear coats, for example, was higher for flexible (polymeric) substrates compared to rigid (steel) substrates (Rutherford et al., 1997; Trezona and Hutchings, 2001). This could be attributed to the much greater elastic modulus of steel which had a significant effect on the magnitude of the forces generated during particle impingement. The effects of other parameters, namely particle velocity, angle of impingement, temperature and particle size, on the erosion durability were investigated by Trezona et al. (2000a). The erosion durability was directly proportional to coating thickness. Therefore, a *specific erosion resistance* may be a more suitable measure of the resistance of coatings to particle impingement. This parameter is defined as follows:

$$Q_t = \frac{Q_C}{h_C} \quad (5.56)$$

The physical unit of this parameter is $\text{kg}/(\text{m}^2 \mu\text{m})$. Typical values for the specific erosion resistance are listed in Table 5.17. Based on accurate profile measurements and SEM inspections, Trezona and Hutchings (2001) found that a *critical coating thickness* existed for typical coating materials; if this coating thickness was reached, any individual particle impact led to the total detachment of the remaining coating material from the substrate.

5.9 Debonding of Organic Coatings

5.9.1 Indentation Debonding

The situation of the gradual penetration of an indenter pressed against a thin polymer film adhered to a metal substrate is illustrated in Fig. 5.53. At first, the indenter contacts the coating only. As the force increases, the indenter penetrates to the metal

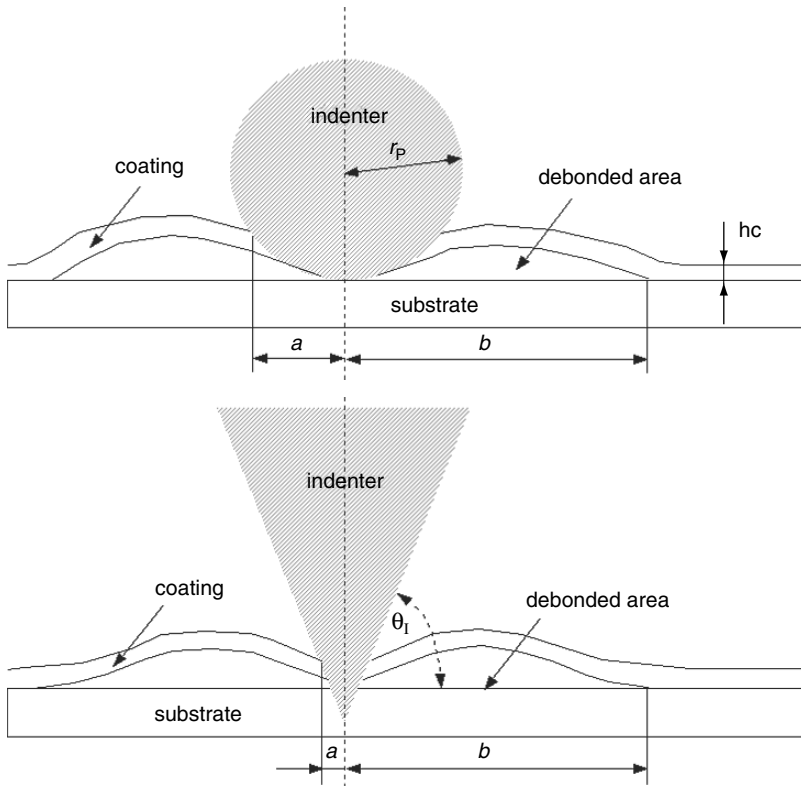


Fig. 5.53 Debonding of a polymer layer from a metal substrate (adapted from Engel and Pedroza, 1983). (a) Blunt (spherical) indenter; (b) Sharp (conical) indenter

level. A large normal compressive stress is exerted through the polymer film, which is dragged into the contact zone.

Ritter and Rosenfeld (1990) distinguished three basic types of debonding, shown schematically in Fig. 5.54. Type “I” occurs when the deformations in the coating remain elastic up to debonding. In type “II”, the coating deformations underneath the indenter are predominantly plastic at debonding, but the substrate is not penetrated. Type “III” occurs when the indenter has penetrated the coating before debonding occurs, so that part of the indentation load is supported directly by the substrate. The failure type for a given system coating/substrate will depend on the properties of the coating, coating thickness, adhesion strength and indenter geometry. Blunt indenters and thick, poorly adhering coatings favour type “I”; whereas sharp indenters and thin, well-adhering coatings favour the types “II” and “III” (Ritter and Rosenfeld, 1990).

Plastic deformations of the substrate metal tend to cause pile-up around the rim of the crater, and further out along the surface a tensile load between film and substrate arises. Separation between coating and steel substrate occurs for the following condition:

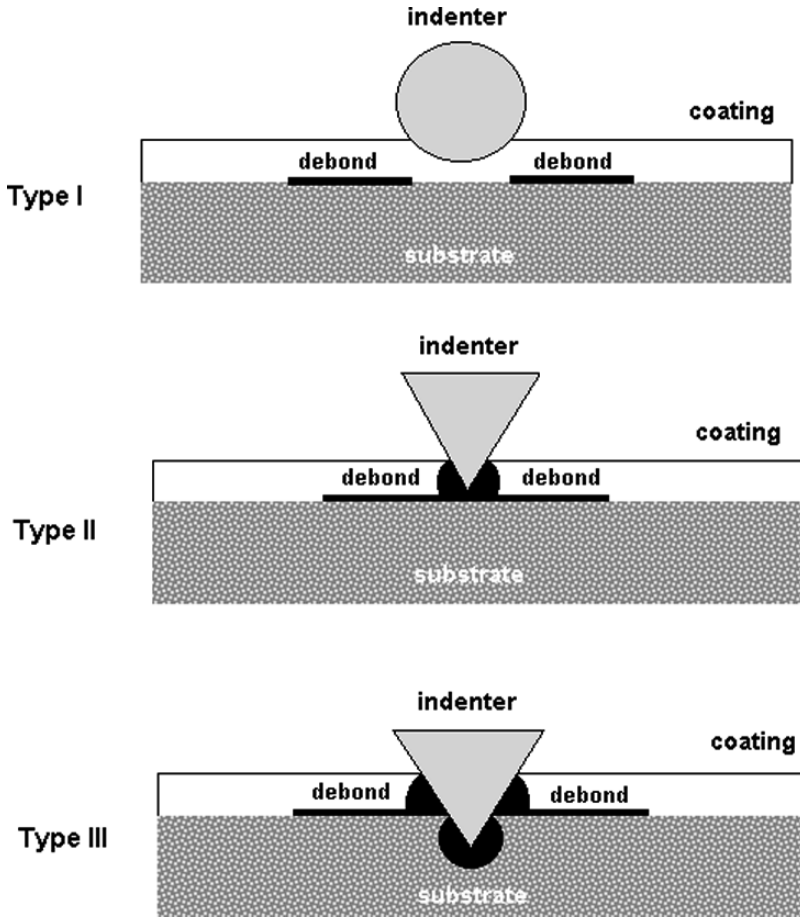


Fig. 5.54 Schematic diagram of three possible types of debonding (adapted from Ritter and Rosenfeld, 1990)

$$\sigma_T > \sigma_B \tag{5.57}$$

The polymer film departed from the substrate along the rim of the indented crater, but it rejoined the substrate beyond an annulus of debonded space, where the tensile stress was insufficient to prevent anchorage. For very sharp indenters, a hole on the bottom of the indentation could be observed frequently (Engel and Pedroza, 1983). Indentation radius (“a” in Fig. 5.53) as well as debonding radius (“b” in Fig. 5.53) had almost linear relationships to the indentation force in the range between 2 and 27 N. Examples are shown in Fig. 5.55. Engel (1985) considered the debonded circular annulus of a polymer coating to be a thin plate which is bent by the applied load. Based on this approach, he derived a maximum radial bending strain. This parameter is denoted as “peel strain”, and it is defined as follows:

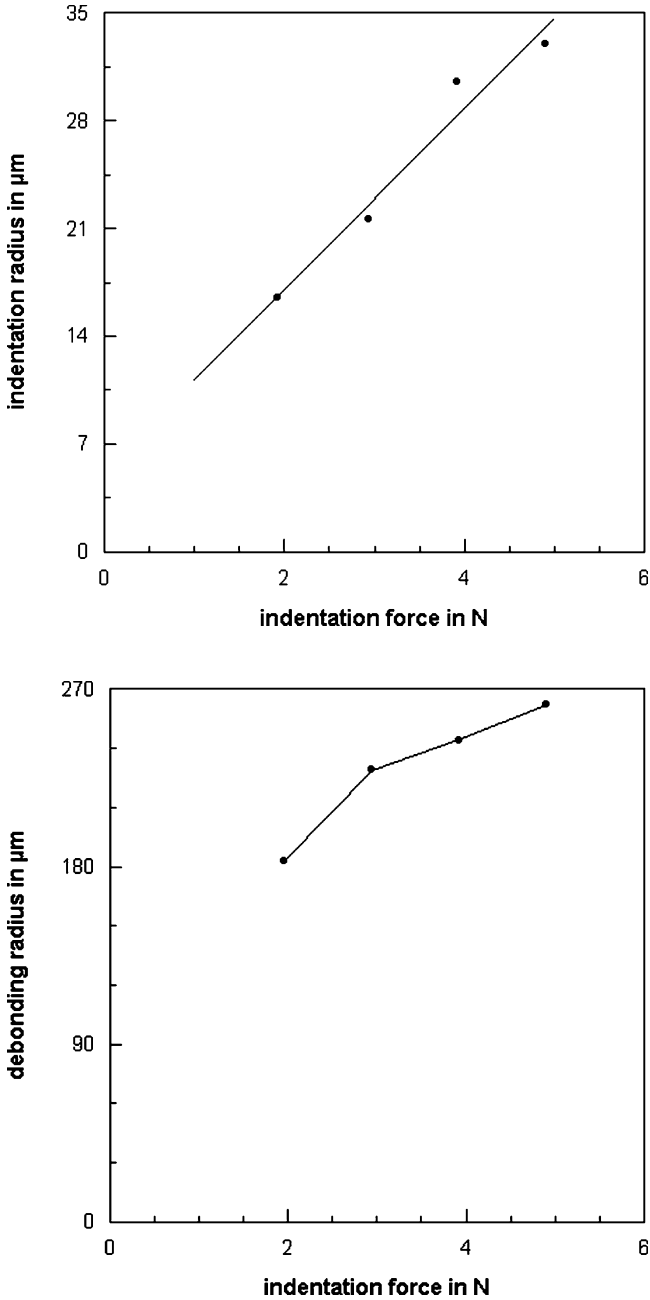


Fig. 5.55 Relationship between indentation force and debonding parameters (results from Engel and Pedroza, 1983). (a) Indentation radius; (b) Debonding radius

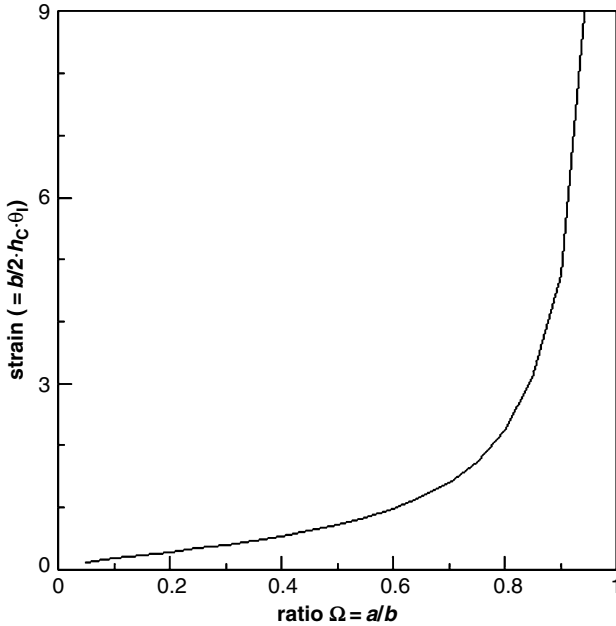


Fig. 5.56 Graphical illustration of (5.59)

$$\epsilon_0 = \frac{2 \cdot \theta_1 \cdot h_c}{b} \cdot \frac{\Omega^2 - [1 + (1 + \Omega^2) \cdot \ln \Omega]}{(2 \cdot \Omega \cdot \ln \Omega)^2 - (1 - \Omega^2)^2} \cdot \Omega \quad (5.58)$$

$$\Omega = \frac{a}{b}$$

The parameters a , b and θ_1 are defined in Fig. 5.53. The peel strain sets the limit of adhesion between a specific combination of substrate and bonded polymer layer. Equation (5.58) is graphically illustrated in Fig. 5.56 For conical indenters with cone angles between $\theta_1 = 14.4^\circ$ and 51° , peel strain was inversely proportional to the indentation force; values for the peel strain were between $\epsilon_0 = 3\%$ and 7% (Engel and Pedroza, 1983).

5.9.2 Impact Debonding

Impact testing of organic coatings is an event very similar to the erosion of a coating by an impinging abrasive particle. The results of such tests can deliver important information about fundamental mechanisms of coating erosion and debonding. Zosel (1977) and Zorll (1975a) inspected impact marks, formed during impact tests, and noted ring cracks and radial cracks accompanied by wall formation (buckling) around the impact centre. Wall formation (buckling) in organic coatings impinged with a steel ball was proven by Zorll (1975a) due to interference microscopic

images. Two examples of such images, illustrating wall formation, are shown in Fig. 5.57. Figure 5.57a illustrates the formation of a single wall in a coating impinged at a low impact velocity. The image shown in Fig. 5.57b is indicative of the formation of multiple walls in a coating impinged at a higher impact velocity. The entire damage area exceeded the contact area by a factor between 100 and 200. These results pointed to the formation and propagation of stress waves in the material. Zorll (1975b) found that only a fraction of the kinetic energy of a steel ball, impinging at low velocity, was dissipated due to the formation of the permanent depression and the wall. The majority of the energy was being distributed in more remote coating locations as well as in the substrate material, but was also absorbed due to elastic rebound. Table 5.18 summarises some results. For higher impact velocities (e.g. $v_p = 50$ m/s), multiple wall formation (buckling) and first cracks could be observed. A similar transition behaviour of coatings was also detected by Breinsberger and Koppelman (1982). Zorll (1975a) found finely ground paint particles (size about $3\ \mu\text{m}$) under the central damage area and concluded that compressive stresses in the range of 850 MPa were responsible for this special feature. Shear stresses, formed at the interface between coating and substrate, were responsible for coating debonding. Zorll (1983) investigated the effects of substrate topography on the failure mode of coating systems (DFT between 50 and $80\ \mu\text{m}$) subjected to impinging steel spheres, and he found that deep, angled profiles promoted cohesive failure; whereas smooth profiles promoted adhesive failure. Therefore, substrate topography may be considered for the modelling of coating removal processes.

It was observed by Zorll (1976) for two-layer coating systems, that the addition of platelet-shaped talcum to the coating reduced the deformation of organic coatings as well as the probability of debonding at higher impact velocities. These results pointed to a reinforcement effect of the talcum platelets. The above-mentioned transition stage between wall formation and cracking did not exist for talcum pigmented coatings, whereas it was registered for iron oxide pigmented coatings. The hardness and pigmentation of the primer determined the response of the entire coating system against impact loading.

Ladstädter (1984) subjected multiple-layered coating systems to high-speed steel bullets and deduced so-called *damage functions*. An example for a damage function is shown in Fig. 5.58. Surprisingly, the author found a reduction in the damaged area for moderate bullet velocities, and he called this effect *softening-effect*. Part of the energy of the impinging particles was dissipated into heat, and it rose coating temperature. A steel ball with a weight of $m_p = 0.5$ g and a velocity of about $v_p = 30$ m/s may rise the temperature in a deformed coating mass of $m_c = 0.2$ mg by a value of 200 K. Mechanical properties of organic materials depend on temperature. Young's modulus of organic coating materials (primer, filler material and top coat), for example, notably decreased if temperature increased (Ladstädter, 1984). For many organic coatings, an increase in 30 K was sufficient to transform the material in the glass-transition stage – the material responded with plastic deformation and could dissipate more energy prior to failure. This aspect is illustrated in Fig. 5.58 for the higher impact velocity. Zosel (1977) could show that complete separation between paint coating and substrate due to delamination occurred only if a certain threshold impact velocity was exceeded.

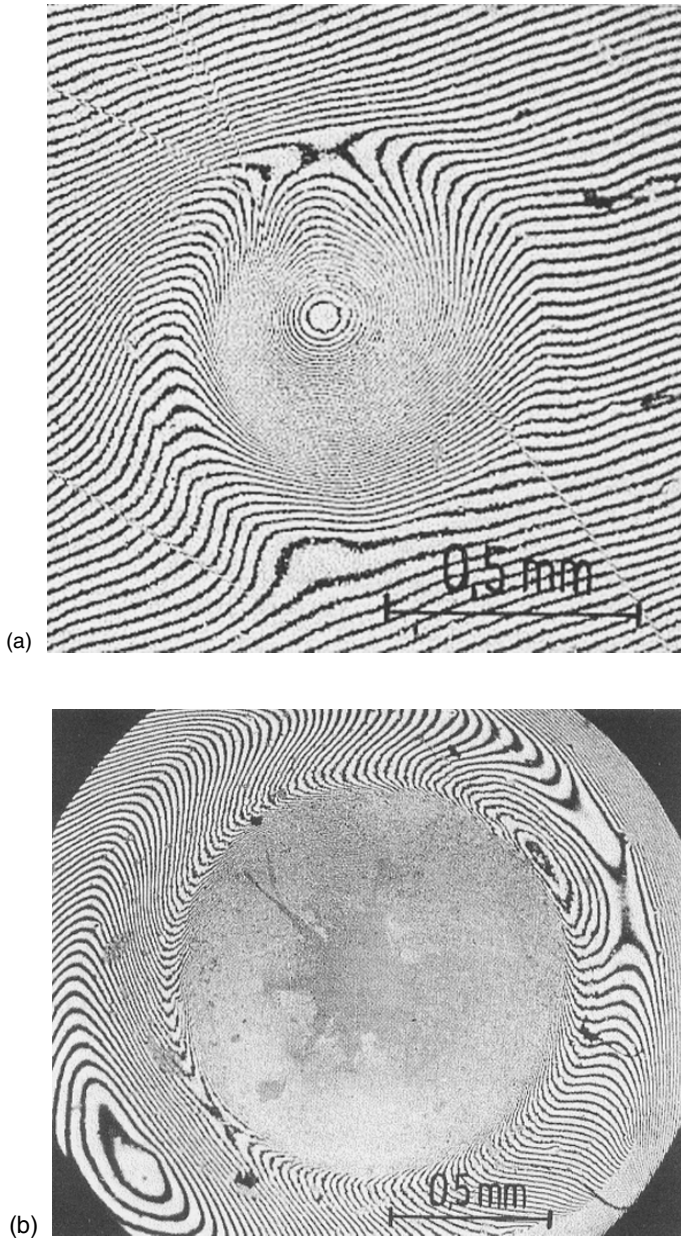


Fig. 5.57 Interference microscopic images of organic coatings (polyurethane, DFT = 100 μm) after steel ball impingement ($d_p = 3.5$ mm); images: Zorll (1975a). (a) Lower impingement velocity ($v_p = 20$ m/s), formation of a single wall; (b) Higher impingement velocity ($v_p = 50$ m/s); formation of multiple walls

Table 5.18 Typical parameters of an impact test for an organic coating (values from Zorll, 1975b); see also Fig. 5.57

Parameter	Value
Ball diameter	3.5 mm
Impact velocity	20 m/s
Ball weight	0.17 g
Kinetic energy ball	34 mJ
Deformed volume (wall)	$5.7 \times 10^{-4} \text{ mm}^3$
Deformed volume (depression)	$18.1 \times 10^{-4} \text{ mm}^3$
Energy absorbed due to deformation	$3 \times 10^{-3} \text{ mJ}$

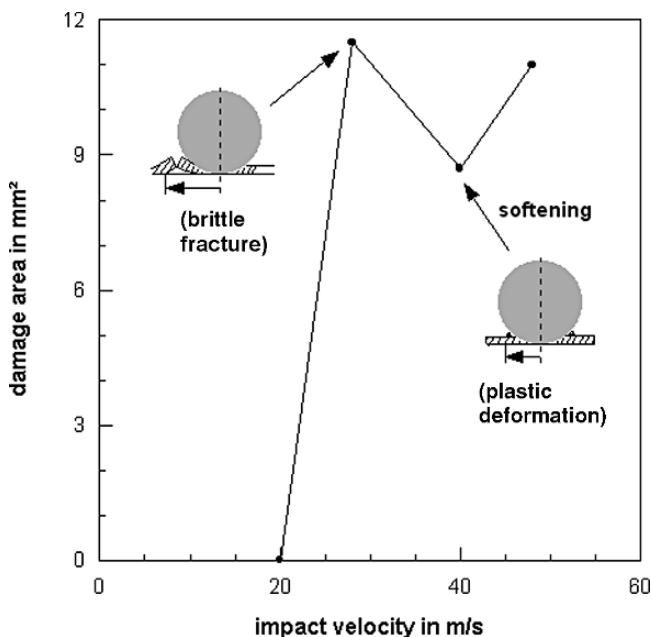


Fig. 5.58 “Damage function” according to Ladstädter (1984)

The value of this critical velocity was dependent of the temperature. It was notable lower for lower temperatures ($\vartheta = -20^\circ\text{C}$ compared with $\vartheta = 23^\circ\text{C}$).

5.10 Coating Removal Models

5.10.1 Ploughing/Delamination Model

A series of papers by Papini and Spelt (1997, 1998a, b) provided some detailed insight in the removal of organic coatings from steel substrate due to spherical abrasive particle impingement. The authors distinguished between ploughing erosion of the bulk coating and coating delamination.

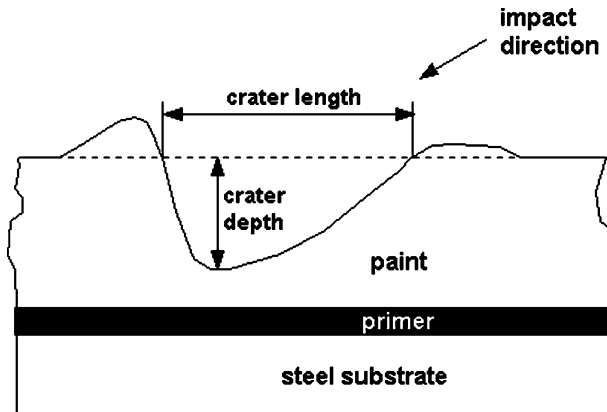


Fig. 5.59 Geometrical situation of ploughing erosion (Papini and Spelt, 1998)

Ploughing erosion occurred at non-rectangular impact. The geometrical situation is illustrated in Fig. 5.59 (see also Fig. 5.21b). At the edge of the impact appeared a certain amount of plastically deformed coating material, which is being knocked off by subsequently impinging particles. The authors modelled this material removal process with an elastic–plastic model, and they obtained good results for crater length, crater depth and rebound parameters (Papini and Spelt, 1998a).

The initiation of the delamination of alkyd paint from steel occurred at a critical shear stress independently on coating thickness. A typical value for an alkyd coating, eroded with impinging glass and steel spheres, was about $\tau_M = 100$ MPa (Papini and Spelt, 1998b). The delamination itself was dominated by a mixed-mode interfacial crack, induced by the buckling of the coating. This situation corresponded to that illustrated in Fig. 5.53a. If the abrasive bead started to penetrate the substrate, coating delamination started, and the coating was going to be removed. A critical impact velocity was needed for this process. For thin coatings (DFT = 20–50 μm), critical velocities were between $v_P = 20$ and 40 m/s (glass beads and steel spheres). Values for critical particle kinetic energies are plotted in Fig. 5.60. It can be seen that the critical particle energy increased linearly with an increase in coating thickness, irrespective of the abrasive type. A range of normal kinetic energies was found where the coating was removed without damaging the steel substrate (Papini and Spelt, 1997). It was also found that coating delamination due to impinging particles had maximum values at normal impact angles ($v_P = 55$ –108 m/s).

5.10.2 Debonding Model

Zouari and Touratier (2000, 2001, 2002) provided a detailed investigation in the removal of a polyurethane coating from an aluminium substrate through impinging spherical particles. They identified the three following failure mechanisms:

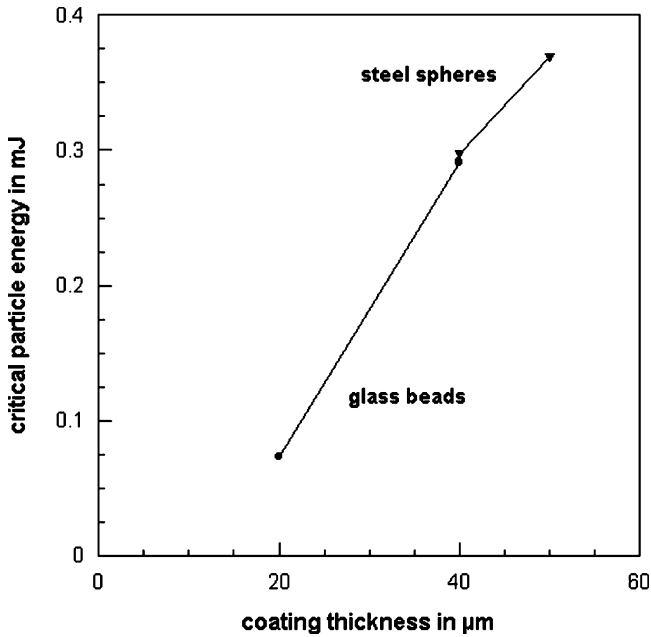


Fig. 5.60 Critical kinetic particle energies for coating delamination (Papini and Spelt, 1998b)

- initiation of delamination due to shear stresses at the interface;
- buckling of the paint film due to compressive stresses originating from particle penetration into the coating;
- delamination of the coating caused by the buckling of the coating film.

This is essentially the mechanism suggested in Sec. 5.10.1. Zouari and Touratier (2002) used a finite element code to numerically model the removal process. Among others, they found that the substrate consumed a high amount of the kinetic energy supplied by the impinging rigid particle (aluminium oxide spheres). The debonding failure criterion assumed by the authors reads as follows:

$$\left(\frac{\sigma_N}{\sigma_{NF}}\right)^2 + \left(\frac{\tau_N}{\tau_M}\right)^2 \leq 1 \quad (5.59)$$

Debonding is assumed to occur if the left-hand side of the equation is greater than unity. The coating resistance parameters can be evaluated from pull-off test results; typical values were $\sigma_{NF} = 50$ MPa and $\tau_M = 200$ MPa (Zouari and Touratier, 2002). Graphical expressions of the results of the numerical simulations can be found in Zouari and Touratier (2002) paper. The authors found that buckling and coating delamination occurred outside the contact area particle-coating, and they estimated the limits for paint buckling and coating delamination.

5.10.3 Effects of a Second Phase in the Coating

Luo et al. (2001) considered the effect of hard fillers in a soft matrix, as found in powder coatings, on the erosion resistance. They developed a simple model for the assessment of the mass loss of a coating subjected to slurry flow. The model reads as follows:

$$\frac{1}{m_C} = \frac{1 - F_f}{m_{\text{matrix}}} + \frac{F_f}{m_{\text{filler}}} \quad (5.60)$$

Here, m_{matrix} is the mass loss of the matrix material, m_{filler} is the mass loss of the filler material, F_f is the volume fraction of the filler and the quantity “ $1 - F_f$ ” is the volume fraction of the matrix.

Chapter 6

Surface Preparation Process

6.1 Definition of Process and Target Parameters

6.1.1 Process Parameters

Blast cleaning can be considered to be an erosion process. Erosion is a tribological term, and it can be discussed based on a tribological system. The tribological system for solid particle erosion is schematically shown in Fig. 6.1. The tribological system features the loading collective, the wear parameters and the bodies involved in the process. The loading collective characterises the *process parameters*.

The blast cleaning process is characterised by numerous process parameters that determine efficiency, economy and quality of the whole process. Therefore, optimisation of the process is a primary requirement for a successful application. Generally, the process parameters in blast cleaning divide as listed below (see also Fig. 6.2).

(1) Pneumatic parameters:

- air (nozzle) pressure, p ;
- nozzle diameter, d_N ;

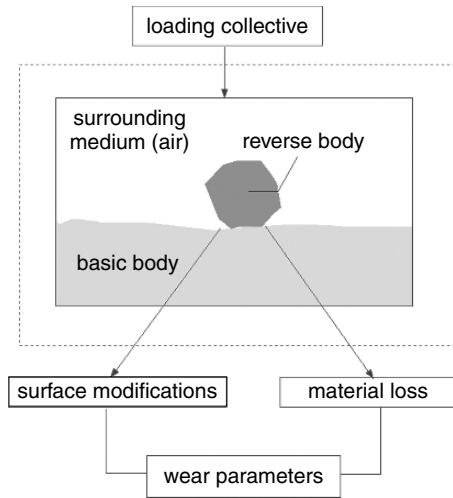
(2) Process parameters:

- stand-off distance, x ;
- impact angle, φ ;
- exposure time, t_E ;
- number of passes, n_S ;

(3) Abrasive parameters

- abrasive mass flow rate, \dot{m}_P ;
- abrasive particle diameter, d_P ;
- abrasive particle size distribution, $f(d_P)$;
- abrasive particle shape;
- abrasive particle hardness, H_P ;
- abrasive recycling capacity.

Fig. 6.1 Tribological system for blast cleaning (solid particle erosion)



6.1.2 Target Parameters

The tribological system shown in Fig 6.1 also features wear parameters, which are basically parameters describing material loss and parameters characterising surface modifications. Parameters for the description of surface modifications are discussed in Chap. 7.12.2. Material loss parameters are denoted *target parameters* in this chapter.

Target parameters are illustrated in Fig. 6.2. The most important target parameter in blast cleaning applications is the cleaning rate, which is given as follows:

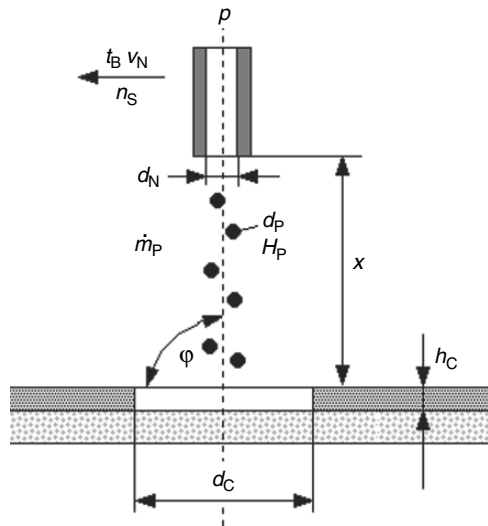


Fig. 6.2 Process parameters and target parameters of blast cleaning processes

$$\dot{A} = \frac{A_M}{t_B} \quad (6.1)$$

In that equation, A_M is the area to be blast cleaned and t_B is the total blast cleaning time. Cleaning rate is usually given in m^2/h . Following an approach of Uferer (1992), the cleaning rate can be expressed in terms of the total kinetic energy of the impinging abrasive particles:

$$\dot{A} = \frac{C_B}{2} \cdot \frac{N_P \cdot m_P}{t_B} \cdot v_P^2 \quad (6.2)$$

The constant C_B is an energy transfer parameter given in s^2/kg . If the thickness of a rust layer or, respectively, a coating system is considered, a volumetric removal rate can be defined as follows:

$$\dot{V}_M = \frac{V_M}{t_B} = \frac{A_M \cdot h_C}{t_B} \quad (6.3)$$

Here, V_M is the removed volume, and h_C is the thickness of the removed material layer. For coatings, h_C equals the dry film thickness. An alternative expression for (6.3) is as follows:

$$\dot{V}_M = A_M \cdot v_N \quad (6.4)$$

Here, v_N is the traverse rate of the nozzle. The unit of the volumetric removal rate is m^3/h .

For optimisation purposes, the consumption of consumable materials need to be considered. The specific abrasive consumption rate, for example, is given as follows:

$$m_S = \frac{\dot{m}_P}{\dot{A}} \quad (6.5)$$

The unit of this parameter is kg/m^2 . Similarly, a specific power consumption (kW/m^2) or a specific fuel consumption (l/m^2) could be defined.

6.2 Effects of Pneumatic Parameters

6.2.1 Effects of Air Pressure

Tilghman (1870), in his original patent, wrote: “*The greater the pressure of the jet the bigger will be the velocity imparted to the grains of sand, and the more rapid and powerful the cutting effect upon the solid surface.*” In most instances, increasing air pressure increases cleaning rate. A 300% increase in cleaning rate was, for example, reported for the blast cleaning of steel with copper slag if air pressure rose from

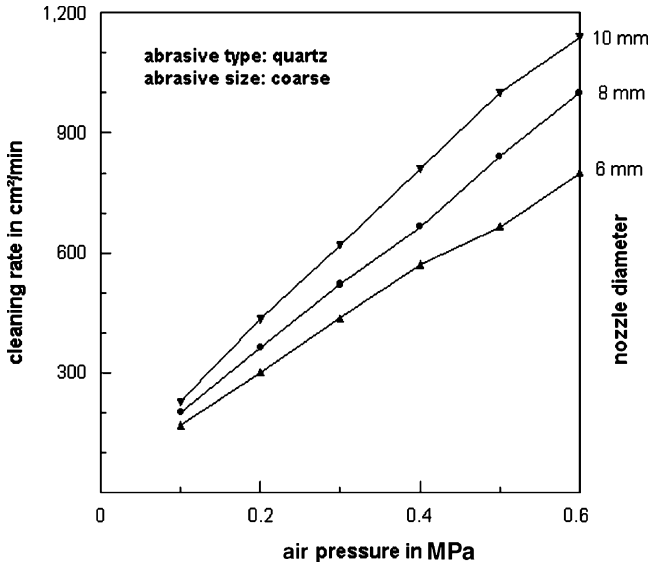


Fig. 6.3 Effects of air pressure and nozzle diameter on cleaning rate (Kalpers, 1949)

$p = 0.53$ to 0.8 MPa (Holt and Austin, 2001). Figures 6.3, 6.4 and 6.9 show general relationships between air pressure and cleaning rate. The higher the nozzle pressure, the more productive is the blast cleaning process in terms of cleaning rate. A linear relationship between air pressure and cleaning rate was also found by Kura (2003) for bar shot, by Kalpers (1949) for grit, and by Seavey (1985) for different non-metallic abrasive materials. A mathematical formulation is:

$$\dot{A} = C_1 \cdot (p - p_C) \quad (6.6)$$

The general structure of this function is the result of complex relationships between pressure and the processes of jet formation, abrasive acceleration and mixing, and material removal. For suction devices, cleaning rate rises according to a square-root relationship with increasing air pressure (Uhlmann et al., 2003). Figure 6.4 provides further insight into the effect of air pressure on cleaning rate. It can be recognised that the pressure influence depended on abrasive material. In the case of copper slag, cleaning rate even dropped at high pressure levels, an effect which can be explained through the friability of this material. At high pressures, this material is fractured in the nozzle and on the substrate surface. Such trends were reported by Gesell (1966) for quartz, copper slag and foundry slag. More information on this issue is delivered in Sect. 2.9. Although (6.6) holds for many cases, the real process can differ from a linear relationship, especially if rather hard target materials are being treated.

The first stage, $p < p_C$, characterises an *incubation stage*. In this pressure range, no material removal takes place, although the removal process is invisibly introduced in the material. The parameter p_C is a threshold value that has to be

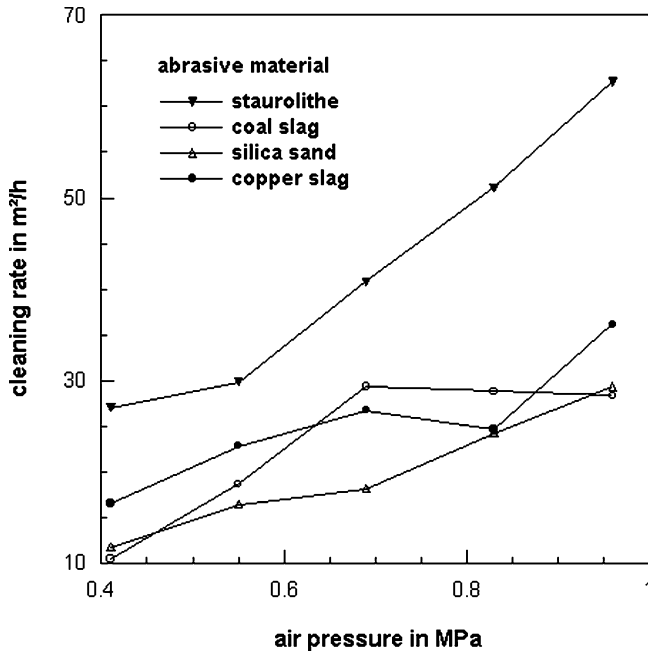


Fig. 6.4 Effects of air pressure and abrasive material on cleaning rate (Seavey, 1985)

exceeded for a measurable material removal. Results of Uferer (1992) deliver a value of $p_C = 0.05$ MPa for the removal of mill scale from steel plates with nickel slag. The threshold pressure could be interpreted as a critical particle impact velocity, which is known from impact testing of organic coatings (Breinsberger and Koppelman, 1982; Ladstädter, 1984). For elastically responding materials, say mill scale, heavy rust or brittle coatings, a threshold concept developed by Evans et al. (1978) for solid particle erosion can be applied. In this model, the threshold velocity of the particles is given by the following equation:

$$v_C \propto K_{Ic}^2 \cdot c_M^{0.33} \tag{6.7a}$$

In that equation, K_{Ic} is the fracture toughness of the target material, and c_M is the velocity of longitudinal waves in the target material. Values for the fracture toughness of some organic coating materials are listed in Table 5.11. This approach is partly verified by the experimental results presented in Fig. 6.5. For plastically responding materials, say soft coatings and most metal substrates, a rather complex model introduced by Yabuki and Matsumura (1999) can be applied. One basic result of this model is that the threshold velocity, required for micro-cutting, has a linear relationship with the material hardness:

$$v_C \propto H_M \tag{6.7b}$$

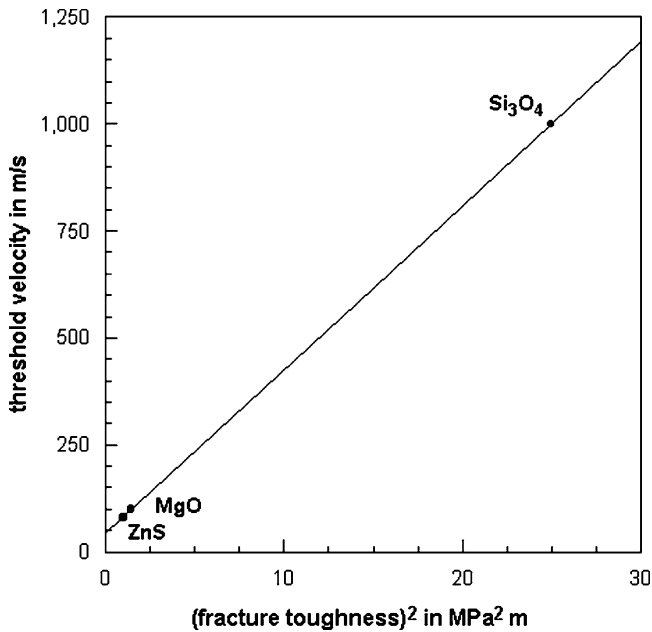


Fig. 6.5 Relationship between threshold particle impact velocity and fracture toughness for brittle target materials (Evans et al., 1978)

Hardness values for some coating materials are listed in Tables 5.1, 5.3 and 5.7–5.10. The threshold values, measured on numerous metals, were too low (between $v_C = 1$ and 3 m/s) that they do not need to be considered in practice (Yabuki et al., 1999). Luo et al. (2001) estimated threshold velocities between $v_C = 6$ and 7 m/s for the slurry erosion of fusion-bonded epoxy powder coatings. Another threshold characteristic is illustrated in Fig. 5.21b, which illustrates the situation for material detachment in a plastically deformable material. It can be seen that a critical particle impact velocity must be exceeded before material removal starts. This value is at about $v_p = 210$ m/s for the situation illustrated in Fig. 5.21b. If this velocity value is not reached, the material only deforms.

Papini and Spelt (1997) provided the idea that coating removal begins only when the coating is fully penetrated for a given coating/substrate/particle system. They derived a critical abrasive impact velocity to cause penetration of the coating to the steel substrate, and they provided a methodology for the calculation of these velocity values. The normal component of the critical penetration velocity increased with larger coating thickness, which was attributed to a relationship between coating thickness and interface shear stress. Typical values for the penetration of alkyd paint layers (DFT = 20–50 μm) were between $v_C = 20$ and 45 m/s. Later, these authors (Papini and Spelt, 1998b) introduced a critical particle energy required for the introduction of coating delamination. This relationship is illustrated in Fig. 5.60, and it can be seen that the threshold energy depended on the coating thickness.

In the second stage, $p > p_C$ – called *linear stage* – cleaning rate increases linearly with an increase in air pressure. Each increase in air pressure leads to a proportional increase in cleaning rate. The factor of proportionality C_1 depends on all the process conditions listed earlier as well as on the properties of the target material. Figure 6.3a reveals a slight effect of the nozzle diameter. For the linear coefficient C_1 exists the following rule of thumb: “For each 7 kPa increase (in pressure) there is a 1.5 percent increase in productivity.” (Drisko, 2002). However, results published by Seavey (1985) have shown that C_1 depended on the abrasive material used. Some results of this investigation are plotted in Fig. 6.4. It can be seen that the proportionality factor was rather low for quartz and coal slag, and that it was higher for copper slag and fine-grained staurolite. In some cases, cleaning rate can even drop if pressure is increased. Such phenomena were reported by Seavey (1985) for the use of coal slag. This feature is illustrated in Fig. 6.4. The reason for this behaviour could be the high degree of friability of the slag material. If the pressure, and thus the abrasive particle impact velocity, becomes too high, the slag particles start to fracture during the impact process and do not work efficiently (see Fig. 6.4). Similar is the situation if rather large abrasive particles are being used, as has been observed by Stallmann et al. (1988) for copper slag and melting chamber slag. It is, therefore, a general recommendation to select an air pressure lower than, or close to, the critical pressure for abrasive impact fragmentation. More information on this issue is provided in Sect. 2.9. Results plotted in Fig. 6.9 show that the coefficient C_1 depends also on the nozzle geometry.

Air pressure determines the velocity of the impinging abrasive particles (see Sect. 3.6.1). This fact was considered by Settles and Garg (1995) who calculated the abrasive particle velocities for the cleaning rate examples provided in Fig. 6.4. They computed the following values for the particle velocity ($p = 0.7$ MPa, $d_N = 9.5$ mm; $\dot{m}_P = 9.7$ kg/min): $v_P = 173$ m/s for the silica sand and $v_P = 210$ m/s for the staurolite. From these results, they concluded that the high productivity of the staurolite abrasive is a result of the higher abrasive particle impact velocity.

Abrasive particle velocity has the strongest influence on the erosion durability of organic coatings, if abrasive size, temperature, impact angle and abrasive particle velocity are being considered (Trezona et al., 2000a). For polymeric paint films, a power-law dependency of the erosion resistance (given in kg/m²) on the abrasive particle velocity can be expected (Rutherford et al., 1997). The following relationship can be assumed:

$$R_E \propto \frac{1}{v_P^q} \quad (6.8)$$

Here, q is a velocity exponent. By fitting experimental results obtained with multi-layer organic coating systems applied to galvanised steel substrates, this exponent was found to be $q = 3.5$ (Rutherford et al., 1997), which points to a stronger relationship as for the erosion of bulk polymers ($q = 2.5$).

Particle impact velocity affects the erosion rate according to a power law. A suitable relationship is as follows:

$$E_R \propto v_P^\phi \quad (6.9)$$

A simple model developed by Rosenberger (1939) for blast cleaning processes delivered a velocity parameter of $\phi = 2.0$.

Power exponents for brittle material removal modes are listed in Table 5.13. Power exponents for polymer coatings (for hydroabrasive erosion) are listed in Table 6.1. For rubber, the power exponent depended on the fatigue-function parameter β_F (see Sect. 5.6.4). Detailed relationships were $\phi = 2 \cdot \beta$ for normal impact angles; and $\phi = \beta_F + 1$ for oblique impact angles (Arnold and Hutchings, 1992, 1993). Slikkerveer (1999) found values between $\phi = 2.87$ and 4.0 for different elastomers, whereby the high value characterised the behaviour of the most “rubber-like” material. For polymers, power exponent values between $\phi = 1.7$ and 2.8 were found (Zhang et al., 1995); and for the slurry erosion of fusion-bonded epoxy powder coatings, power exponents between $\phi = 4.0$ and 5.5 were reported (Luo et al., 2001). A power law with $\phi > 1$ could also describe the influence of the particle velocity on the volume of removed lips during the erosion of polymers (Walley and Field, 1987). Henning and Brauer (1986) found that the power exponent depended on impact angle and abrasive diameter. For PMMA, the exponent was found to vary between $\phi = 2.7$ and 3.2, whereas the latter value was for high impact angles. For rubber, values between $\phi = 2.5$ and 5.0 were found, whereby the precise value depended on the diameter of the impinging particles. Volume loss measurements performed by Tangirala (1998) on brittle iron scale delivered a power exponent slightly larger than unity.

If the Almen intensity was being considered as the target parameter, which is a familiar procedure in shot peening applications, the relationship between shot velocity and Almen intensity was linear (Linnemann et al., 1996).

Rajesh et al. (2004) investigated the effects of impact angle and material type on the particle impact velocity effects. They eroded seven types of polyamides at impact velocities of $v_p = 80$ m/s and, respectively, $v_p = 140$ m/s, which was a velocity increase of +75%. Their results are listed in Table 6.2, and the results witnessed a notable effect of the impact angle on the percentage of increase in the erosion rates. The highest increase of +240% was found for PA11 impinged at an angle of $\varphi = 30^\circ$. For an impact angle of $\varphi = 90^\circ$, however, the increase in erosion rate due to the higher impact velocity was +79% only. For the material PA12, the gain in erosion rate was larger for the high impact angle, which was not found for the other materials.

Fokke (1999) investigated the relationships between the kinetic energy of impinging abrasive particles, the impact area and the volume removed in epoxy-based

Table 6.1 Velocity exponents for polymer coatings (Zolotar, 1973); hydroabrasive erosion, $v_p = 5\text{--}17$ m/s

Material	Velocity exponent
Epoxy	3.06
Epoxy-phenol formaldehyde resin	3.20
Methacrylate resin	3.13
Phenol formaldehyde liquid	3.10
Vulcanite	3.02
Phenol formaldehyde powder	3.40

Table 6.2 Percentage increase in erosion rate for an impact velocity increase from $v_p = 80$ m/s to $v_p = 140$ m/s (Rajesh et al., 2004). Variable impact angle

Polyamide	Increase in erosion rate in %	
	30°	90°
PA 6	180	70
PA 11	240	70
PA 12	190	60
PA 12 (L 20)	160	210
PA 66	180	130
PA 66/610	220	30
Aromatic PA	200	50

organic coatings. For the blast cleaned area as the target parameter, the following linear trend was found:

$$A_M = \varepsilon_M \cdot E_P \quad (6.10)$$

The coefficient ε_M is the inverse specific erosion energy (m^2/J), and it depends on impact angle. The inverse specific energy decreased notably if impact angle increased (Fokke, 1999). The volume of removed paint showed a power-law relationship to the impact energy:

$$V_M = 3.1 \cdot 10^{-13} \cdot E_P^{1.5} \quad (6.11)$$

Here, V_M is given in m^3 , and the particle impact energy is given in mJ. Results of measurements are presented in Fig. 6.6. The power exponent of 1.5 is right between two exponents estimated by Wood (1999) for the erosion of different metallic and ceramic coatings by a slurry flow. This author found a value of 1.17 for normal impact angles, and a value of 1.98 for an oblique ($\varphi = 30^\circ$) impact angle.

Some results from scale removal experiments (with blast wheels) are provided in Fig. 6.7. The graph shows critical energy conditions for scale removal as functions of impact velocity, abrasive diameter and particle kinetic energy. This graph very well supports the threshold conception mentioned earlier. The removal of the mill scale becomes possible only if a certain impact velocity is exceeded for a given abrasive size. The effect of the impact velocity was pronounced in the range of small abrasive particles. Although these results were obtained with a wheel blast machine, the basic idea will work the same way for air blast machines.

6.2.2 Effects of Nozzle Diameter and Nozzle Length

Figure 6.8 shows typical relationships between cleaning rate and nozzle diameter for two air pressure levels. The cleaning rate almost linearly increases with an increase in the nozzle diameter. A simple expression is:

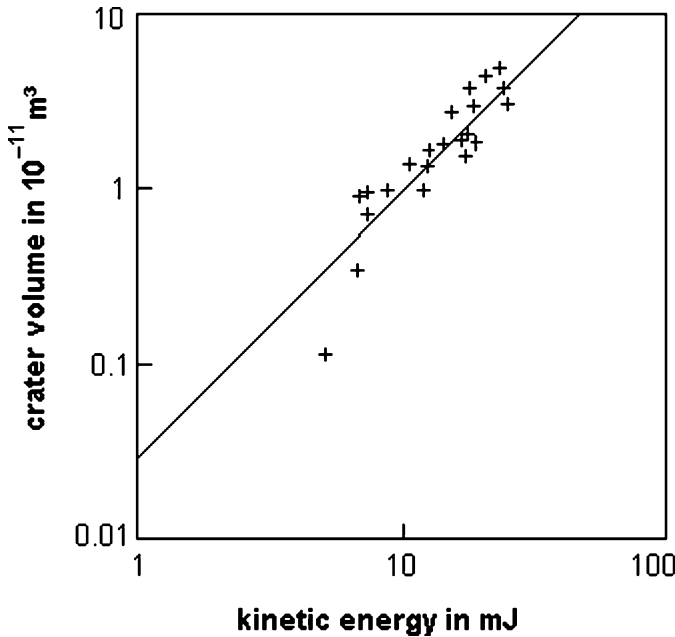


Fig. 6.6 Effect of particle kinetic energy on volume of removed paint (Fokke, 1999)

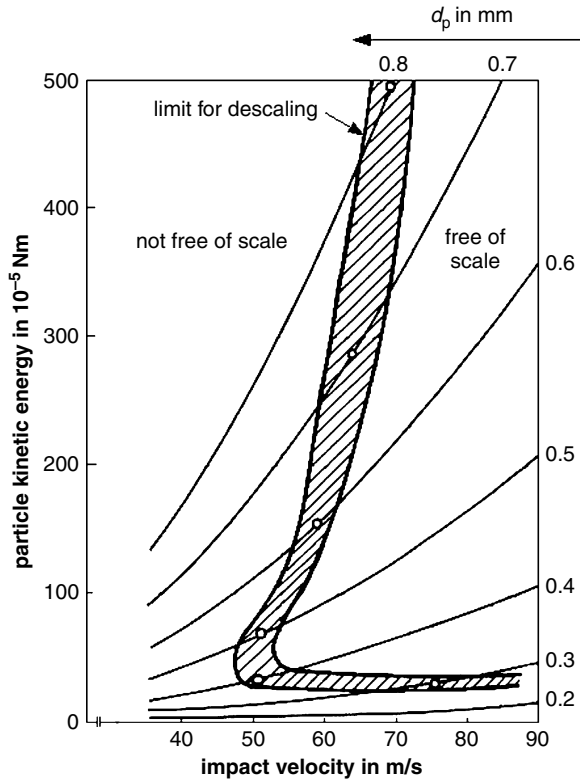
$$\dot{A} = C_2 \cdot d_N^{\chi_N} \quad (6.12)$$

with $\chi_N < 1$.

The major contribution of the nozzle diameter to the material removal process is the determination of air mass flow rate as well as of abrasive mass flow rate (if a fixed ratio between air mass flow rate and abrasive mass flow rate is desired). Both parameters increase if nozzle diameter rises (see Sects. 3.2 and 4.3.2). Nozzle diameter also affects the size of the blasted area (see Sect. 3.4). A threshold diameter does not seem to exist, although practice shows that a minimum nozzle diameter should not be undercut in order to realise a satisfying performance. The proportionality factor C_2 seems to decrease slightly with an increase in air pressure for the conditions in Fig. 6.8.

It is important to note that a trend as shown in Fig. 6.8 can be realised only if the compressor can deliver a volumetric air flow rate high enough to meet the requirement of a larger nozzle diameter. If the compressor cannot be adjusted to an increasing nozzle diameter, the working lines of compressor and nozzle will not intersect (see Fig. 4.3). The cleaning rate will drop if the nozzle diameter increases. This case is illustrated in Fig. 4.37, where the drop in cleaning rate for the larger nozzle diameter is almost 40%. The reason is the pressure drop in the system which leads to a deteriorated cleaning process. The limit for an increase in nozzle diameter is, therefore, the capacity of the compressor.

Fig. 6.7 Threshold conditions for mill scale removal from steel substrates (Weidenhaupt, 1970)



Uferer (1992) introduced a nozzle-shape factor, f_N , which depends on nozzle length. Cleaning rate is assumed to rise linearly with an increase in this parameter. For cylindrical nozzles, f_N depends on nozzle length; and for Laval nozzles, f_N depends on air pressure. Table 6.3 lists some typical values. According to these values, Laval nozzles would provide a higher cleaning rate.

6.2.3 Effects of Nozzle Design

A number of investigations depicted a notable influence of nozzle design parameters on the efficiency of blast cleaning processes. Djurovic et al. (1999), for example, noted an effect of the nozzle cross-section shape on the removal of organic coatings from aluminium substrates with starch media. The width of the traces formed in the paint layer was 26 mm for a round nozzle exit, but 46 mm for a rectangular nozzle exit; this was an increase of about 180%. It is also known that the energy distribution at the target surface notably depends on the nozzle exit geometry. These relationships are displayed in Figs. 3.33, 3.34 and 3.51.

Further effects of nozzle geometry were investigated by Kline et al. (1988) and Plaster (1972). Results of descaling tests with different nozzle types are summarised

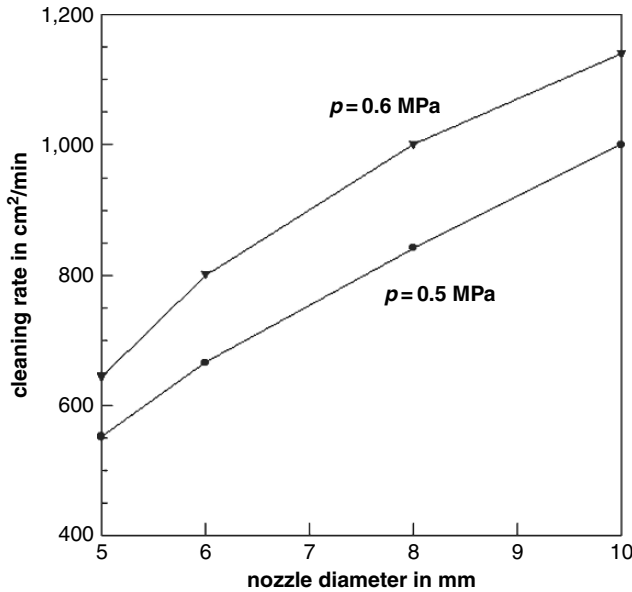


Fig. 6.8 Effect of nozzle diameter on cleaning rate (Kalpers, 1949)

in Fig. 6.9. It can be seen that scale mass loss rate increased with increasing pressure for all nozzle types, which verifies the trends discussed in Sect. 6.2.1. However, the individual trends depended on nozzle geometry. The maximum mass loss was obtained at all pressure levels if a convergent–divergent (Laval) nozzle was utilised. For the highest pressure level, however, this advantage vanished, and a divergent nozzle with a bell-shaped inlet section performed equally.

Kline et al. (1988) performed laboratory and site experiments with a number of different nozzles at higher compressor pressures. The authors cleaned mill scale bearing steel plates to a near-white surface standard, and they tested four different types of nozzles: a standard Laval nozzle, a nozzle with wide throat design, a double Laval

Table 6.3 Blasting nozzle coefficient f_N (Uferer, 1992)

Cylindrical nozzle	
Nozzle length in mm	f_N
50	0.60
80	0.85
100	0.93
120	1.00
150	1.05
Laval nozzle	
Nozzle air pressure in MPa	f_N
<0.3	1.0–1.1
0.3–0.6	1.1–1.3

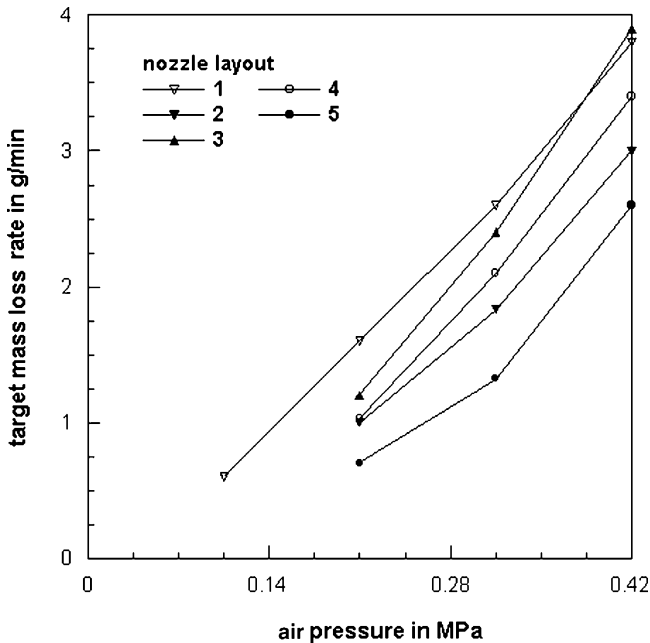


Fig. 6.9 Effects of nozzle design and nozzle pressure on the removal of mill scale (Plaster, 1972). Nozzle layout: 1 – convergent–divergent (Laval) nozzle; 2 – bell-mouthed convergent nozzle; 3 – bell-mouthed divergent nozzle; 4 – bell-mouthed convergent–divergent (Laval) nozzle; 5 – convergent–parallel nozzle (lined with tungsten carbide sections). Abrasive type: crushed chilled cast iron shot; nozzle diameter: $d_N = 9.5$ mm

nozzle and a Laval nozzle with a distinctively large exit end opening. Results of these investigations are plotted in Figs. 6.10 and 6.11. The graph in Fig. 6.10 provides results of laboratory tests. No apparent improvement could be achieved with the wide throat nozzle. This design will benefit only from a larger blast hose that is able to take advantage of the wider throat cross-section (see Sect. 4.5). The double Laval nozzle gave little or no significant improvement compared to the standard Laval design. Productivity could significantly be improved by using the wide exit opening design; the results indicated an improvement of about +50%. The gain was probably due to the larger blast pattern obtained with this nozzle. Measurements of the blast pattern sizes indicated a diameter of 102 mm for the wide exit opening nozzle compared to a diameter of 76 mm for the standard Laval nozzle. Results of field tests are plotted in Fig. 6.11. A laminar flow nozzle was included to these tests, which featured a very smooth transition throat between the convergent and divergent nozzle sections. This design did not deliver a productivity improvement. The double Laval nozzle generated about +10% more productivity improvement over the standard Laval nozzle at all pressure levels. The large exit opening design was significantly more effective than the standard Laval nozzle at the two higher pressure levels. A higher nozzle pressure was beneficial to the cleaning efficiency for all nozzle types, but it was most influencing if the large exit opening design was utilised.

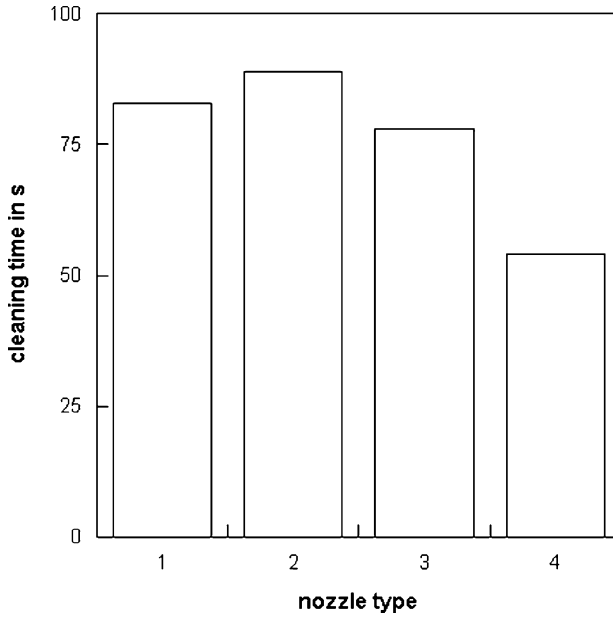


Fig. 6.10 Effects of nozzle design and nozzle pressure on the removal of mill scale (Kline et al., 1988); results of laboratory tests. Nozzle layout: 1 – standard Laval nozzle; 2 – nozzle with wide throat; 3 – double Laval nozzle; 4 – nozzle with distinctively large exit opening

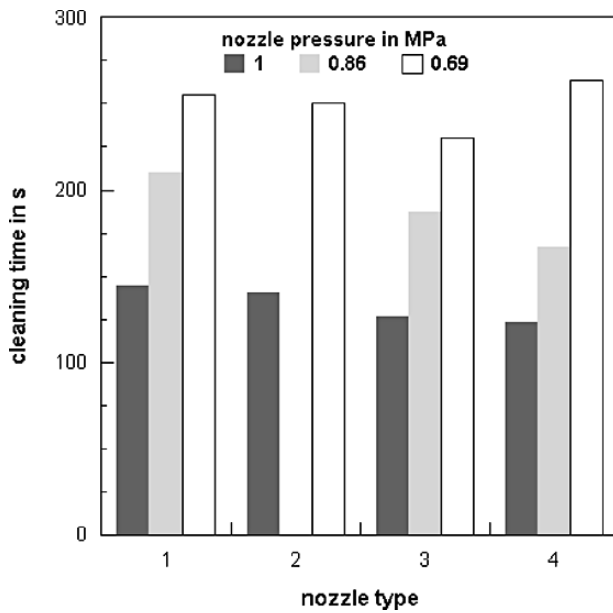


Fig. 6.11 Effects of nozzle design and nozzle pressure on the removal of mill scale (Kline et al., 1988); results of site tests. Nozzle layout: 1 – standard Laval nozzle; 2 – laminar flow nozzle with soft flow transition; 3 – double Laval nozzle; 4 – nozzle with distinctively large exit opening

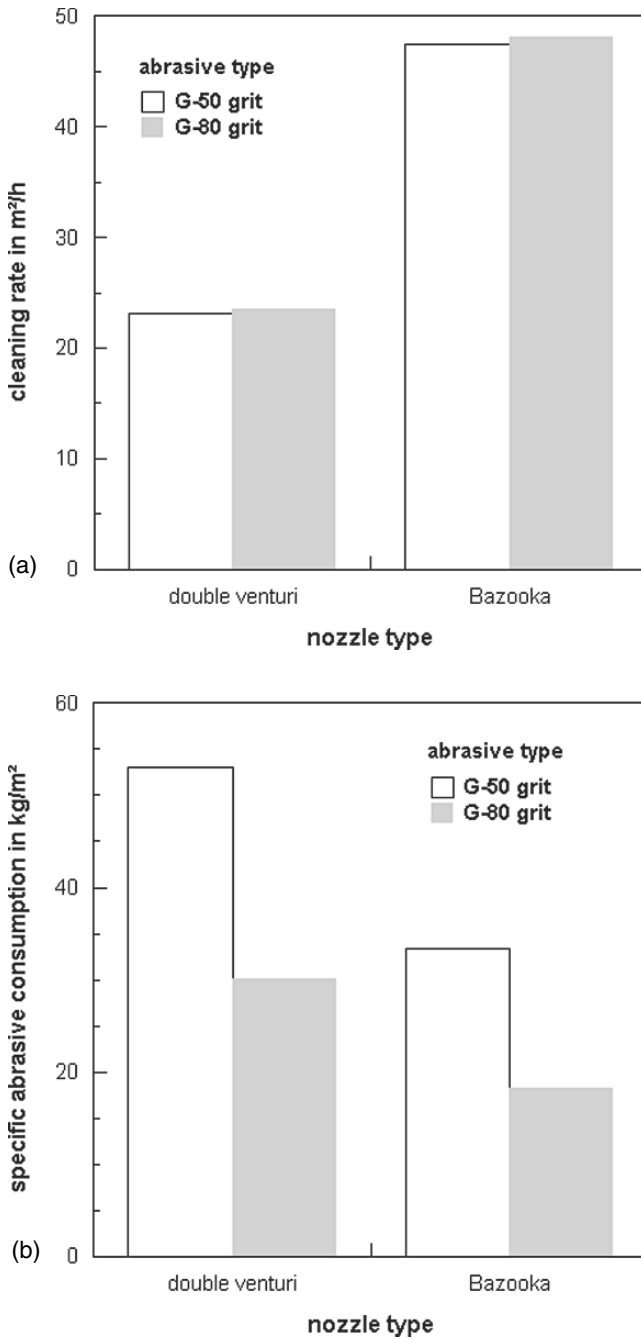


Fig. 6.12 Effects of nozzle design and abrasive type on target parameters (Hitzrot, 1997). “Double venturi” corresponds to nozzle “3” in Figs. 6.10 and 6.11; “Bazooka” corresponds to nozzle “4” in Figs. 6.10 and 6.11. (a) Effects on cleaning rate; (b) Effects on abrasive consumption

Figure 6.12 illustrates the effects of abrasive particle size on the nozzle design. With respect to cleaning rate, shown in Fig. 6.12a, the size of the abrasives did not affect the cleaning rate for a given nozzle design. The Bazooka nozzle type delivered higher efficiency values compared with the double Laval nozzle, whether small or large steel grit particles were used. If, however, the specific abrasive consumption was considered, the situation changed. This aspect is illustrated in Fig. 6.12b. The double Laval nozzle, fed with smaller steel grit particles, was more efficient than the Bazooka type nozzle, fed with larger steel grit particles. For a given nozzle design, abrasive size affected the specific abrasive consumption notably, whereby the smaller steel grit particles led always to a more efficient performance.

Figure 6.13 displays results of erosion experiments performed by Hamann (1987) with different nozzle configurations. Figure 6.13a applies to the removal of mill scale from steel plates with steel shot, whereas Fig. 6.13b applies to the removal of a PVC plate with nickel slag. It can be recognised that a convergent–divergent nozzle with a specially designed inlet section (nozzle type “4”) was the most effective design for both experimental situations. With regard to the removal of the mill scale, a cylindrical nozzle with a bell-shaped inlet section (nozzle type “2”) was more efficient than a convergent–divergent nozzle (nozzle type “3”). However, the opposite trend could be found during the treatment of the PVC targets, where the convergent–divergent nozzle performed more effectively. It can also be seen that a convergent–divergent nozzle with a short convergent section (nozzle type “2”) was very efficient for the removal of mill scale, but it did not show an equally good performance during the treatment of the PVC samples.

A convincing conclusion from the presented results is that an optimum nozzle design does not exist in general. The nozzle design must be adapted to the entire cleaning system, which includes abrasive material, process parameters and target material response.

Hutans (1986) placed a pipe between nozzle exit and surface to be blast cleaned in order to reduce the effects of interactions between the abrasive–air flow and the surrounding air. He reported notable improvements in terms of cleaning rate, specific abrasive consumption and specific energy consumption. The savings were larger for blast cleaning in an open environment compared to blast cleaning in a hall.

6.3 Effects of Performance Parameters

6.3.1 Effects of Stand-off Distance

Results of Remmelts (1969) on the effect of variations in stand-off distance on the cleaning rate for mill scale are displayed in Fig. 6.14. Such a trend was also found for the removal of coatings from metal substrates (Uhlmann et al., 2003). Three regions can be distinguished in the graph: an initial region, an optimum region and a decreasing region. The optimum stand-off distance is in the range between $x = 57$ and 67 mm. These values are close to the SSPC Surface Preparation Commentary,

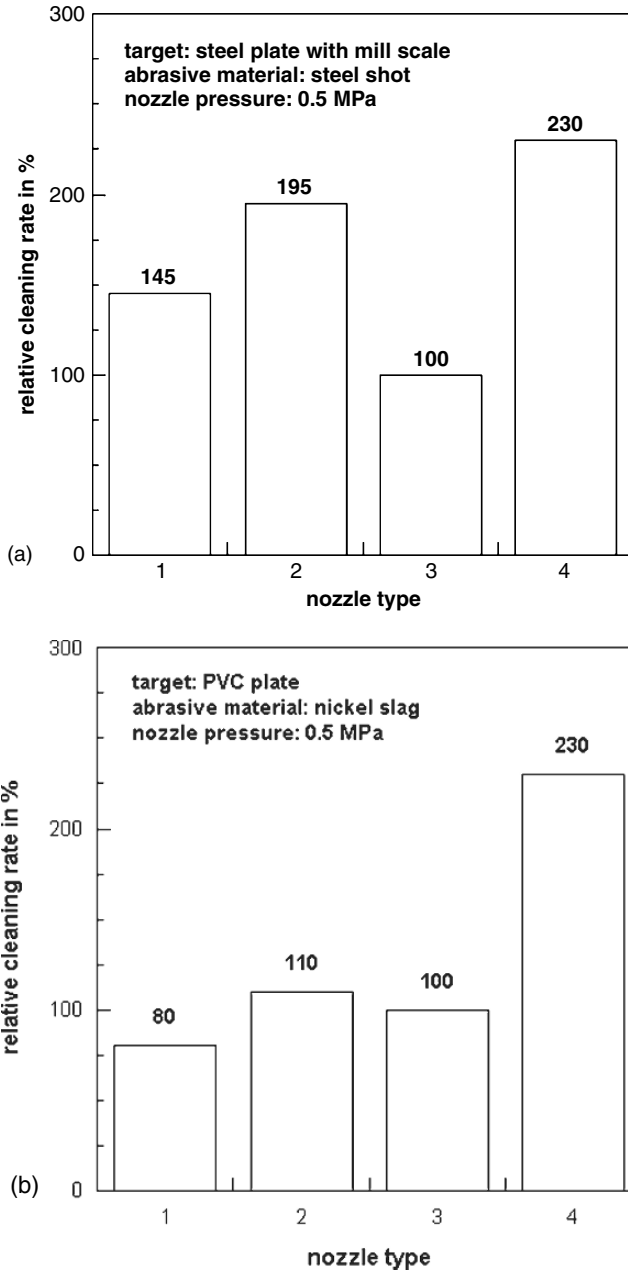


Fig. 6.13 Effects of nozzle design on material removal efficiency (Hamann, 1987). Nozzle layout: 1 – cylindrical nozzle with bell-shaped inlet section; 2 – divergent–convergent nozzle with short divergent section; 3 – standard divergent–convergent nozzle (Laval); 4 – divergent–convergent nozzle with additional inlet flow section. (a) Removal of mill scale from steel plates with steel grit; (b) Erosion of PVC samples with nickel slag

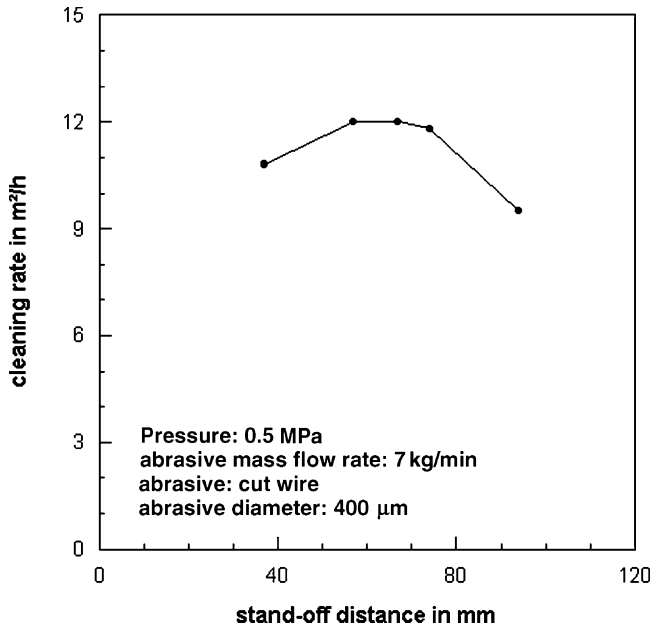


Fig. 6.14 Effect of stand-off distance on cleaning rate for mill scale (Remmelts, 1969)

which states the following: “For optimum cleaning rate, the nozzle to surface distance is around 46 cm.” This optimum distance can vary depending on the type of substrate, material to be removed and process parameters to be adjusted. An older regulation for the removal of mill scale and rust from ship steels due to blast cleaning recommended optimum stand-off distances between $x = 40$ and 60 cm (STG, 1963).

It was shown in Sect. 3.6.6 that abrasive particle velocity increases further after the particles have exited the nozzle (see Figs. 3.46 and 3.47). This phenomenon explains partly the existence of an optimum stand-off distance for blast cleaning processes. Another aspect is the increase in jet diameter and, thus in the size of the blasted area (see Fig. 3.22). This issue is discussed in Sect. 3.4.

Uferer (1992) introduced a stand-off distance parameter f_x , whose values are listed in Table 6.4 for different abrasive materials. It can be seen that slag and quartzsand are much more sensitive to variations in stand-off distance than steel

Table 6.4 Values for the stand-off distance coefficient f_x for the removal of rust (Uferer, 1992)

Abrasive material	Value for f_x				
	Stand-off distance in mm				
	250	300–400	500	600	750
Steel wire	–	0.90	1.00	1.00	1.00
Slag and quartz	0.95	1.05	1.00	0.85	0.65

wire. This result agrees with the trends shown in Fig. 3.40, where it can be seen that the increase in particle velocity after the nozzle exit was more distinct for the slag material (at least for the convergent–divergent nozzle).

6.3.2 Effects of Relative Particle Distance

The relative distance between particles in the particle stream according to (3.45) affects the erosion of materials. Results cited by Ciampini et al. (2003a) showed a drop in erosion rate from a constant value of unity for low L_P^* -values to much lower erosion rates at a L_P^* of about 17. This result was attributed to a sudden increase in interference between incidental and rebounding particles at the higher L_P^* -numbers.

Balasubramaniyan (1998) has shown that the volume loss of eroded brittle materials was very sensitive to changes in the relative particle distance if $L_P^* < 1$. This would mean that changes in the stream density are critical to the material removal process for $\rho_S^* > \pi/6$.

6.3.3 Effects of Impact Angle

The effect of variations in impact angle on the cleaning rate for mill scale is displayed in Fig. 6.15 for two abrasive mass flow rates. A maximum cleaning rate could be noted at an angle of $\varphi = 45^\circ$ which is rather typical for plastically responding materials. The lowest cleaning rate was found at perpendicular impact for both parameter conditions. These results neither verified the general recommendation in the SSPC Surface Preparation Commentary: “An 80 to 90 degree angle is best suited for removing mill scale or heavy rust and for cleaning pitted areas”, nor did the scale removal model presented in Sect. 5.6. However, abrasive mass flow rate seemed to play an additional role, as illustrated in Fig. 6.15, and the lower value for the abrasive mass flow rate did not reveal a “ductile” behaviour of the scale. If elastically responding materials, namely heavy rust, heavy mill scale, brittle coatings, need to be removed, a normal impact angle is often the right choice. Averbchenko et al. (1970), for example, determined maximum values for the erosion rate of brittle enamel coatings at normal impact angles. For the removal of rust (no platy rust) from steel plates, Uferer (1992) found an increase in cleaning rate if impact angle rose from $\varphi = 45^\circ$ to 90° . Tangirala (1998) noted a maximum volume loss of iron scale if the impact angle was $\varphi = 90^\circ$.

Maximum erosion rates at low impact angles are rather typical for materials being removed by micro-cutting or, respectively, ploughing processes (see Sect. 5.5.2). Such trends were also observed for organic coating materials by Kotnarowska (2003), Zahavi and Schmitt (1981, 1982) and Trezona et al. (2000a); for rubber by Arnold and Hutchings (1992) and Slikkerveer (1999); for enamel coatings by Parslow et al. (1997) and for polyethylene by Walley and Field (1987).

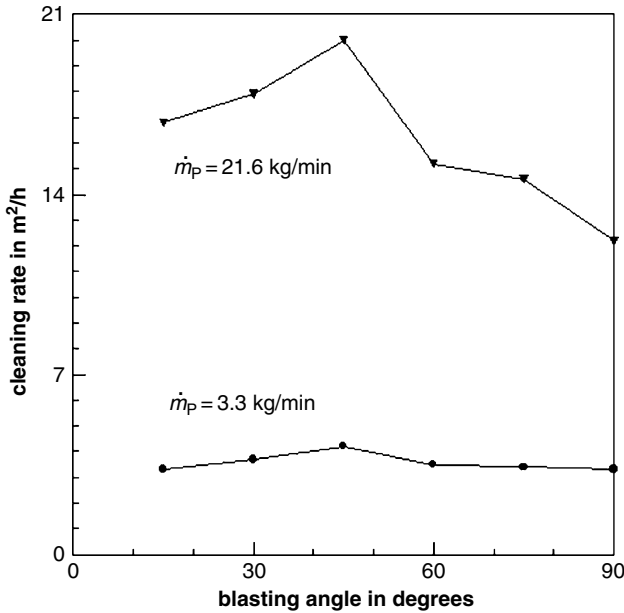


Fig. 6.15 Effects of blasting angle and abrasive mass flow rate on cleaning rate for mill scale (Remmelts, 1969)

An example is provided in Fig. 6.16 which shows that the type of the epoxy coating system did not affect the location of the optimum impact angle. Zahavi and Schmitt (1981, 1982) eroded rather thin organic coatings (DFT between 30 and 75 μm) with quartz sand ($d_p = 210\text{--}297$ μm) at a moderate impact speeds ($v_p = 42$ m/s) and investigated the effects of impact angle variations. They found that changes in impact angle were more affective to the erosion of rather hard polyurethane coatings. For elastomeric coating materials, the mass loss due to erosion was almost unaffected if the impact angle exceeded a value of about $\varphi = 45^\circ$.

Optimum impact angles for the erosion of rubber by impinging solid particles were found between $\varphi = 15^\circ$ and 20° (Arnold and Hutchings, 1992). Slikkerveer (1999) derived the following relationship between impact angle and erosion rate of rubber materials:

$$E_R = a \cdot (1 + b \cdot \cos^c \varphi) \quad (6.13)$$

The regression parameters had the following values: $a = 0.0072\text{--}0.037$; $b = 2.7\text{--}8.7$ and $c = 2.2\text{--}8.0$. The regression parameter a is the erosion rate at normal impact ($\varphi = 90^\circ$), and the parameter c describes the transition from oblique to normal impact.

Fokke (1999) introduced the inverse specific erosion energy [see (6.10)], and he found a dependence with the impact angle. The inverse specific erosion energy decreased with an increase in impact angle in the impact angle range between $\varphi = 30^\circ$

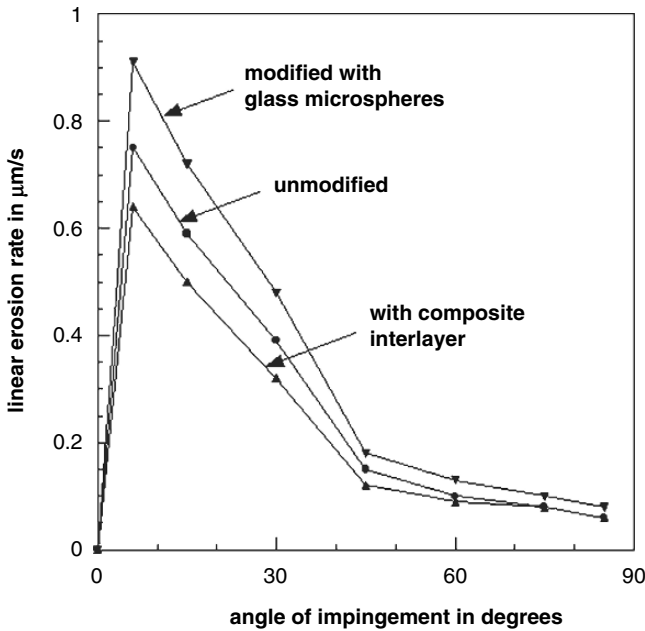


Fig. 6.16 Effect of blasting angle and coating composition on coating removal (Kotnarowska, 2003)

and 45°. For impact angles larger than $\varphi = 45^\circ$, impact angle did not affect the inverse specific erosion energy.

Uferer (1992) introduced an impact angle factor f_ϕ , which has a linear effect on the cleaning rate for the removal of mill scale and rust. Typical values for this parameter are listed in Table 6.5.

6.3.4 Effects of Exposure Time

Removal rate and cleaning rate increase with an increase in exposure time. The respective functional relationship can be described as follows:

$$\dot{A} \propto (t_E - t_I)^{n_t} \tag{6.14}$$

Table 6.5 Values for the blasting angle coefficient f_ϕ (Uferer, 1992)

Blasting angle	Coefficient f_ϕ	
	For mill scale	For rust
30°	1.5	–
45°	1.6	0.6
60°	1.25	–
90°	1.0	0.84

This relationship can be considered a removal kinetics, whereby values for the exponent range between $n_t = 0$ and 1. Therefore, the efficiency of cleaning processes and of material removal processes drops with an increase in exposure time. If the deposit or coating is completely removed from a substrate, $n_t = 0$. It was shown that the precise values for n_t depended, among others, on abrasive type and size (Raykowski et al., 2001). Some relationships are listed in Table 6.6. The parameter t_I is an incubation period which must be exceeded in order to generate a measurable material removal. Equation (6.14) has the same structure as (5.47), which was derived by Schmithals (1961) for the blast cleaning of mill scale.

An alternative exposure parameter is the local exposure time, which is given as follows:

$$t_E = d_J / v_N \quad (6.14a)$$

The jet diameter can sometimes be replaced by the nozzle diameter ($d_J = d_N$). A general plot of local exposure time versus volumetric erosion is shown in Fig. 6.17. It can be seen that the erosion rate (slope of the curve) increased notably at low exposure times. If the local exposure time increases further, efficiency (in terms of the slope of the curve) dropped. From this point of view, short local exposure times (high traverse rates) are recommended. A threshold exposure time (t_I), which separates the incubation period from the erosion period, is also shown in Fig. 6.17. A threshold (incubation) period was found by Friedrich (1986) for the particle erosion of polymers. The actual magnitude of the incubation time depended on the brittleness of the polymers. More brittle polymers did not exhibit a notable incubation period. D'Emanuele et al. (1992) found for copolymer materials that the duration of the incubation period depended on the initial molecular weight of the polymers. These authors characterised the incubation period as a time during which a rapid decrease in polymer molecular weight occurred. Threshold periods are also known from other abrasive jet applications, namely hydroabrasive machining (Momber and Kovacevic, 1998), but also from hydroblasting applications (Momber, 2003, 2005a). The most probable explanation is that erosion of the coating starts after a period of damage accumulation by subsequently impinging abrasive particles (see Fokke, 1999). Threshold limits do not seem to exist for the removal of rather soft coatings. The removal rate should have a maximum at rather short relative exposure times (see Fig. 6.17). After a certain time, a further increase in exposure time reduces the removal rate.

Table 6.6 Removal kinetic power parameter, based on measurements from Raykowski et al. (2001) ($p = 0.35$ MPa, $\varphi = 90^\circ$, $x = 38$ cm)

Abrasive type	Particle diameter in μm	n_t -value
Glass beads	125–177	0.56
	177–250	0.47
	420–590	0.47
Steel shot	90–200	0.51
	90–300	0.60

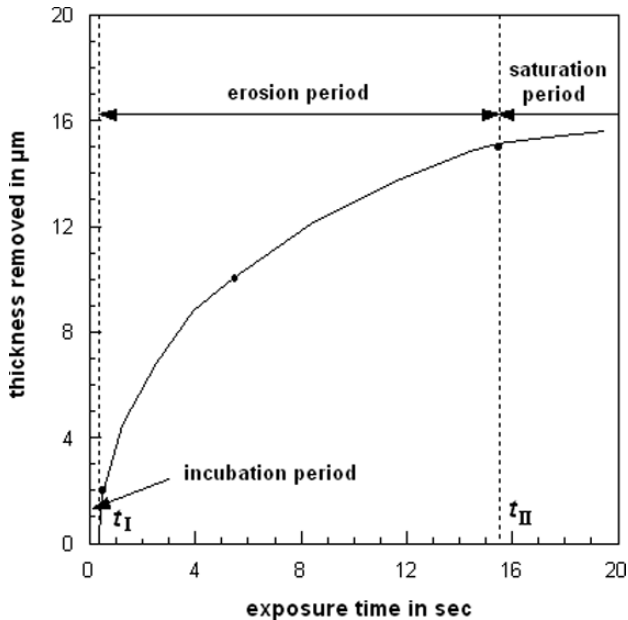


Fig. 6.17 Effect of local exposure time on the removal of a deposit from a turbine blade (based on results of Raykowski et al., 2001)

The qualitative relationship displayed in Fig. 6.17 corresponds well with measurements of area coverage values performed by Tosha and Iida (2001). The authors found an initial increase in the area coverage, which was followed by a saturation level at higher exposure times. Both ranges were separated by a “full coverage time”. Coverage time increased if abrasive particle diameter increased, and if abrasive particle velocity decreased (see Sect. 3.5.4). This transition parameter may be close to the exposure time (t_{II}) defined in Fig. 6.17, which separates erosion period and saturation period. This time mark should not be exceeded in order to guarantee effective cleaning conditions. A similar transition parameter – the minimum number of impinging abrasive particles for the complete coverage of an area of 1 m^2 – was defined by Fokke (1999). This particular parameter mainly depended on the kinetic energy of the impinging particles (see Sect. 6.5).

6.3.5 Effects of Number of Passes

If the optimum exposure time, t_0 , is known, a strategy for multi-pass material removal can be developed. The optimum exposure time can simply be introduced several times into the duration that corresponds to the desired volumetric removal rate. This approach delivers the following relationship:

$$n_S = \frac{\dot{V}_M}{\dot{V}_{M(t_E=t_0)}}; n_S = 1, 2, 3 \dots \quad (6.15)$$

If, for example, a deposit with a thickness of $h_C = 16 \mu\text{m}$ must be removed from a substrate, a local exposure time of $t_E = 20 \text{ s}$ is required. The optimum exposure time for $dh_C/dt_E = \text{max}$ shall be $t_0 = 2 \text{ s}$, which gives $h_C(t_E = t_0) = 6 \mu\text{m}$. The theoretical number of steps calculated from (6.15) is $n_S = 16/6 = 2.67$. In practice, $n_S = 3$. The entire exposure time required to remove the desired coating mass is thus $t_E = 3.2 = 6 \text{ s}$ which is about 30% of the time for a one-step removal. The gain in efficiency is, therefore, as high as +70%. This example is based on Fig. 6.17.

6.4 Effects of Abrasive Parameters

6.4.1 Effects of Abrasive Mass Flow Rate

Effects of variations in abrasive mass flow rate on blast cleaning processes were investigated by Bae et al. (2007), Hareux and Riac (1986), Holt and Austin (2001) and Kura (2003). Figures 6.18 and 6.19 show typical relationships between abrasive mass flow rate and cleaning rate. Similar relationships were found for the removal of epoxy coatings from steel plates with steel grit (Bae et al., 2007); and for abrasive erosion of polyurethane and rubber (Zhang et al., 1995). The relationship can be expressed according to a reaction kinetics model (Momber, 1995):

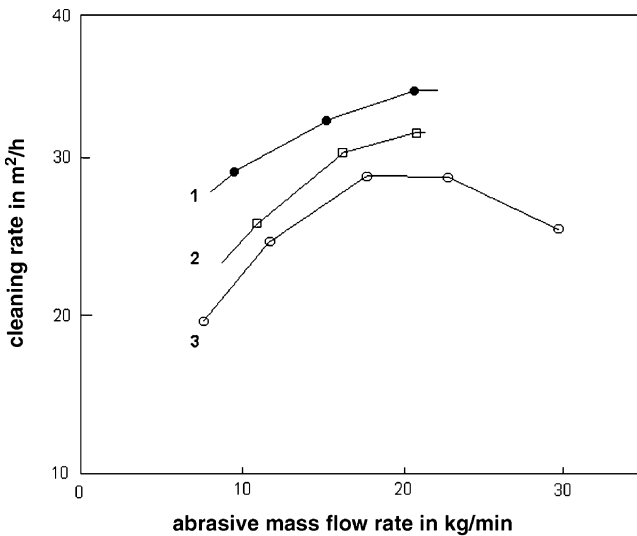


Fig. 6.18 Effect of abrasive mass flow rate on cleaning rate (Hareux and Riac, 1986). Abrasive material: aluminium oxide 700; nozzle types: 1 – long Laval nozzle, $d_N = 9.5 \text{ mm}$; 2 – short Laval nozzle, $d_N = 9 \text{ mm}$; 3 – cylindrical nozzle, $d_N = 10 \text{ mm}$

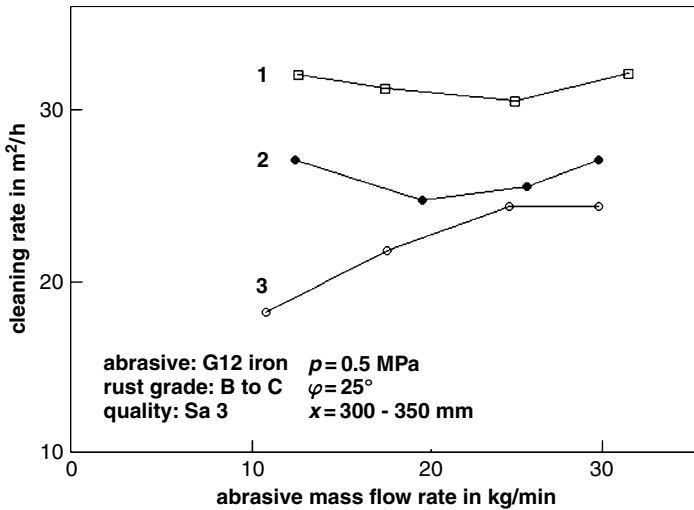


Fig. 6.19 Effect of abrasive mass flow rate on cleaning rate (Hareux and Riach, 1986). Abrasive material: iron shot G12; nozzle type: 1 – long Laval nozzle, $d_N = 9.5 \text{ mm}$; 2 – cylindrical nozzle, $d_N = 10 \text{ mm}$; 3 – short Laval nozzle, $d_N = 9 \text{ mm}$

$$\dot{A} = k \cdot \dot{m}_p^m \tag{6.16}$$

In the equation, the power exponent, m , is a function of the abrasive mass flow rate. For small abrasive mass flow rates, $m = 1$. For the erosion of polymers, values between $m = 0.5$ and 1.0 were estimated (Zhang et al., 1995). For the slurry erosion of fusion-bonded epoxy powders, values between $m = 0.5$ and 0.6 were recorded (Luo et al., 2001). The value for m decreases up to $m = 0$ for optimum abrasive mass flow rates, and it becomes $m \downarrow 0$ for high abrasive mass flow rates. From the point of view of abrasive consumption, the optimum range is at low abrasive mass flow rates and $m = 1$. In this range, each increase in abrasive mass flow rate leads to a proportional rise in the material removal rate. Such effects are known from abrasion tests of organic coatings, where mass loss linearly increases with the number of abrasion cycles (Cambruzzi et al., 2005). Fokke’s (1999) erosive cleaning model also leads to a linear relationship between cleaning rate and abrasive mass flow rate (see Sect. 6.5). Results plotted in Figs. 6.18 and 6.19 show that an optimum mass flow rate depends on abrasive type and the nozzle configuration. It seems from the plot in Fig. 6.18, which is valid for aluminium oxide, that the optimum mass flow rate shifted to higher values if convergent–divergent nozzles (“1” and “2”) were applied. For this nozzle type, the conditions for maximum cleaning rates were not yet reached. The cylindrical nozzle, however, featured a maximum cleaning rate at an abrasive mass flow rate of $\dot{m}_p = 17 \text{ kg/min}$. For equal abrasive mass flow rates, the convergent–divergent nozzles generated a higher cleaning rate compared with the cylindrical nozzle. The advantage of the convergent–divergent nozzles seems to become even more pronounced at higher abrasive mass flow rates. The situation is

different in Fig. 6.19, which is valid for iron grit. In that case, only the curve for the short convergent–divergent nozzle (denoted “3”) showed an optimum range for the abrasive mass flow rate. It was at about $\dot{m}_p = 25 \text{ kg/min}$. The other two nozzle types did not show any optimum range. In particular, the long convergent–divergent nozzle (denoted “1”) was rather insensitive to changes in the abrasive mass flow rate. The cylindrical nozzle behaved completely different compared with the situation in Fig. 6.18. Whereas this nozzle exhibited an optimum performance at moderate values for the mass flow rate ($\dot{m}_p = 15\text{--}20 \text{ kg/min}$) in Fig. 6.18, it performed worst in that same abrasive mass flow rate range in Fig. 6.19.

The abrasive mass flow rate determines the number of impinging abrasive particles as well as their kinetic energies. The higher the abrasive mass flow rate, the higher the number of particles involved in the blast cleaning processes. Assuming no interaction between the individual abrasive particles in the course of acceleration, each increase in abrasive mass flow rate leads to a proportional increase in material removal. This holds for relatively low abrasive mass flow rates. It is known from wheel blasting, that a certain abrasive mass exists, which guarantees a complete coverage of a given surface with erosion pits. This critical abrasive mass is typical for a given substrate material, and it depends on abrasive material density and abrasive particle diameter (Safar, 1973). For rather high abrasive mass flow rates, damping mechanisms, particle collision, the generation of debris films and overlap effects may occur. Also, the limited kinetic energy of the air flow distributes over a very high number of particles, which leads to a decrease in the kinetic energy of the individual particles. This effect cancels the positive effect of the higher impact frequency. Figure 2.17 schematically illustrates these relationships. It is also known that an increase in the mass flow ratio abrasive/air reduces the velocity of the particles at the nozzle exit; this is true especially for smaller abrasive particles (see Sect. 3.6.2).

The location of the optimum abrasive mass flow rate depends on the deformation behaviour of the target materials. Whereas materials with the ability of plastic deformation reach the optimum at comparatively high abrasive mass flow rates; elastically responding materials reach the optimum region at lower abrasive mass flow rates. This difference is due to the higher sensitivity of brittle materials to the loading intensity provided by the abrasive particles. In contrast, a material responding with plastic deformation is more sensitive to the frequency of the impacting particles. Therefore, an increase in the abrasive mass flow rate is beneficial for these materials to overcome their plastic-deformation capability.

Experimental investigations have shown that the cleaning rate generally exhibited a maximum at an optimum number of turns on the abrasive metering valve (Holt and Austin, 2001; Kura, 2003; Bae et al., 2007). An example is shown in Fig. 6.20. It can be seen that the different abrasive materials responded differently to changes in the number of valve turns. The copper slag (denoted “1”), in particular, was very sensitive to changes in the number of turns. It can also be seen that the location of the maximum depended on the abrasive type. Each abrasive material is related to a certain number of turns (respectively to a certain cross-section of the valve opening). The optimum number of valve turns is six for the copper slag, and it is four for the

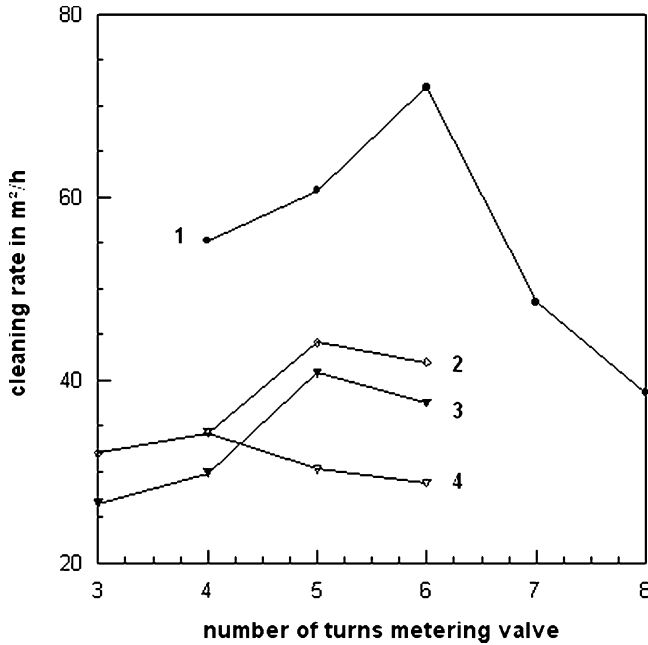


Fig. 6.20 Effect of abrasive metering on cleaning rate (Holt and Austin, 2001). Abrasive material: 1 – copper slag, 2 – hematite, 3 – garnet, 4 – coal slag

coal slag. It is conclusive that the specific abrasive consumption (in kg/m²) must have a minimum value at that particular number of valve turns. It must, however, be taken into account that abrasive mass flow rate does not always have a linear relationship to the number of turns for all abrasive types. This was shown by Holt and Austin (2001). Therefore, the relationship between cleaning rate and abrasive mass flow rate does not always exhibit an optimum range (especially not for high air pressures), whereas the relationship between cleaning rate and number of valve turns always does.

Bae et al. (2007) published cleaning rates obtained during the removal of epoxy paint from steel substrate, whereby the values for the mass flow ratio abrasive/air were varied. The results depicted that cleaning rate decreased if the value for the mass flow ratio abrasive/air rose. The values for the mass flow ratio considered in this study ($R_m = 4-4.4$) were, however, unusually high.

Papini et al. (2003) defined a critical abrasive mass flow rate for significant inter-particle collision to occur. This critical parameter can be calculated as follows:

$$\dot{m}_C = \frac{4 \cdot \Pi_1 \cdot v_P \cdot \rho_P \cdot \pi \cdot r_P^3}{3 \cdot x} \tag{6.17}$$

The variable Π_1 , a dimensionless mass flow rate, is given through the following equation (Papini et al., 2003):

$$\Pi_1 = \frac{\dot{N}_{P1} \cdot x}{v_P} \quad (6.18)$$

Here, the variable \dot{N}_{P1} is a particle frequency at which significant interference (5%) between incident and rebounding particles begins to appear. It was found that this frequency depended, among others, on particle diameter and coefficient of restitution. Papini et al. (2003) performed numerical simulations to estimate values for Π_1 and found that this variable had low values for low x/d_p -ratios. The ratio x/d_p also determined the influence of the coefficient of restitution on Π_1 . If the ratio was $x/d_p < 120$, Π_1 was high for high values for the coefficient of restitution; whereas the opposite trend was found for $x/d_p > 120$. Equation (6.17) can also be expressed in terms of the critical particle mass flux, passing through a nozzle:

$$\dot{m}_N = \frac{\dot{m}_C}{\pi \cdot r_N^2} \quad (6.19)$$

Parslow et al. (1997) performed erosion tests on enamel paints with a film thickness of DFT = 50 μm and found a relationship very similar to that plotted in Fig. 6.19. The authors utilised the abrasive concentration (g/m^3) as the evaluation parameter. At high values for the abrasive concentration, the erosion rate approximated a constant value in all cases. The value, where the erosion rate became stable, may be considered a typical parameter for a given paint material.

Walley and Field (1987) introduced an *incubation number* for the erosion of polymers. This number was defined as the number of impacts that have to occur on an impact zone before it contributes to a net mass loss. The incubation numbers were rather large for polymers, suggesting that the amount of deformation needed before material is removed was also large. This parameter had a strong relationship to the impact angle. If impact angle increased, the incubation number increased as well.

Glatzel and Brauer (1978) applied the *collision number* according to (2.12) to erosion processes, and they found that the mass loss decreased with an increase in the collision number according to the following relationship:

$$\Delta m_M \propto e^{-2 \cdot c_k} \quad (6.20)$$

6.4.2 Effects of Abrasive Flux Rate

Abrasive flux rate can be defined as follows:

$$\dot{m}_F = \frac{m_P \cdot \dot{N}_P}{A_C} \quad (6.21)$$

It expresses the mass of abrasive particles impinging a given cross-section during a defined time interval. Its physical unit is $\text{kg}/(\text{m}^2 \text{ s})$. Flux rate, thus, can characterise

the impingement frequency. Detailed studies have shown that abrasive flux rate had comparatively little influence on the erosion of brittle materials and metals, but it was a sensitive parameter for the erosion of polymers and elastomers (Walley and Field, 1987; Arnold and Hutchings, 1989). Some results obtained on rubber are displayed in Fig. 6.21. It can be seen that erosion rate decreased as flux rate increased. The effects of varying flux rates were very pronounced in the range of small flux rates. The reasons for this behaviour were attributed to chemical degradation processes in the rubber material, and they were in detail discussed by Arnold and Hutchings (1989). The same trend was noted by Djurovic et al. (1999) for the removal of organic coatings from aluminium substrates with starch media. The authors found that cleaning efficiency dropped if specific abrasive consumption (kg/m^2) increased. Ciampini et al., 2003a) performed a simulation of the flux rate on abrasive particle interactions. They calculated critical values for the flux rate for negligible particle interactions. The critical value depended on the particle diameter. Typical values are listed in Table 6.7.

Henning and Brauer (1986) applied the frequency number according to (2.11), and they found an increase in the erosion rate with an increase in the particle frequency number. The progress of the erosion rate function did not depend on the material type; it had equal values for glass, aluminium, rubber and PMMA.

Hutchings (1981) derived a critical specific abrasive mass (kg/m^2) needed for the incubation of erosion processes in metals. This critical parameter was defined as follows:

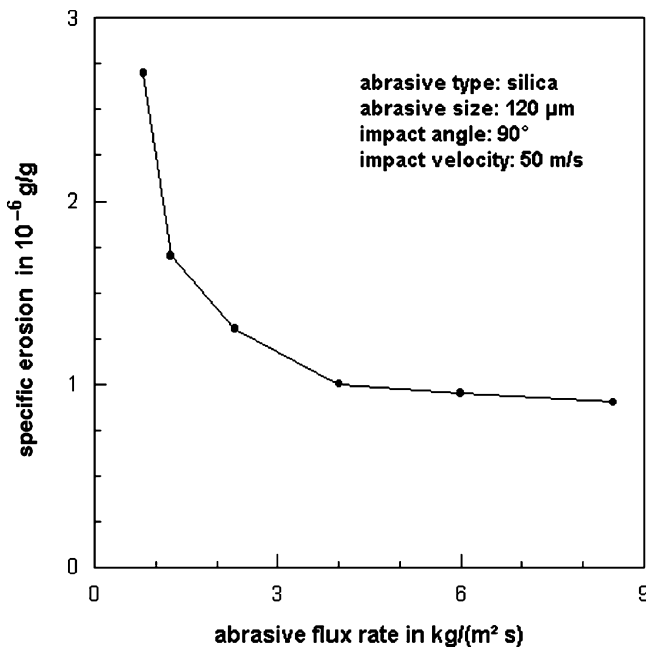


Fig. 6.21 Effect of abrasive flux rate on specific erosion in rubber (Arnold and Hutchings, 1989)

Table 6.7 Critical flux rates for negligible particle interactions (Ciampini et al., 2003a)

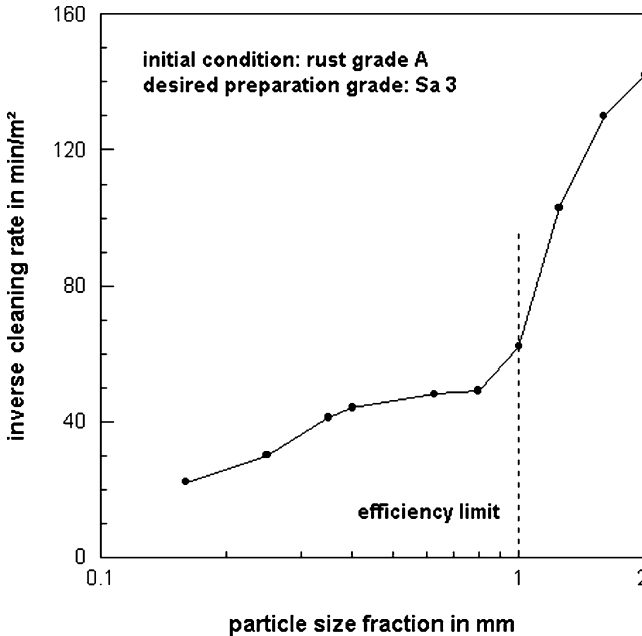
Particle diameter in μm	Critical flux rate in $\text{kg}/(\text{s} \cdot \text{m}^2)$
69	0.07
231	0.9
700	8.0

$$m_A \propto \varepsilon_C \cdot \frac{d_P}{v_P^2} \quad (6.22)$$

The power exponent for the particle velocity corresponded very well with experimentally estimated values (which were between 1.9 and 2.5 for aluminium). The parameter ε_C is a critical strain generated in the target material.

6.4.3 Effects of Abrasive Particle Diameter

Figure 6.22 illustrates a typical relationship between abrasive particle diameter and inverse cleaning rate for descaling. The time required to clean a given area was rather unaffected for small particle sizes. For particle diameters larger than $d_P = 1,000 \mu\text{m}$, cleaning time suddenly rose, and the descaling process became very inefficient. The relationship between cleaning rate and abrasive particle diameter can be characterised as follows:

**Fig. 6.22** Effect of abrasive particle size on inverse cleaning rate for mill scale (Neumann, 1976)

$$\dot{A} \propto d_p^{\theta_p} \tag{6.23a}$$

with $\theta_p < 0$.

It is important to note that the condition $\theta_p < 0$ holds for the relationship between particle size and cleaning rate as the target parameter. Figure 6.23 shows how a variation in abrasive particle size can be utilised for cleaning rate optimisation if a desired profile roughness must be realised. For a given roughness of $R_z = 25 \mu\text{m}$, the specific rate varied between 60 min/m^2 (for $d_p = 1.0 \text{ mm}$) and 130 min/m^2 (for $d_p = 1.6 \text{ mm}$). This is a tremendous potential for cleaning process optimisation. The results plotted in Fig. 6.24 further verify the positive effect of smaller abrasive particles. For steel descaling, cleaning rate dropped for comparative mass flow rate values if larger abrasives were utilised. This effect is illustrated in Fig. 6.24a. The same trend between cleaning rate and abrasive particle size was reported by Bigos (1959) for the blast cleaning of steel panels with different abrasive materials (iron grit, sand and slag); by Balcar (1986) for the removal of bronze from steel substrates with glass beads; and by Bae et al. (2007) for the removal of epoxy coatings from steel substrates with steel grit. Results of the latter authors are provided in Fig. 6.24b. It can be seen that the relative cleaning rate notably dropped if larger abrasive particles were utilised for the removal of the epoxy primer. Figure 6.25 illustrates the effect of the abrasive size on the specific abrasive consumption. For comparative cleaning rates (about $\dot{A} = 30 \text{ m}^2/\text{h}$), abrasive consumption was lowest for the smallest particle size and the lowest abrasive mass flow rate. Bullett and

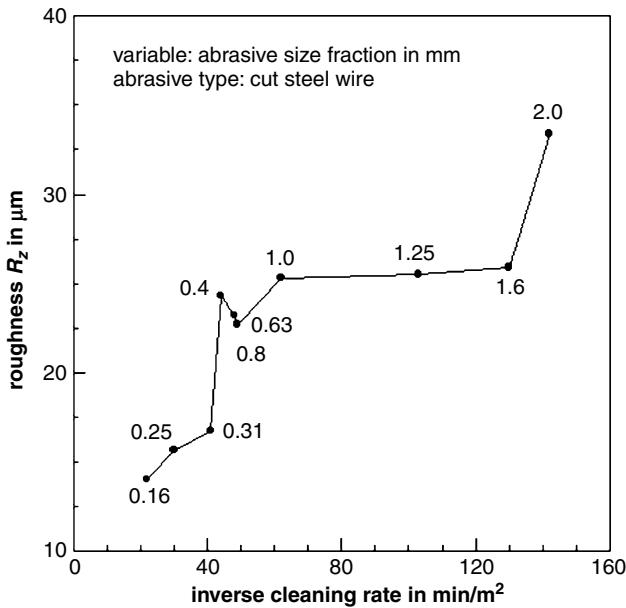


Fig. 6.23 Effects of final substrate roughness and abrasive particle size on inverse cleaning rate for mill scale (Neumann, 1976)

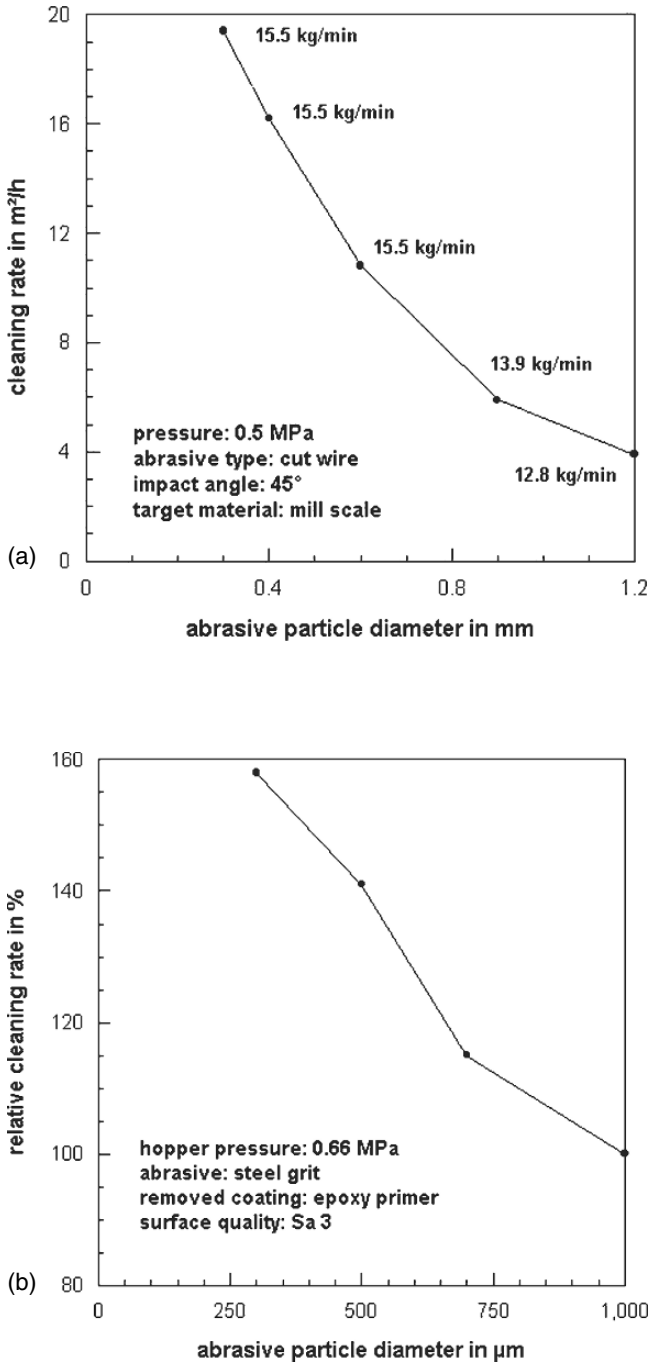


Fig. 6.24 Effect of abrasive particle size on cleaning rate. (a) Removal of mill scale (Remmelts, 1969); (b) Removal of epoxy primer (Bae et al., 2007)

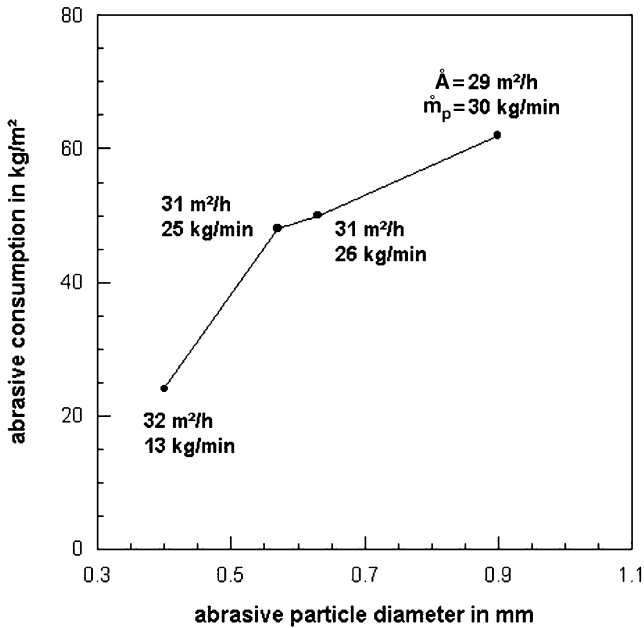


Fig. 6.25 Effects of abrasive particle size on specific abrasive consumption and cleaning rate (Hareux and Riac, 1986)

Dasgupta (1969) investigated the effect of abrasive size variation on the cleaning quality. They doped steel panels with ferrous sulphate and performed blast cleaning tests in order to remove this contaminant. Results of this study are displayed in Fig. 6.26 which reveals that a desired cleanliness (retained ferrous sulphate) could be achieved much earlier if smaller abrasive particles were utilised.

It seems, similar to the discussion in Sect. 6.3.3, that overlap and area coverage effects were important. Tosha and Iida (2001) have shown that the surface density of erosion dents in steel decreased with an increase in abrasive size according to a d_p^{-2} -relationship. Therefore, smaller particles guaranteed a closer coverage of the eroded surface. Smaller abrasive particle diameters also reduce the time where full area coverage starts [see (3.40)]. These findings support the recommendation in the SSPC Surface Preparation Commentary: “*Decreasing abrasive particle size can dramatically increase cleaning rate. The general rule is to use the smallest size abrasive that will do the job.*” Larger abrasive particle size may be beneficial for the removal of heavy coatings and scale.

Results of solid particle erosion tests on polymers and rubber are displayed in Fig. 6.27. Such stationary tests deliver different trends than cleaning tests with moving nozzles, because area coverage and overlap effects are not considered. The curves displayed in Fig. 6.27 can be subdivided into two sections: a linear section and a saturation section, whose locations depended on target material. On polyurethane, for example, the linear section was short, and there was some trend that a further increase in abrasive size would reduce erosion rate, similar to the situations shown in Fig. 6.24.

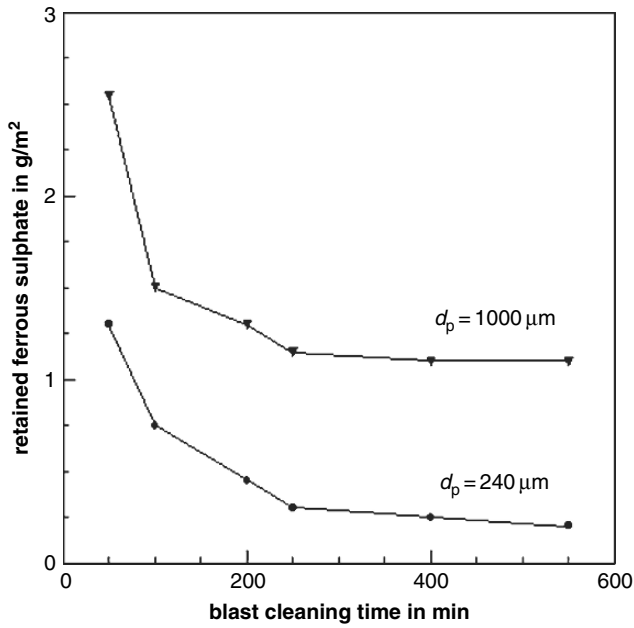


Fig. 6.26 Effect of abrasive particle size on substrate cleanliness (Bullett and Dasgupta, 1969)

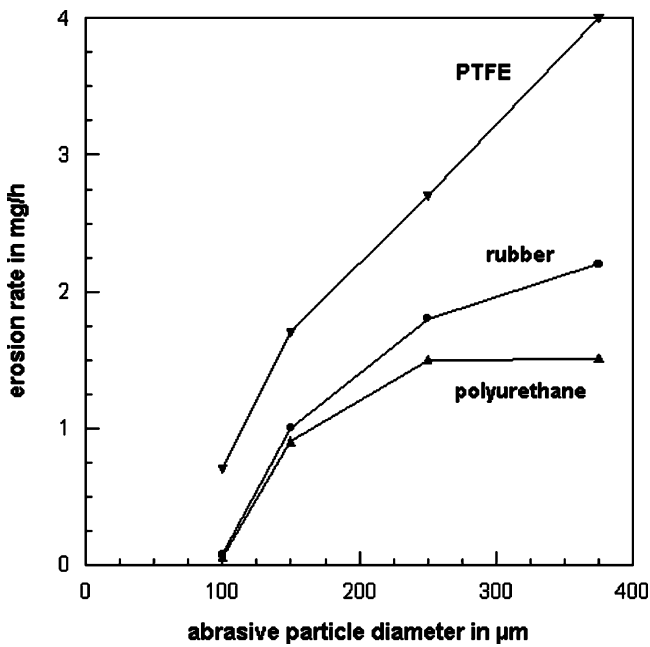


Fig. 6.27 Effect of abrasive particle size on the erosion of organic coatings (Zhang et al., 1995)

For the slurry erosion of fusion-bonded epoxy powder coatings, Luo et al. (2001) recorded two threshold particle diameters, a lower value ($d_p = 80 \mu\text{m}$) and an upper value ($d_p = 410 \mu\text{m}$), which enveloped the linear section. Beyond these two values, any notable particle size effects vanished. In the linear section, erosion rate increased linearly with increasing particle diameter. The reason for this relation was the higher kinetic energy of the larger particles as expressed by $E_p \propto d_p^{2.5}$. (Particle size affects abrasive particle velocity, which leads to a power exponent different from 3.) On the other hand, the number of impinging particles reduces with an increase in the particle diameter (see Sect. 2.6). In addition, abrasive particle velocity decreased if particle diameter increased, especially for low mass flow ratios abrasive/air (see Sect. 3.6.3). These effects became more important in the second range. In this range, the progress of the function dropped because of the reduced impact frequency and the reduced particle velocity. The optimum balance between the kinetic energy of a single abrasive grain and the number of impacting particles was exceeded.

The relationship between erosion rate and abrasive particle diameter can be approximated with a simple power law as:

$$E_R \propto d_p^{\theta_p} \quad (6.23b)$$

with $\theta_p > 0$.

In contrast to (6.23a), the power exponent has values larger than zero. If only the fundamental local material removal process is being considered, θ_p has always positive values. If, however, the cleaning process with a moving nozzle and notable particle interactions is considered, the condition $\theta_p < 0$ holds [see Fig. 6.24 and (6.23a)]. For rubber, the power exponent depends on the fatigue-function parameter: $\theta_p = \beta_F - 1$ (see Sect. 5.7.4 for the fatigue parameter β_F). Depth of both cracked layers and crack separation distance in eroded rubber surfaces increased nearly linearly with increasing particle diameter (Arnold and Hutchings, 1993). For polymers, values for the power exponent in (6.23) were between $\theta_p = 1.0$ and 2.0 (Zhang et al., 1995).

If the complete removal process, including overlap and superposition effects, is considered, values for θ_p may become negative as illustrated in Figs. 6.19a and 6.24 for mill-scale removal and coating removal applications.

Some other aspects that determine the influence of the abrasive particle diameter on the blast cleaning process are the higher impact fracture probability of larger grains (see Sect. 2.2.2) and the relationship between grain size and grain shape (see Sect. 2.3).

Bullett and Dasgupta (1969) investigated the effect of the abrasive particle size on the cleaning intensity. They contaminated rusty steel samples with a layer of ferrous sulphate and blast cleaned the samples with steel grit of two different abrasive sizes: a fine-grained abrasive ($d_p = 240 \mu\text{m}$) and a coarse-grained abrasive ($d_p = 1,000 \mu\text{m}$). The cleaning intensity was assessed based on the amount of retained ferrous sulphate after a given cleaning time. The results revealed that the application of the fine-grained abrasive materials led to much lower amounts of

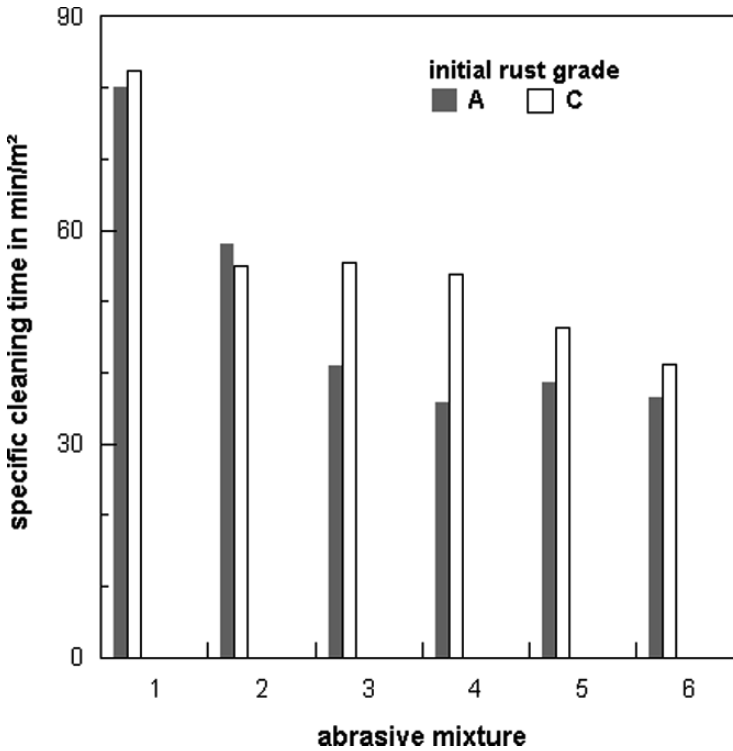


Fig. 6.28 Effects of abrasive mixture and initial cleaning condition on specific cleaning time (Neumann, 1976)

ferrous sulphate at all cleaning time levels. Therefore, an abrasive mixture with a high amount of small particles could guarantee a more thoroughly cleaned substrate.

The effect of abrasive working mixture on the cleaning of steel panels covered with mill scale (grade A), respectively rust (grade C), is illustrated in Fig. 6.28. The mixtures had different particle size class portions. The abrasive mixture “1” (coarse mixture, no grains smaller than $d_p = 315 \mu\text{m}$) could remove mill scale and rust with an equal efficiency, whereas the results for abrasive mixture “4” (medium mixture; no grains larger than $d_p = 1,250 \mu\text{m}$, no grains smaller than $d_p = 315 \mu\text{m}$) showed notable differences in the cleaning rates for the two types of oxide.

Safar (1973) defined a critical abrasive mass required for a complete coverage of the surface with erosion pits. For wheel-driven blasting machines, this critical abrasive mass can be approximated with the following relationship:

$$m_G = 2.09 \cdot \rho_p \cdot \left(\frac{d_p}{d_e} \right)^2 \cdot d_p \quad (6.24)$$

This equation should be applied to even surfaces only. It can be seen that the critical mass has a cubic relationship to the abrasive particle size. Table 6.8 lists

Table 6.8 Critical abrasive mass values for complete specimen coverage (Safar, 1973)

Target material	Abrasive diameter in mm			
	1.3	1.8	2.4	3.4
	Critical abrasive mass in kg/m ²			
Cast iron	143	198	265	375
Bronze	113	157	209	296
Carbon steel	107	148	198	281
Alloyed steel	102	141	189	266
Highly alloyed steel	121	167	224	317

experimental results, showing the effects of abrasive particle diameter and target material.

Peltzer (1955) gave some recommendations about the abrasive size for effective removal of mill scale (see Sect. 5.6.3) and cast sand from castings. Some of his recommendations are listed in Table 6.9.

6.4.4 Effects of Abrasive Particle Shape

Figures 6.29–6.31 show the effect of abrasive shape on the removal of organic coatings. Figure 6.29 deals with the removal of baking enamel from different metal substrates. The use of spherical steel particles led to lower cleaning rates compared with the angular grit particles. This effect was most pronounced for the aluminium substrate, where grit particles (angular shape) were much more efficient than shot particles (rounded shape). For a stainless steel substrate, in contrast, particle shape did not affect the coating removal efficiency. Figure 6.30 illustrates some effects of coating composition. All coatings were more sensitive to the impingement of steel balls compared to the impingement of a cone-shaped particle. It can also be seen that the size of the ball played an additional role. Figure 6.31 shows the effects of particle shape and target material hardness. Grit particles were more effective at both target hardness levels, although the differences in specific volume loss were sensitive to the target material hardness. For the lower target hardness value, particle shape had a pronounced influence on the specific volume loss, whereas only a weak effect was found for the higher target hardness value. Irregular particles may, therefore, be recommended for the removal of rather soft materials. For rubber, impinged at

Table 6.9 Particle size recommendations for the removal of cast sand from castings (Peltzer, 1955)

Casting type	Recommended abrasive size	
	Shot	Grit
Iron casting	S 550–S 320	G 16–G 40
Annealed casting	S 550–S 330	G 18–G 40
Steel casting	S 660–S 390	G 14–G 25

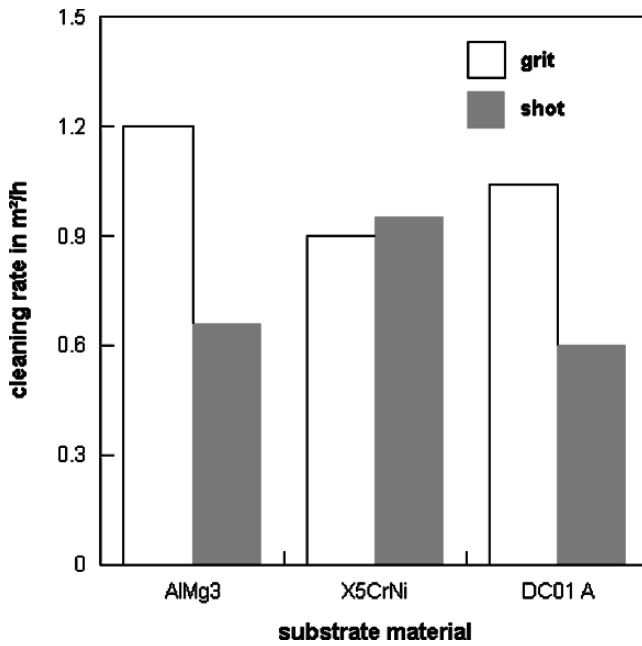


Fig. 6.29 Effect of particle shape on the cleaning rate for baked enamel (Uhlmann et al., 2003)

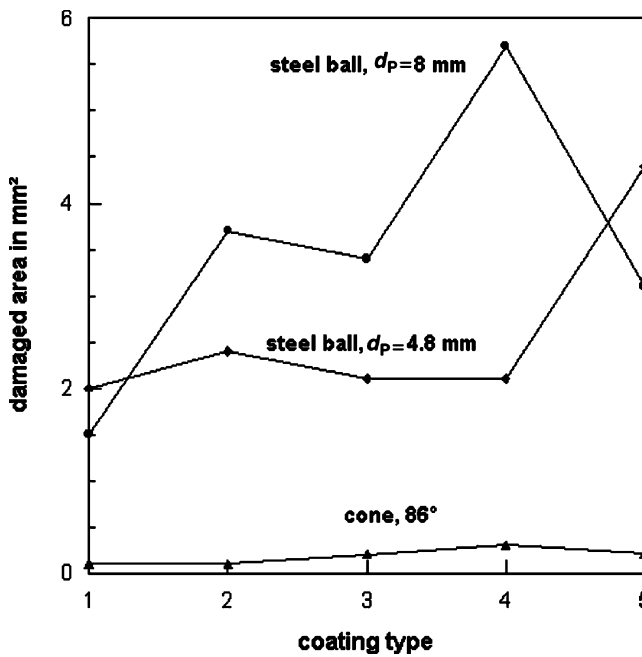


Fig. 6.30 Effect of particle shape on the damage size in different coating types (Breinsberger and Koppelman, 1982). Coating types: 1-DFT = $72 \mu\text{m}$, $150/140^\circ\text{C}$; 2-DFT = $77 \mu\text{m}$, $120/140^\circ\text{C}$; 3-DFT = $78 \mu\text{m}$, $160/140^\circ\text{C}$; 4-DFT = $78 \mu\text{m}$, $160/140^\circ\text{C}$; 5-DFT = $80 \mu\text{m}$, $160/140^\circ\text{C}$

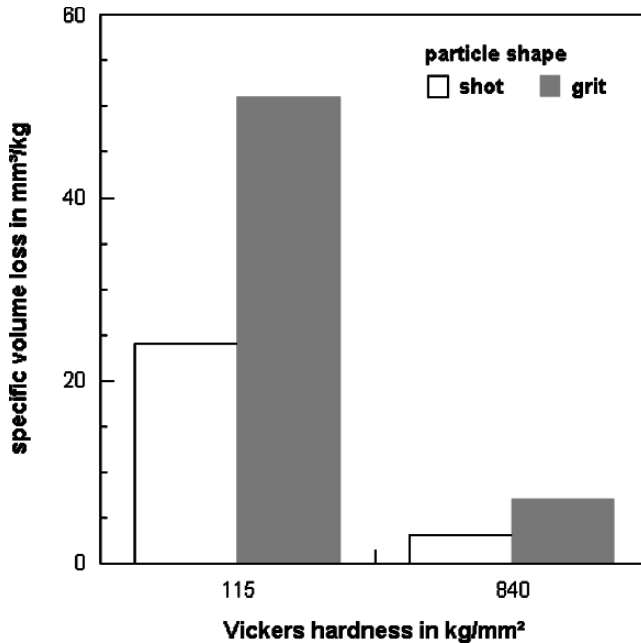


Fig. 6.31 Effects of particle shape and target material hardness on the specific volume loss in steel targets (Wellinger and Uetz, 1955)

oblique impact angles, erosion rate increased substantially for more angular particles (Arnold and Hutchings, 1992).

Basically, these findings support the recommendation given in the SSPC Surface Preparation Commentary: “*Rounded particles are most effective in removing brittle coatings such as mill scale, whereas angular shaped particles are more effective in removing softer coatings such as rust and paint.*”

Systematic studies in the field of solid particle erosion have shown that the abrasive grain shape had an important influence on the material removal regime. Bahadur and Badruddin (1990) related the particle shape influence to the different removal mechanisms, such as micro-cutting for angular particles and micro-ploughing for spherical particles. Cousens and Hutchings (1983) showed that the usually used terms ‘ductile’ and ‘brittle’ behaviour are determined by the abrasive grain shape.

Abrasive particle shape also effects the acceleration of the particles in the blast nozzle (see Sect. 3.6.4). Grit particles tend to have higher velocities than shot particles.

6.4.5 Effects of Abrasive Material Hardness

From investigations of abrasion and solid particle erosion is known that a “transition stage” exists at the point of comparable hardness of abrasive material and target material (Wellinger and Uetz, 1955; Uetz, 1986):

$$\frac{H_M}{H_P} \rightarrow 1.0 \text{ to } 1.5 \tag{6.25}$$

In this region, erosive material removal processes are very sensitive to changes in the relative hardness. Figure 6.32 illustrates these relationships. For the substrate with the high hardness ($H_M = 440 \text{ kg/mm}^2$), the specific mass loss exhibited a high increase if the abrasive hardness exceeded a value of $H_P = 500 \text{ kg/mm}^2$. The corresponding hardness ratio was about $H_M/H_P = 0.9$, which agrees very well with (6.25). For the substrate with the lowest hardness, the progress of the function dropped with an increase in the abrasive material hardness. Beyond a critical hardness ratio between abrasive and target material (at about $H_P/H_M = 2.4$), the progresses of the functions exhibited a steep decrease. Any further increase in the abrasive hardness would not substantially improve the material removal performance. A general rule in the SSPC Surface Preparation Commentary is: “*Select the minimum abrasive hardness that will effectively do the job.*”

Figure 6.33 illustrates the effects of abrasive material hardness on the erosion of rubber. In contrast to Fig. 6.32, there is no unique trend visible in the graph. The maximum specific volume loss occurred at rather low abrasive hardness values ($H_P = 500\text{--}900 \text{ kg/mm}^2$) and not, as could have been expected, at the highest value for the abrasive material hardness. These relationships were contributed to abrasive particle shape effects. The glass and flint particles were characterised by pronounced edges, and they basically removed material due to micro-cutting. For rubber, as a soft material, this erosion mode contributed to high levels of material

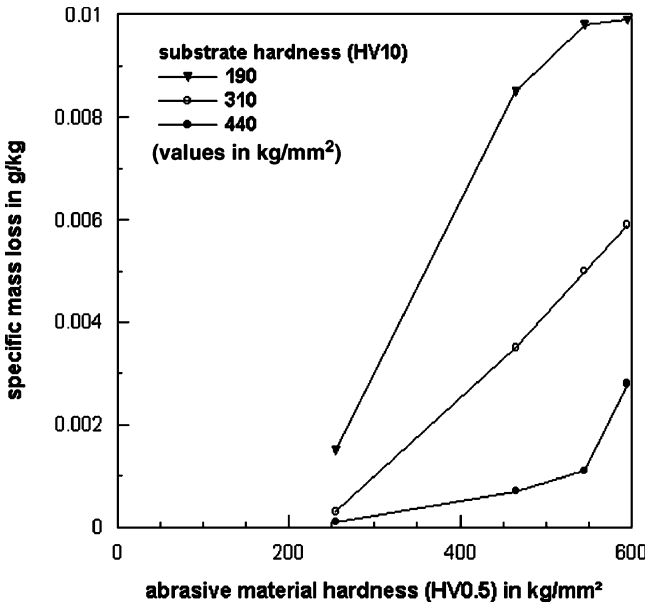


Fig. 6.32 Effect of abrasive material hardness on specific mass removal (Wellinger and Gommel, 1967). Process parameters: abrasive type: cut steel wire; $d_p = 400 \mu\text{m}$; $v_p = 70 \text{ m/s}$

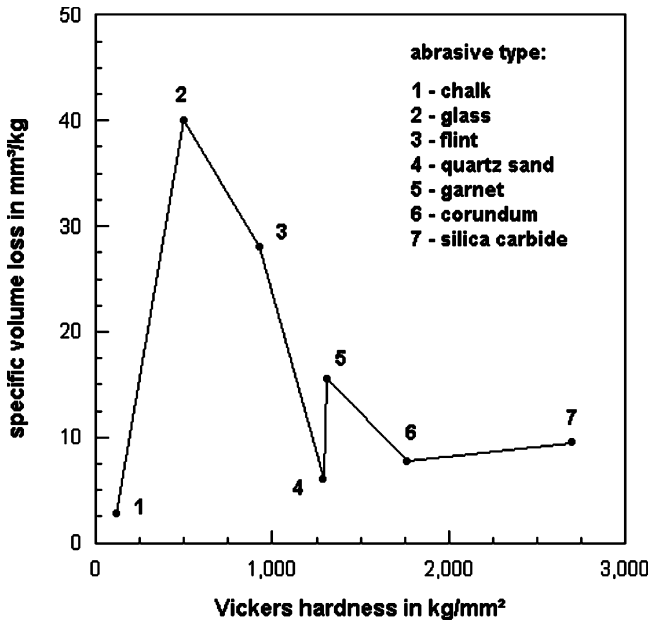


Fig. 6.33 Effect of abrasive material hardness on specific volume loss in rubber (Wellinger and Uetz, 1955)

removal. Particle shape was, therefore, much more important to the rubber material than abrasive material hardness.

Wellinger et al. (1962) investigated the effects of tensile strength of abrasive materials (cut steel wire) on the specific material loss of steel target and found a relationship very similar to that shown in Fig. 6.32. The authors found that the influence of the abrasive material tensile strength vanished for very high values of target material hardness.

6.5 Removal Models

Rosenberger (1939) probably provided the first, simple material removal model for blast cleaning processes whereby the material removal due to the impingement of an individual abrasive particle was considered a machining process.

Fokke (1999) developed a model for the estimation of the cleaning efficiency for the removal of organic coatings from steel substrates due to blast cleaning. The model is based on a geometric description of the coating area removed during the impingement of an individual abrasive particle. Fokke (1999) obtained this area due to precise surveys of impact craters.

For a chosen kinetic energy of a particle (see Sect. 2.6.2 for additional information), a minimum number of particles, which is required to erode an impacted area of 1 m^2 , can be computed as follows:

$$N_{P\min} = \frac{1}{\varepsilon_M \cdot E_P} \quad (6.26)$$

The number is a minimum because its establishment assumes that the impact areas of all particles do not overlap. The physical unit of the minimum number is m^{-2} . The parameter ε_M was experimentally estimated by Fokke (1999); an example is provided in Fig. 6.6. Typical values were between $\varepsilon_M = 2.6 \times 10^{-5}$ and $2.9 \times 10^{-5} m^2/J$; they depended on coating hardness and abrasive particle size. A dimensional analysis of the size of craters formed in the coating as a result of particle impingement delivered the following relationship:

$$\frac{V_C}{d_p^3} = \psi_M \cdot \left(\frac{E_P}{H_M \cdot d_p^3} \right)^{1.5} \quad (6.27)$$

The parameter ψ_M is a dimensionless scaling parameter. For a given coating material (given coating hardness), this relationship can be simplified as follows:

$$V_C = \psi_N \cdot E_P^{1.5} \cdot d_p^{1.5} \quad (6.28)$$

The parameter ψ_N is an empirical parameter with the unit ($m^{4.5}/J^{1.5}$). If the abrasive particle size is known, values for ψ_N can be estimated due to linear regressions of experimental results as presented in Fig. 6.6. When a number of particles each remove a volume V_C from $1 m^2$ of substrate, the coating layer is reduced by an average thickness Δh_C , the total number of impacts required to totally remove the coating down to the substrate, reads as follows:

$$N_P \cdot N_{P\min} = \frac{n_C}{V_C} \quad (6.29)$$

For a given particle diameter, the number of particles impinging a given area depends on abrasive mass flow rate and traverse speed. The traverse speed can be expressed by the cleaning rate because this parameter is nothing else than an area traversed during a given time period. This reflection leads to the following equation:

$$\dot{A} = \frac{\dot{m}_P}{N_P \cdot N_{P\min} \cdot V_P \cdot \rho_C} \quad (6.30)$$

The linear relationship between cleaning rate and abrasive mass flow rate corresponds well with the results provided in Sect. 6.4.1 for small and moderate abrasive mass flow rates. The inverse relationship between cleaning rate and abrasive particle size also verifies experimental results obtained on mill scale and soft coatings (see Sect. 6.4.3). It is also conclusive that cleaning rate may reduce for coating materials with higher density values.

Uferer (1992) derived an empirical model for the removal of mill scale and rust from steel substrates. The final equation reads as follows:

Table 6.10 Constants for the model of Kambham et al. (2006)

Constant	<i>a</i>	<i>b</i>	<i>c</i>	<i>d</i>	<i>e</i>	<i>f</i>
Value for rusted panels	-129.40	9,405.97	2,943.53	-235,051.25	-12,593.40	-16,946.26
Value for painted panels	542.45	-67,478.23	-806.87	3,532,289.80	10,379.03	-145,564.76

Table 6.11 Variable range for the model of Kambham et al. (2006)

Variable	Unit	Range
Air pressure	psi	80–120
Abrasive mass flow rate	lbs/min	8–26

$$A_S = \frac{\dot{A}}{\dot{m}_p} = (K_0 \cdot K_1 \cdot \dot{m}_p - a_0 \cdot K_1^2 \cdot \dot{m}_p^2) \cdot f_p \cdot f_N \cdot f_X \cdot f_\phi \quad (6.31)$$

The parameter A_S is the specific cleaning rate in m^2/kg ; it is actually the inverse version of (6.5). Values for the parameter constants f_N , f_X and f_ϕ are provided in Tables 6.3–6.5. The constants K_0 , K_1 and α_0 must be established due to a standard blast cleaning test. Uferer (1992) recommended the following parameter configuration for such a standard test: $p = 0.25$ MPa, $x = 50$ cm and $\phi = 90^\circ$.

Kambham et al. (2006) issued a model for the removal of rust and coatings from steel substrates due to dry blast cleaning. The model is based on regression statistics. The authors performed numerous blast cleaning trials and applied a standard data-fit method. The final equation reads as follows:

$$\dot{A} = a + \frac{b}{p} + \frac{c}{\dot{m}_p} + \frac{d}{p^2} + \frac{e}{\dot{m}_p^2} + \frac{f}{p \cdot \dot{m}_p} \quad (6.32)$$

The cleaning rate is given in ft^2/h . The regression parameters a to f for the two removal modes “rust” and “coating” are listed in Table 6.10. Table 6.11 lists the parameter ranges for the two process variables. Because the regression coefficients are in the range of about 0.6 only, the use of the model may be restricted to the determination of qualitative trends only. Another limit of the model is its restriction to coal slag as an abrasive material.

6.6 Efficiency of Blast Cleaning

6.6.1 Erosion Efficiency

The efficiency of the erosion process is difficult to evaluate. Following Thiruvengadam’s (1967) erosion resistance model (which is, rigorously taken, valid

for liquid drop impact), a probable approach involves the strain energy density defined in (5.2). This parameter characterises the amount of energy stored in a stressed volume. If this parameter is being related to the specific material removal energy, the efficiency can be approximated as follows:

$$\Phi_E = \frac{E_{SD}}{E_{sp}} \cdot 100 \quad (6.33)$$

The specific energy is given through E_P/V_M . From Fig. 6.6, respectively (6.11), one obtains $E_{sp} \propto E_P^{-1/2}$. A particle with a kinetic energy of 10 mJ removes a paint volume of 10^{-11} m^3 (see Fig. 6.6), which results in a specific energy of $E_{sp} = 10^3 \text{ MJ/m}^3$. A typical value for the elastic strain energy density of an organic paint is $E_{SD} = 5 \text{ MJ/m}^3$ from Table 5.6. For these numbers, (6.33) delivers a material removal efficiency of $\Phi_E = 0.5\%$. If additional energy dissipation due to plastic deformations is assumed, an erosion efficiency of about 1% is an approximate value. This order of magnitude corresponds with results from calculations for hydro-abrasive erosion of steel (Momber et al., 1996). Mineral grinding processes also have a mechanical efficiency in the range of one percent only (Schubert, 1988).

6.6.2 General Aspects of Process Efficiency

Numerous factors affect the efficiency of blast cleaning processes. Experience show that the most important factors are the following:

- (1) existing coating type, adhesion and condition;
- (2) substrate material properties;
- (3) experience and organisation of the working crew;
- (4) geometry and accessibility of the objects.

The aspects (1) and (2) are considered for shipyard operations in a benchmarking report (Appleman et al., 1998).

The criterion “existing coatings” is treated in terms of “type of surface” and “coating hardness”, whereas the latter term basically characterises the resistance of the coatings against the action of impinging abrasive particles during blast cleaning. In terms of “type of surface”, four categories are being distinguished:

- Light rust, light mill scale or loose paint: This is a deteriorated surface which requires little effort to clean.
- Tight rust or tight mill scale: This is new structural steel from the mill.
- Thin paint or rusted thin paint: This is previously coated steel plate where the coating thickness is in the range of $DFT = 120$ to $175 \mu\text{m}$.
- Thick paint, heavy mill scale, or heavily pitted rust: This can be steel plate where the coating thickness in the range of, or greater than, $DFT = 200$ to $250 \mu\text{m}$.

In terms of “coating hardness”, the report distinguished between the following three categories:

- hard coatings: typically chemically cured coatings (epoxy, urethane, zinc-filled coatings);
- soft coatings: typically a more readily deformed surface (alkyd, latex, chlorinated rubber);
- no coating: new mill scale bearing steel.

Numerous remarks on the effects of mechanical properties of coatings on the erosion process are delivered in Chap. 5.8. A further example is shown in Fig. 6.34. The graph illustrates the effect of the target material (e.g. metallic coating) on the specific erosion. It can be seen that specific erosion increased notably in the range of low hardness values. If the hardness was rather high, it did not affect the erosion process. These results correspond to the relationships discussed in Sect. 6.4.5. An additional point of interest, however, is the effect of the air pressure on the erosion of the target material. Pressure effects were very pronounced in the range of low hardness values. However, for higher values of target hardness ($H_M > 700 \text{ kg/mm}^2$), the gain of the higher pressure seemed to vanish.

The aspect (3) is illustrated in ISO 12944-4, which states the following: “*Personnel carrying out surface preparation work shall have... sufficient technical knowledge of the processes involved.*” This includes knowledge about the equipment being used, the basic principles of blast cleaning and the effects of major process parameters. Health and safety training is another important issue of personnel qualification. Experience shows that trained blasters can outperform untrained blasters by a factor

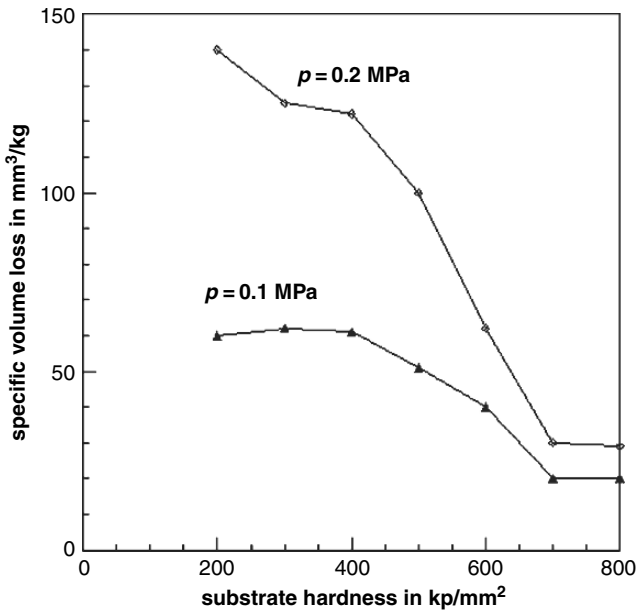


Fig. 6.34 Effect of substrate hardness and air pressure on specific volume loss in metal (Gommel, 1967a)

of about two. Training and qualification counts even more if high-level surface preparation operations are being performed, which would include, among others, the treatment of stainless steel, tank coating surface preparation, or the preparation of substrates for metal-sprayed coatings.

Regarding aspect (4), a detailed investigation has shown that accessibility can dramatically affect efficiency as well as quality of blast cleaning. For steel bridge structures with delicate geometry, only 25–30% of the interior limited access surface could be cleaned by blast cleaning. Also, profile depth was only 85% of the values generated during normal blast cleaning procedures (Bullard et al., 2002). Some results are listed in Table 6.12. Based on the data, blast cleaning inside gap widths of 0.3–0.6 cm on 10-cm-deep back-to-back angles did not reach approximately 50–75% of the total angle depth. That is, only 25–50% of the interior surface was being cleaned. For 5-cm-deep back-to-back angles, 25–50% remained uncleaned, while 50–75% was prepared. Blast cleaning penetration increased when gaps were 1.2 cm and wider, but was also somewhat dependent on angle depth. Cleaning rate also depends on work location. Examples from the ship building industry are listed in Table 6.13. It can be seen that cleaning rate can drop up to 75% for very complex structural shapes.

6.6.3 Aspects of Site Management

Site management has a notable effect on efficiency especially if site environment is not a stable factor in blast cleaning. Here, experience is again an issue. However, other problems are of importance as well, namely the following (related basically to external site applications):

- Work delay occurs while operators are waiting for broken equipment to be repaired.
- Preventive maintenance is being performed during the blast shift and subsequently displaces operators who would be blasting regularly.
- Relocating a compressor or a blast machine is often a timely process. The technician must evaluate the desired location of the unit, search for a suitable power source and obtain the connecting cables before work can continue. Hose lines must also be replaced.

Table 6.12 Abrasive blast penetration at typical difficult-to-access areas (Bullard et al., 2002)

Gap width in cm	Depth cleaned in cm		Area cleaned in %	
	10 cm angle	5 cm angle	10 cm angle	5 cm angle
0.31	2.38	2.40	24	48
0.66	4.60	3.50	46	70
1.25	4.48	5.00	45	100
1.88	9.15	5.00	92	100
2.50	9.63	5.00	96	100

Table 6.13 Cleaning rates modifications due to work location in the ship building industry (NSRP, 1998b)

Location	Relative cleaning rate in %
Hull section; easily reached	100
Complex steel shape; less than 8.25 m elevation	75
Hull section; 8.6–25 m high	75
Complex steel; 8.6–25 m high	75
Hull section; 26–50 m high	50
Complex steel; 26–50 m high	50
Interior tank spaces; little structural steel	50
Interior tank spaces; complex structural shapes	25

- Electrical outages and power supply problems disrupt entire teams during operation. When electrical services on the site are interrupted, qualified technicians must be utilised to restart the units.
- Lack of hose management causes significant delay time, especially if long distances between compressor and blast machine, respectively between blast machine and nozzle, need to be bridged.
- Dressing and inspecting personal protective equipment is a time-consuming function of the manual operator.
- Cranes are often unable to make lifts at night due to poor lighting. Therefore, compressors, abrasive hoppers and other equipment cannot be moved at appropriate speed.

6.6.4 Aspects of Operators' Fatigue

A further aspect that affects efficiency is operator fatigue, especially if the equipment is run manually. Typical problems associated with fatigue can be summarised as follows:

- The grit hoses are supported partly by the operator as he works. Both the weight of the hose and the pull from horizontal friction increase the fatigue. Fatigue increases if hose diameter increases. Wipe hoses are, therefore, frequently used.
- The weight of the nozzle is fatiguing to the operator; this weight is completely supported by the arms and neck of the operator.
- In order to reach surfaces behind obstructions, an operator is forced to position his nozzle in awkward angles. This strain is magnified if the operator stands in a basket on a high-reach.
- While blasting overhead in areas with low clearance, the operator is often forced to a squatting position to blast; this directs forces to the knees.
- Working in overhead areas with tall clearances, the operators are often forced to reach overhead with the nozzle to make contact with the surface. This compounds forces in the elbows and shoulders.
- Operators are often uncomfortable due to dust.

- Operators are often uncomfortable due to cumbersome personal protective equipment.
- Operators often have their vision obstructed by dirty safety glasses.
- Operators often have their vision impaired by poor lighting at night.
- Operators often do not practice sound ergonomic principles as they confirm their duties.
- Operator's efficiency decreases in productivity as their shift progresses. Even after standard breaks, production at the end of the shift is significantly less than at the beginning.

A major conclusion drawn from these observations is the performance of ergonomic training (which may be done by contractors) and the development of ergonomic support devices (which may be done by manufacturers).

Fatigue due to the jet flow reaction force can be approximated as follows:

$$F_R = \dot{m}_A \cdot v_A + \dot{m}_P \cdot v_P \quad (6.34)$$

It can be seen that an efficient nozzle, which delivers high exit velocities for air and abrasive particles, is associated with an increase in fatigue. The same is true for the use of large-diameter nozzles, which allow for high air and abrasive mass flow rates. If typical values from Chap. 2.6 are taken ($\dot{m}_A = 10$ kg/min, $\dot{m}_P = 15$ kg/min, $v_A = 500$ m/s and $v_P = 180$ m/s), a corresponding reaction force of $F_R = 130$ N can be calculated. The reaction forces generated by a blast cleaning nozzle flow were measured by Kline et al. (1988) for different nozzle designs, and values between $F_R = 49$ and 67 N were estimated experimentally. These results are notably lower than the calculated value, which is most probably due to impulse losses during the acceleration process and the flow of the jet through the surrounding air. Therefore, (6.34) delivers rather overestimated values in terms of reaction force assessment. Rosenberg et al. (2006) developed a biomechanical model for the approximation of hand forces and wrist moments. For blast cleaning with steel shot, they reported force values of $F_R = 26$ N at the hand, and moment values of 3 Nm at the wrist.

Critical, respectively permissible, reaction force values do not exist by law for blast cleaning applications. For hydroblasting applications, however, such permissible limits exist, and they may be applied for comparative purposes (Momber, 2003, 2005a). For the operation of hand-held water jet guns, the permissible limit is, for example, at $F_R = 150$ N, which is more than three times higher than the values measured for dry blast cleaning. Another parameter which helps to assess the severity of fatigue due to the jet flow reaction force is the weight of the operator. Experience from water jetting applications shows that a gun can be handled in a safe and efficient way if the reaction force of the jet does not exceed one-third of the weight force of the operator. The weight force of an operator (blaster) is simply:

$$F_W = 9.81 \cdot m_O \quad (6.35)$$

whereby the weight of the operator is given in kg. The fatigue condition is then:

$$\frac{F_W}{3} > F_R \tag{6.36}$$

The weight force of a 75-kg operator, for example, is $F_W = 735 \text{ N}$; one-third of this value is $F_R = 245 \text{ N}$, which again is much higher than typical values estimated for blast cleaning.

6.7 Weld Seam Cleaning

Experimental results of weld seam cleaning with different treatment methods were reported by Remmelts (1969) and Blomquist (1997). Some results are summarised in Table 6.14. It can be seen that the proper selection of the abrasive type can have a considerable effect on the cleaning rate. The cleaning rate was high for crystal grit and rather low for steel grit. Vacublast and manual grinding resulted in very low cleaning rates.

Remmelts (1969) investigated the effects of weld type, abrasive size and abrasive mass flow rate in more detail. Results of his study are provided in Table 6.15. The results verify the higher cleaning capability of non-metallic abrasive materials. Cleaning speed was higher and specific abrasive consumption was lower if copper slag was used instead of cut steel wire.

Table 6.14 Cleaning rates for weld seam cleaning (Blomquist, 1997)

Method	Weld seam length in m	Cleaning speed in m/min
Blast cleaning with steel grit	115	1.3
Blast cleaning with aluminium oxide	67	2.1
Blast cleaning with crystal grit	50	2.3
Manual grinding	14	0.03
Vacublast	4	0.93

Table 6.15 Cleaning speeds for weld seam cleaning (Remmelts, 1969). Parameters: $p = 0.5 \text{ MPa}$, $d_N = 10 \text{ mm}$, $x = 56 \text{ cm}$; ship plate (12 mm), arc welding

Type of weld	Abrasive type	Abrasive size in μm	Abrasive mass flow rate in kg/min	Cleaning speed in m/h	Abrasive consumption in kg/m
Butt weld	Cut wire	400	18.7	270	4.2
		900	16.4	135	7.3
Fillet weld (vertical)	Copper slag	900	5.7	180	1.9
	Cut wire	400	18.7	108	10.4
Fillet weld (flat)	Copper slag	400	8.9	126	4.3
	Cut wire	400	18.7	101	11.1
	Copper slag	400	8.9	119	4.5

6.8 Underwater Applications

Blast cleaning can be performed under submerged conditions. Typical applications would include the cleaning of steel piles prior thickness measurements, the cleaning of submerged constructions for inspections and the removal of rust and deteriorated coating systems. However, just a few systematic investigations about the efficiency of submerged blast cleaning applications have been performed. Donker (1985) and Donker and Richter, (1982, 1988) conducted a number of tests at water depths between 10 and 50 m with a special adapter in front of a standard blast cleaning nozzle. This adapter created an air shroud between nozzle exit and target surface. A special bypass-control avoided the penetration of water into the grit hose and kept the abrasive material dry. The experimental conditions are listed in Table 6.16, and results are provided in Table 6.17. The cleaning rate of up to $\dot{A} = 7 \text{ m}^2/\text{h}$ was high and comparable to cleaning rates for atmospheric blast cleaning. The authors found, however, that cleaning rate depended on initial surface condition (see Fig. 6.35a). The values for the specific abrasive consumption, provided in Fig. 6.35b, were notably higher than values for atmospheric blast cleaning, and they also depended on the initial condition. Tar epoxy was the most difficult to remove material.

A very special submerged application is “blast zincing” (Groot et al., 1982; Donker and Richter, 1988). In that application, zinc-coated abrasive particles are used as a blasting media, and the particles, either being embedded in the steel substrate or forming a protective layer on the steel surface, are considered to act as sacrificial anodes. The idea is illustrated in Fig. 6.36. Typical performance data for blast zincing is an efficiency of $\dot{A} = 3 \text{ m}^2/\text{h}$ and a specific abrasive consumption of $\dot{m}_S = 112 \text{ kg/m}^2$ (Donker and Richter, 1988).

Table 6.16 Experimental conditions for underwater blast cleaning tests for water depths up to 30 m (Donker and Richter, (1982))

Parameter	Value
Nozzle type	Laval nozzle
Nozzle diameter	10 mm
Grit hose diameter	32 mm
Air pressure	0.8 MPa
Air volumetric flow rate	10 m ³ /min
Abrasive type	Quartz sand
Abrasive size	1.0–2.0 mm
Abrasive mass flow rate	10 kg/min

Table 6.17 Results of underwater blast cleaning tests (Donker and Richter, 1982)

Parameter	Value
Cleaning rate	2–7 m ² /h
Maximum roughness	40 μm
Preparation grade	Sa 2 ^{1/2} and P Sa 2 ^{1/2}

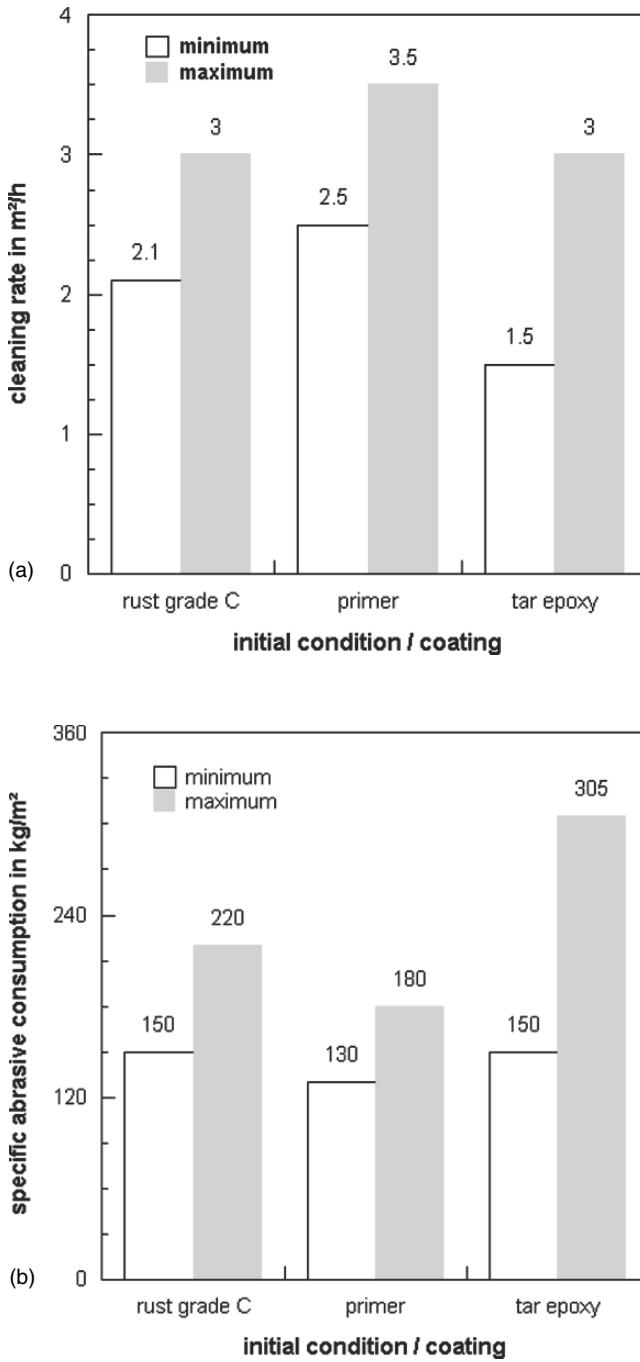


Fig. 6.35 Results of submerged blast cleaning tests (Donker and Richter, 1982); see Table 6.12 for the corresponding operation parameters. (a) Cleaning rate; (b) Specific abrasive consumption

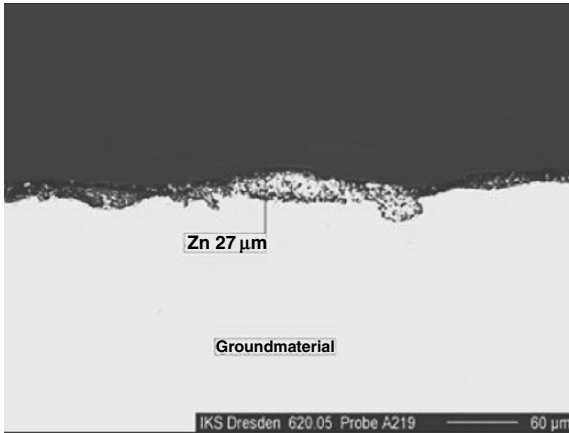


Fig. 6.36 Steel surface blasted with zinc-coated abrasives (Photograph: IKS Dresden)

6.9 Cost Aspects

Dry blast cleaning consumes a notable part of steel refurbishment budgets. A typical value for a 28,400m² project is 42% (Trotter, 2001). For comparison: paint supply cost = 22.1%; painting cost = 20.7% and scaffolding cost = 15.1%. Some cost features for a typical dry blast cleaning system are listed in Table 6.18.

Cost structures for blast cleaning processes are provided in Fig. 6.37. A general cost structure may include the following positions:

- investment air compressor;
- investment blast pot;
- investment hose lines;
- nozzle wear (see Sect. 4.6.2);
- fuel (or electricity, respectively);
- abrasive material (see Chap. 2);
- operators' wages.

The costs of blast cleaning per square metre (m²) can be calculated as follows:

$$C_{SP} = \frac{(60 \cdot \dot{m}_P \cdot C_P + C_E + C_{LB}) + (60 \cdot \dot{m}_P \cdot C_D + C_{EC} + C_{LC})}{\dot{A}} \quad (6.37)$$

This is a slightly modified version of an equation suggested by Holt and Austin, (2001). Here, the costs types C_E , C_{LB} , C_{EC} and C_{LC} are given in \$/h, whereas the costs types C_P and C_D are given in \$/kg. The abrasive mass flow rate must be given in kg/min. For given costs for labour, disposal, equipment and abrasive material, it is the abrasive mass flow rate makes the difference.

Table 6.18 Cost structures of various preparation methods (Anonymous, 2002)

Direct operating costs ^a	Preparation method	
	Blast cleaning (Sa 2) ^b	Robotic hydroblasting (HB 2) ^c
Labour		
Crew required	20	6
Labour cost per man/hour	20	40
labour cost/hour	400	240
Total in m ² /h	200	200
Hours spent per 10,000 m ²	50	50
Total labour cost	20,000	12,000
Consumables		
Grit cost and disposal coat/h	1,050	32
Fuel cost/h (machine)	117.5	48.80
Fuel cost/h (vacuum)	–	20
Fuel cost/h (filtration)	–	10
Jets cost/h	–	20
Wear cost (seals, nozzles, etc.)	–	10
Misc. filtration expenses cost/h	–	10
Hours spent per 10,000 m ²	50	50
Total consumables cost	58,360	7,444
Equipment use/maintenance		
Diesel engine cost/h	25	10
Smaller engine cost/h	–	7.50
Compressor cost/h	187.50	–
Hours spent per 10,000 m ²	50	50
Total engine maintenance cost	10,625	875
Total cost to clean 10,000 m ²	88,985	20,319
Cost per square metre	8.90	2.03

^aAll cost in US\$; grit consumption: 50 kg/m²

^bISO 8501-1

^cHydroblasting Standard, International Paint

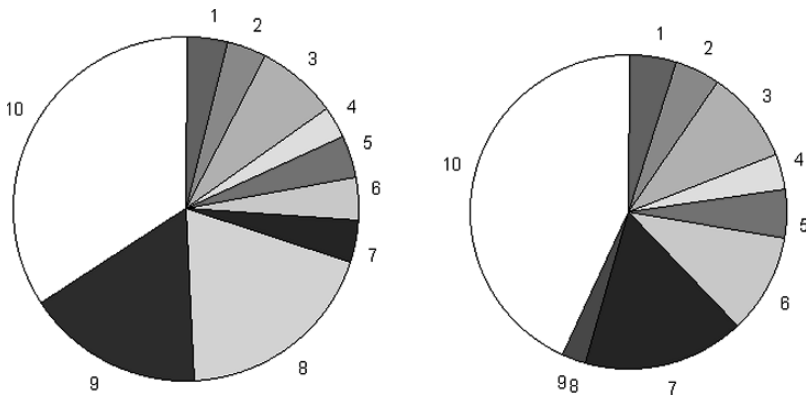


Fig. 6.37 Cost structure of a blast cleaning job (Lyras, 1991). Left: Conventional blast cleaning (1- primer, 2- small equipment, 3- vac truck, 4- compressors, 5- fuel, 6- equipment, 7- abrasive material, 8- disposal, 9- overhead, 10- total labor); Right: recyclable blast cleaning (1- primer, 2- small equipment, 3- vac truck, 4- compressors, 5- fuel, 6- equipment, 7- overhead, 8- abrasive material, 9- disposal, 10- total labor)

Table 6.19 Results of comparative cost calculations (Pi and Hoogstrate, 2007)

Parameter	Value	
	Traditional regime	“Optimal” regime
Initial nozzle diameter in mm	3.2	4.4
Nozzle lifetime in hours	300	78
Average cleaning rate in m ² /h	3.8	4.2
Number of used nozzles	1	3.46 (4)
Total working time in hours	300	270
Cost in /m ²	42.2	38.8
Total cost in	48,411	44,482

Pi and Hoogstrate (2007) developed an alternative cost calculation model which in particular considered effects of nozzle wear. These authors introduced the concept of an “*optimal exchange nozzle diameter*”. This parameter corresponds to the optimum lifetime of a blast cleaning nozzle. Results of calculations are provided in Table 6.19.

Chapter 7

Health, Safety and Environment

7.1 Safety Features of Blast Cleaning

7.1.1 General Safety Aspects

General aspects of health, safety and environment (HSE) for blast cleaning applications are summarised in Fig. 7.1. ISO 12944-4 states the following for surface preparation in general: “*All relevant health and safety regulation shall be observed.*” Blast cleaning owns an injury potential. General sources of danger to blast cleaning operators include the following:

- reactive forces generated by the exiting air-abrasive mixture (see Sect. 6.6.4);
- hose movements;
- uncontrolled escape of pressurised air;
- damaged parts being under pressure;
- dust and aerosol formation;
- sound emitted from equipment and blasting jet;
- impact from rebounding abrasive material and debris from the impact point.

It is generally recommended to carry out a risk assessment of the actual environment where a blast cleaning job will be done before starting the job. This risk assessment may include (French, 1998):

- how access is to be gained?
- is there a need for scaffolding?
- is there confined space?
- what is the surface like where the operators will have to stand?
- the availability of day light or artificial light;
- the presence of electrical supplies/equipment;
- nature of contaminate: Is it toxic? Is it a pathogen? Is it asbestos based? Is it harmful or corrosive?
- general layout that will allow visual contact between the blast cleaning team;
- permit requirements;

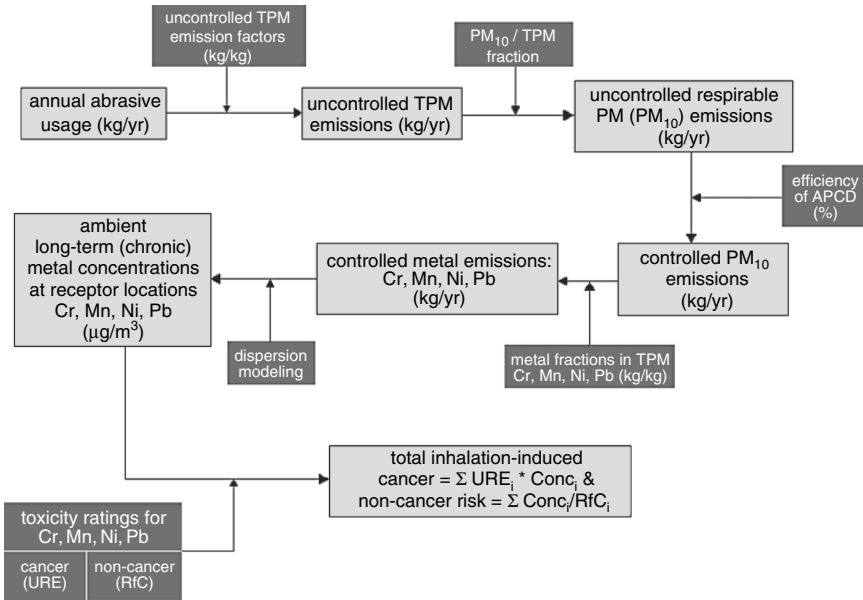


Fig. 7.1 HSE risk analysis for blast cleaning processes (Kura, 2005)

- safety of access (e.g. working on motorways or hazardous areas such as refinery where flameproof equipment and earthing to avoid static electricity may be required);
- who or what will be affected by flying debris?
- is noise a problem?
- will containment be necessary?
- where will the effluent go? (for wet blast cleaning and slurry blast cleaning)

In that context, ISO 12944-4 states the following: “*Personnel carrying out surface preparation work shall have suitable equipment and sufficient technical knowledge of the processes involved.*”

7.1.2 Risk of Explosion

Some source of explosion during blast cleaning can be electric discharge sparks. Safety hazard analyses identified that static electric charges occur in the following three circumstances:

- small particles flowing through piping;
- small particles passing through fine filters or nozzles;
- abrasive particles impinging fixed parts.

Table 7.1 Results of spark measurements during blast cleaning (Stuvex Belgium)

Parameter	Method	
	Dry blast cleaning	Wet blast cleaning
Voltage at the blast cleaned surface in V	500	2–3
Voltage of static electricity at the nozzle in V	5,000–10,000	0

Results of spark measurements performed on oil containers with dry blast and wet blast cleaning techniques are listed in Table 7.1. Dry blast cleaning generated high levels of voltage at the blast cleaned surface as well as at the nozzle. The use of wet blasting equipment helped to keep these levels low. Elbing (2002) reported about measurements of the electrostatic charging of steel during the blast cleaning with carbon dioxide pellets. The author measured values as high as 3,000 V, and he found that the discharge current increased with an increase in air pressure and stand-off distance. The discharge current was rather high for shallow impact angles, but reached a lower saturation level for impact angles $\varphi > 50^\circ$.

The electrostatic discharge in hose lines due to friction between hose wall and flowing abrasive particles can be managed through the use of blast cleaning hoses with low electric resistance. Values for the electrical resistance lower than of $10^3 \Omega/\text{m}$ are considered to allow a safe charge elimination (BGR 132, 2003).

The effects of impinging abrasive particles on the ignition of explosive gas mixtures are not well understood. Dittmar (1962) highlighted the fact that sparks must create a certain temperature field in order to ignite gas mixtures. Duration and intensity of the temperature field determine the danger of explosion. The author cited experimental results from machining operations, and he reported that the formation and subsequent combustion of small metal chips generated temperatures up to 2,300°C. These high temperatures were much more critical than the temperatures reached at the tool–chip interface during the material removal process (see Fig. 5.17 for the situation during blast cleaning). Smaller chips generated higher temperatures than larger chips. Dittmar (1962) also reported that rusted steel substrates were much more sensitive to spark generation compared with clean steel substrates.

7.2 Emission of Air Sound

There are four major sources of air sound generated during blast cleaning operations:

- sound emitted from the pressure generating unit (compressor, engine and power transmission);
- sound emitted from the abrasive air jet travelling through the air;
- sound emitted from the erosion site;
- sound emitted from accompanying trades.

Two other items of concern are noise generated by air supply in the helmet and sound attenuation of the helmet.

State-of-the-art air compressors are regularly equipped with sound insulating hoods or even placed in containers. Thus, the air sound emission is limited up to 70–75 dB(A). More critical is the air sound emitted by the jet. This noise is generated due to friction between the high-speed jet and the surrounding air as well as due to turbulences. Thus, the sound level depends on the relative velocity between jet and air, and on the surface exposed to friction. Consequently, air sound level increases as compressor pressure, nozzle diameter and stand-off distance increase. This is verified in Fig. 7.2 where the effect of the nozzle pressure on the noise level is shown. The noise level increased almost linearly with increasing air pressure. Equal trends have been reported for the noise emitted during dry blast cleaning with carbon dioxide pellets (Elbing, 2002).

Fig. 7.3 illustrates results of measurements performed at different blasting sites, where dry blast cleaning, shot blast cleaning and wet blast cleaning were applied. Figure 7.3a includes results from measurements at a dry blast cleaning site. The actual blast cleaning application generated the highest noise levels. Figure 7.3b and d shows results from measurements at wet blast cleaning sites. The noise generated during the actual wet blast cleaning application was lower than the noise level measured for the dry blast cleaning in Fig. 7.3a. Figure 7.3c contains results from measurements at a shot blast cleaning site. The noise level was again lower than the noise level for the dry blast cleaning process mentioned in Fig. 7.3a, which was due to the facts that no air was involved in the mechanically driven shot blast cleaning process, and that the blast cleaning head was sealed. It can be recognised that

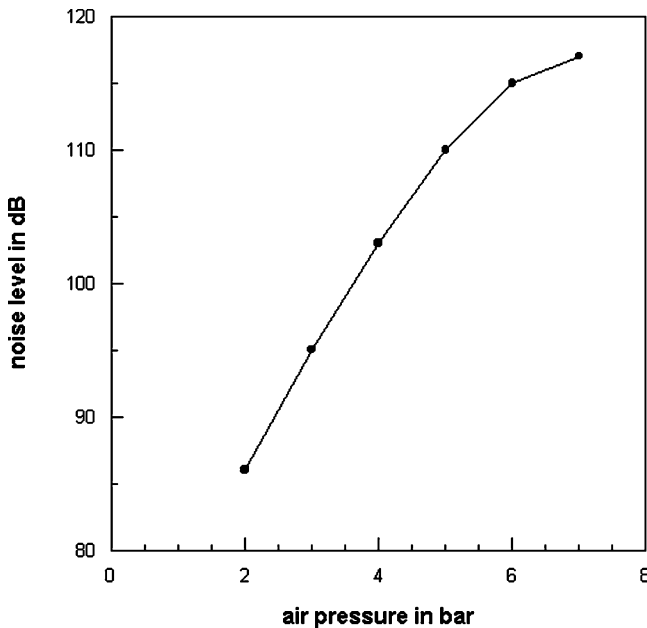


Fig. 7.2 Effect of compressor pressure on noise level (Schaffner, 1997)

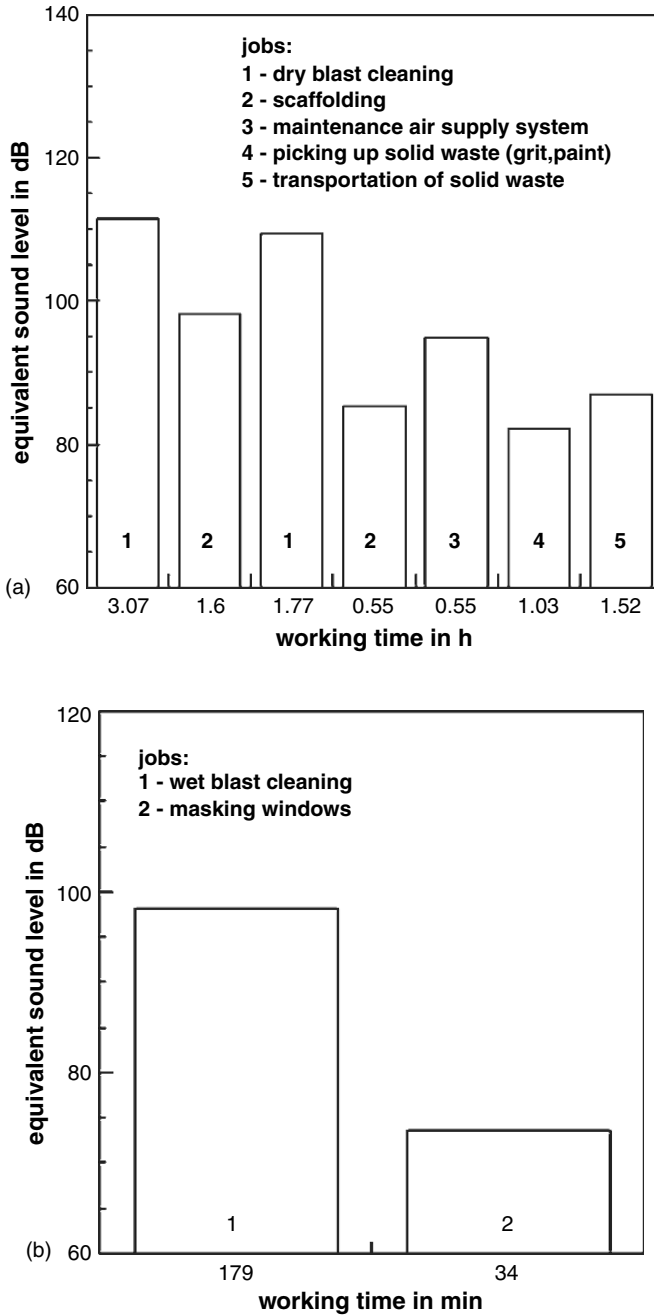


Fig. 7.3 Results from noise-level measurements during steel surface preparation jobs (Knipfer and Funke, 1997). (a) Dry blast cleaning; (b) Wet blast cleaning; (c) Shot blast cleaning; (d) Wet blast cleaning

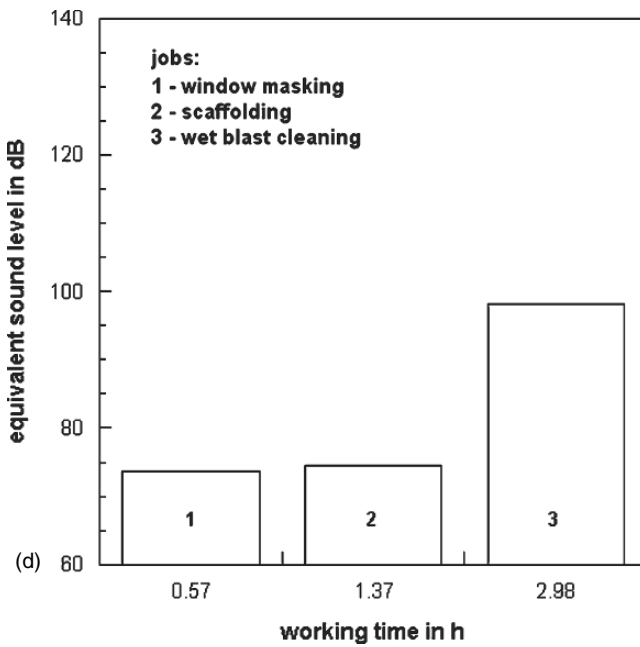
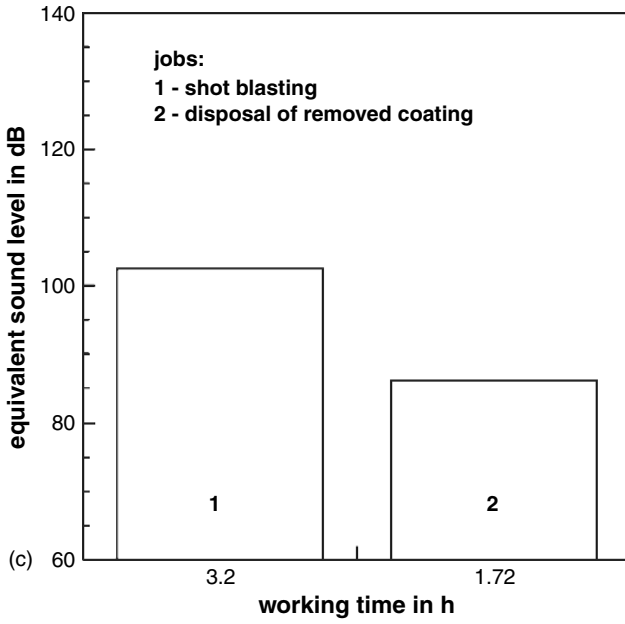


Fig. 7.3 Continued

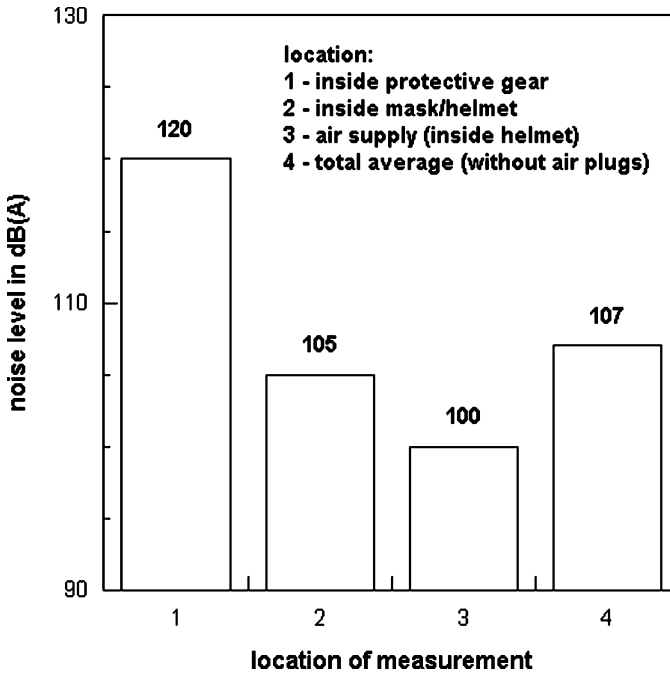


Fig. 7.4 Noise levels at different locations (Ognedal and Harbak, 1998)

the actual blasting operations (dry blast cleaning, shot blast cleaning and wet blast cleaning) generated the highest noise levels among all trades. Shot blast cleaning (which works with shrouded blasting tools) and wet blast cleaning are comparatively silent. Noise emission can notably be reduced if shrouded or sealed tools are used.

Figure 7.4 shows results of air noise measurements performed inside the helmet of blasters. Ognedal and Harbak (1998) concluded from these measurements that blast cleaning may create loss of hearing to the workers, if no additional hearing protection is provided.

The permissible air noise level depends on the exposure time. This is illustrated in Fig. 7.5 based on regularity limits stated in the German standard ‘BGV B3 Lärm’. It can be concluded from the graph that ear protection equipment must be worn by any personally involved blasting cleaning operator (see Sect. 7.8).

7.3 Emission of Body Sound

Body sound characterises waves, which carry noise and travel through solid materials. Therefore, even if windows, doors, etc. are properly closed to lock out airborne noise, persons may any way experience certain noise levels. This noise is generated due to vibrations; they occur during the tool impact and depend on the acoustic properties, especially on the sound velocity and the acoustic impedance, of both

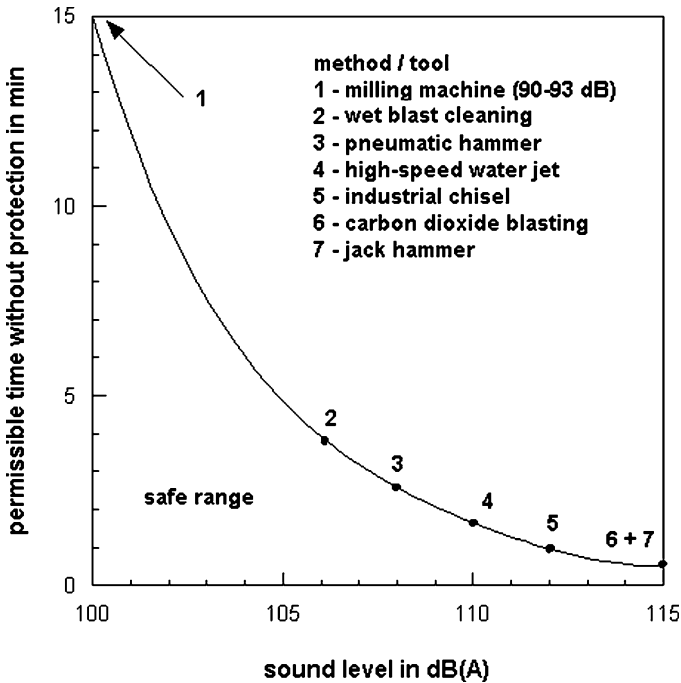


Fig. 7.5 Critical exposure times for different preparation tools (solid line according to BGV B3 Lärm; points from different sources)

the material to be subjected and the preparation tool. The evaluation parameters of the vibration are its amplitude and velocity (frequency). No measurements are available from dry blast cleaning operations. However, there are some measurements available from concrete facades treated with other surface preparation tools. Amplitudes and vibration velocities generated by the tools are plotted in Fig. 7.6. The two mechanical methods generated rather high values for vibration velocities, whereas the application of water jets led to low vibration velocities.

7.4 Emission of Dust

A mist of paint debris and broken abrasive particles is generated during dry blast cleaning in the immediate environment of the operator. An example is shown in Fig. 7.7. A simple model for the evaluation of dust during the blast cleaning of mould casings was introduced by Engelberg (1967).

Unfortunately, the dust is difficult to control. The only way to prevent it is the use of shrouded tools. Another way to protect the operator is the application of mechanically guided tools or robotic machinery. Anyway, both methods fail as it comes to the cleaning of complex structures. A reduction in dust exposure is possible by adding water to the air particle flow (wet blast cleaning and slurry blast

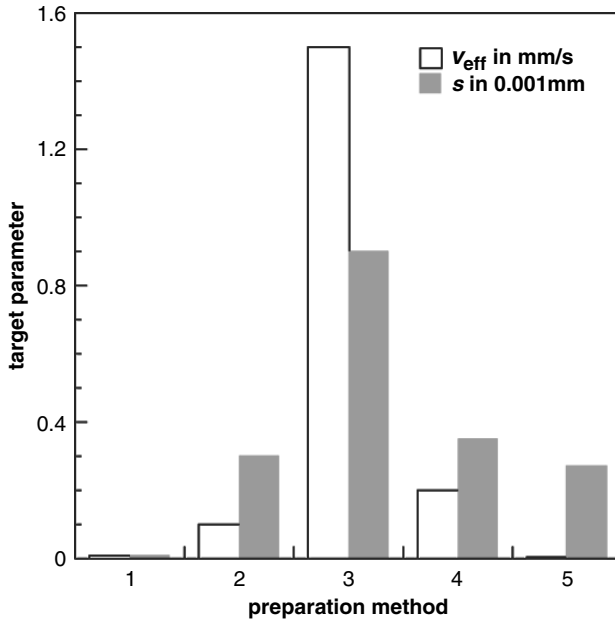


Fig. 7.6 Measurements of body sound emitted from different surface treatment tools (Werner and Kauw, 1991); v_{eff} – effective vibration velocity; s – vibration amplitude. Preparation methods: 1 – water jetting, 2 – hammer and chisel, 3 – jack hammering, 4 – pneumatic hammer, 5 – angle grinder



Fig. 7.7 Dust formation during dry blast cleaning (Photograph: Muehlhan AG, Hamburg)

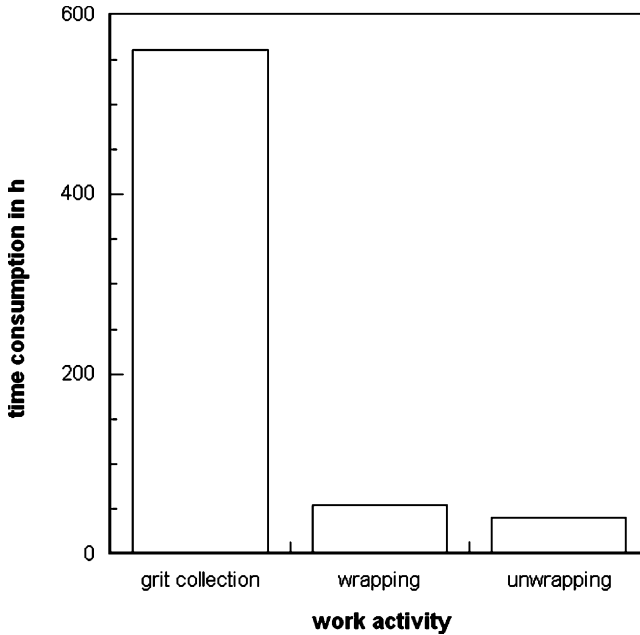


Fig. 7.8 Additional working time in a shipyard due to dust formation (Navy cargo ship in a dry-dock)

cleaning). Reviews on such methods are provided by Momber and Schulz (2006) and in SSPC (2006).

Some problems associated with dust formation are illustrated in Fig. 7.8. A very high amount of working time is required to wrap and unwrap the object (in the certain case a marine vessel in a drydock) before and after blast cleaning, and to clean up the yard site after the blast cleaning job. Several hundreds of additional working hours were spent in the example shown in Fig. 7.9. For a ship hull of about 8,000 m², 5 to 7 days for wrapping up the vessel using an eight-man crew would be required. Unwrapping would require another 4 to 5 days (Nelson, 1996).

Brantley and Reist (1994) investigated the exposure to respirable dust at ten different blast cleaning sites where quartz sand was used. Their results revealed that in general, downwind respirable silica concentration varied as distance raised. The concentration of respirable silica (mg/m³) reduced with distance from the source (feet) according to the following relationship:

$$m_D \propto x^{-1.17} \quad (7.1)$$

The geometry of the worksite and the position of the workers affected concentrations observed by orders of magnitude. The values measured for respirable dust varied between 0.01 and 10 mg/m³. Randall et al. (1998) reported on measurements performed during the removal of lead-based paint from a steel bridge with blast

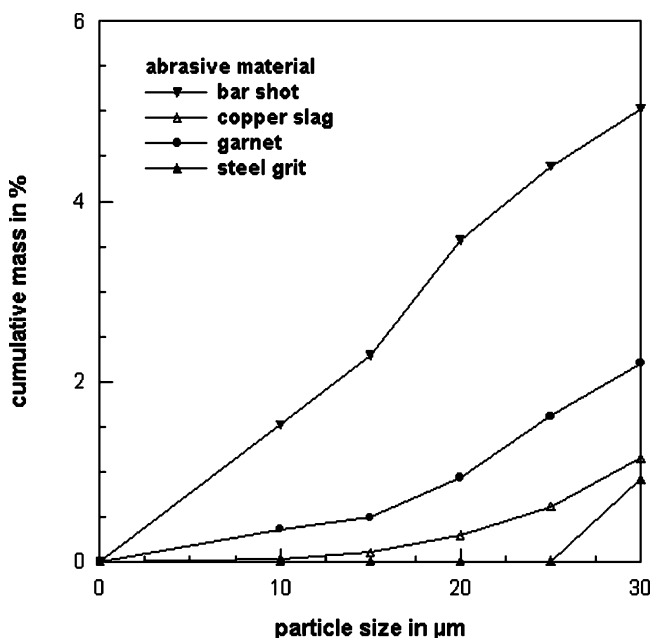


Fig. 7.9 Effects of abrasive type on the particle size distribution functions of dust (Kura, 2005)

cleaning. The authors measured total dust, respirable dust, total lead exposure and the exposure of respirable lead. Results of these measurements are listed in Table 7.2. The values are all above the permissible limits. This situation required the implementation of feasible engineering and work practice controls and the provision of personal protective equipment (PPE) and hygiene facilities supplemented by use of respirators.

Particle size distributions of airborne particles from blast cleaning operations were analysed by Kura (2005) with different methods. Some results are plotted in Fig. 7.9, and it can be seen that the type of abrasive determined the size distribution functions. Steel grit formed rather large dust particles, whereas the dust particles were small for bar shot.

Table 7.2 Air sampling analysis results from the removal of paint from a steel bridge (Randall et al., 1998)

Sampling point	Exposure in $\mu\text{g}/\text{m}^3$			
	Total dust ^a	Respirable dust ^b	Total lead	Respirable lead ^c
Background	300	100	5	*
Blast cleaning area	20,600	6,300	200	100
Blaster 1	4,000	400	50	*
Blaster 2	44,600	6,200	450	120

^aOSHA PEL: 15,000 $\mu\text{g}/\text{m}^3$

^bOSHA PEL: 5,000 $\mu\text{g}/\text{m}^3$

^cOSHA PEL: 50 $\mu\text{g}/\text{m}^3$

*Not detectable

Kura et al. (2006) investigated the effects of nozzle pressure, abrasive feed rate (in terms of number of turns of metering valve) and abrasive mass flow rate on the emission of dust during blast cleaning. Dust emission increased as the nozzle pressure increased if painted panels were blast cleaned. If rusted panels were blast cleaned, dust emission was almost independent of nozzle pressure. The influence of the abrasive feed rate on the emission of particulate matter was sensitive to the nozzle pressure. For low and moderate pressures ($p = 0.55\text{--}0.69$ MPa), the emission increased with an increase in the number of valve turns. For higher pressures ($p = 0.83$ MPa), however, the emission showed maximum values at a moderate number of turns. The emissions for rusted panels were almost independent of the abrasive mass flow rate, whereas the emissions for painted panels again showed a complex relationship to abrasive mass flow rate and nozzle pressure. Results reported by Kjernsmo et al. (2003) are presented in Fig. 7.10. The emission of respirable dust increased for higher nozzle pressures. It can also be seen that quartz sand generated more dust than copper sand at equal nozzle pressures ($p = 0.7$ MPa). But this trend turned upside down if water was

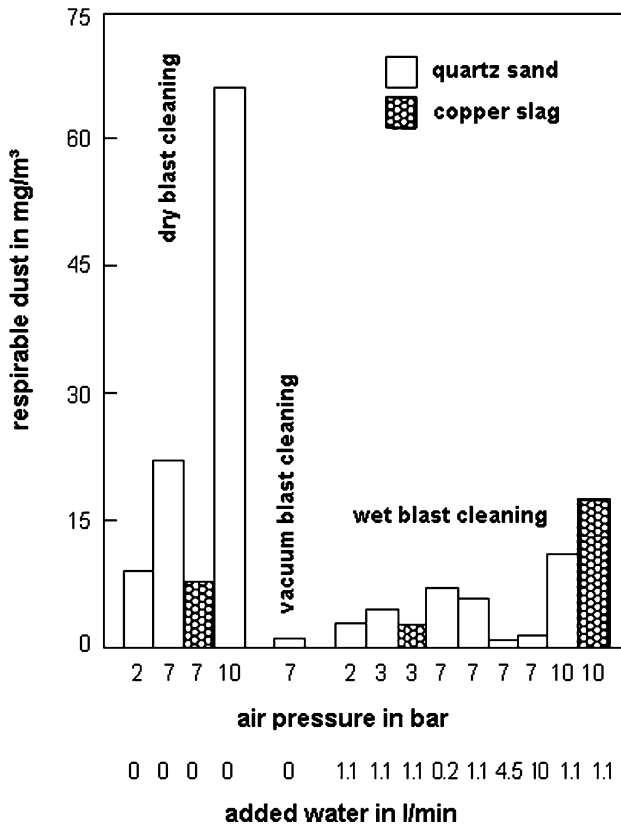


Fig. 7.10 Effects of abrasive type, nozzle pressure and water addition on the formation of respirable dust (Kjernsmo et al., 2003)

added to the nozzle flow; in that case, the dust emission was higher for the copper slag compared with that of quartz sand at equal high nozzle pressure ($p = 1.0$ MPa) and equal water flow rate (1.1 l/min). The graphs also illustrate the effect of water addition. The version with the highest amount of added water (4.5 l/min) generated the lowest dust level among all tested configurations.

Greenburg and Winslow (1932) performed an early thorough study into the effects of location, abrasive type and fresh air supply on the concentration of dust during blast cleaning operations. Some results are listed in Table 7.3. It can be seen that the use of a mineral abrasive (sand at that time), even when mixed with a metallic abrasive material, created much higher dust concentrations compared to the use of a metallic abrasive. Kjærnsmo et al. (2003) reported on the effects of abrasive type on respirable dust concentration. As shown in Fig. 7.11, quartz sand generated the highest amount of dust (which agreed with the results shown in Fig. 7.10), whereas cast iron generated very low dust levels. Mineral-based abrasive materials are usually more critical to dust formation compared with metallic abrasive materials.

Kura (2003) and Kura et al. (2006) provided the following statistical model for the assessment of parameter effects on dust emission during dry blast cleaning:

$$E_f = a_1 + a_2 \cdot p + a_3 \cdot \dot{m}_p + a_4 \cdot p^2 + a_5 \cdot \dot{m}_p^2 + a_6 \cdot p \cdot \dot{m}_p \tag{7.2}$$

Here, E_f is a specific dust emission factor, given in g/ft^2 . The pressure is given in psi and the abrasive mass flow rate is given in lbs/min. This relationship holds for coal slag and bar shot, and for air pressures between $p = 0.55$ and 0.83 MPa. The constants a_1 to a_6 are regression parameters whose values as listed in Table 7.4.

Plitzko et al. (1998) investigated the effects of abrasive type and water addition on the concentration of respirable dust during the blast cleaning of metal substrates. Some of their results are plotted in Fig. 7.12. It is clear from this graph that even the use of a slurry system (method “5”) could not avoid the exposure of impermissibly high dust concentrations. For dry blast cleaning with quartz, the permissible workplace limit was exceeded by a factor of 940. The use of an alternative abrasive material and the addition of water allowed for the reduction of this value, but the permissible limit was still exceeded by a factor of 4.

Katsikaris et al. (2002) noted an effect of the desired substrate surface cleanliness on the concentration of respirable dust. The respirable dust concentration was $399 \mu\text{g}/\text{m}^3$ for a cleanliness degree of Sa 2 and $525 \mu\text{g}/\text{m}^3$ for a cleanliness degree of Sa 2 $^{1/2}$.

Table 7.3 Results of dust measurements for different abrasive materials (Greenburg and Winslow, 1932)

Abrasive material	Dust concentration in 10^6 particles per cubic metre		
	Minimum	Maximum	Average
Sand	6.5	86.9	27.1
Steel	1.4	9.2	4.3
Sand/steel mixture	1.4	66.9	27.8

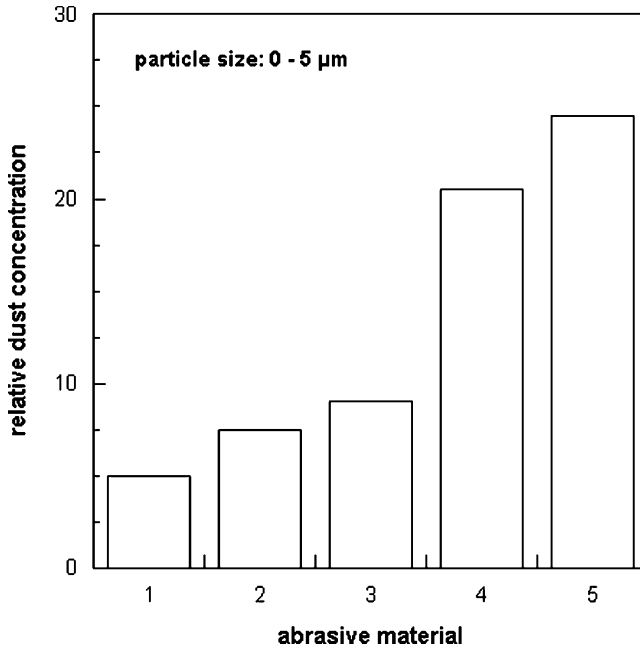


Fig. 7.11 Effects of abrasive material on the formation of dust (Kjernsmo et al., 2003). 1 – cast iron, 2 – aluminium oxide, 3 – aluminium silicate, 4 – olivine, 5 – quartz sand

Dust concentration, especially in confined spaces, can be reduced due to the utilisation of ventilation systems. As shown in Fig. 7.13, ventilation could drop dust concentration to very low values. Critical parameters were ventilation time and system size. The longer the ventilation time, the lower was the dust concentration. It was also shown that small ventilation systems can work very efficiently.

Blast cleaning operators must usually wear respiratory equipment, combined with a separate fresh air supply. It was already shown in an early investigation by Greenburg and Winslow (1932) that the amount of air delivered is of fundamental importance in determining the degree of protection of respiratory devices. Results of their measurements are provided in Fig. 7.14. It can be seen that the dust concentration under the helmet reduced with an increase in air supply. The graphs also illustrate the effects of screens in front of the blaster's eyes. A glass screen notably contributed to a reduction in dust concentration under the helmet.

Table 7.4 Regression coefficients for (7.2)

Target parameter in g/ft ²	Coefficients					
	a_1	a_2	a_3	a_4	a_5	a_6
E_f for painted steel	263.73	2.58	-57.17	-0.03	-0.85	0.71
E_f for rusted steel	-206.40	4.13	8.99	-0.01	1.04	-0.24

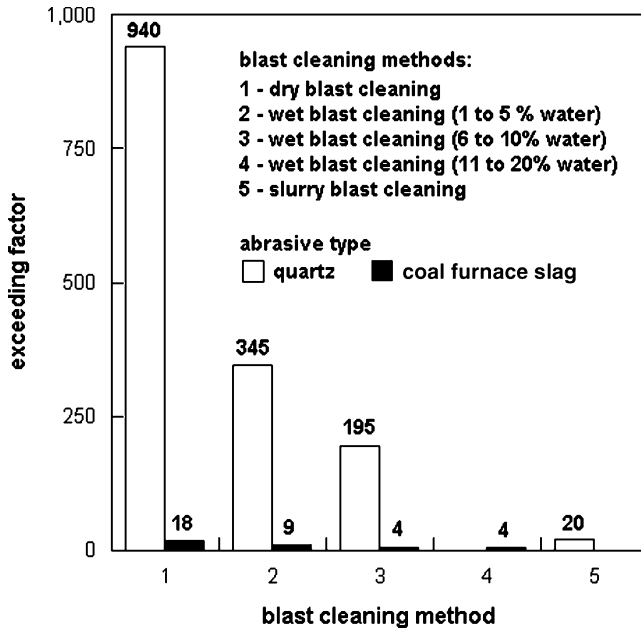


Fig. 7.12 Exceeding of critical dust concentrations for different blast cleaning variations (Plitzko et al., 1998)

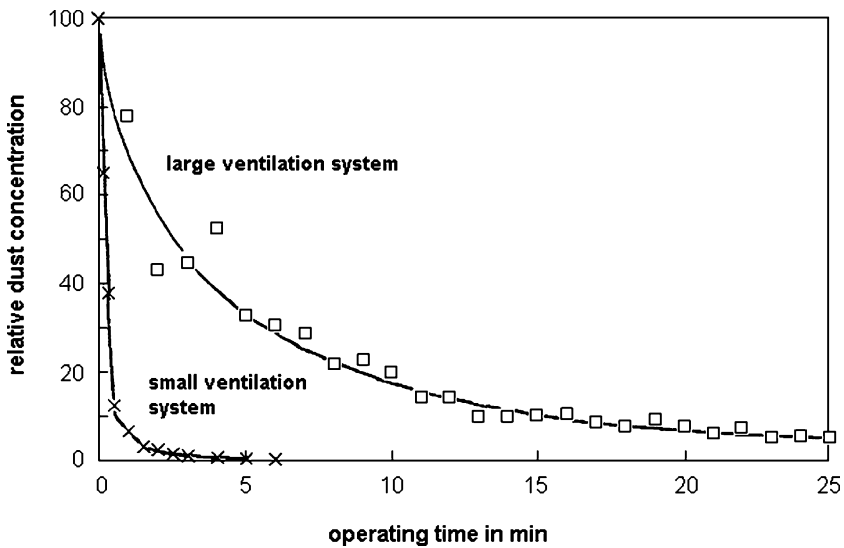


Fig. 7.13 Effects of ventilation on dust concentration (Mickelsen and Johnston, 1995)

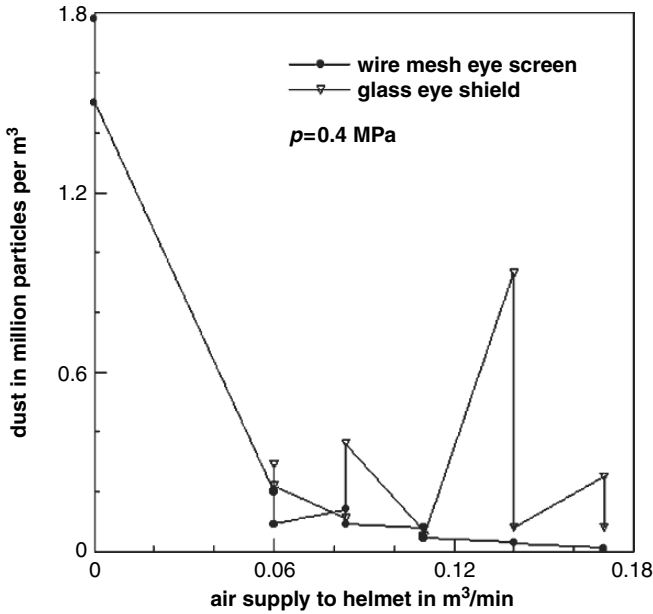


Fig. 7.14 Relationships between air supply to helmet, helmet screen design and dust concentration in helmets (Greenburg and Winslow, 1932)

An extensive database on site measurements of the exposure of workers to total dust, respirable dust, total crystalline silica and respirable crystalline silica can be found in Heitbrink's (1999) report.

7.5 Emission of Airborne Metals

7.5.1 Airborne Lead

Because many old coatings contain lead, there is a critical situation as the lead may enrich the operator's blood due to breathing the aerosol. There are the following two critical levels:

- Action Level (OSHA AL: $30 \mu\text{g}/\text{m}^3$): If an operator works in an area at or above that level, the employer must give medical surveillance and training in the hazards of working with lead.
- Permissible Exposure Limit (OSHA PEL: $50 \mu\text{g}/\text{m}^3$): This limit is for the average amount of lead in the air over an 8-h day.

Extensive studies have shown that airborne lead concentration does not depend on the main lead concentration in coating systems to be removed (NIOSH, 1997); the correlation between these parameters is very weak (correlation = 0.22). It is, therefore, the surface preparation method that determines airborne lead. Salome

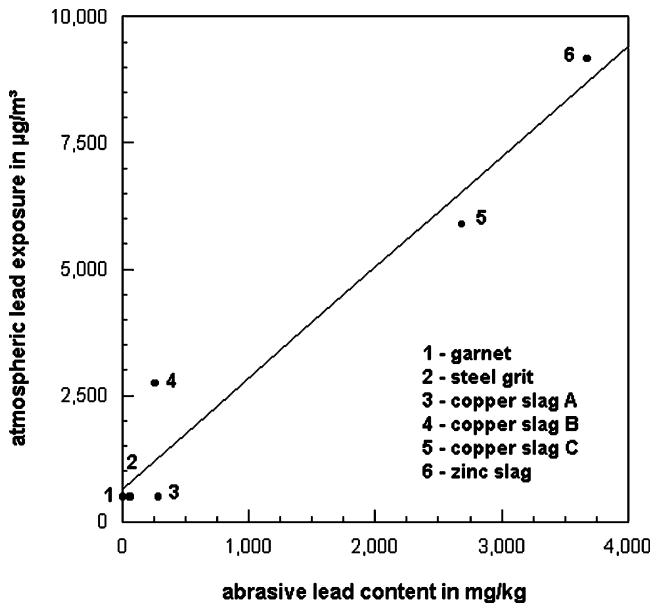


Fig. 7.15 Relationship between lead content in paint and airborne lead exposure for different abrasive materials (Salome and Morris, 1996)

and Morris (1996) have shown that the lead content also affected the amount of atmospheric lead exposure during blast cleaning. Some of their results are plotted in Fig. 7.15. A linear correlation with a correlation coefficient of 0.971 was found.

Blasters and painters are particularly endangered by lead exposure; this was verified by a comprehensive medical surveillance programme designed to prevent lead toxicity in bridge workers, including blasters. Some results of these studies are shown in Fig. 7.16, and it can be seen that painters and blasters experienced the highest blood lead levels among all job categories. Cannon et al. (1996) performed a blood lead monitoring during steel bridge rehabilitation work where lead containing paint was blast cleaned. The authors did not find remarkable differences in blood lead levels for blasters, foremen, operators and painters. The only job classification with an average blood lead level greater than a critical level of 20 µg/dl was represented by the foremen. These rather low and evenly distributed blood lead levels were probably due to the fact that the worksite was properly managed with ongoing training, reinforcement of personal protection and hygiene practices, industrial hygiene monitoring and frequent medical surveillance. Conroy et al. (1996) monitored the blood lead levels of bridge workers, including blasters, sweepers, foremen, equipment operators, helpers and supervisors. They estimated blood lead levels were in the range between 26 and 77 µg/dl. Although the certain value depended on the type of work and the work season, they were higher compared to the values reported in the study mentioned earlier. Several reasons accounted for the



Fig. 7.16 Blood lead levels for bridge workers (Maurer et al., 1995)

blood lead elevation: the airborne lead emissions were very high for this project (see Table 7.5), there was lack of water, and the workers did smoke and eat at the construction site. Schulz et al. (2005) also reported on unusually high blood lead levels for workers who were involved in a blast cleaning project, including abrasive collection, machine maintenance and abrasive distribution. Reasons for the high levels were inappropriate air delivery, use of wrong filters and very high air temperatures.

A number of measurements of airborne lead exposure to blast cleaning sites were performed over the years. Some results are displayed in Table 7.6. It can be read from the table that dry blast cleaning generates rather high quantities of lead containing aerosols. Further results of systematic measurements of air samplings in a containment were reported by Jarrett (2003), who found lead concentrations between 400 and 6,000 µg/m³ for blasters. Lange (2002) monitored the lead exposure

Table 7.5 Personal exposure to airborne lead by job title and activity (Conroy et al., 1996)

Activity	Airborne lead concentration in µg/m ³	
	Range	Median
Blasters and sweepers	12–4,401	366
Equipment operators	14–1,400	219
Foremen	26–3,423	160

Table 7.6 Measured airborne lead levels for different preparation methods

Object/condition	Lead level in $\mu\text{g}/\text{m}^3$	Reference
Hydroblasting		
Galvanised communication towers	1.5–29	Holle (2000)
Structural steel construction	2–12	Dupuy (2001)
Dock side container crane	2.2 ^a	Marshall (2001)
	0.79 ^{a,b}	Marshall (1996)
	<0.99 ^{a,c}	Marshall (1996)
Slurry blast cleaning		
Highway overpass structure	10.4–34.4	Anonymous (1997)
Steel bridge	45.7–305 ^c	Frenzel (1997)
	40.1–52.7 ^d	Frenzel (1997)
Vacuum blast cleaning		
Steel bridge	27–76 ^c	Mickelsen and Johnston (1995)
Dry blast cleaning		
Blast room	1–100,000	Adley and Trimber (1999)
Steel bridge (blaster)	36–4,401	Conroy et al. (1996)
Steel bridge (sweeper)	12–3,548	Conroy et al. (1996)
Steel bridge (foreman)	12–3,423	Conroy et al. (1996)
Steel bridge (equipment operator)	39–1,900	Conroy et al. (1996)
Steel bridge (helper)	22–501	Conroy et al. (1996)
Steel bridge (operator)	50–450 ^d	Randall et al. (1998)
Petrochemical tank	3.31 ^{a,c}	Frenzel (1997)
Blast cleaning with pliant media		
Offshore oil platform (blaster)	4,990	Miles (2000)
Offshore oil platform (containment)	980	Miles (2000)
Ice blasting		
Steel bridge	175	Snyder (1999)

^aTWA 8 h^bDownwind^cGun operator^dOutside containment

during the removal of lead-based paint from a water tank by blast cleaning, and he noted that the exposure to the blaster on top of the tanks was much higher than the exposure to the blasters working on ground or in a crane.

Tinklenberg and Doezema (1998) constructed a chart where the exposure to operators was plotted against the content of heavy metals in paints, and they suggested a procedure how to read critical heavy metal amounts in paints. For inorganic zinc-rich primers, the following examples were provided. To keep operator exposure to less than a permissible exposure limit ($50 \mu\text{g}/\text{m}^3$), the lead concentration in paints should not exceed a value of 280 mg/kg. To keep operator exposure to less than an action level limit ($30 \mu\text{g}/\text{m}^3$), the lead concentration in paints should not exceed a value of 170 mg/kg.

Kaufmann and Zielasch (1998) reported about long-term air monitoring during the refurbishment of a steel bridge in Switzerland. The job was started with dry blast cleaning. However, this method was soon replaced by hydroblasting, mainly

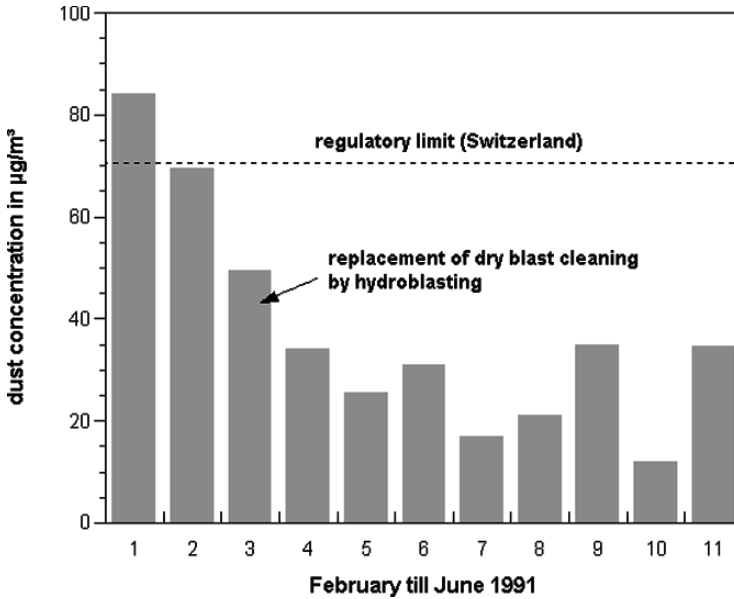


Fig. 7.17 Long-term air monitoring during steel blasting (Kaufmann and Zielasch, 1998)

because of the high dust emission that exceeded regulatory limits. This situation is illustrated in Fig. 7.17. Note that during the introductory phase of the project, where dry blast cleaning was applied, the legal limit of $70 \mu\text{g}/\text{m}^3$ was exceeded. After dry blast cleaning was replaced by a hydroblasting method that featured a robotic tool as well as limited gun operations, the regulatory limit could be met during the entire project which lasted over three years (1991–1994).

7.5.2 Other Airborne Metals

A high number of carefully measured data on metal concentrations in airborne particulates emitted during blast cleaning tests were reported by Kura (2005) for a number of abrasive materials.

The exposure of workers to a number of heavy metals during different blast cleaning applications in a ventilated blasting chamber was investigated by Tinklenberg and Doezema (1998). Results of their study are listed in Table 7.7. The data clearly indicated that during blast cleaning, the operators were exposed very well above the permissible exposure limits for lead and cadmium. Even for a paint with a reduced level of cadmium and for cured paint, blast cleaning resulted in exposure above the permissible exposure limits for both lead and cadmium. Tinklenberg and Doezema (1998) designed a chart where the exposure to operators was plotted against the content of heavy metals in paints, and they suggested a procedure how to read critical heavy metal amounts in paints. To keep operator exposure to less than

Table 7.7 Exposure to heavy metals during dry blast cleaning of zinc-rich coatings (Tinklenberg and Doezeema, 1998); based on 2 h of sampling

Materials	Metal content in $\mu\text{g}/\text{m}^3$					
	Arsenic	Zinc	Lead	Cadmium	Chromium	Copper
Mill scale	*	169 \pm 73	11 \pm 3	*	24 \pm 9	55 \pm 20
Blast cleaned steel	*	162 \pm 28	9 \pm 3	*	24 \pm 9	61 \pm 13
	*	120,675 \pm 41,761	107 \pm 26	55 \pm 17	23 \pm 10	50 \pm 23
	*	82,922 \pm 28,179	71 \pm 17	40 \pm 11	17 \pm 6	35 \pm 19
Primer	*	105,680 \pm 13,046	99 \pm 15	52 \pm 5	17 \pm 2	45 \pm 7
	*	121,162 \pm 45,994	96 \pm 19	56 \pm 14	16 \pm 3	46 \pm 10
Topcoat	*	93,637 \pm 21,441	71 \pm 11	37 \pm 6	14 \pm 5	30 \pm 14
Primer	*	178,266 \pm 55,541	106 \pm 26	12 \pm 3	25 \pm 6	50 \pm 7

*Results below detectable limits

a permissible exposure limit, the cadmium concentration in an inorganic zinc-rich primer should – as an example – not exceed a value of 12 mg/kg. Airborne cadmium was measured during a bridge blast cleaning project by Conroy et al. (1996). The median concentration inside the bridge containment was 15.7 $\mu\text{g}/\text{m}^3$, which exceeded the permissible level (OSHA PEL: 5 $\mu\text{g}/\text{m}^3$).

Results of an exhausting study which considered surface condition and wind velocity are provided in Table 7.8. A general trend between wind velocity and metal emission could not be installed based on this data. Iron was the dominating metal in all cases, even where a painted surface was blast cleaned. Permissible exposure times depended very much on the location of the blast cleaning application. Some examples are listed in Table 7.9. It can be seen that the permissible limit for arsenic exposure was reached after 15 min in a blasting room, whereas it was reached after 60 min for an outdoor application.

Table 7.8 Summary of emission factors for metals blast cleaned with silica sand (Kinsey et al., 1994; Anonymous, 1997)

Operation conditions	Emission factor in kg per kg abrasive					
	Cadmium	Chromium	Iron	Manganese	Nickel	Lead
Clean surface						
8 km/h	1.4×10^{-6}	1.5×10^{-6}	1.1×10^{-4}	1.5×10^{-7}	1.1×10^{-6}	1.1×10^{-6}
10 km/h	*	3.3×10^{-6}	2.0×10^{-4}	2.4×10^{-7}	1.6×10^{-6}	1.2×10^{-6}
24 km/h	8.0×10^{-7}	5.4×10^{-6}	1.8×10^{-4}	7.0×10^{-8}	3.0×10^{-6}	3.9×10^{-6}
Painted surface						
8 km/h	2.1×10^{-7}	2.1×10^{-6}	1.0×10^{-4}	2.9×10^{-7}	8.6×10^{-7}	2.8×10^{-6}
10 km/h	*	4.0×10^{-6}	1.6×10^{-4}	1.2×10^{-6}	1.5×10^{-6}	5.6×10^{-6}
24 km/h	7.6×10^{-8}	7.4×10^{-6}	1.5×10^{-4}	1.2×10^{-7}	8.1×10^{-6}	6.3×10^{-6}
Oxidised surface						
8 km/h	3.1×10^{-7}	3.2×10^{-7}	1.4×10^{-4}	4.2×10^{-7}	4.2×10^{-7}	4.5×10^{-6}
10 km/h	*	3.0×10^{-6}	1.9×10^{-4}	2.4×10^{-7}	3.4×10^{-6}	4.9×10^{-6}
24 km/h	3.1×10^{-9}	3.7×10^{-6}	2.2×10^{-4}	8.6×10^{-8}	4.0×10^{-6}	6.6×10^{-6}

*Cadmium was not detected

Table 7.9 Time required to reach OSHA PEL for copper slag (Stephenson et al., 2002)

Contaminant	Time to reach OSHA PEL in min		
	Booth time	Outdoor time	Room time
Total particulate	22	40	15
Arsenic	37	60	15
Lead	37	60	63

7.6 Emission of Minerals and Organic Compounds

7.6.1 Asbestos Fibres

Many old linings contain asbestos. Asbestos fibres are known to be responsible for lung cancer. Results of asbestos emission during the preparation of steel substrates with different methods were reported by Binder (2001), Goergens (2002) and Schröder (2000). Some results are shown in Figs. 7.18 and 7.19. More information is provided in Table 7.10. It can be seen that all preparation methods that contain a liquid phase (wet blast cleaning, water jetting) generate rather low asbestos concentrations.

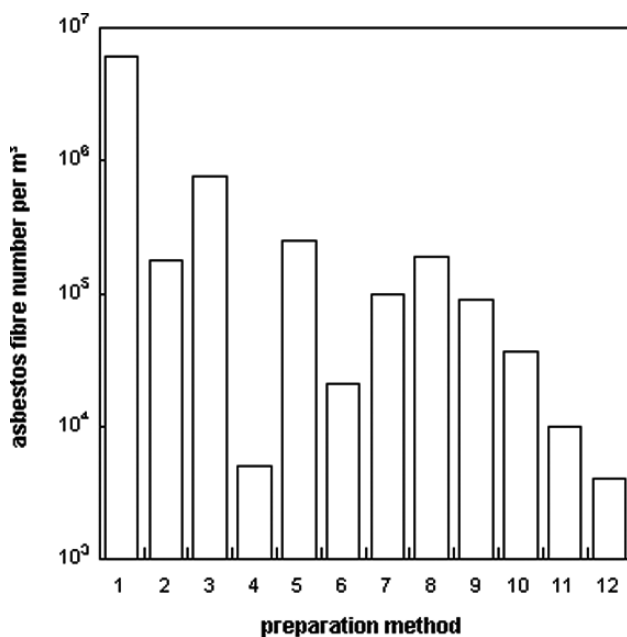


Fig. 7.18 Results of asbestos monitoring (Schröder, 2000). Treatment methods: 1 – dry blast cleaning; 2 – wet blast cleaning; 3 – wet blast cleaning; 4 – abrasive water jetting (85 MPa); 5 – hydroblasting (200 MPa); 6 – abrasive water jetting (120 MPa); 7 – hydroblasting and dry blast cleaning; 8 – wet blast cleaning; 9 – hydroblasting (240 MPa); 10 – wet blast cleaning (copper slag); 11 – water cleaning (13 MPa); 12 – water cleaning (15 MPa)

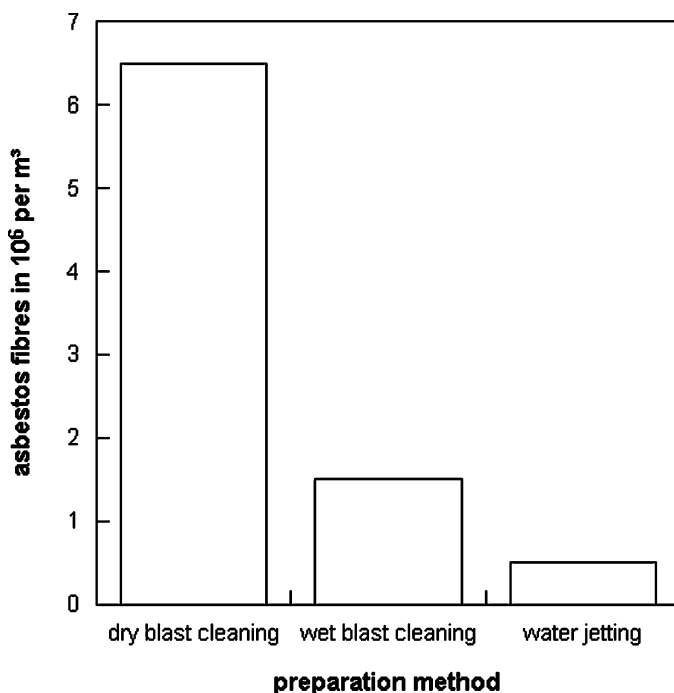


Fig. 7.19 Emission of asbestos fibres for different treatment methods (Goergens, 2002)

7.6.2 Organic Compounds

Tar epoxy coatings contain polycyclic agents, namely polycyclic aromatic hydrocarbons (PAH). Results of measurements of hydrocarbon exposure during paint

Table 7.10 Asbestos and PAH emissions during the coating removal from steel substrates (Schröder, 2000)

Method	Number of measurements	Number of fibres per cubic metre	PAH-value in $\mu\text{g}/\text{m}^3$
Flame cutter	8	881	Regulatory limit ^a exceeded
Needle hammer	1	<5,845	–
	1	14,933	–
	1	281,000	80–130
Burner	7	30,000–165,000	14–48
Hand-held grinder	1	25,000	50–152
Water jet (13 MPa)	1	5,000–10,000	Regulatory limit undercut
Grinding	2	20,000–45,000	–
Scraping	2	<5,000	Regulatory limit undercut
Flame cutter	2	Up to 38,000	Regulatory limit exceeded
Flex sawing (150°C)	1	98,074	–
Water jet	1	<4,045	–
Plane grinding	2	20,000–45,000	Regulatory limit exceeded

PAH Polycyclic Aromatic Hydrocarbons

^aLimit: 2 $\mu\text{g}/\text{m}^3$

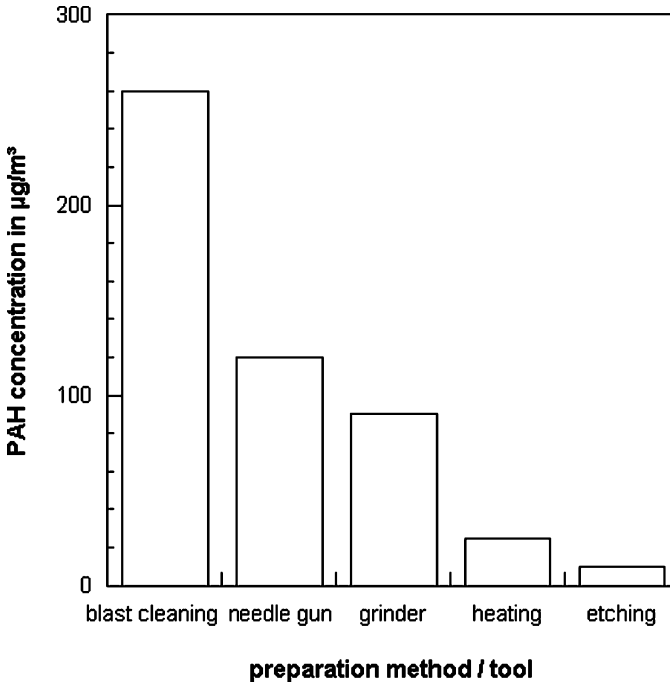


Fig. 7.20 Emissions of PAH for different treatment methods (Goergens, 2002)

removal operation with different treatment methods are reported in Fig. 7.20 and Table 7.10. The Benzo[a]pyren (BaP), mentioned in Fig. 7.20, is a certain type of polycyclic aromatic hydrocarbide. Binder (2001) performed a qualitative assessment of surface preparation methods in terms of emissions. The results of his procedure are listed in Table 7.11. It can be seen that dry blast cleaning has the lowest capability to suppress airborne contaminants. The best data provided high-pressure water jetting with integrated vacuum.

7.7 Vibrations to the Operator

Vibrations generated over a longer period of time in the arms of operators may cause so-called *white fingers*. The vibration generated by the tool is transmitted through the operator's hand where it does some damage to the blood vessels in the fingers (VDI, 1987). Therefore, regulations state minimum working hours depending on the intensity of the vibrations. The intensity is usually given by an acceleration value a_v . Results of measurements obtained from different surface preparation tools are shown in Fig. 7.21. Note from this figure that any point above the solid line is critical to health. Exposure time is the total time vibrations enter the hand per day, whether continuously or intermittently. Requirements for daily

Table 7.11 Assessment scheme for “emission safety” (Binder, 2001)

Method	Achievable limits	
	Asbestos (fibres per cubic metre)	PAH ($\mu\text{g}/\text{m}^3$)
Dry blast cleaning	6,000,000	$\gg 2$
Vacuum blast cleaning	(>150,000)	(>2)
Wet blast cleaning	>150,000/15,000	>2/ ± 2
High-/ultra-high pressure water jetting	>15,000	± 2
Water jetting with vacuuming	(<15,000)	<2
Inductive heating	<15,000	± 2
Etching	± 0	± 0
Sweeping after Etching	<15,000	>2/ ± 2

Parentheses indicate assumptions

exposure may be summarised as follows (Cooke et al., 2001; see also EC-Machine Guideline):

- $a_V = 1 \text{ m/s}^2$ is considered to be potentially hazardous and is the threshold for health risk alert and the need for preventive measures, including workers education.

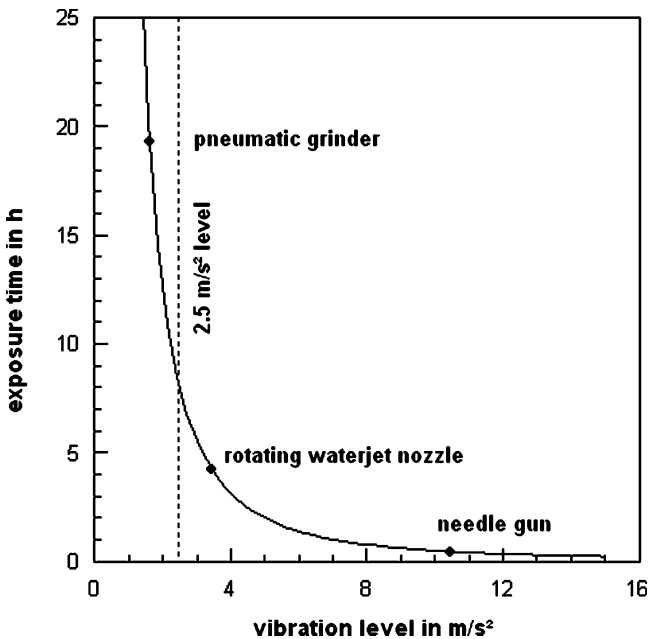


Fig. 7.21 Limits for exposure of the hand per day to vibrations (solid line according to Siebel and Mosher (1984); points from different sources)

Table 7.12 Vibration exposure to blast cleaning operators (Cooke et al., 2001)

Latent interval in years	Hose exposure	Vibration level in m/s^2	
		Highest mean	Highest peak
16	Entirely	2.66	13.0
3	Mostly	3.6	–
22	Mostly	3.6	–

Table 7.13 Vibration measurements on blast cleaning nozzle and hose (Cooke et al., 2001)

Situation	Mean vibration level in m/s^2			
	x-direction	y-direction	z-direction	Total
Right hand on nozzle	1.35	2.66	<1	2.98
	1.91	1.32	<1	2.32
	1.58	1.15	<1	1.95
Left hand on hose	1.00	1.43	<1	1.74
	2.24	1.93	<1	2.96
	1.08	1.36	<1	1.74

Compressor pressure: $p = 0.11 \text{ MPa}$

- $a_V = 2.5 \text{ m/s}^2$ is the threshold for vibration measurement assessment values to be put into the instructions and sales literature and, if the value is less than 2.5 m/s^2 , that fact shall be stated.
- $a_V = 5 \text{ m/s}^2$ is the ceiling level; if the vibration levels cannot be attenuated, exposure time has to be reduced and systematic health surveillance is required if there is daily exposure.
- $a_V = 20 \text{ m/s}^2$ is an enhanced risk situation; in addition to the measurements required at 5 m/s^2 , the offending equipment must be marked.

Cooke et al. (2001) examined a number of working situations in terms of hand-arm vibrations; among them in four cases the blast cleaning equipment was used. Results of their examination are listed in Table 7.12. The critical exposure of $a_V = 1.0 \text{ m/s}^2$ was exceeded in all cases over a period of many years. Results of more detailed measurements during a blast cleaning application are reported in Table 7.13. The vibration levels were high in y -direction and negligible in z -direction. The results also showed high fluctuations caused by the unsteady flow of air and abrasive material through hose and nozzle.

7.8 Personal Protective Equipment

Blast cleaning has a certain injury potential to blasters, and PPE must be worn during blast cleaning processes. Required PPE for blast cleaning operators includes the items listed below (BGV D26, 1999).

1. For free blast cleaning:
 - respiratory protection;

- body protection covering shoulder and body;
 - protective gloves;
 - protective shoes.
2. For free blast cleaning, if poisonous, cancerous, fruit-hurtful or genotype-affecting agents can be exposed:
- smooth and tear-resistant one-part protective suits (combination suits) in connection with respiratory protection.
 - The combination suits must be ventilated, and they cannot have external pockets;
 - Breathing air supply must be organised in a way that a sufficient and salubrious air supply is guaranteed even if fresh air supply is interrupted.
 - protective gloves;
 - protective shoes.
3. For staying close to blast cleaning machines:
- eye protection.
4. For cleaning and waste disposal:
- respiratory protection;
 - protective clothing.

Typical personnel protective clothing and equipment for blast cleaning operators are shown in Figs. 7.22 and 7.23.

Inert substances can cause severe injuries when forcefully injected into the hand. Belsole et al. (1982) described a hand injury subsequent to a pressurised injection of abrasive material. While removing rust from a ship hull, an operator lost control of the grit hose, injuring his left hand. The exact mechanism of injury was unclear, but the hand was struck by the abrasive particle jet and crushed against a steel beam. Roentgenograms could not detect a fracture. However, pinch and grip strengths of the hand were markedly reduced, and diminished sensibility was noted on the fingers of the hand. Only 8 months after the accident, it was found that the radial digital nerve was infiltrated with abrasive material that caused these phenomena. Similar cases were reported by Gelsdorf (1987) and Noetel (1987). A deadman control is, therefore, a mandatory part of any blast cleaning device. This control item must guarantee that no abrasive material leaves the nozzle if the operator loses control over the nozzle or grit hose.

7.9 Confined Spaces

Surface preparation jobs as well as painting jobs are often performed in confined spaces, namely manholes, pipelines, storage vessels, bridge box beams, interior tower cells and ballast tanks. A typical example is shown in Fig. 7.24. Not all



Fig. 7.22 Personnel protective equipment (Photograph: Muehlhan AG, Hamburg)

confined spaces are considered hazardous. However, they must be considered hazardous if they contain or have the potential to contain the following: (Osha, 1993):

- Hazardous atmospheres: This includes (1) lack of oxygen; (2) presence of explosive gases and vapours and (3) presence of toxic dusts, mist and vapours.
- Engulfment hazards: This includes spaces containing materials such as salt, coal, grain and dirt, which can easily shift and trap an operator.
- An internal configuration (slopes or inward configurations) that could trap or asphyxiate: This includes spaces where the bottoms are sloped or curved (e.g. narrow openings at the bottom of a silo) may trap or asphyxiate operators.
- Any other recognised serious hazards: This includes moving parts, power connections, liquid, and anything else that can cause bodily harm. This special situation requires special training because it is reported that operators are still getting hurt in confined spaces. The most important things to understand hazards in confined spaces are as follows (Platek, 2002):
- What hazard will be encountered?
- What equipment or means will offer protection from those hazards?
- How the equipment is used?
- Who can perform the work?
- What happens if something goes wrong?

When a confined space is evaluated, three questions regarding that space should be answered:

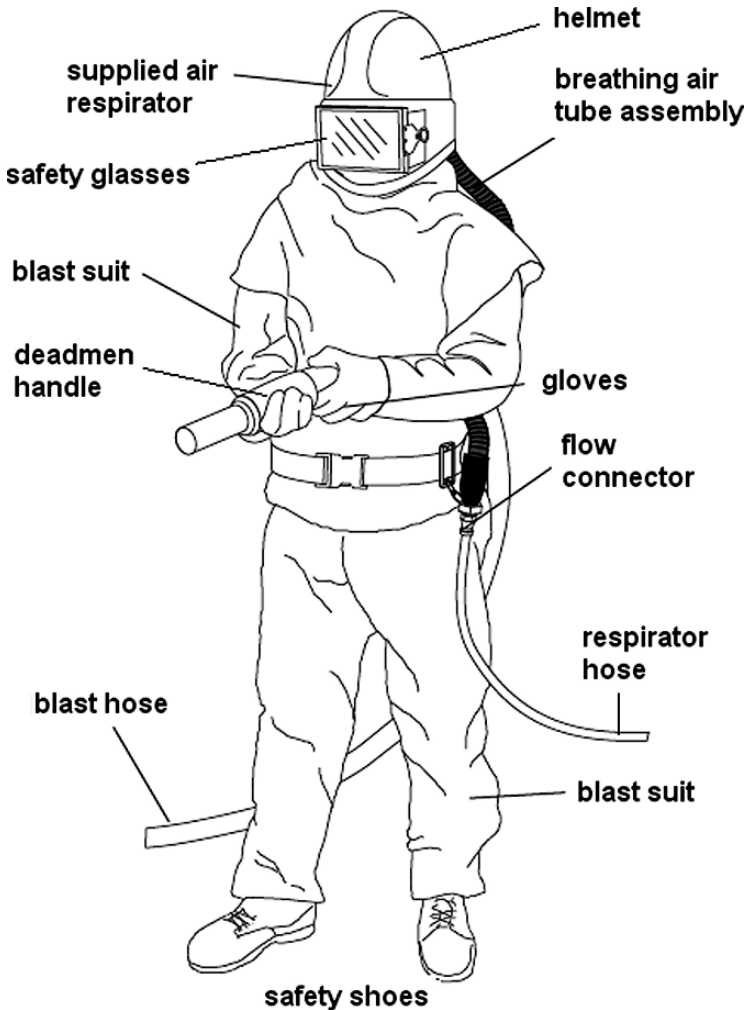


Fig. 7.23 Personnel protective equipment (Clemco Inc., Washington)

- Is the space large enough that the operator can place a part or whole of his body into it?
- Does it have limited entry and exits?
- Is it designed to work continuously?

Training and education are the major methods to reduce risks if work is performed in confined spaces. OSHA 29 CFR 1910.146 states: “The employer shall provide training so that all employees whose work is regulated by this section acquire the understanding, knowledge, and skills necessary for the safe performance of the duties assigned under this section.” Adequate training must be delivered when permit-required confined spaces are encountered and for all of the duties performed



Fig. 7.24 Blast cleaning in a confined space (Photograph: Muehlhan AG, Hamburg)

in and around a confined space. Further information and recommendations can be found in IACS (2003).

7.10 Soil Contamination

Soil contamination due to heavy metals is another health and environmental issue associated with blast cleaning. Lange (2002) performed a systematic investigation into the contamination of soil during the removal of lead-based paint from a steel tank with blast cleaning. The lead concentration in the paint varied between 0.2 and 6.9 wt.%. Soil samples were collected in certain distances from the tank before, during

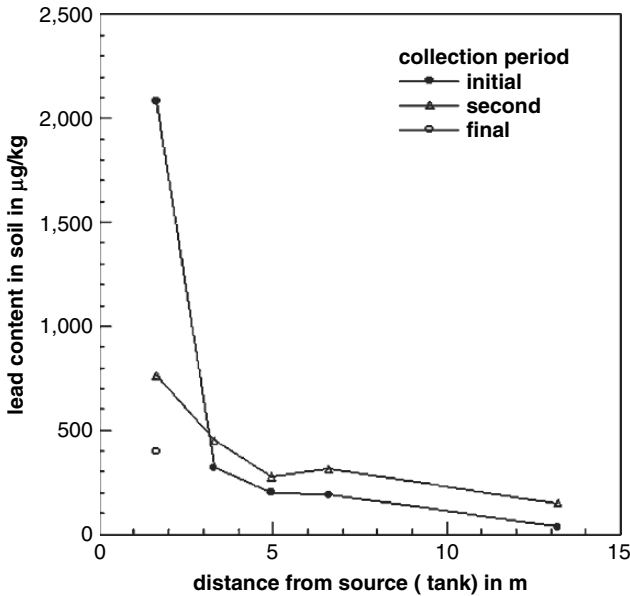


Fig. 7.25 Effect of stand-off distance on lead concentration in soil at a blast cleaning site (Lange, 2002)

and after the blast cleaning operation. Data from this study are plotted in Fig. 7.25. Concentration of lead in the soil generally decreased through distance from the tank. The author also found notable statistical differences among the samples collected during the different periods. The lead content was lowest immediately beneath the tank after the blast cleaning operation. The reasons were machine movements, cleaning operations and the spoilage of sand around the base of the tank.

7.11 Waste Disposal

7.11.1 General Disposal Problems

Waste can result from a variety of activities related to surface preparation and coatings work. Surface preparation, in particular, can produce a considerable amount of waste, mainly spent blasting media and old removed paint or rust products. The problem is illustrated in Fig. 7.26. The image was taken during a ship repair project where copper slag was used in order to remove a deteriorated coating system. The graph plotted in Fig. 7.8 illustrates the high amount of working time to be spent for collecting spent abrasive material in a shipyard.

Especially older paint systems contain hazardous materials such as heavy metals, dioxine, PCBs, etc. A recent report stated that in the USA about 581,000 steel structures contain lead-based coatings, mainly highway bridges, rail bridges and oil



Fig. 7.26 Solid waste to be dealt with after blast cleaning of a ship construction (Photograph: Lightgow Assoc.)

tanks (Randall et al., 1998). Typical examples for hazardous substances contained in paint systems are listed in Table 7.14. Most of these substances are not degradable; their health (and disposal) risk is essential:

- lead is extremely poisonous;
- PCB has chronic toxic effects;
- tar derivatives are carcinogenic;
- chromium-containing dust causes cancer and alters DNA.

These substances can also irritate the skin and cause eczema. A major problem with the removal of these paint types is the contamination of air and soil. Chromium, for example, may affect micro-organisms and prevent the air exchange of the soil. Any blasting medium (solid or liquid) is contaminated with these substances. For spent abrasive materials, for example, the lead contamination level can be as high as 840 mg/kg (Carlson and Townsend, 1998), the zinc contamination level can be as high as 37,000 mg/kg and the cadmium contamination level can be as high as 13 mg/kg. (Table 7.15 provides more data.). Potential concerns with ship maintenance facility abrasive waste are listed in Table 7.16. Concentrations of leachable metals in spent abrasives that are of particular danger to groundwater are listed in Table 7.17. For these reasons, methods that prevent or reduce the uncontrolled formation of dry dust and do not generate solid waste are superior from the point of view of health and ecology.

A management flow chart for waste abrasive blast cleaning media as recommended by Carlson and Townsend (1998) is provided in Fig. 7.27. This chart fea-

Table 7.14 Hazardous substance analysis of paint systems

Substance	Content in paint (%)	Reference
Cadmium	0.014 ^a	Dupuy et al. (2001)
	0.003–0.01	Marshall (2001)
Chromium	0.86 ^a	Dupuy et al. (2001)
	1.65	Holle (2000)
	2.99	Holle (2000)
	0.093–0.21	Marshall (2001)
Lead	0.31–13.5	Dupuy et al. (2001)
	0.132–0.710	Marshall (2001)
	6.14	Holle (2000)
	11.11	Holle (2000)
PCB	14–20	Mickelsen and Johnston (1995)
	0.12	Holle (2000)
Zinc ^b	0.16	Holle (2000)
	80–85	Tinklenberg and Doezeema (1998)

^aMaximum values^bZinc rich paint

tures a number of test and recycling cycles. A duty of care that addresses waste generation, control and disposal, which is a statutory duty that applies to producers, holders, carriers of waste and those who treat waste, has four major aims (Abrams, 1999):

- to prevent any other person from depositing, disposing of, or recovering controlled waste (residential, commercial and industrial) without a waste management licence or in a manner likely to cause environmental pollution or harm to health;
- to ensure that waste is safely and securely contained, both in storage and transport, in such a way that it cannot escape;
- to ensure that if waste is transferred then it only goes to an authorised person;
- to ensure that when waste is transferred there is a clear, written description of it so that the person receiving the waste can handle it properly and safely without committing any offence.

Table 7.15 Comparison of metals in virgin and in spent abrasive material (Carlson and Townsend, 1999)

Condition	Metals in mg/kg					
	Arsenic	Chromium	Iron	Lead	Nickel	Zinc
No. of samples	15	15	15	15	15	15
Detection limit	0.05	5.0	5.0	25.0	5.0	5.0
Minimum	<0.05	12.6	827	<25	4.8	24.3
Maximum	0.08	59.1	2,801	99.5	53.1	4,328
Geometric mean	0.05	32.8	1,300	36.6	13.2	211
Geometric standard deviation	0.04	1.6	1.4	2.3	2.2	5.8
Arithmetic mean	0.06	35.6	1,380	47.3	18.1	760
Arithmetic standard deviation	0.04	13.3	523	29.4	16.1	1,173

Table 7.16 Concerns with abrasive waste from ship maintenance (Carlson and Townsend, 1999)

Metal	Direct exposure		Groundwater leaching
	Residential	Industrial	
Arsenic	Yes	Possibly	No
Cadmium	No	No	No
Chromium	No	No	No
Copper	Yes	No	Possibly
Iron	Yes	No	Possibly
Lead	No	No	Possibly
Nickel	No	No	No
Selenium	No	No	No
Zinc	No	No	Yes ^a

^aCompare with Table 7.17

The following steps are helpful to meet the obligations mentioned above:

- Identification of all types of activity involved in the project (e.g. paint removal; storage of chemicals, fuels and paints; application of paint).
- Identification of all sources of waste in terms of “waste streams” (e.g. dry removed paint, blasting water, abrasive and its packaging, dust, chemicals and their packaging, wet paints, fuel), and the estimation of the quantities of waste from each process step prior to the job start.
- Determination of a means of handling and storing waste in order to control and minimise pollution risks. This could include the following:
 - Minimising the amount of abrasives or contaminated water that can be done by some type of containment with extraction if necessary;
 - Storage of contaminated waste in a properly bonded area;
 - Examination of transfer methods from the storage area to the waste contractor to minimise risk of spillage.

7.11.2 Abrasive Material Disposal

The absolute annual abrasive consumption in North America is listed in Table 7.18. The total consumption, which is about 3.3 million tonnes per year, must be disposed or recycled, respectively. Figure 7.28 shows typical values for solid disposal mea-

Table 7.17 Leachable metals in spent abrasive (Tinklenberg and Doezeema, 1998)

Condition	Leachable metals in mg/l					
	Arsenic	Zinc	Lead	Cadmium	Chromium	Copper
Virgin abrasive	<0.2	<0.3	<0.2	<0.03	<0.05	<0.1
After metal cleaning	<0.2	<0.3	<0.2	<0.03	<0.05	<0.1
After zinc-rich paint removal	*	770	0.23	0.01	*	*

*Results below detection limits

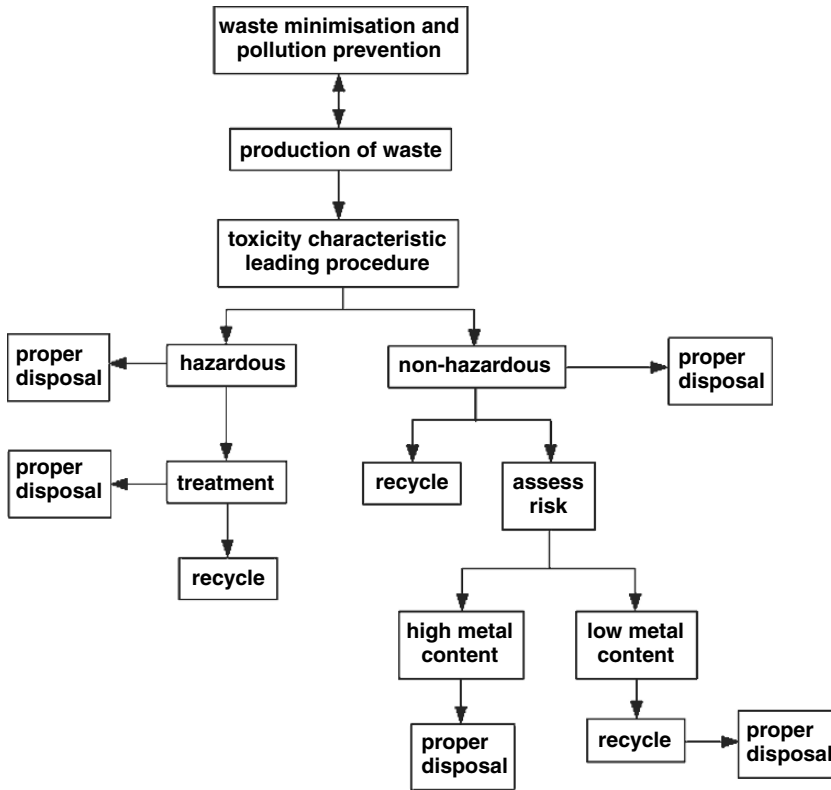


Fig. 7.27 Waste management scheme for blast cleaning processes (Carlson and Townsend, 1998)

sured during the treatment of a ship hull. The specific disposal rate is defined as the ratio between cleaning rate and solid particles collected during the treatment:

$$R_D = \frac{\dot{m}_P + \dot{m}_C}{\dot{A}} \tag{7.3}$$

Therefore, the physical unit is kg/m². Grit blasting usually generates a rather

Table 7.18 Annual abrasive consumption in North America (Hansink, 1998)

Abrasive type	Consumption in tonnes per year
Silica sand	2,000,000
Coal slag	750,000
Copper slag	100,000
Steel grit	300,000
Staurolite	70,000
Garnet	30,000
All others	50,000

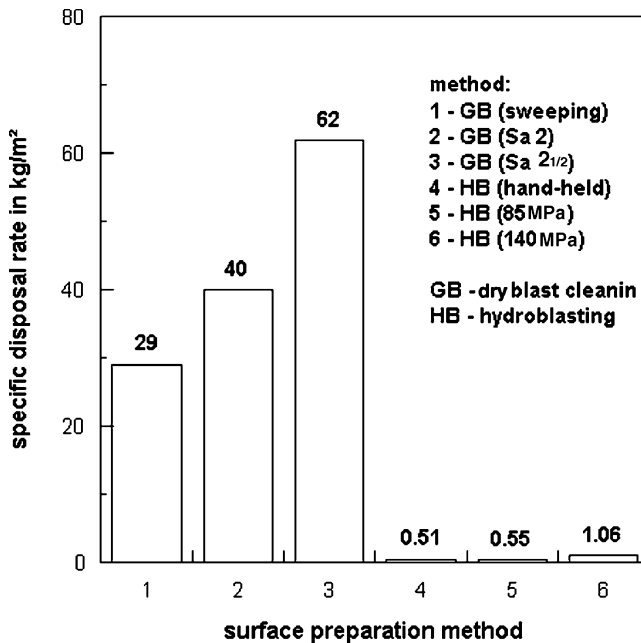


Fig. 7.28 Disposal rates for ship hull treatment (Palm and Platz, 2000)

high amount of solids which is basically due to the abrasive materials spent for the surface preparation. The specific disposal rate increases if the desired surface preparation level increases. It is lowest for simple sweeping jobs and highest for a high-quality surface (Sa 2^{1/2}). Using average values for blast cleaning, the specific amount of abrasives spent to remove a given mass of paint is about 60 kg/kg. The values plotted in Fig. 7.28 are taken from a ship hull cleaning project. A typical value for steel bridge surface preparation by blast cleaning is $R_D = 42 \text{ kg/m}^2$; in that case, a surface of 120,000 m² was blasted with 5 t of abrasive material (Ochs and Maurmann, 1996). Another example is reported by Kaufmann (1998): for a 10,000-m² highway steel bridge, a total of 50 t of abrasive material was required; this corresponds to an abrasive disposal rate of $R_D = 50 \text{ kg/m}^2$. More examples are listed in Table 7.19.

A comparative cost calculation for the treatment of railway bridges by blast cleaning and hydroblasting was performed by Meunier and Lambert (1998). Considering an average abrasive consumption of 40 kg/m², the following statements could be made:

- supplying abrasives before the blast cleaning stop starts: 350 FrF/t (equivalent to 14 FrF/m²) = 19%;
- recovery, transport of waste and discharge of abrasives (average distance 100 km): 24 FrF/m² = 32%;

Table 7.19 Typical abrasive consumption values for blast cleaning applications

Abrasive type	Abrasive consumption in kg/m ²	Efficiency in m ² /h	Method	Reference
Copper slag	26.2	10.7	Slurry blast cleaning	Da Maia (2000)
Copper slag ^a	25.0	12.2	Slurry blast cleaning	Da Maia (2000)
Sand	22.3	9.2	Slurry blast cleaning	Da Maia (2000)
Bauxite	31.9	–	Dry blast cleaning	Uhlendorf (2000)
Coal slag	50	4	Dry blast cleaning	Cluchague (2001)
Copper slag	40	–	Dry blast cleaning	Belto and Assersen (2002)
Dolomite	129.6	5.7	Dry blast cleaning	Andronikos and Eleftherakos (2000b)
Garnet	108.6	10.5	Dry blast cleaning	Andronikos and Eleftherakos (2000b)
Nickel slag	91.4	12.0	Dry blast cleaning	Andronikos and Eleftherakos (2000b)
Olivine	105.6	8.7	Dry blast cleaning	Andronikos and Eleftherakos (2000b)
Steel grit	40	–	Dry blast cleaning	Belto and Assersen (2002)
Coal slag	12	8	Thermo blasting	Cluchague (2001)

^aRecycled

- right to discharge abrasives according to French Class 1 (tax): 900 FrF/t (equivalent to 36 FrF/m²) = 49%.

This corresponds to total cost of 74 FrF/m² (=100%). It is interesting to note that about 50% of the costs are due to the disposal of the spent abrasive material only.

7.11.3 Contamination of Abrasive Material and Leachable Metals

Because of the intense contact between abrasive material and the material to be removed, abrasive material is usually contaminated. The contaminants may, in particular, include heavy metals and organic compounds. Table 7.20 lists the results of comparative measurements of metal contents in a virgin and a spent mineral abrasive material used for the removal of zinc-based paint. The unused abrasive

Table 7.20 Comparison of metals in virgin and in spent abrasive material (Tinklenberg and Doezeema, 1998)

Condition	Metals in mg/kg					
	Arsenic	Zinc	Lead	Cadmium	Chromium	Copper
Virgin	<11.0	<170	<11.0	<1.6	<4.0	<2.5
After steel cleaning	<10.0	<60.0	<10.0	<1.5	<4.0	<5.0
After zinc-rich paint removal	*	37,000	37	13	12	18

*Below detectable limit

Table 7.21 Leachable metals in spent abrasive material (Tinklenberg and Doezema, 1998)

Condition	Metals in mg/l					
	Arsenic	Zinc	Lead	Cadmium	Chromium	Copper
Virgin	<0.2	<0.3	<0.2	<0.03	<0.05	<0.1
After steel cleaning	<0.2	<0.3	<0.2	<0.03	<0.05	<0.1
After zinc-rich paint removal	*	770	0.23 ^a	0.099	*	*

*Below detectable limit

^aOne reading

material did not contain heavy metals in high amounts. The blast cleaning of bare steel did not notably change the amounts of heavy metals in the abrasives compared with the unused abrasives. As expected, the abrasive material spent during coating removal contained in particular a very high level of zinc, which may become critical in term of disposal and recycling. Table 7.15 lists the results of measurements from waste samples collected from blast cleaning contractors. Cadmium, copper and selenium were below their respective detection limit for all samples.

Leachable metals are critical to ground water, and their concentration should not exceed certain critical levels. Wastes classified as hazardous must be treated to leachable levels below 0.5 mg/l for lead, 0.11 mg/l for cadmium and 0.60 mg/l for chromium (Drozd 2000). Wastes that do not exhibit the hazardous characteristics for these metals do not require post-treatment. Some industrial areas use topical stabilisers to prevent spent abrasive material and paint debris from exhibiting the hazardous characteristics for lead. These substances work by reducing the solubility of the lead, thus stabilising it so that it will not leach into the environment when it comes in contact with a liquid. Drozd (2000) performed a study on the efficiency of four stabilisers and found them very effective at eliminating the hazardous characteristics of lead. However, only one of the stabilisers was capable at eliminating the hazardous characteristics of cadmium, and none for chromium.

Measurements on leachable metals in spent abrasive materials, used for the removal of zinc-rich inorganic primers, were performed by Tinklenberg and Doezema (1998). Results of their measurements are listed in Table 7.21. The results showed that the blast cleaning of a zinc-rich paint could easily produce a waste that will leach zinc above 500 mg/l, which would classify the waste to be hazardous. Other metals were not considered to be critical. Results from leaching tests for abrasive waste collected from shipyards and contractor sites are provided by Carlson and Townsend (1999).

7.11.4 Paint Waste

Typical specific chip disposal rates are between 0.3 and 1 kg/m² (see previous section). For the treatment of 3,320 m² of a maritime steel construction, 2.7 t of paint were disposed; this is a disposal rate of 0.8 kg/m² (Uhlendorf, 2000).

7.12 Recycling of Abrasive Materials

7.12.1 Contamination with Residue

A mobile abrasive material recycling unit for large-scale applications is shown in Fig. 7.29. Table 7.22 lists typical values for the recyclability of numerous abrasive materials.

Spent abrasive material is usually contaminated with residue originating from the material which was blast cleaned. Residue could be metals, soluble substances and organic compounds.



Fig. 7.29 Mobile abrasive recycling unit for large-scale applications (Photograph: Muehlhan AG, Hamburg)

Table 7.22 Workability parameters of abrasive materials (Stieglitz, 1996)

Abrasive material	Number of life cycles	Specific consumption in kg/m ²
Melting chamber slag	1	30–60
Copper slag	1	30–60
Garnet	3–6	10–20
Secondary corundum	10–20	5–15
Fused corundum	10–30	3–10
Sintered bauxite	10–30	3–10
Glass beads	10–30	10
Plastics beads	5–200	1–5
Ceramics	300	1–5
Hard cast	150–500	0.5–0.8
Steel cast (HV 700–900)	800–1,200	0.3
Steel cast (HV 550–750)	1,500–2,500	0.2
Steel cast (HV 400–600)	3,000–5,000	0.1
Cut steel wire	4,000–9,000	0.03

Katsikaris et al. (2001) described a procedure for the recycling of ferrous-nickel slag. Their investigation programme included sieve analysis, electric conductivity, chloride content and organic content. Some results are displayed in Fig. 7.30. Figure 7.30a shows results from electric conductivity readings. The recycled abrasive samples exhibited slightly lower levels compared with the unused sample. Similar is the situation in Fig. 7.30b where the amount of sodium chloride is plotted against the number of cycles. The recycling was, therefore, not critical to soluble substances in the abrasive material. Results of organic content monitoring are listed in Table 7.23. The organic content depended on the abrasive particle sizes; it was high for the large particle fraction ($d_p > 1,400 \mu\text{m}$). For the larger particles, an accumulation of organic compounds could be noted.

Katsikaris et al. (2002) investigated the efficiency of recycled ferrous-nickel slag. They found that specific abrasive consumption notably increased if the slag was reused. Whereas for the first usage cycle, the specific abrasive consumption was 99 kg/m^2 ; it increased to 125 kg/m^2 after three usage cycles.

7.12.2 Use for Construction Materials

The use of paint-contaminated abrasive particles as aggregate material for mortar–cement-based concrete and asphalt concrete was investigated by Madany et al. (1991) and Taha et al. (2001). Madany et al. (1991) used copper slag as a replacement ma-

Table 7.23 Organic content in recycled ferrous nickel slag (Katsikaris et al., 2001)

Grain size in μm	Organic content in wt. %	
	One recycling cycle	Two recycling cycles
<150	1.25	1.61
150–1,400	0.14	0.11
>1,400	6.91	46.14

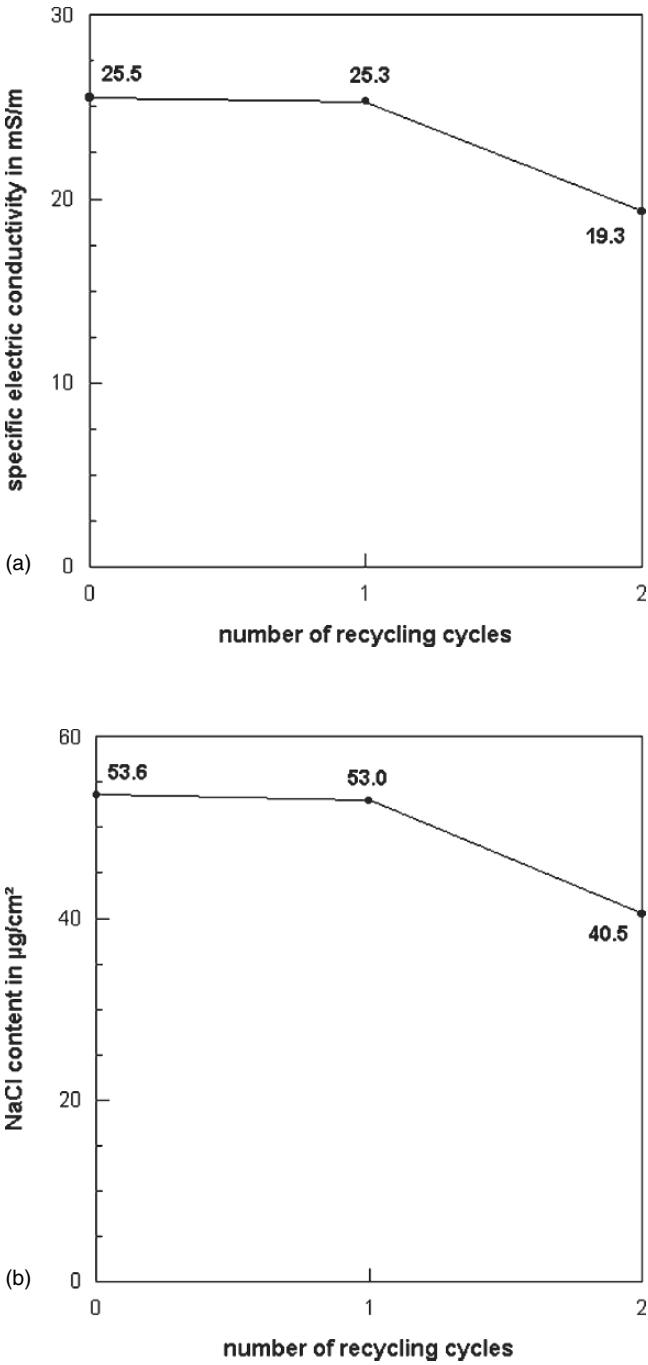


Fig. 7.30 Effects of recycling cycles on soluble substances in abrasive materials (Katsikaris et al., 2001). (a) Results of specific electric conductivity readings; (b) Results of NaCl readings

terial for sea sand as fine aggregate. They produced mortar samples from ordinary Portland cement and spent abrasive material at weight ratios of 1:1, 1:3 and 1:4. The different mixture ratios, and thus the addition of spent abrasive material, did not deteriorate the 28-day compressive strengths (between 33 and 35 MPa). Concrete samples provided 28-day compressive strengths at 12 MPa. Taha et al. (2001) did not specify the type of abrasive material they used, but mentioned that the waste material contained paint chips and paint particles and other debris generated during the blast cleaning process. Sand was partially and completely replaced by this waste material. The 28-day compressive strengths of cement–mortar specimens were as high as 55 MPa for the specified samples. The authors could also prove that asphalt concretes, modified with abrasive material waste, had high skid resistance values.

Chapter 8

Surface Quality Aspects

8.1 Surface Quality Features

Quality features of substrate surfaces determine the performance and properties of applied coating systems. Related to the performance of corrosion protective coating systems, ISO series 8502 states the following: “The performance of protective coatings of paint and related products applied to steel is significantly affected by the state of the steel surface immediately prior to painting. The principal factors to influence this performance are:

- (1) the presence of rust and mill scale;
- (2) the presence of surface contaminants, including salts, dust, oil and greases;
- (3) the surface profile.”

Numerous regulative standards are issued to define these factors, and testing methods are available to quantify them. Blast cleaned surfaces show some distinct features, and extensive experimental studies were performed to address this special point, often in direct comparison to other surface preparation methods.

Figure 8.1 shows a scanning electron microscope image of a steel substrate after blast cleaning. A general distinction can be made between primary and secondary substrate surface features. *Primary surface features* may include those properties which are part of coating specifications. They include the following features:

- visual cleanliness;
- chemical cleanliness;
- physical cleanliness;
- profile properties;
- surface integrity.

Secondary surface features may include properties which are determined by, and depend on, primary features. They may include the following features:

- surface energy;
- wettability;
- adhesion of coating to substrate.

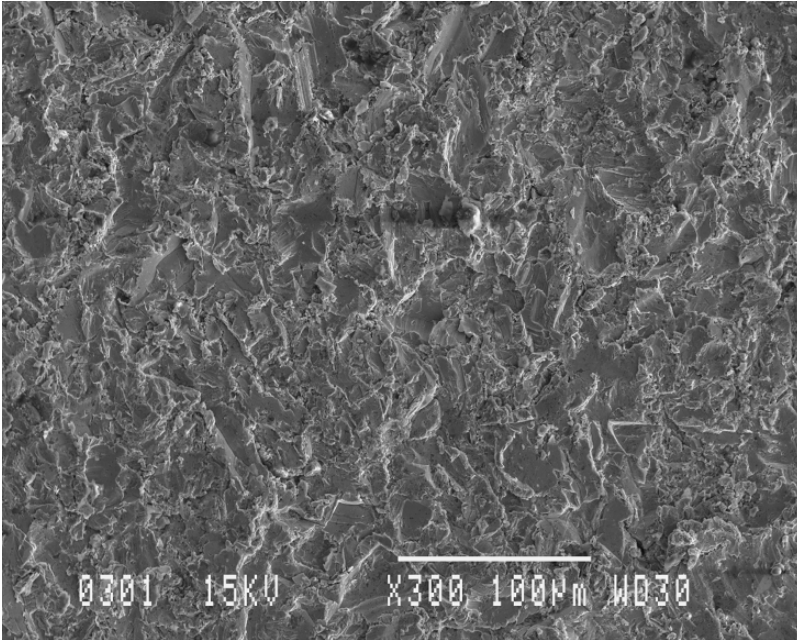


Fig. 8.1 Morphology of a blast cleaned low-carbon steel substrate. Parameters: $p = 0.475$ MPa; $d_N = 8$ mm; $\varphi = 90^\circ$; abrasive: aluminium oxide; $\dot{m}_p = 19$ g/s; $d_p = 165$ μm (Photograph: author)

8.2 Visual Cleanliness

8.2.1 Visual Standards

A number of regulatory standards have been developed in order to define and to characterise steel surfaces prepared by blast cleaning. These standards are more or less based on the standard preparation grades given in ISO 8501-1 (uncoated parts of the surface) and ISO 8501-2 (partial surface preparation). Visual blast cleaning standards cover the following two issues:

- initial condition (rusty steel or shop primer);
- visual surface preparation definition (visible contaminants and cleaning degrees).

Table 8.1 provides a general review on current visual surface preparation standards. Visual standards should always be used in conjunction with the written text, and they should not be used as a substitute of a written standard. The standards listed in Table 8.1 are limited to hot-rolled steel surfaces prepared for painting. They are applicable also to steel substrates that show residues of firmly adhering paint or other foreign matter in addition to residual mill scale. Therefore, care must be taken in applying these standards to other substrate materials.

Table 8.1 Contents of visual blast cleaning standards

Standard	Surface reference for			
	Rusty steel	Coating/primer	Flash rust	Cleaning degree
ISO 8501-1	x			x
ISO 8501-2	x	x		x
International Slurry blasting Standard ^a	x		x	x
SSPC – NACE	x		x	x

^aIssued by International Paint, Newcastle

8.2.2 Initial Conditions

Initial conditions have a notable effect on the performance of coatings applied to blast cleaned steel substrates. The effects of rust grades and preparation grades on coating lifetime are illustrated in Fig. 8.2. It can be seen that lifetime decreased if rust grade increased and if preparation grade decreased. A high rust grade (“C” or “D”) required a higher degree of surface preparation in order to guarantee equal coating lifetimes. The low surface preparation standard Sa 1 was extremely sensitive to changes in the initial conditions. Rust grade “A” (adhering mill scale but little, if any, rust) was least sensitive to changes in surface preparation degree, but

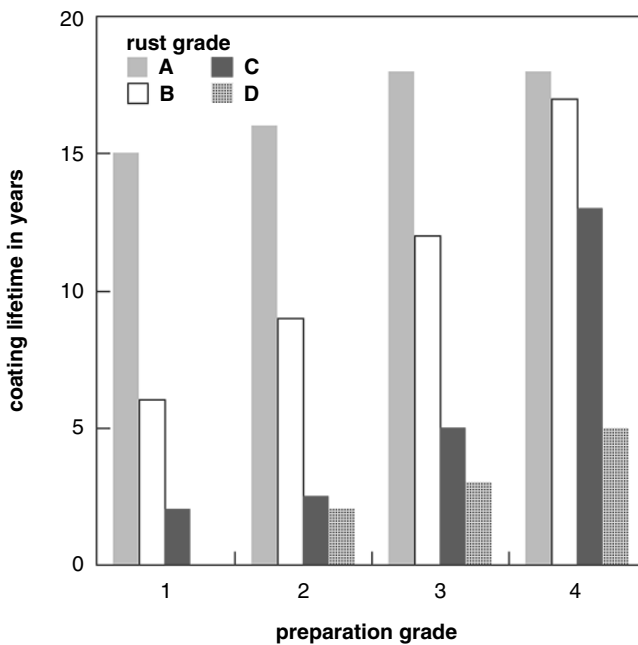


Fig. 8.2 Effects of rust grade and preparation grade on coating lifetime (Bahlmann, 1982). Preparation grades: 1 – brushed; 2 – Sa 1; 3 – Sa 2; 4 – Sa 3 (see Table 8.2 for preparation grades)

if rust grade “C” was present, an increase in the surface preparation grade could substantially extend coating lifetime.

Initial conditions are designated in several visual standards (see Table 8.1). These conditions can be subdivided into two groups:

- (1) rusty steel;
- (2) primers or coatings.

The initial steel grades apply to uncoated steel surfaces that are deteriorated due to corrosion (either thermal or atmospheric oxidation). Rust grades are illustrated in Fig 8.3. These rust grades are defined as follows:

- Steel grade A: Steel surface largely covered with adhering mill scale but little, if any, rust;
- Steel grade B: Steel surface which has begun to rust and from which the mill scale has begun to flake;
- Steel grade C: Steel surface on which the mill scale has rusted away from which it can be scraped, but with slight pitting visible under normal vision;
- Steel grade D: Steel surface on which the mill scale has rusted away and on which general pitting is visible under normal vision.

Previously coated steel surfaces are designated in ISO 8501-2. There are a large number of possible systems and coating conditions. The cleaning results do not depend only on the intensity of cleaning in these cases, but also essentially on type, thickness and adhesion of the coating systems, and on earlier surface preparation steps. For these reasons, only analogous applications to real cases can usually be derived. The coated steel surfaces considered in visual blast cleaning standards include the following coating/primer systems and conditions:

- coatings:
 - iron oxide shop primer;
 - corrosion protection system;

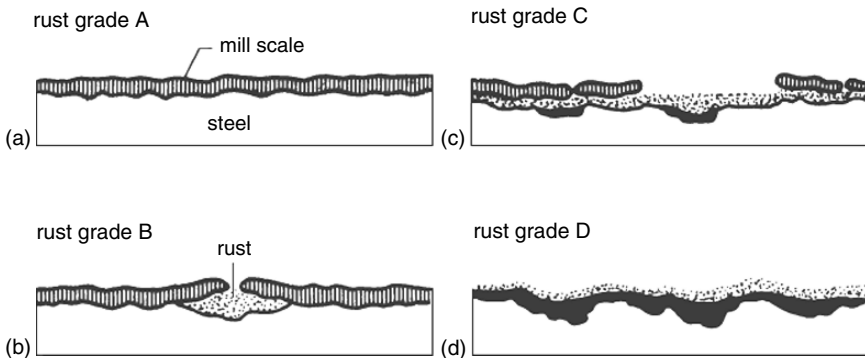


Fig. 8.3 Initial surface conditions according to ISO 8501-1 (adapted from Kjærnsmo et al., 2003). (a) Rust grade “A”; (b) Rust grade “B”; (c) Rust grade “C”; (d) Rust grade “D”

- a sound coating;
- an unsuitable coating;
- conditions:
 - upper side of a hatch cover;
 - upper side of a steel girder;
 - new construction work: tubes in a power station.

Other designations for coated substrate surfaces apply to coating failure schemes, mainly according to the degree of rusting as defined in ISO 4648-3. These particular cases will be discussed in Sect. 9.1.

8.2.3 Preparation Grades

Effects of blast cleaning preparation grades on the performance of a metal-sprayed coating are shown in Fig. 8.4. It can be seen from the graphs that pull-off strength increased if the preparation grade increased. The curves for iron grit and silica sand showed almost equal linear trends, whereas the trend was different if copper slag was used as a blast cleaning medium. One reason for the different trend of copper slag could be the high friability of copper slag. Because the very thorough

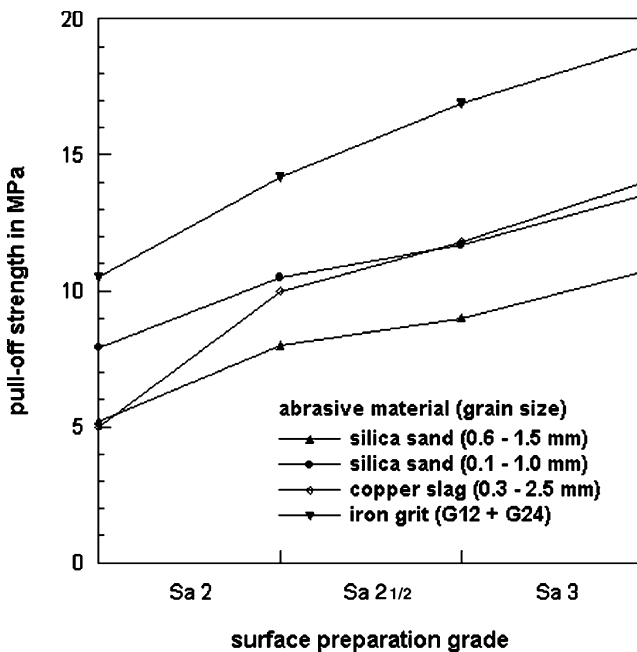


Fig. 8.4 Effects of blast cleaning preparation grades on pull-off strength of arc-sprayed aluminium (Bardal et al., 1973)

preparation grade Sa 3 required a very intense material treatment, slag particles were fractured. The fracture debris did not effectively contribute to the material removal process. The surface texture was changed, leading to a deteriorated bond between substrate and coating, and the initially sharply rising curve started to drop.

Preparation grades as defined in ISO 8501-1 indicate the following two designations:

- method of surface preparation;
- degree of cleaning.

The preparation method dry blast cleaning is designated by the letters “Sa” throughout the standard. Degrees of cleaning range from “1” to “3”. These degrees are defined in Table 8.2. The preparation grades are defined by written descriptions of the surface appearance after the blast cleaning operation, which are also provided in Table 8.2, together with representative photographic examples.

Cleaning degrees are defined according to the presence of visible contaminants. These visible contaminants include the following substances:

- rust;
- previously existing coatings;
- mill scale;
- foreign matter.

Table 8.2 Blast cleaning preparation grades and cleaning degrees (ISO 8501-1)

Preparation grade		Designation	Description of surface (when viewed without magnification)
Preparation method	Cleaning degree		
Sa	1	Light blast cleaning	The surface shall be free from visible oil, grease, dirt, dust, and from poorly adhering ^a mill scale, rust, paint coatings and foreign matter.
Sa	2	Thorough blast cleaning	The surface shall be free from visible oil, grease and dirt, and from most of the mill scale, rust paint coatings and foreign matter. Any residual contamination shall be firmly adhering.
Sa	2½	Very thorough blast cleaning	The surface shall be free from visible oil, grease and dirt, and from mill scale, rust, paint coatings and foreign matter. Any remaining traces of contamination shall show only as slight stains in the form of spots or stripes.
Sa	3	Blast cleaning to visually clean steel	The surface shall be free from mill scale, rust, paint coatings and foreign matter. It shall have a uniform metallic colour.

^aMill scale, rust or paint coating is considered to be poorly adhering if it can be removed by lifting with a blunt putty knife

Table 8.3 Cleaning degrees for different blast cleaning designations; see also Table 8.2

Standard	Preparation method	Cleaning degree			
		1	2	2½	3
ISO 8501-1 (Sa)	Sa	1	2	2½	3
ISO 8501-2 (Sa)	P Sa	–	2	2½	3
SSPC	–	SP 7	SP 6	SP 10	SP 5
NACE	–	4	3	2	1
NACE wet blasting	WAB	–	6	10	–
International Slurry Blasting Standard ^a	SB	–	2	2½	–

^aIssued by International Paint, Newcastle

The highest cleaning degree always requires that the surface shall be free of all these matters, and it shall have a metal finish. The term “foreign matter” may include larger amount of water-soluble salts and welding residue. Comparative degrees of cleaning as defined for other surface preparation methods than dry blast cleaning are listed in Table 8.3. The achievable preparation grade depends on a number of parameters, namely air pressure, abrasive type and abrasive particle size. Effects of abrasive types were already investigated in an early study conducted by Nieth (1955). This author related the cleanliness to the capability of impinging abrasive particles to deform the substrate. Heavily deformed substrates, which are characterised by folded and bended surface sections, often contained traces of rust and mill scale after blast cleaning. With respect to the abrasive particle size, a comparative investigation of Snyder and Beuthin (1989) has shown that coarse as well as very fine silica sand generated high surface preparation grades (90–95% cleaned to Sa 3; 5–10% cleaned to Sa 2½), whereas medium and fine silica sand generated lower preparation grades (75% cleaned to Sa 3; 25% cleaned to Sa 2½). If copper slag and coal slag were used, the highest preparation grade (Sa 3) could not be achieved. Copper slag delivered 10% cleaned to Sa 2½ and 90% cleaned to Sa 2, whereas coal slag delivered 75% cleaned to Sa 2½ and 25% cleaned to Sa 2.

An early approach to replace the rather imprecise and subjective visual assessment through a physically founded parameter was due to Bullett and Dasgupta (1969). The parameter “reflectivity” of a steel surface, measured with an optical method, was applied for the assessment of the surface cleanliness. Results of reflectivity measurements are shown in Fig. 8.5. Reflectivity increased if treatment time increased, and the progress of the function was very pronounced in the range of short treatment times. A reflectivity value of 360 corresponded to a visually estimated preparation grade Sa 2½. If this preparation grade was achieved, further blast cleaning action delivered a marginal increase in reflectivity only. The value of maximum reflectivity may vary from steel to steel, or with different abrasive materials, but for each combination there is a rapid initial increase with time of blast cleaning towards the asymptotic value. Bullett and Dasgupta (1969) could also show that reflectivity values dropped if a blast cleaned steel was exposed to an open environment. A reflectivity value of 60%, measured immediately after blast cleaning, dropped down to a value of 10% after 24 h of exposure. Apps (1969) applied a reflectance meter for substrate cleanliness assessment, and

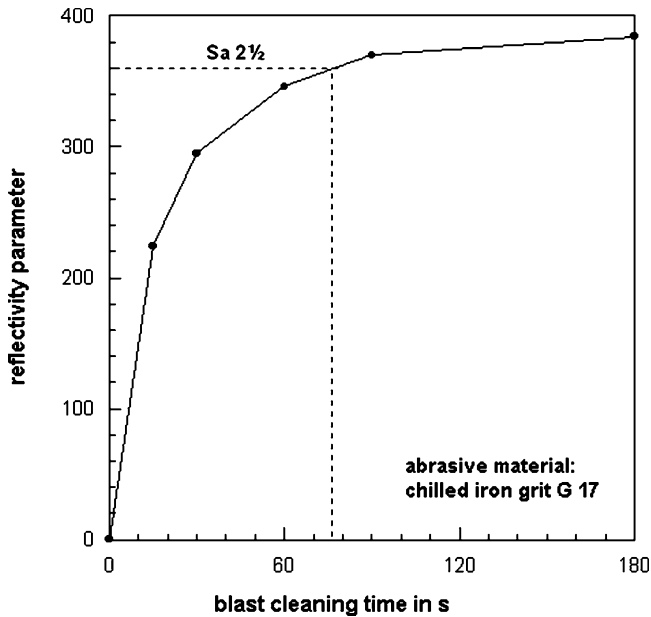


Fig. 8.5 Reflectivity of a blast cleaned steel surface as a function of treatment time (Plaster, 1973)

he investigated the effects of different process parameters on reflectivity. He found that reflectivity dropped with an increase in blasting angle. This author could also show that reflectivity depended on abrasive type and condition. Reflectivity values were high for new and for well-worn chilled iron grit, and they were low for worn, dusty grit. Blasting pressure and stand-off distance did not have any significant effect on reflectivity. Bardal (1973) also made an approach to express visual cleanliness in terms of reflectivity. Reflectivity was defined in his study as the percentage of reflectivity of a base sample, which was a light grey tile. Thus, the unit of reflectivity was percent (%). Some results are displayed in Table 8.4. One striking result is that reflectivity was not a feature of cleanliness standard alone, but also depended on abrasive type. For a cleaning standard of Sa 3, for example, reflectivity was only about 60% for copper slag, but it was about 80% for silica sand. The explanation for this result was the dark colour of the almost black copper slag. Slag debris embedded into the substrate surface

Table 8.4 Effects of surface preparation grade and abrasive type on reflectivity (Bardal, 1973)

Preparation grade	Reflectivity in %	
	Copper slag	Silica sand
Sa 2	40	60
Sa 2 ^{1/2}	50	75
Sa 3	60	80

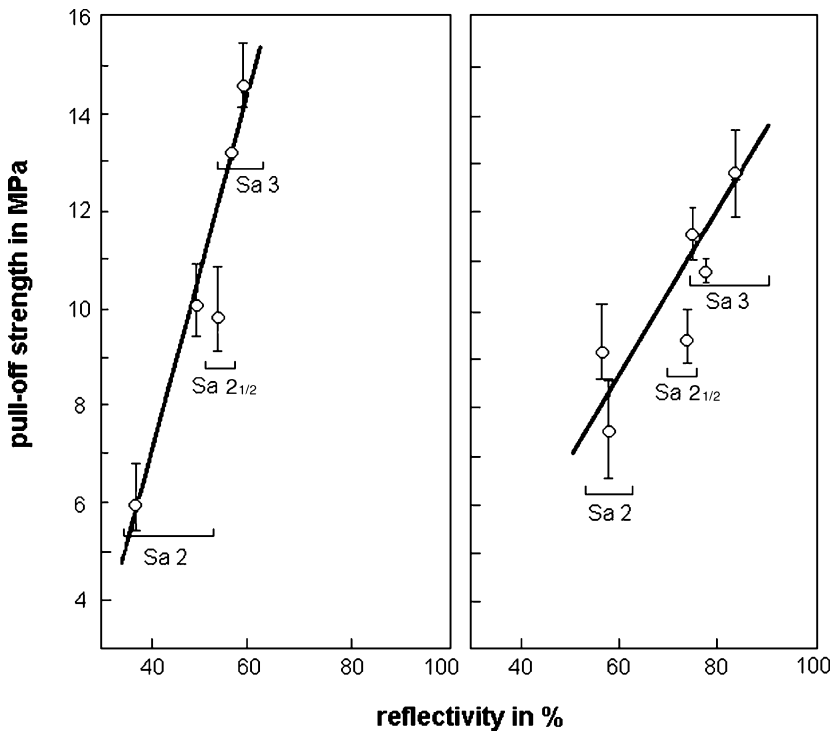


Fig. 8.6 Relationship between reflectivity, abrasive type and pull-off strength for metal-sprayed coatings (Bardal, 1973). Left: Copper slag ($d_p = 300-2, 500 \mu\text{m}$); right: Silica sand ($d_p = 600-1, 500 \mu\text{m}$)

reduced reflectivity (see Fig. 8.7 and Sect. 8.5) for more information on this issue). It could, however, be shown that reflectivity had a unique relationship to the pull-off strength values for sprayed metal coatings. Results of these investigations are exhibited in Fig. 8.6. The graphs in the figure verify that reflectivity alone is not a sufficient measure of the coating carrying capability of a blast cleaned substrate; abrasive type is another considerable parameter. For equal values of reflectivity of 60%, the substrate prepared with copper slag (left graph) delivered a pull-off strength of about $\sigma_A = 13 \text{ MPa}$, whereas the substrate prepared with silica sand (right graph) delivered a pull-off strength of about $\sigma_A = 9 \text{ MPa}$ only.

Hochweber (1971) introduced a method for the assessment of surface preparation grades which deployed the differences in the electric resistances between metal substrate and a measurement zone. This parameter, denoted transition resistance, was very low if the substrate featured a high degree of cleanliness. The author found the following relationships between surface preparation grade and transition resistance: Sa 1 = 1.0Ω ; Sa 1 to Sa 2 = 0.5Ω ; Sa 2 = 0.1Ω ; Sa 2^{1/2} and Sa 3 = 0.05Ω .

More recently, Terrat and Boissel (1995) developed a method for the assessment of the cleanliness of metal substrates based on the measurements of the electrical

surface potential decay. This method proved to be capable to distinguish between clean metal, oxidation products and oil layers.

8.2.4 Special Remarks

The following factors can influence the result of the visual assessment (ISO 8501-1):

- initial state of the steel surface other than any of the standard rust grades A to D;
- colour of the steel itself;
- regions of different roughness;
- surface irregularities, such as dents;
- marks from tools;
- uneven lighting;
- shadowing of the surface profile caused by angled projection of abrasive;
- embedded abrasives.

The latter aspect is considered through a supplement to ISO 8501-1, which illustrates the differences in surface appearance, including colour, which are obtained when the same surface is prepared by blast cleaning with different abrasive materials to the same preparation grade. The situation is shown in Fig. 8.7. This situation is further illustrated by the results of reflectivity measurements as provided in Table 8.4.

For previously coated surfaces, which have been prepared for re-painting, only photographs with rust grades “C” and “D” should be used for visual assessment. The surfaces should be examined either in good diffuse daylight or in equivalent artificial illumination. For rust grades, the worst grade is evident.

Some recent developments revealed the use of vision sensing systems (Carew et al., 2001; Chen and Chang, 2006) and image analysing methods (Gupta et al., 2003; Trujillo and Sadki, 2004; Greverath et al., 2005) for the assessment of blast cleaned steel substrates. Two examples are shown in Figs. 8.8. and 8.9. The graph in Fig. 8.8 shows a pixel histogram for a steel substrate, which was prepared according to a surface preparation grade Sa 3 (bare metal). The dimension for the x -axis was the hue-value of the colour. The rather continuous signal characteristics without a dominating peak, characterised a clean substrate without discolouration. The results shown in Fig. 8.9, where differences in peak location and peak height for two close surface preparation grades in a green-colour histogram could be recognised, showed that colour measurements have promise for detecting subtle differences in blast cleaned surfaces. Software solutions are under development for the automatic detection and quality assessment of blast cleaned substrates (Gupta et al., 2003). An example is provided in Fig. 8.10.

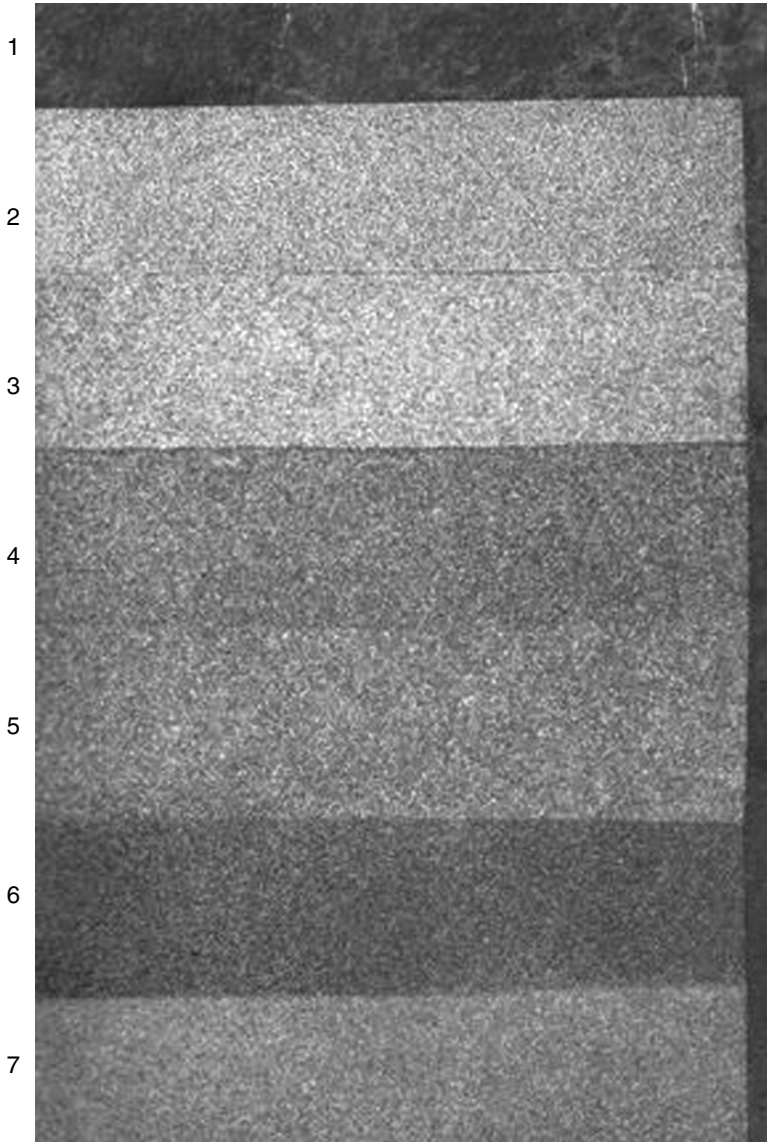


Fig. 8.7 Effects of abrasive materials on visual appearance of blast cleaned steel substrates (ISO 8501-1/1). Substrate condition: 1-Original mild steel plate (rust grade C); 2-blast cleaned to Sa 3 with high-carbon cast steel shot (S 100, Vickers hardness: 390–530 HV); 3-blast cleaned to Sa 3 with steel grit (G 070, Vickers hardness: 390–530 HV); 4-blast cleaned to Sa 3 with steel grit (G 070, Vickers hardness: 700–950 HV); 5-blast cleaned to Sa 3 with chilled iron grit (G 070); 6-blast cleaned to Sa 3 with copper refinery slag; 7-blast cleaned to Sa 3 with coal furnace slag

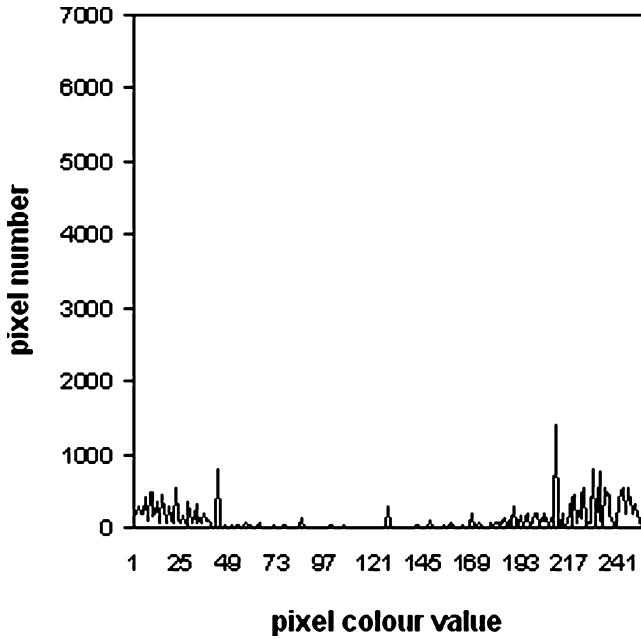


Fig. 8.8 Hue histogram of a blast cleaned stainless steel substrate (Momber, 2005b). Surface preparation grade: Sa 3 (bare metal)

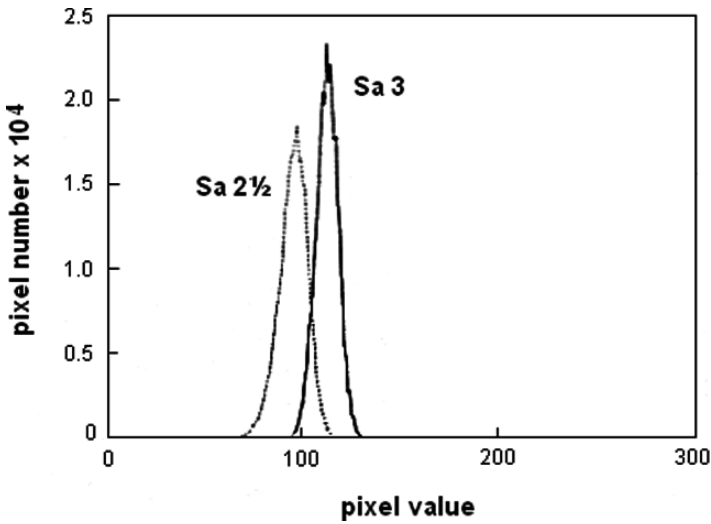


Fig. 8.9 Histogram of the green element in a colour spectrum for two blast cleaning preparation grades (NWU, 1995)

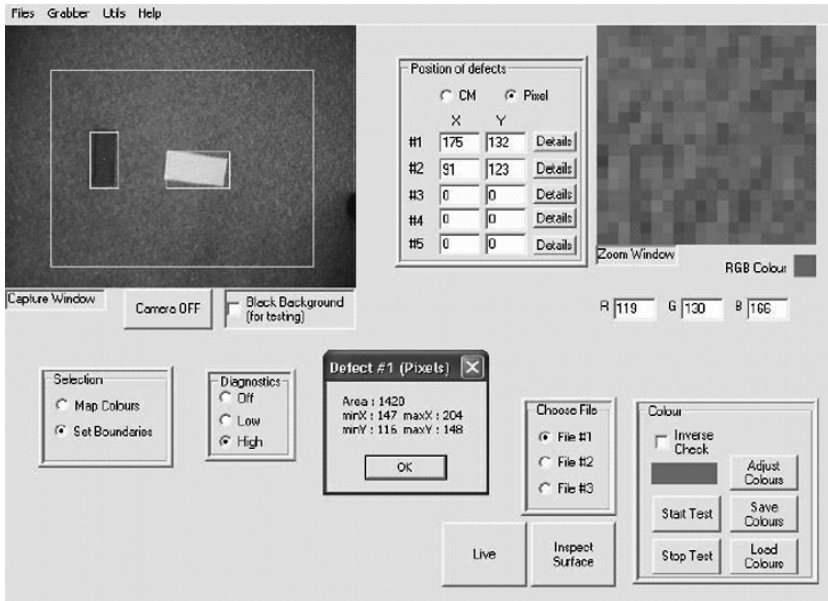


Fig. 8.10 User interface depicting two defects on simulated substrate surfaces (Gupta et al., 2003)

8.3 Dissolved Substances

8.3.1 Definitions and Measurement

Chemical cleanliness mainly considers the presence of dissolved substances on the prepared substrate surface. These substances include dissolved iron and certain salts. Soluble salts, namely chlorides, phosphates, nitrates and sulphates, are very widespread on steel substrates. A major source is sea salt, which affects especially ships, offshore structures and waterfront constructions. However, soluble salts can also arise from chemical processes, cooling towers, agricultural processes and burning of sulphur-containing coal. The detrimental effect of water-soluble contaminants at the steel/paint interface is well known. The amount of salts, especially chlorides, on blasted surfaces is essential for the performance of the applied coating systems. It is often thought that salt contamination is an issue for repair and maintenance of existing structures only. However, new construction work can be affected by salt contamination as well. An example is displayed in Fig. 8.11 showing the contamination of mechanically cleaned steel panels, which were stored on seashore locations, through atmospheric salts. After 12 months of storage, most of the panels displayed high salt contents. Before such panels can go into production, they must be thoroughly cleaned in order to remove salts. Permissible salt levels are specified in accordance to the field of application of the coating system, for example according to atmosphere (air and water) or operation temperature.

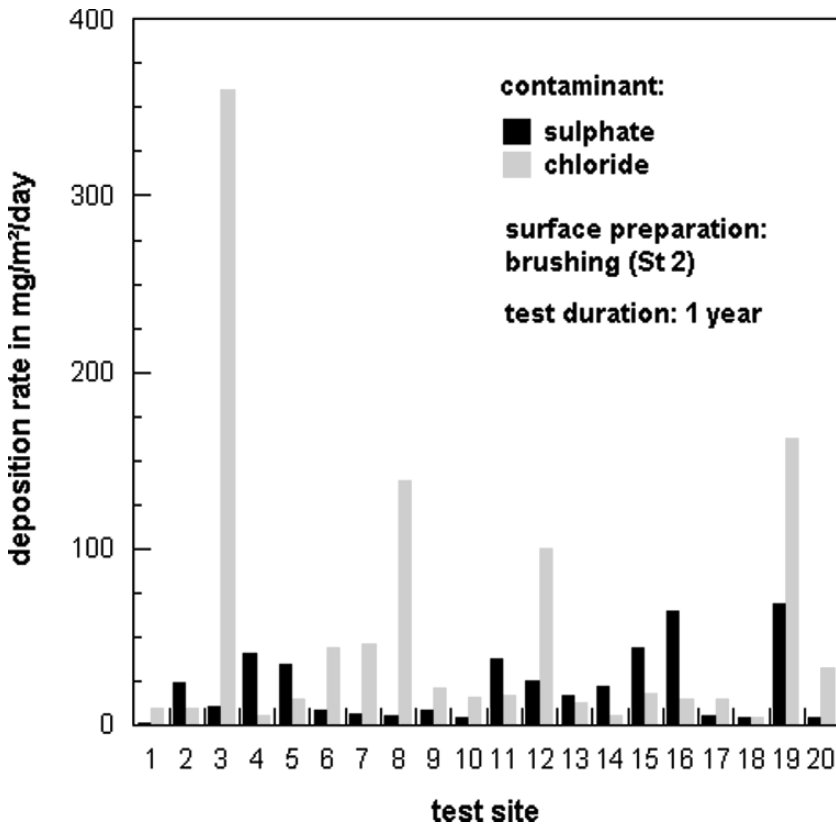


Fig. 8.11 Effects of storage conditions on salt contamination of power tool cleaned steel panels (Flores and Morcillo, 1999). Designations 1–20: locations in Europe and Latin America

Surface contamination by soluble salts has always been an issue for the corrosion protection industry. It was, however, the replacement of lead-based paints (Pb_3O_4) by other paint types due to environmental concerns that caused a different look at salts with respect to coating performance. Salt occupancy applies to non-visible surface contaminants according to SSPC-TU 4. Table 8.5 provides a description of non-visible surface cleanliness definitions. The level of non-visible contaminants that may remain on the surface is usually expressed as mass per unit area, much often in $\mu\text{g}/\text{cm}^2$. The prime salts most commonly encountered are chlorides, sulphates and nitrates. Ferric chlorides, however, tend to be more soluble than other salts of lower formula weight. They, therefore, usually produce rather high osmotic pressures (see Appleman, 2002).

There are several methods used to estimate the salt level on blast cleaned steel substrates, namely:

- Direct salt measurement (swab method or adhesive cell method): salt concentration (ppm or mg/l), cross-section (cm^2) and volume (ml) must be known to estimate salt contamination ($\mu\text{g}/\text{cm}^2$);

Table 8.5 Description of non-visible surface cleanliness definitions (SSPC-SP 12/NACE No. 5)

Term	Description of surface
NV-1	Free of detectable levels of soluble contaminants, as verified by field or laboratory analysis using reliable, reproducible methods.
NV-2	Less than 7 $\mu\text{g}/\text{cm}^2$ of chloride contaminants, less than 10 $\mu\text{g}/\text{cm}^2$ of soluble ferrous ion levels, or less than 17 $\mu\text{g}/\text{cm}^2$ of sulphate contaminants as verified by field or laboratory analysis using reliable, reproducible test methods.
NV-3	Less than 50 $\mu\text{g}/\text{cm}^2$ of chloride or sulphate contaminants as verified by field or laboratory analysis using reliable, reproducible test methods.

- Measurement of electric conductivity (total soluble substances): usually expressed in $\mu\text{S}/\text{cm}$ for liquid solutions;
- Spectrometry: cannot deliver results in terms of salt content per cross-section ($\mu\text{g}/\text{cm}^2$).

The latter method cannot only detect a certain salt type, but also its components: in the case of chlorides, its components, such as sodium hypochloride, chlorine oxide, chlorine dioxide or hydrochloric acid, can be detected (Trotter, 2001). Information about the testing of steel substrates for soluble salts and soluble iron corrosion products as well as analysis methods is provided in several parts of ISO 8502.

8.3.2 Effects of Dissolved Substances on Coating Performance

Chloride content on the substrate significantly influences the performance of coating systems. Rust development under the paint film and osmotic blistering are commonly observed at an early stage in organic coatings applied over contaminated steel substrates. This was verified through laboratory and site experiments performed by Mitschke (2001), Morcillo et al. (1989a), Kaiser and Schütz (2001) and Soltz (1991). The investigations of the authors have shown the following:

- chlorides significantly reduced the capability of paint to penetrate and enclose rust (Fig. 8.12);
- time to osmotic blistering decreased if chloride concentration increased (see Table 8.6);
- maximum service temperature of linings decreased if chloride concentration increased (an increase by 1.0 $\mu\text{g}/\text{cm}^2$ lowers the maximum service temperature by about 6°C);
- number of blisters increased if chloride concentration increased (see Fig. 8.13);
- much higher levels of sulphate contamination (>100–250 $\mu\text{g}/\text{cm}^2$) were required to cause coating blistering compared to chloride. Therefore, blistering from seawater sulphate contamination does not appear to be a primary problem.

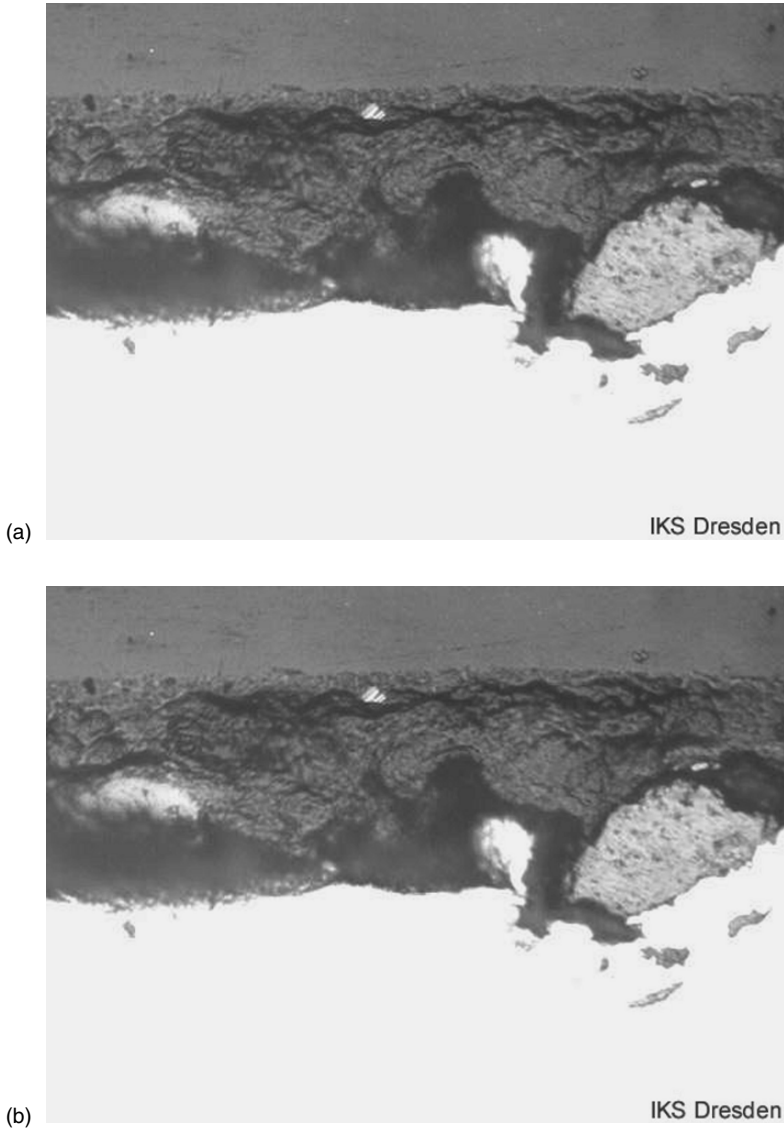


Fig. 8.12 Effects of rust contamination on paint penetration capability. (a) Clean rust; (b) Sulphate-contaminated rust; (c) Chloride-contaminated rust. Magnification: $200\times$ (Photographs: Institut für Korrosionsschutz GmbH, Dresden)

The very extensive study performed by Soltz (1991) also contains an investigation about the effect of chloride-contaminated abrasives on the coating performance.

However, the major criterion for salt content is the safe or, respectively, permissible salt level that prevents under-rusting or blistering of the applied paint system. There are different values available in the literature; some are summarised



Fig. 8.12 Continued

in Tables 8.7 and 8.8. It must be considered that these global values may be modified for certain applications and coating systems; in such cases, paint manufacturers shall be consulted. Zinc-based systems are far less vulnerable to salt concentration than barrier systems, for example. Thresholds for chlorides and sulphates also depend on DFT of the applied paints; this statement is verified by the values listed in Table 8.8. Further information is provided by Alblas and van London (1997). It is important to realise that each different coating/substrate system is likely to have various parameters, including the chloride levels it can tolerate, that are unique to itself.

It is known that the capability of a primer to penetrate existing rust layers depends on the contamination level (CL) of the rust. The penetration capability is weak if the rust contains salts. This was verified through comparative metallographic studies by Kaiser and Schütz (2001) on clean and contaminated, respectively, steel samples (see Fig. 8.12). The authors defined three levels of salt contamination:

- (1) NaCl: $<0.5 \mu\text{g}/\text{cm}^2$; Na_2SO_4 : $<5 \mu\text{g}/\text{cm}^2$;
- (2) NaCl: $0.81 \mu\text{g}/\text{cm}^2$; Na_2SO_4 : $112.6 \mu\text{g}/\text{cm}^2$;
- (3) NaCl: $87.6 \mu\text{g}/\text{cm}^2$; Na_2SO_4 : $18.8 \mu\text{g}/\text{cm}^2$.

If the samples were almost clean [case (1)], the coating material enclosed and integrated the rust completely. The liquefied coating material penetrated up to the substrate surface, and it was able to wet the substrate. This case is shown in Fig. 8.12a. Penetration capability of the liquefied paint material decreased if the rust contained sulphate [case (2)]; rust particles were not enclosed completely in that case, and flaws occurred between substrate and coating. These flaws are clearly visible in Fig. 8.12b. The worst results, as illustrated in Fig. 8.12c, were obtained with highly chloride-contaminated rust [case (3)]. Large gaps with widths of 30–40 μm appeared between

Table 8.6 Time to failure by blistering for linings (Mitschke, 2001)

Chloride level in $\mu\text{g}/\text{cm}^2$	Time to blistering in weeks at various temperatures				
	88 °C	77 °C	66 °C	54 °C	43 °C
Epoxy novolac, DFT 320 μm					
0.6	>56	>56	>56	>56	>56
1.4	>56	>56	>56	>56	>56
3.9	>56	>56	>56	>56	>56
5.3	>56	>56	>56	>56	>56
7.6	>56	36	>56	>56	>56
Epoxy, DFT 193 μm					
0.6	3	26–36	>56	>56	>56
1.4	6	26–36	>56	>56	>56
3.9	6	26–36	>56	>56	>56
5.3	5	26	>56	>56	>56
7.6	2	2	4	10	>56
Epoxy, DFT 239 μm					
0.6	36	11	12	>56	>56
1.4	3	7	12	>56	>56
3.9	1.5	3	7	>56	>56
5.3	1.5	3	7	>56	>56
7.6	1.5	1.5	3	5	3
Epoxy novolac, DFT 262 μm					
0.6	>56	>56	>56	>56	>56
1.4	>56	>56	>56	>56	>56
3.9	>56	>56	>56	>56	>56
5.3	>56	>56	>56	>56	>56
7.6	>56	>56	>56	>56	>56
Epoxy, DFT 252 μm					
0.6	1.5	>56	>56	>56	>56
1.4	1.5	1.5	4	>56	>56
3.9	1.5	1.5	3	>56	>56
5.3	1.5	1.5	10	>56	>56
7.6	1.5	1.5	3	>56	>56
Epoxy, DFT 252 μm					
0.6	36–43	>56	>56	>56	>56
1.4	36–43	43–56	>56	>56	>56
3.9	3	3	>56	>56	>56
5.3	23	23	>56	>56	>56
7.6	3	3	43–56	>56	>56

coating and substrate. This gaps contained rust particles that were not incorporated into the paint. This caused deteriorated adhesion between steel and paint system.

Tests on contaminated substrates, performed by Allan et al. (1995), showed that the level of dissolved salts not only affected the value of adhesion strength, but also the type of adhesion of coatings to substrates. With zero contaminants, the mode of failure was cohesive within the primer coat. As the salt level increased, progressively

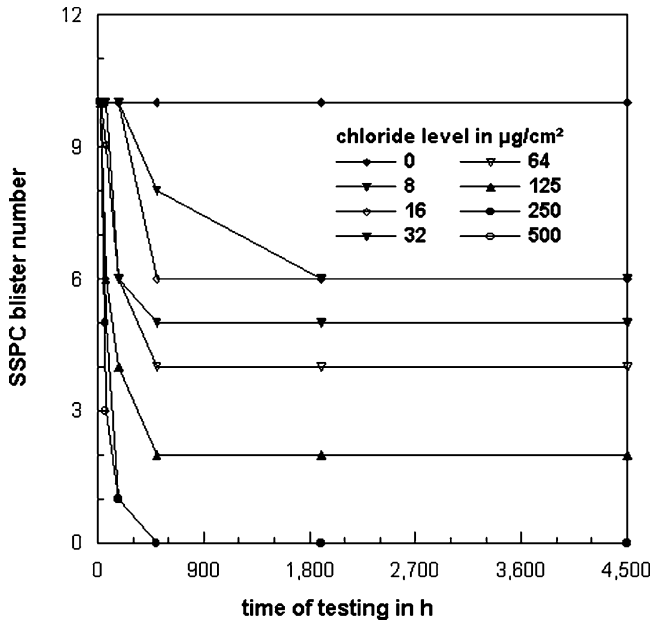


Fig. 8.13 Effects of chloride contamination on blistering intensity (Soltz, 1991)

less primer remained adhered to the steel surface. At higher CL, there was a change from mixed to total adhesive failure of the primer.

Table 8.9 lists further quantitative results. They confirm that with chloride-contaminated steel substrates exhibited the lowest values for adhesion strength, and the highest values for degree of blistering and rusting for all coating systems. These results were caused by the reduced rust penetration capability of the applied paint systems. Thus, rust, in itself, is not a problem; rather it is the contaminants that the rust contains.

Chandler (1966), in an early study on the effects of salts in rust, could show that the presence of sulphates and chlorides in rust increased the corrosion of steel, and this increased with the amount of salts in the rust. Some results of this study are

Table 8.7 Permissible chloride levels on steel substrates

Institution	Permissible chloride content in µg/cm²
NASA	5
IMO (DE 48/12)	5
SSPC/NACE	7
US Navy (non-immersion service) ^a	5
US Navy (immersion service) ^a	3
Norsok (M-501)	2
Hempel (non-immersion service) ^b	19.5
Hempel (immersion service) ^b	6.9

^aCited in Appleman (2002)

^bHempel Paints A/S, Longby, Denmark

Table 8.8 Critical salt thresholds that result in early paint deterioration (Morcillo and Simancas, 1997; Appleman, 2002)

Coating system	DFT in μm	Salt thresholds in $\mu\text{g}/\text{cm}^2$	
		Chloride (Cl)	Sulphate (SO_4)
Unknown	125–225	7–30	70–300
	25–35	>1	–
	7–11	6–25	9–35
	Thin films	7	16
	100–150	–	58.8
	60–190	6–30	100–250
	130–180	5–10	50–100
Epoxy phenolic	One coat	1	–
Epoxy polyamide	Three coats	5	–
Coal tar epoxy	254	50	–
Fusion-bonded epoxy	–	<3	–
Tank lining epoxy	–	10–20	–
Epoxy mastic	Two coats	7	–

displayed in Fig. 8.14. The figure also illustrates that contaminated rust layers were much more sensitive to changes in relative humidity than clean rust or blast cleaned substrates were. Calabrese and Allen (1978) compared the corrosion behaviour of steel plates originally covered with atmospheric (industrial) corrosion products and mill scale. They found that industrially corroded and blast cleaned steel quickly formed new corrosion products, and they attributed this effect to chloride and sulphate trapped in folded substrate regions, which then became active corrosion sites

Table 8.9 Evaluation of coatings for rusted substrates; after one year environmental weathering (Kaiser and Schütz, 2001)

Coating	DFT in μm	Rust contamination	Blistering ^a	Rust ^b degree	Adhesion ^c strength MPa	Failure type
Noverox +	204 \pm 22	None	0	Ri 0	1.3 \pm 0.6	A/B10, B/C90
HS epoxy	213 \pm 17	NaCl	5/2	Ri 0	1.1 \pm 0.6	A/B100
	199 \pm 20	Na ₂ SO ₄	3/2	Ri 0	1.4 \pm 0.2	A/B40, B/C60
Noverox +	213 \pm 24	None	0	Ri 0	3.7 \pm 1.4	A/B50, C50
DS-mica	221 \pm 16	NaCl	5/2	Ri 1	3.2 \pm 1.0	A/B70, C30
	208 \pm 21	Na ₂ SO ₄	0	Ri 1	4.0 \pm 0.8	A/B20, C80
Antitrust +	173 \pm 15	None	0	Ri 0	1.0 \pm 0.6	B/C100
HS epoxy	192 \pm 18	NaCl	5/2	Ri 0	1.9 \pm 0.6	A/B100
	182 \pm 21	Na ₂ SO ₄	4/2	Ri 0	1.9 \pm 0.6	A/B40, B/C60
Antitrust +	181 \pm 17	None	0	Ri 0	4.2 \pm 1.0	A/B20, C80
DS-mica	178 \pm 9	NaCl	5/2	Ri 1	3.6 \pm 1.2	A/B80, C20
	169 \pm 11	Na ₂ SO ₄	0	Ri 0	4.3 \pm 1.5	A/B20, C80
Noxyde	148 \pm 15	None	2/2	Ri 0	2.1 \pm 0.4	A/B80, B20
	136 \pm 11	NaCl	5/2	Ri 2-3	2.0 \pm 0.9	A/B80, B20
	151 \pm 10	Na ₂ SO ₄	3/2	Ri 0	2.9 \pm 0.4	A/B90, B10

^aISO 4628-2^bISO 4628-3^cISO 4624

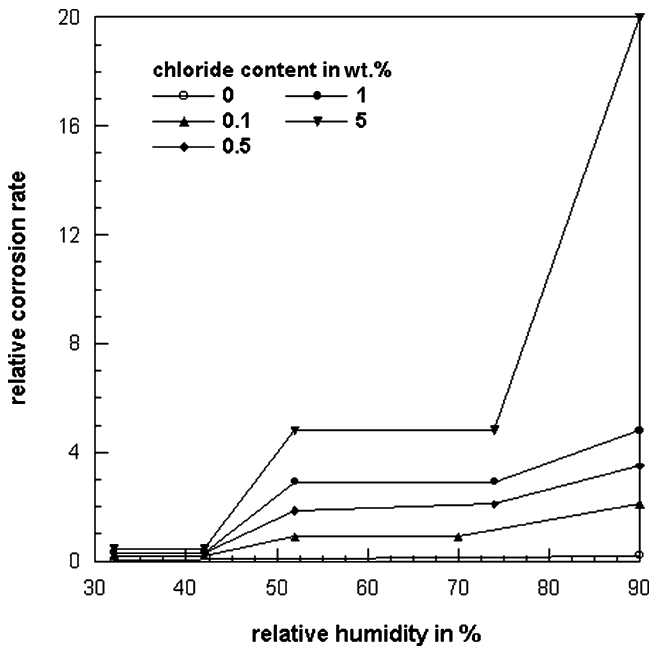


Fig. 8.14 Effects of salt contamination and relative humidity on relative corrosion rate in mild steel (Chandler, 1966)

(see Fig. 8.15). The authors developed a schematic, and suggested an oxidation cycle, which depicted the formation of new surface corrosion products of an industrially corroded, blast cleaned and environmentally tested steel substrate.

8.3.3 Substrate Cleanliness After Blast Cleaning

A number of investigations were performed in order to evaluate the chloride content of steel substrates prepared by different surface preparation methods; this includes the studies of Allen (1997), Brevoort (1988), Dupuy (2001), Forsgren and Applegren (2000), Kuljian and Melhuish (1999), Momber (2003), Momber and Koller (2005), Morris (2000), Trotter (2001), NSRP (1998a) and Van der Kaaden (1994). Some results of these studies are summarised in the Tables 8.10 and 8.11. A notable reduction in chloride level could be noted if wet blast cleaning and hydroblasting were applied. In both these applications, the water flow involved in the preparation process entered pores, pits, pockets, etc., and it swept the salt away. This mechanism was verified by results of SEM inspections of hydroblasted steel substrates (Trotter, 2001). Mechanical methods, such as needle gunning or wire brushing, did not remove soluble salts with the same reliability. Striking features were the high values for soluble iron, potassium and chloride after dry blast cleaning as listed in Table 8.12. Obviously, rust and sea salt could not be removed efficiently by this method. A study that included other salts (sulphates, phosphates and nitrates)

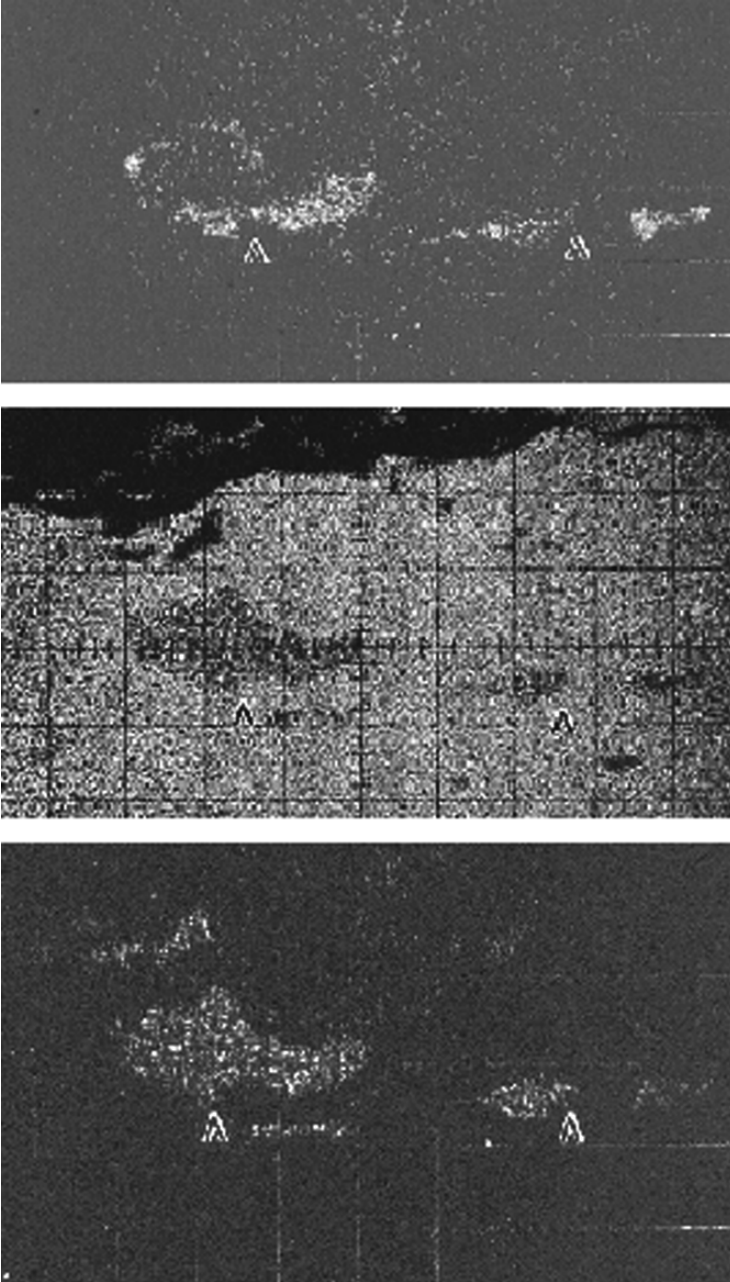


Fig. 8.15 EPA mapping of a dry blast cleaned steel substrate (Calabrese and Allen, 1978). Upper: chloride; centre: iron; lower: oxygen

Table 8.10 Chloride levels measured after different pretreatment methods (Forsgren and Applegren, 2000)

Method	Chloride level in $\mu\text{g}/\text{cm}^2$		
	Bresle (10 min)	SSM (10 s) ^a	SSM (10 min) ^a
No pretreatment	44.8	47.5	61.3
	54.8	72.8	96.3
	15.2	*	*
	24.8	*	*
Wet blast cleaning	1.6	1.4	2.7
	1.6	0.7	2.0
	0	1.7	3.1
	3.2	1.5	4.1
Hydroblasting	1.6	15.2	–
	0.8	1.8	4.2
	0	2.4	4.6
	1.2	0.1	2.1
	2.4	4.8	10.3
	1.2	0	1.0
Wire brush	0	0	0.8
	28.8	63.5	–
	16.0	32.6	58.9
	23.2	15.2	25.0
Needle gun	17.6	18.1	30.3
	27.6	19.9	42.6
	21.2	20.9	35.0
	26.8	41.3	96.1
Dry blast cleaning	29.6	20.6	31.5
	4.4	8.3	14.8
	6.8	10.8	16.5

*No measurements

^aSurface saltmeter

was performed by Howlett and Dupuy, (1993). This study showed the same trends for these types of salts as for the chlorides. It was further found that blast cleaning did not remove chlorides to safe levels 50% of the time.

Calabrese and Allen (1978) showed through SEM images that dry blast cleaned steel surfaces exhibited layered and cusp surfaces. Folds were formed during the blast cleaning process, and impurities were trapped in these folds. EPA mapping indicated numerous elements present in the traps immediately under the blasted surface, among them are chlorine and oxygen. Examples of these measurements are provided in Fig. 8.15. Calabrese and Allen (1978) showed also that surfaces that had traces of chlorine and sulphur after the blast cleaning process, quickly underwent new corrosion. Neal (1999), also based on SEM imaging, could detect micro-pits, which contained chlorides, directly underneath the surface of dry blast cleaned steel substrates. An example for this situation is provided in Fig. 8.16. Fairfull and Weldon (2001) investigated the influence of different abrasive materials on the

Table 8.11 Surface contaminant results from different preparation methods (Howlett and Dupuy, 1993)

Substrate	Contaminant	Salt level in $\mu\text{g}/\text{cm}^2$			
		Surface preparation method			
		Uncleaned	Dry blast cleaned	Hydroblasted	Hydro-abrasive blast cleaned
A-36 steel with mill scale	Sulphates	40	3	0	4
	Phosphates	0	0	0	3
	Chlorides	2	2	1	0
	Nitrates	0	6	0	6
A-285 Grade 3 steel with mill scale	Sulphates	5	5	0	1
	Phosphates	0	1	0	6
	Chlorides	4	3	1	1
	Nitrates	0	11	1	3
Rusted water service pipe	Sulphates	5	2	1	2
	Phosphates	1	2	0	6
	Chlorides	28	32	1	0
	Nitrates	6	1	1	8
Intact coating on water service pipe	Sulphates	8	4	0	0
	Phosphates	0	2	0	3
	Chlorides	6	1	1	0
	Nitrates	4	2	1	5
H ₂ S scrubber plate	Sulphates	39	7	0	3
	Phosphates	0	0	0	2
	Chlorides	12	8	0	1
	Nitrates	0	1	0	3
Heat exchanger shell	Sulphates	7	4	0	0
	Phosphates	0	0	0	7
	Chlorides	17	31	0	0
	Nitrates	0	3	0	6

Table 8.12 Soluble substances on prepared surfaces (Navy Sea System Comm)

Element	Soluble substance in $\mu\text{g}/\text{cm}^2$	
	Hydroblasted	Dry blast cleaned
Nickel	0.006	0.057
Zinc	0.063	1.512
Manganese	0.003	0.031
Magnesium	0.021	0.672
Calcium	0.121	1.989
Copper	0.033	0.250
Aluminium	0.003	0.352
Lead	0.015	0.045
Iron	0.018	9.450
Potassium	0.414	0.513
Sodium	0.855	42.03
Chloride	0.846	62.55
Sulphate	0.211	1.260
Total	2.611 (100%)	120.71 (4623%)

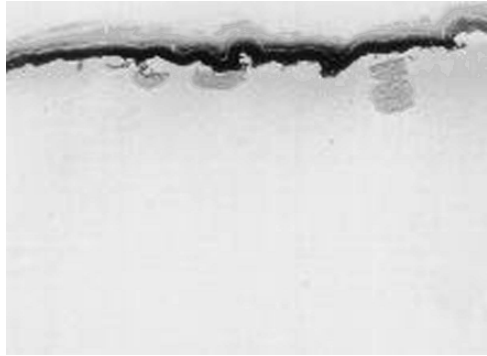


Fig. 8.16 Chloride-filled pits underneath a dry blast cleaned steel surface (Neal, 1999)

contamination of blast cleaned steel substrates. They found that the use of a certain type of coal slag led to a notable contamination of the substrate with sulphates. The sulphate level reached values as high as $9 \mu\text{g}/\text{cm}^2$, whereas the sulphate level was as low as $1 \mu\text{g}/\text{cm}^2$ for other abrasive materials (iron oxide, nickel slag, steel grit, olivine, garnet, etc.).

Appleman (2002, 2003) ranked surface preparation methods according to their relative salt removal capability as follows:

- hydroblasting with abrasives: 1.00;
- hydroblasting: 0.95;
- wet blast cleaning: 0.90;
- dry blast cleaning: 0.83–0.90;
- high-pressure water washing: 0.85;
- hand and power tool cleaning: 0.25.

The salt removal capacity of blast cleaning depended on the designated surface preparation degree as follows (Appleman, 2003):

- commercial blast cleaning (Sa 2): 0.83;
- near white blast cleaning (Sa 2 $\frac{1}{2}$): 0.84;
- white metal blast cleaning (Sa 3): 0.90.

Johnson (1997) introduced an alternative method for the extraction of chlorides from bridge steels. After being dry blast cleaned, the steel may be allowed to set overnight, so chlorides and oxides rise to the surface and dry outside the contaminated pits which could not be cleaned by blast cleaning, and removing the dry, visible blotches by a subsequent blast cleaning step.

Recommended methods for the removal of water-soluble contaminants from steel substrates are listed in Table 8.13.

Table 8.13 Recommended procedures for removal of water soluble contaminants (ISO 12944-4)

Procedure	Remarks
Water cleaning	Fresh water. Pressure ($p < 70$ MPa) may be used.
Steam cleaning	Rinse with freshwater.
Alkaline cleaning	Aluminium, zinc and certain other types of metal coating may be susceptible to corrosion if strongly alkaline solutions are used. Rinse with freshwater.

8.4 Organic Films

8.4.1 Definitions and Measurement

Organic films, mainly consisting of oil or grease, can come from a variety of sources: diesel fumes, lubrication oils from compressors and power tools, or from contaminated abrasives. They have detrimental effects on the performance of protective coatings. Reasons may be the separation of wet coatings from the substrate material as well as the influence of the wetting behaviour of the surfaces. It may generally be distinguished between hydrophobic and hydrophilic films (see Sect. 8.9 for more details on wettability). Table 8.14 lists some typical examples. Grease, motor oil and silicone lead to a reduction in wettability, whereas NaOH and H₂SO₄ contributed to good wettability. However, contact angle, as a measure of wettability, does not allow a precise indication of grease contamination. This aspect is illustrated in Fig. 8.17. It can be seen that contact angle first rose in a linear fashion if grease contamination increased, but it then started to drop if grease level reached high levels. The utilisation of contact angle measurements requires a smooth surface with a roughness less than $R_z = 15 \mu\text{m}$ (Meyer and Schulz, 2001). Piatti et al. (1959) utilised a modified Mettler analysis balance for wettability estimation, and they could show that degreasing improved wettability of austenitic steel by almost +50%.

An accepted standard for the assessment of organic films does not exist. Some recommended procedures are listed in Table 8.15. In practice, the water spray

Table 8.14 Contact angles to contaminated concrete substrates (Gelfant, 1995)

Contaminant	Contact angle in °	Wettability
Laitance	0–20	Hydrophobic
Milk	30–70	Hydrophobic
Vegetable oil	30–60	Hydrophobic
Oleic acid	30–40	Hydrophobic
Silicone	90–100	Hydrophilic
Motor oil	60–80	Hydrophilic
Grease	40–70	Hydrophobic
Hydraulic fluid	20–30	Hydrophobic
Na ₂ SiO ₃	0	Hydrophobic
NaCl	0–20	Hydrophobic
NaOH	0	Hydrophobic
H ₂ SO ₄	0	Hydrophobic

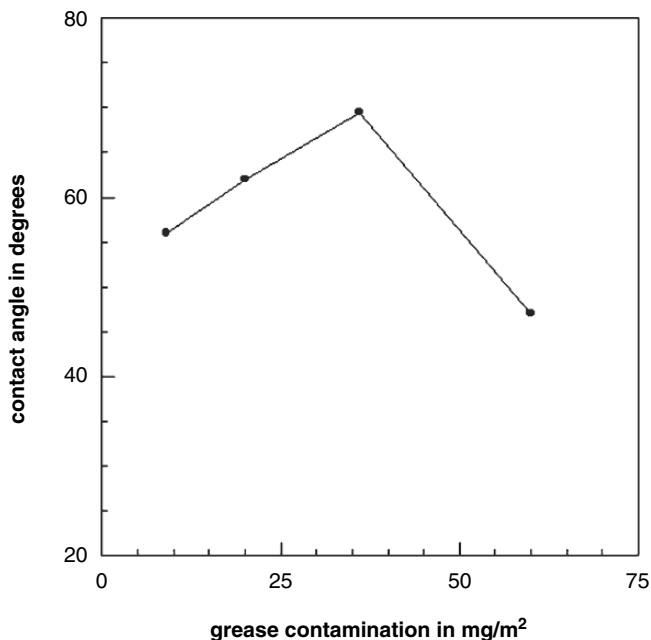


Fig. 8.17 Relationship between grease contamination and contact angle (Meyer and Schulz, 2001). Wetting liquid: water

method as illustrated in Fig. 8.18a is frequently used. If the substrate is greasy or oily, water will not wet these surface sections. It will rather flow besides the contaminated areas. On the hydrophobic greasy and oily sections, the water will not form a film, but will bubble up. Another method, recommended for practice use, is the chalk test as illustrated in Fig. 8.18b. A piece of soft chalk will mark the clean steel surface, but not the contaminated sections. However, this method works for dry grease or oil films only.

8.4.2 Effects of Oil and Grease on Coating Performance

DIN-Fachbericht 28 (2002) defines oil and grease levels to be safe at concentrations lower than $5 \mu\text{g}/\text{cm}^2$. For values higher than $300 \mu\text{g}/\text{cm}^2$, the risk of coat-

Table 8.15 Assessment methods for grease and oil (DIN-Fachbericht 28)

Method	Decision
Water rinsing tests	Yes/no
Water spray test	Yes/no
Grease red-test	Yes/no
Fluorescence test	Yes/no
Solvent extraction	Quantitative
Combustion	Quantitative

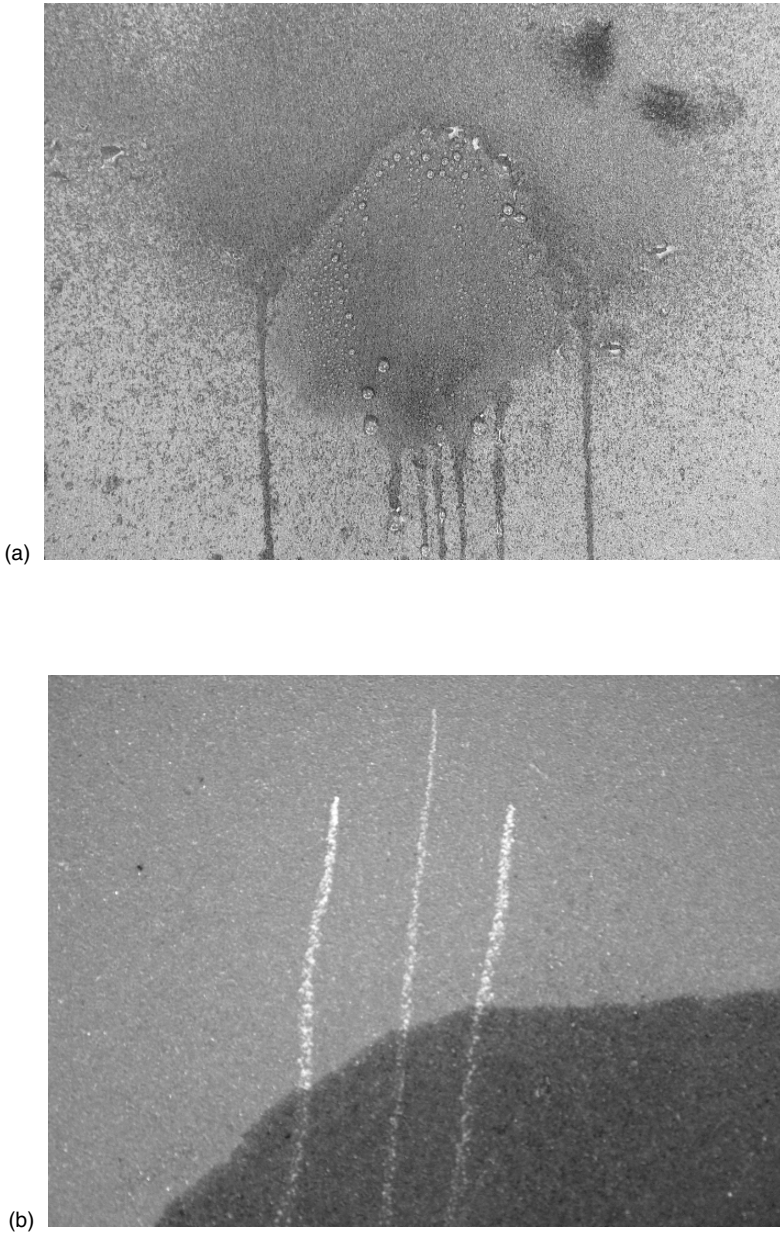


Fig. 8.18 Site methods for grease detection. (a) Water spray tests; (b) Chalk tests (Photographs: Muehlhan AG, Hamburg)

ing failure is high in general, whereby the probability of coating failure depends on coating type and coating thickness. A study about the effects of organic contaminants on the behaviour of certain organic coatings was performed by Weldon et al. (1987). Results of their measurements are listed in Table 8.16. In terms of adhesion to the substrate, the organic coating systems performed well up to a contamination level of about $600 \mu\text{g}/\text{cm}^2$. The inorganic zinc-based coating was most sensitive to grease contamination; it failed at a grease level as low as $320 \mu\text{g}/\text{cm}^2$. Cyclic freeze-thaw-immersion tests of contaminated and subsequently painted panels showed very good results for the organic coating systems, but again a worse performance of the zinc-based coating. An opposite trend was observed for the results of salt fog tests on panels with artificial scribes. In that case, the zinc-based paint performed best. This, however, is a well-known phenomenon. It is the self-healing capability of the zinc that prevents under-rusting and blistering at the scribe (Pietsch et al., 2002; Baumann, 2003; Binder, 2003; Momber and Schulz, 2005). Rider et al. (1999) investigated the effects of organic contaminants on the bond durability of blast cleaned aluminium epoxy joints. After contamination with kerosene, bond durability decreased notably. However, solubility of the liquid organic system into the contaminant material played an additional role. Gause (1989) investigated the effect of a corrosion inhibiting grease (Conoco HD-2) on the peel strength between steel substrates and an insulation rubber bonded with an adhesive. Results of this study are shown in Fig. 8.19, and it can be seen that the grease contamination led to a rapid drop in peel strength. For contamination levels in excess of $2,500 \text{mg}/\text{m}^2$, no direct bond between steel and adhesive could be observed.

Sofyan et al. (2005) reported about the deteriorated bond between HVOF-sprayed WC-Co coatings and steel substrate due to oil on the substrate. Large voids could be observed between coating and substrate, which were signs that the coating did not completely cover the substrate surface.

Table 8.16 Effects of organic contaminants on adhesion of coatings to steel substrates (Weldon et al., 1987)

Contamination level in $\mu\text{g}/\text{cm}^2$	Numeric adhesion rate according to ASTM D3359 ^a									
	Light oil		Motor oil				Grease			
	Alkyd	Epoxy	Alkyd	Epoxy	Vinyl	Zinc	Alkyd	Epoxy	Vinyl	Zinc
40	5	5	–	–	–	–	–	–	–	–
80	5	5	5	5	5	5	5	5	5	5
160	5	5	–	–	–	–	–	5	–	–
320	5	5	5	5	5	1	5	5	4	1
600	5	5	–	–	5	0	–	0	4	0
1,200	5	5	4	5	4	0	5	–	0	0
2,400	5	–	–	–	–	–	–	–	–	–

^aScale between 0 (very poor) and 5 (very good)

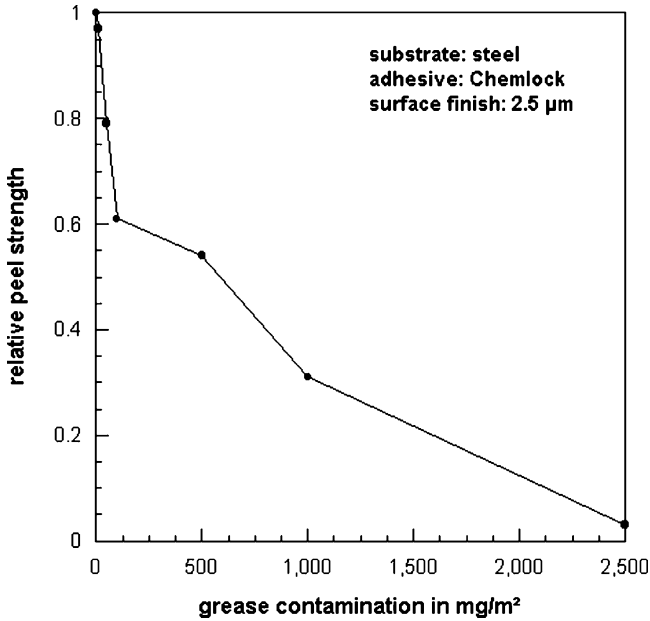


Fig. 8.19 Effects of corrosion-inhibiting grease on peel strength between steel substrate and adherent insulation rubber (Gause, 1989)

8.4.3 Substrate Cleanliness After Blast Cleaning

Blast cleaning is not a suitable method for degreasing. Degreasing must usually be performed before the blast cleaning work starts. However, quantitative demands can usually not be found in data sheets. State-of-the-art methods include steam cleaning, hot-water jetting and chemical degreasing (Van Oojj, 1984). Table 8.17 provides further details.

Table 8.17 Recommended procedures for removal of grease and oil (ISO 12944-4)

Procedure	Remarks
Water cleaning	Fresh water with addition of detergents. Pressure (<70 MPa) may be used. Rinse with fresh water.
Steam cleaning	Fresh water. If detergents are added, rinse with fresh water.
Emulsion cleaning	Rinse with fresh water
Alkaline cleaning	Aluminium, zinc and certain other types of metal coating may be susceptible to corrosion if strongly alkaline solutions are used. Rinse with fresh water.
Organic-solvent cleaning	Many organic solvents are hazardous to health. If the cleaning is performed using rags, they will have to be replaced at frequent intervals as otherwise oily and greasy contaminants will not be removed but will be left as a smeared film after the solvent has evaporated.

8.5 Dust and Embedded Abrasive Particles

8.5.1 Definitions and Measurement

Dust and embedded abrasive debris are common place on blast cleaned surfaces. A collection of examples is provided in Figs. 8.20–8.23. The avoidance of this phenomenon is a critical argument in blast cleaning operations. *Dust* is defined as “*loose particulate matter present on a steel surface prepared for painting, arising from blast-cleaning or other surface preparation processes, or resulting from the action of the environment.*” (ISO 8502-3). *Embedded particles*, in contrast, are tightly anchored in the surface. Dust and embedded particles may act as separators between substrate and coating system. It was shown in a study by Soltz (1991) that this phenomenon applied to larger size grit particles if they were left on surfaces and then painted over. If abrasive particles are notably contaminated with salts they may even cause rusting and blistering (compare Sect. 8.3.2). This can happen even with small amounts of fine dust (Soltz, 1991). Certain studies were performed to investigate dust adherence and particle embedment during blast cleaning operations. The first systematic investigation on this particular issue was probably that of Zaat (1960). The analysis of particulate contaminants on substrates surfaces can be done by applying the following methods:

- optical microscope (Zaat, 1960; Doherty, 1974; Fairfull and Weldon, 2001);
- secondary electron mode of SEM (Fairfull and Weldon, 2001; Momber et al., 2002a, 2004);
- back-scattered mode of SEM (Amada et al., 1999; Momber et al., 2002a, 2004);
- EDXA plots from SEM imaging (Momber and Wong, 2005a; Momber et al., 2002a; Possart et al., 2002).

Two images taken with the secondary electron mode of an SEM are provided in Fig. 8.20. This imaging mode delivers a three-dimensional view on the surface, and it can be seen clearly in Fig. 8.20b how abrasive fragments are just loosely adhere to the steel substrate. An example for the use of the back-scattered mode of an SEM is shown in Fig. 8.21. In that imaging mode, changes in the grey level are indicative of different chemical elements. The white grey sections correspond to steel, whereas the dark grey sections correspond to abrasive material. Two EDXA plots are shown in Fig. 8.22. The plot in Fig. 8.22a was taken from an untreated low-carbon steel sample. The different peaks are all contributed to the chemical composition of the material, whereby the highest peak is for iron (Fe). The plot in Fig. 8.22b was taken after blast cleaning with aluminium oxide. In contrast to the plot for the untreated steel, this plot contains a second dominant peak for aluminium (Al), which is indicative of contamination due to abrasive debris.

Cross cut sections of coated samples were analysed by Momber (2004) and Zaat (1960) in order to directly assess effects on coating adhesion to the substrate. Examples for this type of sample preparation are shown in Fig. 8.23. The images provide interesting information about the substrate structure. A heavily deformed top

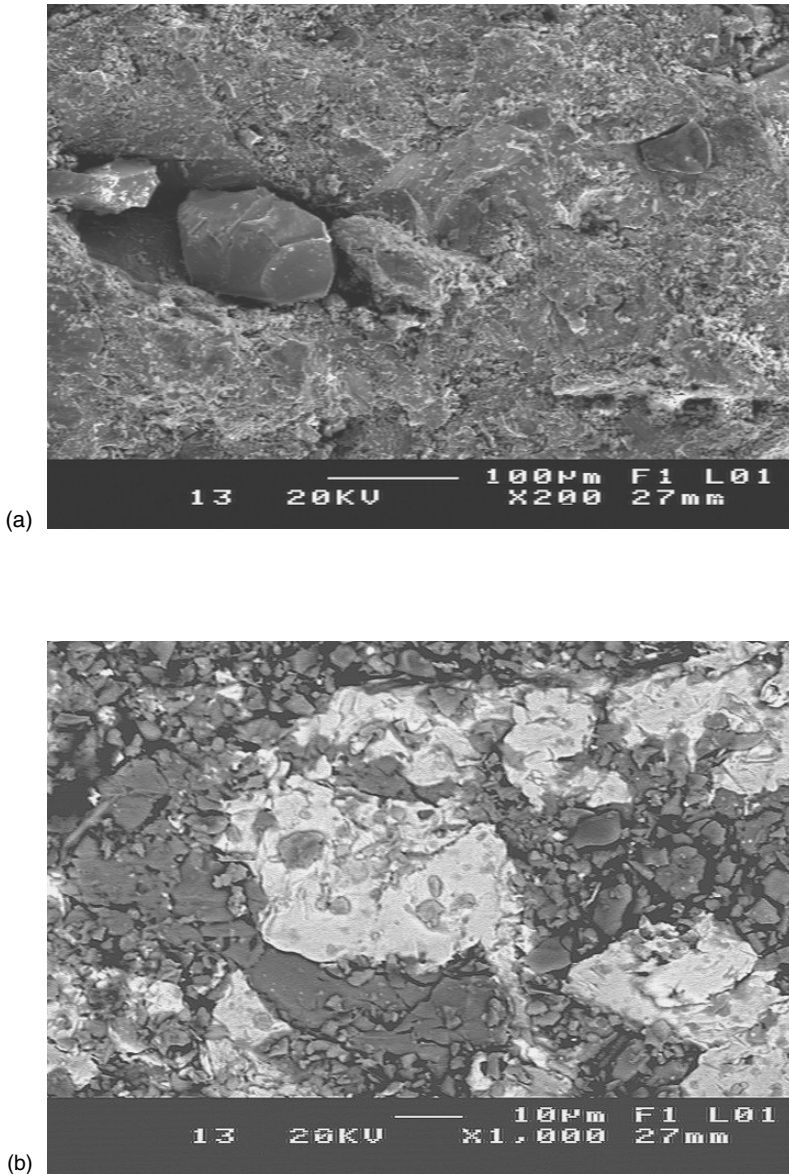


Fig. 8.20 Dust and embedded debris in carbon steel after blast cleaning. (a) Copper slag debris embedment; (b) Dust of broken copper slag debris. No fine cleaning was performed (Photographs: Muehlhan AG, Hamburg)

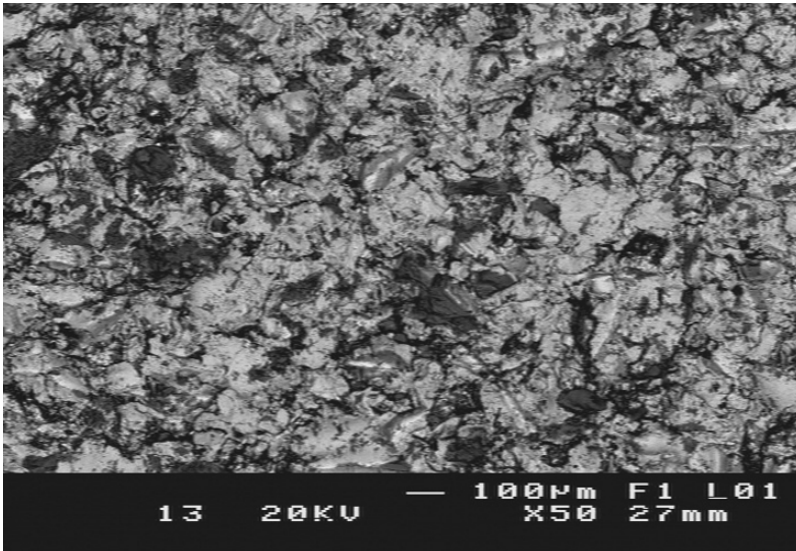


Fig. 8.21 Back-scattered SEM image of embedded aluminium oxide in carbon steel after blast cleaning. No fine cleaning was performed (Photograph: Muehlhan AG, Hamburg)

section can be recognised in Fig. 8.23a, which features lips still attached to the surface. Also visible is the high number of abrasive debris (copper slag) trapped underneath such lips. The image in Fig. 8.23b provides a magnified view on the cross-section of a blast-cleaned steel. A pocket with a length of about $50\ \mu\text{m}$ can be recognised which is completely filled with abrasive (copper slag) fragments. A second, smaller void, also filled with abrasive debris, is situated underneath that pocket.

The modification of metal substrates due to abrasive debris occurs due to two effects. The first effect is the embedment of individual debris in the substrate. This case is illustrated in Fig. 8.20a. A large copper slag fragment can be recognised, which is locked in the steel structure. The second effect is the formation of a loosely adhering dust layer, consisting not only of abrasive debris but also of removed substrate material. An example for this situation is provided in Fig. 8.20b. A large number of copper slag fragments (dark sections), with dimension of some micrometres, which are smeared over the substrate surface, can be seen. The image in Fig. 8.21 covers both effects. In that image, changes in the grey level are indicative of different chemical elements. The very dark grey areas were detected to be copper slag fragments.

Dust grade can be assessed by applying the tape method according to ISO 8502-3. The procedure, together with a typical result of a dust assessment test, is illustrated in Fig. 8.24. Dust can be evaluated according to the size of the particles and the number of the particles. Particle size classes are listed in Table 8.18, whereas particle number classes are displayed in Fig. 8.25. This procedure can, however, be utilised for the detection of debris that are loosely adhering to the substrate. Embedded abrasive fragments cannot be evaluated. Dust classes are rarely specified in data sheets. The demands are rather qualitative. The IMO-resolution for ballast

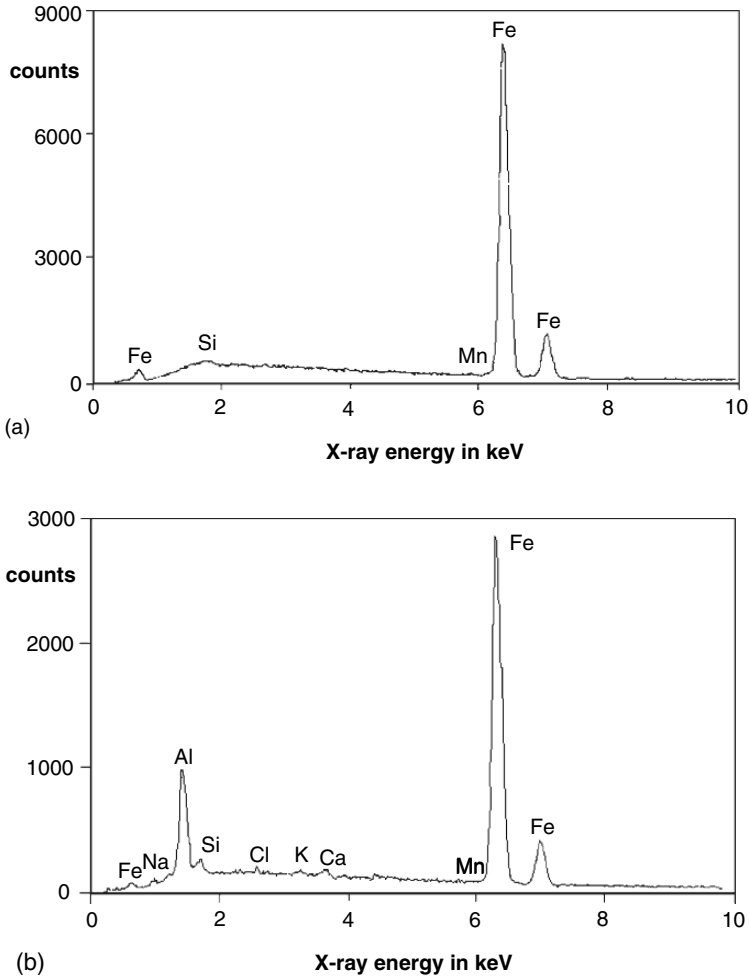


Fig. 8.22 EDXA plots illustrating embedded grit residue (Momber and Wong, 2005a). (a) Untreated surface; (b) Blast cleaned surface

water tanks in ship building (IMO, 2005) states, for example, that a dust class “1” is the limit for coatings in the ship new construction industry.

8.5.2 Effects of Dust and Particle Embedment on Coating Performance

Embedded particles and loose debris dust deteriorate the adhesion of coatings to the substrate. Figure 8.26 shows results of measurements of the adhesion strength as a function of the amount of embedded grit. The adhesion strength between the sprayed

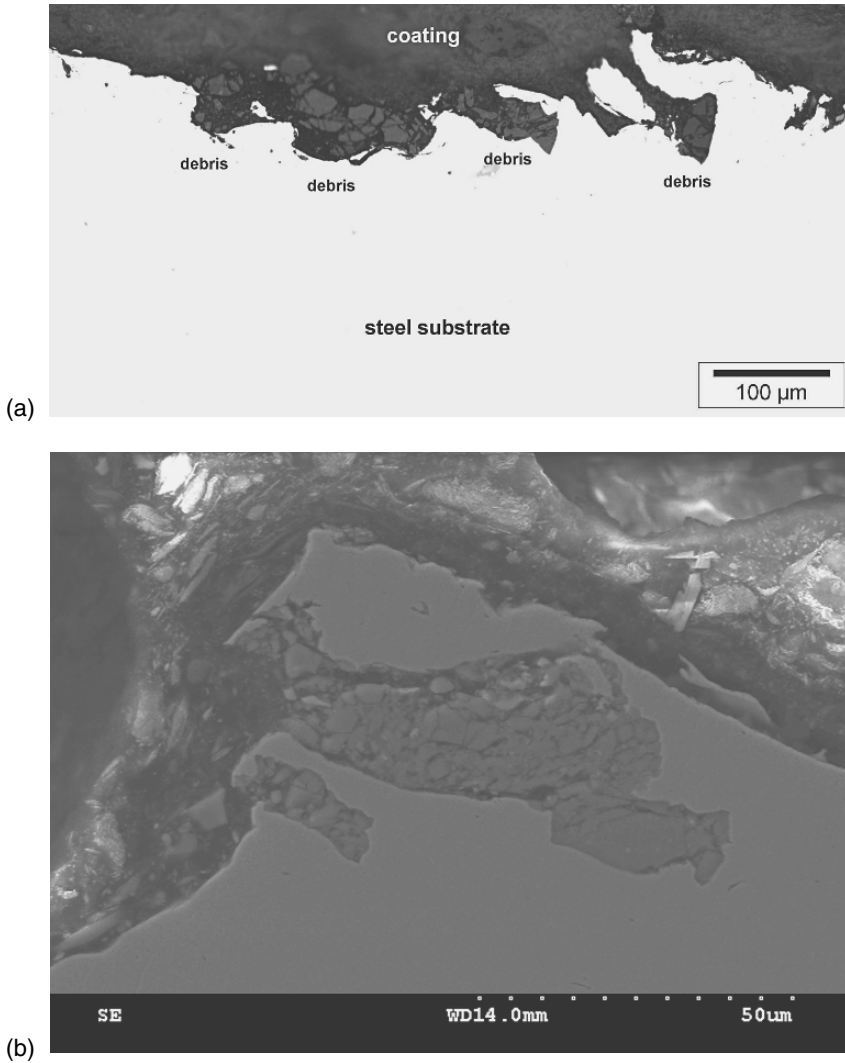


Fig. 8.23 SEM images of polished cross-sections of dry blast cleaned and then coated steel substrates. **(a)** General view; **(b)** Closer view. No fine cleaning was performed. Note copper slag debris accumulation in pits (Images: Muehlhan AG, Hamburg)

ceramic coating and the substrate significantly reduced as the substrate surface contained embedded particles. Similar results were reported by Momber et al. (2004) for organic coatings, whereby the authors argued that the rheological properties of the wet paint films played an important role. Maruyama and Kobayashi (2004) have shown that the adhesion of flame-sprayed copper powders to carbon steel substrates improved notably if the substrates were ultrasonically cleaned after blast cleaning. The improvement in adhesion strength was as high as +400%. Other authors,

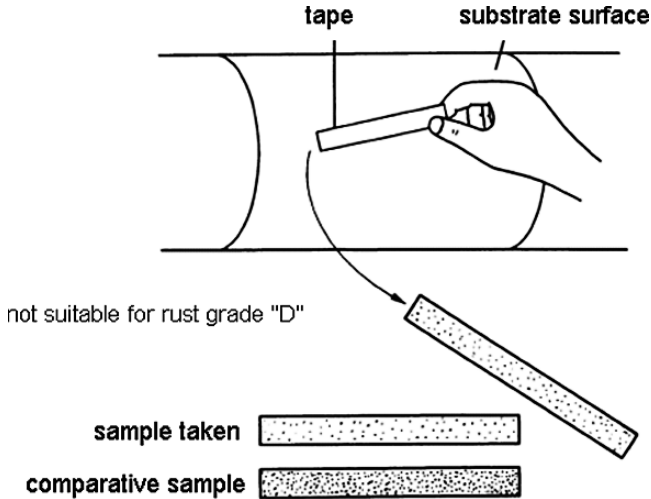


Fig. 8.24 Tape test according to ISO 8502-3 for dust assessment

e.g. Day et al., (2005), found only a random correlation between surface contamination and bond strength of thermally sprayed coatings.

The SEM images displayed in Fig. 8.23 illustrate how abrasive debris form local barriers between substrate and coating. Such images can also be found in Zaat's (1960) early paper. Debris is trapped in cavities generated during the blast cleaning of the substrate. Momber and Koller (2005) and Momber et al. (2004) found that some paint types were extremely sensitive to such dusty substrates, and that these sensitive systems failed in a cohesive fashion at low loads if tested for adhesion with a pull-off tester. Zinc-based primers seemed to be rather insensitive to dust on steel substrates. During the pull-off tests, the coatings failed frequently in the interface between primer and top coat. The adhesion to the dusty substrate was, therefore, better than the inter-coat adhesion for this coating type (Momber and Koller, 2005).

Embedded particles also affect the mechanical behaviour of steel substrates. Kloos et al. (1981) performed a study on the modification of fatigue properties of a high-strength steel (55Cr3) due to embedded non-metallic particles. If the

Table 8.18 Dust size classes (ISO 8502-3)

Class	Description of dust particles
0	Particles not visible under $\times 10$ magnification.
1	Particles visible under $\times 10$ magnification but not with normal or corrected vision (usually particles less than $50\ \mu\text{m}$ in diameter).
2	Particles just visible with normal or corrected vision (usually particles between 50 and $100\ \mu\text{m}$ in diameter).
3	Particles clearly visible with normal or corrected vision (particles up to $0.5\ \text{mm}$ in diameter).
4	Particles between 0.5 and $2.5\ \text{mm}$ diameter.
5	Particles larger than $2.5\ \text{mm}$ in diameter.

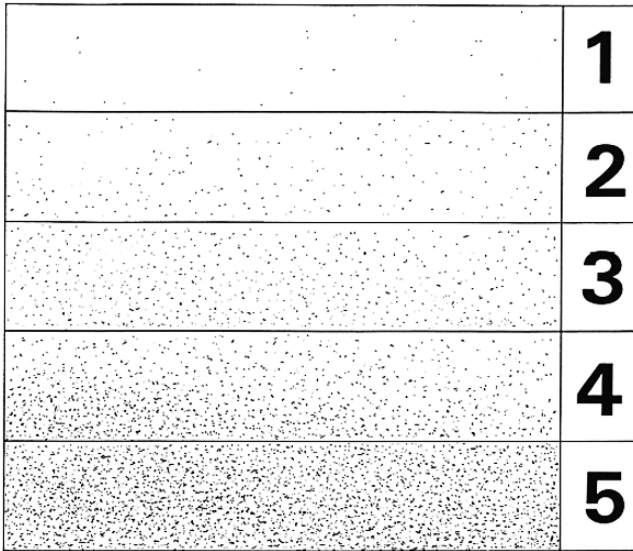


Fig. 8.25 Dust class definitions according to ISO 8502-3

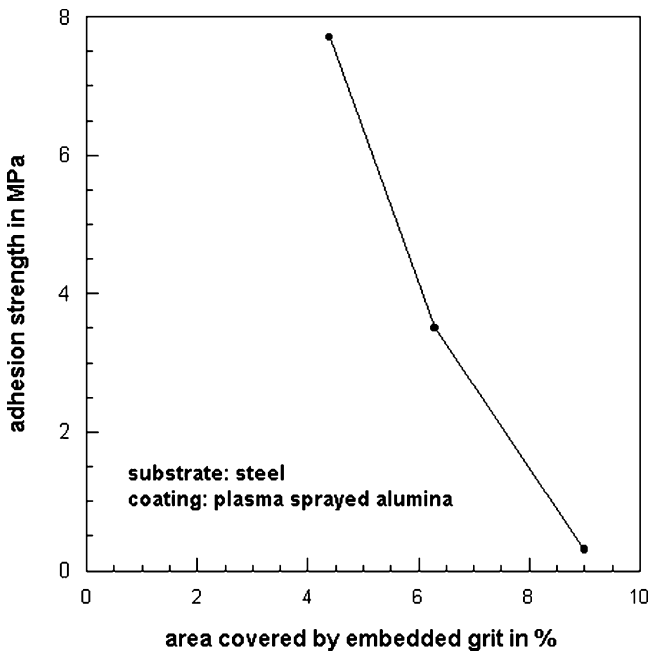


Fig. 8.26 Effects of abrasive debris embedment on pull-off strength of a plasma-sprayed alumina coating on a steel substrate (Griffith et al., 1999)

particle size exceeded a value of $25\ \mu\text{m}$, they notably reduced the fatigue stress reversals. For particle sizes between 25 and $150\ \mu\text{m}$, the relationship between inclusion size and fatigue stress reversal followed an inverse power function, whereby the power exponent depended on the stress amplitude. The same trend was found for the relationship between inclusion size and a fatigue strength number (product of fatigue strength and fatigue cycle number to failure). Embedded particles smaller than $25\ \mu\text{m}$ did not affect the fatigue properties systematically.

Dirt contamination also affects surface energy and wettability of the substrates (see Sects. 8.8 and 8.9).

8.5.3 Substrate Cleanliness After Blast Cleaning

Experimental results of different authors have shown that particle embedment in, and contamination by abrasive debris of, metal substrates after blast cleaning can vary between very low values of about 1% and high values of about 50%. The first systematic investigation on abrasive particle embedment after blast cleaning was probably that of Zaat (1960). This author investigated the effects of different abrasive materials, namely zirconium, quartz sand, steel cut wire, aluminium oxide and cast iron. A part of his results is plotted in Table 8.19. The size of the embedded debris was between 10 and $100\ \mu\text{m}$. The larger debris belonged to the abrasive particles with rather large diameters (cast iron, $d_p = 590\ \mu\text{m}$; corundum, $d_p = 750\ \mu\text{m}$), whereas the small debris belonged to the zirconium with a small initial grain size ($d_p = 120\ \mu\text{m}$). The number of the embedded debris was between 5 and 42 pieces per centimetre. It depended on the blasting direction. The number of embedded debris was usually higher in the direction perpendicular to the blasting direction. The highest numbers were detected after blast cleaning with corundum. The percentage of embedment was highest for the corundum as well. The percentage of the debris contamination layer, which loosely covered the substrate after blast cleaning, also showed the highest value for blast cleaning with corundum. The very different values for the percentage of embedment and the percentage of loose contaminants show how important it is to distinguish between these two types of substrate modification. Substrates blast cleaned with steel cut wire did not show any modification due to debris embedment.

Detailed investigations, performed by Amada et al. (1999), Bahbou et al. (2004), Doherty (1974) and Wigren (1988), have revealed that dust layers as well as particle embedment depended mainly on impact angle and abrasive type. The effect of changes in impact angle is shown in Fig. 8.27. An increase in embedment could be noted as impact angle increased. Maximum embedment occurred at an impact angle of $\varphi = 90^\circ$. These results corresponded to earlier findings of Doherty (1974) who could prove that, after blast cleaning of cold-rolled steel with quartz sand and mineral slag, more abrasive particles were lodged for $\varphi = 60^\circ$ and 90° compared with $\varphi = 30^\circ$ and 45° .

Doherty (1974) conducted investigations into the effects of air pressure and stand-off distance. He found that relationships between these two process parameters

Table 8.19 Abrasive embedment and surface contamination due to abrasive debris for different abrasive materials (Zaat, 1960)

Abrasive type	Abrasive size in μm	Debris size in μm	Number of debris per cm		Embedded surface in %	Contaminated surface in %	Steel chip length in μm
			Parallel ^a	Perpendicular ^a			
Zirconium	120	10	5.5	8	0.004	45	40
Quartz sand	390	20	5.5	9	0.02	50	60
Cast iron	580	60–100	9	13	0.4	55	80
Cut wire	650	–	–	–	0	50	150
Corundum (S)	720	30–50	27	42	1	60	150
Corundum (K)	750	50–100	24	28	2	75	150
Cut wire	970	–	–	–	0	55	200

^aRelated to blasting direction

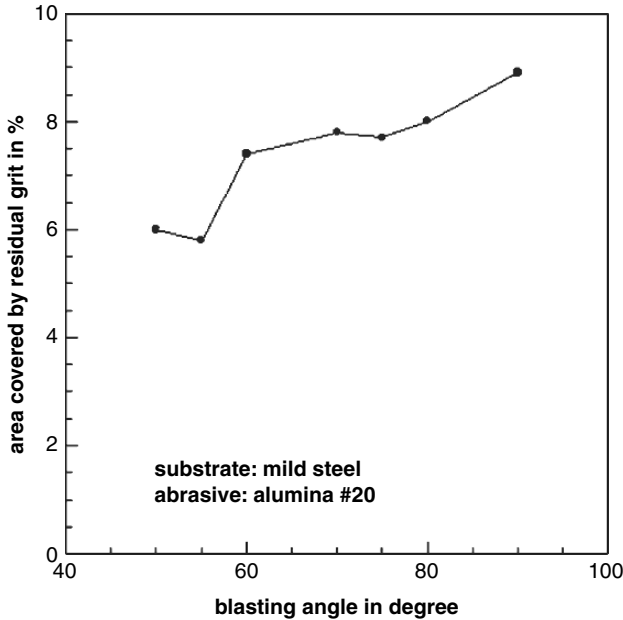


Fig. 8.27 Effects of blasting angle on abrasive debris embedment (Amada et al., 1999)

and the sizes of the particles lodged in the substrate. If pressure decreased and stand-off distance increased, the lodged particles became larger. The size of the embedded particles varied between 80 and 800 μm . Measurements performed by Wigren (1988) have shown that particle embedment decreased with an increase in stand-off distance, whereas an increase in air pressure promoted the embedment of abrasive debris. The latter effect was also noted by Jones and Gardos (1971). An optimisation procedure proposed by Wigren (1988) is shown in Fig. 8.28. According to the proposed procedure, blast cleaning time (t_1-t_3), air pressure and impact angle can be varied in a way that grit embedment has minimum values for a given roughness.

The dependence of particle embedment on abrasive type is illustrated in Tables 8.19 and 8.20. The dramatically different results for the investigated abrasive materials illustrate the effect of grit type and morphology. It seemed from the results listed in Table 8.20 that slag materials (except nickel slag) were rather sensitive to grit embedment. Experiments with copper slag showed that the comminution (breakdown) behaviour of individual particles during the impact at the steel surface seemed to play a notable role. It was apparent that the embedment was not simply due to discrete particles embedded in the substrate, but rather due to extreme breakdown of the slag abrasive into minute particles, or a physical smearing of the grit over the surface (Fairfull and Weldon, 2001). A distinct relationship between hardness of abrasive particles and their embedment in substrate surfaces could not be found. Interestingly, embedment was very intense for abrasive mate-

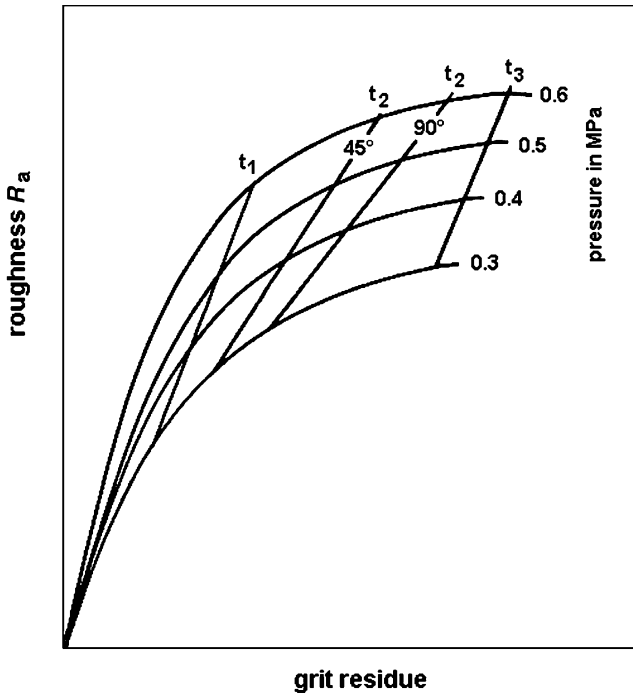


Fig. 8.28 Optimisation procedure for minimising abrasive particle embedment (Wigren, 1988)

rials with moderate hardness values (see Table 8.20). A direct comparison of two abrasive types was performed by Yankee et al. (1991) for the blast cleaning of a titanium substrate, whereas aluminium oxide (high hardness) delivered a contamination level of 12% and silicone carbide delivered a contamination level of only 7%. Day et al. (2005) compared roughness values and abrasive embedment values, and they found that both parameters can be related to each other for given abrasive particle

Table 8.20 Embedment of abrasive debris in a carbon steel (Measurements: Fairfull and Weldon, 2001)

Abrasive type	Embedment (visual) in %	Knoop hardness
Coal slag A	11.1	630
Coal slag B	25.3	669
Copper slag	41.5	523
Garnet A	2.1	1,111
Garnet B	4.7	1,779
Iron oxide	0.7	1,136
Nickel slag	1.2	960
Olivine	15.1	860
Silica sand	2.9	791
Staurolite	0.1	150
Steel grit	4.1	239

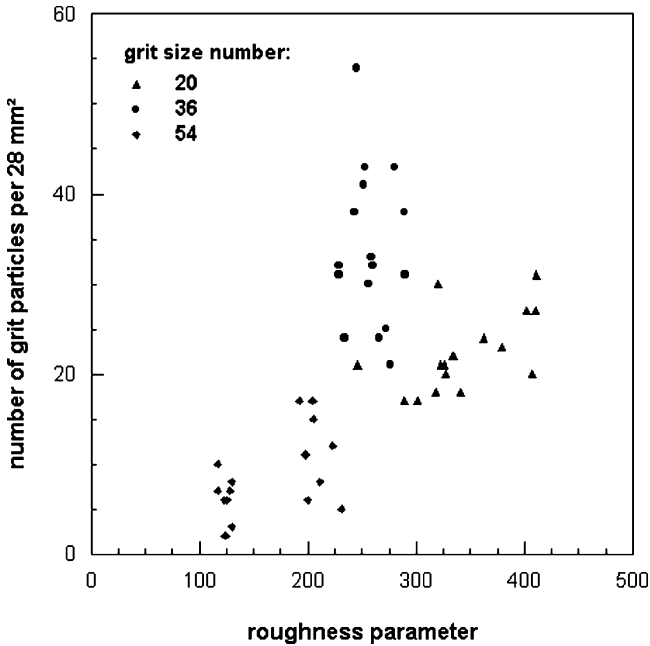


Fig. 8.29 Relationships between substrate roughness, abrasive particle size and abrasive contamination (Day et al., 2005)

sizes. Results of their study are displayed in Fig. 8.29. It can be seen that particle contamination was more severe for a given abrasive particle size if substrate roughness increased. Larger abrasive particles (small grit size number) formed deeper profiles, but also promoted grit embedment.

Neal (1999) found typical grit contamination levels between 10% and 25% on the back side of fusion-bonded epoxy that was applied to a dry blast cleaned pipeline surface. Schuh et al. (2004) detected alumina abrasive debris embedment in blast cleaned titanium substrates, and they found grit contamination levels as high as 42%. Yankee et al. (1991) found grit contamination levels of 12% on titanium substrates blast cleaned with aluminium oxide. Compared to the values for a carbon steel, as listed in Table 8.20, these values are rather high. Obviously, more abrasive material was fragmented during the impingement on the hard titanium surface, and the fragments were smeared across the surface.

A special effect, frequently observed during blast cleaning, is “overblasting” due to multiple blast cleaning steps. This phenomenon applies to the blast cleaning of already blast cleaned surfaces (as usually occurring in blast cleaning of deteriorated coatings). As shown by the results listed in Table 8.21, overblasting increased the grit contamination level due to additional particle embedment. Wigren (1988) found that abrasive embedment quickly increased during short exposure times, but the progress of embedment dropped if a certain critical exposure time (between 2.5 and 3 s) was exceeded. These relationships are illustrated in Fig. 8.28.

Table 8.21 Particle embedment due to overblasting (Momber and Wong, 2005a)

Number of blast cleaning steps	Particle embedment in %
0	0
1	6.7 ± 2
2	7.4 ± 3

Day et al. (2005) performed a statistical analysis on the effect of certain process parameters on the contamination level and derived the following relationship:

$$CL = -0.33 \cdot G_N + 0.24 \cdot p + 0.44 \cdot n_s + 2.87 \cdot x + 0.12 \cdot \varphi \quad (8.1)$$

The CL (contamination level) is given as the total number of embedded particles found in an area of 28 mm². The grit number (G_N) is given in mesh; p is given in psi; x is given in inch and φ is given in degrees.

8.5.4 Fine Cleaning

Fine cleaning is essential after dry blast cleaning. However, quantitative demands can usually not be found in coating data sheets. For fusion-bonded epoxy, a maximum level for dirt contamination of up to 30% is mentioned to be acceptable (Neal, 1999). Dusty contaminants can be removed by certain methods, including blowing with compressed air (Peters and Meister, 1997), vacuuming, water rinsing and ultrasonic cleaning. In the pipe coating industry, acid washing is frequently used as well. Figure 8.30 illustrates the effect of cleaning on CL and hot cathodic disbonding. Interestingly, although phosphoric acid washing could reduce the degree of contamination, it did not notably improve cathodic bond. One possible reason could be that acid cleaning lowered and smoothed the surface profile. This latter effect is illustrated in Fig. 8.31. Subsequent grinding can also help to eliminate the detrimental effect of embedded grit. This is verified by the results listed in Table 8.22. Wetting force increased if a blast cleaned substrate was subsequently polished with paper. The explanation is that polishing process removed embedded abrasive debris, which improved the wettability of the steel substrate (see Sect. 8.9.3). Yankee et al. (1991) could prove that the efficiency of cleaning methods depended on the abrasive type to be removed. Ultrasonic cleaning was, for example, very efficient for the removal of silicone carbide debris from titanium substrates (cleaning efficiency of 50%), but it was inefficient for the removal of aluminium oxide (cleaning efficiency of 10%). However, for both abrasive types, ultrasonic cleaning was slightly superior over air blasting.

Burgess et al. (2002) investigated the effectivity of several post-blast cleaning methods for stainless steel samples blast cleaned with corundum abrasives ($p = 0.4$ MPa). Before the secondary cleaning, the level of deposited debris was between 7% and 8%. After ultrasonic cleaning, the level could be lowered down to 5.4%, and after a combination of acid etching and ultrasonic cleaning, the level went down to 3%.

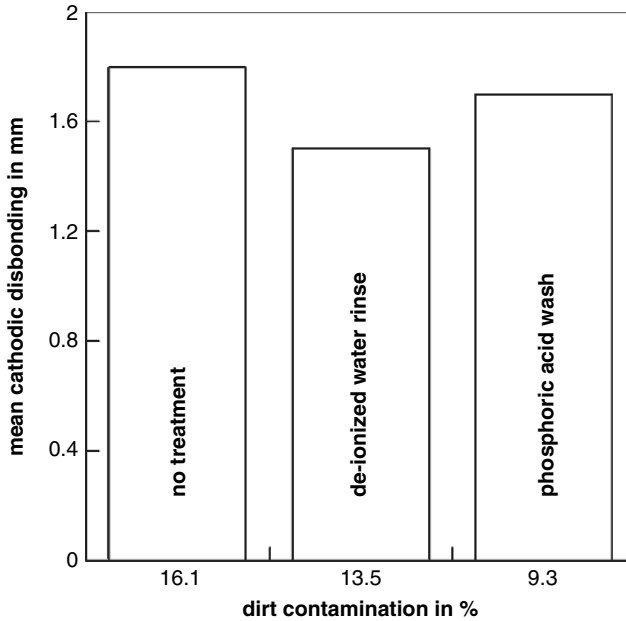


Fig. 8.30 Effects of cleaning methods for debris removal on cathodic disbonding (Neal, 1999)

8.6 Roughness and Profile of Substrates

8.6.1 Definitions and Measurement

Standards for the application of coatings rank the profile of a surface as one of the three major properties that influence coating performance. Substrate roughness is frequently specified by coating manufacturers for coating systems, but not for all. Profile parameters of blast cleaned surfaces can be subdivided into six groups; this includes the following (Griffith et al., 1997; Siegmann and Brown, 1998; Amada and Satoh, 2000):

- height parameters (e.g. average roughness);
- height distribution parameters (e.g. skew and kurtosis);
- bearing parameters;
- angle parameters (e.g. peak slope);
- spacing parameters (e.g. peak spacing);
- fractal dimensions.

Height parameters play an most important role for the assessment of blast cleaned surfaces in practice; they include average statistical roughness (R_a), maximum roughness (R_{max}) and average maximum roughness (R_z). Angle parameters include e.g. average peak slope (Griffith et al., 1997, 1999). Spacing parameters include, among others, peak count (Roper et al. 2005). Weidenhaupt (1970) provided a

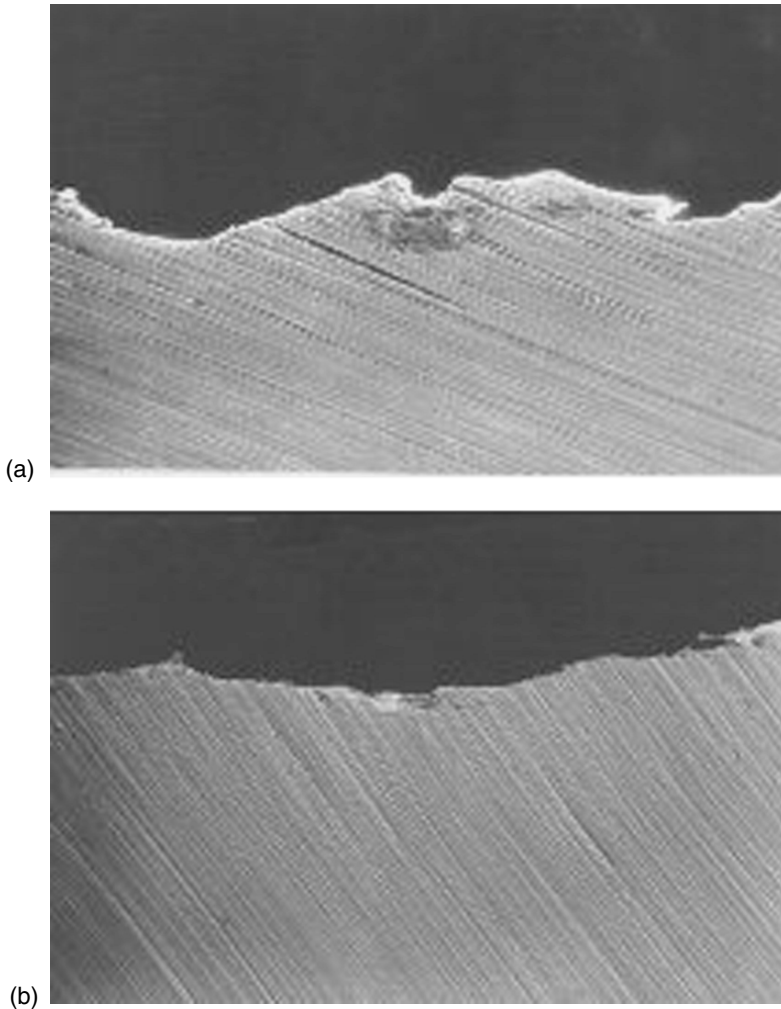


Fig. 8.31 Substrate profile modification due to acid etching (Neal, 1999). (a) Before etching; (b) After etching

number of experimental results for different profile parameters for blast cleaned steel substrates.

The blast cleaning process generates isotropic surfaces, in contrast to grinding and polishing that form anisotropic surfaces. These relationships can be recognised if polar plots of treated surfaces are evaluated. A polar plot of a steel surface treated with different methods is shown in Fig. 8.55. The shape of the plot characterises the surface type. The elliptic shape for the polished surface (inner plot) is typical for an anisotropic surface. The value for the profile parameter (peak spacing) depends on the measurement direction: it is high in 90° -direction. The polar plots for the blast cleaned surfaces, in contrast, are of circular shape. The value of the profile parameter

Table 8.22 Wettability of IN718 after surface treatment; wetting liquid: AMS4777 (Solomon et al., 2003)

Blast cleaning process	Maximum wetting force in N/m
With Al ₂ O ₃	-0.18
	0.09
	0.60
With Al ₂ O ₃ + polishing with paper (400 μm)	0.99

does not depend on the measuring direction. The diameters of the circles express the peak spacing values in the example shown in Fig. 8.55. Doherty (1974) delivered a more detailed study about the effects of blast cleaning parameters on the isotropy of blast cleaned substrates. He found that blast cleaning angle and abrasive material greatly influenced isotropy. This author also distinguished blast cleaned substrates into two types: “normal type” (which is isotropic) and “machine type” (which is anisotropic). “Normal type” areas showed a highly disturbed random surface; this type was produced when large blasting angle and smaller abrasive particles were used. “Machine type” areas, in contrast, had a directionality that varied a little to each side of the blast direction; this type occurred at shallow blasting angle and for larger abrasive particles. For $\varphi = 30^\circ$, all individual cutting marks on the substrate were directed in the blast direction; whereas for $\varphi = 45^\circ$, direction of the cutting marks varied at about 30° to either side of the blast direction. The criteria for generating a “normal type” (isotropic) surface were defined as follows by Doherty (1974): $p > 0.55$ MPa, $\varphi > 45^\circ$, $x < 100$ cm.

Methods of how to evaluate substrate roughness prior to the application of corrosion protective coatings are outlined in ISO 8503. The following four methods are specified:

- profile comparator (ISO 8503-1, ISO 8503-2);
- microscope (ISO 8503-3);
- stylus instrument (ISO 8503-4);
- replica method (ISO 8503-5).

The comparator method delivers qualitative results only; it distinguishes between “fine”, “medium” and “coarse” profiles. Table 8.23 provides a comparison between comparator values and corresponding quantitative roughness values. Profile comparators were basically developed for steel abrasives, in detail for steel shot (comparator profile “S”) and steel grit (comparator profile “G”). Despite this limitation,

Table 8.23 Steel substrate profile parameters (ISO 8503-1)

Comparator value	Roughness value (R_{y5}) ^a in μm	
	Grit	Shot
Fine	25–60	25–40
Medium	61–100	41–70
Coarse	101–150	71–100

^a R_{y5} denotes the average of five in-line measurements

Table 8.24 Classification of peak count (Roper et al., 2006)

Classification	Peaks per cm
High	40–60
Medium	30–40
Low	20–30

comparators are used throughout the corrosion protection industry to evaluate profiles formed by other, non-metallic abrasive materials. Roper et al. (2006) performed a classification of peak count as “high”, “medium” and “low”; the corresponding quantitative values are listed in Table 8.24.

Many commercial portable stylus instruments read the following profile parameters: R_a , R_z (R_{y5}) and R_{max} . These parameters are illustrated in Fig. 8.32. However, the arithmetical mean roughness (R_a) is not specified in coating data sheets; however, the two other parameters sometimes are. It is of interest to see how reproducible profile measurements are. This aspect was investigated by Chandler and Shak (1966) and Neal (1999). Some values of Neal (1999) study are provided in Table 8.25. Standard deviations of roughness values measured by four different operators with different levels of experience, who each measured a profile 10 times at a steel pipe, did not exceed a value of $6.3 \mu\text{m}$. Chandler and Shak (1966) found that the difference in roughness readings of four different operators varied between 7% and 20%.

Prazak and Eremias (1972) provided an alternative method for estimating a surface roughness factor of metals, which was based on estimating the exchange current of a redox system on a passivated metal surface by measuring the polarisation resistance. This relative roughness factor was defined as follows:

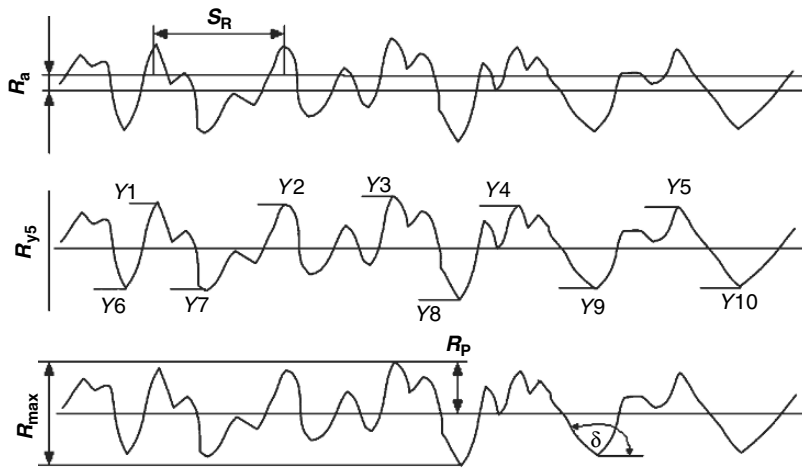


Fig. 8.32 Surface roughness (profile) parameters (Hempel Book of Paints); extended by the author

Table 8.25 Reproducibility of replicate tape profile measurements on dry blast cleaned steel pipes (Neal, 1999)

Parameter	Roughness value in μm				
	Operator				
	1	2	3	4	All
Mean	69.8	70.3	61.2	61.7	65.8
Standard deviation	2.5	4.8	7.4	2.5	6.3
Range	7.6	15.2	25.4	7.6	33.0

$$R_{RF} = \frac{R_{Pst}}{R_P} \quad (8.2)$$

Here, R_{Pst} is the polarisation resistance of an electrode with a standard area, and R_P is the measured polarisation resistance. Because this latter parameter depends on the chemical composition of the metal, the method works only for comparing the surfaces of materials of equal chemical compositions.

8.6.2 Effects of Roughness on Coating Performance

Roughness and profile parameters notably affect the adhesion between substrate and coating to be applied. Respective investigations on many coating types can be found in the literature. Griffith et al. (1997) found that adherence of plasma-sprayed aluminium oxide coatings to steel substrates improved if substrate average roughness, average peak slope and peak spacing (Fig. 8.33b) of the profile increased. The effect of the average roughness on the adhesion is shown in Fig. 8.33a, and it can be recognised that adhesion increased in a linear fashion with an increase in roughness. The effect of variations in peak spacing on the adhesion is illustrated in Fig. 8.33b. The adhesion initially steeply increased with an increase in peak spacing, but it dropped if a certain value for the peak spacing (ca. $S_R = 250\mu\text{m}$) was exceeded. If this case occurred, adhesion between substrate and coating reduced. Therefore, profile parameters must be optimised in order to obtain a maximum adhesion.

Hofinger et al. (2002) performed fracture experiments on interfaces between steel substrates and plasma-sprayed coatings. Their results, listed in Table 8.26, showed that a higher amount of energy was required to separate coating and substrate if substrate roughness increased. Packham (2002) has shown that the adhesion (in terms of the critical energy release rate) of a zinc coating to steel exhibited maximum values at moderate roughness (R_a) values. For high R_a -values, the adhesion deteriorated.

Bergmann (1994) could show that substrate type played an important role. As shown in Fig. 8.34, a higher roughness could deteriorate the adhesion of ceramics coatings plasma sprayed to a certain substrate. Whereas general trends could be established for the zirconium substrate and the aluminium-titanium substrate, the adhesion of the coating applied to the aluminium oxide substrate was very sensitive to changes in substrate roughness. Both facts could be probably explained through

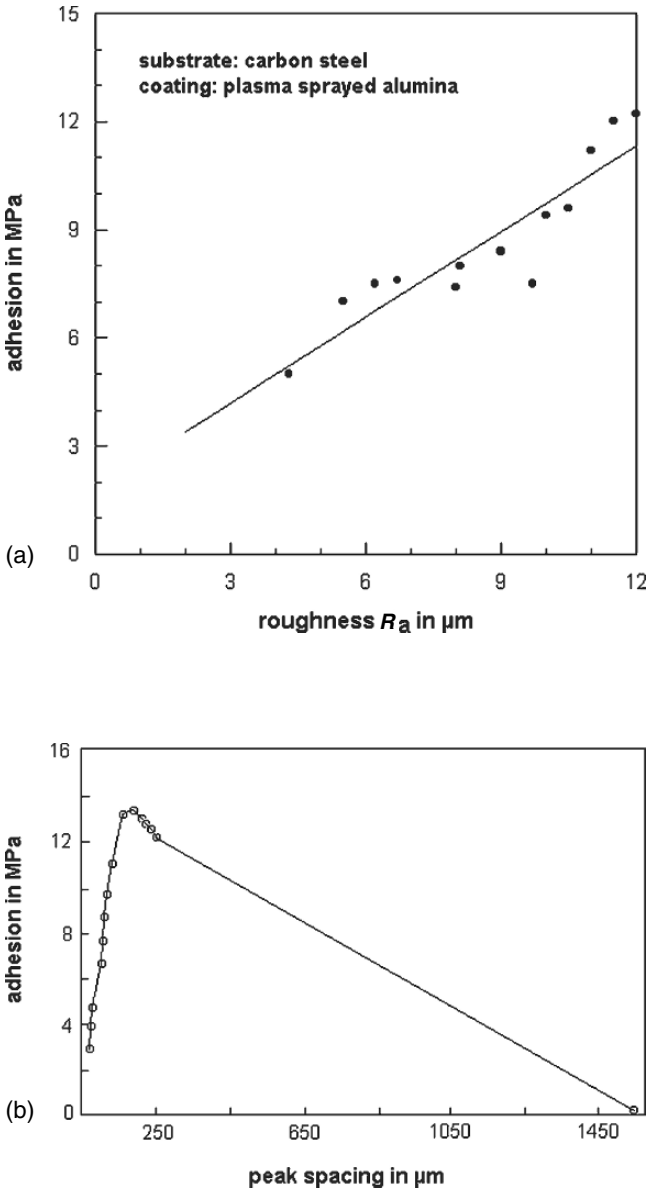


Fig. 8.33 Effects of roughness parameters on the adhesion of plasma-sprayed alumina coatings to a steel substrate (Griffith et al., 1997). (a) Effects of average roughness; (b) Effects of profile peak spacing

Table 8.26 Roughness effect on interface fracture energy (Hofinger et al., 2002)

Roughness in μm		Interface fracture energy in N/m
R_a	R_z	
1.3	9.6	500 ± 30
2.2	15.4	530 ± 50
4.8	29.7	580 ± 40

the different thermal residual stresses which depended on the physical properties of both the materials involved in interface formation. It is, therefore, always the combination of substrate and coating material which determines roughness effects. Results displayed in Fig. 8.35, however, show that abrasive grain shape played some role as well. The experimental points marked “1” were for cut steel wire, and only if these points were excluded, roughness had a definitive relationship to adhesion.

Siegmann and Brown (2002) performed systematic tests into the effect of steel substrate profile parameters on the adhesion of metal-sprayed coatings. They found an almost linear relationship between R_a and adhesion strength; however, the relationship was restricted to roughness values $R_a > 3 \mu\text{m}$. The authors also found that the size of the contact area between substrate and coating was of decisive importance. For contact areas larger than $100 \mu\text{m}^2$, a correlation between profile parame-

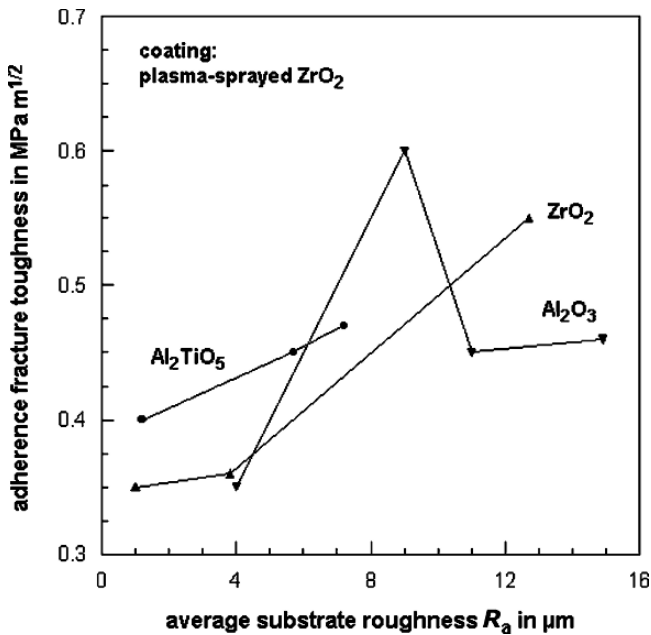


Fig. 8.34 Effects of substrate-coating combination on the roughness influence on the adhesion between ceramic substrates and a plasma-sprayed ceramic coating (Bergmann, 1994)

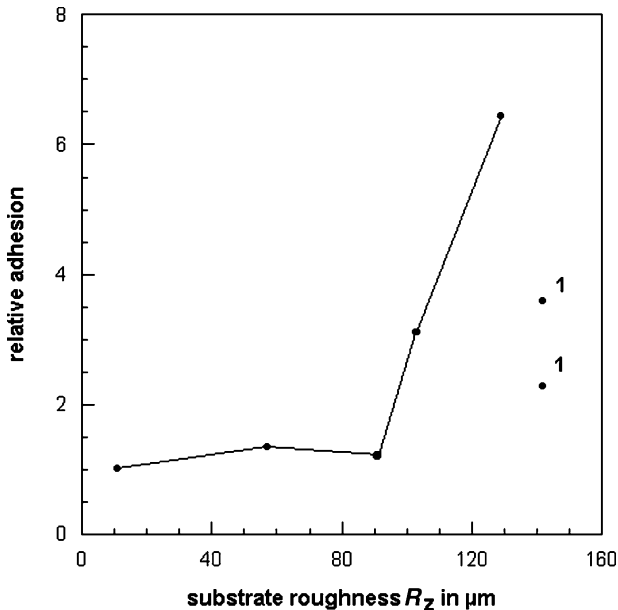


Fig. 8.35 Effects of abrasive particle size and shape on roughness and coating adhesion (Bahlmann, 1982); 1 – cut steel wire

ters and adhesion could be established. Van Tijum and De Hosson (2005) found an almost linear relationship between the relative surface area of a steel substrate and the interface strength between substrate and a polyethylene, but this relationship held only if the increase in surface area was smaller than +150%.

Maruyama and Kobayashi (2004) performed a study about the adhesion of flame-sprayed copper powder to blast cleaned carbon steel substrates. The blast cleaning was carried out with aluminium oxide ($d_p = 116\text{--}1,850\mu\text{m}$) at an air pressure of $p = 0.55\text{ MPa}$. The authors did not find a unique relationship between the maximum roughness (R_{max}) and the adhesion strength. Although the adhesion strength initially increased with an increase in roughness, it dropped at higher roughness values. Thus, an individual roughness parameter could not characterise the quality of the bond between substrate and coating. Maruyama and Kobayashi (2004) introduced a dimensionless “increase ratio of surface area” (see Fig. 8.32). This parameter neither showed any unique relationship to the adhesion strength; best results for the adhesion strength were obtained for moderate values (at about 1.2) for the increase ratio.

Morcillo et al. (1989) investigated the effects of numerous parameters on roughness influence. Some results are displayed in Fig. 8.36. In that example, an organic primer was applied to steel substrates with varying roughness values. It can be seen that rust grade increased (respectively, lifetime of the primer decreased), if the maximum roughness (R_{max}) had high values. The best performance could be realised if the primer was applied over the smoothest profile. It was found that there was a

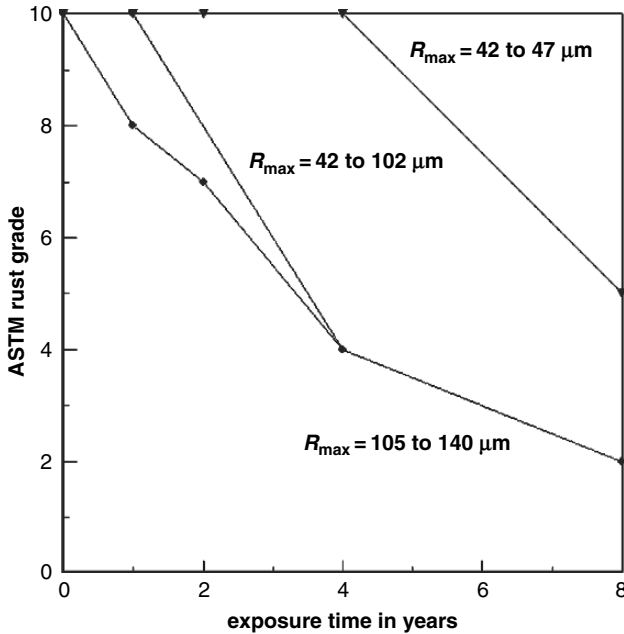


Fig. 8.36 Effects of profile roughness modification and exposure time on the corrosion rate of steel-coated panels (Morcillo et al., 1989)

critical surface profile, the value of which was determined by the environment along with the type and thickness of the coating system. As the coating system increased in thickness, the effect of the surface profile on coating performance diminished. The critical surface profile was found to be a function of the aggressiveness of the environment: a more aggressive environment resulted in a lower critical profile (which corresponded to a higher film thickness over the roughness peak). Bigos (1959) performed investigations into the rusting of organic coatings, and he found that the rusting over roughness peaks was severe for profile values of $R_{max} = 100\text{--}200 \mu\text{m}$, whereas rusting was considerable for profile values of $R_{max} = 81\text{--}86 \mu\text{m}$, and no rusting occurred for profile values of $R_{max} = 33\text{--}51 \mu\text{m}$. Keane et al. (1976) observed similar effects on different coating types. They found that alkyd and vinyl primers performed better over relative small substrate profiles than over very rough profiles in a light industrial environment. The authors concluded that the coating performance seemed to be ordinarily related to the paint thickness over a relative small number of highest peaks out of a total of about 30,000 to 100,000 peaks per 6 cm^2 . There were more high peaks and apparently more thin spots of paint films over coarse substrate surfaces. Table 8.27 lists typical values for critical paint film thicknesses which must be applied over a coarse profile in order to achieve a demanded lifetime for four paint types as functions of the substrate thickness. Trulove (1966) performed detailed measurements of the film thickness of organic paints over peaks and troughs of shot blast cleaned steel substrates, and he could

Table 8.27 Critical film thickness values for coating lifetime (Keane et al., 1976)

Surface profile in μm	Critical film thickness in μm			
	Salt spray test		Mild industrial exposure	
	Alkyd	Vinyl	Alkyd	Vinyl
56	18	23	13	20
61	23	30	23	20
51	30	20	13	20
74	18	20	13	13
127	43	46	25	28

show that the reduction in film thickness (as a fraction of the average film thickness) over peaks had an almost linear relationship to the maximum roughness (R_{max}) of the substrates.

Bardal (1973), and later Roper et al. (2005), introduced an additional surface profile parameter – peak count as illustrated in Fig. 8.32, and they found that this parameter could suitably be related to coating performance, especially for long exposure times. Roper et al. (2005) showed that if profile height was kept constant, peak count could affect the performance of a coating as determined through pull-off adhesion strength, scribe undercut, and in some cases cracking. Some results of this study are shown in Fig. 8.37. Figure 8.37a illustrates the effects of peak count and exposure time on the pull-off strength, whereas Fig. 8.37b illustrates the effects

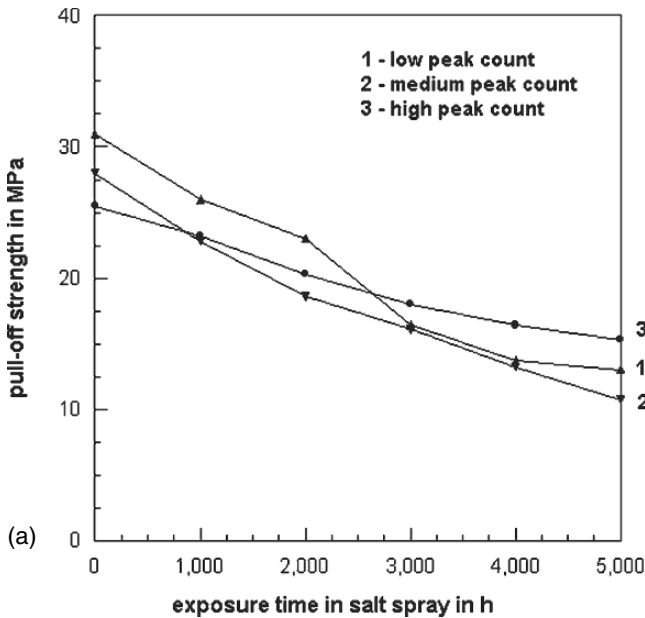


Fig. 8.37 Effects of peak spacing on coating performance (Roper et al., 2005). (a) Pull-off strength; (b) Delamination after salt spray test

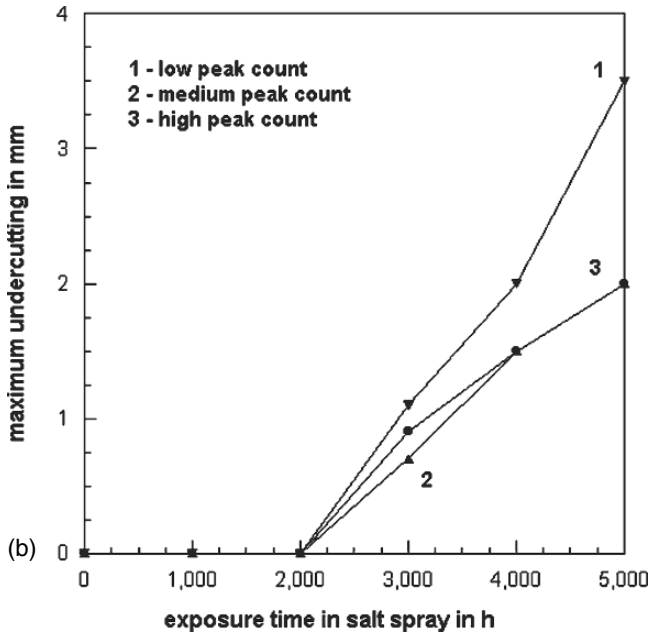


Fig. 8.37 Continued

of both parameters on the delamination at an artificial scribe. High values for the peak count improved the performance of the coating at long exposure times. It was also found that coatings with low wetting capability were less sensitive to changes in peak count. Results of respective measurements are listed in Table 8.28. Feist et al. (1988) investigated the effect of the groove distance of a profile on the adhesion of sprayed zinc and sprayed aluminium to steel substrates. Results of this study are illustrated in Fig. 8.38. Pull-off strength, as a measure of adhesion, dropped notably if a certain critical groove distance was exceeded. In the graph, this critical value was about $S_R = 250 \mu\text{m}$. For substrates with equal values for $R_Z = 500 \mu\text{m}$, pull-off strength of sprayed zinc dropped from $\sigma_A = 10 \text{ MPa}$ for $S_R = 200 \mu\text{m}$ down to $\sigma_A = 4 \text{ MPa}$ for $S_R = 500 \mu\text{m}$ (Feist et al., 1988).

Roughness and adhesion are not always related to each other in a unique fashion, as shown by the examples in Fig. 8.39 which applies to the adhesion between a steel

Table 8.28 Effects of peak count on coating performance (Roper et al., 2005)

Coating	Exposure time in h	Improvement from low to high peak count in %	
		Pull-off strength	Undercutting
A	5,000	43	43
B	5,000	90	62
C	5,000	100	70
D	5,560	13	83
E	4,222	79	60
F	4,222	-4	57

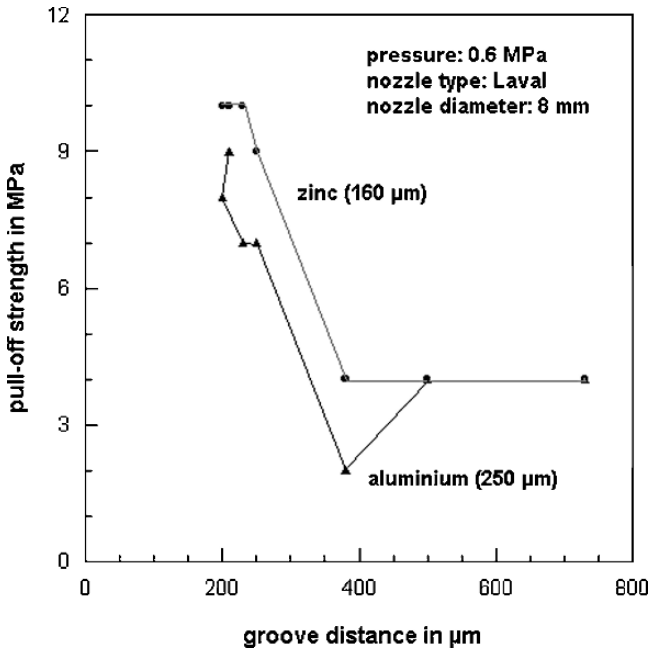


Fig. 8.38 Effects of groove distance on adhesion of metal-sprayed coatings (Feist et al., 1988)

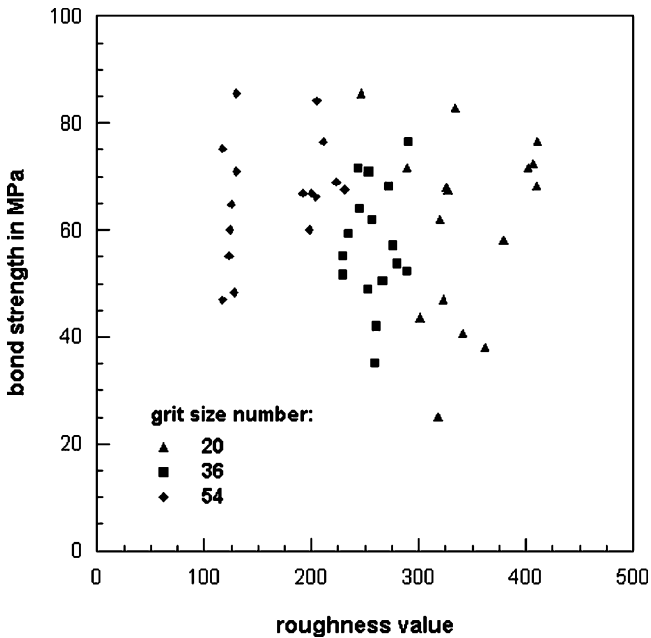


Fig. 8.39 Relationships between substrate roughness, abrasive size number and adhesion (Day et al., 2005)

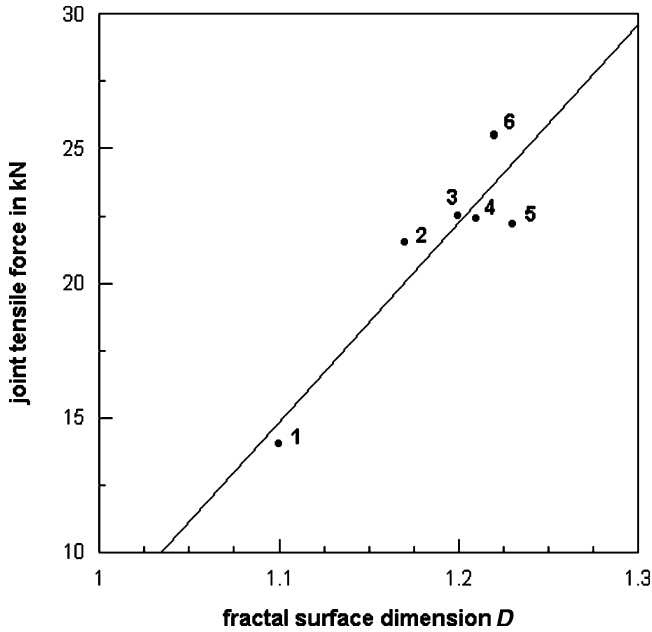


Fig. 8.40 Relationship between fractal surface dimension and the tensile force required to separate a joint (Mannelqvist and Groth, 2001). Surface preparation: 1 – degreased; 2 – blast cleaned with glass beads; 3 – steel brush; 4 – Scotch-Brite pad; 5 – water blasted; 6 – blast cleaned with quartz particles

substrate and a thermally sprayed coating. High roughness values did not necessarily lead to high adhesion. Even if the abrasive particle size is being considered, the relationships did not improve.

Surface profiles can be described by more advanced methods, namely by fractals. Certain authors exploited fractal parameters to characterise blast cleaned surfaces (Mannelqvist and Groth 2001; Siegmann and Brown 2002; Bahbou et al., 2004; Van Tijum and De Hosson 2005), and it was shown that fractal surface parameters could suitably be linked to the bond strength of adhesive joints between two materials. An example is shown in Fig. 8.40. Here, a fractal parameter, denoted “ D ”, showed a satisfying relationship to the tensile strength of a stainless steel joint; no such relationship could be noted for the conventional average roughness (R_a). Van Tijum and De Hosson (2005) introduced a parameter “relative surface area”, and they could theoretically show that this profile parameter had a linear relationship to the strength of the interface between steel and polymer if the increase in surface area was less than 150%. The deviation from the linear relationship became important for small values for the Young’s modulus of the polymer.

Sancaktar and Gomatam (2001) performed tests on the strengths of single lap joints of rolled steel. The strength was measured with a tensile testing machine at different crosshead speeds. Both failure load and ultimate displacement were estimated. The results depicted an effect of the viscosity of the adhesive materi-

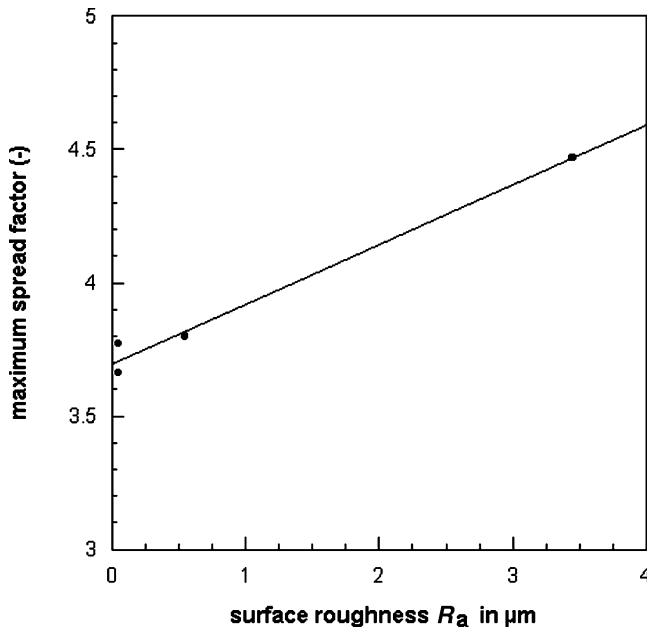


Fig. 8.41 Profile roughness effects on splat formation of liquid paint drops (Siavoshani, 2001)

als. For a low-viscosity adhesive (5–7 Pa s), the two strength parameters increased if the roughness (R_a) of the adherend increased. For a high-viscosity adhesive (170–225 Pa s), no distinctive relationship could be found between roughness of the adherend and strength values of the joint. Surface roughness studies of Rider et al. (1999) established that increasing the adherend roughness from a flat surface to a more profiled roughness, increased the fracture energy of an aluminium-epoxy joint exposed to humid conditions by two orders of magnitude.

Roughness parameters of substrates affect the splat formation of impinging drops of liquefied coating materials. One example is provided in Fig. 8.41. It can be seen that the spread factor increased if average roughness of the substrate increased. Similar results were reported by Sancaktar and Gomatam (2001) for the relationship between substrate roughness (R_a) and adhesive spread parameter. The adhesive (resin) diameter initially increased with an increase in roughness, but started to drop at rather high values for the average roughness. Substrate roughness also affects flattening degree and cooling of plasma-sprayed coatings (see Sect. 9.7). Experimental and numerical results reported by Ivosevic et al. (2006) indicated that an increase in magnitude of the mean roughness promoted splat instability (namely jetting and satellite break-up) and the formation of radial fingers. It was also observed that the increase in surface roughness may result in lower spreading ratio of thermally sprayed polymer particles. Ma et al. (2006) studied the effect of the roughness (R_a) of blast cleaned substrates on the splat formation of HVOF-sprayed tungsten carbide. The results showed that with an increase in roughness, the restriction to

flattening was enhanced in a way that the number of spherical to nearly spherical splats reduced, whereas the number of splats with complex morphologies increased. A comprehensive review on these issues is given by Fauchais et al. (2004). Splat morphology can be subdivided into two types: disc-shaped and splash-shaped. The disc-shaped type can be expected for blast cleaned substrates with an isotropic surface. The splash-shaped type will mainly develop on ground or polished substrates with an anisotropic surface. This was verified by SEM inspections performed by Griffith et al. (1997). Splat type notably affects the contact between substrate and first coating layer. Metallurgical sections through interfaces between carbon steel substrates and plasma-sprayed aluminium oxide coatings verified that about 90% of the good contact areas were covered with disc-shaped splats, whereas about 75% of the poor contacts were covered with splash-shaped splats (Griffith et al. (1997).

Detailed investigations of Hansen (1972) revealed that substrate roughness had a notable effect on the appearance of finished organic coating, namely on gloss.

Emrich (2003) performed a detailed investigation on the quality of adhesive bonds in aluminium joints. Based on the results of transmission electron microscopy (TEM) inspections, he argued that the macroscopic profile (roughness in the sense as discussed above) did not have a notable effect on the bond quality. It was rather the microscopic level ($< 1 \mu\text{m}$) of the substrate which determined the adhesion between adhesive and substrate. This dimensional level is close to the dimensions of the applied polymers.

8.6.3 Profile Parameters of Blast Cleaned Metal Substrates

8.6.3.1 Introduction

Based on the scenario shown in Fig. 8.42, Chernyavskii (1984) and Knotek and Elsing (1987) developed analytical models for the estimation of the maximum roughness of shot blasted steel substrates. Chernyavskii (1984) solution reads as follows:

$$R_{max} \propto v_p \cdot \sin \varphi \cdot m_p^{1/2} \cdot \sigma_f^{-1/2} \quad (8.3)$$

Knotek and Elsing (1987) derived the following relationship:

$$R_{max} \propto v_p \cdot x \cdot m_p^{1/2} \cdot \sigma_f^{-1/2} \quad (8.4)$$

Both equations provide equal trends for particle velocity, abrasive particle mass and yield strength of the substrate material. The yield strength of the target material is for many metals (Tabor, 1951) and polymers (Pickles and Hutchings, 1997) related to the hardness. It can, therefore, be replaced by the substrate material hardness: $\sigma_f \propto H_M$. This approach has been made by Sorokin et al. (1983). Profile parameters are affected by certain material and process parameters, among them particle

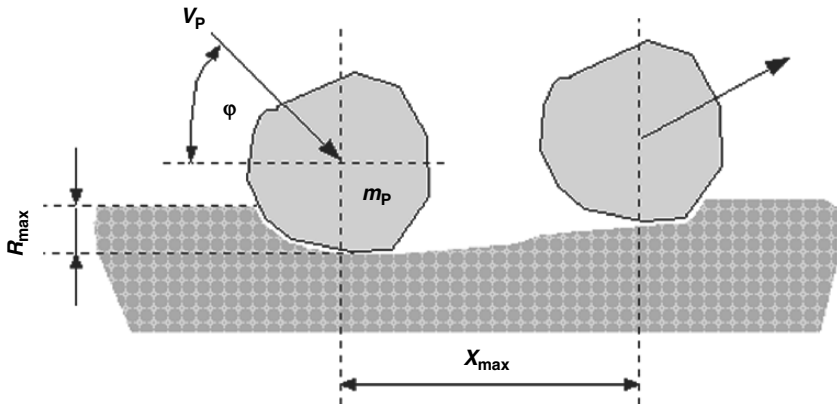


Fig. 8.42 Model for profile formation on a steel substrate due to an impinging abrasive particle (Chernyavskii, 1984)

velocity, blasting angle, blasting time, surface cleaning grade, abrasive hardness, substrate hardness and abrasive working mixture.

8.6.3.2 Effects of Blasting Angle

The effect of the blasting angle on profile values of a carbon steel substrate was investigated by several authors (Keane et al., 1976; Mellali et al., 1994; Ishikawa

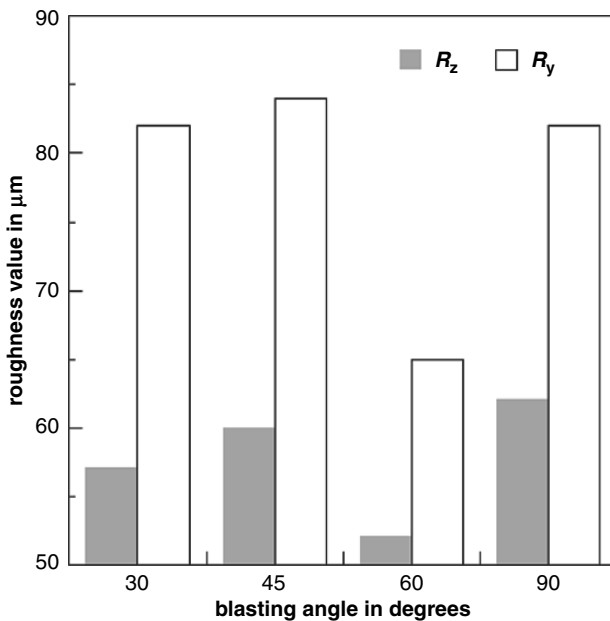


Fig. 8.43 Effects of blasting angle on substrate roughness parameters (Ishikawa and Tobe, 2003)

and Tobe, 2003; Barnett and Burgess, 2007). Results of Ishikawa and Tobe (2003) are provided in Fig. 8.43. There is some range in the neighbourhood of a 60° angle where roughness was rather low. Shallow as well as high blasting angles promoted high roughness values. Similar results were reported by Siegmann and Brown (1998) for the blast cleaning of steel with aluminium oxide abrasives. Mellali et al. (1994), however, who also utilised aluminium oxide with a grain size of $d_p = 1.4$ mm, noted an influence of substrate properties on the blasting angle effect. For rather hard substrate materials ($HV_5 = 200$), average roughness (R_a) dropped only slightly for shallower blasting angles; but for a soft steel, average roughness rapidly fell if the blasting angle was lower than $\varphi = 60^\circ$. Highest roughness values were always obtained at perpendicular impingement. How impact angle affects the appearance of the substrate profile is illustrated in Fig. 8.44. It can be seen that very uneven coarse surface profiles were formed if the blast cleaning was performed at moderate angles.

Bahbou et al. (2004) blast cleaned titanium alloys with aluminium oxide ($p = 0.4$ MPa, $d_p = 160\text{--}400$ μm , $\dot{m}_p = 1.5$ kg/min) and found maximum values for R_a and R_z at perpendicular blasting angles, whereby the parameter R_z was more sensitive to changes in the blasting angle.

8.6.3.3 Effects of Stand-off Distance

The effect of the stand-off distance between nozzle and substrate surface on roughness parameters is not well established. Whereas some authors found that stand-off distance does not seem to affect roughness (Siegmann and Brown 1998; Varacalle et al., 2006), others found a clear, almost linear, increase in roughness (R_z) for longer stand-off distances (Karpinos et al., 1979). Wigren (1988) found that stand-

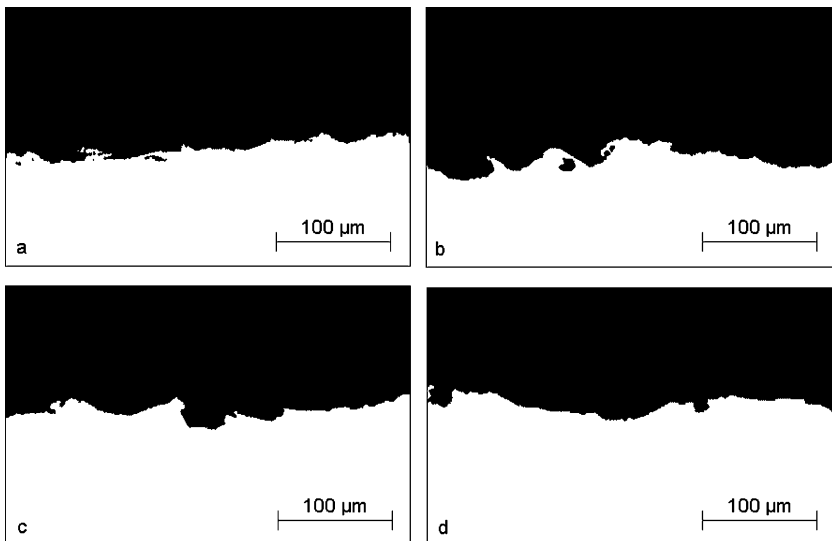


Fig. 8.44 Effects of blasting angle variations on profile shape (Amada and Satoh, 2000); polished cross-sections. (a) $\varphi = 45^\circ$; (b) $\varphi = 60^\circ$; (c) $\varphi = 75^\circ$; (d) $\varphi = 90^\circ$

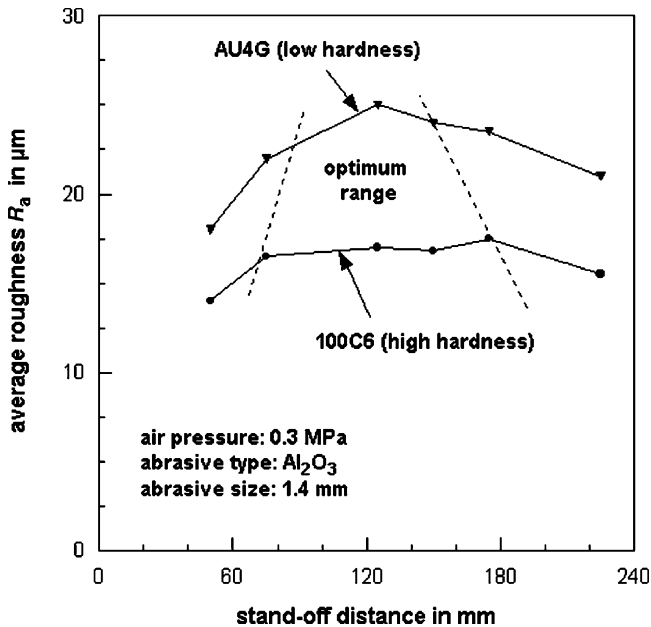


Fig. 8.45 Effects of stand-off distance and substrate material on average roughness (Mellali et al., 1994)

off distance affected roughness if a certain distance was exceeded. Values for this threshold distance depended on air pressure: for $p = 0.4 \text{ MPa}$, the critical stand-off distance was about $x = 250 \text{ mm}$. Mellali et al. (1994) noted an optimum range for the stand-off distance where maximum values for the average roughness (R_a) could be achieved. This optimum stand-off distance range depended on substrate hardness. Results of their investigations are displayed in Fig. 8.45. The optimum range was wider for substrate materials with rather high hardness values. With this optimum stand-off distance, rebound effects deteriorate the removal process; for stand-off distances beyond the optimum value, reduced kinetic energy of the impinging particles is assumed to cause the drop in roughness. Effects of substrate materials were also noted by Karpinos et al. (1979), who utilised cast iron shot ($d_p = 400\text{--}750 \mu\text{m}$) for the treatment of different metals. Whereas the roughness (R_z) almost linearly increased with longer stand-off distances for carbon steel samples and copper samples, stand-off distance changes did not show a notable effect on the roughness for aluminium samples.

8.6.3.4 Effects of Air Pressure and Abrasive Particle Velocity

It was already Tilghman (1870) who mentioned an effect of air pressure on surface profile: “The less the pressure of the blast, the finer is the grain of the de-polished surface.” An increase in air pressure usually leads to deeper profiles (Münster and Spähn, 1979; Wigren, 1988; Kniewald, 1993; Varacalle et al., 2006; Barnett and Burgess, 2007). Some authors noted a linear relationship between

air pressure and substrate roughness (Wiedenhaupt, 1970; Karpinos et al., 1979; Stallmann et al., 1988; Staia et al., 2000; Minaki et al., 2004; Sofyan et al., 2005). Gesell (1973) cited experimental investigations on the effects of particle impingement velocity on substrate roughness, which can be summarised with the following relationship:

$$R_t = C_R \cdot V_P \cdot d_P \quad (8.5)$$

The constant C_R considers effects of equipment and blast cleaning process. A linear relationship between abrasive impingement velocity and roughness was found by Weidenhaupt (1970) for the descaling of steel with cut steel wire and steel shot, which were accelerated with a wheel blast machine. However, for larger wire particles ($d_P > 700 \mu\text{m}$), the relationship between impingement velocity and roughness tended to a power relationship with a power exponent less than unity. Results of these measurements are provided in Fig. 8.46. Weidenhaupt (1970) theoretically derived a relationship between the roughness and the kinetic energy of the impinging abrasive particles: $R_t \propto E_P^{1/2}$. Tosha and Iida (1990) found an almost linear relationship between the impingement velocity of cast steel particles and the maximum roughness of steel and titanium samples, whether steel grit or steel shot was being used.

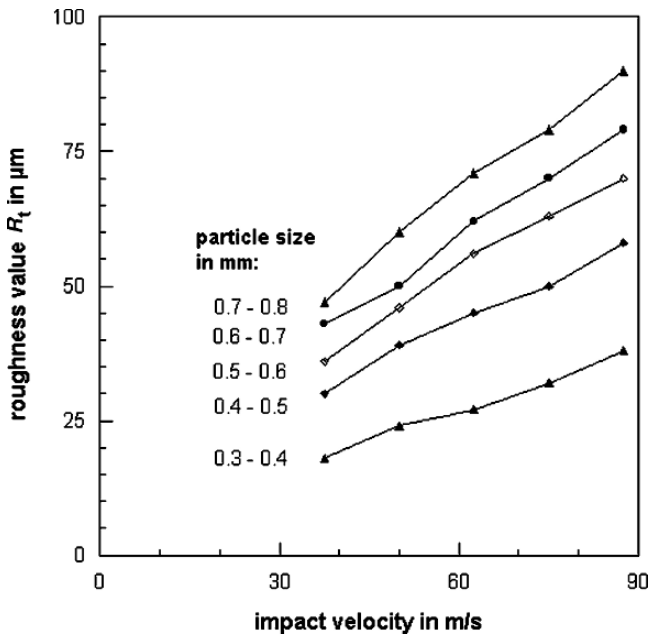


Fig. 8.46 Effects of particle impact velocity and particle size on substrate roughness (Weidenhaupt, 1970)

8.6.3.5 Effects of Abrasive Particle Size and Shape

It was already Tilghman (1870) who mentioned an effect of particle size on surface profile: “*The finer the sand, the finer is the grain of the depolished surface.*” Later, Bigos (1959) reported that the roughness of blast cleaned steel plates increased almost linear with an increase in abrasive particle diameter. The progress of the curve was almost independent of the abrasive type (sand, slag, iron shot and iron grit). A linear relationship between average roughness and abrasive particle diameter was also reported by Bullett and Dasgupta (1969) for the use of chilled iron grit. The authors also noted a linear relationship between abrasive particle diameter and increase in surface area after blast cleaning. Effects of changes in abrasive mixtures on profile parameters are depicted in Fig. 8.47. The average maximum roughness (R_z) was most sensible to changes in the abrasive mixtures. An interesting detail was the different trends for the conventional roughness parameters (R_z and R_a) and for the roughness angle (δ_q). Whereas the values for the roughness values increased from condition “1” to “6”, the roughness angle had minimum values at for the conditions “1” and “6”. The influence of abrasive particle size and shape on the average roughness and maximum roughness is depicted in Fig. 8.48. It can be seen that both roughness values increased in an almost linear fashion with an increase in particle size, irrespectively if shot or grit was used. A linear relationship between abrasive

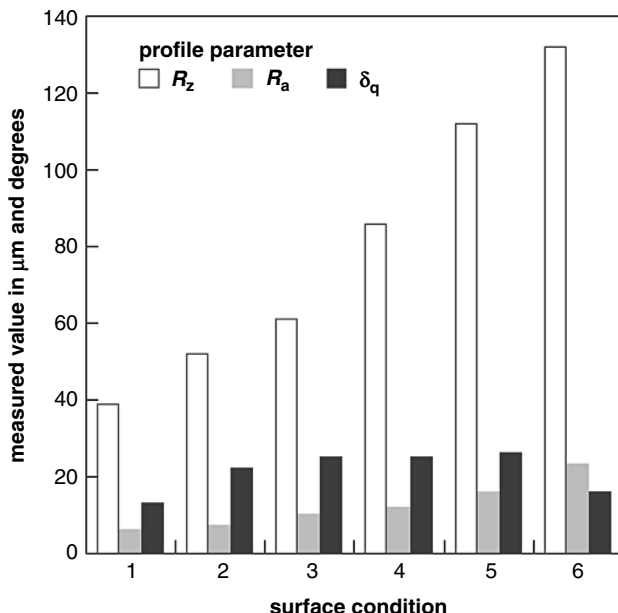


Fig. 8.47 Effects of abrasive mixtures on profile parameters of chromium–nickel steel (Beck and Arndt, 1996). Mixtures: 1 – untreated scale; 2 – garnet ($d_p = 250\text{--}500\ \mu\text{m}$, one run); 3 – garnet ($d_p = 500\text{--}1,000\ \mu\text{m}$), two runs; 4 – garnet ($d_p = 500\text{--}1,000\ \mu\text{m}$), one run; 5 – garnet (new abrasives); 6 – cast steel grit ($d_p = 1,000\text{--}2,400\ \mu\text{m}$)

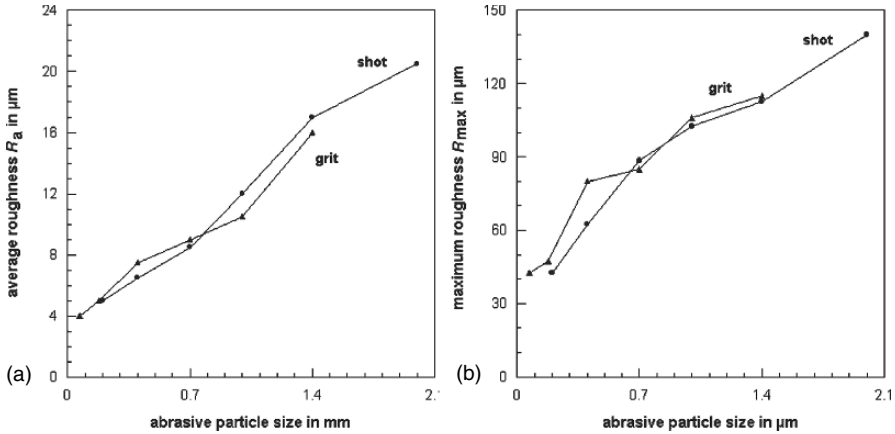


Fig. 8.48 Effects of abrasive particle size and shape on substrate roughness (Morcillo et al., 1989). (a) Average roughness, R_a ; (b) Maximum roughness, R_{max}

particle size and average roughness (R_a) was also found by Mellali et al. (1994) for metal substrates, blast cleaned with aluminium oxide; by Kniewald (1993) for steel and copper, blast cleaned with steel grit; and by Abukawa et al. (2004) for steels, blast cleaned with aluminium oxide. Tosha and Iida (1990) found an almost linear relationship between the diameter of cast steel particles and the maximum roughness of steel and titanium samples, whether steel grit or steel shot was being used. These results verify (8.5). The graphs in Fig. 8.48 also show that particle shape was not of much influence to the profile. Keane et al. (1976) noted a more complex relationship between roughness and abrasive particle size. Although these authors found a linear relationship between roughness and abrasive particle size for some abrasive materials (sand and steel shot), they could also observe a power relationship for other abrasive materials (steel grit and iron grit). A more general expression of (8.5) is, therefore, the following form:

$$R \propto d_p^{n_p} \quad (8.6)$$

In this equation, the parameter n_p characterises the effects of other abrasive and target parameters. For $n_p = 1$, a linear relationship appears, and (8.5) is valid. Weidenhaupt (1970) presented experimental results which verified that the relationship between roughness and particle size depended on substrate hardness. Some results of his work are illustrated in Fig. 8.49. If substrate hardness decreased (respectively abrasive/substrate hardness ratio increased), the relationship was linear ($n_p = 1$) as depicted in Fig. (8.48). For higher substrate hardness values (respectively lower abrasive/substrate hardness ratio), however, power functions with exponents $n_p < 1$ better fitted the relationship. Thus, (8.6) may be modified for this special effect as follows:

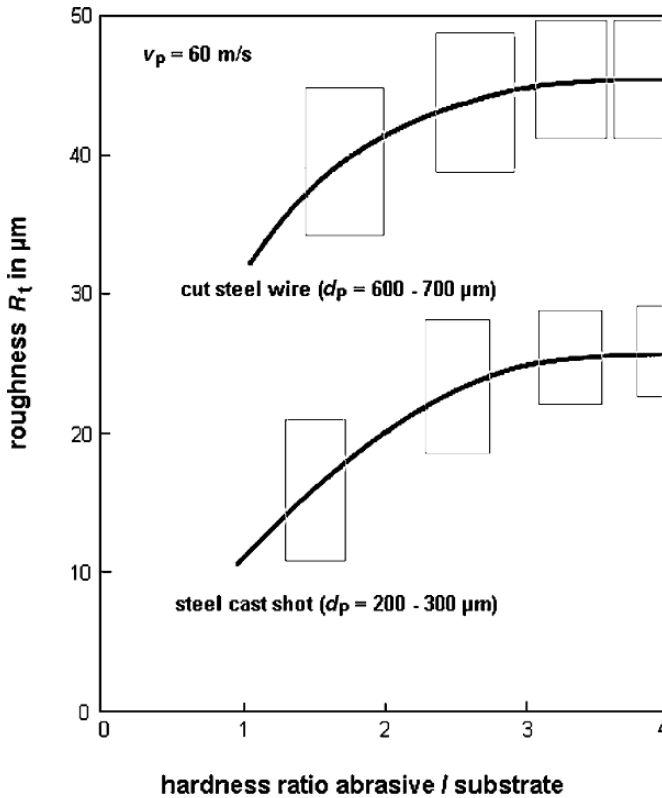


Fig. 8.49 Effects of abrasive type and abrasive hardness on roughness (Weidenhaupt, 1970)

$$R \propto d_p^{f(H_M)} \tag{8.6a}$$

$$n_p = f(H_M)$$

The value of the function $f(H_M)$ increases if substrate hardness decreases. For $f(H_M) = 1$, the relationship equals (8.5). Wheel blast cleaning results for the descaling of steel, Weidenhaupt (1970) and results from Kniewald (1993) on copper substrates suggested that grit size effects were more pronounced for higher grit impact velocities. Slutzky et al. (1988) performed a statistical study into steel grit size effects on selected roughness parameters; results are listed in Table 8.29. Prazak

Table 8.29 Linear regressions ($y = ax+b$) between abrasive particle size and roughness parameters (Slutzky et al., 1988); abrasive: steel grit, substrate: low-carbon steel, preparation grade: Sa $2\frac{1}{2}$

Roughness value	Correlation equation	Correlation coefficient
R_{max}	$y = 0.041x + 9.512$	0.930
R_z	$y = 0.031x + 7.581$	0.931
R_a	$y = 0.006x + 1.028$	0.936

and Eremias (1972) performed test in order to investigate abrasive size effects on the relative roughness factor given by (8.2). Their results are listed in Table 8.30. It can be seen that the values for the relative roughness factor increased with an increase in abrasive particle size.

The effect of abrasive particle diameter on the peak count was investigated by Keane et al. (1976). The authors found that the peak count slightly decreased with an increase in abrasive particle diameter, whereas roughness notably increased if larger abrasive particles were used. This example illustrates again the complex relationship between substrate topography features and abrasive particle size.

Weidenhaupt (1970) investigated effects of abrasive particle shape on substrate roughness. If cut steel wire was utilised as a grit material for descaling, cylindrical particles formed deeper profiles than spherical particles at equal impact velocities. Results of this investigation are plotted in Fig. 8.49. Weidenhaupt (1970) also found the following relationship between substrate roughness and abrasive particle kinetic energy: $R_t \propto E_P^{n_E}$. The power exponent was independent of abrasive particle size ($d_P = 300\text{--}800\ \mu\text{m}$), but showed a weak dependence on the abrasive particle shape. For round cut steel wire, $n_E = 0.343$; for cylindrical cut steel wire, $n_E = 0.337$. A theoretical value, derived by Weidenhaupt (1970), is $n_E = 0.5$.

Cross-sections, cut through blast cleaned steel substrates, are shown in Fig. 8.50. The effect of the abrasive types on the profile can be recognised clearly. Corundum and steel grit, for example, produced rather irregular profiles with a pronounced peak-valley structure as illustrated in Fig. 8.50b, whereas glass beads and plastics abrasives formed smooth, regular profiles as illustrated in Fig. 8.50a. Uhlmann et al. (2003) performed a study about the effects of abrasive materials (chilled cast, corundum, plastics and glass beads) on the roughness of different substrate materials. Corundum produced highest roughness values for all substrate materials, but the roughness for an ordinary construction steel was much higher than for a chromium–nickel steel. Martin (1997) compared glass beads, corundum and steel grit for the preparation of pipeline steel, and he found that steel grit formed the deepest profile, followed by corundum and glass beads. Spherical abrasive materials always produced rather shallow profiles.

Yankee et al. (1991) highlighted the influence of the abrasive particle type on the roughness characteristics of blast cleaned profiles. They found notable differences in the roughness characteristics between titanium substrates impinged with silicone carbide and, respectively, aluminium oxide abrasives. Aluminium oxide particles

Table 8.30 Abrasive particle size effects of the relative roughness factor (Prazak and Eremias, 1972)

Abrasive particle diameter in μm	Relative roughness factor
Ground substrate (for comparison)	3.0
300	8.9
600	10.2
900	12.5
1,200	13.7

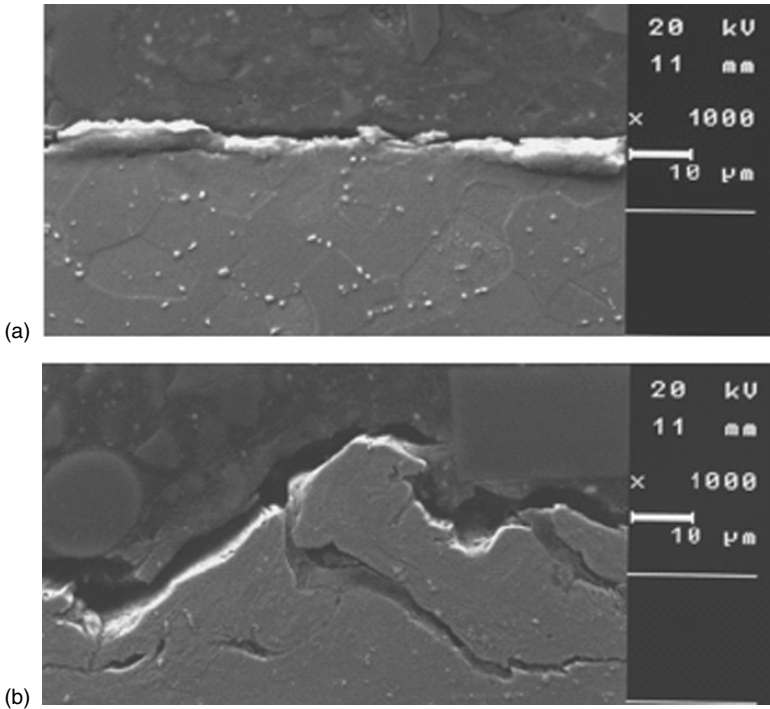


Fig. 8.50 Cross-sections, cut through blasted steel substrates, showing abrasive size effects on substrate profile (Uhlmann et al., 2003); test conditions: $p = 0.6$ MPa; $\varphi = 90^\circ$; $v_T = 0.4$ m/min; $x = 150$ mm; substrate: steel (DC01 A). **(a)** Abrasive material: Plastic pellets “Duroplast” ($d_p = 200\text{--}600\ \mu\text{m}$); **(b)** Abrasive: steel cast grit ($d_p = 120\text{--}420\ \mu\text{m}$)

appeared to produce consecutive sharp peaks and deep valleys, while silicone carbide particles produced a series of shallow peaks between deep valleys. To achieve an equal roughness on the substrate for both abrasive types, completely different process parameters needed to be adjusted. This is illustrated by the results listed in Table 8.31. Table 8.32 lists the effects of abrasive type and size on maximum roughness and peak count. It can be seen that the peak count could be notably affected if the abrasive mixture was changed.

Table 8.31 Blast cleaning parameters resulting in equivalent surface roughness R_a (Yankee et al., 1991)

Parameter	Abrasive material	
	Silicone carbide	Aluminium oxide
Air pressure in MPa	0.65	0.34
Stand-off distance in mm	76	127
Blasting angle in $^\circ$	60	90
Blasting time in s	90	20
Average roughness in μm	3.49	3.50

Table 8.32 Effects of abrasive type and size on profile parameters (Roper et al., 2006)

Abrasive	R_{max} in μm	Peak count in peaks/cm
G-40 steel grit	50–112	48–72
G-25 steel grit	75–137	36–48
G-18 steel grit	100–175	20–30
20/40 flint silica sand	25–87	52–88
20/40 boiler slag	20–75	40–72

Beitelman (2003) applied the shape designations according to Fig. 2.7 to crushed steel grit (G50) and investigated their effects on the roughness of low-carbon steel substrates. Highest roughness values (R_Z) were obtained with sub-rounded particles. Peak density dropped with an increase in particle angularity.

The effects of abrasive material recycling on the profile of blast cleaned steel substrates were investigated by Mellali et al. (1994). The authors used aluminium oxide ($d_p = 500\text{--}1,400\mu\text{m}$), and they found that the average roughness (R_a) continuously decreased with an increase in the number of recycling cycles (a total of five recycling steps were performed). The intensity in drop of roughness depended on the original abrasive diameter; it was most severe for the largest abrasive particles. This result can be explained by the higher friability of the larger particles (see Sect. 2.9.2).

8.6.3.6 Effects of Abrasive Material Hardness

The hardness of the abrasive material has a moderate effect on the roughness. A metallic abrasive material should be at least four points harder on the Rockwell C scale (HRC) than the substrate. This restriction is due to the deformation of abrasive materials with lower hardness values during impact. A steel grit with a hardness of $H_p = 45$ HRC, for example, is known to quickly round up if used for the blast cleaning of steel substrates (Roper et al. 2006). It is, therefore, not the absolute hardness of the abrasive material, but rather the ratio between abrasive material hardness and target material hardness, which determines the roughness. Illustrative examples are provided in Fig. 8.49. The values for the roughness increased with an increase in the hardness ratio abrasive/substrate. The increase was very pronounced in the range of low values for the hardness ratio, but less intense in the range of higher values. If the hardness ratio had very high values (>3), any further increase in abrasive material hardness did not affect the substrate roughness at all.

8.6.3.7 Effects of Specific Abrasive Rate

Effects of specific abrasive rate (abrasive mass per blast cleaned area) are cited by Gesell (1973). It was shown that roughness had a maximum at moderate values for the specific abrasive rate (between $m_s = 4$ and 8 g/cm^2). For lower or higher values of the specific abrasive rate, roughness values dropped. The exact optimum

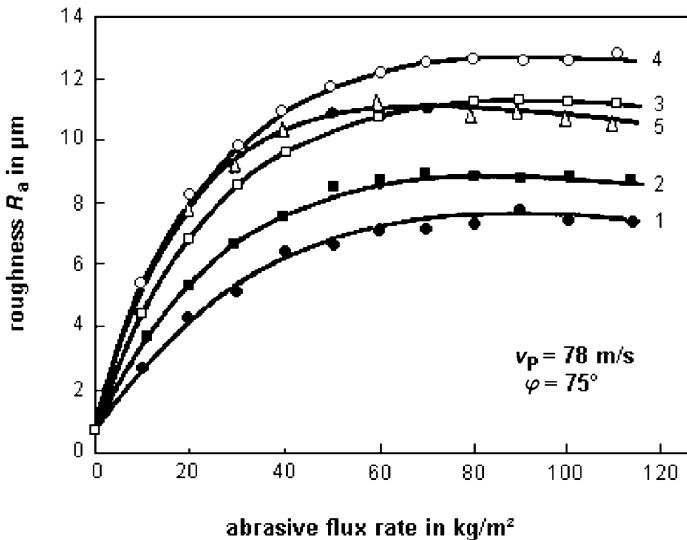


Fig. 8.51 Effects of specific abrasive rate on substrate roughness (Kniewald, 1993). Abrasive material: 1 – steel shot ($d_p = 560 \mu\text{m}$); 2 – steel shot ($d_p = 710 \mu\text{m}$); 3 – steel shot ($d_p = 900 \mu\text{m}$); 4 – steel shot ($d_p = 1,120 \mu\text{m}$); 5 – corundum ($d_p = 1,120 \mu\text{m}$)

depended on abrasive size. Kniewald (1993) investigated the effect of specific abrasive rates up to $m_s = 120 \text{kg/m}^2$ on the roughness of steel substrates treated with steel grit and aluminium oxide. Results of this study are displayed in Fig. 8.51. Whereas average roughness (R_a) increased rapidly in the range of low specific abrasive rates, it approached a saturation level at higher rates. The point where the saturation started, was the point where the most effective overlap of impact craters occurred. Its location depended on the abrasive type and size. The saturation level was quickly reached for fine-grained steel grit and aluminium oxide. For the aluminium oxide, roughness even seemed to drop for the highest specific abrasive mass values. Values in excess of $m_s = 60 \text{kg/m}^2$ did not lead to any further increase in surface profile.

Minaki et al. (2004) utilised rather small abrasive mass flow rates ($\dot{m}_p = 50\text{--}300 \text{g/min}$, aluminium oxide, mesh 700, $p = 0.15\text{--}0.4 \text{MPa}$, $\varphi = 90^\circ$, $d_N = 8 \text{mm}$), and they found that the roughness (R_a) featured maximum values at moderate values for the abrasive mass flow rate (at about $\dot{m}_p = 100 \text{g/min}$).

8.6.3.8 Effects of Blasting Time

Wigren (1988) introduced a parameter “blasting time”, which he defined as follows:

$$t_B = \frac{3.2 \cdot r_j^2 \cdot n_s}{\pi \cdot V_T \cdot \phi_F} \tag{8.7}$$

In this equation, t_B is the blasting time in s, r_j is the radius of the hit area (jet radius)

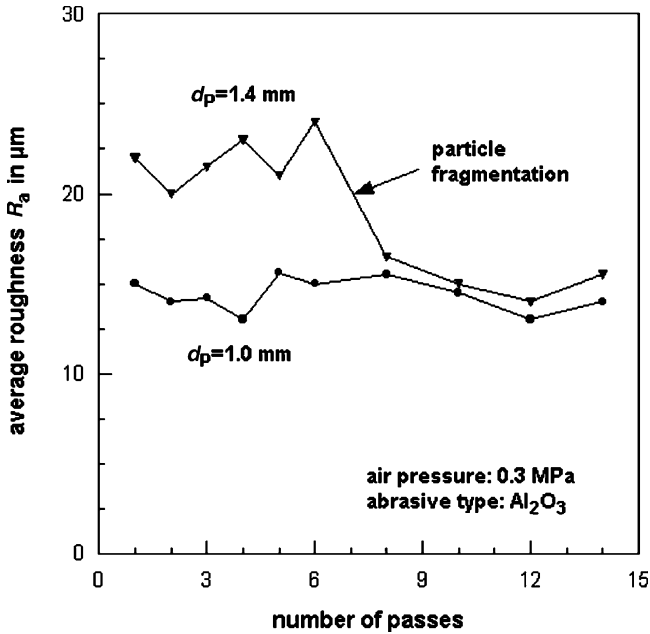


Fig. 8.52 Effects of number of cleaning steps on substrate profile (Mellali et al., 1994)

in mm, n_S is the number of passes, ϕ_F is the diameter of fixture in mm and v_T is the traverse rate in mm/s. Roughness (R_a) increased very quickly for short blasting times between $t_B = 2.5$ and 3.0 s, and it then rested at a certain saturation level, or even slightly dropped. Any further increase in blasting time did not add profile, but only an increase in grit embedment took place (see Sect. 8.6.5). Saturation effects were also reported by Celik et al. (1999) for the blast cleaning of stainless steel with aluminium oxide, and by Jones and Gardos (1971) for the blast cleaning of stainless steel with garnet. Mellali et al. (1994) observed the effect illustrated in Fig. 8.52. Average roughness (R_a) dropped suddenly at a certain number of cleaning passes (corresponds to blasting time), if rather coarse abrasive particles were used. This phenomenon can be explained through particle comminution effects. The coarse particles were crushed during the first blasting passes, and their grain size was reduced (see Sect. 2.9.2). In turn, roughness values dropped if the substrate was impinged by the smaller particles. Mellali et al. (1994) verified this explanation through comparative sieve tests.

8.6.3.9 Effects of Substrate Material

Structure and mechanical properties of the substrate materials affect the topography formation process. Effects of different substrate materials on substrate roughness are depicted in Table 8.33, where it can be seen that hot-rolled steel allowed higher roughness values compared with cold-rolled steel. The differences in roughness led

Table 8.33 Effects of target steel type on roughness (Sancaktar and Gomatam, 2001). Air pressure: 0.55 MPa; abrasive: aluminium oxide #54

Steel type	Roughness value in μm		
	R_a	R_{max}	R_z
Cold-rolled steel	2.4	23.5	18.9
Hot-rolled steel	3.9	43.8	28.7

to differences in the strength of adhesive joints. Whereas the strength increased up to +51% for joints of cold-rolled steel, it improved up to +100% for joints of hot-rolled steel (Sancaktar and Gomatam, 2001) (values related to untreated substrates).

Uhlmann et al. (2003) investigated the roughness of three metal substrates, blast cleaned with different abrasive materials. The roughness was always highest for an ordinary construction steel, followed by that of an aluminium alloy and a chromium–nickel steel. Wigren (1988) depicted an almost reverse linear relationship between the average roughness of blast cleaned metal substrates and their values for Young’s modulus: the higher Young’s modulus, the lower the roughness values. This effect was also observed by Mellali et al. (1994), who impinged different metal substrates with aluminium oxide particles, for the relationship between Young’s modulus and average roughness (R_a).

Keane et al. (1976) investigated the effects of different material composition of steel plates (caused by different heat treatment regimes) on their influence on the roughness after blast cleaning. They found that small variations in the composition of the steels did not affect the profile height if the substrate quality was high after blast cleaning (Sa 2 $\frac{1}{2}$, Sa 3). If the substrate quality was lower (Sa 2), even slight deviations in the steel composition did affect the values for the profile height.

Siegmann and Brown (1998) adapted a fractal parameter, called “area-scale fractal complexity” (ASFC), which was found to be linearly related to the arithmetic roughness. The authors could show that this profile parameter decreased according to a reverse linear relationship if hardness of the substrate materials increased. Thus, roughness decreased with rising substrate material hardness. Weidenhaupt (1970) performed blast wheel cleaning tests with cast shot and wire cut, and he noted a certain relationship between the hardness ratio abrasive/substrate and the roughness. If the hardness ratio exceeded a value of $H_p/H_M = 3$, no further increase in substrate roughness occurred (see Fig. 8.49). Abukawa et al. (2004) performed blast cleaning tests on steel samples with aluminium oxide particles, and they found that a lower substrate hardness promoted higher roughness values (R_a). This trend was also observed by Mellali et al. (1994). These results are in agreement with the model of Sorokin et al. (1983) for metals. The authors derived a relationship: $R \propto H_M^{-1/2}$. Abukawa et al. (2004) noted, however, that a certain steel did not follow the above-mentioned trend, and they concluded that other hardness-related factors (morphology, heat treatment regime) should be considered. Jones and Gardos (1971) reported interesting relationships between original substrate roughness, substrate roughness and final substrate roughness. They found that the original roughness affected the roughness after blast cleaning if hard stainless steel was treated. For the treatment of soft stainless steel, not such effects could be determined.

Karpinos et al. (1979), who propelled cast iron shot ($d_p = 400\text{--}750\ \mu\text{m}$) on steel samples, noted an influence of the stand-off distance on the effects of target material variations. Whereas the roughness (R_Z) was higher for aluminium substrates compared with copper substrates for low stand-off distances, the trend was opposite for longer stand-off distances.

Weidenhaupt (1970) noted effects of scale composition on the roughness values of blast cleaned iron metals. The values for the roughness (R_t) were rather low for FeO; moderate for a mixture Fe₃O₄/FeO; rather high for Fe₃O₄. The initial condition of the steel also affects roughness. Heavily weathered or corroded plates, for example, had relatively high surface profiles after blast cleaning.

8.6.3.10 Effects of Surface Preparation Grade

The surface preparation grade characterises the severity of the substrate treatment, and it can be assumed that changes in the surface preparation grade may be related to changes in the profile parameters. Keane et al. (1976) reported some results on the blast cleaning of steel substrates with steel grit, respectively steel shot. They found that the roughness (profile height) very slightly increased if surface preparation degree improved. The values for the roughness were highest for Sa 2 and lowest for Sa 3, either shot or grit has been used, but the trends were statistically insignificant. The peak count of the profile (in number of peaks per unit length) was independent of the surface preparation grade.

8.6.3.11 Effects of Accessibility

Bullard et al. (2002) investigated effects of accessibility to a structure on profile parameters. The roughness of surfaces in gaps with widths between 0.31 and 2.5 cm was about 85% of the values generated during “normal” blast cleaning procedures. The surface profile fell within a typical specification range between 37 and 67 μm . Similarly, the average peak density was approximately 87% of the values generated during “normal” blast cleaning processes.

8.6.3.12 Statistical Assessment Models

Statistically designed experiments were performed by Varacalle et al. (1995, 2006) in order to assess the effects of air pressure, stand-off distance, blasting angle, abrasive material and blasting machine type on the roughness of steel substrates. For SiO₂ as abrasive medium, Varacalle et al. (1995) derived the following regression equation:

$$R_Z = 7.14 - 0.085 \cdot x + 0.61 \cdot p - 0.79 \cdot x \cdot p \quad (8.8)$$

In this equation, R_Z is given in microns; x is given in inch and p is given in ψ . In a subsequent study, the authors derived the following regression equation for the blast cleaning of low-carbon steel with different abrasive materials (Varacalle et al., 2006):

$$R_Z = C_1 + C_2 \cdot x + C_3 \cdot p + C_4 \cdot x^2 + C_5 \cdot p^2 + C_6 \cdot x \cdot p \quad (8.9)$$

In this equation, R_Z is given in 10^{-2} cm; x is given in cm and p is given in kPa. Values for the regression parameters C_1 to C_6 are listed in Table 8.34 for a number of abrasive materials.

Day et al. (2005) performed a statistical analysis on the effect of certain process parameters on the roughness and derived the following relationship:

$$R = -0.33 \cdot G_N + 0.24 \cdot p + 0.44 \cdot n_s + 2.87 \cdot X + 0.12 \cdot \varphi \quad (8.10)$$

In this equation, the grit number (G_N) is given in mesh; p is given in psi; x is given in inch and φ is given in degrees.

8.6.4 Height Distribution Parameters

Height distribution parameters represent the symmetry and sharpness of the profile. Because of the nature of the material removal process, the profiles of blast cleaned surfaces very often feature a Gaussian profile type. Parameters which characterise symmetry and sharpness of a profile include skew and kurtosis. Figure 8.53 shows plots of skew and kurtosis against the average roughness for four different samples. The graph proves that the mean values for skew and kurtosis were closely to the theoretical values for a Gaussian surface type (which are “0” for skew and “3” for kurtosis).

The results plotted in Fig. 8.53 show further that overblasting did not produce a Gaussian surface. Although the skew values remained at about zero, the kurtosis values were higher than 3, which was due to the higher portion of flat areas. A high kurtosis value is, therefore, indicative of overblasting effects.

8.6.5 Profiles of “Overblasted” Steel Substrates

Further interesting aspects associated with blast cleaning are illustrated in Figs. 8.54 and 8.55. Figure 8.54 shows the influence of multiple blast cleaning (overblasting) on roughness values of a steel substrates. The virgin steel is denoted “0”, blast cleaned steel is denoted “I” and twice blast cleaned steel is denoted “II”. As expected, a single blast cleaning step (as performed during new construction jobs) increased any roughness parameter. The second blast cleaning step (as performed during the stripping of worn coatings or rust), however, again decreased the roughness. This overblasting caused the surface to have a high number of flat regions, a lower peak to valley height and a significant number of laps and tears due to folding and plastic deformation. These phenomena were verified by comparative SEM studies by Momber and Wong (2005a). Other authors (Griffith, 2001) described similar phenomena. An example is provided in Fig. 8.55. The polar plots in this

Table 8.34 Regression parameters for (8.9) (Varacalle et al., 2006)

Abrasive material	Regression parameter					
	C_1	C_2	C_3	C_4	C_5	C_6
HG 16	-7.65×10^{-3}	2.9×10^{-3}	2.29×10^{-4}	-1.88×10^{-4}	-8.76×10^{-7}	1.20×10^{-5}
HG 18	-7.37×10^{-3}	2.29×10^{-3}	2.29×10^{-4}	-1.88×10^{-4}	-8.76×10^{-7}	-1.19×10^{-5}
HG 25	-8.33×10^{-3}	2.49×10^{-3}	2.29×10^{-4}	-1.88×10^{-4}	-8.76×10^{-7}	-1.20×10^{-5}
HG 40	-9.58×10^{-3}	2.44×10^{-3}	2.24×10^{-4}	-1.88×10^{-4}	-8.76×10^{-7}	-1.20×10^{-5}
Copper slag	2.79×10^{-3}	2.21×10^{-4}	1.07×10^{-4}	1.10×10^{-5}	-4.60×10^{-7}	-7.72×10^{-6}
Coal slag	-3.40×10^{-3}	1.02×10^{-3}	1.17×10^{-4}	1.10×10^{-5}	4.60×10^{-7}	-7.72×10^{-6}
Chilled iron	-1.52×10^{-3}	7.37×10^{-4}	1.14×10^{-4}	1.11×10^{-5}	-4.60×10^{-7}	-7.72×10^{-6}

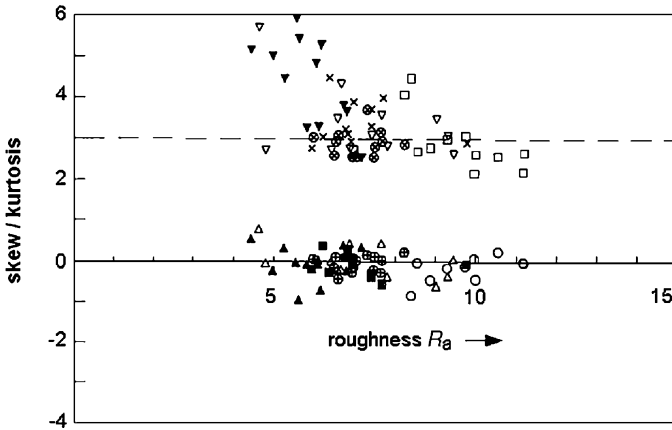


Fig. 8.53 Relationships between blast cleaning conditions, roughness and profile distribution parameters (Griffith et al., 1996). Legend: Δ skew (5.5 μm); ∇ kurtosis (5.5 μm); \circ skew (10 μm); \square kurtosis (10 μm); \blacksquare skew (6.5 μm); \times kurtosis (6.5 μm); \oplus skew (7.5 μm); \otimes kurtosis (7.5 μm); \blacktriangle skew (overblasted); \blacktriangledown kurtosis (overblasted)

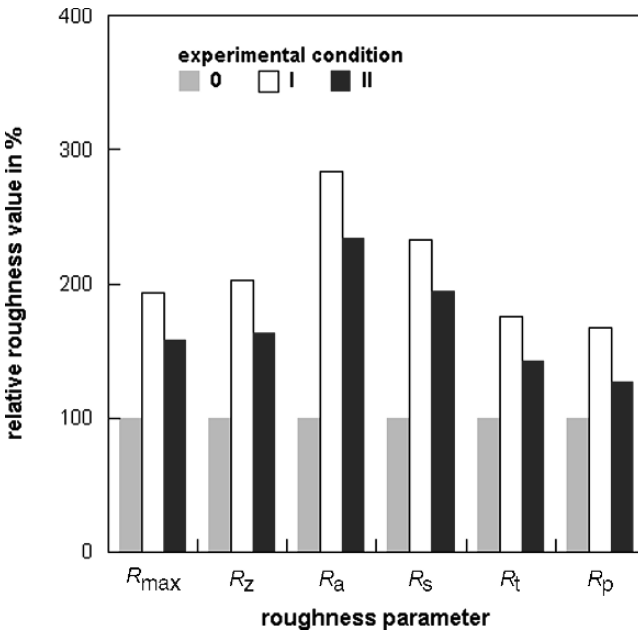


Fig. 8.54 Effects of overblasting on profile roughness parameters (Momber and Wong, 2005a). Experimental condition: 0 – untreated; I – one blast cleaning step; II – two blast cleaning steps; substrate: low-carbon steel

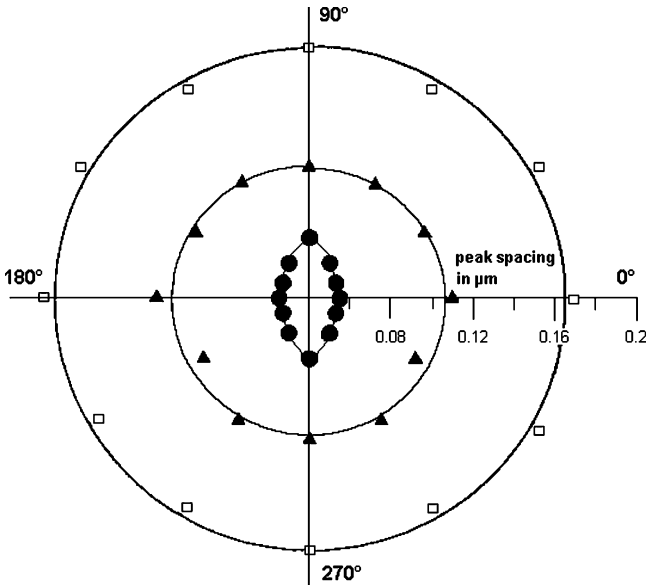


Fig. 8.55 Overblasting effects on peak spacing (Griffith, 2001). Legend: ● ground sheet, ▲ overblasted, □ correctly blasted

figure show the effects of blast cleaning steps on the peak spacing. Values for peak spacing were about $S_R = 0.17 \mu\text{m}$ after the first blast cleaning step, but they reduced down to about $S_R = 0.1 \mu\text{m}$ after a second blast cleaning step. Oppermann (1993), who discussed test results obtained on steel samples impinged with steel shot, found that the roughness (R_Z) of the substrate was a function of the area coverage. For an optimum value of the area coverage, the roughness exhibited maximum values.

Siegmann and Brown (1998, 2002) found that roughness increased as a steel substrate was blast cleaned five times compared with a substrate that was blast cleaned once. If, however, the substrate was blast cleaned 10 times, roughness decreased again. Samples of these tests as well as images of generated profiles are shown in Fig. 8.56. Broughton and Lodeiro (2002) blast cleaned aluminium samples at exposure times up to $t_B = 120 \text{ s}$, and they found that the values for R_a as well as R_q started to decrease if an exposure time of about $t_B = 60 \text{ s}$ was exceeded. Similar results were obtained by Celik et al. (1999) for R_a -values. Wigren (1988) found even much lower critical exposure times, between $t_B = 2.5$ and 3 s . If exposure time increased further, the average roughness of numerous metal alloys started to drop, whereas the levels of grit embedment increased further. There existed a balance between roughness, abrasive embedment and blast cleaning parameters. To achieve high roughness and low percentage of abrasive embedment, higher air pressures and shorter exposure times are preferred over lower air pressures and longer exposure times. Further examples which illustrated these relationships are shown in Figs. 8.28 and 8.29.

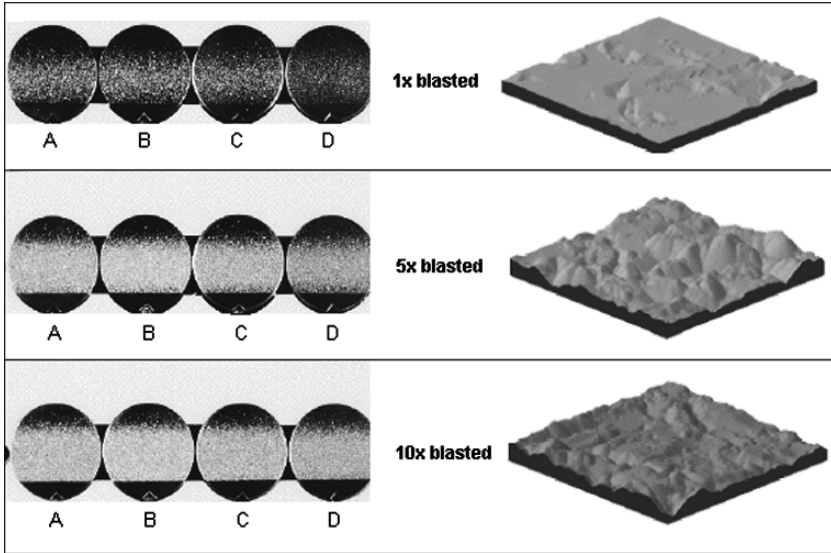


Fig. 8.56 Images of overblasted steel substrates (Siegmann and Brown, 2002)

8.7 Surface Integrity

8.7.1 Introduction

Substrate surface integrity is characterised by near-surface properties of the substrate materials, which may include the following:

- hardness;
- residual stresses;
- fatigue limit;
- stress–strain behaviour;
- metallurgical properties;
- chemical surface state.

Scholtes and Vöhringer (1993) subdivided the consequences of blast cleaning applications on metal surfaces into the following categories:

- changes in dimension;
- changes in topography;
- generation of, and changes in, the number of lattice disturbances (dislocations);
- changes in residual stress;
- changes in phase composition;
- changes in texture condition;
- crack formation;
- changes in density.

The authors also provided a comprehensive review about the effects of blast cleaning applications on these processes.

Guan et al. (2005) performed X-ray diffraction (XRD) and TEM measurements on blast cleaned aluminium samples. The samples were blast cleaned with silica particles with sizes between $d_p = 50$ and $70 \mu\text{m}$ at an air pressure of $p = 0.3 \text{ MPa}$, and they were subsequently annealed. The authors noted a gradual change in the target material grain size from a near-surface nano-crystalline layer through a transition zone to the core of the material samples. Jiang et al. (2006) performed blast cleaning tests on titanium samples with silica grit particles with sizes between $d_p = 200$ and $300 \mu\text{m}$ at a rather high air pressure of $p = 2.1 \text{ MPa}$. They applied high-resolution optical microscopy for structure assessment, and they distinguished three separate material zones: a severely deformed surface zone, a zone deformed mainly by twinning and an un-deformed substrate zone. A conclusion of the work was, that the two upper regions were likely responsible for the enhancement of near-surface material properties, namely fatigue, wear resistance and corrosion resistance. Twinning in the near-surface region blast cleaned steel panels was also reported by Klinger et al. (2002).

There is evidence in the engineering literature that the mechanical state of metallic substrates affects the mechanical properties of applied coatings. Results obtained by Osawa et al. (2005), for example, indicated that the delamination resistance of WC-cermet coatings during impact loading depended on hardness and degree of work hardening of substrate materials. Substrates with higher work-hardening coefficients indicated a higher delamination resistance of the coatings.

8.7.2 Substrate Hardness

Modifications in substrate hardness due to blast cleaning were reported by several authors (Rommelts, 1969; Doherty (1974); Leistikow and Kraft, 1974; Bond and Martin, 1984; Tosha and Iida, 1990; Fang and Chuang, 1999; Rhouma et al., 2001; Momber and Wong, 2005a; Jiang et al., 2006). Fang and Chuang (1999) investigated the surface properties of numerous metallic building materials after blast cleaning with angular silicone carbide abrasives. The particle velocity was rather low ($v_p = 30 \text{ m/s}$). Results of Vickers hardness measurements are shown in Fig. 8.57. It can be seen that surface treatment by blast cleaning altered the hardness. The relative change was highest for the 6063-Al alloy. Interestingly, hardness was almost unaffected after blast cleaning for the weathering steel (ARC-TEN). This material, however, featured an already high initial hardness. Fang and Chuang (1999) also found that the final Vickers hardness depended on blasting angle; it increased if blasting angle rose. It was also found that Vickers hardness of the substrate material increased for higher erosion rates. In a log-log plot, this relationship was reciprocal (Fang and Chuang, 1999). Reasons for hardness modification are mainly plastic deformations of impinged sections, and the embedment of hard abrasive particles in the surface. The latter effect can be excluded during the measurements if cross-sections of blast cleaned samples are inspected.

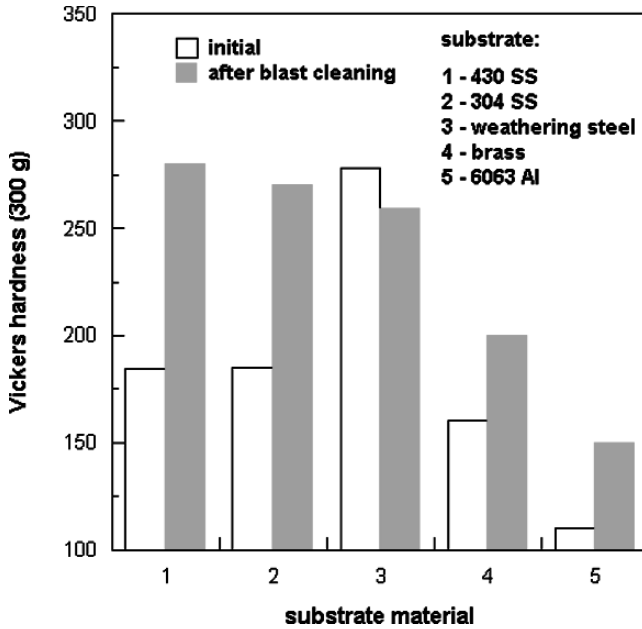


Fig. 8.57 Changes in micro-hardness due to blast cleaning (Fang and Chuang, 1999)

Effects of blast cleaning on the micro-hardness of low-carbon steel were investigated by Momber and Wong (2005a). Results of hardness measurements performed on cross-sections are shown in Fig. 8.58. Average values and standard deviations for the hardness are listed in Table 8.35. It was found that micro-hardness of the near-surface zone increased after blast cleaning. From Fig. 8.58, a depth of the hardened layer of at least 80 μm could be concluded. The increase in hardness was about +20% for one blast cleaning step, and it was about +50% for two blast cleaning steps. Remmelts (1969) published very similar results for blast cleaned steel substrates. He additionally found that larger abrasive particles had a more pronounced effect on surface hardening. The effect of abrasive particle size vanished at distances of about 250 μm. A hardness increase in the near-surface range of steel due to blast cleaning was noted by Bond and Martin (1984), and a hardness increase in the near-surface range of titanium due to blast cleaning was noted by Jiang et al. (2006). The latter authors explained the surface hardening effect by assuming the formation of a nano-crystalline surface layer in course of the blast cleaning process.

Table 8.35 Hardness variation of low-carbon steel due to blast cleaning with alumina abrasives (Momber and Wong, 2005a)

Number of blast cleaning steps	Vickers hardness in kg/mm ²	
	Average	Standard deviation
0	126	8
1	149	13
2	191	17

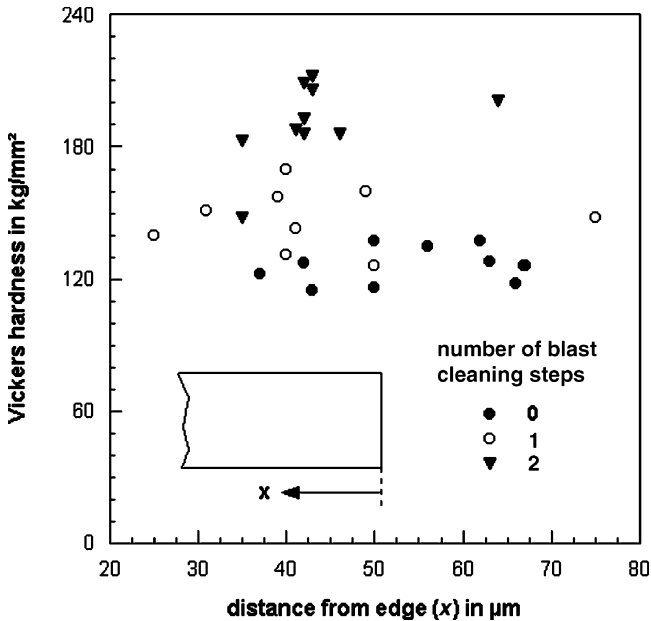


Fig. 8.58 Effects of blast cleaning on near-surface micro-hardness of low-carbon steel (Momber and Wong, 2005a)

Tosha and Iida (1990) investigated effects of abrasive particle shape on hardness modification, and they could show that the surface hardness after blast cleaning was lower than that after shot peening. However, the depths of work-hardening layers produced due to blast cleaning were larger than those produced due to shot peening. The general surface hardness distributions were independent of substrate material (steel, respectively titanium).

The effects of varying abrasive particle sizes on the micro-hardness of near-surface layers of austenitic stainless steel were evaluated by Rhouma et al. (2001). The authors used quartz particles with three different particle size classes ($d_p < 50 \mu\text{m}$; $d_p = 80\text{--}120 \mu\text{m}$; $d_p = 120\text{--}200 \mu\text{m}$). Both the depth of the cold worked layer and the level of hardness (HV 50) increased with an increase in the abrasive particle size. The largest particles ($d_p = 200 \mu\text{m}$) provided an increase in hardness up to $H_M = 350 \text{HV}$, and they extended the hardened layer to a depth of $350 \mu\text{m}$.

Tosha and Iida (1990) investigated the effects of process parameters on surface hardening. Variations in blasting angles did not notably affect hardness distributions in titanium; an increase in blasting angle only slightly decreased the size of the affected near-surface zone. Maximum hardness as well as thickness of the hardened layers exhibited a pronounced linear relationship to the kinetic energy of an impinging abrasive particle.

8.7.3 Residual Stresses

Peening is known to generate residual stresses in the near-surface region of metals. A very thorough review on the formation of residual stresses during shot peening is given by Herzog et al. (1996).

Blast cleaning can also alter the stress state in the near-surface zone of metal substrates. A Cr–Mo steel, for example, with an initial residual compressive stress value of $\sigma_R = 80$ MPa, featured residual stresses between $\sigma_R = 500$ and 600 MPa after it was blast cleaned with aluminium oxide abrasives (Guilemany et al., 1996). Residual stresses in metals impinged by cast steel particles initially (after 5–10 s blasting time) increased to high values, but dropped at longer blast cleaning times. The temporal location of the residual stress maximum depended on impact angle; it shifted to shorter blasting times for perpendicular impact (Tosha and Iida, 1990). Jiang et al. (2006) measured the depths of zones of residual stresses in thin aluminium samples, blast cleaned with silica oxide ($d_p = 200$ – 300 μm , $p = 0.3$ MPa), and they reported a depth of about 70 μm , whereby the maximum residual stress was measured in a depth of about 10 μm . Otsubo et al. (2003) noted the formation of compressive residual stresses of $\sigma_R = 600$ MPa at a depth between 50 and 100 μm in austenitic stainless steel. The authors suggested that the formation of a martensite phase in that area was related to this effect. Subsequent annealing released the residual stresses in the blast cleaned specimens.

Effects of blast cleaning parameters on residual surface stresses were investigated by Andziak and Brezezinski (1999), Badawi et al. (1986), Birley and Owens (1979), Da Silva Rocha et al. (2003), Guilemany et al. (1996), Ishikawa and Tobe (2003) and Zinn et al. (2002). Results of investigations of Andziak and Brezezinski (1999) are shown in Fig. 8.59. It can be recognized that the amplitude of the residual stress depended on abrasive material. Spherical abrasives, namely glass beads, generated higher residual stresses compared with irregular aluminium oxide particles. If steel cast particles were utilised, shot particles generated notably higher residual stresses compared with steel grit particles (Tosha and Iida, 1990). Figure 8.60 illustrates the effects of blasting angle variations on residual stresses of a blast cleaned carbon steel substrate. The values for the residual stresses notably changed, and they exhibited a maximum at a blasting angle of $\varphi = 45^\circ$. It was however, shown that the effect of blasting angle additionally depended on blasting time and air pressure (Guilemany et al., 1996).

Tosha and Iida (1990) showed that the magnitudes of the residual stresses depended on abrasive particle size and abrasive velocity. The larger the abrasive particle size was, the smaller were residual stresses, whether shot or grit particles were being used. Badawi et al. (1986) measured longitudinal and transversal residual stresses formed after the blast cleaning of steel substrates with aluminium oxide of different grain sizes. The results displayed in Fig. 8.61 revealed that residual stresses increased if abrasive particle size increased. Rhouma et al. (2001), who blast cleaned austenitic stainless steel with quartz particles ($d_p = 50$ – 200 μm), could not find a definite effect of abrasive size on stress amplitudes. Effects of particle impact velocity ($v_p = 15$ and 35 m/s) depended on abrasive particle shape. For grit particles,

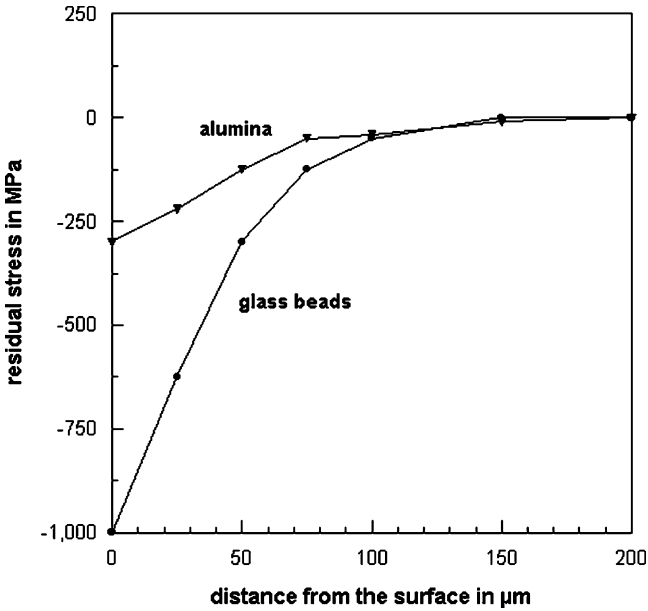


Fig. 8.59 Effects of abrasive type on residual stresses in stainless steel (Andziak and Brezezinski, 1999)

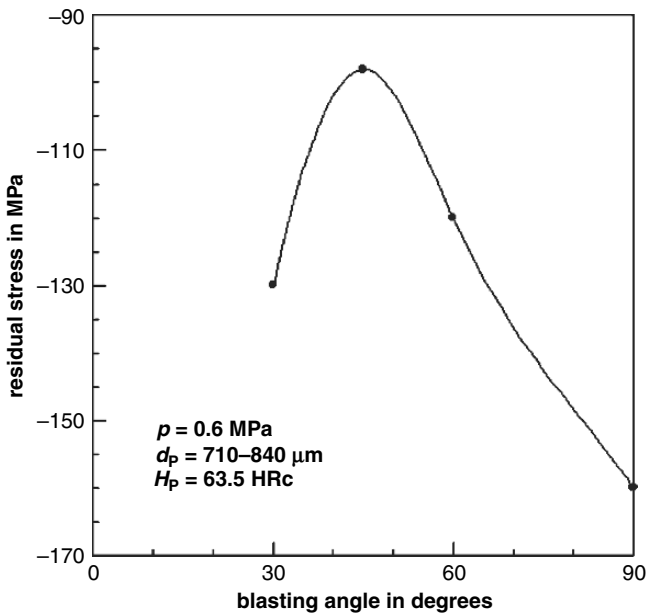


Fig. 8.60 Effects of blasting angle on residual stresses (Ishikawa and Tobe, 2003)

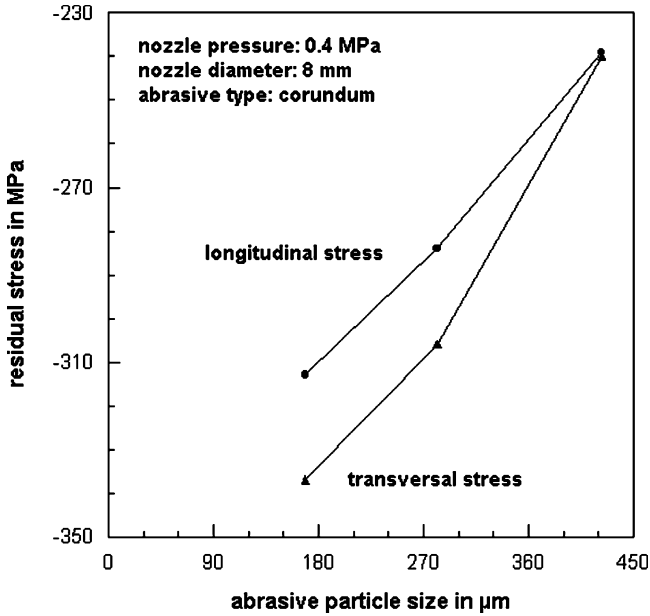


Fig. 8.61 Effects of abrasive size on residual stresses (Badawi et al., 1986)

residual stress decreased if particle velocity increased. For shot particles, the opposite trend occurred, whereas the significance of the velocity effects was rather low. Birley and Owens measured residual stresses after the blast cleaning of an aluminium alloy, and they found that the amplitude of the stresses increased if both air pressure and abrasive particle (aluminium oxide) diameter increased. Changes in impact angle had only marginal effects on the stress amplitude.

The intensities of residual stresses in the near-surface zone of a CrMo-steel, blast cleaned with aluminium oxide, were found to decrease with an increase in blasting time as well as with a decrease in air pressure. An increase in stand-off distance lead to a slight decrease in residual stresses for 45° blasting angles (Guilemany et al., 1996).

Zinn et al. (2002) investigated the residual stress depth distribution of 42CrMo_4 steels, blast cleaned with steel shot at moderate impact velocities ($v_p = 25\text{--}45$ m/s), and they found that the depth of the stressed layer increased with an increase in impact velocity. Results obtained by Schwarzer et al. (2002) could prove this trend for higher impact velocities ($v_p = 20\text{--}80$ m/s). The authors also performed numerical simulations of the peening process, and they showed that the depth of the residual stress zone increased with an increase in shot diameter and dropped for higher impact angles.

Petit-Renaud (2002) performed a statistical analysis for air pressure driven peening processes and derived statistical models. For the estimation of the maximum residual compressive stress generated in a steel after peening, he derived the following model:

$$\begin{aligned} \sigma_{R_{\max}} = & C_1 + C_2 \cdot t_B + C_3 \cdot d_N + C_4 \cdot p + C_5 \cdot \varphi + C_6 \cdot \dot{m}_p + C_7 \cdot p^2 \\ & + C_8 \cdot t_B \cdot p + C_9 \cdot d_N \cdot \dot{m}_p \end{aligned} \quad (8.11)$$

For the estimation of the depth where the maximum residual compressive stress is generated in a steel after peening, Petit-Renaud (2002) derived the following model:

$$\begin{aligned} h(\sigma_{R_{\max}}) = & C_1 + C_2 \cdot t_B + C_3 \cdot p + C_4 \cdot x + C_5 \cdot \varphi + C_6 \cdot \dot{m}_p + C_7 \cdot \varphi^2 \\ & + C_8 \cdot t_B \cdot p + C_9 \cdot p \cdot \varphi + C_{10} \cdot x \cdot \varphi \end{aligned} \quad (8.12)$$

The values for the constants C_1 to C_{10} are listed in Table 8.36. The physical units for the variables are as follows: t_B is given in s, d_N is given in inch, p is given in bar, x is given in mm, φ is given in degrees and \dot{m}_p is given in kg/min.

8.7.4 Substrate Fatigue Strength

Shot peening with steel beads is known to increase fatigue strength of the substrate material by inducing compressive surface stresses. However, it can be expected that blast cleaning also affects the fatigue performance. The relationship between fatigue strength and number of cycles to failure can be expressed as follows:

$$\sigma_F \propto A_F \cdot N_F^{m_F} \quad (8.13)$$

In this equation, A_F represents the fatigue strength coefficient, and m_F represents the fatigue exponent. Both parameters depend on material properties and testing conditions. Values are listed in Table 8.38.

Effects on fatigue parameters of metal as a result of blast cleaning was reported by several authors (Strizhalo et al., 1974; Kloos and Macherauch, 1987; He et al., 1996; Ibrahim and Berndt, 1998; Hernandez et al., 2000; Jiang et al., 2006). Changes in fatigue strengths of metal wires due to blast cleaning with different

Table 8.36 Model constants for (8.11) and for (8.12); Petit-Renaud (2002)

Constant	Target parameter	
	$\sigma_{R_{\max}}$ in MPa	$h(\sigma_{R_{\max}})$ in μm
C_1	-1, 158	35.8
C_2	58.6	3.11
C_3	9.94	15.3
C_4	-118	-2.14
C_5	-58.3	6.46
C_6	10.2	-5.58
C_7	88.8	-5.34
C_8	17.5	3.83
C_9	26.3	4.33
C_{10}	-	-2.53

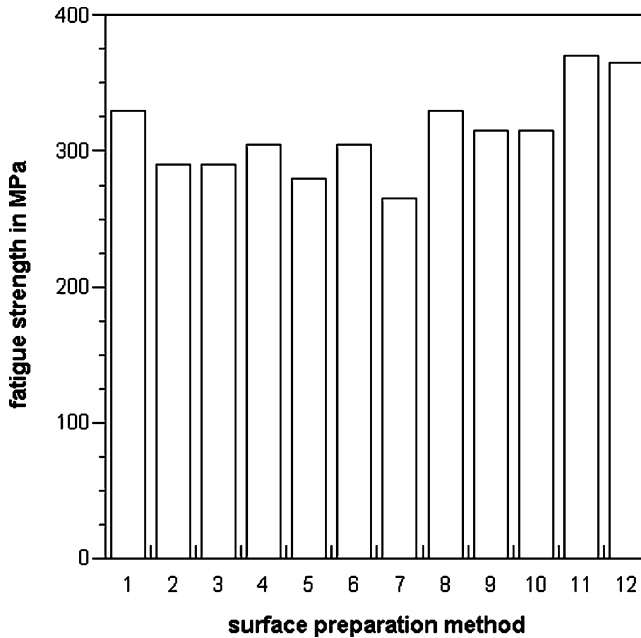


Fig. 8.62 Effects of abrasive types on fatigue strength of steel wires (Kloos and Macherauch, 1987). Surface preparation condition: 1 – as received; 2 – acid pickled; 3 – round sand; 4 – sand dust; 5 – sand dust + carborundum; 6 – sand dust ($p = 0.45 \text{ MPa}$, $\varphi = 90^\circ$); 7 – sand dust ($p = 0.45 \text{ MPa}$, $\varphi = 20^\circ$); 8 – steel shot ($d_p = 300 \mu\text{m}$) + steel grit ($d_p = 800 \mu\text{m}$); 9 – steel grit (75%: $d_p = 800 \mu\text{m}$, 25%: $d_p = 300 \mu\text{m}$); 10 – steel grit (25%: $d_p = 800 \mu\text{m}$, 75%: $d_p = 300 \mu\text{m}$); 11 – steel shot ($d_p = 500 \mu\text{m}$); 12 – steel shot ($d_p = 300 \mu\text{m}/500 \mu\text{m}$) + steel grit ($d_p = 800 \mu\text{m}$)

abrasives are illustrated in Fig. 8.62. Fatigue strength increased as steel shot and steel grit, respectively, were used. Blast cleaning with mineral abrasive materials did not enhance fatigue properties. Although the results applied to certain situations and a certain material, they clearly demonstrated effects of blast cleaning on fatigue behaviour of metallic substrate materials. He et al. (1996) showed for metal coatings on steel that interfacial fatigue limit generally increased if the substrates were blast cleaned. Plain blast cleaning (fatigue limit: $\sigma_F = 850 \text{ MN/m}^2$) was much more effective than grinding (fatigue limit: $\sigma_F = 450 \text{ MN/m}^2$), but a hybrid method consisting of plasma nitriding and subsequent blast cleaning (fatigue limit: $\sigma_F = 1,750 \text{ MN/m}^2$) had the highest capability of fatigue limit improvement. Table 8.37 lists results of comparative fatigue experiments performed by Ibrahim and Berndt (1998) on steel after different surface preparation procedures. Blast cleaning moderately reduced fatigue life (-6%) compared with polished samples at room temperature, but fatigue life increased ($+20\%$) after blast cleaning at elevated temperatures. For aluminium substrates, fatigue life could always be increased compared with the polished samples, at room temperature

Table 8.37 Statistics of fatigue life of SAER steel (Ibrahim and Berndt, 1998)

Specimen condition	Number of cycles to failure			Standard deviation	Coefficient of variation in %	Relative fatigue life
	Minimum	Mean	Maximum			
Polished (room temperature)	8,200	12,833	18,000	3,120	24	1
Polished (370 C)	7,200	8,366	10,700	1,098	13	0.65
Blast cleaned ^a (room temperature)	9,400	12,088	14,600	1,667	14	0.94
Blast cleaned ^a (370 C)	7,000	10,011	16,400	3,003	30	0.78
Coated WC-Co (room temperature)	248,700	660,688	1,000,100	313,015	47	51.48
Coated WC-Co (370 C)	21,000	35,688	64,800	15,868	44	2.78

^aAbrasive type: aluminium oxide; abrasive size: grade 24, blasting pressure: 0.5 MPa

(+67%) as well as at elevated temperature (+200%). More details were provided by Ibrahim and Berndt (1998).

Jiang et al. (2006) investigated the fatigue performance of titanium which was blast cleaned with silica grit ($d_p = 200\text{--}300\ \mu\text{m}$). They found that blast cleaning increased the fatigue strength of titanium by up to +11%. The fatigue strength was $\sigma_F = 270\ \text{MPa}$ for untreated samples and $\sigma_F = 300\ \text{MPa}$ for blast cleaned samples. Strizhalo et al. (1974) performed low-cycle fatigue tests (2 cycles per minute) on titanium alloy sheet samples. They subdivided a low-fatigue curve into three sections, characterising (1) no rupture, (1) quasi-static rupture and (3) fatigue rupture. The authors showed that blast cleaning ($p = 0.6\ \text{MPa}$, abrasive: sand, $d_p = 25\text{--}200\ \mu\text{m}$) could reduce fatigue strength as well as fatigue life, but it did not change the typical three-section-shape of the low-fatigue curves.

Hernandez et al. (2000) investigated the fatigue behaviour of an AISI 4340 steel which was blast cleaned with aluminium oxide. Some of their results are listed in Table 8.38. The values show that blast cleaning lead to a significant reduction in the fatigue properties of the material. Microscopic inspection of the blast cleaned surfaces indicated that fatigue processes were initiated at abrasive debris retained in the near-surface region of the substrate. The debris acted as nucleation sites for fatigue initiation.

Table 8.38 Fatigue parameters for AISI 4340 steel (Hernandez et al., 2000) See (8.13)

Condition	Fatigue parameter	
	A_F in MPa	m_F
Untreated	1,605	0.075
After blast cleaning ^a	1,245	0.066

^aBlasting pressure: 0.62 MPa; abrasive type: aluminium oxide; abrasive size: grit 24

8.7.5 *Substrate Deformation Behaviour*

Spindler (1958) investigated the effects of blast cleaning on the stress–strain behaviour of unalloyed steel plates, and he noted a thickness effect. For 1.0-mm thick plates, the yield point disappeared after blast cleaning; for 3.0-mm thick plates, the yield point was less dominant after blast cleaning; for 5.0-mm to 8.0-mm thick plates, no effect of the blast cleaning process could be noted.

8.7.6 *Substrate Deflection*

Abukawa et al. (2004) investigated the deflection (distortion) of steel samples blast cleaned with aluminium oxide particles. They introduced the idea that a stress mismatch, which occurred during blast cleaning, generated a bending moment in the substrate material. They measured deflections with a coordinate measuring machine, and they noted relationships between the intensity of deflection and blast cleaning parameters. Deflection increased if abrasive particle diameter and nozzle air pressure (thus, kinetic energy of the impinging particle) increased. The authors also found a relationship between substrate roughness and deflection.

Jiang et al. (2006) blast cleaned aluminium sheets (thickness 0.8 mm) with silica particles ($d_p = 200\text{--}300\ \mu\text{m}$, $p = 0.3\ \text{MPa}$), and they observed that the sheet were bent. This effect was explained by the compressive stresses formed at the one side of the sheets.

8.7.7 *Tribological Parameters*

Guan et al. (2005) performed wear tests on blast cleaned aluminium samples. Among others, they measured adhesive forces and friction coefficients with an atomic force microscope (AFM) under a load of 10 nN. The blast cleaned sample featured the lowest values for both parameters. For higher loading forces (49 mN), when mechanical ploughing dominated the friction force, the results were different. As evidenced in Fig. 8.63a, the coefficient of friction was lower for the blast cleaned sample compared with the value for the annealed sample, but the lowest value was found for the samples which were blast cleaned and subsequently annealed. Values for the wear resistance, as manifested through the volume loss during a micro-scale wear test, are plotted in Fig. 8.63b. Blast cleaning did not improve the wear resistance, but a combination of blast cleaning and subsequent annealing could improve the wear resistance. It was assumed that the formation of a nano-crystalline surface layer was responsible for the higher performance of the substrates treated with blast cleaning and subsequent annealing.

Zhang and Zhou (1997) investigated the effects of blast cleaning on the wear resistance of diamond coatings applied to tungsten carbide substrates. The authors found that the wear rate (g/m) of a diamond coating applied to a ground surface

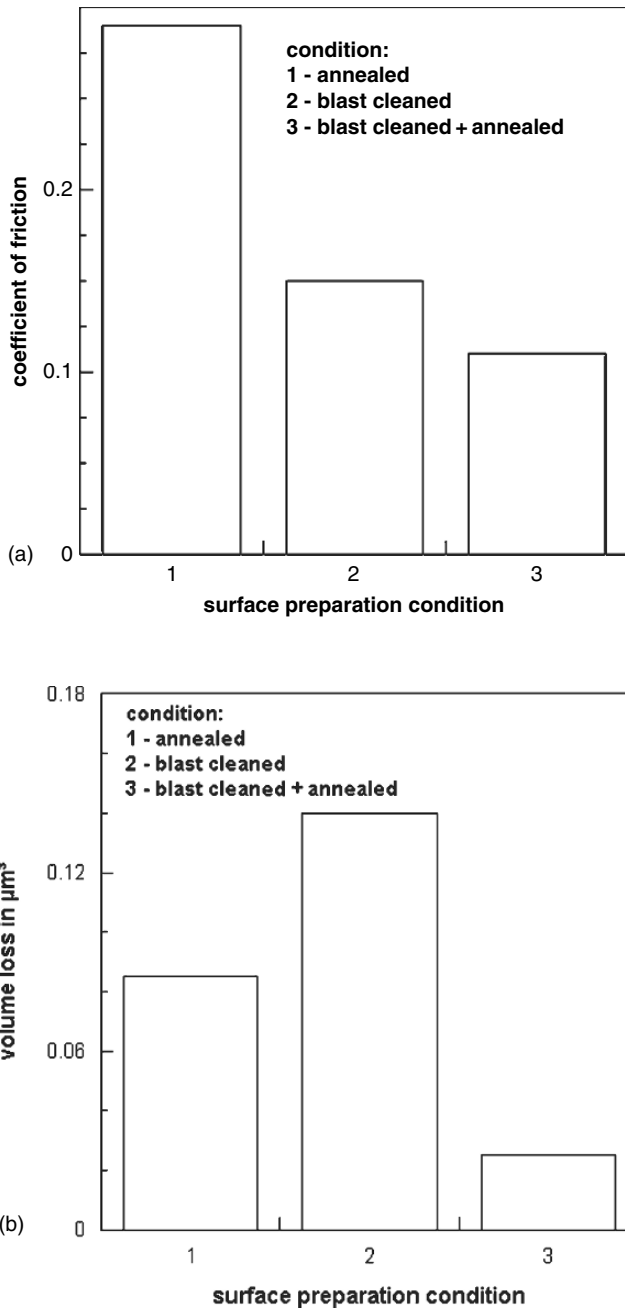


Fig. 8.63 Effects of blast cleaning on tribological properties of aluminium (Guan et al., 2005). Blast cleaning conditions: abrasive material: silica grit; abrasive size: 50–70 μm ; air pressure: 0.3 MPa. (a) Coefficient of friction (micro-tribometer); (b) Volume loss during micro-scale wear test

was between 5 to 14 times higher than those of diamond coatings applied to blast cleaned (aluminium oxide, mesh 120 to 500, $p = 0.3$ MPa) surfaces.

Da Silva Rocha et al. (2003) investigated the influence of different surface preparation methods on the performance of tool steel after plasma nitriding. Methods considered included polishing, grinding and blast cleaning (aluminium oxide, $d_P = 700\text{--}850\ \mu\text{m}$, $p = 0.35$ MPa). The authors observed a significant effect of the surface state prior to nitriding concerning the flank wear of drilling tools. Tools which were blast cleaned before nitriding exhibited the best performance, respectively lowest wear. If the nitrogen concentration was high (76 vol-%), the pre-treatment of the steel with blast cleaning notably reduced torque and contact force during drilling. This latter result was attributed to the formation of an interfacial layer with a low coefficient of friction. Further results of interest included the effects of surface preparation on the diffusion of nitrogen and carbon. This issue is in detail described in the original paper.

8.7.8 Weld Seam Morphology

Blast cleaning is one of the several techniques to place oxides in the surface of steel plates to increase weld penetration. Villafuerte and Kerr (1993) performed a systematic study on the effects of blast cleaning on the grain morphology of weld seams formed by gas tungsten arc (GTA) welding. They utilised glass beads, silica and corundum particles ($d_P = 150\text{--}250\ \mu\text{m}$) at an air pressure of $p = 0.55$ MPa. A surface preparation prior to welding was very influential to the solidification grain structure. For untreated steel, the presence of any equiaxed grains was generally limited to the surface of the welds. In steels that underwent a columnar-to-equiaxed transition (CET), blast cleaning not only increased the percentage of equiaxed grains at the weld surface, but also extended the equiaxed region to the interior. This effect, however, was restricted to steels having high amounts of titanium, nitrogen and aluminium, and high amounts of sulphur. The authors constructed maps which allow for the reading of the percentage of equiaxed grains as functions of steel composition and abrasive type.

8.7.9 Near-surface Layer Chemical Composition

Numerous authors found changes in the chemical composition of the near-surface layer of blast cleaned substrate materials (Watts and Dempster, 1992; Jopp, 1995; Martin, 1997; Anagreh and Dorn, 2002; Possart et al., 2002; Emrich, 2003). Changes in chemical surface stages due to blast cleaning (with glass beads and aluminium oxide) were found to influence the curing reactions of epoxy systems (Bockenheimer et al., 2002). An example is provided in Fig. 9.6. Possart et al., (2002) assessed changes in chemical compositions of near-surface layers of aluminium due to the application of different preparation methods. Some results are listed in Table 8.39.

Table 8.39 Mean chemical composition (XPS measurements) of the near-surface layer (10 nm) for treated aluminium samples (Possart et al., 2002)

Method	Element in %						
	Al	O	Mg	Si	Na	Ca	C
Etched	27.6	42.3	<0.1	1.8	<0.1	–	16.6
Glass bead blasted	25.2	39.2	0.4	1.8	12.8	1.0	16.9
Al ₂ O ₃ blasted	44.3	32.8	0.6	0.4	4.2	0.2	16.3

After blast cleaning with glass beads, the surface was completely covered with considerable amounts of sodium (Na) and calcium (Ca), which must have been transferred by the glass beads. An even accumulation of sodium (Na) was also found after blast cleaning with aluminium oxide, even though the blasting medium contained only very little sodium (2.7%). Equal results were obtained by Emrich (2003), who performed blast cleaning experiments on aluminium (AlMg₃) samples. Aluminium surfaces under intense mechanical treatment, as due to particle impingement during blast cleaning, seemed to develop some particular affinity for the alkali oxides in the blasting media. There was some general trend that the final state of the exposed surface depended on material removal mode and on material removal capacity of the utilised abrasive materials. If not much material was removed but rather deformed, elements of the abrasive materials were more probably transferred to the substrate surface. If, in contrast, notable amounts of substrate material were removed, bulk properties of the substrate may have determined the state of the newly formed surface. Further evidence is delivered in Fig. 8.64, where the changes in surface chemistry of an ordinary construction steel due to blast cleaning are established based on X-ray photoelectron spectroscopy (XPS) analyses. The use of aluminium oxide, for example, dragged aluminium into the near-surface zone, whereas glass beads added silica to the metal surface. Emrich (2003), who noted element contamination after blast cleaning of aluminium (AlMg₃) with corundum and glass beads, concluded that the contaminated layer reduced the shear strength of a subsequently generated adhesion joint, even if the substrate had high roughness values.

Jopp (1995) applied XPS for the analysis of the surface chemistry of a steel substrate (St 37) which was blast cleaned with corundum and, respectively, glass beads. Results of this study are displayed in Fig. 8.65. The designation “unsputtered” corresponds to the very upper layer of the treated steel substrate, whereas the designation “sputtered” is related to surfaces bombarded with argon ions, which allows for the estimation of a depth profile of the surface chemistry. It can be seen that both abrasive materials contributed to a contamination of the steel. The corundum induced aluminium into the surface (Fig. 8.65a), whereas the glass beads induced silica (Fig. 8.65b). Both abrasive materials also induced a certain amount of sodium into the surface. If the upper layers were removed due to argon ion impingement, the ratio between iron and the contaminating elements steadily increased. The ratio Fe to Al, for example, increased from 1.5 (for an unsputtered substrate) to 2.36 (for 2 min sputtering time) up to 3.3 (for 12 min sputtering time). Similar was the trend for the ratio Fe to Si.

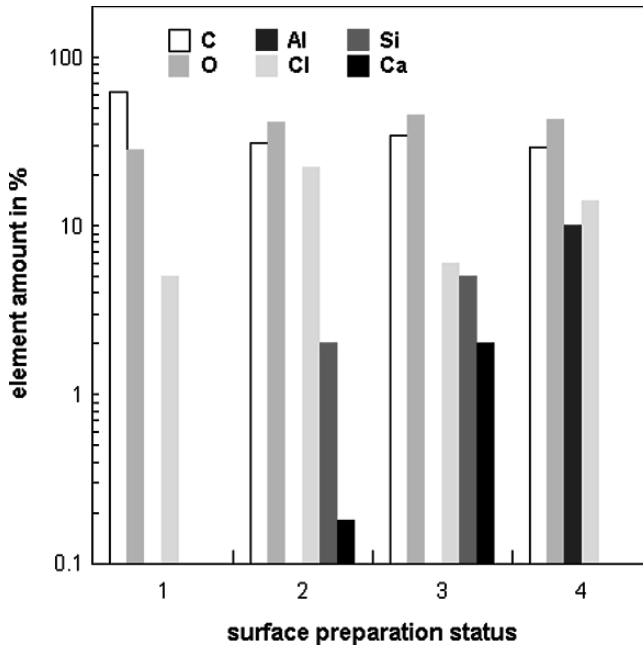


Fig. 8.64 Variations in near-surface chemistry of steel St 37 due to blast cleaning (Martin, 1997). Surface preparation status: 1 – degreasing with acetone; 2 – blast cleaned with steel shot ($d_p = 355\text{--}1,180\ \mu\text{m}$); 3 – blast cleaned with glass beads ($d_p = 100\text{--}200\ \mu\text{m}$); 4 – blast cleaned with corundum ($d_p = 150\text{--}210\ \mu\text{m}$)

Grant et al. (2004) investigated the chemical composition of aluminium alloy surfaces after being treated with different surface preparation methods. The methods used included wiping (with acetone), hand abrading (Scotch Brite) and blast cleaning (with aluminium oxide). The authors deployed X-ray photoelectron spectroscopy (XPS) for the substrate evaluation. After blast cleaning, a large reduction in carbon (C), to a level about one-half of that before blast cleaning was measured. Other important changes included an increase in aluminium (Al) concentration and a decrease in magnesium (Mg) concentration. New elements introduced due to blast cleaning included sodium (Na) and fluorine (F). Measurements of the variations of near-surface chemical composition for aluminium alloys due to blast cleaning with corundum particles and polymer spheres were performed by Anagreh and Dorn (2002a,b).

Tolpygo et al. (2001) performed a systematic study about the effects of blast cleaning (abrasive: aluminium oxide) on the chemical cleanliness of a platinum-modified nickel-aluminide coating prior to the deposition of a thermal barrier coating. The blast cleaning led to contamination by various impurities from the abrasive material, in particular, alkali elements (Li, Na, K, Mg, Ca and Sr) and titanium. During the subsequent high-temperature oxidation, these impurities became incorporated into the growing scale. Their results suggested that impurities introduced by

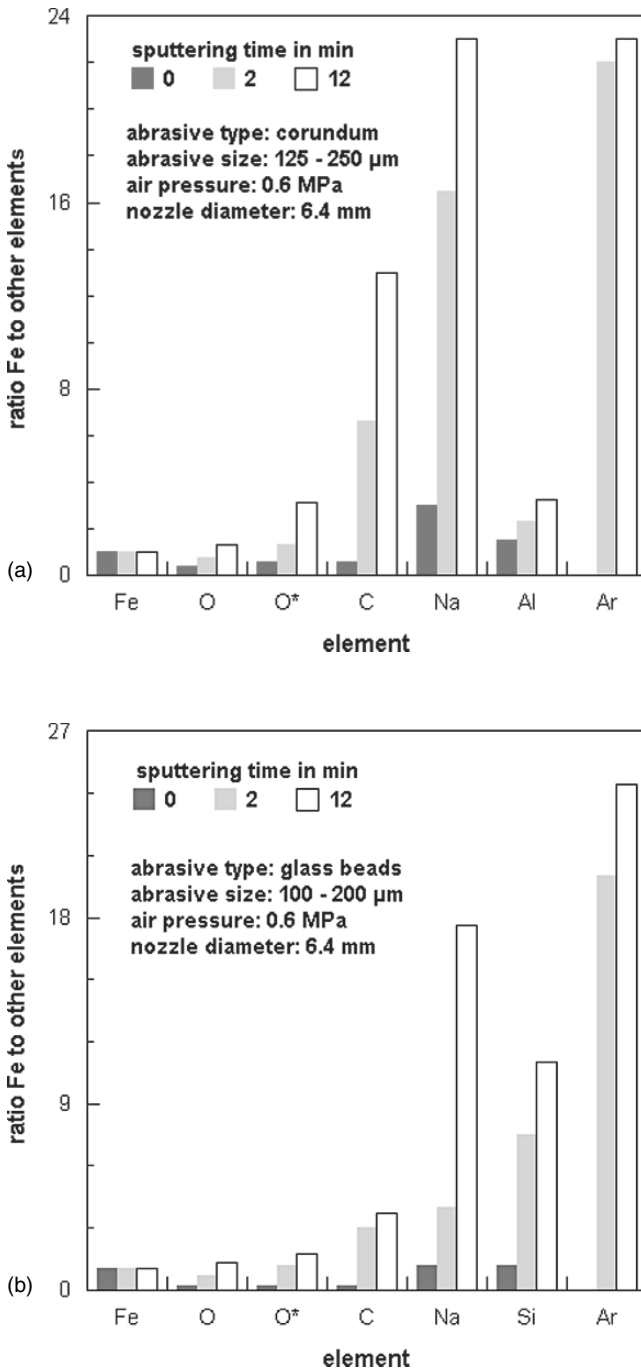


Fig. 8.65 Results of XPS analysis of steel St 37 blast cleaned with different abrasive materials (Jopp, 1995). (a) Abrasive material: corundum; (b) Abrasive material: glass beads

blast cleaning prior to the thermal barrier coating deposition are expected to have a strong detrimental effect on the coating durability.

8.7.10 Corrosion Resistance

Investigations into the corrosion resistance of steel substrates treated with different surface preparation methods were performed by several authors. Rhouma et al. (2001) estimated the effects of different surface preparation methods on the pitting corrosion and stress corrosion cracking (SCC) of austenitic stainless steel samples. Pitting corrosion was assessed based on potentiodynamic polarisation tests. The resistance to SCC was analysed by immersing the samples in an $MgCl_2$ solution (40 g/l), heated at $140^\circ C$, during 48 h. Results of these investigations are listed in Table 8.40. It can be seen that subsequent blast cleaning of ground steel with quartz particles ($d_p = 50$ to $200 \mu m$) improved the resistance against SCC. This was probably due to the formation of compressive stresses during blast cleaning (see Sect. 8.7.3). If exposed to seawater, blast cleaning also led to better pitting resistance. Pitting potential was 110 mV for the ground samples, 320–360 mV for the blast cleaned samples and 500 mV for wire brushed samples. Similar trends were found by Ladwein and Gümpel (2004) in terms of critical pitting potential. It can be seen from the results plotted in Table 8.41 that the critical pitting potential was lowest for ground steel, followed by blast cleaned steel and pickled steel. Jopp (1995) found notable effects of the surface preparation method on the free corrosion potentials of iron samples (Fe 99.5). Free corrosion potentials were highest for degreased surfaces, followed by surfaces blast cleaned with glass beads, and surfaces blast cleaned with corundum. This trend, however, was time dependent. For rather long exposure times (about 40 min) the differences in the corrosion potential vanished, and the corrosion potentials of all prepared surfaces approached a saturation level.

A study about the pitting corrosion of a duplex stainless steel, treated with different surface preparation methods, was performed by Salah-Rousset et al. (1996).

Table 8.40 Influence of surface treatment on the corrosion resistance of AISI316L stainless steel (Rhouma et al., 2001)

Treatment method	Pitting corrosion parameter		
	Pitting corrosion potential in mV/SCE	Repassivation potential in mV/SCE	Stress corrosion cracking
As ground	110	–200	Cracks
Blast cleaned ($d_p < 50 \mu m$)	320	–110	No cracks
Blast cleaned ($d_p = 80\text{--}120 \mu m$)	360	–150	No cracks
Blast cleaned ($d_p = 120\text{--}200 \mu m$)	360	–150	No cracks
Wire brushed (280 rpm)	500	–130	Cracks
Wire brushed (900 rpm)	500	–150	No cracks

Blast cleaning conditions – abrasive type: quartz; air pressure: 0.4 MPa; blasting angle: 45°

Table 8.41 Corrosion resistance and surface energy of duplex stainless steel (steel 1.4301) after surface preparation (Ladwein and Gumpel, 2004)

Preparation method	Critical pitting potential in V	Surface energy in mN/m ^a
Grinding (60 g)	0.18	36
Grinding (120 g)	0.21	38
Blast cleaning ($\varphi = 45^\circ$)	0.30	60
Blast cleaning ($\varphi = 90^\circ$)	0.31	–
Pickling	0.72	51
Electro-polishing	–	47

^aSessile drop method

The authors utilized polishing, grinding and blast cleaning for surface treatment and performed electrochemical tests in artificial and natural seawater. It was found that the polished steel with the smoothest surface had the best corrosion resistance in artificial seawater; it showed the highest values for the pitting potential and for the protection potential. The blast cleaned samples performed worst in artificial seawater. It could, however, be shown, that the blast cleaned samples performed best in the natural seawater. The average number of pits with a depth larger than 500 μm in the steel was much lower (one) compared with ground samples (nine). The authors contributed this superior behaviour to the lower susceptibility of the blast cleaned samples to microbiologically influenced corrosion (MIC). The compressive stresses induced during the blast cleaning process made the samples more resistant against stress crack corrosion (SSC), whereas metallurgical changes in the blast cleaned regions helped to resist MIC. Polarization curves conducted under laboratory conditions were unable to duplicate this beneficial role of blast cleaning.

Andronikos et al. (1998) deployed rather unusual abrasive materials (dolomite, marble, olivine) and investigated the effects of these materials on the corrosion rate (in term of weight loss per time) of uncoated and coated (chlorinated rubber) steel specimens. The authors found that the contribution of the abrasive materials depended on the coating condition. Marble performed best for the uncoated steel and garnet performed best for a steel coated with chlorinated rubber with aluminium flakes. For a steel coated with chlorinated rubber with a red mud pigment, all abrasive materials performed equally good after an exposure time of 100 days.

Otsubo et al. (2003) investigated the corrosion resistance of an austenitic stainless steel, and they found that the corrosion resistance deteriorated if the samples were blast cleaned (aluminium oxide 24, $p = 0.6 \text{ MPa}$, $d_N = 8 \text{ mm}$, $\varphi = 75^\circ$). The polarization curves were measured in a H_2SO_4 -solution at a temperature of 303 K. The corrosion potentials (V) of the blast cleaned samples were lower than, and the passivation current densities ($\mu\text{A}/\text{cm}^2$) were higher than, those of mechanically ground samples. Immersion tests in a NaCl-solution also revealed a deteriorated performance of the blast cleaned samples. Although the authors noted the formation of a martensite phase at the blast cleaned substrate, they contributed the deteriorated corrosion resistance to the rather coarse profile of the substrate surface.

The effects of surface preparation on the corrosive performance of aluminium samples (AlMg_3) was investigated by Emrich (2003). He noted the formation

of aluminium hydroxide after the treatment of the original substrate (AlMg₃) by blast cleaning, degreasing (acetylene) and acid pickling. The author found further, that blast cleaning with corundum ($p = 0.6$ MPa) led to the shifting of the pitting corrosion potential to higher potential differences (from -0.9 to -0.95 V), which eventually deteriorated the resistance of the material against pitting corrosion. The blast cleaned samples also exhibited rather high values for the free corrosion potential (-1.2 V). After a period of about 130 h, however, the corrosion potential rested on a stable range between -1.1 and -1.12 V versus the reference electrode (Ag/AgCl), irrespectively on the surface preparation method. Emrich (2003) also argued that the cold deformation of the surface during blast cleaning (see Sect. 8.7.3), and the accompanying formation of edge dislocations and helicoidal dislocations, may become the origin of corrosively determined material removal.

Jiang et al. (2006) performed electrochemical tests in order to evaluate the corrosion resistance of titanium substrates. They measured potentiodynamic polarisation curves in a 3.5% sodium chloride solution. The results indicated that blast cleaning delivered a lower corrosion current density (A/cm^2) compared to as-received samples. The lowest corrosion current density, however, was estimated for a combination of blast cleaning and subsequent annealing. The authors contributed this result to the formation of a nano-crystalline layer with a high density of grain boundaries, which in turn were beneficial to the formation of a passive film. Jopp (1995) compared the anodic polarisation curves of surfaces (Fe 99.5) treated with different methods. The highest current (A) values were measured for a surface blast cleaned with corundum, followed by a surface blast cleaned with glass beads and by a degreased surface. This author also estimated the metal loss due to the exchange current and found the following values: $73 \mu m/a$ for degreasing, $172 \mu m/a$ for corundum and $87 \mu m/a$ for glass beads. Thus, blast cleaning deteriorated the corrosion resistance of the material.

Celik et al. (1999) found that the corrosion of a steel substrate, coated with a plasma-sprayed alumina coating, exposed to an H_2SO_4 solution, depended on the roughness of the substrate. The corrosion resistance was lower for the substrates with higher roughness values. For $R_a = 3.37 \mu m$, the corrosion rate was 0.018 cm/year; whereas for $R_a = 4.02 \mu m$, the corrosion rate was 0.024 cm/year.

Confente et al. (1995) prepared low-carbon steel rods with different methods and exposed them also to an H_2SO_4 -solution. They measured corrosion current densities and corrosion potentials. Results of these measurements are listed in Table 8.42. Mechanically prepared rods (brushed, blast cleaned) behaved much more reactive

Table 8.42 Corrosion resistance of low-carbon steel rods in an H_2SO_4 solution (Confente et al., 1995)

Preparation method	Current density in mA/cm^2	Corrosion potential in mV
Pickling	0.06	-466
Brushing	3.48	-486
Blast cleaning	2.58	-478

than pickled rods in an acid environment, which was attributed to surface hardening effects and to a reviving effect on the surface due to the elimination of any chemisorbed species.

A special problem is the formation of protective oxide layers on stainless steel substrates exposed to boiling water in nuclear power plants (water temperature: 280°C, water pressure: 12 MPa). During growth, these layers incorporate radioactive ^{60}Co in their structures, which is considered a serious health problem. The thicknesses of the oxide layers and the incorporation of ^{60}Co in the oxide layers depended on the surface preparation method being used. Results of an investigation of Rao et al. (1986) on a nuclear grade stainless steel are listed in Tables 8.43 and 8.44. A notable result was the high rate of oxidation after blast cleaning, as evidenced in Table 8.44. The oxide thickness was very large for the blast cleaned steel. This result was explained by the authors through the high level of silica (25%), embedded in the substrate after blast cleaning with the silica sand (indicated in bold in Table 8.44), and through the rather rough topography of the blast cleaned surfaces. Both these factors would contribute to high levels of ^{60}Co buildup. Subsequent electropolishing was, therefore, recommended for this special area of application.

Another corrosion issue is “metal dusting”, which is a catastrophic form of carburisation leading to the disintegration of iron-, nickel- and cobalt-base alloys into powdery mixtures of graphite, metal particles, carbides and oxides. Lin et al. (2004) exposed stainless steel samples, which were in the conditions as-ground, blast cleaned and pre-oxidised, to a mixed gas (CO/CO_2) at high temperatures up to 700°C and investigated the resistance of the surfaces to metal dusting. The abrasive material was aluminium oxide ($d_p = 200\text{--}250\mu\text{m}$), propelled at an air pressure of $p = 0.7\text{ MPa}$. The authors noted that blast cleaning assisted carbon deposits and filamental carbon formation, and it favoured the formation of a protective chromium-rich oxide on the steel. These processes helped to prevent metal dusting.

Ruttmann and Günther (1965) investigated the effects of blast cleaning on the lifetime of welded steel samples exposed to a boiling MgCl_2 solution (140°C). The lifetime criterion was the start of SCC. The authors varied abrasive type, air pressure and exposure time. Some results are displayed in Table 8.45. It can be seen that the untreated samples cracked after 3 h, whereas the blast cleaned samples did not show any cracking even after 9.5 days. The use of steel grit (not listed in Table 8.45) was very effective, but glass beads particles performed excellent as well. The use of

Table 8.43 Effects of surface preparation methods on the buildup of ^{60}Co in oxide layers of stainless steel samples subjected to boiling water in nuclear power reactors (Rao et al., 1986)

Preparation method	Steel grade	^{60}Co buildup in $\mu\text{Ci}/\text{cm}^2$
Electro-polishing	309	7.0
As received	309	14.1
Blast cleaned (silica sand)	316 NG	12.7
Acid pickled	316 NG	4.5

Table 8.44 Effects of surface preparation methods on the formation of oxide layers in stainless steel (Rao et al., 1986)

Preparation method	Oxide thickness in Å	Oxide layer composition in % (at 50 Å depth)
Cold rolled	~ 100	Fe-27, Cr-7, Ni-4, C-4, O-50
Acid pickled	~ 100	Fe-25, Cr-8, Ni-4, C-15, O-45
Blast cleaned (silica sand)	~ 2,000	Fe-20, Cr-5, Si-22, Ni-3, O-16, C-25
Acid pickled + electropolished	~ 120	Fe-16, Cr-3, Ni-2, O-56 (P, Na < 5)
Blast cleaned + electropolished	~ 70	Fe-30, Cr-16, Ni-3, O-40 (P, Na < 5)

corundum particles delivered good results, but they were not as good as those for the use of glass beads. An increase in air pressure and blast cleaning time improved resistance against SCC. For ferritic steel, exposed to a boiling $\text{Ca}(\text{NO}_3)_2$ solution (113°C), very similar results could be observed. Blast cleaning extended the time to SCC from 48 h for untreated samples up to 227 h for samples blast cleaned with steel shot and corundum. Münster and Spähn (1979) provided results on the corrosion behaviour of blast cleaned weld seams of Cr–Ni steels. The authors found that blast cleaning with glass beads delivered a cleaning quality comparable to that after acid cleaning. Table 8.46 lists results of the corrosion resistance tests. As can be seen, brushing and grinding led to corrosion as well as SCC. The results for the blast cleaned samples were all good, whether quartz sand, slag or glass beads were being used.

Tolpygo et al. (2001) performed a study into the oxidation of a platinum-modified nickel-aluminide coating after blast cleaning with aluminium oxide. During high-temperature oxidation, impurities originating from the blast cleaning process became incorporated in the growing scale and significantly accelerated the oxide growth.

Leistikow and Kraft (1974) provided a detailed investigation on the hot steam (600°C, 500 hours) corrosion resistance of an austenitic CrNi-steel. The steel substrate was prepared by electro-polishing, rolling, needle gunning, grinding, turning, sanding and blast cleaning (corundum, $d_p = 250\text{--}500\ \mu\text{m}$, $p = 0.8\ \text{MPa}$). The corrosion resistance was measured in terms of specific mass loss. Samples characterised by very smooth surfaces (ground, sanded, turned) experienced the lowest specific mass loss (between 11 and 22 mg/dm^2). Blast cleaned samples performed worse (41 mg/dm^2), but their corrosion resistance was equal to that of the

Table 8.45 Time to SCC of a welded austenitic (X10CrNiTi189) steel (Ruttmann and Günther, 1965)

Method	Abrasive	Pressure in MPa	Time in s	Time to SCC in h
As received	–	–	–	3
Blast cleaned	Glass beads	0.3	30	227
	Glass beads	0.3	60	227
	Corundum	0.3	30	12
	Corundum	0.6	30	60
	Corundum	0.6	60	108

Table 8.46 Results of corrosion and SCC tests on Cr–Ni steel (Münster and Spähn, 1979)

Treatment	Corrosion in water + H ₂ SO ₄	SCC in boiling MgCl ₂ (35%)
As received	Localised corrosion	SCC
Acid cleaning	No damage	SCC
Brushing	Localised corrosion	SCC
Grinding	No damage	SCC
Blast cleaning ^a (glass beads)	No damage	O.K.
Blast cleaning ^a (quartz sand)	No damage	O.K.
Blast cleaning ^a (slag)	No damage	O.K.

^aPressure: $p = 0.6$ MPa

needle-gunned substrate (41 mg/dm²), and it was better compared to samples which were rolled (143 mg/dm²) and electro-polished (296 mg/dm²). The authors found a relationship between the degree of surface deformation (surface hardness) and the corrosion resistance. Corrosion resistance was low if degree of deformation was high, and vice versa. A high degree of deformation promoted the formation of thin, almost defect-free, chromate-rich layers with a high corrosion protection potential.

8.8 Surface Energy and Work of Adhesion

8.8.1 Definitions and Measurement

If a liquid drop that rests on a substrate surface is going to be removed, a certain amount of energy will be required. The situation is illustrated in Fig. 8.66. This energy is known as work of adhesion, and it can be calculated as follows:

$$W_A = \gamma_S + \gamma_L - \gamma_{SL} \quad (8.14)$$

Here, γ_S is the specific surface energy of the substrate, γ_L is the surface tension of the liquid and γ_{SL} is the interfacial free energy. These parameters are illustrated in Fig. 8.66a. It can be seen from (8.14) that, for a given coating material, work of adhesion can be increased if specific surface energy of the substrate rises. Surface energy is the sum of contributions from different intermolecular forces, namely dispersion and polar forces. Therefore, the following relationship applies:

$$\gamma = \gamma^d + \gamma^p \quad (8.15)$$

Here, the superscript “d” stands for dispersion and “p” stands for polar. For metal surfaces, the contribution of dispersion forces is usually larger than that of polar forces. Adhesives, in contrast, usually own a high polar component. An alternative expression of (8.14) is:

$$W_A = \gamma_L \cdot (1 + \cos \theta_C) \quad (8.16)$$

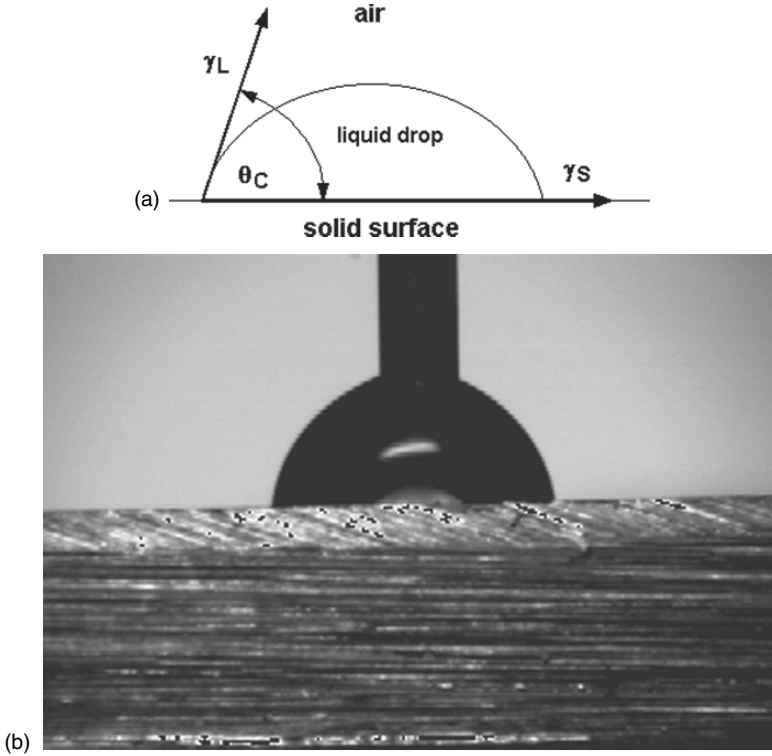


Fig. 8.66 Fundamentals of contact angle estimation. (a) Energy balance; (b) Contact angle to low-carbon steel (Momber and Wong, 2005a)

Here, θ_C is the contact angle (see Sect. 8.9.1). Whenever the two variables in that equation can be measured experimentally, work of adhesion can be calculated. The relationship between work of adhesion and contact angle as expressed by (8.16) is illustrated in Fig. 8.67. It can be seen that the work of adhesion has a maximum value at a contact angle of $\theta_C = 0^\circ$, which corresponds to complete wetting. Work of adhesion is zero for $\theta_C = 180^\circ$, which counts for complete non-wetting. Values for the work of adhesion between different adhesives and steel as estimated with this relationship are listed in Table 8.47. It can be seen that high values for the work of adhesion promote a high interfacial fracture energy. This relationship is confirmed by experimental results published by Berg (2002). A standard equation for the discussion of wetting effects is the Young equation, which reads as follows:

$$\gamma_{SL} = \gamma_S - \gamma_L \cdot \cos \theta_C \quad (8.17)$$

Based on this equation, a method for the assessment of the paintability of a substrate was developed by Zisman (1972). The method works as follows. For the assessment of the paintability, the contact angles of various liquids to a substrate

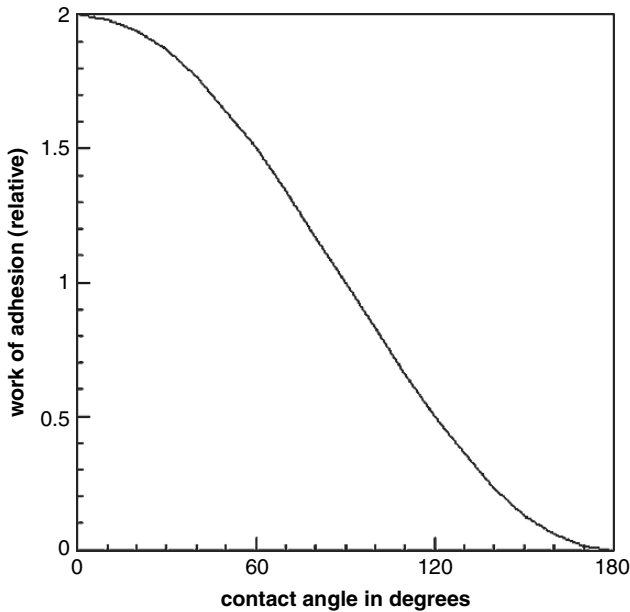


Fig. 8.67 The relationship between work of adhesion and contact angle as expressed by (8.16)

surface are determined, and the cosines of the contact angles are plotted against the surface tension of the liquids (Zisman, 1972). The plot is extrapolated to $\cos \theta_C = 1$ ($\theta_C = 0^\circ$), and the intersection point determines the critical surface energy of the substrate. The procedure is illustrated in Fig. 8.68. The critical surface energy in about $\gamma_S = 33 \times 10^{-5} \text{ N/cm}$ ($=33 \text{ mJ/m}^2$) for the example plotted in that figure. More values are listed in Table 8.48. A very similar procedure was suggested by Miller (1973) for the assessment of the critical surface energy of metal substrates. This author could show that a certain minimum amount of substrate surface energy was a requirement to maintain a good adhesion between substrate and applied

Table 8.47 Work of adhesion and interfacial fracture energy for different adhesives and steel (Penn and Defex, 2002)

Adhesive	Work of adhesion in mJ/m^2	Interfacial fracture energy in mJ/m^2
Water (ice), -23°C	144.4	$19,300 \pm 3,300$
Water (ice), -10°C	144.4	$16,300 \pm 3,030$
Diiodomethane, -23°C	101.6	$2,490 \pm 579$
Diiodomethane, -16°C	101.6	$4,710 \pm 1,100$
Diiodomethane, -6°C	101.6	^a
Bromonaphthalene, -23°C	89.2	$1,120 \pm 102$
Bromonaphthalene, -10°C	89.2	^a
Hexadecane, -4°C	55.4	^a
Hexadecane, $+5^\circ\text{C}$	55.4	^a

^aCohesive failure in adhesive

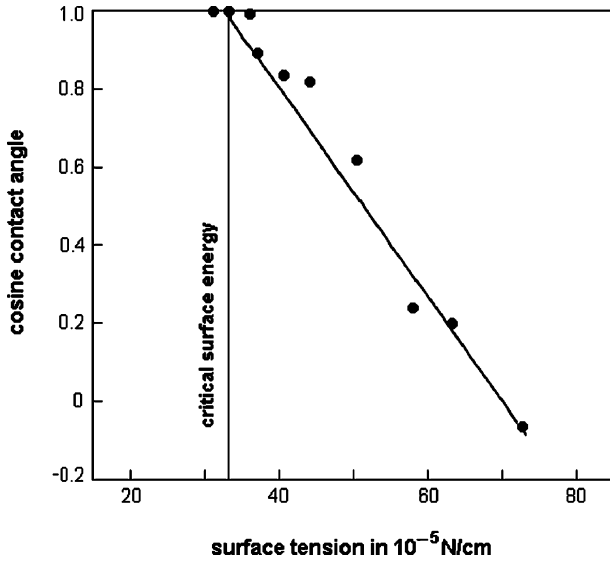


Fig. 8.68 Zisman’s plot for wettability assessment (Zisman, 1972)

coating. For an epoxy-polyamide paint, applied to chromated clad aluminium, this critical threshold was about $\gamma_s = 40 \text{ mJ/m}^2$.

It is common in the coating industry to refer to low energy and high energy surfaces. Steel substrates belong to high energy surfaces. Table 8.49 lists surface tension (energy) values for different resins in liquefied state and after hardening. Hardening does not alter the surface energy notably and can, therefore, be utilised for calculations with dry films.

8.8.2 Effects of Substrate Surface Energy on Corrosion and Coating Performance

Ladwein and Gumpel (2004) performed a study into the corrosion resistance of duplex stainless steel as a function of surface preparation. The measure of the corrosion

Table 8.48 Critical surface energies of substrates; data generated according to the procedure shown in Fig. 8.68 (Schoff, 1992)

Substrate	Critical surface energy in mJ/m ²
Zn-phosphated steel	45–56
Fe-phosphated steel	43
Tin-plated steel	35
Treated aluminium extrusions	33–35
Untreated steel	29
SMC polyester	23

Table 8.49 Surface tension values for resins (Chair for Plastics Technology, University of Erlangen)

Resin type	Surface tension in mN/m (mJ/m ²)	
	Liquid state	Hardened
Epoxy/polyamine	40.8	47.7
Polyester (I)	36.1	45.1
Polyester (II)	36.1	47.5
Polyester (III)	36.1	47.7
Alkali-resistant polyester	36.1	46.7
Metacrylate	–	38.4

was the critical pitting potential – the lower the value for this parameter, the lower the corrosion resistance. Results of this study are listed in Table 8.41. It can be seen that ground substrates performed worse and pickled substrates performed best. Blast cleaned surfaces showed a moderate corrosion resistance, whether the surface was blast cleaned at perpendicular or shallow angle. The authors assumed that the surface energies of the substrates after preparation had a determining effect on corrosion resistance, but experimental results did not confirm this approach completely (see Table 8.41).

The adhesion strength between polymeric adhesives and metal substrates and between copolymer films and metal substrates was found to linearly increase with higher metal surface energy (Basin, 1984; Vakula and Pritykin, 1991). However, it is usually not the value for the total surface energy alone that determines adhesion. The polar components of the surface energies play important roles as well. High adhesion between substrate and coating can be expected if the polar components of their surface energies are of equal order, thus $\gamma_S^P = \gamma_L^P$. Examples are shown in Fig. 8.69.

8.8.3 Surface Energies of Blast Cleaned Substrates

As shown in Table 8.41, the surface energies of metal substrates depend on the type of surface preparation. For the condition in Table 8.41, surface energy was high for blast cleaning, and rather low for grinding. Kogan et al. (1993) utilised the surface potential of a surface for the assessment of the activated state, and they found that blast cleaning contributed to an increase in surface potential of a steel substrate compared with mechanical machining. The use of corundum generated a higher surface potential value than the use of shot.

Harris and Beevers (1999) utilised results of contact angle measurements to estimate the surface energies of steel and aluminium substrates blast cleaned with different aluminium oxide abrasives. The effects of the abrasive media on surface energies are listed in Table 8.50. It can be seen that the Pink and White abrasives produced similar surface energy characteristics, but the Brown abrasive delivered a lower total surface energy with higher dispersive and lower polar components

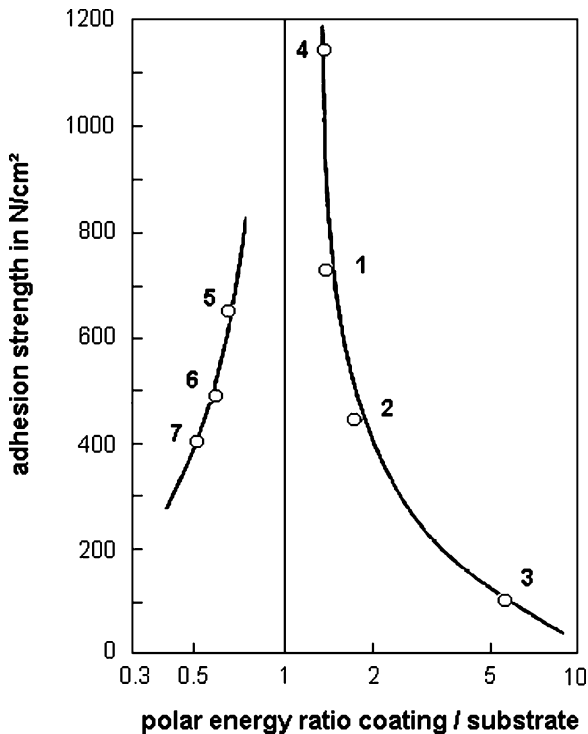


Fig. 8.69 Adhesion strength as a function of the ratio of polar surface energy components of paint and substrate (Potente and Krüger, 1978). Substrates: 1 – post-chlorinated PVC; 2 – styrene-acrylonitrile-copolymer; 3 – polypropylene; 4 – polystyrene; 5 – PVC; 6 – polyamide-6; 7 – PMMA; coating: alkyd-based

than the other abrasive types. The effects of surface roughness and abrasive type on surface energies of blast cleaned substrates are shown in Fig. 8.70. With the Pink and White abrasives, the smoother surfaces exhibited higher surface energy readings than the 60 mesh abrasives, but with the Brown abrasives, surface energy values appeared to be independent of roughness. The changes in surface energy after blast cleaning are associated with chemical changes on the surfaces. These changes in surface composition are due to residues from the abrasive media, and the impurities vary between different abrasive types (see Sect. 8.7.8). Smaller abrasive sizes apparently left a greater percentage of contaminant residues on the surface.

Emrich (2003) measured the specific surface energies of aluminium substrates (AlMg_3) prepared with different surface preparation methods. The surface energy after blast cleaning with aluminium oxide ($p = 0.6 \text{ MPa}$) was $\gamma_s = 52 \text{ mJ/m}^2$. This value was higher than those measured after degreasing with acetone, but lower than those estimated after pickling. Emrich (2003) also measured the polar and disperse components of the surface energies. The surface energy of aluminium substrates,

Table 8.50 Contact angle and surface energy data for blast cleaned and solvent wiped substrates (Harris and Beevers, 1999)

Surface treatment	Contact angles in °		Total surface energy in mJ/m ²
	De-ionised water	Diiodomethane	
Mild steel	68 ± 5	37 ± 7	46 ± 3
Solvent wiped			
Blast cleaned (Brown 180/220)	52 ± 7	18 ± 4	57 ± 3
Blast cleaned (Brown 60)	61 ± 4	21 ± 4	52 ± 2
Blast cleaned (Pink 180/220)	8 ± 3	27 ± 3	74 ± 1
Blast cleaned (Pink 60)	28 ± 4	30 ± 3	68 ± 2
Blast cleaned (White 180/220)	6 ± 2	26 ± 4	74 ± 1
Blast cleaned (White 60)	34 ± 10	25 ± 3	65 ± 5
Aluminium alloy			
Solvent wiped			
Blast cleaned (Brown 180/220)	76 ± 4	33 ± 3	44 ± 1
Blast cleaned (Brown 60)	75 ± 5	30 ± 4	46 ± 2
Blast cleaned (Pink 180/220)	34 ± 3	31 ± 3	64 ± 2
Blast cleaned (Pink 60)	51 ± 3	35 ± 5	54 ± 2
Blast cleaned (White 180/220)	28 ± 6	30 ± 3	68 ± 3
Blast cleaned (White 60)	59 ± 3	28 ± 4	52 ± 2

which were degreased with acetone showed almost no polar component. The surface energy of the substrates blast cleaned with aluminium oxide showed a well-balanced ratio between polar and disperse component, whereby the polar component had a value of $\gamma_L^p = 27 \text{ mJ/m}^2$, and the disperse component had a value of $\gamma_S^d = 25 \text{ mJ/m}^2$. Surface energies of samples which were pickled with acid also showed a good balance between polar and disperse components.

Broughton and Lodeiro (2002) applied the Wilhelmy plate method for the assessment of wettability parameters, and they found an increase in the surface energy of mild steel from $\gamma_S = 34 \text{ mJ/m}^2$ for an untreated substrate to a value of $\gamma_S = 51 \text{ mJ/m}^2$ after blast cleaning with aluminium oxide abrasives. This values corresponds well with that measured by Emrich (2003). Broughton and Lodeiro (2002)

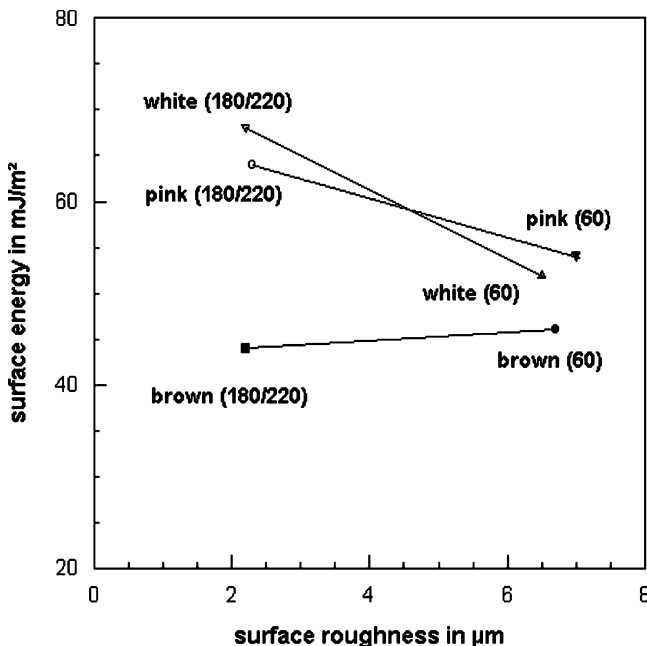


Fig. 8.70 Relationship between surface roughness and surface energy for a blasted aluminium alloy (Harris and Beever, 1999)

could also show that blast cleaning increased the disperse component of surface energy only (from initially $\gamma_S^d = 32.1$ up to 50.4 mJ/m^2 after blast cleaning), whereas the polar component of surface energy was reduced due to blast cleaning (from initially $\gamma_S^d = 1.8$ down to 0.5 mJ/m^2 after blast cleaning).

An alternative measure for the reactivity of substrates is the carbon content. The higher the carbon content, the lower the reactivity to the formation of bond forces. Emrich (2003) measured the carbon content on aluminium substrates (AlMg_3) treated with different surface preparation methods, and he found that blast cleaning with aluminium oxide ($p = 0.6 \text{ MPa}$) generated highly reactive, low-carbon (15 atom%) surface. Degreasing with acetone, in contrast, formed a rather low-reactive, high-carbon (33 atom%) surface.

8.9 Wettability of Metal Substrates

8.9.1 Definitions and Measurement

The contact between the liquid coating and the substrate is the result of a wetting procedure. Wettability is often defined through the contact angle of a liquid drop to the substrate. Contact angle is given by the Young equation [see (8.17)]:

$$\gamma_S = \gamma_{SL} + \gamma_L \cdot \cos \theta_C \quad (8.18)$$

The parameters are defined in (8.15) and (8.17). Equation (8.18) is illustrated in Fig. 8.71. For complete wetting, the contact angle has a value of $\theta_C = 0^\circ$; and for no wetting, the contact angle has a value of $\theta_C = 180^\circ$. For low contact angles (usually less than $\theta_C = 90^\circ$), the substrate is considered hydrophilic against the liquid, whereas it is considered hydrophobic for high contact angles. Another parameter which can characterise wettability is the spreading of a liquid over a solid surface. The spreading coefficient is related to the surface tension of the liquid and the contact angle as follows (Crawford and Atkinson, 1996):

$$S_{LS} = \gamma_L \cdot (\cos \theta_C - 1) \quad (8.19)$$

Many factors influence contact angle measurements, the main ones being substrate contamination, substrate roughness and substrate chemical heterogeneity, substrate temperature, but also test duration (Hitchcock et al., 1981; Hazlett, 1993; Shanahan, 1993; Hong et al., 1994; Duncan and Lodeiro, 2004). Examples are illustrated in Figs. 8.72 and 8.73. The effect of changes in surface roughness can be evaluated with Wenzel's (1936) equation:

$$\begin{aligned} \cos \theta_R &= r_R \cdot \cos \theta_0 \\ r_R &= \frac{A_R}{A_0} \end{aligned} \quad (8.20)$$

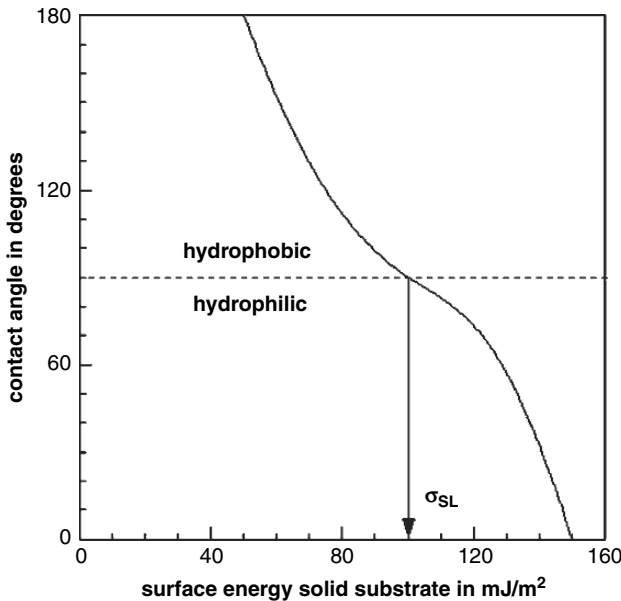


Fig. 8.71 Graphical solution to (8.18)



Fig. 8.72 Effects on contact angle formation (Fraunhofer Society, München). Conditions: left – initial condition; centre – effect of roughness; right – effect of contamination

Here, r_R is a so-called “roughness factor” considering the profile of a rough surface, θ_R is the contact angle of the rough surface, A_R is the true (rough) surface and A_0 is a perfectly smooth surface. For a completely smooth (untreated) surface, $r_R = 1$ and $\theta_R = \theta_0$. Equation (8.20) is graphically illustrated in Fig. 8.74. It can be seen that the contact angle decreases if roughness increases for $\theta_C < 90^\circ$ (wetting, hydrophilic), and that the contact angle increases if roughness increases for $\theta_C > 90^\circ$ (no wetting, hydrophobic). Experimental work of Hitchcock et al. (1981) has shown that the roughness factor can be linked to the profile roughness. For very smooth substrates ($R_a < 0.1 \mu\text{m}$), the authors derived the following relationship:

$$r_R = 1 + 50 \cdot \left(\frac{R_a}{S_R}\right)^2 \tag{8.21}$$

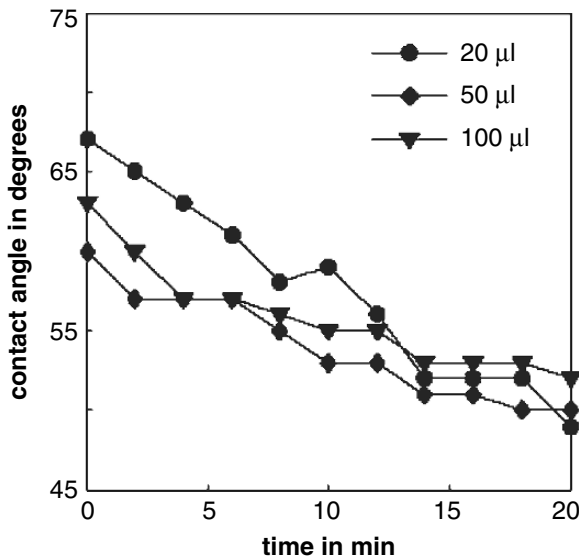


Fig. 8.73 Effects of test duration and drop volume on contact angle to a blasted substrate (Roero, 2005)

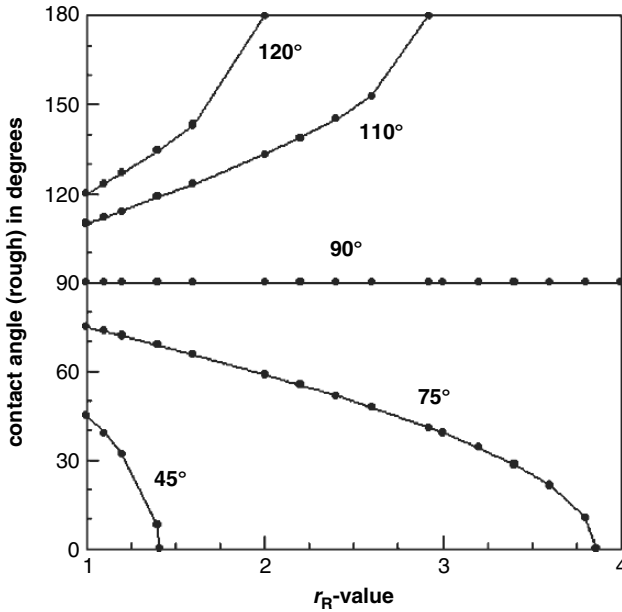


Fig. 8.74 Graphical expression of Wenzel's equation (8.20)

In a more general way, R_a is the average amplitude and S_R the average wavelength of the surface feature (see Fig. 8.32). Minaki et al. (2004) performed measurements of R_a and S_R for different blast cleaning conditions (aluminium oxide, mesh 700, $p = 0.15 - 0.4$ MPa, $\dot{m}_P = 100$ g/min, $t_B = 1 - 10$ s, $d_N = 7$ mm, $\varphi = 90^\circ$). From the results they reported, typical values for R_a/S_R are between 10^{-3} and 10^{-2} . An example for the roughness effect based on experimentally estimated values is shown in Fig. 8.75 for a hydrophilic surface. As depicted by (8.20), contact angle dropped with an increase in roughness. The same result was reported by Sancaktar and Gomatam (2001) for the contact angles of epoxy adhesives to hydrophobic steel substrates. For very smooth substrates ($R_a < 0.1$ μm), Hitchcock et al. (1981) found that the contact angle showed a linear relationship with the profile parameter ratio R_a/S_R . Effects of substrate contamination on contact angle to substrate are represented in Table 8.14. Hong et al. (1994) found on aluminium plates that oxidation could significantly reduce the contact angle for distilled water.

The most commonly used method for contact angle measurement is the sessile drop method, whereby θ_C is directly measured for a liquid drop resting on a flat surface of the solid. This procedure is illustrated in Fig. 8.66b. Other methods are outlined by Adamson (1990) and Berg (1993). The sessile drop method delivers three different types of contact angles as illustrated in Fig. 8.76: advancing angle, receding angle and equilibrium angle. The difference between advancing angle and receding angle:

$$H_\theta = \theta_A - \theta_R \quad (8.22)$$

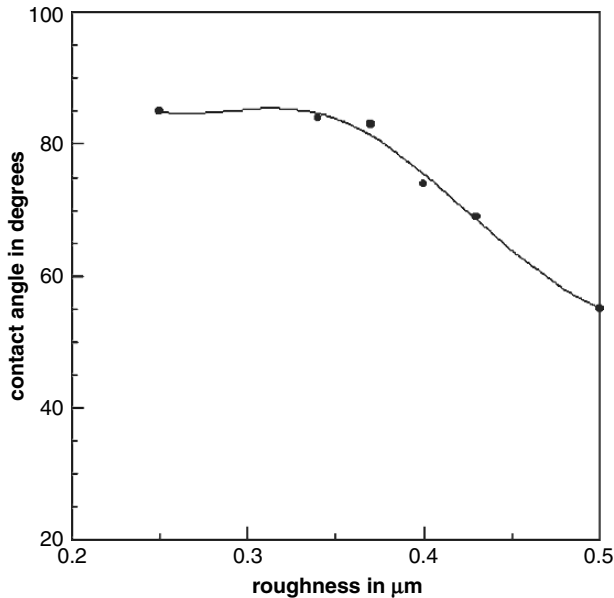


Fig. 8.75 Effects of roughness on contact angles to a hydrophilic aluminium substrate (Duncan and Lodeiro, 2004)

is referred to as contact angle hysteresis, which occurs for a number of reasons. Reasons related to substrate conditions are roughness, surface heterogeneity, diffusion and swelling (Baldan, 2004).

8.9.2 Effects of Wettability on Coating Performance

Mayfarth and Schubert (1989) highlighted the effect of wettability on coating adhesion. They found experimentally for austenitic steel that the best coating performance can be achieved if a maximum wettability can be achieved. It was rather the wettability, and not the roughness, which promoted good adhesion.

Wettability of a substrate influences the process of coating formation, especially the formation of wet films (Vincent, 2001). This was shown, among others, due to investigations of splash morphologies for sprayed coating materials (Griffith et al., 1997; Fauchais et al., 2004). From (8.16) and Fig. 8.67, contact angle affects the work of adhesion between substrate and wet film. If wettability increases (contact angle decreases), work of adhesion rises. However, a definite relationship between wettability and cured coatings is difficult to prove because it is very difficult to exclude other effects. Nevertheless, Fig. 8.77 shows, as an example, how the wettability of a substrate by an adhesive affected the shear strength of an aluminium joint. The better wettability (the lower contact angle) was, the higher was shear strength. The same trend was observed by Minaki et al. (2005) for the adhesion of

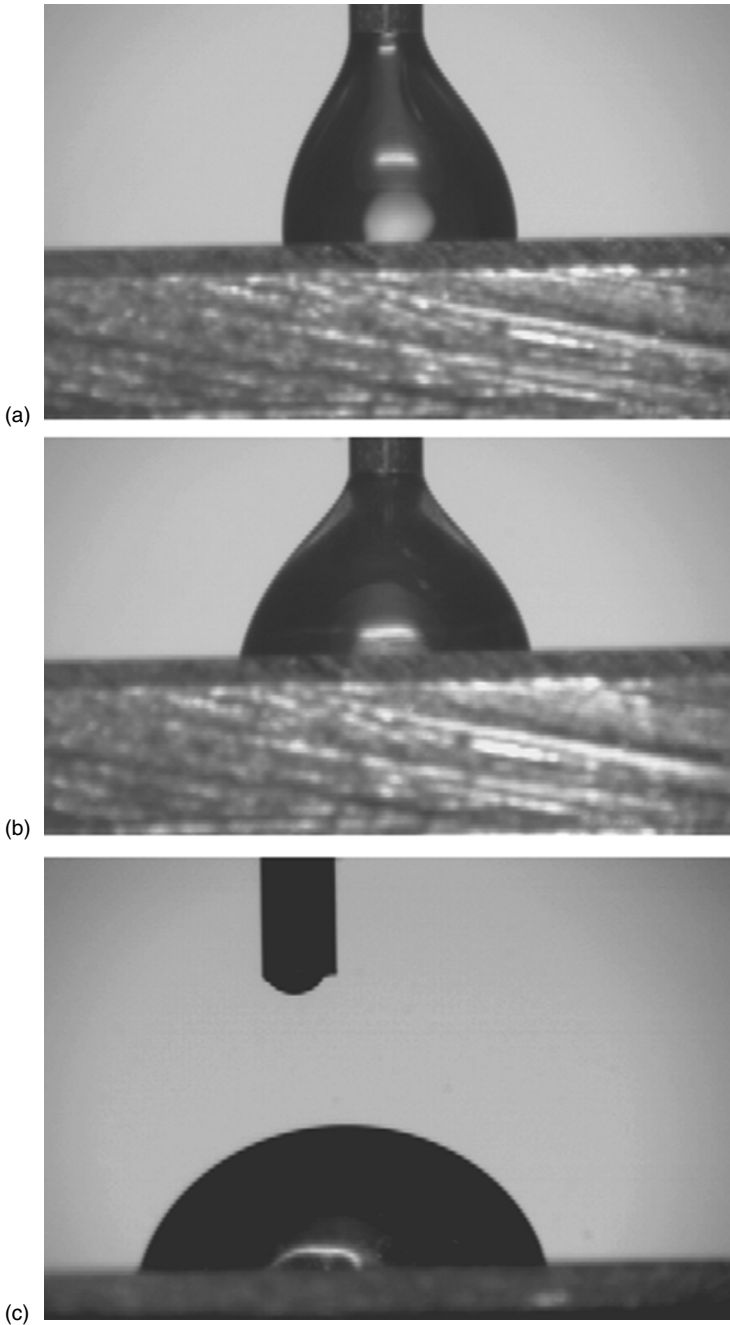


Fig. 8.76 Contact between liquid drop and substrate surface after blast cleaning (Momber and Wong, 2005a). (a) Advancing contact angle; (b) Receding contact angle; (c) Equilibrium contact angle

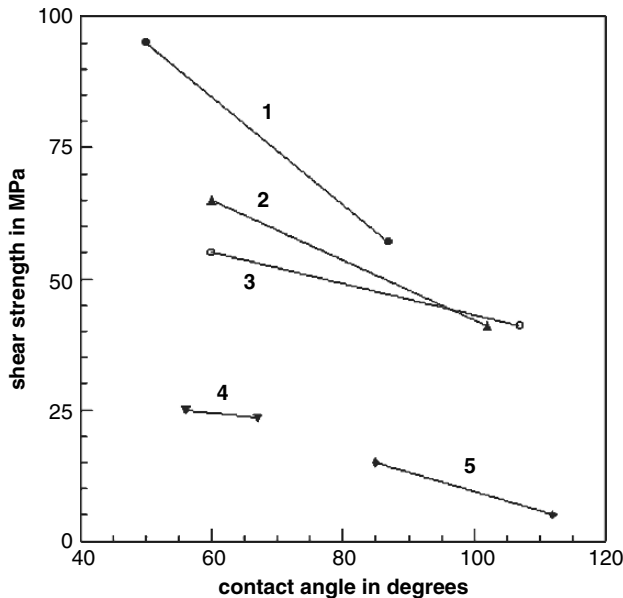


Fig. 8.77 Relationship between contact angle and joint shear strength (Asthana and Sobczak, 2000). Material pairings: 1 - AlSi₁₁/AlN; 2 - Al/AlN; 3 - A/AlN; 4 - AlTi₆/AlN(1); 5 - AlTi₆/AlN(2)

plated titanium nitride to blast cleaned stainless steel substrates. Adhesion increased for smaller contact angles.

Tamai and Tanaka (1967) introduced the idea that the advancing contact angles measured on the reverse sides of polymer coatings peeled off from different metal substrates are a measure of the peel strength between the coating and the individual metal. The order of contact angle values for the different substrates was: Au ($\theta_C = 76^\circ$), Fe ($\theta_C = 70^\circ$), Al ($\theta_C = 67^\circ$), Ni ($\theta_C = 62^\circ$) and Cd ($\theta_C = 50^\circ$). The same order was obtained in terms of knife-edge breaking strength between substrate and polymer film.

8.9.3 Wettability of Blast Cleaned Metal Substrates

Solomon et al. (2003) performed wetting experiments on blast cleaned substrates which were later brazed. They found notable effects of blast cleaning media on wettability. Some results are displayed in Table 8.51. Blast cleaning with aluminium oxide yielded surfaces that were most poorly wet. Best wetted surfaces were produced with Ni-Cr-Fe abrasive, and SiC abrasives were intermediate compared to the other two media. Debris embedment into the blast cleaned substrates was the major reason that affected wettability, and this was the reason for the good performance of Ni-Cr-Fe blasted substrates, because this abrasive did not become embedded in the surface. If a substrate, subsequently blast cleaned with aluminium oxide, was

Table 8.51 High-temperature wetting test results on IN718 after surface treatment; wetting liquid: AMS4777 (Solomon et al., 2003)

Blast cleaning process	Maximum wetting force in N/m
With Al ₂ O ₃	-0.18
	0.09
	0.60
With Al ₂ O ₃ + polishing with paper (400 μm)	0.99
Polishing only with paper (400 μm)	1.25
With SiC	1.24
	1.29
	1.07
With Ni-Cr-Fe alloy	0.48
	1.28
	1.25
	0.98

mechanically ground, it improved in terms of wettability. The reason was the removal of the embedded debris (see Table 8.22).

Broughton and Lodeiro (2002) reported about contact angle measurements on blast cleaned mild steel substrates; advancing contact angles only slightly decreased from $\theta_C = 90.5^\circ$ – 86.9° after the surface was blast cleaned with aluminium oxide, and receding contact angles only slightly decreased from $\theta_C = 31.1^\circ$ to 30.2° after blast cleaning. Rider et al. (1999) found that the contact angle of water to aluminium substrates was reduced due to blast cleaning. The contact angle of the received sample was $\theta_C = 80^\circ$, and this high value could be lowered down to $\theta_C = 5^\circ$ due to blast cleaning with aluminium oxide powder ($d_p = 50 \mu\text{m}$). Sancaktar and Gomatam (2001) could show that contact angles of a resin to a cold-rolled steel also reduced after blast cleaning with aluminium oxide (from $\theta_C = 42^\circ$ for the untreated substrate to $\theta_C = 15^\circ$ after blast cleaning), and they contributed this result to an increase in roughness due to blast cleaning (compare with Fig. 8.75). Similar results were found by Momber and Wong (2005a) for low-carbon steel substrates, although the reduction was only marginal. More interestingly, the latter authors found that the contact angle increased notably after a second blast cleaning step; this effect could not be explained by geometric arguments and may have been caused by changes in the chemical state of the surface. A similar situation is shown in Fig. 8.78. In contrast to (8.20) as well as to Fig. 8.75, contact angle of the hydrophilic surface increased with an increase in roughness. The explanation is due to changes in the chemical composition of the substrate surface due to abrasive particle impingement (Harris and Beevers, 1999). These results clearly documented the limits to Wenzel's approach, which is a plain geometric approach. Momber and Wong, 2005a) considered contact angle hysteresis according to (8.22), and they found that it was low for an untreated surface ($H_\theta = 7^\circ$) and high for blast cleaned surfaces ($H_\theta = 18$ – 24°). Kallio et al. (2005) performed abrasion tests on uncoated stainless steel and found that contact angle of water to the substrate decreased as the number of abrasion cycles rose.

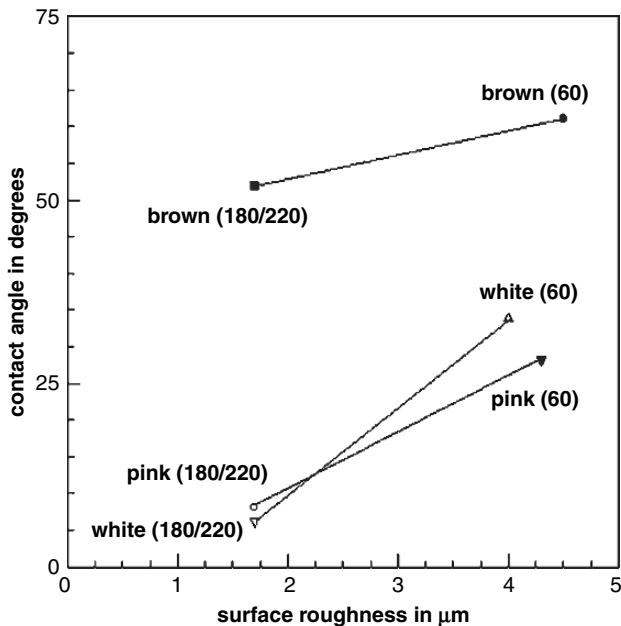


Fig. 8.78 Effects of abrasive type and size on substrate roughness and contact angle (Harris and Beever, 1999); substrate: steel; wetting liquid: de-ionised water

Minaki et al. (2005) blast cleaned martensite stainless steel with aluminium oxide ($p = 0.2 - 0.4 \text{ MPa}$, mesh 700, $\dot{m}_p = 50-300 \text{ g/min}$, $\varphi = 90^\circ$, $d_N = 8 \text{ mm}$) and performed contact angle measurements with water. The authors found that the contact angle decreased as air pressure and blasting time increased. In general, the substrate surface featured rather high contact angles ($\theta_C = 75-107^\circ$), which pointed to rather hydrophobic surfaces.

Uhlmann et al. (2006) measured contact angles and specific energies of AlMg_3 substrates after the treatment with impinging dry ice particles. The estimated contact angles were between $\theta_C = 50^\circ$ and 80° , and the estimated specific surface energies were between $\gamma_S = 10$ and 50 mN/m . Contact angles decreased with an increase in dry ice mass flow rate, whereas the specific energies increased with an increase in dry ice mass flow rates.

A study on the wettability of aluminium substrates (AlMg_3) with different wetting liquids (demineralised water, glycerine and diiodmethane) was performed by Emrich (2003), who measured the values of the advancing contact angle. For substrates blast cleaned with aluminium oxide ($p = 0.6 \text{ MPa}$), he obtained the following results: demineralised water (70% polar): $\theta_C = 30^\circ$; glycerine (40% polar): $\theta_C = 60^\circ$; diazomethane (disperse): $\theta_C = 35^\circ$. These contact angles were lower than those for substrates degreased with acetone, but higher than those obtained for substrate prepared by pickling. These results illustrated the effect of the polar, respectively disperse,

components of the testing liquids, although no trend could be established between contact angle and the percentage of polar, respectively disperse, component.

Sancaktar and Gomatam (2001) investigated the effects of different surface preparation methods on the contact angle of an organic adhesive to rolled steel substrates. For cold-rolled steel, the authors found that blast cleaning (aluminium oxide, mesh 54, $p = 0.55$ MPa) generated lower contact angles ($\theta_C = 15^\circ$) compared to etching ($\theta_C = 19^\circ$) and to the untreated substrate ($\theta_C = 41^\circ$). For hot-rolled steel, the substrate formed after etching generated somewhat lower contact angles ($\theta_C = 14^\circ$) than the blast cleaned substrate ($\theta_C = 18^\circ$). The untreated hot-rolled steel featured a high contact angle of $\theta_C = 50^\circ$.

A study into the wettability of liquefied organic coatings to welded metals was performed by Fedko and Tomas (1998); this seems to be the only study which considered organic coating materials as wetting liquid. Some results of this investigation are summarised in Fig. 8.79. It can be seen that “sand” blasting generated very high contact angles compared to grinding. Therefore, the conditions for wetting the weld substrate by the coatings notably deteriorated. Deterioration effects

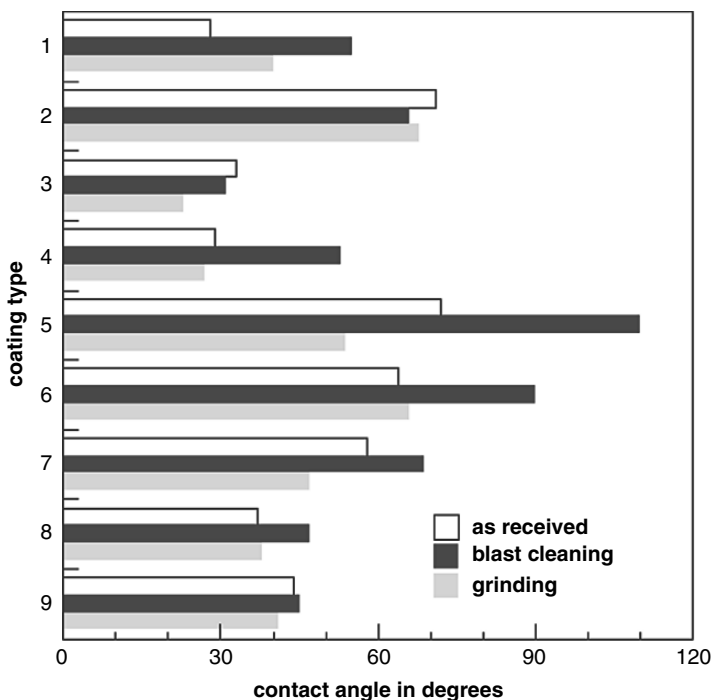


Fig. 8.79 Effects of surface properties on wettability of welded metals by liquefied organic coatings (Fedko and Tomas, 1998). Wetting liquids: 1 – aqueous solution (KBZh); 2 – TsZhS (not specified); 3 – AD (not specified); 4 – aqueous solution of chalk; 5 – MZhS (not specified); 6 – AzhS (not specified); 7 – silicon cream; 8 – emulsion with surface-active agent (P3-1); 9 – emulsion with surface-active agent (P3-2)

occurred namely in case of the aqueous solutions (coatings “4” and “5”), whereas the emulsions (coatings “8” and “9”) were less affected. These two latter materials were modified with surface-active agents (soap and calcinated soda), which explains their superior capability to wet even the blast cleaned substrate efficiently.

8.10 Electron Transport Properties

Baer and Wagner (1973) presented measurements of the low-temperature electrical and thermal resistivities of several high-purity tungsten rods. They performed treatments with etching, electropolishing and blast cleaning, and they observed several effects of the surface conditions on the electron transport properties. Both the electrical and thermal resistivities were substantially affected by blast cleaning and etching. Some results for the electrical resistivity are presented in Fig. 8.80. It can be seen that etching and blast cleaning increased the values for the electrical resistivity. The same trend was found for the thermal resistivity. The original paper delivers further information.

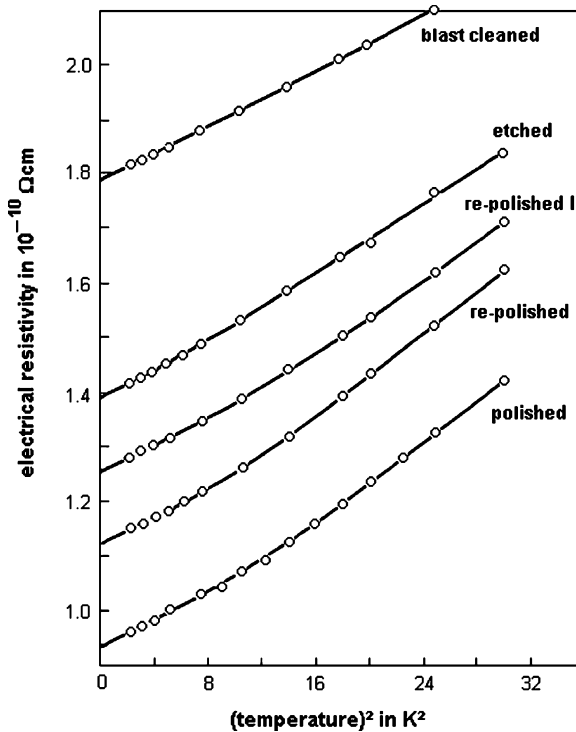


Fig. 8.80 Electrical resistivity as a function of temperature for various surface preparation conditions (Baer and Wagner, 1973)

Gladun et al. (1977) investigated the effects of blast cleaning (corundum, $d_p = 27 - 31 \mu\text{m}$) on the low temperature thermal conductivity of a single-crystal niobium specimen. Above a temperature of 2 K, the results of the untreated and the blast cleaned samples were in accord, whereas below 2 K the differences of the sample surfaces, caused by the blast cleaning process, were discernible.

Chapter 9

Coating Performance

9.1 Corrosion Protection Performance of Organic Coatings

9.1.1 Definitions and Methods

There is no single parameter or property that can characterise the corrosion protection capability or performance of coating systems. It is rather a mixture of parameters that must be considered. The same problem applies to testing methods. Standard parameters for the assessment of the behaviour of corrosion protective coatings are summarised in Fig. 9.1. Basically, the performance of undamaged and artificially injured coating systems is evaluated. Examples for the effects of different surface preparation methods on the corrosion at artificial scribes are provided in Fig. 9.2. It can be seen that the performance was worst for the untreated sample and best for the blast cleaned sample. Samples prepared with power tools showed moderate performance.

Failure evaluation of coating systems involves the following three conditions (ISO 4628-1):

- failure size;
- failure distribution;
- failure intensity.

Some authors tried to generalise results of visual inspection methods. Vesga et al. (2000) introduced a *KIV*-value (Constant-Inspection-Visual) for the assessment of primers applied to substrates prepared with different surface preparation methods. The *KIV*-value reads as follows:

$$KIV = 100 - \sum (\text{corrosion products} + \text{blister size} + \text{blister density}) \quad (9.1)$$

The criteria for the assessment of the three performance parameters are listed in Table 9.1. The term “corrosion products” corresponds to the degree of rusting according to ISO 4628-2, whereby “blister size” and “blister density” correspond to the degree of blistering according to ISO 4628-3. The higher the *KIV*-value, the better the coating performs. A freshly applied defect-free coating at $t = 0$ has a value

Fig. 9.1 Coating performance assessment parameters according to ISO 4628

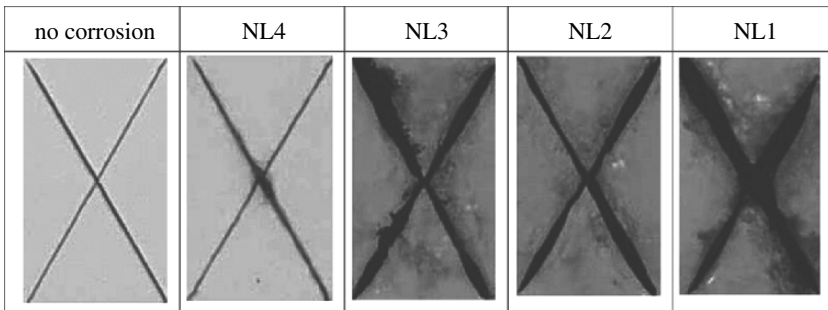
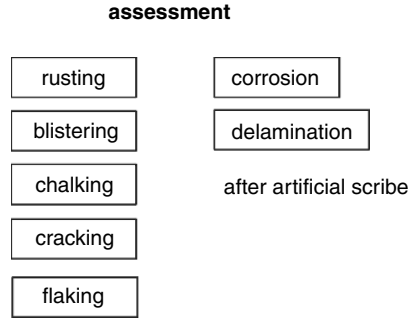


Fig. 9.2 Effects of surface preparation on underscribe corrosion (Kim et al., 2003). NL1 – untreated; NL2 – grinding (light rust removed); NL3 – grinding (rust completely removed); NL4 – dry blast cleaning

of $KIV = 100$. A coating with a value of $KIV = 36$ shows the worst performance. Figure 9.3 illustrates results of this procedure: KIV -values are plotted against the testing duration as functions of different surface preparation methods. The values for KIV decrease, as expected, with an increase in testing time, and they also show a dependence on the surface preparation method, at least for long exposure times.

Artificially injured coatings play a role for laboratory tests, such as for the neutral salt spray tests. In these cases, the artificial scribes simulate mechanical damage to the coating systems. Test duration depends on the corrosivity of the environment the coatings have been designed for. Examples are listed in Table 9.2. For certain

Table 9.1 Criteria for degree of blistering and degree of rusting (ISO 4628-1)

Criterion	Defect quantity	Defect size
0	No (resp. not visible) defects	Not visible at 10 × magnification
1	Very few defects	Visible only at 10 × magnification
2	Few defects	Just visible with unaided eye
3	Moderate number of defects	Clearly visible with unaided eye (up to 0.5 mm)
4	Considerable number of defects	Range between 0.5 and 5.0 mm
5	High number of defects	Larger than 5.0 mm

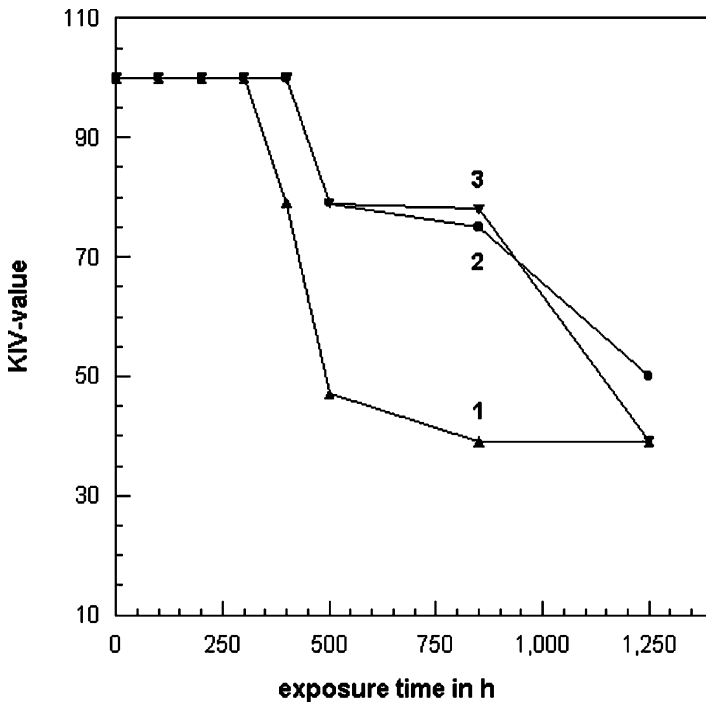


Fig. 9.3 Relationship between KIV and surface preparation methods (Vesga et al., 2000). Preparation methods: 1 – wet blast cleaning; 2 – wet blast cleaning with inhibitor; 3 – dry blast cleaning

application, for example for the use of coatings for offshore structures, special test regimes have been developed. An example is displayed in Fig. 9.4.

The methods for the damage and failure assessment are visually determined, although certain parameters, namely degree of rusting and degree of blistering, can be alternatively assessed by more objective methods, such as computerised image analysis methods (Momber, 2005b). Examples are provided in Fig. 9.5.

Table 9.2 Relationships between corrosivity and test conditions for coatings according to ISO 12944-6 (Projected coating durability: >15 years)

Corrosivity category ^a	Test duration in hours			
	Chemical resistance	Water immersion	Water condensation	Neutral salt spray
C2	–	–	120	–
C3	–	–	240	480
C4	–	–	480	720
C5-I	186	–	720	1,440
C5-M	–	–	720	1,440
Im1	–	3,000	1,440	–
Im2	–	3,000	–	1,440
Im3	–	3,000	–	1,440

^a Defined in ISO 12944-1




day 1	day 2	day 3	day 4	day 5	day 6	day 7
UV/condensation — ISO 11507			salt spray — ISO 7253			low-temp. exposure at (-20±2) °C
						

Fig. 9.4 Coating performance testing regime for offshore applications according to ISO 20340

Bockenheimer et al. (2002) performed investigations into the curing reactions of epoxy systems applied to aluminium, and they found different degrees of conversion of epoxy groups on the pretreated surfaces. Results of this study are plotted in Fig. 9.6. It can be seen that blast cleaning notably reduced the final degree of conversion of the epoxy groups. A distinct effect of the abrasive type could also be noted. The authors could further show that blast cleaned surfaces not only influenced the formation of the network structure in the near-interphase region, but also far from substrate.

9.1.2 Coating Performance After Blast Cleaning

9.1.2.1 Introduction

Systematic investigations about the effects of different surface preparation methods on the performance of organic coatings are provided by Allen (1997), Morris (2000), Momber et al. (2004) and Momber and Koller (2005, 2007). The first three authors mainly dealt with the adhesion of organic coatings to steel substrate; their results are presented in Sect. 9.2.

Vesga et al. (2000) utilised the *KIV*-criterion mentioned in Sect. 9.1.1. Results are provided in Fig. 9.3. For comparatively short exposure times ($t < 300$ h) and long exposure times ($t = 1,250$ h), this parameter was insensitive to surface preparation methods. At moderate exposure times, primer performance depended notably on surface preparation method. Primers applied over wet blast cleaned substrates deteriorated very quickly after a threshold time level was passed. The decrease in the resistance of primers applied over dry blast cleaned substrates was moderate after the threshold exposure time was exceeded. The addition of an inhibitor to the water for wet blast cleaning did not notably improve the performance of primers for longer exposure times. An inhibitor improved the situation basically for moderate exposure times only. Vesga et al. (2000) found that electrochemical impedance spectroscopy (EIS) can be utilised for the evaluation and assessment of the protective performance of organic coating systems. Pore resistance values measured on primers applied over steel substrates prepared with dry blast cleaning and wet blast cleaning showed the same qualitative trend as the *KIV*-values.

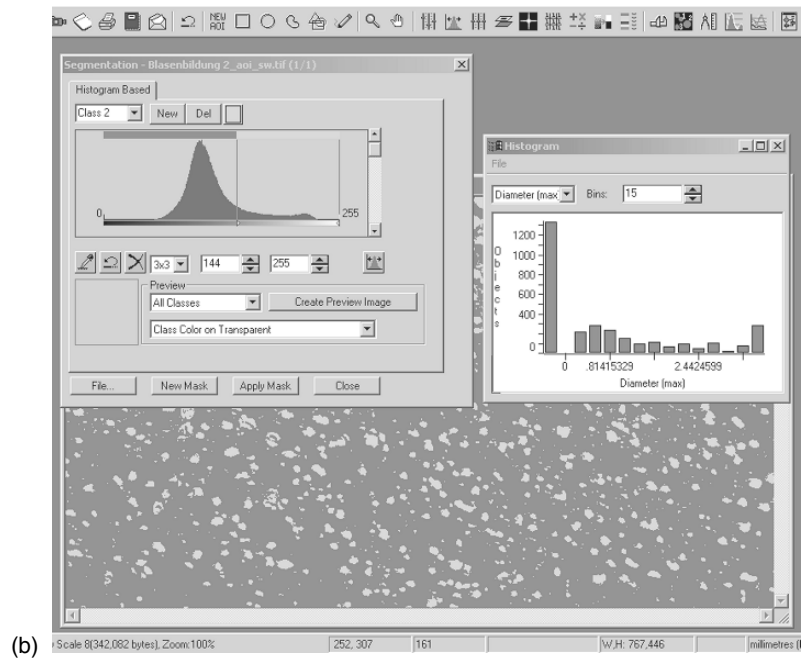
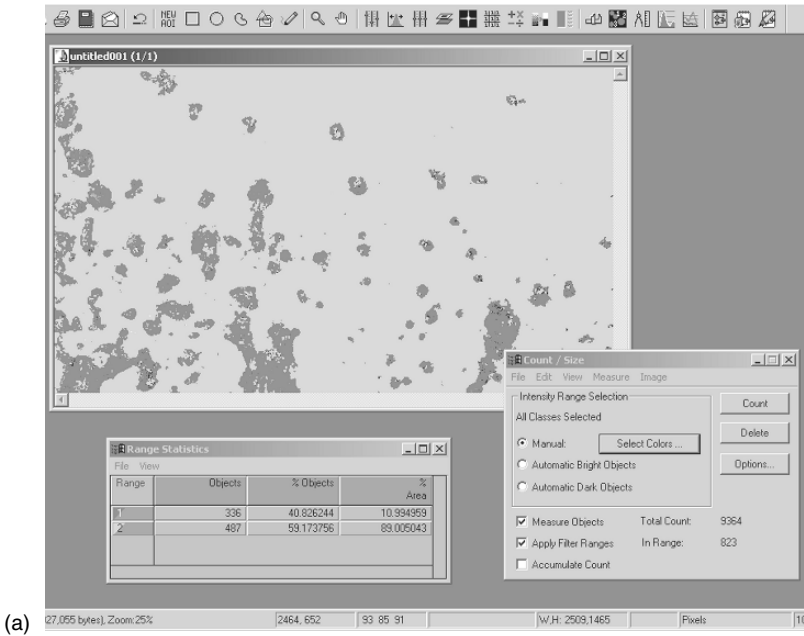


Fig. 9.5 Assessment of coating damaged based on digital image processing (Images: Muehlhan AG, Hamburg). (a) Degree of rusting; (b) Degree of blistering

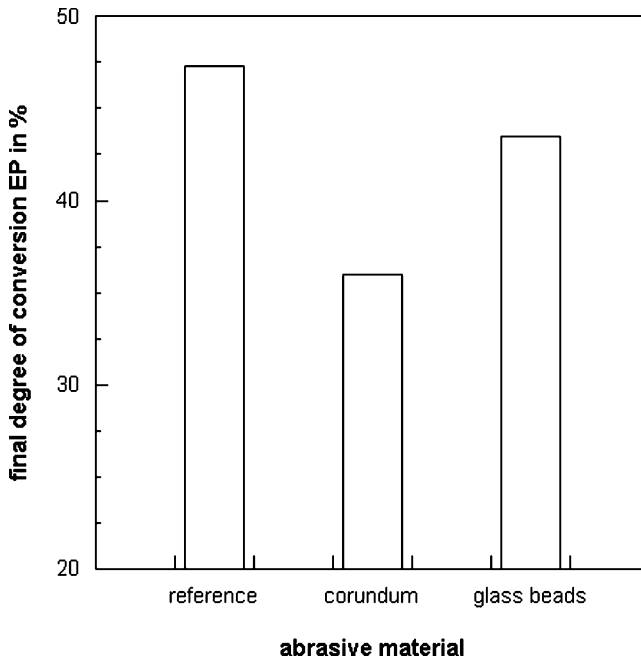


Fig. 9.6 Final degree of conversion of epoxy groups for 2 μm films on aluminium (Bockenheimer et al., 2002)

9.1.2.2 Coating Delamination

Results of measurements of coating delamination at artificial scribes were reported by several authors (Haagen et al., 1990; Van der Kaaden, 1994; Pietsch et al., 2002; Momber and Koller, 2005, 2007; Claydon, 2006). Some results are displayed in Fig. 9.7. Coatings applied to wet blast cleaned substrates showed the lowest delamination rate, whereas coatings applied to dry blast cleaned substrates performed worst. These results were attributed to substrate contamination due to broken abrasive debris. If blast cleaning was compared with manual surface preparation, delamination widths were larger for blast cleaned substrates, at least for epoxy coatings with zinc phosphate fillers subjected to wetting–drying cycles (Pietsch et al., 2002). Results of respective tests are shown in Figs. 9.8 and 9.9. Delamination of zinc phosphate primers at the artificial scribe on blast cleaned substrate occurred due to cathodic delamination. Using zinc dust primers, especially the edges of the scribe were cathodically protected by the anodic dissolution of zinc. Because of the formation of zinc oxides, increasing exposure time can lead to a deactivation of zinc dust and a progression of the corrosion process. Haagen et al. (1990) investigated the delamination of coatings on non-rusted substrates, and they found that blast cleaned surfaces were superior over mechanically ground surfaces. Some of their results are listed in Table 9.3. Figure 9.10 illustrates the effects of abrasive types on coating delamination. The coatings tested showed worse performance over shot

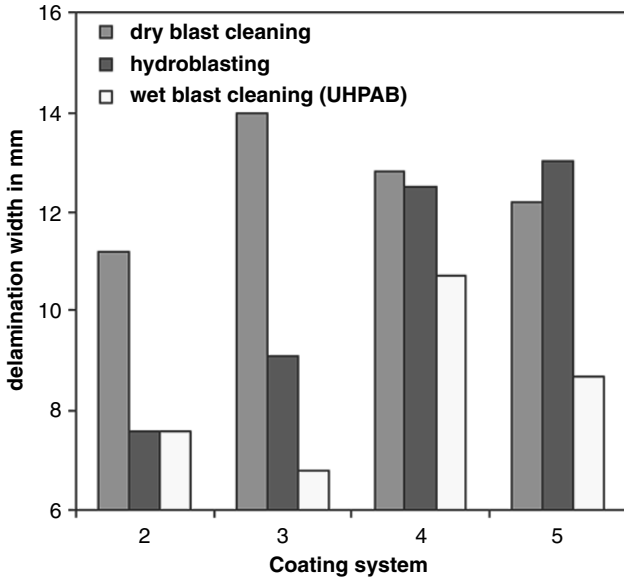


Fig. 9.7 Delamination of organic coatings for different surface preparation methods (Momber and Koller, 2005)

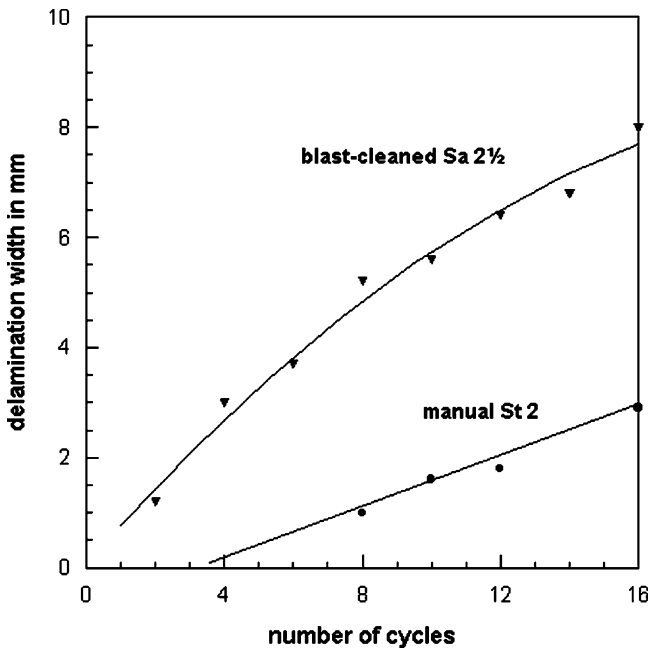


Fig. 9.8 Surface preparation influence on delamination of organic coatings at artificial scribe (Pietsch et al., 2002). Coating: epoxy/polyurethane; Primer: epoxy/zinc-phosphate

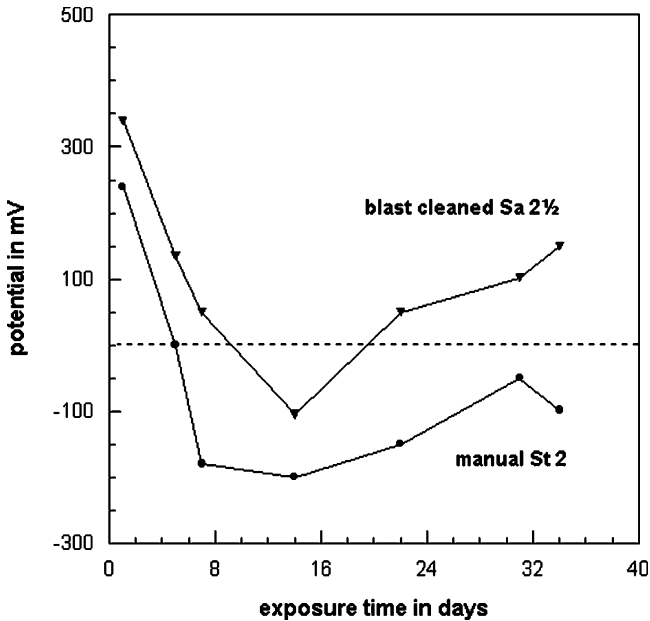


Fig. 9.9 Surface preparation method effects on electric potential below an intact coating (Pietsch et al., 2002). Primer type: zinc dust based primer

blasted steel compared with coatings applied to grit blasted steel during a cyclic corrosion test. If a salt spray test was considered, both abrasive types delivered comparative results. Van der Kaaden (1994) performed a comparative study into the performance of organic coating systems applied to dry blast cleaned and wet blast cleaned steel substrates. The hot-rolled substrates were pre-rusted. Results of this study are listed in Table 9.4. The results reveal the tight relationships between surface preparation method, testing regime, coating type and delamination width. Whereas the wet blasting version with the larger water flow rate (7.0l/min) showed the best results for the chlorinated rubber in the salt spray test, it performed

Table 9.3 Effects of surface preparation method and test solution on the delamination of coatings after salt spray tests (Haagen et al., 1990), Coating: 2-pack epoxy with micaceous iron ore

Test solution	Delamination in mm	
	Polished	Blast cleaned
NaCl (0.117%)	2–3	2
NaCl (saturated)	4–5	0.5–1
NaCl (5%)	Ca. 11	Ca. 5
NH ₄ NH ₃ (3.2%)	Ca. 1	0
NH ₄ NH ₃ (0.85%)	5–7	2–3
NH ₄ Al(SO ₄) ₂	2–3	0
NH ₄ Cl (2.14%)	0.5	0
CaCl ₂ (2.8%)	1–2	0

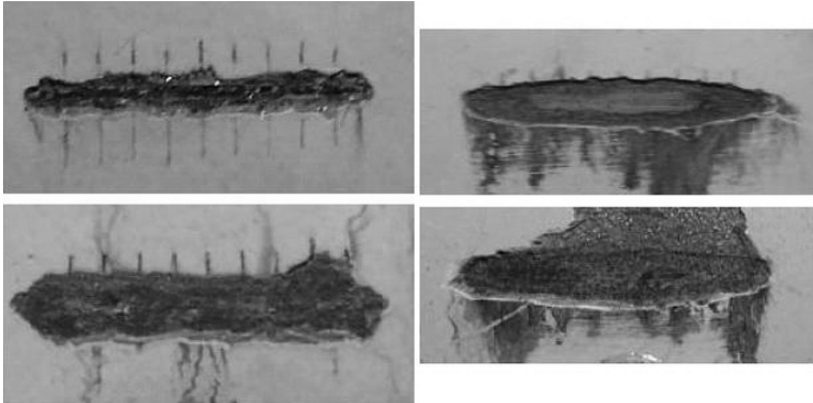


Fig. 9.10 Effects of blast cleaning method on delamination of zinc epoxy primers at an artificial scribe (Claydon, 2006). Upper images: dry blast cleaning with grit; Lower images: dry blast cleaning with shot. Left: after cyclic corrosion test; right: after salt spray test

worst for the high-solid epoxy in the seawater test with cathodic protection. The results for the tests with cathodic protection are of special interest. If the results for chlorinated rubber, obtained during the seawater test, are considered, the preferred surface preparation method would be wet blast cleaning with a low water volume (1.6 l/min). As far as cathodic protection was added, the preferred surface preparation method would be wet blast cleaning with a high volume of water (7.0 l/min). The opposite trend could be recognized if high-solid epoxies were applied to the blast cleaned surfaces.

Emrich (2003) investigated the delamination of adhesive bonds in aluminium (AlMg₃) samples. He subjected the samples to a salt spray test over a period of

Table 9.4 Delamination of organic coatings at an artificial scribe (Van der Kaaden, 1994)

Preparation method	Coating system	Delamination in mm			
		Sea water (1 year)	Sea water with cathodic protection (1 year)	Artificial rain water (1 year)	Salt spray test (3,000 h)
Dry blast cleaning	Chlorinated rubber	1.4	814.9	76.1	9.5
	Vinyl/tar	2.5	7.9	55.6	6.0
	Coal tar/epoxy	0.0	0.0	59.1	8.5
	High-solid epoxy	13.3	19.4	65.8	5.5
Wet blast cleaning (1.6 l/min)	Chlorinated rubber	1.2	831.3	77.3	8.0
	Vinyl/tar	0.0	0.0	61.0	6.8
	Coal tar/epoxy	0.0	0.0	46.1	8.3
	High-solid epoxy	13.3	30.0	56.9	4.5
Wet blast cleaning (7.0 l/min)	Chlorinated rubber	8.6	703.8	81.3	6.3
	Vinyl/tar	0.0	0.0	110.1	5.3
	Coal tar/epoxy	0.0	0.0	63.8	8.9
	High-solid epoxy	3.9	43.8	20.3	6.0

2,000 h, and he noted a severe delamination of the adhesive on substrates which were blast cleaned with corundum ($p = 0.6 \text{ MPa}$). The delamination was much more severe than delaminations estimated for samples where the substrates were degreased with acetylene. Samples with substrates that were treated by pickling did not show any delamination. If an accelerated corrosion test (6 h in a 5% NaCl solution, subjected to an external current) was applied to the samples, the ranking was different. The samples with the degreased substrates exhibited the most severe delamination, followed by the blast cleaned samples. The best performance was again shown by the samples prepared with pickling.

9.1.2.3 Degree of Rusting

Measurements of the degree of rusting for paints applied to substrates prepared with different surface preparation methods were performed by Grubitsch et al. (1972) and Kogler et al. (1995). Results of the latter authors are displayed in Fig. 1.4. Figure 9.11 shows the effects of different abrasive materials on the degree of rusting of coated (zinc dust) steel panels. There exists the following power relationship between exposure time and degree of rusting:

$$\text{DR} \propto t_E^{k_R} \quad (9.2)$$

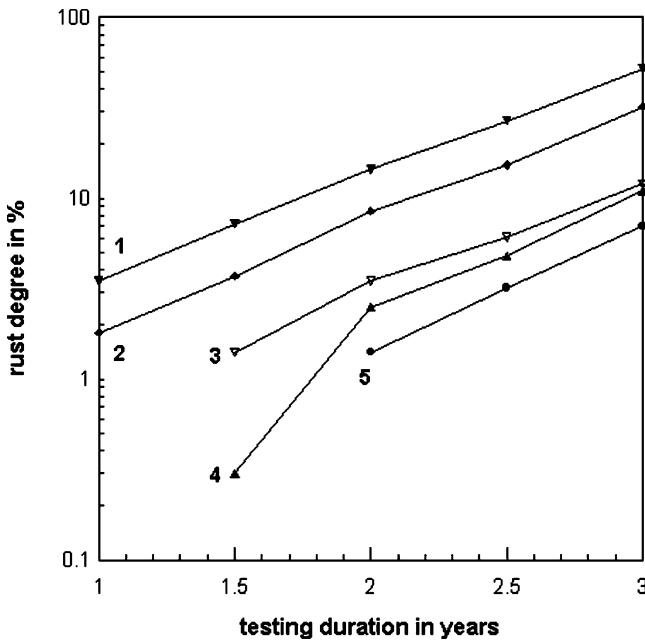


Fig. 9.11 Relationship between ageing kinetics and abrasive materials (Grubitsch et al., 1972). Abrasive materials/method: 1 – slag; 2 – quartz; 3 – aluminium oxide; 4 – steel grit; 5 – etching

Table 9.5 Ageing kinetics parameter in (9.2) for different abrasive materials (Grubitsch et al., 1972)

Abrasive type/method	Grain size in mm	Parameter k_R
Quartz	1.0–2.0	2.6
Corundum	0.8–1.0	–
Slag	1.0–2.0	2.4
Steel grit	0.8–1.0	–
Etching with H ₂ SO ₄	–	–

This relationship could be exploited to describe the kinetics of ageing of a coating system. The power exponent k_R depended on abrasive material type. Values for this parameter are provided in Table 9.5. It can be seen that not only the type of abrasive material determined the ageing kinetics, but also its fineness.

Further results are listed in Table 9.6 where the failure times of two coating systems are listed. The failure time was defined as the time when the first rusting was visible on the coatings. Failure time strongly depended on the abrasive type. For the alkyd paint, for example, failure occurred after 3 months if aluminium oxide was used, but the failure time could be delayed up to 114 months when wet sand was used as an abrasive material. For the acrylic paint, the trend was opposite. Here, the coating applied to the substrate that was blast cleaned with aluminium oxide, showed the best performance.

9.1.2.4 Degree of Blistering

The degree of blistering of organic coatings is sensitive to the type of surface preparation. A systematic study on this issue was undertaken by Kim et al. (2003). Deterioration curves for a coating system, based on the results of long-term blistering tests (251 days) on artificially injured samples, are plotted in Fig. 9.12. Blistering was most severe for the untreated steel and least severe for the blast cleaned substrate. Blast cleaning was more efficient than power tool cleaning. The general relationship

Table 9.6 Effects of abrasive material type on failure times of organic coatings (Boocock, 1992)

Abrasive material	Failure time in months	
	Alkyd paint	Acrylic latex paint
Dry sand	101	114
Wet sand	114	38
Steel shot (S-280)	75	16
Steel grit (G-12)	89	38
Coal slag (coarse)	68	16
Coal slag (fine)	3	–
Staurolite	89	38
Flint	89	94
Copper/coal slag	89	114
Aluminium oxide	3	>126

Surface preparation grade: SP 10 for all samples

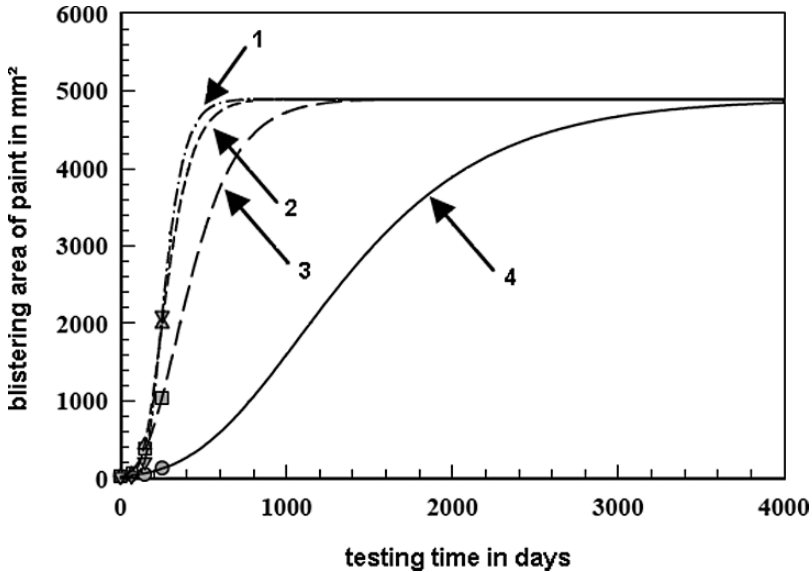


Fig. 9.12 Effects of surface preparation methods on the blister formation kinetics (Kim et al., 2003). Preparation method: 1 – no cleaning; 2 – grinding (light rust removed); 3 – grinding (rust completely removed); 4 – blast cleaning

between exposure time and degree of blistering is essentially equal to (9.2), whereby the power exponent depended on the surface preparation method.

9.2 Adhesion and Adhesion Strength

9.2.1 Definitions and Measurement

9.2.1.1 Definitions

According to Bullett and Prosser (1972) “the ability to adhere to the substrate throughout the desired life of the coatings is one of the basic requirements of a surface coating, second only to the initial need to wet the substrate.” Adhesion bases on adhesive forces that operate across the interface between substrate and applied coating to hold the paint film to the substrate. These forces are set up as the paint is applied to the substrate, wets it and dries. The magnitudes of these forces (thus, the adhesion strength) depend on the nature of the surface and the binder of the coating. Five potential mechanisms cause adhesion between the surfaces of two materials (see Fig. 9.13):

- physical adsorption;
- chemical bonding;
- electrostatic forces;

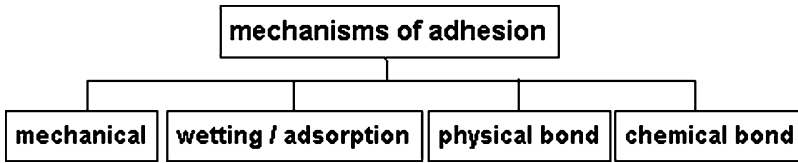


Fig. 9.13 Mechanisms of adhesion

- diffusion;
- mechanical interlocking.

In the mechanical interlocking mechanism, the macroscopic substrate roughness provides mechanical locking and a large surface area for bonding; the paint is mechanically linked with the substrate. Adhesive bonding forces could be categorised as primary and secondary valency forces as listed in Table 9.7. Adhesion depends on numerous factors, including those summarised in Fig. 9.14. It is instructive to note that the adhesion is to a certain amount a “test parameter” depending on test conditions and specifications. Adhesion values get a comparative meaning only if assessed under equal test conditions.

9.2.1.2 Adhesion Measurement

Adhesion between substrate and organic coating can be evaluated on site by different methods, including the following:

- pull-off testing; for coating dry film thickness DFT > 250 μm;
- X-cut testing;
- cross-cut testing; for coating dry film thickness DFT < 250 μm;
- falling ball impact;
- penknife disbondment.

For adhesive bonds, metallic coatings and ceramic coatings, other, more advanced testing methods (peel tests, indentation debonding tests, scratch tests, beam-bending tests, etc.) are available; a recent extensive review was delivered by Lacombe (2006). Berndt and Lin (1993) and Lin and Berndt (1994) provided a review about methods used to define and measure the adhesion of coatings or deposits formed by thermal spraying; their review included tensile adhesion test, double cantilever beam test, scratch test and bending test.

The pull-off test delivers quantitative information about the strength of the bond (usually given in N/mm², respectively MPa), while the picture of the rupture provides information about the weakest part of the system. The adhesion strength (referred to as pull-off strength if measured with the pull-off test) is the relationship between applied force and loaded cross-section:

$$\sigma_A = \frac{F_A}{A_A} \tag{9.3}$$

Table 9.7 Bonding forces and binding energies (Hare, 1996)

Force	Type	Description	Example	Binding energy in kcal/mole
Ionic	Primary valency	Bonding formed by transfer of valency electrons from the outer shell of an electron-donating atom into outer shell of an electron-accepting atom, to produce a stable valency configuration in both.	Metal salts	150–250
Covalent	Primary valency	Bonding formed when one or more pairs of valency electrons are shared between two atoms.	Most organic molecules	15–170
Co-ordinate	Primary valency	Covalent type bond where both of shared pair are derived from one of the two atoms.	Quaternary ammonium compounds	100–200
Metallic	Primary valency	Bonding in bulk phase of metals between positively charged metallic ions and the electron cloud in the lattice points of the structure.	Bulk metals	27–83
Hydrogen bonding	Secondary valency	Forces set up between the unshared electrons on a highly electronegative atom on one molecule and the weak positive charge from the 'exposed' proton of a hydrogen atom.	Water	<12
Dispersion	Secondary valency	Weak forces in all molecules that are associated with temporary fluctuations in electron density caused by the rotation of electrons around atomic nuclei.	Most molecules	<10
Dipole	Secondary valency	Intermolecular forces set up between weak and electronegative charge on one polar molecule and electropositive charge on a second polar molecule.	Polar organics	<5
Induction	Secondary valency	Very weak dipole-like forces between non-polar molecules set up by weak dipoles induced by the proximity of other strongly polar molecules.	Non-polar organics	<0.5

Frequently, adhesion strength is given in kN, which is the unit of a force. Obviously, this information is useful only if the loaded cross-section is known. It can, however, be used as a comparative measure if the loaded cross-section is a constant, exactly defined value.

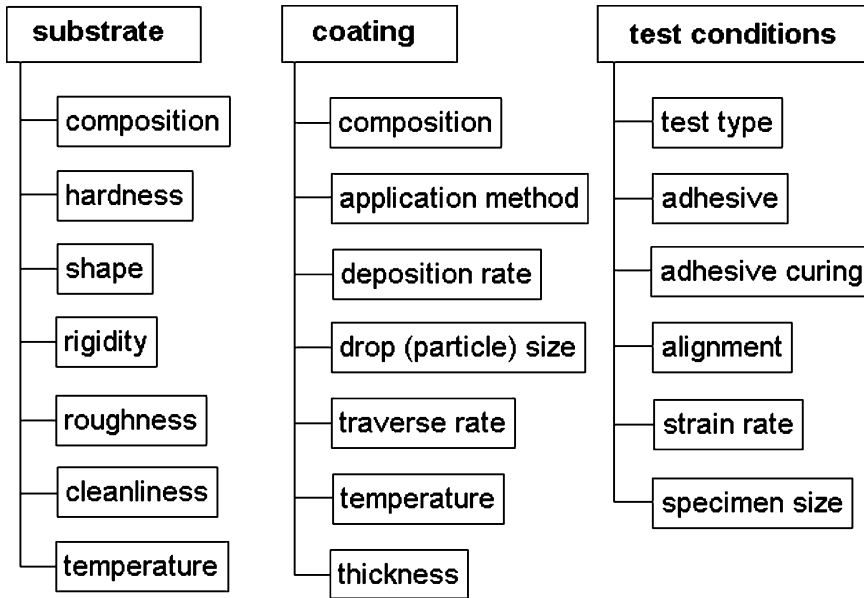


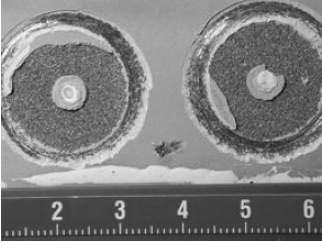
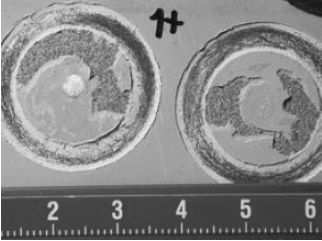
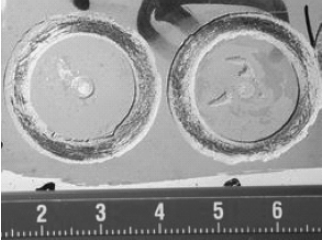
Fig. 9.14 Influence factors on the adhesion of coatings to steel substrates (James, 1984)

Typical failure types to be observed during pull-off tests are either adhesive failure (substrate-coating), cohesive failure (internal coating failure) or mixed adhesive-cohesive failure. More detailed designation is mentioned in Table 9.8. Strictly spoken, a plain adhesion failure will never occur in a coating-substrate system. This restriction is reinforced by XPS (X-ray photoelectron spectroscopy) measurements performed by van den Brand et al. (2004) and Watts and Dempster (1992), who found traces of polymeric material on the substrate surface of a metal-polymer interfacial fracture, which appeared to be a purely adhesive failure from an optical examination.

Time and environmental conditions are important parameters in the experimental estimation of adhesion parameters. Because the hardening of coating materials is a reaction kinetics process, the bond between substrate and coating, respectively adhesive, is a time-domain process. Emrich (2003), for example, measured the shear strength of an aluminium-adhesive joint subjected to a salt spray test. The aluminium substrate (AlMg₃) was blast cleaned with corundum ($p = 0.6$ MPa). Prior to the salt spray exposure, the shear strength had a value of 15.5 MPa. After a period of 2,000 h, however, the shear strength had dropped down to a value of 4.5 MPa only. This author could also show that the adhesion of the adhesive was extremely sensitive to ageing when the adhesive was applied to blast cleaned substrates. Other surface preparation methods, namely degreasing with acetylene and pickling, were much less sensitive to ageing effects. Further experimental information on these aspects is available in the literature, and it will be discussed in the following sections.

Desired adhesion depends on the certain case of application. The US Navy, for example, has defined a general minimum pull-off strength of $\sigma_A = 3.4$ MPa

Table 9.8 Failure modes after pull-off testing of organic coatings (Momber and Koller, 2005)

Method	Failure figure	Failure type ^a
Dry blast cleaning		100% A/B
Hydroblasting		60% B, 40% A/B (left) 70% B, 30% A/B (right)
Wet blast cleaning (Ultra-high pressure abrasive blasting)		100% B

^aA/B-adhesive failure coating/substrate

B-cohesive failure coating

measured per ASTM D4541 (Kuljan and Holmes, 1998). Demands for marine constructions are listed in Table 9.9.

9.2.2 Adhesion of Coatings and Adhesives to Metal Substrates

Sobiecki et al. (2003) conducted a study into the effects of surface preparation methods on the structure of the interfacial zone between steel substrate and a tungsten carbide coating. They found that the porosity in the interfacial zone depended on the surface preparation prior to the coating process. The porosity was lowest for grinding and highest for blast cleaning.

Several systematic studies were performed to estimate the adherence of coating systems to steel panels prepared by different methods. Long-term tests in salt water were performed by Allen (1997) and Morris (2000). These studies included hand wire brushing, needle gunning, hydroblasting and blast cleaning. The

Table 9.9 Critical adhesion strength values for some coatings (Norsok, 2004); using equipment according to ISO 4624, and carry out test when coatings are fully cured

Coating type/Application	DFT in μm	Pull-off strength in MPa (absolute minimum)	Failure mode
Thermally sprayed aluminium (or alloys)	200	7.0	–
Thermally sprayed zinc (or alloys of zinc)	100	5.0	Cohesive
Potable water tanks	–	5.0	–
Tanks for crude, diesel and condensate	–	5.0	–
Process vessels (<0.3 MPa, <75°C)	–	5.0	–
Process vessels (<7 MPa, <80°C)	–	5.0	–
Process vessels (<3 MPa, <130°C)	–	5.0	–
Vessels for storage of methanol, etc.	–	5.0	–
Fire protection (cement based)	–	2.0	–
Fire protection (epoxy based)	–	5.0	–

results, listed in Tables 9.10 and 9.11, illustrated the complex relationships between preparation methods and applied coating systems. Cross-cut, measured after 36 months, was almost independent on the preparation method for many epoxy coatings; exceptions were coal tar epoxy and pure epoxy tank lining, where wire brushing and needle gunning showed worse results compared to hydroblasting and blast cleaning. Penknife disbondment and impact resistance, both measured after 24 months, showed worst results for the mechanical methods (especially for the wire brushing). Impact resistance was more a function of the coating system than of the preparation method; thus, blast cleaned substrates were, on the whole, only slightly superior to manual preparation under the conditions of the impact testing. Regarding the pull-off strength, measured with a commercial adhesion tester, blast cleaning methods were superior to mechanical methods. Some results are shown in Fig. 9.15. There was a certain trend for the blast cleaning methods that pull-off adhesion increased with time. Under simulated ballast tank conditions, coatings applied to blast cleaned surfaces performed far better than coatings applied to mechanically prepared substrates, and equal to those on hydroblasted surfaces. It was observed that paint failure type was often a mixture of cohesive and adhesive failures, and the appearance of the certain mode was denoted in percent (see Table 9.8). However, as shown in Tables 9.10 and 9.11, substrate failure (denoted “S”) and coat detachment occurred usually from mechanically prepared surfaces, whereas glue failure (denoted “G”) and inter-coat failure (denoted “I”) were the principal failure mode on most of the blast cleaned and hydroblasted surfaces.

Björgum et al. (2007) investigated the adhesion of repair coating systems for off-shore applications. Pre-rusted steel panels were cleaned with blast cleaning, power tooling and waterjetting. After an accelerated ageing test, the adhesion between coatings and steel substrates was measured with a pull-off device. Although the authors found deviations in the pull-off strength for the different surface preparation methods, these differences were statistically insignificant.

Tests on contaminated substrates showed that the level of dissolved salts affected value and type of adhesion of coatings to substrates. With zero contaminants, the mode of failure was cohesive within the primer coat. As the salt level increased,

Table 9.10 Results of comparative adhesion tests on ballast tank coatings (Allen, 1997)

Method	Adhesion parameter		
	Falling ball impact ^a	Pull-off strength in MPa ^b	Penknife disbondment in mm
Epoxy coating (solvent-less)			
Wire brushing	2	2.8/S	6
Needle gunning	1	2.8/S	5
Hydroblasting (Dw2)	0	6.9/G	0
Hydroblasting (Dw2 FR)	4	3.4/G	0
Hydroblasting (Dw3)	0	3.4/G	0
Hydroblasting (Dw3 FR)	0	4.1/G	0
Blast cleaning (Sa 2½)	1	5.5/G	0
Coal tar epoxy			
Wire brushing	4	2.1/S	10
Needle gunning	3	2.4/S	7
Hydroblasting (Dw2)	0	5.2/I	0
Hydroblasting (Dw2 FR)	2	6.9/I	0
Hydroblasting (Dw3)	0	6.9/I	0
Hydroblasting (Dw3 FR)	2	6.9/I	0
Blast cleaning (Sa 2½)	1	6.6/I	0
Epoxy system			
Wire brushing	2	2.1/S	5
Needle gunning	2	2.8/S	3
Hydroblasting (Dw2)	2	6.9/G	0
Hydroblasting (Dw2 FR)	0	5.5/G	0
Hydroblasting (Dw3)	0	5.2/G	0
Hydroblasting (Dw3 FR)	0	6.9/G	0
Blast cleaning (Sa 2½)	0	5.5/G	0
Glass flake epoxy			
Wire brushing	2	2.8/S	5
Needle gunning	1	4.1/S	3
Hydroblasting (Dw2)	1	6.9/G	0
Hydroblasting (Dw2 FR)	4	5.2/G	0
Hydroblasting (Dw3)	0	3.4/G	0
Hydroblasting (Dw3 FR)	0	5.5/G	0
Blast cleaning (Sa 2½)	0	6.9/G	0

FR flash rust; Dw surface cleanliness according to STG 2222

^a0 = no cracking, no detachment; 1 = slight cracking, no detachment; 2 = slight cracking and detachment; 3 = moderate cracking, no detachment; 4 = moderate cracking, slight detachment

^bFailure mode: G = glue, I = intercoat, S = substrate

progressively less primer remained adhered to the steel surface. At higher contamination level, there was a change from mixed to totally adhesive failure of the primer (Allan et al., 1995). Baek et al. (2006) reported a notable decrease in pull-off strength if the steel substrate was contaminated with chlorides. The drop in adhesion was very pronounced if a chloride concentration of 7 µg/cm² was exceeded.

Kaiser and Schulz (1987) performed cross-cut adhesion tests on coatings applied to zinc surfaces. If the samples were degreased only, the cross-cut adhesion was very low. The adhesion notably improved if the samples were blast cleaned with coal

Table 9.11 Results of comparative long-term adhesion tests after 12, 24 and 36 months (Morris, 2000)

Method	Cross-cut in mm			Impact resistance ^a			Pull-off strength in MPa ^b		
	12	24	36	12	24	36	12	24	36
Solventless epoxy (2 × 125 µm DFT)									
Wire brushing	0	0	0	2	2	3	2.8/S	3.5/S	2.8/S
Needle gunning	0	0	0	1	1	2	2.8/S	5.5/S	5.2/S
Hydroblasting (Dw2)	0	0	0	0	0	1	6.9/S	7.6/I	8.3/G
Hydroblasting (Dw2 FR)	0	0	0	2	3	3	3.5/I	11.0/I	8.6/I
Hydroblasting (Dw3)	0	0	0	0	0	1	3.5/I	11.0/I	10.7/G
Hydroblasting (Dw3 FR)	0	0	0	0	1	1	4.1/I	8.3/I	11.0/I
Blast cleaning (Sa 2 1/2)	0	0	0	1	2	2	5.5/I	12.4/I	10.3/G
Glass flake epoxy (2 × 125 µm DFT)									
Wire brushing	0	0	10	1	1	3	4.1/S	4.1/S	2.1/S
Needle gunning	0	0	2	2	2	3	2.4/S	5.5/S	8.9/S
Hydroblasting (Dw2)	0	0	0	1	1	1	6.9/G	11.0/I	>17.9/G
Hydroblasting (Dw2 FR)	0	0	0	1	2	2	3.4/G	15.2/G	>17.2/G
Hydroblasting (Dw3)	0	0	0	0	0	1	7.6/G	10.3/I	9.7/I
Hydroblasting (Dw3 FR)	0	0	0	1	1	1	6.9/G	16.9/I	>17.2/I
Blast cleaning (Sa 2 1/2)	0	0	0	0	0	1	6.9/G	13.8/G	13.1/G
Low temperature cure glass flake epoxy (2 × 125 µm DFT)									
Wire brushing	0	0	10	1	1	1	2.8/S	4.6/S	7.6/S
Needle gunning	0	0	12	1	1	2	4.1/S	3.4/S	12.1/S
Hydroblasting (Dw2)	0	0	0	2	2	2	6.9/G	17.2/G	16.6/G
Hydroblasting (Dw2 FR)	0	0	0	2	2	2	5.2/G	14.5/I	11.7/G
Hydroblasting (Dw3)	0	0	0	0	0	1	3.4/G	15.2/G	10.3/G
Hydroblasting (Dw3 FR)	0	0	0	0	1	1	5.5/G	16.9/I	13.8/G
Blast cleaning (Sa 2 1/2)	0	0	0	1	1	2	6.9/G	13.8/G	12.4/G
Modified epoxy (2 × 125 µm DFT)									
Wire brushing	0	0	0	1	1	3	4.8/S	5.5/S	2.8/S
Needle gunning	0	0	0	2	3	3	2.1/S	2.8/S	4.1/S
Hydroblasting (Dw2)	0	0	0	0	0	0	6.9/I	12.8/I	10.3/I
Hydroblasting (Dw2 FR)	0	0	0	1	2	2	3.8/I	11.0/I	8.6/I
Hydroblasting (Dw3)	0	0	0	0	0	1	6.9/I	10.8/I	9.7/I
Hydroblasting (Dw3 FR)	0	0	0	0	0	0	4.1/I	15.2/I	7.9/I
Blast cleaning (Sa 2 1/2)	0	0	0	0	0	1	6.9/I	13.1/I	9.7/G

FR flash rust; Dw surface cleanliness according to STG 2222

^a0 = No cracking; 1 = very slight cracking, no detachment; 2 = slight cracking, no detachment; 3 = moderate cracking, no detachment

^bFailure mode: S = substrate, I = intercoat, G = glue

furnace slag. However, the authors noted an additional effect of the coating to be applied. Chlorinated polyvinyl chloride (PVC), for example, performed especially good if the zinc substrate was blast cleaned.

Table 9.12 lists results of changes in adherence of two coatings on aluminium and steel after 500 h in a condensing water environment as a function of the metal pretreatment process. Although the values for the adhesion are higher in the case of the blast cleaned surface, the behaviour after exposure to water was similar for the

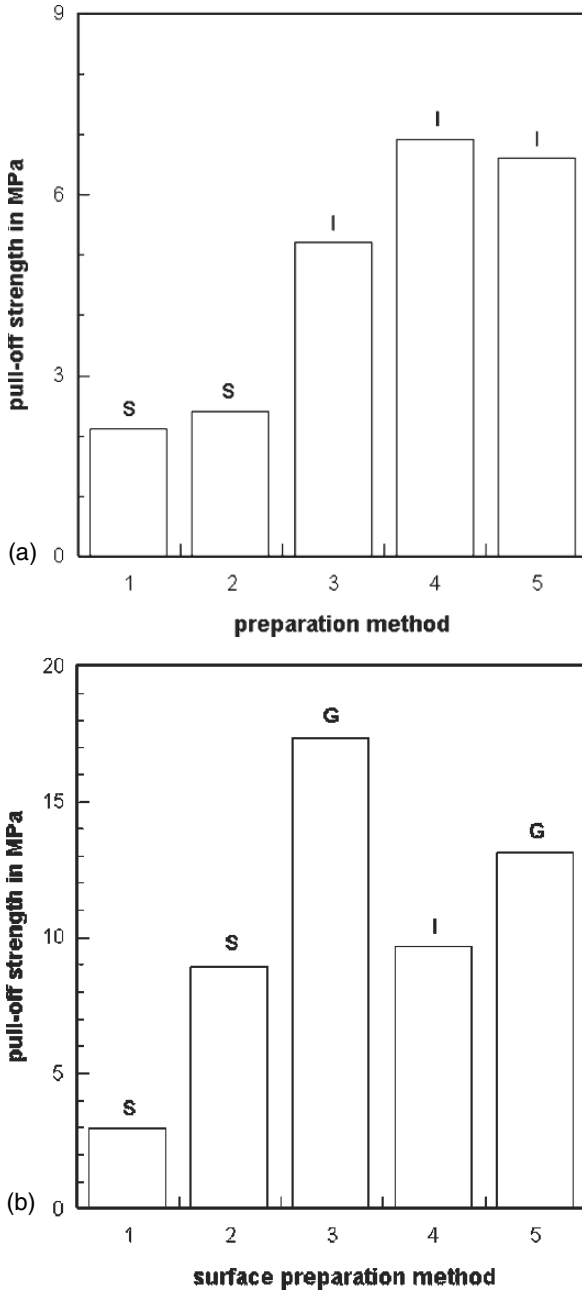


Fig. 9.15 Pull-off strengths after surface preparation-simulated ballast tank conditions. Preparation methods: 1 – hand brush; 2 – needle gunning; 3 – hydroblasting (Dw2); 4 – hydroblasting (Dw3); 5 – dry blast cleaning (Sa 2 1/2); coating thickness: 2 × 125 μm. (a) Coal tar epoxy after 24 months (Allen, 1997); (b) Glass flake epoxy after 36 months (Morris, 2000). See Table 9.11 for “S”, “I” and “G”

Table 9.12 Adherence of coatings after 500 h condensation (Leidheiser and Funke, 1987)

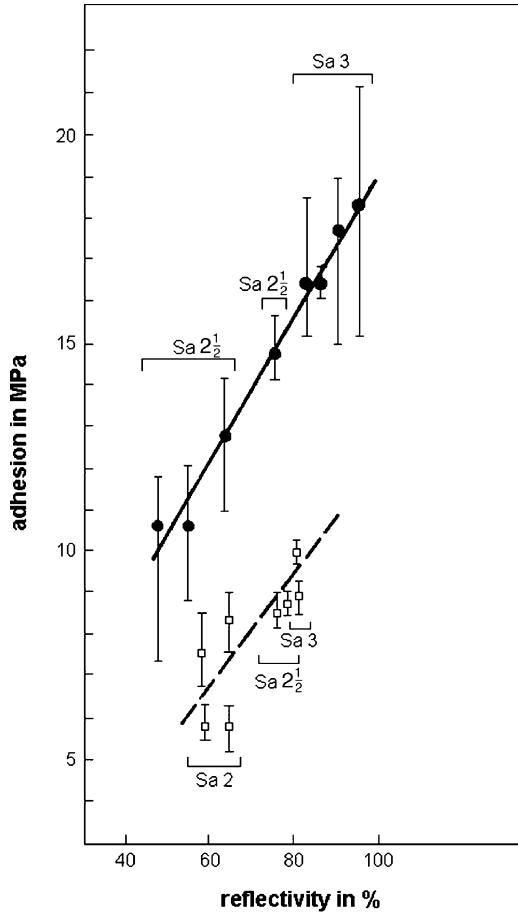
Substrate	Coating	Adhesion before and after water exposure in MPa			
		Degreased		Blast cleaned	
		Before	After	Before	After
Aluminium	Polyurethane	11.4	11.6	27.6	28.2
	Epoxy-polyamide	20.3	22.1	27.6	27.6
Steel	Polyurethane	15.4	3.4	35.9	15.2
	Epoxy-polyamide	19.5	17.4	25.9	21.8

degreased and blast cleaned surfaces. There was very little effect of water exposure for both coatings and for both surface preparation methods in the case of aluminium; both coatings exhibited lower adhesion values after exposure to water for both surface preparation methods in the case of steel.

The effect of cleanliness on the adhesion of thermally sprayed metal coatings to steel substrates is illustrated in Fig. 9.16. Here, substrate cleanliness is characterised through reflectivity. A value of 100% corresponded to the reflectivity of a light grey tile. The higher reflectivity, the higher is surface cleanliness (this relationship holds for a given abrasive material only). It can be seen that high cleanliness promoted high adhesion strength; the relationship was linear for both abrasive types. Another example for the effects of surface cleanliness is illustrated in Fig. 9.17 in terms of surface preparation grade. The relative adhesion of a metal-sprayed coating dropped down to 50%, if the preparation grade was lowered from Sa 3 to Sa 2.

Rider (1987) reported about the bond durability of metals, pretreated with different methods, and adhesives. Wedge style durability tests were conducted, and the durability performance of blast cleaned metallic adherends was compared with standard pretreatments. It was found that blast cleaning at a blasting pressure of $p = 0.45$ MPa led to a notable reduction in the average length of cracks in the adherend-adhesive system. After a root time of 7 h, for example, the crack length was about $l_C = 107$ mm for abrading with distilled water, but it was $l_C = 60$ mm only for blast cleaning. Watts and Dempster (1992), however, who applied wet blast cleaning with aluminium oxide abrasives to adhesively bonded titanium alloys, found that plain blast cleaning did not perform very well; additional preparation steps (anodising and priming) were required to obtain satisfying results. Wedge splitting tests in a corrosive environment were performed by Emrich (2003) for the assessment of adhesion between aluminium substrates and organic adherends. He found that blast cleaning (corundum and glass beads) and subsequent electropolishing reduced the lengths of the cracks in the interface zones between adhesive and substrate compared to samples which were electropolished only. Regarding the two blast cleaning media, the positive effects were stronger for the samples blast cleaned with corundum compared to samples blast cleaned with glass beads. Opposite trends were observed by Emrich (2003) for samples that were blast cleaned and subsequently pickled. In these cases, the pretreatment with corundum and glass beads deteriorated the resistance of the adhesive joint against crack propagation. The shortest crack lengths were measured for the systems where the substrate was pickled only. After an

Fig. 9.16 Effect of substrate cleanliness (reflectivity) on adhesion strength of arc-sprayed aluminium (Bardel, 1974). Parameters: $p = 0.4\text{--}0.6\text{ MPa}$; $d_N = 8\text{--}12\text{ mm}$; $x = 150\text{--}300\text{ mm}$; $\varphi = 60\text{--}90^\circ$. Upper curve: iron grit ($d_p = 100\text{--}900\ \mu\text{m}$), Lower curve: silica sand ($d_p = 600\text{--}1,500\ \mu\text{m}$)



exposure time of about 250 h, however, the influence of the surface preparation methods vanished, and the crack length rested on a stable level of about $l_C = 38\text{ mm}$. The author could also prove that the crack length depended on the surface roughness of the profile. A coarse profile (as achieved after blast cleaning and subsequent pickling) delivered longer cracks than a finer profile (as achieved after blast cleaning and subsequent electropolishing). Emrich (2003) also noted that the deformation behaviour of the adhesive in the wedge splitting test had an additional influence on the results. A rather rigid, less deformable adhesive promoted a quick crack extension.

Bardis and Kedward (2002) performed an investigation into the effects of surface preparation methods on the strength of adhesively bonded composite joints. A double cantilever beam (DCB) test was adapted in order to measure the critical strain energy rates (G_{Ic}) of the bonded systems. Results are displayed in Fig. 9.18. Blast cleaned adherends had higher failure loads and higher G_{Ic} -values than non-blast cleaned ones, though the failure mode did not change. Load displacement curves for the bonded composites also depended on preparation method. Emrich (2003)

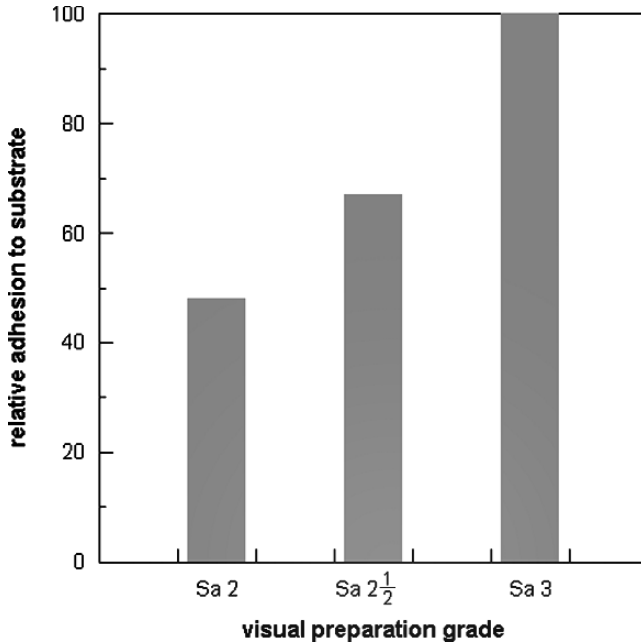


Fig. 9.17 Effects of surface preparation grades on the adhesion strength of metal-sprayed coatings (James, 1984)

estimated the change in the shape of a shear–gliding diagram for adhesive layers. The shear–gliding diagram is comparable with a stress–strain diagram, whereby the stress is replaced by the shear stress, and the strain is replaced by the gliding of the adhesive layer. The results showed that a preparation of the substrate due to blast cleaning (corundum, $p = 0.6$ MPa) and degreasing with acetylene led to a notable change in the shape of the shear–gliding diagram. The use of both methods induced a distinctive drop in shear stress after a number of ten loading cycles in a corrosive medium. However, the shear modulus (ratio between shear stress and gliding) did not change after blast cleaning.

Martin (1997) compared the peel resistance characteristics of pipeline coatings as functions of surface preparation procedures. Results of this study are displayed in Fig. 9.19, which shows results of peel resistance measurements after artificial ageing in a salt spray solution. Blast cleaning could notably improve peel strength, but the level of improvement depended on abrasive type and ageing duration. Aluminium oxide and steel grit delivered very good results, whereas glass beads did not contribute to an improvement in the peel strength. The positive effect of blast cleaning seemed to vanish for long ageing duration; after 16 weeks, the adhesion between coating and substrate was completely deteriorated for the degreased and the glass bead blasted samples. Figure 9.20 illustrates the situation after artificial ageing in a hot water immersion chamber. With the exception of the glass bead blasted samples, the peel resistance curves for the different surface preparation methods ran almost

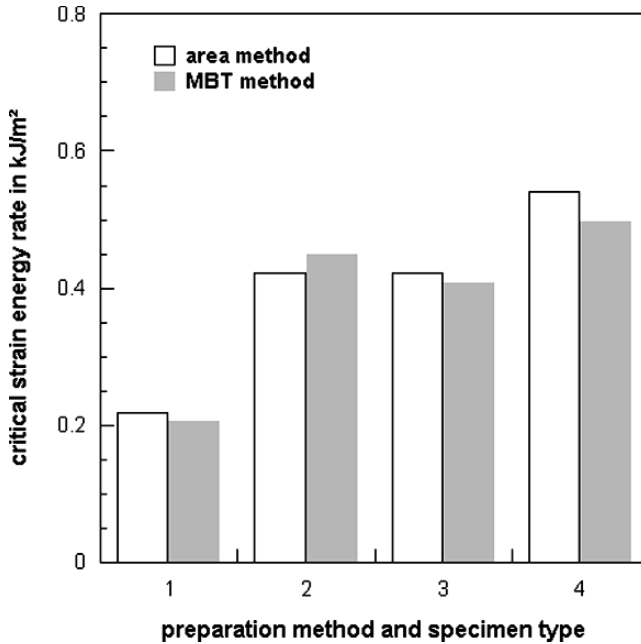


Fig. 9.18 Effect of blast cleaning on the strain energy rate of bonded systems (Bardis and Kedward, 2002). Preparation methods: 1 – RF–RF, no blast cleaning; 2 – RF–RF, blast cleaning; 3 – VB–VB, no blast cleaning; 4 – VB–VB, blast cleaning (RF–RF = release fabric to release fabric orientation; VB–VB = vacuum bag to vacuum bag orientation)

parallel to each other. A gradual reduction in the peel strength with an increase in ageing duration took place. Blast cleaning did not contribute to an improvement in adhesion. However, steel grit showed the best performance among the blast cleaning media in both test situations, and this was contributed to the high roughness at the substrate surface. Substrates with comparative roughness values (glass bead and aluminium oxide) performed quite differently under corrosive environment, and it was concluded that roughness was not the only affecting surface parameter (Martin, 1997). Changes in substrate morphology (contamination) seem to play an important role as well. The worst performance of glass bead can be contributed to the formation of a thin, with Na, Si and Ca, contaminated oxide layer (see Fig. 8.53).

Staia et al. (2000) conducted tests on the adhesion of coatings thermally sprayed on steel substrates. The authors blast cleaned the substrate with aluminium oxide ($d_p = 425\text{--}850\ \mu\text{m}$, $p = 0.34\text{--}0.62\ \text{MPa}$, $\varphi = 75^\circ$) and conducted pull-off tests and interface indentation tests. For the indentation test, they found that critical indentation load, necessary to produce a crack at the interface, as well as the critical length of the crack in the interface between substrate and coating increased if the air pressure increased. Pull-off strength also increased as pressure increased. The authors also found a relationship between air pressure and effects of coating thickness on adhesion. For the rather low air pressure ($p = 0.34\ \text{MPa}$), critical indentation

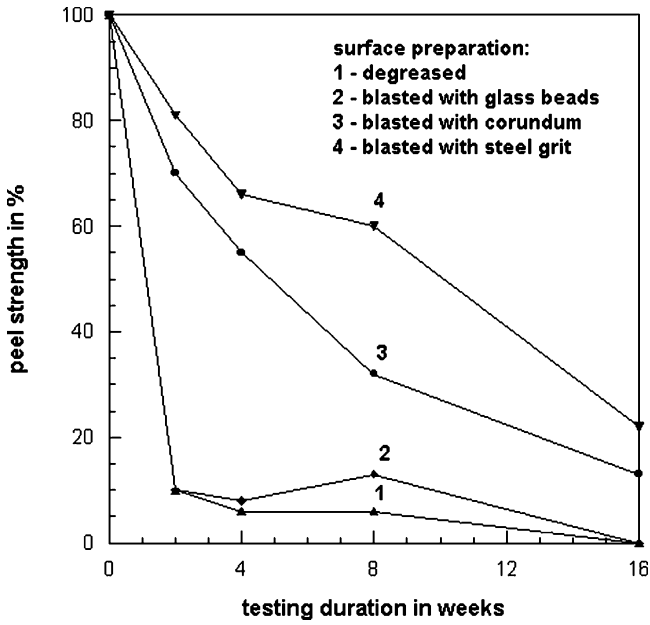


Fig. 9.19 Effects of surface preparation methods on peel resistance of pipeline coatings after salt spray testing (Martin, 1997)

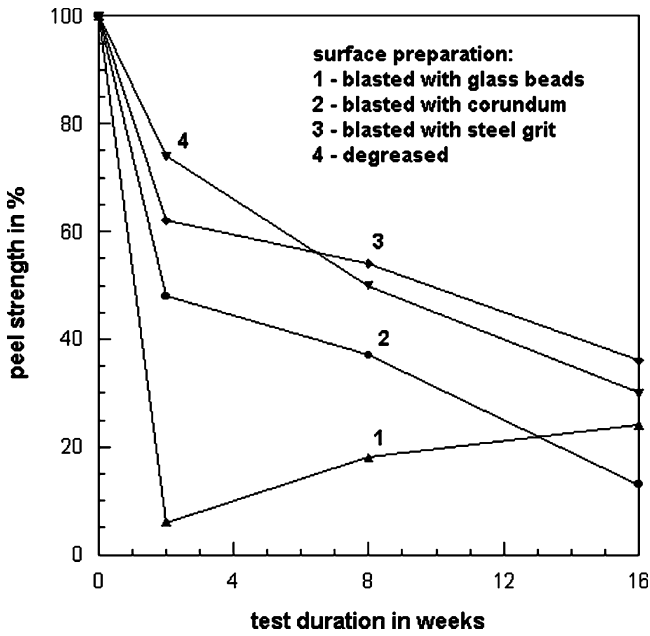


Fig. 9.20 Effects of surface preparation methods on peel resistance of pipeline coatings after immersion tests in 70°C hot water (Martin, 1997)

load depended on coating thickness. This was not the case for the higher air pressures. These results were attributed to the history of residual stress formation in the substrate and the coating material.

Van Rooijen et al. (2005) investigated the effects of chemical and mechanical treatment of steel sheets on the behaviour of fibre–metal laminate (FML). They considered regular steel sheets, molybdenum-enriched steel sheets and aluminium-coated steel sheets. Pretreatment methods were etching and blast cleaning (aluminium oxide, $d_p = 149\text{--}210\mu\text{m}$, $p = 0.2\text{ MPa}$). Peel tests were performed, and it was shown that blast cleaning delivered the highest values for the peel strength (1.62 MPa). The failure mode was cohesive (in the adhesive material) for the blast cleaned samples, which further proved very good adhesion. Etched samples failed at the interfaces between sheet and adhesive; only after a rather long etching time of 3 min, the failure was partially cohesive. Leahy et al. (2003) performed a study into the bonding of fibre reinforced composites to titanium substrates based on a modified wedge test. They deployed blast cleaning (aluminium oxide, mesh 180/220), anodisation, plasma treatment and silicon sputtering as treatment methods. The joints were subjected to 24-hours cycles (wet/dry, cold/hot) for 12 days. The authors reported that a simple blast cleaning was the least successful treatment. The best bond was achieved for the samples treated with a combination of anodisation and subsequent blast cleaning.

Figure 9.21 displays results of furnace cyclic tests on the durability of a multi-layer thermal barrier system. Bond coat surface morphology (not substrate surface

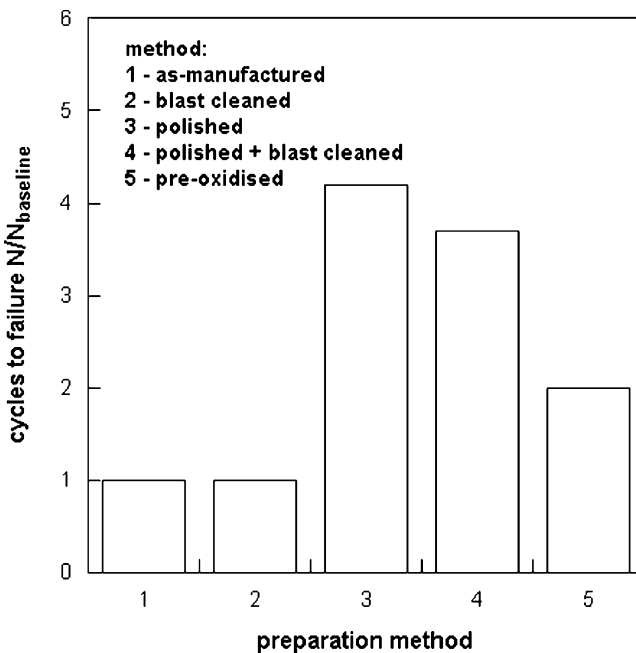


Fig. 9.21 Effects of surface preparation of a bond coat on the failure lifetimes for multi-layer thermal barrier coating systems (Spitsberg et al., 2005). Abrasive type: aluminium oxide

morphology) was varied due to the application of different surface preparation methods, among them combined methods. As the graph clearly shows, the durability was lowest for the systems which were conventionally blast cleaned. Durability could notably be increased if the substrates were treated with a combined method, consisting of polishing and subsequent blast cleaning. Chemical methods also delivered good results. An investigation of the effects of blast cleaning on the durability of thermal barrier coatings (TBS) was also conducted by Xie et al. (2003). The authors blast cleaned a bond coat with aluminium oxide abrasives (grit size 220, $p = 0.2$ MPa, $R_z = 75$ μm) and applied a top coat by means of electron beam physical vapour deposition. The lifetime of the coating and the residual stresses in the thermally grown oxide (TGO) were measured as functions of surface morphology. It was found that the lifetime of the system with the blast cleaned bond coat. The lifetime (thermal spallation cycles) of the systems with blast cleaned bond coats varied over a narrow range of 600 to 750 cycles, whereas the systems with the untreated bond coats featured a wide lifetime range of 190 to 1,917 cycles. This result was attributed to the more consistent surface roughness of the blast cleaned bond coat. Another finding was that the stresses in the thermally grown oxides decreased faster if the bond coat was blast cleaned.

Boue (2005) investigated the effect of surface preparation on the adhesion of coatings to bridge ropes and found that blast sweeping delivered results superior to those measured after simple cleaning. Adhesion strength increased after blast sweeping (e.g. from $\sigma_A = 4.1$ MPa after washing to $\sigma_A = 6.6$ MPa after blast sweeping); percentage of cohesive failure also increased if the ropes were blast swept.

Coating type and thickness also determine the effects of surface preparation methods on pull-off strength. Results were provided by Bordeaux et al. (1991). For TiC-coatings, plasma sprayed on inconel substrates, the authors found that pull-off strength was higher for dry blast cleaned substrates (aluminium oxide, $d_p = 7.4$ μm) compared with machined substrates as long as the coating thickness did not exceed a value of 200 μm . Beyond this thickness value, machined substrates provided better adhesion to the coating. It was also found that the microstructure of the coating was modified if the coating was applied to the machined substrate. Lamellae within the coating were folded due to the rather coarse surface relief. Such foldings resulted in oscillation of the laminations within the coating, which were maximum at the surface and vanished further in the coating.

Loh et al. (2002) found that moisture on the surface of steel substrates affected the adhesion of epoxy to the steel. Results of their measurements are provided in Fig. 9.22. Interface fracture energy steadily degraded with increasing moisture content. For a dry substrate interface, for example, fracture energy was 770 J/m², whereas it was about 50 J/m² only for a moisture content of about 8 wt.%.

For bitumen, pull-off strength depends additionally on temperatures of the substrate and the applied bitumen mass; this was shown by Pawlikowski et al. (1966). Pull-off strength increased if steel substrate temperature rose; pull-off strength was four times higher at a steel temperature of 100°C compared with a steel temperature of 20°C. For a given substrate temperature, pull-off strength only slightly increased with a rise in the temperature of the applied bitumen mass.

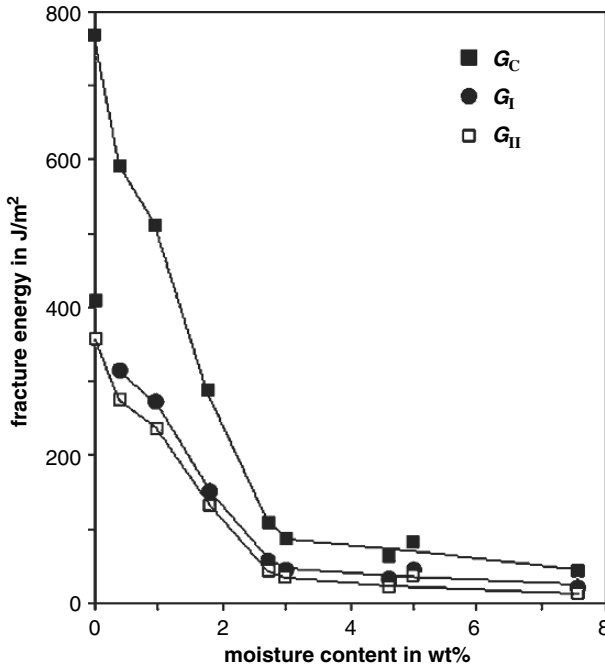


Fig. 9.22 Effect of moisture on the fracture energy of and interface between and epoxy bonded to steel (Loh et al., 2002)

LaBerge et al. (1990) performed tension tests and shear tests to characterise the bond strength of polymer–metal interfaces both for blast cleaned and etched specimens. The Co–Cr substrates were blast cleaned with silica particles ($d_p = 600 - 1,000 \mu\text{m}$), ultrasonically cleaned and then coated with high-density polyethylene (HDPE) powder coatings. The bond strengths for the blast cleaned samples were one order of magnitude lower than those for the etched samples, both for the tension and the shear tests. The authors contributed these results to a high amount of pores in the etched substrates, which promoted interlocking effects between substrate and coating.

Aga and Woldesenbet (2007) investigated the effects of surface preparation on the performance of adhesively bonded graphite/epoxy composites subjected to impact. Although their investigation did not deal with metal substrates, it delivered interesting results in terms of adhesion under impact conditions. The authors performed test with a drop-weight impact machine at different energy levels and estimated the debond areas in the adhesive bond after the testing. The substrate was treated with three surface preparation methods, namely abrading with sandpaper, use of a paper peel plied and blast cleaning ($d_p = 22 \mu\text{m}$, $p = 0.55 \text{ MPa}$). Contact force graphs are shown in Fig. 9.23. The history of the contact forces, but in particular the contact force at the peak of the curves, notably depended on the surface preparation method. The contact force at the peak was highest for the specimen treated with

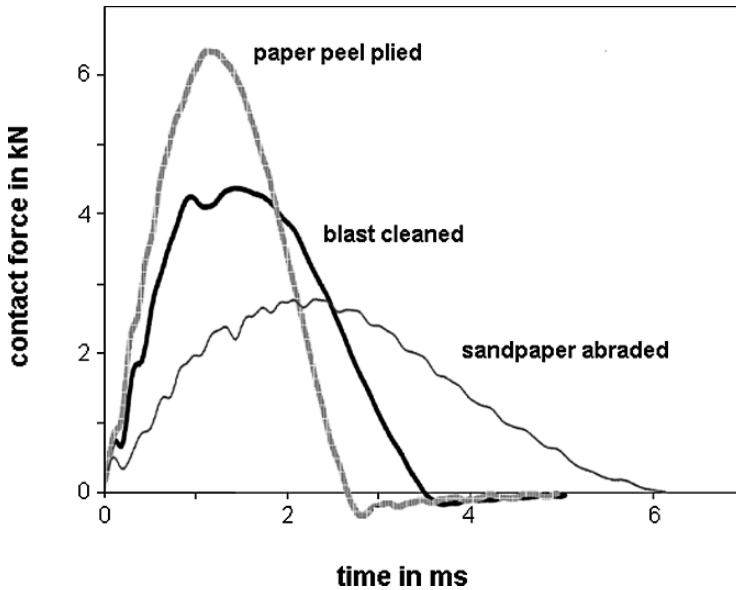


Fig. 9.23 Contact force histories for adhesively bonded graphite/epoxy composite specimens impacted at an energy level of 5.0J (Aga and Woldeesenbet, 2007)

paper peel plied, followed by blast cleaning and treatment with sandpaper. A somewhat different trend was found for the debond areas after the impact tests. Here, blast cleaned samples delivered the largest debond areas, followed by sandpaper treatment and treatment with paper peel plied. The paper-peel ply surface preparation created the most uniform and smoothest surface. The superior performance of the samples treated with that method was contributed to the formation of very low stress concentrations at the uniform, smooth surface.

Sancaktar and Gomatam (2001) performed tests on the strengths of single lap joints of rolled steel. The strength was measured with a tensile testing machine at different crosshead speeds. Both failure load and ultimate displacement were estimated. The results depicted an effect of the viscosity of the adhesive materials. For a low viscosity adhesive (5–7 Pa s), blast cleaning with aluminium oxide ($p = 0.55 \text{ MPa}$) generated the highest values for the failure load (4,200 N) as well as for the ultimate displacement (0.013 mm). For a high viscosity adhesive (170–225 Pa s), the maximum value for the failure load was measured for etched adherends. The authors also proved that the loading rate affected the strength parameters. Strength values were always higher for a loading rate of 1 mm/min compared with the values for a loading rate of 100 mm/min. It turned out that the blast cleaned samples were least sensitive to changes in the loading rate. Surface roughness studies of Rider et al. (1999) established that the application of blast cleaning (aluminium oxide, $d_p = 50 \mu\text{m}$, $m_s = 1.2 \text{ g/cm}^2$) increased the fracture energy of an aluminium-epoxy joint exposed to humid conditions by two orders of magnitude. Whereas an ultra-milled aluminium adherend led to a fracture energy of about $G_{Ic} = 5 \text{ kJ/m}^2$, the blast cleaned aluminium adherend delivered a fracture

energy of about $G_{Ic} = 20 \text{ kJ/m}^2$ (for a crack velocity of 4 mm/s). Neeb et al. (2000) reported on the performance of adhesive bonds. The substrate was aluminium, and the adhesive was a 2-pack epoxy material. The treatment of the substrate included pickling and blast cleaning ($p = 0.6 \text{ MPa}$, $d_N = 3 \text{ mm}$, $\varphi = 90^\circ$). Abrasive materials were glass beads ($d_p = 100\text{--}200 \mu\text{m}$) and corundum ($d_p = 125\text{--}250 \mu\text{m}$). The adhesion was estimated by means of a wedge test. It was found that the substrate treatment method affected the crack length in the joint. Crack length was highest for the samples blast cleaned with glass beads, and it was lowest for the samples blast cleaned with corundum. The authors contributed these results to the conversion rates of the polymers in the joint. The epoxy applied to the aluminium that was blast cleaned with glass beads showed a high conversion rate and a high final cross-linking density (compare Fig. 9.6). This led to a rather brittle adhesion layer. The epoxy applied to the aluminium that was blast cleaned with corundum, in contrast, showed a low conversion rate (compare Fig. 9.6), and it had a high capability of plastic deformation. Liu et al. (2006) conducted a systematic study into the crack growth in sol-gel treated aluminium/epoxy joints prepared with various methods, namely polishing, etching, sanding and blast cleaning (aluminium oxide, $d_p = 50 \mu\text{m}$, $p = 0.62 \text{ MPa}$). Crack growth velocity and strain energy release rate (respectively fracture energy) were assessed by means of a double cantilever beam in a humid environment. The crack growth velocity for a given energy release rate was highest for the polished samples and lowest for the blast cleaned samples. The energy release rate exhibited a strong dependence on the crack growth velocity, which is a known effect for moisture-assisted crack growth. However, the joints formed with the blast cleaned substrates showed the highest values for the energy release rate ($G_{Ic} = 2,615 \text{ J/m}^2$), whereas the lowest value was found for the joints formed with the polished substrate ($G_{Ic} = 440 \text{ J/m}^2$). Minaki et al. (2007) performed a scratch test in order to assess the adhesion of a plated titanium nitride coat. The substrate was blast cleaned with aluminium oxide ($p = 0.2\text{--}0.4 \text{ MPa}$, mesh 700, $\dot{m}_p = 50\text{--}300 \text{ g/min}$, $\varphi = 90^\circ$, $d_N = 8 \text{ mm}$). The authors found that the critical scratch force increased with an increase in air pressure and in blast cleaning time. This result was attributed to the higher values for profile roughness which was believed to promote a better mechanical bond.

Zhang and Zhou (1997) investigated the effects of blast cleaning on the adhesion of diamond coatings applied to tungsten carbide substrates. The adhesion was evaluated through an indentation test. Flaking of the coatings applied to ground substrates was observed at an indentation load of 600 N, whereas the coatings applied to blast cleaned (alumina, mesh 120 to 500, $p = 0.3 \text{ MPa}$) substrates did not show any flaking until the indentation load reached a value of 800 N.

The delay time between blast cleaning and spraying, respectively coating, has a definite effect on the pull-off strength of coatings. Results of systematic investigations were reported by Aapps (1969) for metal-sprayed coatings and by Bullett and Dasgupta (1969) for organic coatings. The results of the authors revealed that the pull-off strength notably dropped for longer delay times if the substrates were exposed to an open environment. A drop in pull-off strength could be prevented if the blast cleaned substrates were stored in a desiccator (Aapps, 1969).

9.2.3 Blast Cleaning Parameters Effects on Adhesion

9.2.3.1 Effects of Blasting Angle

Process parameters also affect adhesion of coatings to substrate. Apps (1969, 1974) and Berndt and Lin (1993) reported about effects of blasting angle and abrasive type on the adhesion of metal-sprayed aluminium coatings. For all situations, optimum values for maximum adhesion could be found at rather high impact angles. In many cases, the optimum blasting angle was at $\varphi = 90^\circ$, but the correct location of the certain optimum angle was affected by the abrasive type. Some results of these investigations are listed in Table 9.13. Amada et al. (1999) found, for aluminium oxide coatings, very low adhesion strengths at low blasting angles, whereas, adhesion was maximum at a blasting angle of $\varphi = 79^\circ$. Ishikawa and Tobe (2003) noted a sensitive relationship between blasting angles and spraying angles. Results of their study are displayed in Fig. 9.24. If both parameters were effectively related to each other, maximum adhesion strength could be achieved. Differences in adhesion strength for different parameter configurations were as high as 300%.

9.2.3.2 Effects of Abrasive Type, Size and Shape

Bahlmann (1982) found that the relative adhesion of organic coatings to steel substrates increased from a value of 1.00 for untreated steel to a value of 1.30 for blast cleaning with round steel grit, and to a value of 6.4 for blast cleaning with irregular chilled casting. Therefore, both hardness and particle shape notably affected adhesion. Similar relationships were reported by James (1984) for thermally sprayed coatings (see Table 9.14). Apps (1974) noted a strong influence of coating thickness on adhesion strength. If, for example, an aluminium coating exceeded a thickness of 200 μm , adhesion to the substrate started to drop. This drop was highly pronounced if copper slag and chilled iron grit were used for blast cleaning, but less important if aluminium oxide abrasive was used.

Varacalle et al. (2006) performed a systematic study into the effects of abrasive types on the pull-off strengths of aluminium, sprayed on a low-carbon steel substrate. Their results, partly listed in Table 9.15, depicted a strong effect. Steel grit delivered the highest adhesion values, whereas chilled iron grit provided the lowest

Table 9.13 Effects of blasting angle and abrasive type on the adhesion of aluminium coatings (Berndt and Lin, 1993); optimum blasting angle designates angles for maximum adhesion strength

Abrasive type	Optimum blasting angle in $^\circ$
New chilled iron grit	90
Used chilled iron grit	90
Worn chilled iron grit	90
Round shot	20
Alumina grit	60
New copper slag grit	40
Worn copper slag grit	30 and 90

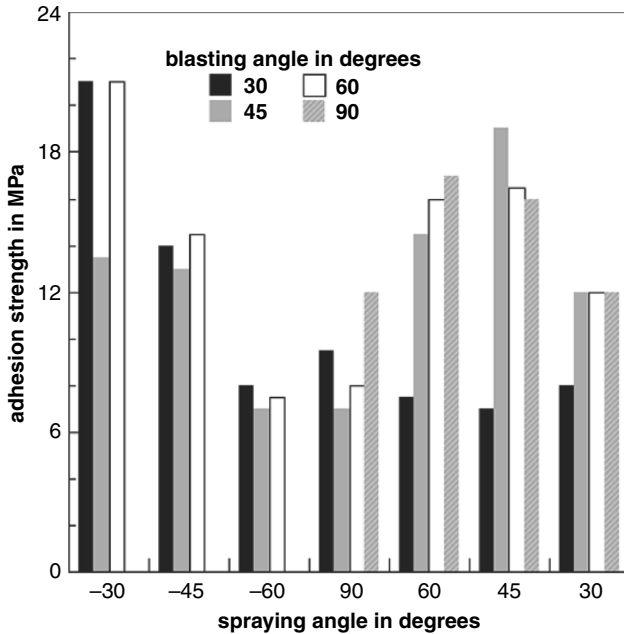


Fig. 9.24 Effects of blast cleaning angle and spraying angle on the adhesion of a metal-sprayed coating (Ishikawa and Tobe, 2003)

pull-off strength values. It is obvious from these studies, that the abrasive type must be adjusted to both substrate and coating properties in order to provide maximum adhesion.

Mannelqvist and Groth (2001) reported about the influence of abrasive type on the adhesion of adhesive epoxy joints to stainless steel panels. Results of their study are displayed in Fig. 9.25. Joint tensile strengths of samples blast cleaned with an irregular abrasive (grit) were notably higher than strengths of samples that were blast cleaned with glass beads. Feist et al. (1988) reported about the effects of numerous abrasive materials on the adhesion of sprayed metal coatings to steel; results are plotted in Fig. 9.26. It can be seen that the abrasive type had a notable

Table 9.14 Effect of abrasive type and coating application on relative adhesion of flame-sprayed zinc and aluminium (James, 1984)

Abrasive	Relative adhesion in %			
	Aluminium		Zinc	
	Arc-sprayed	Flame-sprayed	Arc-sprayed	Flame-sprayed
G 12/24	100	33	28	31
Slag	36	31	23	25
Sand ($d_p = 0.6-1.5$ mm)	72	16	18	17
Sand ($d_p = 0.1-1.0$ mm)	54	-	22	20

Table 9.15 Effect of abrasive type on the adhesion of sprayed aluminium to blast cleaned low-carbon steel (Varacalle et al., 2006)

Abrasive type	Pull-off strength in MPa
Steel grit HG-16	8.21
Steel grit HG-18	8.07
Steel grit HG-25	7.82
Steel grit HG-40	8.48
Copper slag	6.83
Coal slag	7.07
Chilled iron grit	3.62

influence on the pull-off strength values. Even for equal roughness values (say $R_z = 50 \mu\text{m}$), pull-off strength of sprayed aluminium dropped from $\sigma_A = 10 \text{ MPa}$ for basalt or furnish slag to $\sigma_A = 4 \text{ MPa}$ for nickel slag. Similar was the situation for a roughness of $R_z = 80 \mu\text{m}$. Yankee et al. (1991) could also show that abrasive type can play a decisive role in adhesion. For equivalent roughness values and equal cleaning procedures, it was the profile characteristics (thus, the abrasive shape), that determined the adhesion strength. These effects are illustrated in Fig. 9.27. Blast cleaning with aluminium oxide delivered notably higher adhesion strengths. The distinct profile characteristics generated during the blast cleaning with aluminium

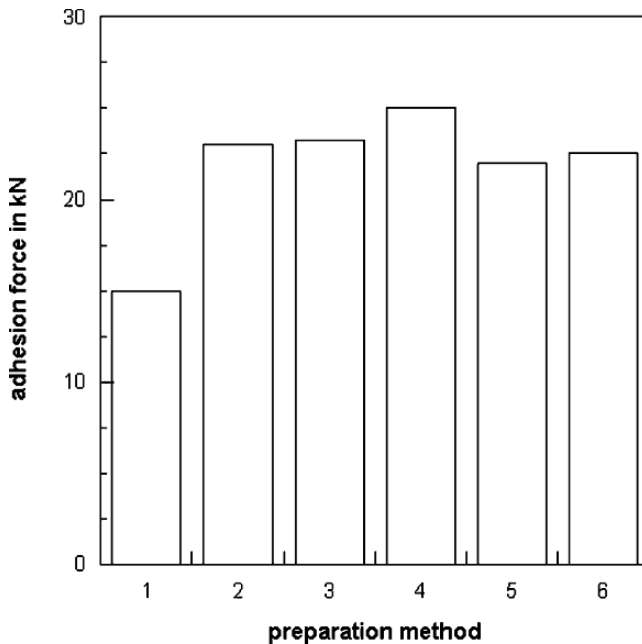


Fig. 9.25 Effects of surface preparation methods on the adhesion of adhesive epoxy joints to steel (Mannelqvist and Groth, 2001). Preparation methods: 1 – degreasing; 2 – Scotch-Brite; 3 – steel brushing; 4 – blast cleaning with grit; 5 – blast cleaning with glass beads; 6 – water blasting

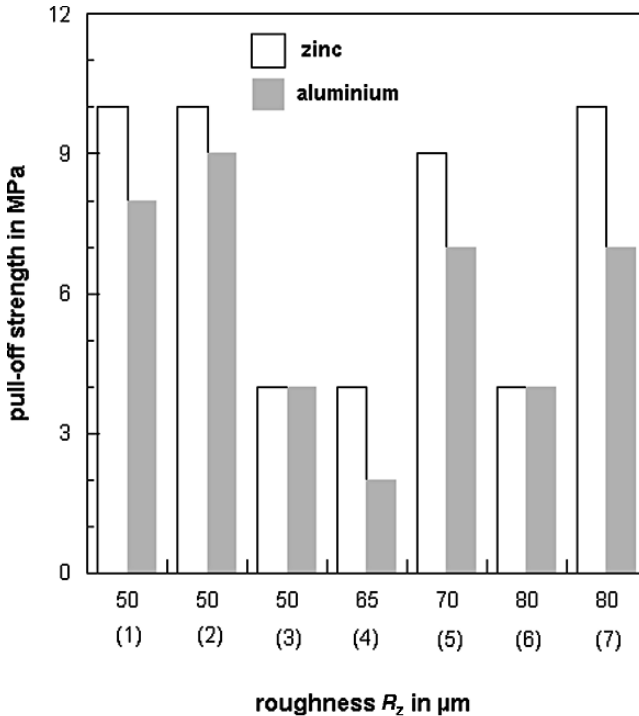


Fig. 9.26 Effects of abrasive materials on the adhesion of metal-sprayed coatings to steel (Feist et al., 1988). Abrasive types: (1) – basalt; (2) – furnace slag; (3) – VV-slag; (4) – electric-furnace slag; (5) – nickel–iron slag; (6) – lead–tin slag. Parameters: $p = 0.6$ MPa; $d_p = 630\text{--}1,250$ μm ; $d_N = 8$ mm; nozzle type: Laval nozzle

oxide seemed to promote a good bond of the thermally sprayed hydroxylapatite coating to the titanium substrate. However, as also shown in Fig. 9.27, intense post-cleaning of the substrate surfaces with ultrasound reduced the differences in adhesion strength, which pointed to additional contamination effects (see Sect. 8.5.3). Brewis et al. (1999) could prove that the preparation of aluminium substrates with carbon dioxide particles (“dry ice blasting”) could notably improve the strength of single-lap shear joints. Joint strength increased from 1,859 N for a degreased surface up to 4,420 N for carbon dioxide blast cleaned surfaces.

Apps (1967) found that the individual influence of the abrasive type to the adhesion of thermally sprayed coatings depended on the blasting angle. Results of his study are plotted in Fig. 9.28. The effect of abrasive deterioration, for example, is much more distinguished if the abrasives were propelled at normal angle. At this angle, even worn steel grit performed better than steel grit that was just used once.

Tests performed on the adhesion of enamel coatings to steel by Sorokin et al. (1977) verified notable effects of particle shape. Steel shot abrasives delivered better bonding conditions than steel grit particles. The coatings were unevenly distributed

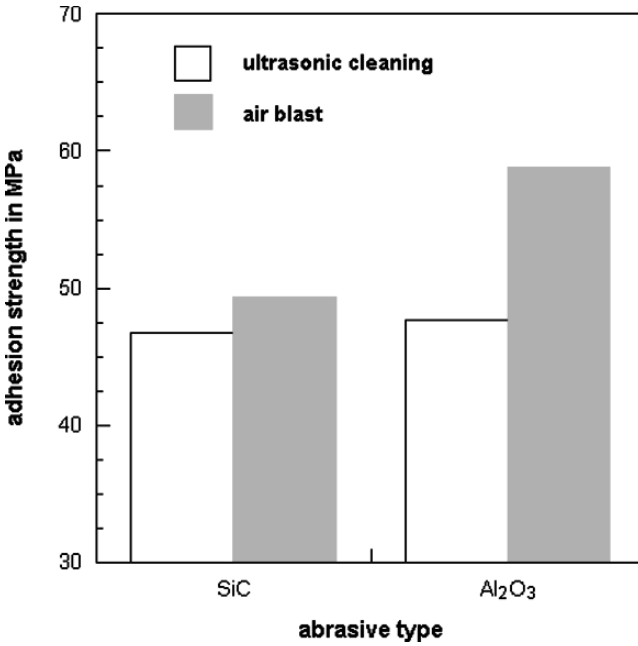


Fig. 9.27 Effects of abrasive type and substrate fine-cleaning on the adhesion of a plasma-sprayed coating to titanium (Yankee et al., 1991)

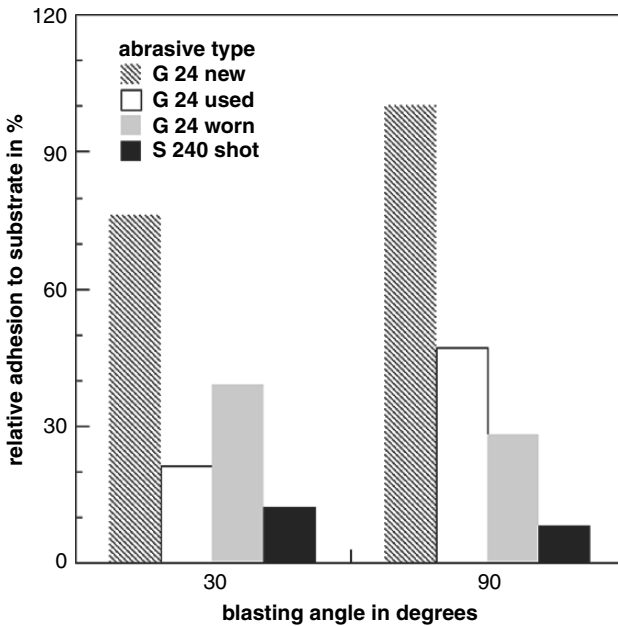


Fig. 9.28 Effects of blasting angle and abrasive quality on the relative adhesion strength of thermally sprayed coatings (Apps, 1967)

over the grit blasted surfaces and peeled during application. Beitelman (2003) applied the abrasive shape designations according to Fig. 2.8 and measured the adhesion performance of organic and metallic coatings to the prepared substrates. Results of this study are provided in Table 9.16. Abrasive particle shape had an influence on the adhesion strength of the metallic coatings, whereas it was insensitive to the adhesion strength of the organic coating. This difference in the coating types was also found for the failure behaviour during the adhesion tests. Particle shape affected the failure type for the metal-sprayed coating, but not that of the organic coating. The amount of cohesion failure of the metal-sprayed coating dropped with a decrease in the angularity of the abrasive particles.

9.2.3.3 Effects of Air Pressure

Apps (1969) performed a systematic study into the effects of blasting pressure variations on the adhesion of metal-sprayed coatings to steel substrates. Although the author noted a certain trend that adhesion increased with an increase in blasting pressure, blasting pressure did not always show a distinct relationship to the adhesion of coatings to steel substrates. An example is illustrated in Fig. 9.29. It seemed that optimum blasting pressure ranges existed which depended on abrasive quality. Worn abrasive materials deteriorated adhesion strength. Sofyan et al. (2005) found an increase in bond between WC-Co coatings and steel if blast cleaning pressure increased.

9.2.3.4 Effects of Stand-off Distance

Apps (1969) performed a systematic study into the effects of changes in stand-off distance on the adhesion of metal-sprayed coatings on steel plates and steel bars, and he did not find any notable trends. The pull-off strength was unaffected by variations in the stand-off distance in the range between $x = 15$ and 90 mm.

9.2.3.5 Statistical Assessment Models

Day et al. (2005) and Varacalle et al. (2006) performed statistical analyses into the effects of numerous process parameters on the adhesion of thermally sprayed coatings to steel substrates. Day et al. (2005) derived the following relationship:

Table 9.16 Abrasive shape effects on the adhesion of coatings to blast cleaned substrates (Beitelman, 2003)

Particle shape ^a	Pull-off strength in MPa		Cohesion failure in %		Adhesion failure in %	
	Organic ^b	Metallic ^c	Organic	Metallic	Organic	Metallic
Very angular	13.3	9.8	100	81	0	19
Angular	13.2	9.4	100	83	0	17
Sub-angular	13.0	9.7	100	86	0	14
Sub-rounded	13.3	8.8	100	45	0	55
Rounded	13.3	8.3	100	44	0	56

^aCrushed steel grit (G-59); see Fig. 2.9 for shape designations

^bZinc-rich organic coating (DFT = 93–130 μm)

^cMetal-sprayed Zn/Al (DFT = 340–500 μm)

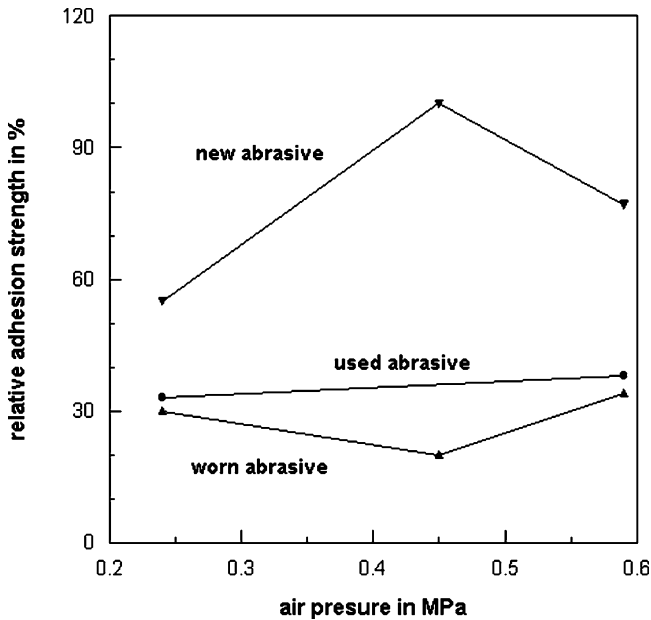


Fig. 9.29 Effects of air pressure and abrasive type on the adhesion of adhesive epoxy joints to steel (Mannelqvist and Groth, 2001)

$$\sigma_A = 38.7 \cdot GN + 76.9 \cdot p + 414.2 \cdot n_S + 182.6 \cdot x + 20.6 \cdot \phi \quad (9.4)$$

In this equation, the adhesion strength is given in psi, the grit number is given in mesh, the pressure is given in psi, the stand-off distance is given in in), and the blasting angle is given in degrees. Varacalle et al. (2006) derived the following relationship for aluminium, sprayed on a low-carbon steel substrate:

$$\sigma_A = 3,518.2 + 457.3 \cdot x + 59.55 \cdot C_G + 8.6 \cdot p_S - 13.78 \cdot x^2 - 0.113 \cdot C_G^2 - 0.012 \cdot p_S^2 \quad (9.5)$$

In that equation, the adhesion strength is given in kPa, the stand-off distance is given in cm, the spray pressure is given in kPa, and the spray gun current is given in A. The equation holds for the use of HG 16 steel grit ($d_p = 1,000\text{--}1,700\ \mu\text{m}$).

9.3 Mechanical Behaviour of Coatings

Surface preparation methods can affect the mechanical behaviour of coatings, mainly those of sprayed metal or ceramic coatings. Examples are provided in Fig. 9.30. In the two graphs, four sections can be distinguished as functions of coating thickness and power density: (1) fusion of the inconel substrate, (2) segmentation

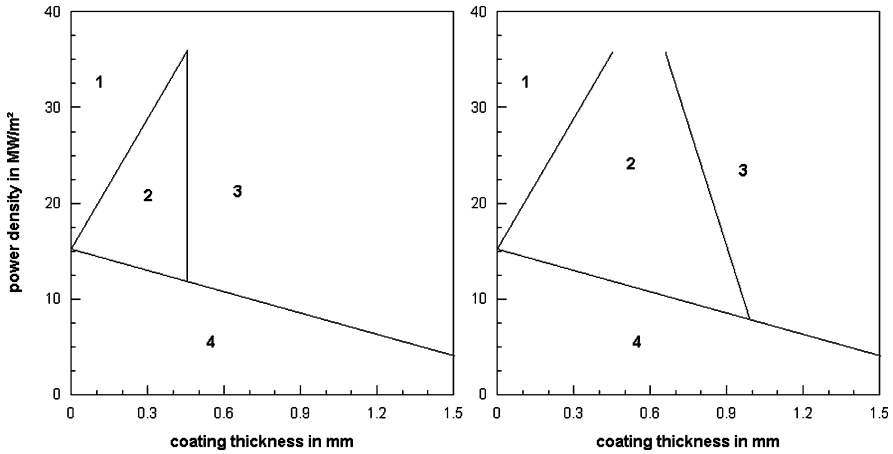


Fig. 9.30 Effects of surface preparation methods on coating failure types during thermal shock tests (Bordeaux et al., 1991). Left: blast cleaning; right: macro-roughening; Failure types: 1 – substrate fusion; 2 – segmentation of coating; 3 – delamination; 4 – no damage

of the coating, (3) delamination and (4) no damage. The no-damage region was not notably affected by the surface preparation method, but the coatings were more sensitive to segmentation if blast cleaning was performed. For blast cleaning, the limit for segmentation was at a coating thickness of about 400 μm , whereas it was at a coating thickness of about 950 μm for the machined substrate. These relationships are of importance for the application of thermal barrier coatings.

Sobiecki et al. (2003) measured the microhardness of tungsten carbide coatings applied to substrates which were prepared with different surface preparation methods, but they did not record any effect.

Bochenin (2005) performed investigation on aluminium coatings deposited by diffusion metallisation on steel substrates. The abrasive material used was iron shot ($d_p = 1,000 \mu\text{m}$); the air pressure was $p = 0.6 \text{ MPa}$. The coated specimens were placed into a furnace, heated to 1,000°C and held for 90 h. The specific weight loss of the coating was defined as a measure for its heat resistance. It was found that heat resistance of the coating could be affected notably due to blast cleaning of the substrate. The heat resistance depended on several blast cleaning parameters. Results are displayed in Fig. 9.31. For the stand-off distance, an optimum value could be detected, whereas heat resistance was highest for a perpendicular blast cleaning angle.

Tolpygo et al. (2001) investigated the behaviour of thermal barrier coatings deposited on (Ni, Pt) Al bond-coat substrates. The samples were cyclically oxidised. Each cycle consisted of 10 h of exposure at 1,150°C, with heating and cooling rates of about 200°C/min. The authors noted that blast cleaning of the substrate with aluminium oxide particles promoted a very high growth rate of the oxide scale. The high oxidation rate was explained by impurities from the blast cleaning

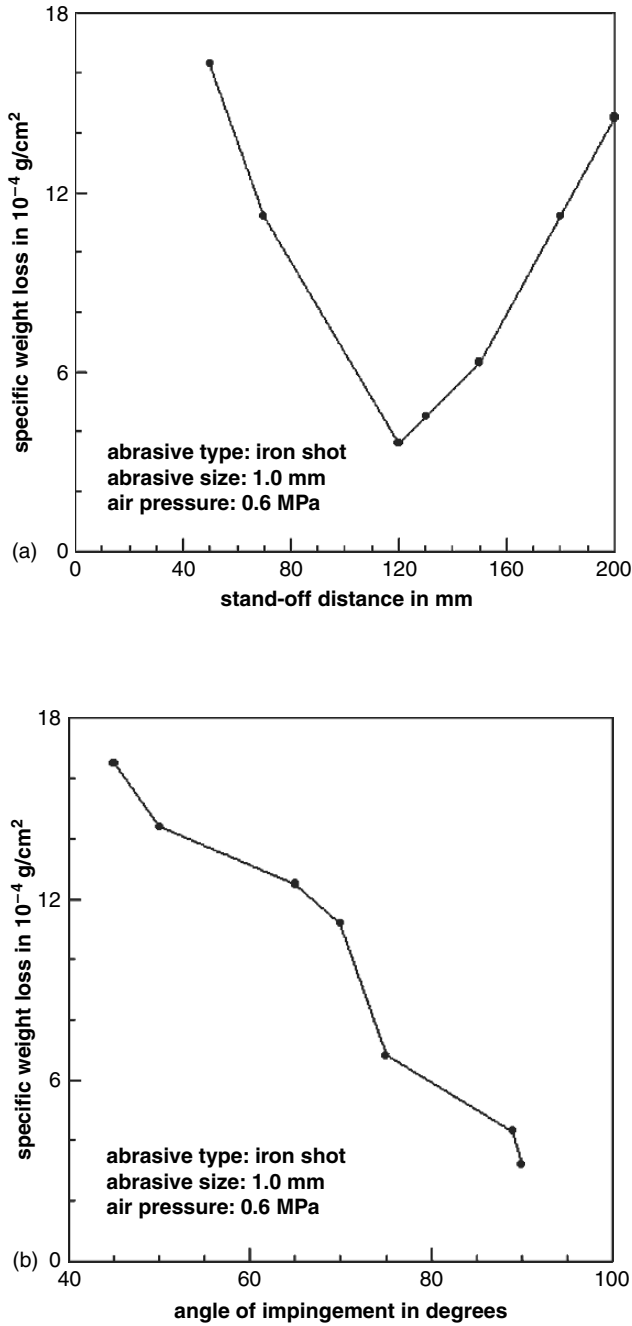


Fig. 9.31 Effects of blast cleaning parameters on the heat resistance of aluminium coatings deposited to a steel substrate (Bochenin, 2005). (a) Effect of stand-off distance; (b) Effect of blasting angle

process (alkali and titanium), which became incorporated into the growing scale and significantly accelerated the oxide growth. The high grow rate resulted in cracking and spalling of the scale followed by a mass decrease after only 30 ten-hour cycles at 1,150°C. The scale formed on the aluminised surfaces had much lower impurity content and a slower growth rate, and they showed an excellent spalling resistance during cyclic oxidation. Based on these results, blast cleaning is expected to have a detrimental effect on the durability of thermal barrier coatings.

A study into the performance of sol-gel-derived coatings over blast cleaned aluminium alloys was conducted by You et al. (2001). The substrate was blast cleaned with aluminium oxide powder ($d_p = 20$ and $100 \mu\text{m}$). The authors found that the coating layer was more uniform for the sampled blast cleaned with the finer abrasives. These coatings also showed a smaller number of cracks after firing compared with the coatings applied over the substrate blast cleaned with the coarser abrasives. The authors attributed these results to effects of substrate roughness.

9.4 Corrosion Protection Performance of Coatings

The corrosion protection performance of organic coatings can be evaluated by means of electrochemical methods. One method that became notably involved in coating testing during the recent years is EIS. The physical and chemical background is complex and beyond the scope of this book. The reader may refer to Baboian (1986). One assessment parameter, however, is the electrical resistance of a coating. If this parameter has high values, corrosion protection capability of the coating is high as well. Studies where effects of different surface preparation methods on the corrosion protection performance of coatings were investigated by means of EIS were conducted by Lin et al. (1992), Santaga et al. (1998), Vesga et al. (2000) and Elsner et al. (2003). Lin et al. (1992) investigated the effects of surface preparation methods on the electrical resistance of rather thin organic coatings. Results of their study are plotted in Fig. 9.32. It appeared that for the coating systems studied, blast cleaning deteriorated the performance of the coatings. The authors contributed this result to areas of “deficient” coating coverage (e.g. peaks of a rough substrate), which occurred at the blast cleaned surfaces.

Figure 9.33 shows results of EIS measurements performed by Vesga et al. (2000) on organic primers applied to blast cleaned steel substrates. The primer behaviour was subdivided into three stages, denoted “R” (resistive), “CR” (capacitive/resistive) and “C” (capacitive) in Fig. 9.33. The value for the resistance at a given time can indicate the state of the primer degradation. The lower this value, the more severe degradation took place. It can be seen that the resistance had rather low values for the primer applied to the wet blast cleaned steel. The resistance of the primer applied to the dry blast cleaned steel was one order of magnitude higher. It was demonstrated that the pore resistance of the primers showed the same qualitative trend over the

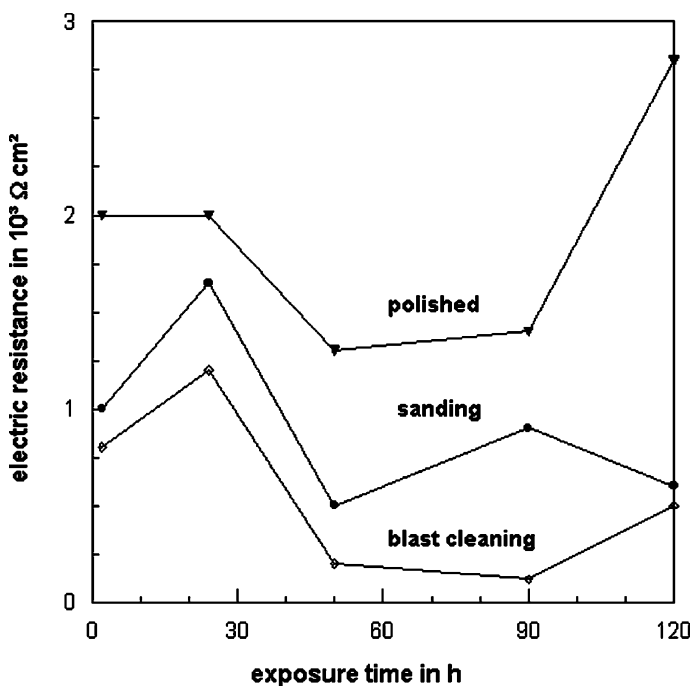


Fig. 9.32 Effects of surface preparation methods on the corrosion protection performance (electric resistance) of thin organic coatings (Lin et al., 1992). Coating: epoxy; substrate: cold-rolled steel; parameters: $p = 0.7$ MPa; $d_p = 150\text{--}300$ μm ; abrasive material: sand

exposure time as the *KIV*-value (see Fig. 9.3). Thus, the resistance seemed to be indicative of the corrosion protective performance of the primer. It can further be seen from the graphs in Fig. 9.33 that the resistive status (“R”) was reached after a shorter period of time for the primer applied to the wet blast cleaned steel substrate. In the status “R”, the primer may swell excessively and irreversibly, taking up extra water and ions from the electrolyte and may be damaged. Vesga et al. (2000) observed that the primer lost adhesion to the substrate in that stage.

Cambruzzi et al. (2005) utilised EIS for the assessment of abraded coating systems. The background of this study is that paint inspectors sometimes claim that a well-adhering primer coat must not be removed during coating repair applications. If this strategy is being followed, the primer is, if not removed, however abraded by the impinging particles. Cambruzzi et al. (2005) applied a special abrasion test to a polyester powder coating and measured the electric resistance after a variety of abrasion cycles. The results shown in Fig. 9.34 depicted a notable deterioration of the corrosion protection performance of the coating. In less than 300 cycles, almost all samples reached values lower than the protection threshold of 10^6 Ω cm². It was observed that the abrasive particle size played an important role in the reduction of the protective properties of the coatings, since the most severe conditions were observed for the coarsest grains.

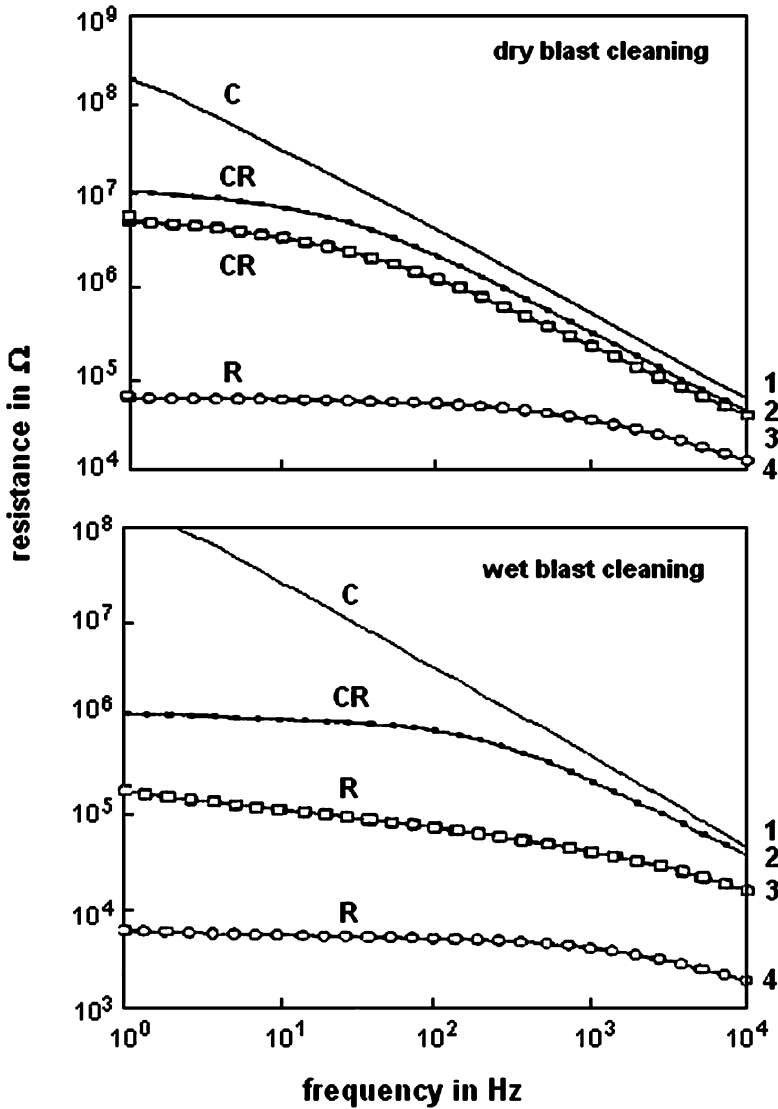


Fig. 9.33 Bode and Nyquist plots for an organic primer applied to blast cleaned steel substrates (Vesga et al., 2000). 1 – initial condition; 2 – after 180 h; 3 – after 360 h; 4 – after 860 h

9.5 Deposition and Transport Phenomena

The deposition rate of a coating is actually not a performance parameter of an already existing coating, but it may affect the behaviour of the final coating. The relationships between deposition rate and blast cleaning processes are not well understood. Heya et al. (2005) performed an investigation in the deposition rate of

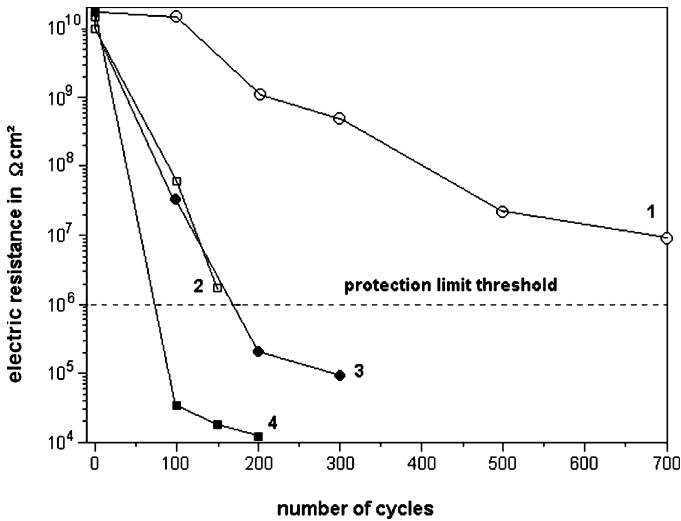


Fig. 9.34 Effects of abrasion damages on the corrosion protection performance (electric resistance) of an organic powder coating (Cambruzzi et al., 2005). Abrasive parameters: 1 – mesh 20–69, 250 g; 2 – mesh 12–20, 250 g; 3 – mesh 20–60, 1000 g; 4 – mesh 12–20, 1000 g)

SiN_x-films on tungsten wires in catalytic chemical vapour deposition (Cat-CVD). If a high deposition rate is required for this process, the temperature is usually increased which is accompanied with a rise in electric power consumption. Heya et al. (2005) blast cleaned the wires with silicon carbide particles with sizes between 10 and 20 μm, and they measured the deposition rates. For a given electric power of 70 kW, the deposition rate increased from about 9 nm/min for untreated wires to 12 nm/min for blast cleaned wires. This result was explained with the higher specific surface of the blast cleaned wires, which was about 35% higher than that of untreated wires.

Another effect worth noting is the influence of profile parameters on the carburisation of turbine blades as witnessed by Locci et al. (2004). Blast cleaning with coarse aluminium oxide provided a more efficient surface condition for carburisation compared with machining and polishing. This effect could directly be contributed to the corresponding surface roughness values. Carbide depth after a 2-hour standard carburisation process was, for example, 33 μm for a roughness of $R_a = 0.34 \mu\text{m}$, but it increased up to 85 μm for a roughness of $R_a = 1.7 \mu\text{m}$.

9.6 Wire Embedment in Polymer Matrices

A special case is the treatment of metal wires, which become embedded in a polymer matrix. The performance of such a reinforced structure depends to a great amount on the bond between steel and matrix. Jonnalagadda et al. (1997)

Table 9.17 Effect of surface preparation on the adhesion between metal wires and a polymer matrix (Jonnalagadda et al., 1997)

Surface preparation of the wires	Interfacial bond strength in MPa	Max. wire displacement in μm	Max. shear stress induced in the matrix in MPa
Untreated	10.5	0.14	5.5
Blast cleaned	30.3	0.11	8.9
Hand sanded	9.0	0.31	4.0
Acid etched	8.1	0.32	4.1

performed investigations into the mechanical contact behaviour of nickel–tungsten wire steels (wire diameter: $150\mu\text{m}$) embedded into a commercial polymer material. The authors utilised different methods for the surface preparation of the wires, including acid etching, blast cleaning and sanding. They estimated interfacial bond strength, wire displacement under load and shear stresses induced in the matrix by means of pull-out tests, interferometry and photoelasticity. Results of these studies are listed in Table 9.17. Blast cleaning significantly increased the bond strength, whereas sanding and acid etching actually reduced the interface strength. Blast cleaning resulted in lower wire displacement and higher interfacial stresses.

9.7 Coating Formation Processes

9.7.1 Spreading and Splashing

The formation of splats from impinging liquid metal or ceramic drops can be accompanied by flattening effects. During flattening, molten material flows radially at high speed, while cooling and possibly solidification of the particle/substrate interface takes place. The first sprayed coating particles, which impinge the substrate, hit a profiled surface that considerably affects the flattening process. Flattening can be characterised by a flattening degree, which is the ratio between final splat diameter and initial splat diameter. It is defined as follows (Moreau et al., 1995):

$$\frac{D_S}{D_0} = f_F \cdot \left(\frac{v_D \cdot \rho_C \cdot D_0}{\eta_C} \right)^{0.2} \quad (9.6)$$

In this equation, D_S is the final splat diameter, D_0 is the initial splat diameter, v_D is the velocity of the impinging drop, ρ_C is the coating material density and η_C is the coating material dynamic viscosity. Figure 9.35 illustrates the effects of different surface preparation methods on the flattening degrees of plasma-sprayed molybdenum on a molybdenum substrate. The flattening degree tended to decrease if substrate roughness increased. It seemed that the constant f_F in (9.6) is a function of

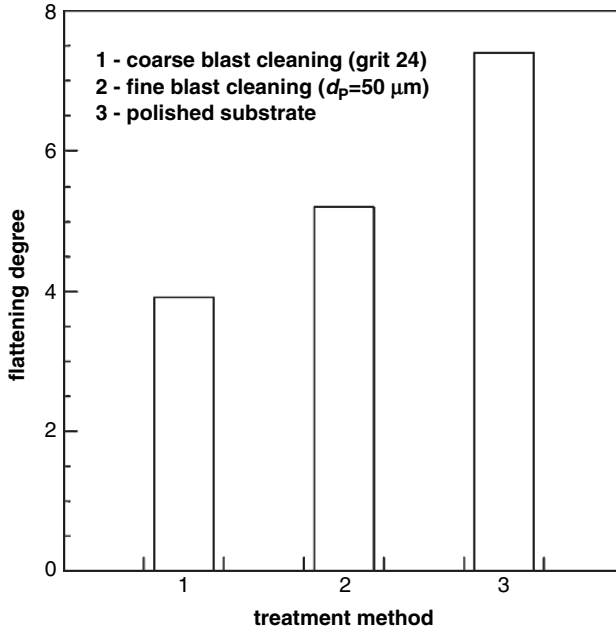


Fig. 9.35 Effects of surface preparation on the flattening degree of plasma-sprayed molybdenum particles (Moreau et al., 1995)

the surface preparation method. It has lower values for the methods which produce rougher surfaces, such as blast cleaning with coarse aluminium oxide particles. Moreau et al. (1995) also found that the surface preparation method affected splat surface and flattening time. The smoother the substrate, the larger the splat surface and the longer the flattening time. The cooling time, in contrast, was found to be longer if the surface was blast cleaned with the coarse aluminium oxide.

Ma et al. (2006) studied the effect of the roughness (R_a) of blast cleaned substrates on the splat formation of HVOF-sprayed tungsten carbide. The results showed that with an increase in roughness, the restriction to flattening was enhanced in a way that the number of spherical to nearly spherical splats reduced, whereas the number of splats with complex morphologies increased.

Liu et al (2006) conducted a study on the spreading kinetics of a wetting liquid for different surface preparation methods, namely polishing, etching, sanding and blast cleaning (aluminium oxide, $d_p = 50 \mu\text{m}$, $p = 0.62 \text{ MPa}$). The substrate was aluminium, and the wetting liquid was hexadecane. Results of their investigations are provided in Fig. 9.36. The relationship between spread radius and time followed a power law:

$$\frac{D_S}{\lambda} \propto t^{k_D} \tag{9.7}$$

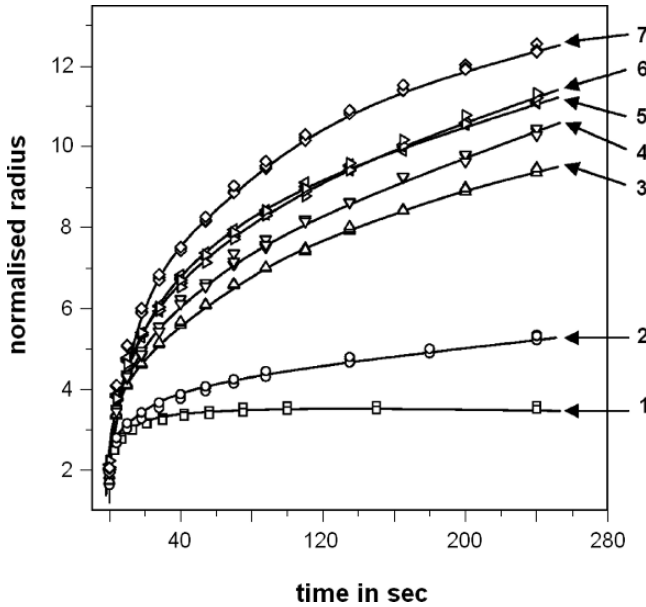


Fig. 9.36 Effects of surface preparation methods on the spreading kinetics of hexadecane on aluminium (Liu et al., 2006). Preparation methods: 1 – polishing; 2 – etching; 3 – sanding (mesh 240); 4 – sanding (mesh 180); 5 - sanding (mesh 120); 6 – blast cleaning; 7 – blast cleaning and subsequent etching. Normalized radius is ratio between spread radius and (drop volume)^{1/3}.

The power exponent k_D was a function of the surface preparation methods. Values for the power exponent are listed in Table 9.18. It can be seen that blast cleaning substrates provided the highest values.

9.7.2 Powder Solidification

Sobolev et al. (2000) conducted a study into the solidification of a WC-Co powder during the high-velocity oxygen-fuel spraying on a copper substrate. They generated two roughness levels on the substrate: smooth due to polishing; rough due to blast cleaning. The authors analysed a number of process parameters of the solidification process, namely solidification rate, cooling rate, thermal gradient, crystal size and

Table 9.18 Spreading kinetics power exponent k_D for different surface preparation methods (Liu et al, 2006)

Surface preparation method	k_D -value
Polishing	0.11
Etching	0.16
Sanding (mesh 240 to 120)	0.27
Blast cleaning (aluminium oxide, $d_P = 50 \mu\text{m}$, $p = 0.62 \text{ MPa}$)	0.29

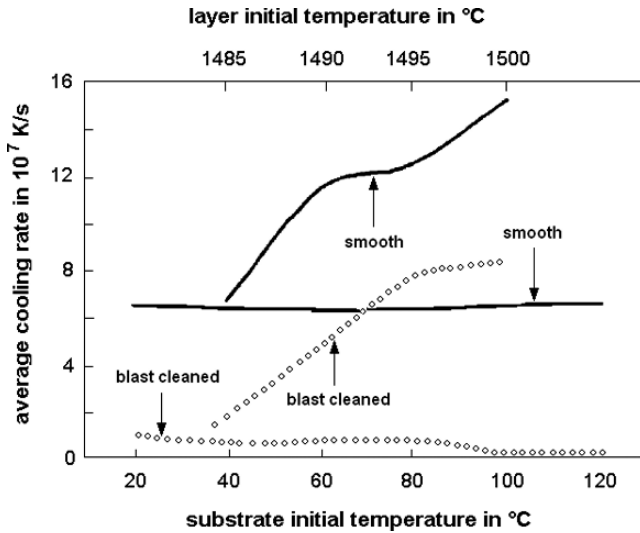


Fig. 9.37 Relationship between solidification rate, initial temperature and surface preparation (Sobolev et al., 2000)

intercrystalline distance. An example is provided in Fig. 9.37. It can be seen that the cooling rate was lower if the powder was sprayed on the blast cleaned substrate. The same trend was found for the thermal gradient and for the solidification rate. The authors also calculated the contact heat transfer coefficient for the substrate-coating interface, and they reported the following values: $6.6 \cdot 10^6 \text{ W}/(\text{m}^2 \cdot \text{K})$ for the polished substrate and $3.33 \cdot 10^6 \text{ W}/(\text{m}^2 \cdot \text{K})$ for the blast cleaned substrate. The basic result was that a rough (blast cleaned) substrate allowed more time for forming a good bond to develop a strongly adherent coating. These results are good examples on how blast cleaning can affect the coating formation process in its very early stage.

9.7.3 Nucleation Processes

Zhang and Zhou (1997) found a relationship between the nucleation density of diamond applied to tungsten carbide and the surface preparation method. It was found that blast cleaning provided the highest nucleation density. The authors related this result to the morphology of the blast cleaned substrate (skewness between -1 and -3 ; compare Fig. 8.53) which provided a suitable contact angle for diamond nucleation.

Machu (1963) discussed the effect of surface treatment on the phosphating process of steel. He pointed out that, from the point of view of electro-chemistry, a high number of activated pits (local anodes) at the steel surface is one preposition

for an efficient phosphating process. The number and the energy state of these pits determine number of crystal nuclei, nucleation rate and crystal growth. Such active pits will be created during mechanical pre-treatment, including blast cleaning. As a result, very fine-grained, thin and corrosion protective phosphate layers are being formed on the steel substrate after blast cleaning.

References

- Abrams, S., 1999, Handling and disposal of waste. *Protect. Coat. Europe*, Vol. 4, 24–29.
- Abukawa, S., Kobayashi, K., Kobayashi, Y. 2004, The relationship of work distortion and surface roughness on grit blasting process. *Proc. Int. Therm. Spray Conf.*, Osaka, 884–889.
- Achtsnick, M., 2005, High performance micro abrasive blasting. *PhD Thesis*, Delft University of Technology, Delft, The Netherlands.
- Achtsnick, M., Geelhoed, P.F., Hoogstrate, A.M., Karpuschewski, B., 2005, Modelling and evaluation of the micro abrasive blasting process. *Wear*, Vol. 259, 84–94.
- Adamson, A.W., 1990, *Physical Chemistry of Surfaces*. 5th edition, John Wiley & Sons, New York.
- Adlassing, K., 1960, Einfluß der Düsenform und des Betriebsdruckes auf die Leistung von Druckluftstrahlanlagen. *Giesserei*, Vol. 47, 211–214.
- Adlassing, K., Jahn, W., 1961, Die Eigenschaften von Strahlmitteln und Düsenwerkstoffen bei Druckluft-Strahlanlagen. *Giesserei*, Vol. 48, 618–622.
- Adler, W.F., 1979, *Erosion: Prevention and Useful Application*. ASTM, New York.
- Adley, D., Trimber, K., 1999, Evaluation of substitute materials for silica sand in abrasive blasting. *J. Protect. Coat. Lin.*, Vol. 16, No. 8, 49–71.
- Aga, Z.A., Woldesenbet, E., 2007, Surface preparation effect on performance of adhesively-bonded graphite/epoxy composites subjected to impact. *J. Adhes. Sci. Technol.*, Vol. 21, No. 1, 51–65.
- Agus, M., Bortolussi, A., Ciccu, R., et al., 1995, Abrasive performance in rock cutting with AWJ and ASJ. *Proc. 8th Am. Water Jet Conf.* (ed. T.J. Labus), Water Jet Technology Association, St. Louis, 31–48.
- Ahland, E.O., 1966, Strömungsvorgänge im vertikalen, feststoffbeladenen Förderrohr mit austretendem Freistrah. *Dissertation*, RWTH Aachen, Germany.
- Alblas, B.P., van Londen, A.M., 1997, The effect of chloride contamination on the corrosion of steel surfaces: a literature review. *Protect. Coat. Europe*, Vol. 2, No. 2, 16–25.
- Albring, W., 1970, *Angewandte Strömungslehre*. Theodor Steinkopf, Dresden.
- Al-Hassani, S.T., 1999, Numerical simulation of multiple shot impact. *Proc. 7th Int. Conf. Shot Peening*, Warsaw, 217–226.
- Allan, S.J., May, R., Taylor, M.F., Walters, J., 1995, The effect of salts on steels and protective coatings. *GEC J. of Research*, Vol. 12, 86–92.
- Allen, B., 1997, Evaluating UHP waterjetting for ballast tank coating systems. *Protect. Coat. Europe*, Vol. 2, No. 10, 38–64.
- Amada, S., Satoh, A., 2000, Fractal analysis of surfaces roughened by grit blasting. *J. Adhes. Sci. Technol.*, Vol. 14, No. 1, 27–41.
- Amada, S., Hirose, T., Senda, T., 1999, Quantitative evaluation of residual grits under angled blasting. *Surf. Coat. Technol.*, Vol. 111, 1–9.
- Anagreh, N., Dorn, L., 2002a, Klebflächenvorbehandlung von Aluminiumoberflächen mit SIP-Haftvermittler. *Materialwiss. Werkstofftech.*, Vol. 33, 657–666.
- Anagreh, N., Dorn, L., 2002b, Einfluss des Strahlmittels auf Oberflächenstruktur und Adhäsionseigenschaften von Aluminiumoberflächen, Teil I+II. *Aluminium*, Vol. 78, 88–94, 194–199.

- Anderson, R.M., Adler, T.A., Hawk, J.A., 1993, Scale of microstructure effects on the impact resistance of Al₂O₃. *Wear*, Vol. 162–164, 1073–1080.
- Andrews, A.F., 2002, Polysiloxane topcoats—product choice for optimum performance. *SSPC 2002—Technical Presentations*, Tampa, FL, November 2002.
- Andrews, D.R., Field, J.E., 1982, The erosion of metals by the normal impingement of hard solid spheres. *J. Phys. D Appl. Phys.*, Vol. 15, 571–578.
- Andrews, E.W., Kim, K.S., 1998, Threshold conditions for dynamic fragmentation of ceramic particles. *Mech. Mater.*, Vol. 29, 161–180.
- Andrews, E.W., Kim, K.S., 1999, Threshold conditions for dynamic fragmentation of glass particles. *Mech. Mater.*, Vol. 31, 689–703.
- Andronikos, G., Valiadis, P., Vassilion, P., 1998, The effect of blasting materials on the corrosion of protected steel in sea water. *Anti-Corr. Meth. Mater.*, Vol. 45, No. 3, 153–157.
- Andronikos, G., Eleftherakos, A., 2000a, Alternative surface preparation methods for ship-repairing. *Proc. PCE Conf. Exhib.*, Technology Publications, Pittsburgh, 253–262.
- Andronikos, G., Eleftherakos, A., 2000b, Alternatives to slag abrasives for blast cleaning of ships. *Protect. Coat. Europe*, Vol. 5, 54–60.
- Andziak, J., Brezezinski, M., 1999, Influence of abrasive blast cleaning and vibrofinishing on surface properties of the stainless steel OH18N9. *Proc. 7th Int. Conf. Shot Blasting*, Warsaw, 60–68.
- Anonymous, 1997, Emission factor documentation for AP-42, Section 13.2.6, abrasive blasting. *Final Report*. EPA Contract 68-D2-0159, September 1997.
- Anonymous, 2002, Advances in high-production robotic UHP water blasting. *Shiprepair and Conversion Technol.*, 2nd Quarter, 35–40.
- Appleman, B.R., 2002, The effect of soluble salts on protective coatings. *SSPC Painting Manual* (ed. R.W. Drisko), Vol. 1, Chapter 2.8, SSPC, Pittsburgh, 119–138.
- Appleman, B.R., 2003, Update on soluble salts: progress and critical issues. *National Shipbuilding Research Program*, Panel SP-3, Key West, FL, 26.2–8, February 2003.
- Appleman, B.R., Weaver, R.E., Boocock, S.K., 1998, User's guide to selecting abrasives. *J. Protect. Coat. Lin.*, Vol. 15, 89–99.
- Apps, R.L., 1967, The effect of grit blasting on the bond strength of flame sprayed aluminium coatings on mild steel. *Proc. 2nd Met. Spray Conf.*, Birmingham, Institute of Welding.
- Apps, R.L., 1969, Grit blasting versus bond strength in metal spraying. *Final Report*, The Welding Institute, Cambridge.
- Apps, R.L., 1974, The influence of surface preparation on the bond strength of flame-sprayed aluminium coatings on mild steel. *J. Vac. Sci. Technol.*, Vol. 11, 741–746.
- Aquaro, D., Fontani, E., 2001, Erosion of ductile and brittle materials. *Meccanica*, Vol. 36, 651–661.
- Arnold, J.C., Hutchings, I.M., 1989, Flux rate effects in the erosive wear of elastomers. *J. Mater. Sci.*, Vol. 24, 833–839.
- Arnold, J.C., Hutchings, I.M., 1992, A model for the erosive wear of rubber at oblique impact angles. *J. Phys. D: Appl. Phys.*, Vol. 25, A222–A229.
- Arnold, J.C., Hutchings, I.M., 1993, Erosive wear of rubber by solid particles at normal incidence. *Wear*, Vol. 161, 213–221.
- Askheim, E., Nokleby, J.O., Carlsson, L., Palm, M., 2001, Why do paints crack? *Protect. Coat. Europe*, Vol. 6, No. 3, 49–55.
- Asthana, R., Sobczak, N., 2000, Wettability, spreading, and interfacial phenomena in high-temperature coatings. *JOM*, Vol. 52, No. 1, e-supplement.
- Averchenko, P.A., Pleskach, V.M., Yurchenko, A.D., Kolesnik, R.I., 1970, Increasing the erosion stability of enamel coatings. *Glass Ceramics*, Vol. 27, No. 10, 342–344.
- Baboiian, R., 1986, *Electrochemical and Technical Corrosion Engineering*. NACE, Houston.
- Badawi, K., Bielle, J., Castex, L., Giraudeau, A., 1986, Influence of sand blasting parameters on the geometrical and mechanical characteristics of 1010 steel sand blasted surfaces. *Advances in Surface Treatments: Technology—Applications—Effects*, Pergamon Press, Oxford, 229–241.

- Bae, H.J., Baek, J.J., Lee, C.S., Shin, C.S., Lee, B.H., Shin, S.R., Beak, K.K., Kim, K.S., 2007, Improvement of blasting productivity by optimizing blasting-related operation parameters. *PACE 2007*, Dallas, TX, February 11–14, 2007.
- Baek, K.H., Park, C.S., Kim, K.H., Chung, M.K., Park, J.H., 2006, Effect of blasted surface contaminants on coating performance. *Corrosion 06*, San Diego, NACE.
- Bahadur, S., Badruddin, R., 1990, Erodent particle characterization and the effect of particle size and shape on erosion. *Wear*, Vol. 138, 189–208.
- Bahbou, M.F., Nysten, P., Wigren, J., 2004, Effect of grit blasting and spraying angle on the adhesion strength of a plasma-sprayed coating. *J. Thermal Spray Technol.*, Vol. 13, No. 4, 508–514.
- Bahlmann, W., 1978, Das richtige Einwegstrahlmittel für das Freistrahlen von Stahlbauten. *Ind. Lackierbetrieb*, Vol. 46, No. 10, 337–341.
- Bailey, A.B., Hiatt, J., 1972, Sphere drag coefficients for a broad range of Mach and Reynolds numbers. *AIAA J.*, Vol. 10, 1436–1440.
- Balasubramanian, B., 1998, Computational modeling of brittle impact erosion mechanisms. *Master Thesis*, West Virginia University, Morgantown, WV, USA.
- Balcar, G.P., 1986, Impact process engineering: a key to success. *Impact Surface Treatment* (ed. S.A. Meguid), Elsevier Appl. Sci. Publ., London, 250–257.
- Baldan, A., 2004, Adhesively-bonded joints and repairs in metallic alloys, polymers and composite materials: adhesives, adhesion theories and surface pretreatment. *J. Mater. Sci.*, Vol. 39, 1–49.
- Ballard, R.L., Sailer, R.A., Larson, B., Soucek, M., 2001, Fracture toughness of inorganic-organic hybrid coatings. *J. Coat. Technol.*, Vol. 73, No. 913, 107–114.
- Bandaru, R.K., 2004, Particle breakage in sand blasting due to impact on ductile materials. *MS Thesis*, West Virginia University, Morgantown, WV, USA.
- Bardal, E., 1973, The effect of surface preparation on the adhesion of arc- and flame-sprayed aluminium and zinc coatings to mild steel. *Proc. 7th Int. Met. Spraying Conf.*, Welding Institute, Cambridge, 215–223.
- Bardal, E., Molde, P., Eggen, T.G., 1973, Arc and flame sprayed aluminium and zinc coatings on mild steel: bond strength, surface roughness, structure and hardness. *Br. Corros. J.*, Vol. 8, 15–19.
- Bardis, J.D., Kedward, K.T., 2002, Surface preparation effects on mode I testing of adhesively bonded composite joints. *J. Compos. Technol. Res.*, Vol. 24, 30–37.
- Barkoula, N.M., 2002, Solid particle erosion behaviour of polymers and polymeric composites. *IVW-Schriftenreihe*, Band 29, Inst. für Verbundwerkstoffe GmbH, Kaiserslautern, Germany.
- Barkoula, N.M., Karger-Kocsis, J., 2002, Processes and influencing parameters of the solid particle erosion of polymers and their composites. *J. Mater. Sci.*, Vol. 37, 3807–3820.
- Barnett, K., Burgess, R.A., 2007, Factors influencing anchor profile. *PACE 2007*, Dallas, TX, February 11–14, 2007.
- Basin, V.E., 1984, Advances in understanding the adhesion between solid substrates and organic coatings. *Prog. Org. Coat.*, Vol. 12, 213–250.
- Bates, R.L., Jackson, J.A., 1980, *Glossary of Geology*. Amer. Geol. Inst., Falls Church.
- Baumann, M., 2003, Korrosions- und Beschichtungsschäden an Stahlwasserbauten. 2. *Tagung Korrosionsschutz in der maritimen Technik*, German. Lloyd, Hamburg, 124–143.
- Baer, D.R., Wagner, D.K., 1973, Effects of surface condition on the transport properties of tungsten. *J. Low Temp. Phys.*, Vol. 13, No. 5/6, 445–469.
- Beck, C., Arndt, U., 1996, Tolerierung und Messung der Rauheit gestrahlter Oberflächen. *Strahlmittel und Strahlverfahrenstechnik*, Seminarunterlagen, IKS Dresden, Germany, March 1996.
- Beitelman, A., 2003, Recycling steel grit. *Protect. Coat. Europe*, Vol. 19, No. 7, 56–59.
- Bellmann, R., Levy, A., 1981, Erosion mechanism in ductile metals. *Wear*, Vol. 70, 1–27.
- Belloy, E., Thurre, S., Walckiers, E., Sayad, A., Gijs, M.A., 2000, The introduction of powder blasting for sensor and microsystem applications. *Sens. Actuators*, Vol. 84, 330–337.

- Belsole, R.J., Nolan, M., Eichberg, R.D., 1982, Sandblasting injury of the hand. *J. Hand Surg.*, Vol. 7, No. 5, 523–525.
- Beltov, S., Assersen, N., 2002, Shipyard blasting and painting facilities. *J. Protect. Coat. Lin.*, Vol. 19, No. 7, 47–48.
- Bendler, H., 1983, *Technisches Handbuch Verdichter*. VEB Verlag Technik, Berlin.
- Berg, J.C., 1993, *Wettability*. Marcel Dekker, New York.
- Berg, J.C., 2002, Semi-empirical strategies for predicting adhesion. *Surfaces, Chemistry and Applications* (eds. M. Chaudhury, A.V. Pocius), Elsevier, Amsterdam, 1–73.
- Bergmann, C.P., 1994, Influence of the substrate roughness on the adherence of plasma sprayed coatings. *Proc. 7th Int. Therm. Spray Conf.*, Boston, MS, June 20–24, 683–686.
- Berndt, C.C., Lin, C.K., 1993, Measurement of adhesion for thermally sprayed materials. *J. Adhes. Sci. Technol.*, Vol. 7, 1235–1264.
- Besztercey, G., Karger-Kocsis, J., Szaplónczay, P., 1999, Solid particle erosion of electrically insulating silicon and EPDM rubber compounds. *Polymer Bull.*, Vol. 42, 717–724.
- Beverloo, W.A., Leniger, H.A., van de Velde, J., 1961, The flow of granular solids through orifices. *Chem. Eng. Sci.*, Vol. 15, 260–269.
- BGR 132, 2003, Vermeidung von Zündgefahren infolge elektrostatischer Aufladungen. Berufsgenossenschaft, Germany, 2003.
- BGV D26, 1999, *BG-Vorschrift Strahlarbeiten*. Steinbruchs-Berufsgenossenschaft, Langenhagen, Germany.
- Bigos, J., 1959, Anchor pattern profile and its effect on paint performance. *Corrosion*, Vol. 15, No. 8, 46–50.
- Binder, G., 2001, Arbeits- und Umweltschutz bei Korrosionsschutzarbeiten. *Mitt. Bundesanstalt Wasserbau*, No. 83, 73–81.
- Binder, G., 2003, Examination of accelerated laboratory tests for corrosion protection. *Protect. Coat. Europe*, Vol. 8, No. 11, 8–16.
- Birley, S.S., Owens, A., 1979, Surface stresses induced by grit blasting. *Anti-Corros.*, Vol. 26, No. 7, 5–7.
- Bitter, J.G., 1963, A study of erosion phenomena, part I+II. *Wear*, Vol. 9, 5–21 and 169–190.
- Björgum, A.J., Knudsen, O.O., Kvernbråten, A.-K., Johnsen, R., 2007, Repair coating systems for bare steel – effect of pre-treatment and conditions during application and curing. *NACE Corrosion Conference*, Houston, Paper 0712.
- Bloch, H.P., 1995, *A Practical Guide To Compressor Technology*. McGraw-Hill, New York.
- Blomquist, P.A., 1997, Simultaneous three-edge pre-weld cleaning. *J. Ship Production*, Vol. 13, No. 4, 242–257.
- Bochenin, V.I., 2005, A radioisotope technique for estimation of heat resistance of aluminium coatings after shot blasting. *Russ. J. Nondestructive Test.*, Vol. 41, No. 12, 775–777.
- Bockenheimer, C., Valeske, B., Possart, W., 2002, Network structure in epoxy aluminium bonds after mechanical treatment. *Int. J. Adhes. Adhesives*, Vol. 22, 349–356.
- Bohl, W., 1989, *Technische Strömungslehre*. 8. Auflage, Vogel-Verlag, Würzburg.
- Böhm, H., Betz, S., Ball, A., 1990, The wear resistance of polymers. *Tribol. Int.*, Vol. 23, No. 6, 399–406.
- Bond, F.C., 1953, Work indexes tabulated. *Trans. AIME Mining Eng.*, 315–316.
- Bond, F.C., 1961, Crushing and grinding calculations, part I and II. *Br. Chem. Eng.*, Vol. 6, 378–385, 543–548.
- Bond, S.D., Martin, J.W., 1984, Surface recrystallization in a single crystal nickel-based superalloy. *J. Mater. Sci.*, Vol. 19, 3867–3872.
- Boocock, S.K., 1992, The effect of abrasives on coating performance. *J. Protect. Coat. Lin.*, Vol. 9, No. 9, 52–61.
- Boocock, S.K., 1994, SSPC research on performance testing of abrasives and salt retrieval techniques. *J. Protect. Coat. Lin.*, Vol. 11, No. 3, 28–39.
- Bordeaux, F., Sait-Jacques, R., Moreau, C., Dallaire, S., Lu, J., 1991, Thermal shock resistance of TiC coatings plasma-sprayed on macroroughened substrates. *Proc. 4th Nat. Therm. Spray Conf.*, Pittsburgh, PA, May 4–10, 127–134.

- Bosshard, R.G., Fritchman, T.T., 1992, Definition of blast pressure in air-operated peening machines. *The Shot Peener*, Vol. 6, No. 3, 20–21.
- Bothen, M., 2000, *Mikro-Abrasive Druckluftstrahlen*. Verlag Köster, Berlin.
- Boue, A., 2005, Eignungsprüfung von Beschichtungssystemen für Brückenseile. *Korrelation von Labortests mit Praxisbedingungen im schweren Korrosionsschutz*, Workshop-Unterlagen, Gesellschaft für Korrosionsschutz e.V., Frankfurt am Main, 98–107.
- Bowden, F.P., Tabor, D., 1964, *The Friction and Lubrication of Solids*, Part II, Clarendon Press, Oxford.
- Branco, J.R., Gansert, R., Sampath, S., Berndt, C.C., Herman, H., 2004, Solid particle erosion of plasma sprayed ceramic coatings. *Mater. Res.*, Vol. 7, No. 1, 147–253.
- Brantley, C.D., Reist, P.C., 1994, Abrasive blasting with quartz sand: factors affecting the potential for incidental exposure to respirable silica. *Am. Ind. Hyg. Assoc. J.*, Vol. 55, 946–952.
- Brauer, H., 1971, *Grundlagen der Einphasen- und Mehrphasenströmung*. Sauerländer-Verlag, Aargau.
- Brauer, H., Kriegel, E., 1963, Untersuchungen über den Verschleiß von Kunststoffen und Metallen. *Chemie-Ing.-Technik*, Vol. 35, 697–707.
- Brauns, E., Determann, H., Kalla, U., 1964, Einfluß der Oberflächenvorbehandlung von Stahl auf das Verhalten von Anstrichen in Seewasser. *Stahl Eisen*, Vol. 84, No. 17, 1082–1087.
- Breinsberger, J., Koppelman, J., 1982, Verhalten von Dreischichtlackierungen im Steinschlagtest. *Farbe Lack*, Vol. 88, 916–920.
- Brevoort, G.H., 1988, Abrasive blasting and salt contamination: a case history. *J. Protect. Coat. Lin.*, Vol. 5, No. 5, 24–71.
- Brewis, D.M., Critchlow, G.W., Curtis, C.A., 1999, Cryoblasting as a pretreatment to enhance adhesion to aluminium alloys: an initial study. *Adhes. Adhesives*, Vol. 19, 253–256.
- Briscoe, B.J., Sinha, S.K., 2003, Scratch resistance and localised damage characteristics of polymer surfaces—a review. *Materialwiss. Werkstofftech.*, Vol. 34, 989–1002.
- Broughton, W.R., Lodeiro, M.J., 2002, Review of surface characterisation techniques for adhesive bonding. *NPL Report MATC(A)66*, National Physics Laboratory, Teddington, UK, February 2002.
- Broughton, W.R., Lodeiro, M.J., 2003, Assessment of characterisation techniques for evaluating surface treatments for adhesive bonding. *NPL Report MATC(A)140*, National Physics Laboratory, Teddington, UK, June 2003.
- Buhlmann, S., 1970, Ein stochastisches Modell der Prallzerkleinerung. *Chemie-Ing.-Techn.*, Vol. 42, No. 5, 277–281.
- Buhrke, H., Kecke, H.-J., Richter, H., 1989, *Strömungsförderer*. Vieweg & Sohn, Braunschweig.
- Bullard, J., Corbett, W.D., Mozelewski, F.A., 2002, Corrosion protection of limited access areas common to bridge structural steel design. *J. Protect. Coat. Lin.*, Vol. 19, No. 9, 46–50.
- Bullett, T.R., Dasgupta, D., 1969, Characterization of blast-cleaned surfaces and its relation to paint performance. *J. Oil Colour Chem. Assoc.*, Vol. 52, 1099–1129.
- Bullett, T.R., Prosser, J.L., 1972, Measurement of adhesion. *Prog. Organ. Coat.*, Vol. 1, 45–71.
- Burgess, R., Laube, D., Gijs, M.A., 1999, Sidhwa, A., Spinner, C., Zheng, S., Chew, T., Gandy, T., Melosky, S., Vetier, J., 2002, Post blast component cleaning techniques to reduce particle generation in etch and deposit chambers. *Mater. Res. Soc. Symp. Proc.*, Vol. 716, 549–554.
- Calabrese, C., Allen, J.R., 1978, Surface characterization of atmospherically corroded and blast cleaned steel. *Corrosion*, Vol. 34, 331–338.
- Calabrese, S.J., Murray, S.F., 1982, Methods of evaluating materials for icebreaker hull coatings. *Selection and Use of Wear Tests for Coatings* (ed. R.G. Bayer), ASME, New York, 157–173.
- Calboreanu, G., 1991, Influence of target hardness on impact damage of shot. *Wear*, Vol. 150, 315–329.
- Cambruzzi, A., Rossi, S., Deflorian, F., 2005, Reduction on protective properties of organic coatings produced by abrasive particles. *Wear*, Vol. 258, 1696–1705.
- Cannon, L.J., Maurer, K.F., Woodmansee, J.T., Arena, S.L., McConnell-Meachen, M., 1996, Keeping workers' blood lead levels down on bridge repainting jobs. *J. Protect. Coat. Lin.*, Vol. 12, 64–69.

- Carew, T., Ghita, O., Whelan, P.F., 2001, A vision system for detecting paint faults on painted slates. *Int. Conf. Control, Autom. Syst.*, IEEE, New York.
- Carlson, J.R., Townsend, T.G., 1998, Management of solid waste from abrasive blasting. *Prac. Period. Hazard., Toxic, Radioact. Waste Manage.*, 72–77.
- Carlson, J.R., Townsend, T.G., 1999, Assessment of waste abrasive blasting media from ship maintenance facilities and sandblasting contractor sites. *Proc. CCSE/ASCE Environ. Eng. Conf.*, 651–660.
- Carter, G., Bevan, I.J., Katardjiev, I.V., Nobes, M.J., 1991, The erosion of copper by reflected sandblasting grains. *Mater. Sci. Eng. A*, Vol. 132, 231–236.
- Celik, E., Demirkiran, A.S., Avci, E., 1999, Effect of grit blasting of substrate on the corrosion behaviour of plasma-sprayed Al_2O_3 coatings. *Surf. Coat. Technol.*, Vol. 116–119, 1061–1064.
- Chandler, K.A., 1966, The influence of salts in rust on the corrosion of the underlying steel. *Br. Corros. J.*, Vol. 1, 264–266.
- Chandler, K.A., Shak, B.J., 1966, The assessment of surface profile after blast-cleaning. *Br. Corros. J.*, Vol. 1, No. 9, 307–316.
- Chaudri, M.M., Walley, S.M., 1978, A high-speed photographic investigation of the impact damage in sodalime and borosilicate glasses by small glass and steel spheres. *Fracture Mechanics of Ceramics* (eds R.C. Bradt et al.), Vol. 3, Plenum Press, New York, 349–364.
- Chen, P.H., Chang, L.M., 2006, Effectiveness of neuro-fuzzy recognition approach in evaluating steel bridge paint conditions. *Can. J. Civil Eng.*, Vol. 33, 103–108.
- Chernyavskii, A.N., 1984, Surface roughness after shot blasting. *Chem. Petroleum Eng.*, Vol. 20, No. 1, 29–33.
- Ciampini, D., Spelt, J.K., Papini, M., 2003a, Simulation of interference effects in particle streams following impact with a flat surface. Part I: theory and analysis. *Wear*, Vol. 254, 237–249.
- Ciampini, D., Spelt, J.K., Papini, M., 2003b, Simulation of interference effects in particle streams following impact with a flat surface. Part II: parametric study and implications for erosion testing and blast cleaning. *Wear*, Vol. 254, 250–264.
- Cizmas, P.G., Slattery, J.C., 2007, Dimensionless correlation for sand erosion of families of polymers. *Wear*, Vol. 262, 316–319.
- Clausen, R., Stangenberg, J., 2002, Device for the determination of impact velocities in shot peening. *Proc. 8th Int. Conf. Shot Peening*, Garmisch-Partenkirchen, 90–94.
- Claydon, D.A., 2006, Performance testing of anti-corrosive coatings. *Proc. PACE Conf.*, Tampa, FL, Conference-CD.
- Cleaver, J.A., Ghadiri, M., 1993, Impact attrition of sodium carbonate monohydrate crystals. *Powder Tech.*, Vol. 76: 15–22.
- Cluchague, P., 2001, New innovations in surface preparation. *Protect. Coat. Europe*, Vol. 6, No. 11, 13–18.
- Confente, M., Geneve, D., Resiak, B., Jallon, M., 1995, Effects of mechanical descaling on the surface of low carbon wire rod for drawing or cold heading. *Wire J. Int.*, No. 2, 238–242.
- Conroy, L.M., Menezes-Lindsay, R.M., Sullivan, P.M., Cali, S., Forst, L., 1996, Lead, chromium, and cadmium exposure during abrasive blasting. *Arch. Environ. Health*, Vol. 51, 95–99.
- Cooke, R., House, R., Lawson, I.J., Pelmeur, P.L., Wills, M., 2001, Hand-arm vibration syndrome from exposure to high-pressure hoses. *Occup. Med.*, Vol. 51, No. 6, 401–409.
- Coulson, J.M., Richardson, J.F., 1968, *Chemical Engineering*, Vol. 2, Unit Operations, Pergamon Press, Oxford.
- Cousens, A.K., Hutchings, I.M., 1983, Influence of erodent particle shape on the erosion of mild steel. *Proc. 6th Int. Conf. Erosion by Liq. Solid Impact*, (ed. J.E. Field), Cavendish Lab., Cambridge, 41/1–41/7.
- Cox, E.P., 1927, A method of assigning numerical and percentage values to the degree of roundness. *J. Paleontol.*, Vol. 1, 179–183.
- Crawford, R., Atkinson, D., 1996, *Liquid Surfaces*. Swinburne University, Melbourne.
- D’Emanuele, A., Hill, J., Tamada, J.A., Domb, A.J., Langer, R., 1992, Molecular weight changes in polymer erosion. *Pharm. Res.*, Vol. 9, No. 10, 1279–1283.

- Da Maia, M.L., 2000, Alternatives to conventional methods and equipment for surface preparation. *Proc. PCE 2000 Conf. Exhib.*, Technology Publication, Pittsburgh, 349–359.
- Dahlhoff, B., 1967, Zusammenhang zwischen Zerkleinerungsgeschwindigkeit und Schallgeschwindigkeit. *Chemie-Ing. Techn.*, Vol. 39, 1112–1116.
- Da Silva Rocha, A., Strohaecker, T., Hirsch, T., 2003, Einfluss unterschiedlicher Oberflächenzustände vor dem Plasmanitrieren auf Eigenschaften und Zerspanungsverhalten des Schnellarbeitsstahls S 6-5-2. *Materialwiss. und Werkstofftechn.*, Vol. 34, 64–73.
- Day, J., Huang, X., Richards, N.L., 2005, Examination of a grit-blasting process for thermal spraying using statistical methods. *J. Therm. Spray Technol.*, Vol. 14, 471–479.
- Deng, J.X., 2005a, Sand erosion performance of B₄C/(W,Ti)C ceramic blasting nozzle. *Advances in Appl. Ceram.*, Vol. 104, 59–64.
- Deng, J.X., 2005b, Erosion wear of boron carbide ceramic nozzles by abrasive air-jets. *Mater. Sci. Eng. A*, Vol. 408, 227–233.
- Deng, J.X., Zheng, Z.C., Ding, Z.L., Wang, J.H., 2003a, Erosion wear of ceramic and cermeted carbide nozzles in dry sand blasting process. *Br. Ceram. Trans.*, Vol. 102, 61–65.
- Deng, J.X., Feng, Y., Ding, Z., Shi, P., 2003b, Wear behavior of ceramic nozzles in sand blasting treatments. *J. Europ. Ceram. Soc.*, Vol. 23, 323–329.
- Deng, J., Liu, L., Ding, M., 2007, Erosion wear behaviours of SiC/(W,Ti)C laminated ceramic nozzles in dry sand blasting processes. *Mater. Sci. Eng. A*, Vol. 444, 120–129.
- DIN 1343, 1990, Referenzzustand, Normzustand, Normvolumen—Begriffe und Werte. Deutsches Inst. für Normung, 01-90.
- DIN-Fachbericht 28, 2002, Korrosionsschutz von Stahlbauten durch Beschichtungen. Prüfung von Oberflächen auf visuell nicht feststellbare Verunreinigungen vor dem Beschichten. Beuth-Verlag GmbH, Berlin.
- Dioh, N.N., Williams, J.G., 1994, The impact behaviour of paints. *J. Mater. Sci.*, Vol. 29, 6091–6096.
- Dittmar, P., 1962, Zündgefahren durch Funken aus metallischen Oberflächen. *Jahrb. Oberflächentechnik*, Vol. 18, 56–66.
- Djurovic, B., Jean, E., Papini, M., Tangestanian, P., Spelt, J.K., 1999, Coating removal from fibre-composites and aluminium using starch media blasting. *Wear*, Vol. 224, 22–37.
- Doherty, C.B., 1974, Surfaces produced by abrasive blasting of steel. *Mater. Perform.*, No. 11, 12–20.
- Donker, B., 1985, Underwater sandblasting for surface treatment of submerged steel and concrete structures. *Proc. 1st Int. Conf. Surf. Eng.* (ed. I.A. Bucklow), Vol. III, The Welding Institute, London, 9–14.
- Donker, B., Richter, U., 1982, Unterwasser-Sandstrahlen mit Druckluft. *Hansa*, Vol. 119, No. 20, 1365–1367.
- Donker, B., Richter, U., 1988, Unterwasser-Konservierung: Erprobungsbericht zum Kooperationsprojekt “Pfahl-Konservierung”. *Internal Report GKSS 88/I/9*, GKSS, Geesthacht, Germany.
- Drisko, R.W., 2002, *SSPC Painting Manual*, Vol. 1, Surface Preparation Specifications, SSPC, Pittsburgh.
- Drozd, S., Race, T., Tinklenberg, K., 2000, Laboratory evaluation of engineered abrasives and surface treatments for mixed-metal blast media wastes. *J. Protect. Coat. Lin.*, Vol. 18, 41–47.
- Duncan, B., Lodeiro, M., 2004, Adhesion durability assessment. *NPL-Report DEPC-MPR-004*, National Physics Laboratory, Teddington, UK, June 2004.
- Dupuy, R., 2001, Ultra-high-pressure waterjetting for maintenance coatings applications. *J. Protect. Coat. Lin.*, Vol. 18, No. 8, 68–75.
- Dupuy, R., Ashworth, R., Frenzel, L., 2001, Turning a liability into an asset – the story of an old power plant. *Proc. 11th Amer. Water Jet Conf.* (ed. M. Hashish), WJTA, St. Louis, Paper 56.
- Elbing, F., 2002, Prozessanalyse und—optimierung des Trockeneinsstrahlens. *1. Treffen Industriearbeitskreis Trockenstrahlen*, Berlin, November, 2002.
- Ellermaa, R.R., 1993, Erosion prediction of pure metals and carbon steels. *Wear*, Vol. 162–164, 1114–1122.

- Elsner, C.I., Cavlacanti, E., Ferraz, O., Di Sarli, A.R., 2003, Evaluation of the surface treatment effect on the anticorrosive performance of plant systems on steel. *Progr. in Organic Coat.*, Vol. 48, 50–62.
- Emrich, S., 2003, Untersuchungen zum Einfluss von Oberflächenchemie und -morphologie auf die Langzeitbeständigkeit geklebter Aluminiumverbunde. *Dissertation*, Universität Kaiserslautern, Germany.
- Engel, P.A., 1976, *Impact Wear of Materials*. Elsevier Science Publication Comp., Amsterdam.
- Engel, P.A., 1985, Indentation debonding test for polymer coatings adhered to a substrate. *Int. J. Adhes. Adhesives*, Vol. 5, 129–132.
- Engel, P.A., Pedroza, G.C., 1983, Indentation-debonding test for adhered thin polymer layers. *Adhesion Aspects of Polymeric Coatings* (ed. K.L. Mittal), Plenum Press, New York, 583–595.
- Engelberg, F., 1967, Staubentwicklung in Schleuderradputzräumen und Entstaubung. *Giesserei*, Vol. 54, No. 6, 144–148.
- Engell, H.-J., 1960, Die Haftfestigkeit von Oberflächenschichten auf Metallen. *Werkst. Korros.*, Vol. 11, 147–151.
- Eprecht, A., 1974, Das mechanische Verhalten von Lackfilmen. *Farbe Lack*, Vol. 80, 505–513.
- Evans, A.G., Gulden, M.E., Rosenblatt, M.E., 1978, Impact damage in brittle materials in the elastic-plastic response regime. *Proc. R. Soc. Lond., Ser. A.*, Vol. 361, 343–356.
- Evans, A.G., Fleck, N.A., Watanabe, M., Maloney, M., Darolia, R., 2006, Scaling laws governing the erosion and impact resistance of thermal barrier coatings. *Wear*, Vol. 260, 886–894.
- Faidi, S.E., Scantlebury, J.D., Young, R.J., 1990, Messung der Haftfestigkeit unter Stoßbelastung. *Farbe Lack*, Vol. 96, No. 11, 853–856.
- Fairfull, C.L., Weldon, D.G., 2001, Salt contaminated abrasives and their effect on coating performance. *Proc. SSPC Conf.*, Atlanta, November 11–14, 2001, 30–44.
- Fang, C.K., Chuang, T.H., 1999, Surface morphologies and erosion rates of metallic building materials after sandblasting. *Wear*, Vol. 230, 156–164.
- Fauchais, P., Fukumoto, M., Vardelle, A., Vardelle, M., 2004, Knowledge concerning splat formation: an invited review. *J. Therm. Spray Technol.*, Vol. 13, 337–360.
- Fedko, V.T., Tomas, K.I., 1998, Wetting the surface of welded components by protective coatings. *Welding Int.*, Vol. 12, 47–49.
- Feist, K., Schulz, W.-D., Eisengräber, A., 1988, Zur Bedeutung der Rauheitsmaße R_a , R_m , R_z und S_m auf die Haftfestigkeit von Spritzmetallschutzschichten. *Korrosion*, Vol. 19, 307–315.
- Finnie, I., 1958, The mechanism of erosion of ductile metals. *Proc. 3rd U.S. Nat. Congr. Appl. Mech.* (eds. R.M. Haythornthwaite, et al.), ASME, New York, 527–532.
- Finnie, I., McFadden, A., 1978, On the velocity dependence of the erosion of ductile metals by solid particle at low angle of incidence. *Wear*, Vol. 48, 181–190.
- Flavenot, J.F., Lu, J., 1990, Influence of ageing of a cut steel wire shot during shot peening. *Proc. 4th Int. Conf. Shot Peening*, Tokyo, 83–93.
- Flores, S., Morcillo, M., 1999, Anticipated levels of soluble salts remaining on rusty steel prior to painting. *Surf. Coat. Int.*, No. 1, 19–24.
- Foghelin, M., 1990, The effect of surface preparation on the durability of paint on galvanized steel. *Proc. 11th Int. Conf. Innov. Technol. Trans. Corros. Control*, Vol. 2, Associazione Italiana, Milan, 2.283–2.291.
- Fokke, M., 1999, *Abrasive Blasting of Metal Surfaces*. Delft University Press, Delft.
- Forsgren, A., Applegren, C., 2000, Comparison of chloride levels remaining on the steel surface after various pretreatments. *Proc. PCE Conf. Exhib*, Technology Publication, Pittsburgh, 271–283.
- Fraenkel, K.H., 1954, *Manual on Rock Blasting*, Vol. II, Atlas Diesel, Stockholm.
- French, M.A., 1998, Safety in high-pressure water jetting. *Water Jet Applications in Construction Engineering* (ed. A.W. Momber), A.A. Balkema, Rotterdam, 387–397.
- Frenzel, L.M., 1997, Continuing improvement initiatives of surface preparation with water jetting. *Proc. 9th Am. Water Jet Conf.*, (ed. M. Hashish), WJTA, St. Louis, 697–716.
- Friedrich, K., 1986, Erosive wear of polymer surfaces by steel ball blasting. *J. Mater. Sci.*, Vol. 21, 3317–3331.

- Gane, N., Murray, M.J., 1979, The transition from ploughing to cutting in erosive wear. *Proc. 5th Int. Conf. Erosion Liq. Solid Impact*, Cavendish Laboratory, 40/1–40/8.
- Gasterstädt, J., 1924, Die experimentelle Untersuchung des pneumatischen Fördervorganges. *Forschungsarbeiten auf dem Gebiet des Ingenieurwesens*, Heft 265.
- Gause, R.L., 1989, A noncontacting scanning photoelectron emission technique for bonding surface cleanliness inspection. *5th Annual NASA NDE Workshop*, Cocoa Beach, Florida.
- Gelfant, F.S., 1995, Contaminated concrete—effect of surface preparation methods on coating performance. *J. Protect. Coat. Lin.*, Vol. 15, No. 12, 60–72.
- Gelsdorf, H., 1987, Sicherheit beim Druckluftstrahlen. *Bau-BG*, No. 1, 24–25.
- Gesell, W., 1966, Ersatz von Quarzsand beim Druckluftstrahlen durch nicht Silikose erzeugende mineralische Strahlmittel. *Stahl Eisen*, Vol. 86, No. 14, 906–912.
- Gesell, W., 1969, Jahresübersicht Putzverfahren und -einrichtungen. *Giesserei*, Vol. 56, No. 18, 552–557.
- Gesell, W., 1973, Strahlmittelfragen—zweite Literatur-Rückschau. *Fachberichte Oberflächentechnik*, Vol. 11, 1–10.
- Gesell, W., 1979, Verfahren und Kennwerte der Strahlmittelprüfung. *VDG-Taschenbuch 5*, Gießerei-Verlag GmbH, Düsseldorf.
- Gillespie, B., 1996, Image analysis of shot peening media. *Proc. 6th Int. Conf. Shot Peening*, San Francisco, CA, 213–222.
- Gillespie, B., Fowler, D.B., 1991, Evaluation of size and shape of shot peening media by image analysis. *SAE Trans.*, Vol. 100, No. 1, 28–39.
- Gillessen, R., Lange, H., Schindler, H., 1995, Bemessungen von Stahlrohren. *Stahlrohr-Handbuch* (ed. Hrsg. B. Sommer), Vulkan-Verlag, Essen, 156–281.
- Gillström, P., Jarl, M., 2004, Replacement of pickling with shot blasting for wire rod preparation. *Scand. Metall.*, Vol. 33, 178–269.
- Gladun, A., Gladun, C., Knorn, M., Vinzelberg, H., 1977, Investigation of the heat conductivity of niobium in the temperature range 0.05–23 K. *J. Low Temp. Phys.*, Vol. 27, 873–886.
- Glatzel, W.-D., Brauer, H., 1978, Prallverschleiß. *Chemie Ing. Technik*, Vol. 50, No. 7, 487–497.
- Glück, B., 1988, *Hydrodynamische und gasdynamische Rohrströmung—Druckverluste*. VEB Verlag für Bauwesen, Berlin.
- Gnyp, L.P., Marukha, M., Heneha, B., Chervatyuk, V., 2004, A device for simultaneous determination of the impact resistance and hardness of insulating coatings of pipelines. *Mater. Sci.*, Vol. 40, No. 2, 291–295.
- Goergens, U., 2002, PAK-Problematik im Stahlwasserbau. *BVK-Fachtagung*, Bundesverband Korrosionsschutz, Köln, March 2002.
- Goldman, D.B., Sutker, B.J., Schmidt, R.G., Suttmeier, P., 1990, Comparative performance of glass beads in suction and direct pressure shot peening applications. *Proc. 4th Int. Conf. Shot Peening*, Tokyo, 9–18.
- Gommel, G., 1967a, Energy, abrasion and comminution in impact processes. *Staub—Reinhalung—Luft*, Vol. 27, No. 1, 54–61.
- Gommel, G., 1967b, Erscheinungen bei stoßender Beanspruchung und ihr Zusammenhang mit Verschleißvorgängen. *Materialprüfung*, Vol. 9, No. 5, 175–178.
- Grabow, G., 2002, Optimalbereiche von Fluidenergiemaschinen – Pumpen und Verdichter. *Forschung im Ingenieurwesen*, Vol. 67, 100–106.
- Grant, J.T., Smith, J.A., Mazza, J.J., 2004, The characterization of Al alloy surfaces at each stage of preparation for adhesive bonding. *Materiali in Technologije*, Vol. 38, No. 5, 223–231.
- Greason, A.N., Aucote, J., Engström, H., 1989, Wear of ceramics in grit blasting. *Brit. Ceram Trans. J.*, Vol. 88, 213–218.
- Green, R.G., Gregory, I.A., Henry, R.M., Hill, E.J., 1981, Measurement of shot velocity at the nozzle of a shot-peening machine. *Proc. Conf. Impact Surf. Treat.*, Elsevier, London, 221–228.
- Greenburg, L., Winslow, C., 1932, The dust hazard in air pressure abrasive blasting. *Int. Arch. Occup. Environ. Health*, Vol. 3, No. 4, 577–599.

- Greverath, W.-D., Momber, A.W., Opel, H., 2005, Device and method for testing surfaces, in particular steel surfaces, with respect to structure, colour intensity and/or colour distribution. Patent No. WO 2005/057127 A1.
- Griffith, A.A., 1921, The phenomena of rupture and flow in solids. *Phil. Trans. Roy. Soc. London*, Ser. A, Vol. 221, 163–198.
- Griffith, B., 2001, *Manufacturing Surface Technology*. Penton Press, London.
- Griffith, B.J., Gawne, D.T., Dong, G., 1996, The erosion of steel surfaces by brit-blasting as a preparation for plasma spraying. *Wear*, Vol. 194, 95–102.
- Griffith, B.J., Gawne, D.T., Dong, G., 1997, The role of grit blasting in the production of high-adhesion plasma sprayed alumina coatings. *Proc. Inst. Mech. Eng., Part B*, Vol. 211, 1–9.
- Griffith, B.J., Gawne, D.T., Dong, G., 1999, A definition of the topography of grit-blasted surfaces for plasma sprayed alumina coatings. *Trans. ASME, J. Manuf. Sci. Eng.*, Vol. 121, 49–53.
- Groot, R.C., Kik, T.A., van Tongeren, H.P., van Ooij, W.J., 1982, Protection of steel by blasting with zinc-coated abrasives and painting under water or in wet conditions. *Proc. 8th Int. Conf. Org. Coat. Sci. Technol.*, Athens, 395–406.
- Groth, K., 1995, *Kompressoren*. Vieweg, Braunschweig.
- Groß, K.-J., 1988, Erosion (Strahlverschleiß) als Folge der dynamischen Werkstoffreaktion beim Stoß. *Dissertation*, Universität Stuttgart, Germany.
- Grubitsch, H., Sammer, R., Willfurth, L., 1972, Über das Korrosionsverhalten von Stahlblechen, die mit verschiedenen Strahlmittel entrostet und mit Zinkstaubanstrich versehen wurden. *Werkst. Korros.*, Vol. 23, 561–564.
- Guan, X.S., Dong, Z.F., Li, D.Y., 2005, Surface nanocrystallization by sandblasting and annealing for improved mechanical and tribological properties. *Nanotechnology*, Vol. 16, 2963–2971.
- Guilemany, J.M., Llorca-Isern, N., Szabo, P.J., 1996, Residual stress characterization of grit blasted steel surfaces. *Surf. Eng.*, Vol. 12, 77–79.
- Gupta, G., Win, T., Messom, C., Demidenko, S., Mukhopadhyay, S., 2003, Defect analysis of grit-blasted or spray-painted surface using vision sensing techniques. *Image Vision Comput.*, NZ, 18–23.
- Haagen, H., Konzelmann, R., Kunz, G., 1990, Einfluß atmosphärischer Salze auf den Korrosionsschutz von Beschichtungen. *Farbe Lack*, Vol. 96, No. 4, 255–260.
- Hamann, J., 1987, Zur Entwicklung von Strahldüsen für das Druckluft-Freistrahilverfahren hoher Strahlleistung. *Korrosion*, Vol. 18, No. 4, 183–192.
- Hamed, A., Mohamed, A., 2001, Simultaneous LDV measurements of gas and particle velocities in two-phase flow. *Proc. 7th Int. Congr. Fluid Dyn. Propul.*, ASME, New York, 1–7.
- Hansen, C.M., 1972, Surface roughness profiles and coatings performance. *J. Paint Technol.*, Vol. 44, No. 570, 61–66.
- Hansink, J.D., 1998, Economics of abrasive selection for shipyard use. *Protect. Coat. Europe*, Vol. 3, No. 5, 24–27.
- Hansink, J.D., 2000, An introduction to abrasives for protective coating removal operations. *J. Protect. Coat. Lin.*, Vol. 17, No. 4, 66–73.
- Hare, C.H., 1996, The mechanical properties of coating films and their characterisation. *Protect. Coat. Europe*, Vol. 1, No. 6, 42–57.
- Hareux, D., Riach, B., 1986, A comparative study of air blasting using different abrasives—parts 1+2. *Corros. Prot. Mater.*, Vol. 5, No 1, 18–34.
- Harris, A.F., Beevers, A., 1999, The effects of grit-blasting on surface properties for adhesion. *Adhes. Adhesives*, Vol. 19, 445–452.
- Hauke, W., 1982, Strömungstechnische Untersuchungen an Düsen für das Druckluftstrahlen. *Maschinenbautechnik*, Vol. 31, No. 2, 87–90.
- Hazlett, R.D., 1993, On surface roughness effects in wetting phenomena. *Contact Angle, Wettability and Adhesion* (ed. K.L. Mittal), VSP, Utrecht, 73–181.
- He, J.W., Hendrix, B.C., Hu, N.S., Xu, K.W., Bell, T., Sun, Y., Mao, K., 1996, Interfacial fatigue limits as measure of cyclic bonding strength of hard coatings. *Surf. Eng.*, Vol. 12, No. 1, 49–54.

- Heitbrink, W.A., 1999, Control technology for crystalline silica exposures in construction: wet abrasive blasting. *Report No. ECTB 247-11*, US Department of Health and Human Services, Cincinnati, December 1999.
- Henning, R., Brauer, H., 1986, Untersuchung des Prallverschleißes ebener Platten. *VDI Forschungshefte*, No. 636, VDI-Verlag, Düsseldorf.
- Hernandez, L., Oliviera, F., Gijs, M.A., 1999 Berrios, J.A., Villalobos, C., Pertuz, A., Cabrera, E., 2000, Fatigue properties of a 4340 steel coated with a Colmonoy 88 deposit applied by high-velocity oxygen fuel. *Surf. Coat. Technol.*, Vol. 133–134, 68–77.
- Hertz, H., 1882, Ueber die Berührung fester elastischer Körper. *Journal für die reine und angewandte Mathematik*, Vol. 92, 156–171.
- Herzog, R., Zin, W., Scholtes, B., Wohlfahrt, H., 1996, Zur Aussagefähigkeit der Almenintensität als Kennwert bei der gezielten Eigenspannungserzeugung durch Kugelstrahlen. *Materialwiss. Werkstofftech.* Vol. 27, 608–617.
- Heya, A., Niki, T., Gijs, M.A., 1999 Takano, M., Doguchi, Y., Yonezawa, Y., Minamikawa, T., Muroi, S., Minami, S., Izumi, A., Masuda, A., Umemoto, H., Matsumura, H., 2005, Improvement of deposition rate by sandblasting of tungsten wire in catalytic chemical vapor deposition. *Jpn. J. Appl. Phys.*, Vol. 44, No. 4A, 1943–1944.
- Heywood, H., 1933, Numerical definition of particle size and shape. *Chem. Ind.*, Vol. 32, 149–154.
- Hitchcock, S.J., Carroll, N.T., Nicholas, M.G., 1981, Some effects of substrate roughness on wet-ability. *J. Mater. Sci.*, Vol. 16, 714–732.
- Hitzrot, H.W., 1997, Reduced volume of spent abrasive in open air blasting. *NSRP Project No. 3-93-6*, July 1997.
- Hochweber, M., 1970, Korrosionsschutz bei Unterwasser- und erdverlegten Stahlkonstruktionen. *Deutsche Farbenzeitschrift*, Vol. 24, 182–186.
- Hofinger, I., Raab, K., Möller, J., Bobeth, M., 2002, Effect of substrate roughness on the adherence of NiCrAlY thermal spray coatings. *ASM J. Thermal Spray*, Vol. 11, 387–392.
- Holle, D., 2000, Ultra-high pressure waterjetting of hazardous coatings on galvanised communication towers. *J. Prot. Coat. Lin.*, Vol. 17, No. 11, 71–85.
- Holt, S., Austin, D.M., 2001, How nozzle pressure and feed rate affect the productivity of dry abrasive blasting. *J. Protect. Coat. Lin.*, Vol. 18, No. 10, 82–104.
- Hong, K.T., Imodojemu, H., Webb, R.L., 1994, Effects of oxidation and surface roughness on contact angle. *Exp. Therm. Fluid Sci.*, Vol. 8, 279–285.
- Hornauer, K.-P., 1982, Untersuchungen zur Umformung von Bauteilen durch Kugelstrahlen. *Dissertation*, RWTH Aachen, Germany.
- Horowitz, I., 1982, *Oberflächenbehandlung mittels Strahlmitteln*. Vulkan-Verlag, Essen.
- Howlett, J.J., Dupuy, R., 1993, Ultrahigh-pressure water jetting for deposit removal and surface preparation. *Mater. Perform.*, Vol. 32, 38–43.
- Huang, H., Zhu, X.H., Huang, Q.K., 1995, Weibull strength distributions and fracture characteristics of abrasive materials. *Eng. Fracture Mech.*, Vol. 52, 15–24.
- Hurst, R.C., Hancock, P., 1972, Measurement of the mechanical properties of growing surface films in oxidising environments. *Werkst. Korros.*, Vol. 23, 773–776.
- Hutans, J., 1986, Wirkungsgraderhöhung des Druckluftstrahlens durch Einsatz des Strahlrohres. *Korrosion*, Vol. 17, No. 1, 38–41.
- Hutchings, I.M., 1977a, Strain rate effects in microparticle impact. *J. Phys. D Appl. Phys.*, Vol. 10, L179–L184.
- Hutchings, I.M., 1977b, Deformation of metal surfaces by the oblique impact of square plates. *Int. J. Mech. Sci.*, Vol. 19, 45–52.
- Hutchings, I.M., 1979a, Mechanical and metallurgical aspects of the erosion of metals. *Proc. Corros./Erosion Coal Convers. Syst. Mater. Conf.* (ed. A.V. Levy), NACE., Houston, 393–428.
- Hutchings, I.M., 1979b, Some comments on the theoretical treatment of erosive particle impact. *Proc. 5th Int. Conf. Erosion Liq. Solid Impact* (ed. J.E. Field), Cavendish Lab., Cambridge, 36/1–36/6.

- Hutchings, I.M., 1981, A model for the erosion of metals by spherical particles at normal incidence. *Wear*, Vol. 70, 269–281.
- Hutchings, I.M., 1992 Ductile-brittle transitions and wear maps for the erosion and abrasion of brittle materials. *J. Phys., D: Appl. Phys.*, Vol. 25, A/212–A/221.
- Hutchings, I.M., Levy, A.V., 1989, Thermal effects in the erosion of ductile metals. *Wear*, Vol. 131, 105–121.
- Hutchings, I.M., Winter, R.E., Field, J.F., 1976, Solid particle erosion of metals: the removal of surface material by spherical projectiles. *Proc. R. Soc. London A*, Vol. 348, 379–392.
- Hutchings, I.M., Macmillan, N.H., Rickerby, D.G., 1981, Further studies of the oblique impact of a hard sphere against a ductile solid. *Int. J. Mechan. Sci.*, Vol. 23, No. 11, 639–646.
- Hutchings, I.M., Deuchar, D.W., Muhr, A.H., 1987, Erosion of unfilled elastomers by solid particle impact. *J. Mater. Sci.*, Vol. 22, 4071–4076.
- IACS, 2003, Confined Space Safe Practice, *Rec. No. 72*, Rev. 1, International Association of Classification Societies, London, October 2003.
- Ibrahim, A., Berndt, C.C., 1998, The effect of high-velocity oxygen fuel, thermally sprayed WC-Co coatings on the high-cycle fatigue of aluminium alloy and steel. *J. Mater. Sci.*, Vol. 33, 3095–3100.
- Iida, K., 1996, The analysis of the shot velocity thrown from the nozzle and the bladed wheel. *Shot Peener*, Vol. 10, No. 4, 36–38.
- Ilyes, A., Brauer, H., 1987, Die Energieumwandlung bei ein- oder mehrmaligem Stoß einer Partikel gegen eine feste Wand. *VDI-Forschungshefte*, No. 640, VDI-Verlag, Düsseldorf.
- IMO, 2005, Performance Standards for Protective Coatings for Dedicated Seawater Ballast Tanks in all Types of Ships and Double-Side Skin Spaces of Bulk Carriers. International Maritime Organization, London.
- Ishii, R., Kawasaki, K., 1982, Limiting particle streamline in the flow of a gas-particle mixture through an axially symmetric nozzle. *Phys. Fluids*, Vol. 25, No. 6, 959–966.
- Ishikawa, K., Tobe, S., 2003, The effect of blasting and spraying angles on adhesive strength of aluminium sprayed coating by wire flame spraying. *Nippon Yosha Kyokai Shi*, Vol. 40, No. 3, 107–112.
- ISO 1217, 1996, Displacement compressors—acceptance tests. 1996–09, International Organization for Standardization, Geneva.
- ISO 12944-4, 1998, Paints and varnishes—corrosion protection of steel structures by protective paint systems—Part 4: types of surfaces and surface preparation. 1998-05-15, International Organization for Standardization, Geneva.
- ISO 8502-3, 1992, Preparation of steel substrates before application of paint and related products—tests for the assessment of surface cleanliness—Part 3: assessment of dust on steel surfaces prepared for painting (pressure-sensitive tape method). 1992-10-01, International Organization for Standardization, Geneva.
- ISO 8573-1, 2001, Compressed air - Part 1: Contaminants and purity classes. International Organization for Standardization, Geneva.
- Ivosevic, M., Gupta, V., Gijss, M.A., 1999 Cairncross, R.A., Twardowski, T.E., Knight, R., Baldoni, J.A., 2006, Effect of substrate roughness on splatting behaviour of HVOF sprayed polymer particles: modelling and experiments. *Int. Therm. Spray Conf. Exhib.*, Seattle, WA, May 15–17, 2006.
- James, D.H., 1984, A review of experimental findings in surface preparation for thermal spraying. *J. Mech. Work. Technol.*, Vol. 10, No. 10, 221–232.
- Jarrett, C., 2003, Evaluation of elevated blood lead in a commercial painter. *Appl. Occup. Environ. Hyg.*, Vol. 18, 808–811.
- Jiang, X.P., Wang, X.Y., Li, J.X., Li, J.X., Man, C.S., Shepard, M.J., Zhai, T., 2006, Enhancement of fatigue and corrosion properties of pure Ti by sandblasting. *Mater. Sci. Eng. A*, Vol. 429, 30–35.
- Johnson, W., 1972, *Impact Strength of Materials*. Chapter 9, Edward Arnold, London.
- Johnson, K.L., 1985, *Contact Mechanics*. Cambridge University Press, Cambridge.
- Johnson, W.C., 1990, Corrosion failure from water-soluble contaminants on abrasives. *J. Protect. Coat. Lin.*, Vol. 7, No. 9, 54–59.

- Johnson, W.C., 1997, Cost-effective extraction of chlorides from bridge steel. *J. Protect. Coat. Lin.*, Vol. 14, No. 1, 82–92.
- Johnson, K.L., Kendall, K., Roberts, A.D., 1971, Surface energy and the contact of elastic solids. *Proc. R. Soc. London A*, Vol. 324, 301–313.
- Johnston, M.H., 1998, Nozzle development for dry media blasting processes. *Abrasive Blast Cleaning News*, Vol. 3, No. 3, 4–7.
- Jones, J.R., Gardos, M.N., 1971, An investigation of abrasive cleaning. *J. Am. Soc. Lubr. Eng.*, Vol. 27, No. 11, 393–399.
- Jonnalagadda, K., Kline, G.E., Sottos, N.R., 1997, Local displacements and local transfer in shape memory alloy composites. *Exp. Mech.*, Vol. 37, No. 1, 78–86.
- Jopp, H., 1995, Ein Beitrag zum besseren Verständnis der Wirkungsweise des Strahlens auf die Festigkeit und Beständigkeit von Metallklebungen. *Dissertation*, Kaiserslautern University, Kaiserslautern, Germany.
- Kaiser, W.-D., Schütz, A., 2001, Hochdruckwasserstrahlen und restrostverträglicher Beschichtungsstoff. *Korrosionsschutz durch Beschichtungen und Überzüge auf Metallen*, Vol. 2, Part 9, Chapter 8.5, WEKA Media, Kissing, 1–26.
- Kaiser, W.-D., Schulz, W.-D., 1987, Duplexsystem Zink plus Anstrich—Teil 2: Untersuchungen zur Optimierung der Haftfestigkeit in Abhängigkeit von Vorbehandlung und Bindemittel. *Korrosion*, Vol. 18, 211–225.
- Kalide, W., 1990, *Einführung in die technische Strömungslehre*. Carl Hanser Verlag, München.
- Kallio, M., Mannila, J., Gijs, M.A., 1999 Vesa, A., Mahlberg, R., Ritschkoff, A.C., Ohlgiöschlagger, T., 2005, Modification of surface properties of metals by sol-gel coatings. *PACE 2005*, Las Vegas, T 59.
- Kalpers, H., 1949, Wirtschaftlichkeitsfragen im Betrieb von Sandstrahlgebläsen. *Metalloberfläche*, Vol. 3, 67–70.
- Kambham, K., Sangameswaran, S., Potana, S., Kura, B., 2006, Productivity and consumption variation in dry abrasive blasting with coal slag. *J. Ship Prod.*, Vol. 22, No. 1, 1–8.
- Kamzolov, V.N., Maslov, B.N., Pirumov, U.G., 1971, Investigation of particle trajectories in Laval nozzles. *Fluid Dyn.*, Vol. 6, No. 5, 849–856.
- Karpinos, D.M., Zilberberg, V.G., Vyaltsev, A.M., Kud, V.S., 1979, Shot-blasting as a mean of preparing surfaces for plasma deposition. *Powder Metall. Met. Ceram.*, Vol. 17, No. 9, 675–678.
- Karuppanam, S., Romero, J.S., Rios, E.R., Rodopoulos, C., Levers, A., 2002, A theoretical and experimental investigation into the development of coverage in shot peening. *Proc. 8th Int. Conf. Shot Peening*, Garmisch-Partenkirchen, 101–107.
- Katsikaris, K., Voutsas, E., Gijs, M.A., 1999, Andronikos, G., Stamataki, S., Magoulas, K., 2002, Recyclinmg ferrous-nickel slag in blast cleaning. *Waste Manage. Res.*, Vol. 20, No. 3, 269–278.
- Katsikaris, K., Voutsas, E., Stamataki, S., Magoulas, K., 2001, Development of recycling process for used ferrous-nickel slag as abrasive material in sandblasting operations. *Proc. 7th Int. Conf. Environ. Sci. Technol.*, Syros, 187–194.
- Kaufmann, B., 1998, Traggrund Stahl: Gibt es Alternativen zum Sandstrahlen? Seminarunterlagen, *Der Traggrund—ein ständiger Konfliktkherd?* Schweizerischer Fachverband für Hydrodynamik am Bau, Würenlingen, Switzerland.
- Kaufmann, B., Zielasch, A.H., 1998, Renovation of steel constructions by a combined waterjetting—waste recycling method. *Water Jet Applications in Construction Engineering* (ed. A.W. Momber), A.A. Balkema, Rotterdam, 313–323.
- Keane, J.D., Bruno, J.A., Weaver, R.E., 1976, *Surface Profile for Anti-Corrosion Paints*. Steel Structures Painting Council, Pittsburgh, PA.
- Kelly, E.G., Spottiswood, D.J., 1982, *Introduction to Mineral Processing*. John Wiley & Son, New York, 21–45.
- Kendall, M.A., Quinlan, N.J., Thorpe, S.J., Ainsworth, R.W., Bellhouse, B.J., 2004, Measurements of the gas and particle flow within a converging-diverging nozzle for high speed powdered vaccine and drug delivery. *Exp. Fluids*, Vol. 37, 128–136.

- Kiesskalt, S., Dahlhoff, B., 1965, Praktische Bedeutung zweier zerkleinerungsphysikalischer Effekte. *Chemie Ing. Technik*, Vol. 37, 277–283.
- Kim, S.R., Nairn, J.A., 2000, Fracture mechanics analysis of coating/substrate systems. Part II: experiments in bending. *Eng. Fracture Mech.*, Vol. 65, 595–607.
- Kim, I.T., Itoh, Y., Kainuma, S., Kadota, Y., 2003, Accelerated exposure tests of painted steel with different surface preparations of steel substrate. *Proc. 9th East Asia Pacific Conf. Struct. Eng. Construct.*, Bali, Indonesia.
- Kinsey, J., Schliesser, S., Murowchick, P., 1994, Development of particular emission factors for uncontrolled abrasive blasting under simulated windy conditions. *Proc. 87th Annual Meeting*, Cincinnati, Air & Waste Management Assoc., Paper 94-WA71.03, 1–12.
- Kirchner, H.P., Gruver, R.M., 1978a, Localized impact damage in a viscous medium (glass). *Fracture Mechanics of Ceramics* (eds. R.C. Bradt et al.), Vol. 3, Plenum Press, New York, 365–377.
- Kirk, D., 2007, Generation of air-blast shot velocity. *The Shot Peener*, Vol. 21, No. 1, 26–30.
- Kirk, D., Abyaneh, M.Y., 1994, Theoretical basis of shot peening coverage control. *Proc. 5th Int. Conf. Shot Peening*, Coventry, 183–190.
- Kjernsmo, D., Kleven, K., Scheie, J., 2003, *Corrosion Protection Inspector's Book of Reference*. Hempel A/S, Lyngby, Denmark.
- Kline, E., Mort, G., LeCompte, J., 1988, Improved productivity from new blast nozzle geometry. *J. Protect. Coat. Lin.*, Vol. 5, 8–12.
- Klinger, C., Kinder, J., Ell, M., Klingbeil, D., 2002, Zwillingsbildung im Schiffbaustahl der M.V. Estonia. *Werkstoffprüfung: Schadensanalyse—Schadensvermeidung* (eds. Hrsg. G. Lange, M. Pohl), Wiley-VCH, Weinheim, 134–154.
- Kloos, K.H., Kaiser, B., Schreiber, D., 1981, Einflüsse unterschiedlicher Reinheitsgrade auf die Dauerschwingfestigkeit des Federstahles 55 Cr 3. *Zeitschrift Werkstofftechnik*, Vol. 12, 206–218.
- Kloos, K.H., Macherauch, E., 1987, Development of mechanical surface strengthening processes from the beginning until today. *Shot Peening Sci., Technol., Appl.*, Garmisch-Partenkirchen, 3–27.
- Kniwald, D., 1993, Vorbehandlung des metallischen und keramischen Substrats durch Strahlen unter keramischen Plasmaspritzüberzügen. *DVS-Berichte*, Band 152, 118–122.
- Knight, C.G., Swain, M.V., Chaudri, M.M., 1977, Impact of small steel spheres on glass surfaces. *J. Mater. Sci.*, Vol. 12, 1573–1586.
- Knipfer, C., Funke, H.-W., 1997, Lärmbelastung an Baustellenarbeitsplätzen, Teil V. *BIA Report*, Hauptverband der gewerblichen Berufsgenossenschaften, St. Augustin, Germany.
- Knotek, O., Elsing, R., 1987, Computer simulation of different surface topographies of metals produced by blasting processes. *Proc. 3rd Int. Conf. Shot Blasting*, Garmisch-Partenkirchen, 361–368.
- Kogan, Y.D., Sazonova, Z.S., Boiko, S.V., Aleksandrov, V.D., 1993, Surface preparation for the application of hardening protective coatings. *Met. Sci. Heat Treat.*, Vol. 35, No. 12, 663–666.
- Kogler, P.A., Ault, J.P., Farshon, C.L., 1995, Environmental acceptable materials for the corrosion protection of steel bridges. *Final Report*, Ocean City Research Corp.
- Komov, G.A., 1966, Investigation of flow of a dust-laden stream in a Laval nozzle. *J. Eng. Phys. Thermodyn.*, Vol. 10, No. 3, 217–219.
- Kotnarowska, D., 1999, Influence of ageing on mechanical properties of epoxide coating. *J. Corros. Sci. Eng.*, Vol. 2, Paper 28.
- Kotnarowska, D., 2003, Influence of organic coating macrostructure on its resistance to erosive wear. *Corros. Sci. 21st Century*, UMIST, Manchester, July 2003.
- Kriegel, E., 1968, Der Strahlverschleiß von Werkstoffen. *Chemie-Ing.-Technik*, Vol. 40, 31–36.
- Kuljian, G., Holmes, B.S., 1998, U.S. Navy experience with waterjetting. *Prot. Coat. Europe*, Vol. 3, No. 16–21.
- Kuljian, G.G., Melhuish, D.C., 1999, Water-jetting productivity study for the marine industry. *Proc. 10th Amer. Waterjet Conf.* (ed. M. Hashish), WJTA, St. Louis, Paper 42.

- Kukera, S.N., Hutchings, I.M., 1984, Yielding of engineering polymers at strain rates of up to 500 s^{-1} . *Int. J. Mech. Sci.*, Vol. 26, 617–623.
- Kumar, R., Verma, A.P., Lal, G.K., 1983, Nozzle wear during the flow of a gas-particle mixture. *Wear*, Vol. 91, 33–43.
- Kura, B., 2003, Clean technologies for industries: role of emission test facility in emissions modeling and health risk reductions. *Risk Assess. Shipyard Emissions*, February 2003.
- Kura, B., 2005, Residual risk from abrasive blasting emissions: particle size and metal speciation. *Final Report No. 2006-317*, University of New Orleans, New Orleans, LA, December 2005.
- Kura, B., Kambham, K., Sangameswaran, S., Silvadasan, X., 2006, Particulate emission and emission factors for speciality sand used in dry abrasive blasting. *J. Ship Prod.*, Vol. 22, No. 1, 33–40.
- LaBerge, M., Drouin, G., Gelinas, C., Champagne, B., Bobyn, J.D., 1990, Adherence of HDPE powder coating on Co-Cr surfaces: effect of substrate preparation and gas sterilization. *J. Biomed. Mater. Res.*, Vol. 24, 1427–1438.
- Lacombe, R., 2006, *Adhesion Measurement Methods—Theory and Practice*. Taylor & Francis, Boca Raton.
- Ladstädter, E., 1984, Grundlagen der Steinschlagsimulation “SPLITT”. *Farbe Lack*, Vol. 90, 646–653.
- Ladwein, T.L., Gümpel, P., 2004, The influence of functional surface properties of stainless steels on corrosion. *Corrosion 2004*, New Orleans, March 2004, 1–6.
- Lange, J.H., 2002, Airborne exposure and soil levels associated with lead abatement of a steel tank. *Toxicol. Ind. Health*, Vol. 18, 28–38.
- Lange, F.F., Evans, A.G., 1979, Erosive damage depth in ceramics: a study on metastable, tetragonal zirconia. *J. Amer. Ceram. Soc.*, Vol. 62, 62–65.
- Lange, G., Schimmöller, H., 1967, Beispiel einer statistischen Auswertung von Härtemessungen. *Materialprüfung*, Vol. 9, No. 4, 143–144.
- Larsen-Basse, J., 1993, Effect of atmospheric humidity on the dynamic fracture strength of SiC abrasives. *Wear*, Vol. 166, 93–100.
- Laugier, M.T., 1986, Effect of hardness on erosion of WC-Co composites. *J. Mater. Sci.*, Vol. 21, 3548–3550.
- Lawn, B.R., 1993, *Fracture of Brittle Solids*. 2nd edition, Cambridge University Press, Cambridge.
- Leahy, W., Young, T., Buggy, M., Barron, V., 2003, A study of environmentally friendly titanium pretreatments for adhesive bonding to a thermoplastic composite. *Materialwissenschaft und Werkstofftechnik*, Vol. 34, 415–420.
- Lecoffe, Y., Bunazzi, X.H., Jouet, F., Huet, D., 1993, Travel—a real time particle velocity measuring system for use in shot peening. *Proc. 5th Int. Conf. Shot Blasting*, Oxford, 61–68.
- Leidheiser, H., Funke, W., 1987, Water disbondment and wet adhesion of organic coatings on metals: a review and interpretation. *JOCCA*, No. 5, 121–132.
- Leistikow, S., Kraft, R., 1974, Verbesserung der Heißdampf-Korrosionsbeständigkeit von Incoloy Alloy 800-Rohrmaterial durch verformende Oberflächenvorbehandlungen. *Werkstoffe und Korrosion*, Vol. 25, No. 1, 12–25.
- Lepand, H., 1963, Neue Erkenntnisse beim Strahlentzndern von Drähten und Stäben. *Stahl Eisen*, Vol. 83, No. 14, 866–870.
- Levin, B.F., Vecchio, K.S., DuPont, J.N., Marder, A.R., 1999, Modeling solid-particle erosion of ductile alloys. *Metall. Mater. Trans.*, Vol. 30A, 1763–1774.
- Levy, A., 1995, *Solid Particle Erosion and Erosion-Corrosion of Metals*. ASM International, Materials Park.
- Li, J., Hutchings, I.M., 1990, Resistance of cast polyurethane elastomers to solid particle erosion. *Wear*, Vol. 135, 293–303.
- Li, L., Kim, J.H., Shukor, M.H., 2005, Grit blast assisted laser milling/grooving of metallic alloys. *Ann. CIRP*, Vol. 54, 183–186.
- Lin, C.K., Berndt, C.C., 1994, Measurement and analysis of adhesion strength for thermally sprayed coatings. *J. Thermal Spray Technol.*, Vol. 3, No. 1, 75–104.

- Lin, C., Tinh, N., McNight, M.E., 1992, Relation between AC impedance data and degradation of coated steel. *Prog. Org. Coat.*, Vol. 20, 169–186.
- Lin, C.Y., Chang, C.H., Tsai, W.T., 2004, Morphological and microstructural aspects of metal dusting on 304L stainless steel with different surface treatments. *Oxidation Met.*, Vol. 62, No. 3/4, 153–174.
- Linnemann, W., 1997, Method and apparatus for determining a real velocity distribution of solid particles travelling in a gas carrier flow for shot peening. *U.S. Patent No. 5,691,483*, Nov. 25, 1997.
- Linnemann, W., Kopp, R., Kittel, S., Wüstenfeld, F., 1996, Shot velocity measurements. *Proc. 6th Int. Conf. Shot Peening*, San Francisco, 118–129.
- Liu, J., Berry, D.H., Seebergh, J.E., Osborne, J.H., Blohowiak, K.Y., 2006, Effect of surface morphology on crack growth at a sol-gel reinforced epoxy/aluminium interface. *J. of Adhesion*, Vol. 82, 487–516.
- Locci, I.V., MacKay, R.A., Garg, A., Ritzert, F., 2004, Successful surface treatment for reducing instabilities in advanced nickel-base superalloys for turbine blades. *NASA/TM-2004-212920*, March 2004.
- Loh, W.K., Crocombe, A.D., Wahab, M.M., Watts, J.F., Ashcroft, I.A., 2002, The effect of moisture on the failure locus and fracture energy of an epoxy-steel interface. *J. Adhes. Sci. Technol.*, Vol. 16, 1407–1429.
- Lukschandel, J., 1973, Die Sandstrahldüse—ein Wirtschaftlichkeitsfaktor. *Fachberichte Oberflächentechnik*, Vol. 11, No. 11, 273–275.
- Luo, S., Zheng, Y., Li, J., Ke, W., 2001, Slurry erosion resistance of fusion-bonded epoxy powder coating. *Wear*, Vol. 249, 733–738.
- Luo, S., Zheng, Y., Li, J., Ke, W., 2003, Effect of curing degree and fillers on slurry erosion behavior of fusion-bonded epoxy powder coatings. *Wear*, Vol. 254, 292–297.
- Lyras, L.G., 1991, The cost of lead paint removal: achieving realistic bid prices. *J. Protect. Coat. Lin.*, Vol. 11, 56–63.
- Ma, Z., Cao, S., Wang, F., Liu, Y., Xiao, X., 2006, Effect of substrate surface roughness on the splat formation in the HVOF spraying of WC-Co. *Trans. Beijing Inst. Technol.*, Vol. 26, No. 4, 373–376.
- Machu, W., 1963, Über den Einfluß einer Vorbehandlung vor dem Phosphatieren auf die Eigenschaften von Phosphatschichten. *Werkstoffe und Korrosion*, Vol. 16, No. 7, 566–574.
- Madany, I.M., Al-Sayed, M.H., Raveedran, E., 1991, Utilisation of copper blasting grit waste as a construction material. *Waste Manage.*, Vol. 11, 35–40.
- Magnee, A., 1995, Generalized law of erosion: application to various alloys and intermetallics. *Wear*, Vol. 181–183, 500–510.
- Mannelqvist, A., Groth, M.R., 2001, Comparison of fractal analyses methods and fractal dimension for pre-treated stainless steel surfaces and the correlation to adhesive joint strength. *Appl. Phys. A*, Vol. 73, 347–355.
- Marcus, D.R., Leung, L.S., Klinzing, G.E., Rizk, F., 1990, *Pneumatic Conveying of Solids*. Chapman and Hall, London.
- Marshall, A.K., 1996, Lead removal with waterjetting. *J. Prot. Coat. Lin.*, Vol. 13, No. 2, 47–51.
- Marshall, A.K., 2001, Waterjetting and recoating dockside at the port of Houston authority. *J. Prot. Coat. Lin.*, Vol. 18, No. 5, 63–69.
- Marshall, D.B., Lawn, B.R., Evans, A.G., 1982, Elastic/plastic indentation damage in ceramics: lateral crack system. *J. Am. Ceram. Soc.*, Vol. 65, 561–566.
- Martin, L., 1997, Untersuchungen der Adhäsion und der Beständigkeit von Beschichtungssystemen für Rohrleitungen. *Dissertation*, Universität Kaiserslautern, Kaiserslautern, Germany.
- Martinez, P., 1994, A contribution to the characteristics of mineral abrasives for water jet cutting. *Geomechanics 94* (ed. Z. Rakowski), A.A. Balkema, Rotterdam, 361–365.
- Maruyama, T., Kobayashi, T., 2004, Influence of substrate surface roughness on adhesive properties of sprayed coating. *Proc. Therm. Spray 2004, Int. Therm. Spray Conf.*, 266–271.
- Maurer, K.F., Castler, L.B., Cullen, M.R., 1995, Making lead paint removal safe in Connecticut. *J. Prot. Coat. Lin.*, Vol. 12, No. 2, 68–76.

- McPhee, W.S., 2001, High productivity vacuum blasting system. *Research Report*, Contract-No. DE-AR26-98FT40367, LTC Teletrak, Inc., Alexandria, VA, USA.
- McPhee, W.S., Ebadian, 1999, High productivity vacuum blasting system. *Proc. Ind. Partnership Environ. Sci. Technol. Conf.*, Washington, US Dept of Energy.
- McPhee, W.S., Lin, C.X., Zheng, B., Kang, H.J., Ade, R., Shea, E., Ebadian, M.A., 2000, High productivity blasting system. *Proc. Ind. Partnership Environ. Sci. Technol. Conf.*, Washington, US Dept of Energy.
- Meguid, S.A., Rabie, A.M., 1986, Evaluation of potential techniques for computer control of shot-peening coverage. *Impact Surface Treatment* (ed. S.A. Meguid), Elsevier, London, 208–220.
- Mellali, M., Grimaud, A., Fauchais, P., 1994, Parameters controlling the sand blasting substrates for plasma spraying. *Proc. 7th Int. Therm. Spray Conf.*, Boston, MS, June 20–24, 227–232.
- Meng, H.C., Ludema, K.C., 1995, Wear models and prediction equations: their form and content. *Wear*, Vol. 181–183, 443–457.
- Meunier, P., Lambert, P., 1998, The experience of SNCF in preparing previously painted metal surfaces by UHP waterjetting. *Protect. Coat. Europe*, Vol. 15, No. 9, 34–37.
- Meyer, D., Schulz, W.-D., 2001, Minimale Verschmutzung bestimmen—Messung kleinster Restfettbelegungen auf Metalloberflächen. *Metalloberfläche*, Vol. 55, No. 6, 13–18.
- Mickelsen, R.L., Johnston, O.E., 1995, Lead exposure during removal of lead-based paint using vacuum blasting. *J. Prot. Coat. Lin.*, Vol. 12, No. 2, 78–84.
- Miles, D., 2000, Offshore oil platform surface preparation using the pilant media blasting technology. *Proc. Sem. Increasing Value Coat.*, Orlando, Reprint, 1–8.
- Miller, R., 1973, Rapid method for determining the degree of cleanliness of metal surfaces. *Mater. Prot. Perform.*, Vol. 12, No. 5, 31–36.
- Minaki, K., Kitajima, K., Minaki, K., Izawa, M., 2004, Improvement of surface texture of stainless steel by utilizing dry blasting. *Proc. 7th Int. Symp. on Advances in Abrasive Technol.*, Bursa, June 2004, 519–524.
- Minaki, K., Kitajima, K., Minaki, K., Izawa, M., Tosha, K., 2005, Improvement of surface texture of stainless steel by utilizing dry blasting: effect of blasting conditions on wettability. *Key Engng. Mater.*, Vol. 291–292, 265–270.
- Minaki, K., Kitajima, K., Nakahira, Y., Minaki, K., Izawa, M., Tosha, K., 2007, Improvement of surface texture of stainless steel by utilizing dry blasting. *Key Engng. Mater.*, Vol. 329, 533–538.
- Mintrop, H., 1941, Untersuchungen über den Stoß einer Kugel gegen eine ebene Platte. *Forschungsgebiete Ingenieurwesen*, Vol. 12., No. 3, 127–136.
- Mitschke, H., 2001, Effects of chloride contamination on the performance of tank and vessel linings. *J. Prot. Coat. Lin.*, Vol. 18, No. 3, 49–56.
- Miyazaki, N., 1996, Effect of Crystallization of thermoplastic polyimide resin on erosion rate. *J. Mat. Sci-Lett.*, Vol. 15, 1422–1423.
- Mohamed, A., Hamed, A., Lehnig, T., 2003, Supersonic rectangular over-expanded jets of single and two-phase flows. *ISABE 2003*, 11–19.
- Momber, A.W., 1995, A generalized abrasive water jet cutting model. *Proc. 8th Am. Water Jet Conf.* (ed. T.J. Labus), Vol. 1, Water Jet Technology Association, St. Louis, 359–371.
- Momber, A.W., 2003, *Hydroblasting and Coating of Steel Structures*. Elsevier Applied Science, London.
- Momber, A.W., 2004a, Eine Übergangsbedingung beim Strahlverschleiß von Gesteinen und Betonen. *Materialwiss. Werkstofftechn.*, Vol. 35, 151–157.
- Momber, A.W., 2004b, Damage to rocks and cementitious materials from solid impact. *Rock Mech. Rock Engng.*, Vol. 37, 57–82.
- Momber, A.W., 2005a, *Hydrodemolition of Concrete Substrates and Reinforced Concrete Structures*. Elsevier Applied Science, London.
- Momber, A.W., 2005b, Digital image analysis for assessing coated and uncoated surfaces. *J. Protect. Coat. Lin.*, Vol. 22, No. 2, 53–56.
- Momber, A.W., 2006, Aspects of salt concentration of prepared steel substrates. *J. Protect. Coat. Lin.*, Vol. 23, No. 2, M2–M8.

- Momber, A.W., Koller, S., 2005, Zur Korrosionsschutzwirkung von organischen Beschichtungssystemen auf gestrahlten Stahloberflächen. *Stahlbau*, Vol. 74, No. 10, 780–787.
- Momber, A.W., Koller, S., 2007, Effects of surface preparation methods on delamination of organic coatings applied to a metal substrate. *J. Protect. Coat. Lin.*, Vol. 24, in print.
- Momber, A.W., Kovacevic, R., 1998, *Principles of Abrasive Water Jet Machining*. Springer-Verlag Ltd., London.
- Momber, A.W., Schulz, R.R., 2006, *Betonuntergrund: Eigenschaften—Verfahren—Prüfung*. Birkhäuser Verlag, Basel.
- Momber, A.W., Wong, Y.C., 2005a, Overblasting effects on surface properties of low-carbon steel. *J. Coat. Technol.*, Vol. 2, 453–461.
- Momber, A.W., Wong, Y.C., 2005b, Geometrical features of wear debris, part I: erosion of ductile steel by solid particle impingement. *J. Mater. Sci.*, Vol. 40, 3517–3522.
- Momber, A.W., Kovacevic, R., Kwak, S., 1996, Investigations in abrasive water jet erosion based on wear particle analysis. *ASME J. Tribol.*, Vol. 118, 759–766.
- Momber, A.W., Wong, Y., Budidharma, E., Tjo, R., 2002a, Profiling of low-carbon steel with supersonic water jets. *Wear*, Vol. 249, 853–859.
- Momber, A.W., Wong, Y.C., Budidharma, E., Tjo, R., 2002b, Hydrodynamic profiling and grit blasting of low-carbon steel. *Tribol. Int.*, Vol. 35, 271–281.
- Momber, A.W., Koller, S., Dittmers, H.J., 2004, Effects of surface preparation methods on adhesion of organic coatings to steel substrates. *J. Protect. Coat. Lin.*, Vol. 21, No. 2, 44–50.
- Moore, D.R., 2001, Adhesion and fracture of polymeric coatings. *Surf. Coat. Int. Part B Coat. Trans.*, Vol. 84, 243–336.
- Morcillo, M., Simancas, J., 1997, Effects of soluble salts on coating life in atmospheric services. *J. Prot. Coat. Lin.*, Vol. 14, No. 9, 40–52.
- Morcillo, M., Feliu, S., Simancas, J., 1989a, Korrosionsschutzbeschichtungen für rostige Untergründe. *Farbe Lack*, Vol. 95, No. 10, 726–728.
- Morcillo, M., Bastidas, J.M., Simancas, J., Galvan, J.C., 1989b, The effect of the abrasive work mix on paint performance over blasted steel. *Anti Corros.* May, 4–8.
- Moreau, C., Gougeon, P., Lamontagne, M., 1995, Influence of substrate preparation on the flattening and cooling of plasma-sprayed particles. *J. Therm. Spray Technol.*, Vol. 4, No. 1, 25–33.
- Morris, M., 2000, Update: evaluating UHP waterjetting as preparation for ballast tank coating. *Protect. Coat. Europe*, Vol. 5, No. 9, 54–59.
- Münster, R., Spähn, H., 1979, Kann das Beizen von Schweißnähten austenitischer CrNi-Stähle durch andere Verfahren ersetzt werden? *Zeitschrift Werkstofftechnik*, Vol. 10, 37–42.
- Muruges, L., Srinivasan, S., Scattergood, R.O., 1991, Models and material properties for erosion of ceramics. *J. Mater. Eng.*, Vol. 13, 55–61.
- Myshanov, A.I., Shirokov, N.N., 1981, Flow of a two-phase medium in a Laval nozzle. *Fluid Dyn.*, Vol. 16, No. 1, 83–86.
- Nadkarni, V.S., Sharma, M.C., 1996, Some aspects of mass flow control of shots in pneumatic systems. *Shot Peener*, Vol. 10, No. 3, 30–34.
- Neal, D., 1999, Good pipe coating starts with properly prepared steel surface. *Corros. Pipe Protect.*, Vol. 82, No. 3.
- Neeb, T., Brockmann, W., Possart, W., Valeske, C., Bockenheimer, C., 2000, Surface modification of metals by mechanical pretreatments. *Proc. 23rd Annual Meeting of the Adhesion Soc.*, February 2000, 437–440.
- Neelakantan, M.N., Green, R.G., 1982, The measurement and control of impact finishing processes. *J. Phys. E: Sci. Instrum.*, Vol. 15, 1332–1336.
- Neilson, J.H., Gilchrist, A., 1968a, An analytical and experimental investigation of the velocity of particles entrained by the gas flow in nozzles. *J. Fluid Mech.*, Vol. 33, 131–149.
- Neilson, J.H., Gilchrist, A., 1968b, Erosion by a stream of solid particles. *Wear*, Vol. 11, 111–122.
- Nelson, D., 1996, Stripped clean. *Workboat Magaz.*, Jan./Febr., 52–59.
- Nettmann, P., 1936, Kraft- und Luftverbrauch von Sandstrahldüsen. *Automobiltechnische Zeitschrift*, Vol. 39, No. 21, 554–555.
- Neumaier, P., 1993, Bestimmung mechanisch-physikalischer Eigenschaften dünner Farb- und Lackschichten. *Farbe Lack*, Vol. 99, No. 8, 683–688.

- Neumann, G., 1976, Neue Erkenntnisse beim Entrosten und Entzundern durch Strahlen mit Strahldrahtkorn. *Neue Hütte*, Vol. 21, 45–51.
- Neumann, G., 1985, Höhere Effektivität des Druckluftstrahlens—die neue ZKS-Richtlinie R 35–84. *Korrosion*, Vol. 16, 160–164.
- Nieth, F., 1955, Die Beschaffenheit der Stahloberfläche bei Anwendung verschiedener Entrostungs- und Entzunderungsverfahren. *Metalloberfläche—Teil A*, Vol. 9, No. 10, 174–178.
- Ninham, A.J., Hutchings, I.M., 1983, A computer model for particle velocity calculation in erosion testing. *Proc. 6th Int. Conf. Erosion Liq. Solid Impact* (eds. J.E. Field, N.S. Corney), Cavendish-Laboratory, Cambridge, Paper 50.
- NIOSH, 1997, Protecting workers exposed to lead-based paint hazards—a report to congress. DHHS (NIOSH) Publication No. 98–112, New York.
- Noetel, K.H., 1987, Korrosionsschutzarbeiten – Sicherheitstechnische und arbeitsmedizinische Aspekte. *Bau-BG*, No. 4, 168–172.
- Norsok, 2004, Surface preparation and protective coating. *Norsok Standard M-501*, Standards Norway, Lysaker, June 2004.
- NSRP, 1998a, Productivity study of hydroblast removal of coatings. *Final Report*. The National Shipbuilding Research Program, NSRP 0520 N3-96-4, US Department of the Navy.
- NSRP, 1998b, User's guide to selection of blasting abrasives. *Final Report*. The National Shipbuilding Research Program, NSRP 0511 N3-95-7, US Department of the Navy.
- NWU, 1995, *Issues Impacting Bridge Painting*. FHWA/RD/94/098, Chapter 7, Northwestern University, Evanston, IL, USA, August 1995.
- Ochs, H.-J., Maurmann, W., 1996, Strahl- und Beschichtungstechnik an der Ruhrtalbrücke. *Bautenschutz Bausanierung*, No. 6, 17–19.
- Oertel, M., 2001, *Prandtl-Führer durch die Strömungslehre*. Vieweg, Braunschweig.
- Ognedal, T., Harbak, R., 1998, Noise from sandblasting. *J. Acoust. Soc. Am.*, Vol. 103, No 5, 2922.
- Ohlsen, J., 1997, Recycling von Feststoffen beim Wasserabrasivstrahlverfahren. *VDI Fortschritt-Berichte*, Reihe 15, No. 175.
- Oosthuizen, P.H., Carscallen, W.E., 1997, *Compressible Fluid Flow*. McGraw-Hill Inc., New York.
- Oppermann, T., 1993, Beitrag über die Schwingfestigkeitssteigerungen in Wöhler- und Betriebsfestigkeitsversuchen durch Reinigungsstrahlen und Festwalzen von konventionell und vereinfacht wärmebehandelten bauteilähnlichen Stahlproben. *Dissertation*, TH Darmstadt, Germany.
- Osawa, S., Itsukaichi, T., Ahmed, R., 2005, Influence of substrate properties on the impact resistance of WC cermet coatings. *J. Therm. Spray Technol.*, Vol. 14, 495–501.
- OSHA, 1993, Permit required confined spaces for general industry. *Title 29 CFR 1910.146*, Final Rule, Dept. of Labor, Jan. 14, 1993.
- Otsubo, F., Kishitake, K., Akiyama, T., Terasaki, T., 2003, Characterization of blasted austenitic stainless steel and its corrosion resistance. *J. Thermal Spray Technol.*, Vol. 12, No. 4, 555–559.
- Packham, D.E., 2002, Surface roughness and adhesion. *Surfaces, Chemistry and Applications* (eds. M. Chaudhury, A.V. Pocius), Elsevier, Amsterdam, 317–349.
- Palm, L., Platz, N., 2000, Innovative Technologien zur Entlackung und Farbbeschichtung von Schiffen im Dock. *Forum Thyssen Krupp*, No. 1, 70–73.
- Papini, M., Spelt, J.K., 1997, Organic coating removal by particle impact. *Wear*, Vol. 213, 185–199.
- Papini, M., Spelt, J.K., 1998a, The plowing erosion of organic coatings by spherical particles. *Wear*, Vol. 222, 38–58.
- Papini, M., Spelt, J.K., 1998b, Indentation-induced buckling of organic coatings—part II: measurements with impacting particles. *Int. J. Mech. Sci.*, Vol. 10, 1061–1068.
- Papini, M., Spelt, J.K., 2002, The mechanics of coatings. *The Mechanics of Adhesion* (eds. D.A. Dillard, A.V. Pocius), Elsevier, Amsterdam, 303–350.
- Papini, M., Ciampini, D., Krajac, T., Spelt, J.K., 2003, Computer modelling of interference effects in erosion testing: effect of plume shape. *Wear*, Vol. 255, 85–97.
- Parslow, G.L., Stephenson, D.J., Strutt, J.E., Tetlow, S., 1997, Paint layer erosion resistance behaviour for use in a multilayer paint erosion indication technique. *Wear*, Vol. 212, 103–109.
- Pashatskii, N.V., Syromyatnikov, N.I., Kovshov, A.N., 1970, Discharge of a gas with solid particles from nozzles at critical velocities. *J. Eng. Phys. Thermophys.*, Vol. 18, No. 4, 440–443.

- Pashatskii, N.V., Syromyatnikov, N.I., Letnitskii, B.A., 1971, Nozzle wear in two-phase flow. *J. Eng. Phys. Thermophys.*, Vol. 21, No. 1, 841–843.
- Paul, K.C., Pal, A.K., Gosh, A.K., Chakraborty, N.R., 2004, Measurements of elastic properties of some coating materials. *Surf. Coat. Int. Part B Coat. Trans.*, Vol. 87, No. B1, 47–50.
- Pawlikowski, S., Aniol, S., Pollo, I., Respondek, E., 1966, Bestimmung der Adhäsionskraft von Bitumenmassen an Stahl. *Werkst. Korros.*, Vol. 17, 468–470.
- Peltzer, O., 1955, Richtige Strahlmittelauswahl bei der mechanischen Entzunderung von Metallen. *Stahl Eisen*, Vol. 75, No. 17, 1115–1117.
- Penn, L.S., Defex, E., 2002, Relation between work of adhesion and work of fracture for simple interfaces. *J. Mater. Sci.*, Vol. 37, 505–513.
- Peters, F., Meister, D., 1997, Abblasen von Sandkörnern von einer ebenen Fläche. *Chemie-Ing. Technik*, Vol. 69, No. 4, 510–512.
- Petit-Renaud, F., 2002, Optimisation of the shot peening parameters. *Proc. 8th Int. Conf. Shot Peening*, Garmisch-Partenkirchen, 119–129.
- Pi, V.N., Hoogstrate, A.M., 2007, Cost optimization of abrasive blasting systems: a new and effective way for using blasting nozzles. *Key Engng. Mater.*, Vol. 329, 323–328.
- Piatti, L., Küng, A., Kaiser, A., 1959, Die Benetzung der Oberfläche von Werkstoffen. *Werkst. Korros.*, Vol. 10, 239–243.
- Pickles, M.J., Hutchings, I.M., 1997, Scratching testing: a means of characterising the in-service performance of automotive polymers. *Proc. Int. Symp. Automot. Technol. Autom.* (ed. D. Roller), ISATA, Florence, 391–298.
- Pietsch, S., Kaiser, W.-D., Stratmann, M., 2002, Korrosionsschutzwirkung von Beschichtungen am Defekt—Einfluß der Oberflächenvorbereitung und der Pigmentierung der Grundbeschichtung. *Werkst. Korros.*, Vol. 53, 299–305.
- Placke, J., 2005, The importance of air compressor maintenance. *Protect. Coat. Europe*, Vol. 10, No. 10, 17–21.
- Plaster, H.J., 1972, *Blast Cleaning and Allied Processes*. Vol. 1, Industrial Newspapers Ltd., London.
- Plaster, H.J., 1993, A tribute to Benjamin Chew Tilghman. *Proc. 5th Int. Conf. Shot Peening*, Oxford, 2–9.
- Platek, M., 2002, Training for confined space entry. *Protect. Coat. Europe*, Vol. 7, 45–52.
- Plitzko, S., Gabelmann, J., Gijjs, M.A., 1999, Johannknecht, A., Kolmsee, K., Kraus, J., 1998, Staubminderung von Strahlsystemen. *Die BG*, No. 10, 616–620.
- Possart, W., Bockenheimer, C., Valeske, B., 2002, The state of metal surfaces after blasting treatment—part I: technical aluminium. *Surf. Interf. Anal.*, Vol. 33, 687–696.
- Potente, H., Krüger, R., 1978, Bedeutung polarer und disperser Oberflächenspannungsanteile von Plastomeren und Beschichtungsstoffen für die Haftfestigkeit von Verbundsystemen. *Farbe Lack*, Vol. 84, 72–75.
- Prazak, M., Eremias, B., 1972, A method for measuring the surface roughness factor of metals. *Corros. Sci.*, Vol. 12, 463–468.
- Preece, C.M., 1979, Erosion. *Treatise on Materials Science and Technology*, Vol. 16, Academic Press, New York.
- Rädiker, W., Wild, M., 1958, Die Entfernbarkeit des Zunders von Stahlblechen. *Stahl Eisen*, Vol. 78, No. 2, 100–103.
- Rajesh, J.J., Bijwe, J., Venkataraman, B., Tewari, U.S., 2004, Effect of impinging velocity on the erosive behaviour of polyamides. *Tribol. Int.*, Vol. 37, 219–226.
- Ramamurthy, A.C., Lorenzen, W.I., Bless, S.J., 1994, Stone impact damage to automotive paint finishes. *Prog. Org. Coat.*, Vol. 25, 43–71.
- Randall, N.X., 2006, Characterization of the surface mechanical properties of paints and polymeric surface coatings. *PACE Conf. 2006*, Tampa, FL, Conference-CD.
- Randall, P.M., Kranz, P.B., Sonntag, M.L., Stadelmaier, J.E., 1998, Evaluation of needle gun and abrasive blasting technologies in bridge paint removal practices. *J. Air Waste Manage. Ass.*, Vol. 48, 264–270.

- Rao, T.V., Vook, R.W., Meyer, W., 1986, Effect of surface treatments on near surface composition of 316 nuclear grade stainless steel. *J. Vac. Sci. Technol.*, Vol. 4, No. 3, 1604–1607.
- Ratner, S.B., Styller, E.E., 1981, Characteristics of impact friction and wear of polymeric materials. *Wear*, Vol. 73, 213–234.
- Ravi-Chandar, K., 2004, *Dynamic Fracture*. Elsevier, Amsterdam.
- Raykowski, A., Hader, M., Maragno, B., Spelt, J.K., 2001, Blast cleaning of gas turbine components: deposit removal and substrate deformation. *Wear*, Vol. 249, 127–132.
- Reade, G.W., Kerr, C., Barker, B., Walsh, F.C., 1998, The importance of substrate surface condition in controlling the porosity of electroless nickel deposits. *Trans. Inst. Met. Finishing*, Vol. 76, No. 4, 149–155.
- Reams, C.A., 1939, *Modern Blast Cleaning and Ventilation*. Penton Publications, Cleveland.
- Rehacek, K., 1982, Exakte Messung der Eindringhärte von Anstrichfilmen mit der Vickers-Pyramide. *Farbe Lack*, Vol. 88, No. 4, 253–263.
- Reiners, E., 1960, Die Prallzerkleinerung von spröden Stoffen bei sehr hohen Aufprallgeschwindigkeiten. *Chemie-Ing.-Technik*, Vol. 32, No. 3, 136–142.
- Remmelts, J., 1968, Optimum conditions for blast cleaning of steel plate. *Br. Corros. J.*, Vol. 3, 88–98.
- Remmelts, J., 1969, Optimum conditions for blast cleaning of steel plate. *Br. Corros. J.*, Vol. 4, 199–206.
- Rhouma, A.B., Braham, C., Fitzpatrick, M.E., Sidhom, H., 2001, Effects of surface preparation on pitting resistance, residual stress, and stress corrosion cracking in austenitic stainless steel. *ASM J. Mater. Eng. Perform.*, Vol. 10, No. 5, 507–514.
- Rider, A.N., 1987, Bond durability of grit-blast and silane treated metallic adherends bonded with room temperature curing adhesives. *DSTO-TR-1187*, Department of Defence, Washington.
- Rider, A.N., Olsson-Jacques, C.L., Arnott, D.R., 1999, Influence of adherend surface preparation on bond durability. *Surf. Interface Anal.*, Vol. 27, 1055–1063.
- Ritter, J.E., Rosenfeld, L.G., 1990, Use of indentation technique for studying delamination of polymeric coatings. *J. Adhes. Sci. Technol.*, Vol. 4, No. 7, 551–571.
- Rizk, F., 1973, Pneumatische Förderung von Kunststoffgranulaten in horizontalen Rohrleitungen unter Berücksichtigung des Gewichtseinflusses im Zusammenhang mit Gut- und Rohrwerkstoffeigenschaften, insbesondere im optimalen Förderbereich. *Dissertation*, Universität Karlsruhe, Germany.
- Roche, S., Pavan, S., Loubet, J.L., Barbeau, P., Magny, B., 2003, Influence of the substrate characteristics on scratch and indentation properties of UV-cured clearcoats. *Prog. Org. Coat.*, Vol. 47, 37–48.
- Roero, C., 2005, Contact angle measurements of sessile drops deformed by a DC electric field. *High Voltage Laboratory Report*, Swiss Federal Institute of Technology, Zurich, Switzerland.
- Roper, H.J., Weaver, R.E., Brandon, J.H., 2005, The effect of peak count or surface roughness on coating performance. *J. Protect. Coat. Lin.*, Vol. 22, No. 7, 52–64.
- Roper, H.J., Weaver, E.F., Brandon, J.H., 2006, Peak performance from abrasives. *J. Protect. Coat. Lin.*, Vol. 23, No. 6, 24–31.
- Rosenberg, B., Yuan, L., Fulmer, S., 2006, Ergonomics of abrasive blasting: a comparison of high pressure water and steel shot. *Appl. Ergon.*, Vol. 37, 659–667.
- Rosenberger, W.A., 1939, *Impact Cleaning*. Penton Publ., Cleveland.
- Ruff, A.W., Ives, L.K., 1975, Measurement of solid particle velocity in erosive wear. *Wear*, Vol. 35, 195–199.
- Rumpf, H., 1965, Die Einzelkornzerkleinerung als Grundlage einer technischen Zerkleinerungswissenschaft. *Chemie-Ing.-Techn.*, Vol. 37, No. 3, 187–202.
- Ruppel, P., Brauer, H., 1990, Prallzerkleinerung durch Serienstoß. *VDI-Forschungshefte*, No. 658, VDI-Verlag, Düsseldorf.
- Ruppel, E., 2003, *Druckluft-Handbuch*. 4th edition, Vulkan-Verlag, Essen.
- Rutherford, K.L., Trezona, R.I., Ramamurthy, A.C., Hutchings, I.M., 1997, The abrasive and erosive wear of polymeric paint films. *Wear*, Vol. 203–204, 325–334.

- Ruttmann, W., Günther, T., 1965, Verhütung von Spannungsrisskorrosion durch Strahlen mit Stahlschrot, Glasperlen und Elektrokorund. *Werkst. Korros.*, No. 2, 104–108.
- Safar, K., 1973, Über den Zusammenhang zwischen der Körnung des Strahlmittels und der Oberflächenrauheit von Gußstücken. *Fachberichte Oberflächentechnik*, Vol. 11, No. 4, 105–110.
- Sakamura, Y., Matsumoto, M., Suzuki, T., 2005, High frame-rate imaging surface pressure distribution using a porous pressure-sensitive paint. *Meas. Sci. Technol.*, Vol. 16, 759–765.
- Salah-Rousset, N.B., Chaouachi, M.A., Chellouf, A., 1996, Role of surface finishing on pitting corrosion of a duplex stainless steel in seawater. *J. Mater. Engng. Perform.*, Vol. 5, No. 2, 225231.
- Salman, A.D., Gorham, D.A., 2000, The fracture of glass spheres. *Powder Technol.*, Vol. 107, 179–185.
- Salome, F., Morris, H., 1996, Occupational exposures and hazardous wastes from abrasive blast cleaning. *Proc. 13th Int. Corros. Conf. Towards Corros. Prot.*, Melbourne, November 1996.
- Sancaktar, E., Gomatam, R., 2001, A study on the effects of surface roughness on the strength of single lap joints. *J. Adhes. Sci. Technol.*, Vol. 15, 97–117.
- Santagata, D.M., Sere, P.R., Elsner, C.I., Di Sarli, A.R., 1998, Evaluation of the surface treatment effect on the corrosion performance of painted coated steel. *Prog. in Organic Coat.*, Vol. 33, 44–54.
- Sato, H., Kanai, H., Gijs, M.A., 1999 Kawai, Y., Moritaka, H., Ishida, M., Iwami, H., Takahashi, Y., 2003, Development of metallic sheating for protection of offshore steel structures using seawater resistance stainless steel. *Nippon Steel Technical Report*, No. 87, 37–42.
- Schaffner, A., 1997, Untersuchung der Lärmbelastung von Arbeitnehmern an Sandstrahlarbeitsplätzen. *Zeitschrift Lärmbekämpfung*, Vol. 44, 150–154.
- Schmithals, P.U., 1961, Die Entfernung des Zunders durch Strahlen. *Stahl Eisen*, Vol. 81, No. 25, 1739–1745.
- Schoff, C.K., 1992, Wettability phenomena and coatings. *Modern Approaches to Wettability* (eds. M.E. Schrader, G.I. Loeb), Plenum Press, New York, 375–395.
- Scholtes, B., Vöhringer, O., 1993, Ursachen, Ermittlung und Bewertung von Randschichtveränderungen durch Kugelstrahlen. *Materialwiss. Werkstofftech.*, Vol. 24, 421–431.
- Schröder, H., 2000, Rechtsgrundlagen bei der Entschichtung von asbesthaltigen Altanstrichen. *Sprechtag der Hafentechnischen Gesellschaft*, Magdeburg, 5. April 2000.
- Schubert, H., 1988, *Aufbereitung fester mineralischer Rohstoffe*. Bd. 1, VEB Deutscher Verlag für Grundstoffindustrie, Leipzig, 21–68.
- Schuh, A., Holzwarth, U., Gijs, M.A., 1999 Kachler, W., Göske, J., Zeiler, G., 2004, Oberflächenuntersuchungen an Al₂O₃-rauhgestrahlten Titanplantaten in der Hüftdoprothetik. *Orthopäde*, Vol. 33, 905–910.
- Schulz, M., Drach, C., Ihrig, A., Triebig, G., 2005, Zur Frage einer Bleiintoxikation als Berufskrankheit bei Korrosionsschutzarbeiten. *Arbeitsmed. Sozialmed. Umweltmed.*, Vol. 40, No. 1, 4–10.
- Schwarzer, J., Schulze, V., Vöhringer, O., 2002, Finite element simulation of shot peening—a method to evaluate the influence of peening parameters on surface characteristics. *Proc. 8th Int. Conf. Shot Peening*, Garmisch-Partenkirchen, 507–515.
- Schwate, W., 1986, *Handbuch Drucklufttechnik*. VEB Deutscher Verlag f. Grundstoffindustrie, Leipzig.
- Seavey, M., 1985, Abrasive blasting above 100 psi. *J. Protect. Coat. Lin.*, Vol. 2, No. 7, 26–37.
- Settles, G.S., Garg, S.T., 1995, A scientific view of the productivity of abrasive blasting nozzles. *J. Protect. Coat. Lin.*, Vol. 12, No. 4, 28–41 and 101–102.
- Settles, G.S., Geppert, S.T., 1997, Redesigning blasting nozzles to improve productivity. *Shot Peener*, Vol. 11, No. 2, 8–12.
- Seville, J.K., Tüzün, U., Clift, R., 1997, *Processing of Particulate Solids*. Blackie Academic & Professional, London.
- SFSA, 1980, Cast steel abrasives. *SFA Designation: 20–66*. Steel Founders Society of America, Rocky River, OH, USA.

- Shanahan, M.E., 1993, Effects of surface flaws on the wettability of solids. *Contact Angle, Wettability and Adhesion* (ed. K.L. Mittal), VSP, Utrecht, 159–171.
- Sheldon, G.L., Finnie, I., 1966, The mechanism of material removal in the erosive cutting of brittle materials. *ASME J. Eng. Ind.*, Vol. 88, 363–400.
- Sheldon, G.L., Maji, J., Crowe, C.T., 1977, Erosion of a tube by gas-particle flow. *ASME J. Eng. Mater. Technol.*, No. 4, 138–142.
- Shipway, P.H., Hutchings, I.M., 1993a, Influence of nozzle roughness on condition in a gas-blast erosion rig. *Wear*, Vol. 162–164, 148–158.
- Shipway, P.H., Hutchings, I.M., 1993b, Attrition of brittle spheres by fracture under compression and impact loading. *Powder Technol.*, Vol. 76, 23–30.
- Shipway, P.H., Hutchings, I.M., 1994, A method for optimizing the particle flux in erosion testing with a gas-blast apparatus. *Wear*, Vol. 174, 169–175.
- Shipway, P.H., Hutchings, I.M., 1995, Measurement of coating durability by solid particle erosion. *Surf. Coat. Technol.*, Vol. 71, 1–8.
- Siavoshani, S.S., 2001, Effect of substrate properties on molten metal droplet impact. *Master Thesis*, University of Toronto, Toronto, Canada.
- Siebel, M.K., Mosher, G.E., 1984, Detecting and controlling vibration. *Mod. Casting*, 34–36.
- Siegel, W., 1991, *Pneumatische Förderung*. Vogel-Buchverlag, Würzburg.
- Siegmann, S., Brown, C.A., 1998, Investigation of substrate roughness in thermal spraying by a scale-sensitive 3-D-fractal analysis method. *Proc. 15th Int. Therm. Spray Conf.*, Nice, 1998, 831–836.
- Siegmann, S., Brown, C.A., 2002, Einfluss der Haftgrundvorbereitung auf die entstehende Topographie und Schichthftung: ein dreidimensionales Fraktalanalyse-Verfahren. 2. *GTV-Kolloquium*, Luckenbach, 2002, 1–11.
- Sigloch, H., 2004, *Technische Fluidmechanik*, 5th edition, Springer, Heidelberg.
- Singh, S.K., Tambe, S.P., Kumar, D., 2004, Effect of pigmentation on fracture toughness of paint films. *J. Mater. Sci.*, Vol. 39, 2629–2632.
- Siviour, C.R., Walley, S.M., Proud, W.G., Field, J.E., 2005, The high strain rate compressive behavior of polycarbonate and polyvinylidene difluoride. *Polymer*, Vol. 46, 12546–12555.
- Skowronnek, J., Germer, A., Ladstädter, E., 1991, Dehneigenschaften von Autolacken bei schlagartiger Beanspruchung. *Farbe Lack*, Vol. 97, No. 1, 14–17.
- Slikkerveer, P.J., 1999, *Mechanical Etching of Glass by Powder Blasting*. Philips Electronics N.V., Eindhoven.
- Slutzky, O., Caprapi, J.J., Pessi, P.L., Meda, J.F., 1988, Grit blasting performance on steel surfaces. *Bull. Electrochem.*, Vol. 4, No. 2, 121–130.
- Snyder, G., Beuthin, L., 1989, Abrasive selection: performance and considerations. *J. Protect. Coat. Lin.*, Vol. 6, No. 3, 46–53.
- Sobiecki, J.R., Ewertowski, J., Babul, T., Wierzchon, T., 2003, The influence of surface preparation on the properties of tungsten carbide coatings produced by gas-detonation method. *Mater. Sci. Forum*, Vol. 426–432, 2587–2592.
- Sobolev, V.V., Guilemany, J.M., Calero, J.A., 2000, Development of coating structure and adhesion during high velocity oxygen-fuel spraying of WC-Co powder on a copper substrate. *J. Thermal Spray Technol.*, Vol. 9, No. 1, 100–106.
- Sofyan, B.T., Stefano, M., Pardede, J.H., Sofyan, E., 2005, Characteristics of HVOF WC-Co coating used for rocket nozzle application. *Mater. Forum*, Vol. 29, 147–151.
- Solomon, H.D., Delair, R.E., Thyssen, J., 2003, The high-temperature wetting balance and the influence of grit blasting on brazing of IN718. *Weld. J.*, 278–287.
- Soltz, G.C., 1991, The effects of substrate contaminants on the life of epoxy coatings submerged in sea water. *National Shipbuilding Research Program*, Tasks No. 3-89-2, March 1991, 1–96.
- Sorokin, V.M., Shetulov, D.I., Tsvetkov, V.I., Kuznetsov, V.S., Gafiatov, N., 1977, Influence of surface preparation techniques on the quality of vitreous enamel coatings. *Chem. Petroleum Eng.*, Vol. 13, No. 9, 824–826.
- Sorokin, G.M., Eroshkin, V.P., Grigorev, S.P., 1983, Calculation of the depth of penetration of an abrasive particle in abrasive-impact wear. *Chem. Petroleum Eng.*, Vol. 19, No. 6, 230–232.

- Spangenberg, M., 1972, Zur Haftfestigkeit von Walzzunder auf unlegiertem Stahl. *Werkst. Korros.*, Vol. 23, 880–886.
- Sparks, A.J., Hutchings, I.M., 1993, Effects of erodent recycling in solid particle erosion testing. *Wear*, Vol. 162–164, 139–147.
- Spindler, H., 1958, Beeinflussung der ausgeprägten Streckgrenze von weichem Stahl durch Sandstrahlen. *Die Naturwissenschaften*, Vol. 45, No. 23, 566–567.
- Spitsberg, I.T., Mumm, D.R., Evans, A.G., 2005, On the failure mechanisms of thermal barrier coatings with diffusion aluminide bond coatings. *Mater. Sci. Eng. A*, Vol. 394, 176–191.
- SSPC, 2006, Wet abrasive blast cleaning. SSPC-TR2/NACE/6G198SSPC/NACE *Joint Technical Report*, Final Draft, 2006
- SSPC-AB 2, 2004, *Abrasive Specification No. 2: Cleanliness of Recycled Ferrous Metallic Abrasives*. Revised version, The Society for Protective Coatings, New York.
- Staia, M.H., Ramos, E., Carrasquero, A., Roman, A., Lesage, J., Chicot, D., Mesmacque, G., 2000, Effect of substrate roughness induced by grit blasting upon adhesion of WC-17%Co thermal sprayed coatings. *Thin Solid Films*, Vol. 377–378, 657–664.
- Stallmann, K., Sieber, W., Hauser, H., 1988, Strahlentrosten—Optimierung des Strahlmittels und der Strahlbedingungen. *Materialwiss. Werkstofftech.*, Vol. 19, 133–137.
- Stephenson, D., Spear, T., Seymor, M., Cashell, L., 2002, Airborne exposure to heavy metals and total particulate during abrasive blasting using copper slag abrasive. *Appl. Occup. Environ. Hyg.*, Vol. 17, No. 6, 437–443.
- Stevenson, A.N., Hutchings, I.M., 1995a, Scaling laws for particle velocity in the gas-blast erosion test. *Wear*, Vol. 181–183, 56–62.
- Stevenson, A.N., Hutchings, I.M., 1995b, The influence of nozzle length on the divergence of the erodent particle stream in a gas-blast erosion rig. *Wear*, Vol. 189, 66–69.
- STG, 1963, Richtlinien für das Reinigungsstrahlen von Schiffsblechen und Formstahl. *STG 4303*, Schiffbautechnische Gesellschaft, Hamburg, Januar 1963.
- Stieglitz, U., 1996, Strahlmittelauswahl und Abfallvermeidung. *J. Oberflächentechnik*, Vol. 36, No. 10, 62–67.
- Strizhalo, V.A., Zasimchuk, E.E., Morozov, B.S., Bega, N.D., Kuzema, Y.A., Illjin, A.A., 1974, Effect of sand blasting on the low cycle fatigue of titanium alloys. *Strength Mater.*, Vol. 6, No. 9, 1083–1086.
- Strojny, A., Moody, N.R., Emerson, J.A., Even, W.R., Gerberich, W.W., 2000, Interfacial fracture of thin polymer films on aluminium. *Mater. Res. Soc. Symp.*, Vol. 629, 5.13.1–5.13.6.
- Tabor, D., 1951, *The Hardness of Metals*. Clarendon Press, Oxford.
- Taha, R., Al-Alawi, D., Al-Nabhani, M., Pillay, A.E., Al-Hamadi, A., 2001, Recycling of paint-contaminated grit. *J. Environ. Monit.*, Vol. 3, 421–424.
- Tamai, Y., Tanaka, S., 1967, Contact angle characteristics and breaking strength of paint plastic films. *J. Appl. Polym. Sci.*, Vol. 11, 297–304.
- Tangestanian, P., 1999, Starch media blast cleaning: properties and performance of masking tapes and aged paint films. *Master Thesis*, University of Toronto, Toronto, Canada.
- Tangestanian, P., Papini, M., Spelt, J.K., 2001, Starch media blast cleaning of artificially aged paint films. *Wear*, Vol. 248, 128–139.
- Tangirala, R., 1998, Computational models of particle size effects on brittle oxide scale erosion. *Master Thesis*, West Virginia University, Morgantown.
- Tashiro, H., Tomita, Y., 2004, Numerical study of air compressibility during horizontal pneumatic transport. *Particulate Sci. Technol.*, Vol. 22, 139–149.
- Terrat, J.-P., Boissel, J., 1995, A new device for checking surface contamination based upon electrical measurement. *Microchim. Acta*, Vol. 120, 183–193.
- Thiruvengadam, A., 1967, The concept of erosion strength. *ASTM STP 408*, American Society for Testing of Material, Philadelphia, 22–41.
- Tilghman, B.J., 1870, Improvement in cutting and engraving stone, metal, glass, etc. *US States Patent* 108,408, October 18, 1870.
- Timoshenko, S.P., Goodier, J.N., 1970, *Theory of Elasticity*. 3rd edition, McGraw-Hill, New York.

- Tinklenberg, G.L., Doezema, D.M., 1998, Health concerns for workers using zinc-rich coatings. *J. Protect. Coat. Lin.*, Vol. 15, 36–46.
- Tolpygo, V.K., Clarke, D.R., Murphy, K.S., 2001, The effect of grit blasting on the oxidation behavior of a platinum-modified nickel-aluminide coating. *Metall. Mater. Trans.*, Vol. 32A, 1467–1478.
- Tong, J., Zhang, M., Jiang, M., Ren, L., 1998, Free-abrasive wear of an enamel coating. *J. Mater. Sci.*, Vol. 17, 523–525.
- Tosha, K., Iida, K., 1990, Stock removal and surface residual stress of grit blasted titanium. *Proc. 4th Int. Conf. Shot Peening*, Tokyo, 435–444.
- Tosha, K., Iida, K., 2001, On the area coverage of grit blasting. *Proc. Int. Conf. Shot Peening Blast Cleaning* (ed. M.C. Sharma), Bophal, 160–166.
- Trezona, R.I., Hutchings, I.M., 2001, Resistance of paint coatings to multiple solid particle impact: effect of coating thickness and substrate material. *Prog. Org. Coat.*, Vol. 41, 85–92.
- Trezona, R.I., Hutchings, I.M., Ramamurthy, A.C., 1997, A new technique for determining the micro-scale abrasion resistance of automotive clearcoats. *Proc. Int. Symp. Automot. Technol. Autom.* (ed. D. Roller), Automotive Automation Ltd, Croydon, 913–920.
- Trezona, R.I., Pickles, M.J., Hutchings, I.M., 2000a, A full factorial investigation of the durability of automotive clearcoats. *Tribol. Int.*, Vol. 33, 559–571.
- Trezona, R.I., Weakley, A.P., Hutchings, I.M., 2000b, Effect of weathering on the mechanical durability of automotive clearcoats. *Surf. Coat. Int.*, Vol. 83, 580–587.
- Trotter, L.E., 2001, Comparison of surface preparation using different methods. *Proc. 11th Am. Waterjet Conf.* (ed. M. Hashish), WJTA, St. Louis, 745–763.
- Truelove, R.K., 1966, Shotblasted ships plate—the significance of profile and its effect on the performance of protective coatings. *J. Oil Colour Chem. Assoc.*, Vol. 49, No. 1, 57–88.
- Trujillo, M., Sadki, M., 2004, Sensitivity analysis for texture models applied to rust steel classification. *Mach. Vis. Appl. Ind. Insp.*, XII (eds. J.R. Price, F. Meriaudeau), Vol. 5303, SPIE Bellingham, 161–169.
- Uetz, H., 1986, *Abrasion und Erosion*. Carl Hanser Verlag, München-Wien.
- Uetz, H., Föhl, J., 1978, Wear as an energy transformation process. *Wear*, Vol. 49, 253–264.
- Uetz, H., Gommel, G., 1966, Temperaturerhöhung und elektrische Aufladung beim Stoss einer Stahlkugel gegen eine Stahlplatte. *Wear*, Vol. 9, 282–296.
- Uferer, R., 1992, Optimales Druckluftstrahlen unter variablen Bedingungen. *Dissertation*, Universität Karlsruhe, Germany.
- Uferer, R., 1993, Optimales Druckluftstrahlen unter variablen Bedingungen. *J. Oberflächentechnik*, Vol. 33, No. 7, 36–40.
- Uhlendorf, H.-J., 2000, Korrosionsschutzmaßnahmen an Hafenanlagen in der Jade. *Hansa*, Vol. 137, No. 8, 75–79.
- Uhlmann, E., El Mernissi, A., Dittberger, J., Krieg, M., 2003, Einfluss des Strahlmittels beim Druckluftstrahlen. *J. Oberflächentechnik*, Vol. 43, No. 2, 62–70.
- Uhlmann, E., El Mernissi, A., Hollan, R., 2006, Adhäsive Oberflächen-Eigenschaften: Was bringt das Trockeneisstrahlen? *J. Oberflächentechnik*, Vol. 46, No. 2, 44–47.
- Urbanovich, L.I., Kramchenkov, E.M., Chunosov, Y.N., 1995, Effect of the parameters of impact action and mechanical and thermal properties of materials on the intensity of their gas-abrasive erosion. *Mater. Sci.*, Vol. 31, No. 2, 263–267.
- Vakula, L.V., Pritykin, L.M., 1991, *Polymer Adhesion: Physico-Chemical Principles*. Ellis Horwood, New York.
- Van den Brand, J., van Gils, S., Terryn, H., Sivel, V.G., de Witt, J.H., 2004, Changes in epoxy-coated aluminium due to exposure to water. *Progr. Organic Coat.*, Vol. 51, 351–364.
- Van der Kaaden, 1994, Wet blasting studied to replace dry blasting in Netherlands shipyards. *J. Protect. Coat. Lin.*, Vol. 11, No. 5, 79–86.
- Van Ooij, W.J., 1984, Interfacial interactions between coatings and metals related to adhesion and corrosion protection. *Organic Coatings: Science and Technology* (ed. G.D. Parfitt), Athens, Greece, 1984, 277–289.

- Van Rooijen, R.G., Sinke, J., van der Zwaag, S., 2005, Improving the adhesion of thin stainless steel sheets for fibre laminate (FML) applications. *J. Adhes. Sci. Technol.*, Vol. 19, No. 16, 1387–1396.
- Van Tijum, R., De Hosson, J.T., 2005, Effects of self-affine surface roughness on the adhesion of metal-polymer interfaces. *J. Mater. Sci.*, Vol. 40, 3503–3508.
- Varacalle, D.J., Lundberg, L.B., Hartley, R.S., Walker, J., Riggs, W.L., 1995, Surface preparation via grit-blasting for thermal spraying. *Proc. 8th Natl. Therm. Spray Conf.*, Houston, TX.
- Varacalle, D.J., Guillen, D.P., Deason, D.M., Rhodaberger, W., Sampson, E., 2006, Effect of grit-blasting on substrate roughness and coating adhesion. *J. Therm. Spray Technol.*, Vol. 15, No. 3, 348–355.
- Vasek, J., Martinec, P., Foldyna, J., 1993, Influence of properties of garnet on AWJ cutting process. *Proc. 7th Am. Water Jet Conf.*, (ed. M. Hashish), Vol. 1, Water Jet Technology Association, St. Louis, 365–387.
- VDI, 1987, Einwirkung mechanischer Schwingungen auf den Menschen—Beurteilung, *VDI-Richtlinie 2057/Blatt 3*, Mai 1987.
- Verspui, M.A., With G., Dekkers, E.C., 1997, A crusher for single particle testing. *Rev. Sci. Instrum.*, Vol. 63, No. 3, 1553–1556.
- Vesga, L.F., Vera, E., Panqueva, J.H., 2000, Use of electrochemical impedance spectroscopy to evaluate the performance of a primer applied under different surface preparation methods. *Prog. Org. Coat.*, Vol. 39, 61–65.
- Villafuerte, J.C., Kerr, H.W., 1993, The effect of abrasive cleaning on columnar-to-equiaxed transitions in ferritic stainless steel GTA welds. *International Trends in Welding Science and Technology* (eds. S.A. David, J.M. Vitek), ASM International, Materials Park, 187–191.
- Vincent, L.D., 2001, The importance of wetting a substrate. *Mater. Perform.*, No. 2, 40–41.
- Wadell, H., 1933, Sphericity and roundness of rock particles. *J. Geol.*, Vol. 41, 316–331.
- Wagner, W., 1990, *Strömungstechnik und Druckverlustberechnung*. Vogel Buchverlag, 2nd Ed., Würzburg.
- Walley, S.M., Field, J.E., 1987, The erosion and deformation of polyethylene by solid-particle impact. *Philos. Trans. R. Soc. London*, Vol. A321, 277–303.
- Walley, S.M., Field, J.E., Yennadhiou, P., 1984, Single solid particle impact erosion damage on polypropylene. *Wear*, Vol. 100, 263–280.
- Walley, S.M., Field, J.E., Greenglass, M., 1987, An impact and erosion study of polyetheretherketone. *Wear*, Vol. 114, 59–71.
- Watts, J.F., Dempster, B.R., 1992, A comparative study of the influence of surface pretreatment on the failure characteristics of adhesively bonded titanium. *Surf. Interface Anal.*, Vol. 19, 115–120.
- Weber, M., 1974, *Strömungs-Fördertechnik*. Krauskopf, Mainz.
- Weidenhaupt, W., 1970, Über den Einfluß der Entzunderungs- und Ziehbedingungen auf die Oberflächen-Feingestalt von Stab- und Profilstahl. *Dissertation*, RWTH Aachen, Germany.
- Weldon, D.G., Bochan, A., Schleiden, M., 1987, The effect of oil, grease, and salts on coating performance—a laboratory evaluation. *J. Protect. Coat. Lin.*, Vol. 17, No. 6, 46–55.
- Wellinger, K., Gommel, G., 1967, Vielfachstoßuntersuchungen Stahlkugel—Stahlplatte im Zusammenhang mit Strahlmittelzertrümmerung und Strahlverschleiß. *Arch. Eisenhüttenwesen*, Vol. 38, No. 5, 355–362.
- Wellinger, K., Uetz, H., 1955, Gleitverschleiß, Spülverschleiß, Strahlverschleiß unter der Wirkung von körnigen Stoffen. *VDI-Forschungshefte*, No. 449, 1–40.
- Wellinger, K., Uetz, H., Gommel, G., 1962, Gütekennwerte von Strahlmitteln und deren Veränderung während des Strahlvorganges. *Stahl Eisen*, Vol. 82, No. 21, 1436–1445.
- Wenzel, R.W., 1936, Resistance of solid surfaces to wetting by water. *Ind. Eng. Chem.*, Vol. 28, 988–994.
- Werner, M., Kauw, V., 1991, High pressure water jet system—a new process for cleaning defective mortar joints in historic masonry. *Proc. 9th Int. Brick/Block Masonry Conf.*, Vol. 3, Berlin, 1639–1644.

- Wiederhorn, S.M., Lawn, B.R., 1979, Strength degradation of glass impacted with sharp particles. *J. Am. Ceram. Soc.*, Vol. 62, 66–70.
- Wigren, J., 1988, Grit-blasting as surface preparation before plasma spraying. *Thermal Spray—Advances in Coating Technology* (ed. D.L. Houck), ASM International, Materials Park, 99–104.
- Wille, R., 2005, *Strömungslehre*. 8. Auflage, Springer, Berlin.
- Winter, R.E., Hutchings, I.M., 1974, Solid particle erosion studies using single angular particles. *Wear*, Vol. 29, 181–194.
- Wirtz, H., 1962, *Strahlverfahrenstechnik*. Prost & Meiner-Verlag, Coburg.
- Wolak, J., Worm, P., Patterson, I., Bodoia, J., 1977, Parameters affecting the velocity of particles in an abrasive jet. *ASME J. Eng. Mater. Technol.*, Vol. 99, No. 4, 147–152.
- Wood, G.C., Hodgkiess, T., 1972, The hardness of oxides at ambient temperatures. *Werkst. Korros.*, Vol. 23, 766–773.
- Wood., R.J.K., 1999, The sand erosion performance of coatings. *Mater. Designs*, Vol. 20, 179–191.
- Xie, L., Sohn, Y., Jordan, E.H., Gell, M., 2003, The effect of bond coat grit blasting on the durability and thermally grown oxide stress in an electron beam physical vapor deposited thermal barrier coating. *Surface Coat. Technol.*, Vol. 176, 57–66.
- Yabuki, A., Matsumura, M., 1999, Theoretical equation of the critical impact velocity in solid particles impact erosion. *Wear*, Vol. 233–235, 476–483.
- Yabuki, A.; Matsuwaki, K.; Matsumura, M., 1999, Critical impact velocity in the solid particles erosion of metallic materials. *Wear*, Vol. 233–235, 468–475.
- Yankee, S.J., Bletka, B.J., Salsbury, R.L., 1991, Quality control of hydroxylapatite coatings: the surface preparation stage. *Proc. 4th Natl. Therm. Spray Conf.*, Pittsburgh, PA, May 4–10, 475–479.
- Yashima, S., Kanda, Y., Sano, S., 1987, Relationships between particle size and fracture energy or impact velocity required to fracture as estimated for single particle crushing. *Powder Technol.*, Vol. 51, 277–282.
- You, C., Oh, S., Kim, S., 2001, Influences of heating condition and substrate-surface roughness on the characteristics of sol-gel-derived hydroxyapatite coatings. *J. Sol-Gel Sci. Technol.*, Vol. 21, 49–54.
- Zaat, J.H., 1960, Voruntersuchungen über die Strahlreinigung von Stahlkonstruktionen. *Schiff Hafen*, Vol. 12, No. 7, 624–637.
- Zahavi, J., Schmitt, G.F., 1981, Solid particle erosion of polymeric coatings. *Wear*, Vol. 71, 191–210.
- Zahavi, J., Schmitt, G.F., 1982, Solid particle erosion of coatings on transparent polycarbonate and reinforced composites. *Selection and Use of Wear Tests for Coatings* (ed. R.G. Bayer), ASTM STP 769, New York, 28–70.
- Zehnder, A.T., Ramamurthy, A.C., Bless, S.J., Brar, N.S., 1993, Stone impact damage to automotive paint finishes: measurement of temperature rise due to impact. *Int. J. Impact Eng.*, Vol. 13, No. 1, 133–143.
- Zhang, B., Zhou, L., 1997, Effect of sandblasting on adhesion strength of diamond coatings. *Thin Solid Films*, Vol. 307, No. 1–2, 21–28.
- Zhang, S.W., Wang, D., Yin, W., 1995, Investigation of abrasive erosion of polymers. *J. Mater. Sci.*, Vol. 30, 4561–4566.
- Zhang, S., Panat, R., Hsia, K.J., 2003, Influence of surface morphology on the adhesive strength of aluminium/epoxy interfaces. *J. Adhes. Sci. Technol.*, Vol. 17, 1685–1711.
- Zieler, W., 1965, Auswahl und Beurteilung von Strahlmitteln unter Berücksichtigung der beim Strahlen erzielbaren Oberflächenbeschaffenheit. *Fachberichte Oberflächentechnik*, Vol. 3, No. 3, 75–84.
- Zieler, W.; Lepand, H., 1964, *Strahlen und Strahlmittel*. Carl Hanser Verlag, München.
- Zinn, W., Schulz, J., Kopp, R., Scholtes, B., 2002, The influence of the velocity of a peening medium on the almen intensities and residual stress states of shot peened specimens. *Proc. 8th Int. Conf. Shot Peening*, Garmisch-Partenkirchen, 161–166.
- Zisman, W.A., 1972, Surface energetics of wetting, spreading, and adhesion. *J. Paint Technol.*, Vol. 44, No. 564, 42–57.

- Zolotar, A.I., 1973, Wear of materials under hydroabrasive conditions. *Chem.Petroleum Eng.*, Vol. 9, No. 1, 76–79.
- Zorll, U., 1975a, Untersuchungen über Deformation und Reißbildung an Lackschichten bei stoßartiger Belastung. *Farbe Lack*, Vol. 81, 505–509.
- Zorll, U., 1975b, Schlagfestigkeitsbestimmung von Blechlackierungen nach dem Kugelstoßversuch. *Metalloberfläche*, Vol. 29, 577–616.
- Zorll, U., 1976, Untersuchungen über den Einfluß der Grundbeschichtung auf die Schlagfestigkeit von Zweischichtlackierungen. *Farbe Lack*, Vol. 82, 821–826.
- Zorll, U., 1983, Untergrundeinflüsse auf das Verhalten von Korrosionsschutzbeschichtungen bei stoßartiger Belastung. *Werkst. Korros.*, Vol. 34, 514–519.
- Zorll, U., 1984, Korrosionsschutz mit Hilfe organischer Schutzschichten und deren Charakterisierung. *Fresenius Z. Anal. Chem.*, Vol. 319, 675–681.
- Zosel, A., 1977, Ein Gerät zur Untersuchung der Schlagfestigkeit von Lackfilmen. *Farbe Lack*, Vol. 83, 9–12.
- Zouari, B., Touratier, M., 2000, Numerical simulation of aeronautical paint layer decoating. *Finite Elements: Techniques and Developments* (ed. B.H. Topping), Civil-Comp Ltd., Edinburgh, 231–236.
- Zouari, B., Touratier, M., 2001, Simulation of decoating of a paint layer by using media blasting. *Proc. 4th Int. ESAFORM Conf. Met. Forming*, University of Liege, 655–657.
- Zouari, B., Touratier, M., 2002, Simulation of organic coating removal by particle impact. *Wear*, Vol. 253, 488–497.
- Zum Gahr, K.-H., 1987, *Microstructure and Wear of Materials*. Elsevier, Amsterdam.

List of Symbols

\dot{A}	Cleaning rate
A_A	Adhesion cross-section
A_a	Auerbach constant
a_C	Contact radius
A_C	Cross-section
A_D	Dynamic stress strain parameter
A_F	Fatigue strength coefficient
A_G	Area of Particle Spread
A_M	Area to be cleaned
A_P	Abrasive particle cross-section
a_p	Particle acceleration
A_R	Rough surface area
A_S	Specific cleaning rate
a_V	Tool acceleration value
A_0	Smooth surface area
c	Speed of sound
C_A	Area coverage
C_B	Energy transfer parameter
C_D	Disposal cost
c_D	Particle drag coefficient
C_E	Equipment cost
C_G	Spray gun current
c_K	Collision number
C_L	Labour cost
c_M	Longitudinal wave velocity
c_P	Isobaric heat capacity
C_P	Abrasive material cost
C_R	Roughness factor
c_R	Particle concentration
C_S	Sutherland parameter
C_{SP}	Specific cost

C_{TP}	Abrasive parameter
c_V	Isochoric heat capacity
C_λ	Friction parameter for abrasive hoses
d^*	Particle size distribution parameter
d_B	Blast pot abrasive outlet valve diameter
d_e	Erosion pit diameter
d_E	LAVAL nozzle exit diameter
d_H	Hose diameter
d_J	Jet diameter
d_N	Nozzle (throat) diameter
d_P	Abrasive particle diameter
d_{PG}	Geometric mean particle diameter
d_{PSt}	Statistical particle diameter
DR	Degree of rusting
D_S	Final splat diameter
d_V	Diameter abrasive metering valve
d_{VK}	Diameter compressor outlet valve
D_0	Initial splat diameter
E_A	Young's modulus abrasive material
E_F	Particle fragmentation energy
E_f	Dust emission factor
E_i	Particle energy stored in workpiece
E_P	Abrasive particle kinetic energy
\dot{E}_P	Particle stream energy flow
E_R	Erosion rate
e_R	Coefficient of restitution
E_{SD}	Strain energy density
E_p	Specific energy
E^*	Secondary energy absorption
F_A	Adhesion force
F_C	Contact force
F_D	Drag force
F_f	Volumetric filler fraction
F_P	Abrasive volume fraction
Fr	Froude number
F_R	Jet reaction force
F_W	Weight force
F_X, F_Y	Cutting forces
g	Acceleration
G_N	Grit number
G_{Ic}	Fracture energy (critical energy release rate)
h_A	Enthalpy of air
H_B	Brinell hardness
h_C	Layer thickness
H_d	Dynamic hardness

h_L	Depression depth/lateral crack formation depth
H_M	Target material hardness
H_N	Nozzle material hardness
H_P	Abrasive material hardness
H_v	Vickers hardness
h_Z	Thickness mill scale
H_θ	Contact angle hysteresis
\dot{I}_A	Air impulse flow
I_P	Particle impulse
k	Reaction kinetic parameter
k_E	Elastic parameter
K_F	Force ratio
k_H	Internal hose wall roughness
K_R	Mass flow ratio parameter
K_R	Coating ageing parameter
K_S	Mill scale resistance parameter
k_Z	Metering valve flow parameter
K_{Ic}	Fracture toughness
L	Machining geometry parameter
l_C	Crack length
l_H	Hose length
l_N	Nozzle length
L_P	Abrasive particle spacing
L_P^*	Relative abrasive particle spacing
L_R	Radial crack length
m	Abrasive mass flow power exponent
M_0	Sieve overflow
Ma	Mach number
\dot{A}_A	Air mass flow rate
m_C	Removed coating mass
\dot{A}_C	Critical particle mass flow rate
m_D	Dust mass concentration
m_F	Fatigue exponent
m_f	Flow distribution parameter
\dot{A}_F	Abrasive flux rate
m_G	Critical abrasive mass
m_M	Removed target mass
\dot{A}_N	Abrasive flux rate
m_O	Operator weight
\dot{m}_P	Abrasive particle mass
\dot{m}_P	Abrasive mass flow rate
m_S	Specific abrasive consumption rate
m_{SC}	Mill scale mass
m_W	Weibull modulus
n_C	Compressor rotor rotational speed

n_d	Particle diameter exponent
n_e	Impact angle exponent
N_F	Fatigue cycle number
n_E	Energy power exponent
n_m	Abrasive mass flow exponent
n_M	Particle size distribution parameter
N_P	Abrasive particle number
n_P	Particle size power exponent
\dot{N}_P	Abrasive particle impingement frequency
\dot{n}_P	Particle frequency number
N_R	Radial crack number
n_S	Number of passes
n_t	Exposure time power exponent
n_V	Particle velocity exponent
n_ρ	Particle density exponent
p	Static air pressure
P^*	Power availability
p_0	Atmospheric pressure
p_B	Back pressure
p_C	Threshold air pressure
p_E	Nozzle exit pressure
P_F	Particle fragmentation power
p_G	Gauge pressure
P_H	Theoretical isentropic compressor power
P_K	Actual power rating compressor
P_P	Particle power
p_S	Spray pressure
P_S	Specific power rating compressor
q	Velocity exponent
\dot{Q}_A	Air volumetric flow rate
\dot{Q}_C	Erosion durability
\dot{Q}_0	Theoretical compressor air volumetric flow rate
q_0	Unit compressor air volume
Q_t	Specific erosion resistance
R	Mass loss ratio
R_a	Average roughness
R_D	Specific disposal rate
Re	Reynolds number
Re_H	Reynolds number hose flow
R_E	Erosion resistance
R_H	Hardness ratio
r_i	Indent radius
r_i	Scar radius
R_i	Individual gas constant
r_J	Jet radius

R_{\max}	Maximum roughness
r_N	Nozzle radius
r_N^*	Dimensionless nozzle radius
R_P	Polarization resistance
r_P	Particle radius
r_P^*	Dimensionless particle radius
R_{PST}	polarization resistance standard
r_{PL}	Abrasive particle transition radius
r_R	Roughness factor
R_{RF}	Relative roughness factor
R_Y	Average maximum roughness
R_Z	Average maximum roughness
S_{LS}	Spreading coefficient
S_P	Abrasive particle shape parameter
S_R	Peak spacing
S_V	Solid by volume in paint
T	Absolute temperature
t	Time
t_a	Acceleration time
t_B	Blasting time
T_D	Toughness parameter
T_E	Nozzle exit temperature
t_E	Exposure time
t_F	Critical exposure time
t_i	Incubation time
T_K	Absolute temperature after compression
T_N	Normative temperature
t_O	Optimum exposure time
v_A	Air flow velocity
v_{AP}	Saltation velocity
v_C	Abrasive particle threshold velocity
V_C	Crater volume
v_D	Drop velocity
v_{EL}	Threshold particle velocity for elastic response
v_F	Air flow velocity
v_H	Critical abrasive velocity
v_L	Laval velocity
V_M	Removed material volume
\dot{V}_M	Volumetric removal rate
v_{\min}	Critical conveying velocity
v_N	Nozzle traverse rate
v_{opt}	Optimum air flow velocity
v_P	Particle volume
v_P	Abrasive particle velocity
\dot{v}_P	Average abrasive particle velocity

v_{PL}	Critical abrasive velocity
v_{Pt}	Threshold abrasive velocity for fragmentation
v_{rel}	Relative velocity
v_S	Particle settling velocity
v_T	Nozzle traverse rate
W_A	Work of adhesion
x	Stand-off distance; dimensional direction
x^*	Dimensionless stand-off distance
x_w	Moisture pressure dew point
Y_M	Young's modulus target material
Y_P	Young's modulus abrasive material
y_t	Machining geometry parameter
z	Dimensional direction
α_B	Erosion exponent
α_C	Crack geometry coefficient
α_F	Particle friction exponent
α_L	Crack geometry parameter
α_M	Contact parameter
α_N	Nozzle exit coefficient
α_P	Nozzle coefficient
β_F	Fatigue parameter
β_P	Focus coefficient
χ_C	Paint loss correction factor
χ_G	Particle geometry parameter
χ_N	Nozzle diameter power exponent
χ_P	Abrasive assessment parameter
Δh_C	Thickness reduction
Δp	Pressure gradient
Δp_A	Pressure loss air hose
Δp_P	Pressure loss due to abrasive addition
Δp_T	Pressure loss abrasive hose
δ_H	Thickness laminar boundary layer
δq	Roughness angle
ε	Strain
ε_0	Peel strain
ε_C	Specific energy parameter
ε_D	Mill scale deformation degree
ε_M	Inverse specific erosion energy
ε_Y	Yield strain
ϕ	Velocity power exponent
ϕ_D	Particle disintegration number
ϕ_F	Fixture diameter
ϕ_E	Erosion efficiency
Φ_E	Erosion efficiency
ϕ_P	Reduction parameter

γ^d	Dispersive specific surface energy
γ_L^l	Specific surface energy – liquid
γ^p	Polar specific surface energy
γ_S	Specific surface energy – solid
γ_{SL}	Specific surface energy solid–liquid
η_A	Dynamic viscosity
η_C	Dynamic viscosity of liquefied coating
η_{Kd}	Dynamic losses compressor
η_{Km}	Mechanical losses compressor
η_N	Nozzle efficiency
ϕ	Impact angle
ϕ_L	Laval nozzle coefficient
κ	Isentropic exponent
λ_A	Air flow friction parameter
λ_P	Abrasive particle flow friction parameter
ν_A	Kinematic viscosity
ν_M	Poisson ratio target material
ν_P	Poisson ratio abrasive material
ω	Nozzle flow parameter
Π_1	Dimensionless abrasive mass flow rate
θ_C	Contact angle
θ_J	Jet expansion angle
θ_P	Particle diameter power exponent
ρ_A	Gas density
ρ_B	Abrasive bulk density
ρ_C	Coating material density
ρ_N	Normative air density
ρ_P	Abrasive material density
ρ_S	Particle stream density
σ	Stress
σ^*	Strength parameter
$\sigma_{0.1}$	Elastic deformation limit
σ_A	Adhesion strength
σ_B	Bond strength
σ_E	Failure stress
σ_f	Yield stress
σ_F	Fatigue strength
σ_{Fr}	Fracture stress
σ_M	Adhesion strength mill scale
σ_N	Stress normal to interface
σ_{NF}	Normal failure stress
σ_R	Residual stress
σ_{Rmax}	Maximum residual stress
σ_T	Tensile stress
σ_V	Erosion strength

σ_{VP}	Standard deviation particle velocity
τ_M	Shear failure stress
τ_N	Shear stress
ξ_K	Friction parameter air hose armatures
ξ_P	Friction parameter abrasive hose armatures
ϑ	Celsius temperature
ϑ_R	Rolling temperature
ν_S	Specific gas volume
μ_F	Particle friction parameter
ω_P	Rotational particle speed
Ψ	Outflow function
Ψ_F	Machining parameter
Ψ_M	Dimensionless coefficient
Ψ_N	Empirical coefficient

Index

- Abrasive mass flow rate, 31, 53, 62–63, 84, 88, 94–96, 107, 119–128, 140, 153, 259–261, 264–268, 306–307
- Abrasive metering, 118–127
- Abrasive particle, 367–378, 387, 392, 394–400, 414–419
- Adhesion, 464–489
 - strength, 464–489
- Adhesive force, 423, 464
- Ageing kinetics, 462–463
- Air
 - air-borne metals, 310–314
 - mass flow rate, 59–66, 67, 79–80, 123, 129, 158, 250
 - pressure, 94, 120–122, 129, 136–137, 159, 243–247, 283, 397
 - quality, 116–118
 - sound, 297–301
 - velocity, 67, 98, 103, 106, 140, 143–146, 158
- Aluminium oxide, 155–156, 378–379, 384–385, 387, 396, 400, 403–406, 417, 419, 422, 438–439, 441, 444, 462, 475–479, 492
- Aluminium substrate, 421, 438–439, 448
- Area coverage, 90
- Artificial scribe, 365, 390, 453–454, 458, 459, 461
- Asbestos, 316

- Blasius equation, 132
- Blasting time, 395, 403, 405–406, 417–419
- Blast machine, 118–128
- Body sound, 301–302
- Boron carbide, 155–156, 161, 162
- Brittleness, 198, 216, 218, 262

- Cadmium, 314–315, 326, 331–332
- Carbon dioxide, 118, 297, 298, 486
- Cathodic disbonding, 5, 379–381
- Chemical cleanliness (dissolved substance), 349–361
- Cleaning rate, 127, 153–154, 228, 242–243, 245, 247–249, 251–252, 256–261, 264–267, 270–271, 276–278, 282–283, 289–291
- Cleanliness, visual, 338–346
- Coal slag, 247, 267, 283, 307, 343, 361
- Coal tar, 469
- Coefficient of restitution, 182–184, 268
- Compressor, 62, 107–108, 109–117, 159, 250, 298
- Confined space, 321–324
- Constant-Inspection-Visual (KIV), 453–456
- Contact angle, 362–363, 435–436, 438, 441–450
- Contact force, 192, 480–481
- Contact radius, 192
- Contact time, 193–194
- Contamination, 35–36, 324–325, 331–332
- Conveying velocity, 128, 140, 143, 145–146
- Copper slag, 127, 243–244, 247, 266, 307, 341, 343–345, 369
- Corrosion resistance, 429–434, 438
- Cutting wear, 203
- Cut wire, 15–16

- Damage number, 189–191
- Debonding, 167, 229–232, 233–238
- Deformation wear, 203
- Degreasing, 362, 366, 427, 431, 439, 441
- Degree of blistering, 355, 453–454, 463–464
- Degree of rusting, 341, 453–454, 462–463
- Delamination model, 236–237
- Density, 90–92, 100, 453
- Deposition, 494–495
- Design pressure, 81–83
- Disintegration number, 47–49

- Dissolved substance, 349–361
 Dry film thickness, 175, 225, 227, 243
 Dust emission, 306–307, 314
- Elastomers, 210–221
- Electrochemical impedance spectroscopy (EIS), 456, 492, 493
- Energy absorption, 51–53, 185–189
- Epoxy, 36, 173–174, 177, 222, 225, 264–265, 267, 271, 456–458, 479–482
- Erosion
 durability, 228–229, 247
 efficiency, 283–284
 rate, 37, 161, 162, 185, 200, 205, 207, 217–219, 247–248, 259–262, 268–269, 275
 resistance, 214–221, 223–228
- Explosion, 296–297
- Exposure time, 31, 90, 92, 155, 261–264, 301–302, 318–320, 388–390
- Fatigue, 287–289
 limit, 413, 421
 strength, 374, 420–422
- Flattening, 393, 496–497
- Flow velocity, 66–68, 129–130, 131, 136–137, 140, 142, 144, 146–147, 152, 155
- Flux rate, 75, 214, 268–270
- Focus coefficient, 79
- Fractal, 380, 392, 391, 407
- Fracture
 energy, 185, 200, 216, 393, 435–436, 479–482
 mechanics, 8, 172–173, 181–182, 205
 toughness, 172–173, 177, 181–182, 245–246
 zone, 37–38
- Fragmentation, 42–47, 49–53, 247
- Friction coefficient, 191–192, 423
- Friction number, 131, 132–136, 137, 148–150
- Froude number, 145–146, 148–150
- Garnet, 10, 21, 24, 46, 127, 406
- Gas constant, 55
- Gasterstädt equation, 150–151
- Glass bead, 31, 35, 36–38, 41, 44, 79, 94, 104, 122, 237, 402, 417, 425–427, 428–433, 473
- Glass sphere, 38, 41, 46, 78, 100, 196
- Grease on Coating Performance, 363–366
- Grinding, 379, 381, 433, 468
- Grit, 3, 8, 17, 18, 100, 123–124, 256, 266, 277, 287, 321, 344, 370, 376–378, 398–406, 479
- Hardness
 abrasive, 36–37, 279–281, 404
 nozzle, 155–164
 substrate, 414–416
- Hardness ratio, 161, 189, 280, 400, 404, 407
- Height distribution, 409
- Hertzian crack, 38, 194
- Hose diameter, 129–130, 132, 136–138, 142–146, 151, 153–154
- Hose line, 115, 128–137
- Hydroblasting, 262, 288, 313, 330, 357, 468
- Impact angle, 183–184, 203–205, 201–213, 217–222, 237, 241, 248–249, 259–261
- Impact frequency, 31, 212–214, 266, 275
- Impurity, 492
- Incubation period, 214, 262
- Indentation debonding, 229–233
- Initial condition, 290, 338–340
- Ientropic compression, 112–113
- Jet structure, 77–84
- Kinetic energy, 30–33
- Laminar layer, 132
- Lateral crack, 196–200, 205
- Laval nozzle, 64, 68–71, 75, 80, 89–90, 97, 251–256
- Laval pressure, 60, 67
- Lead, 34–35, 310–314, 350
- Mach number, 59, 71–72, 154
- Mass flow ratio, 87, 96, 101–103, 123–124, 144, 145, 149, 151–152, 266–267, 275
- Metal dusting, 432–434
- Metal-sprayed coating, 286, 341, 345, 386, 391, 473, 475, 482, 486
- Metering valve, 119–120, 122, 127, 266, 306
- Mill scale, 4, 174–175, 207–210, 252–254, 257–259, 275–277
- Moisture, 114, 116, 479–482
- Needle gunning, 357, 468–472
- Nikuradse equation, 132–133
- Nozzle
 diameter, 31, 64, 67, 87, 97, 103–106, 115–116, 119–120, 143, 145, 153–154, 159–160, 163, 244, 249–252
 geometry, 63–68, 81, 85, 123–126, 155, 162, 247, 251–252
 length, 73, 79, 101–102, 125–126, 163
 wear, 155–164

- Oil, 109–110, 116, 118, 362, 363
- Organic coatings, 167–181
- Organic film, 362–365
- Outflow function, 59–60
- Overblasting, 378–379, 409–412
- Oxides, 167–181
- Particle
 - acceleration, 72–74
 - collision, 266, 267
 - diameter, 24–29, 43, 52, 74, 94, 100, 122–123, 147, 270–277
 - embedment, 367–379
 - shape, 17–21, 49–50, 100, 277–281, 400, 402, 488
 - size, 24–32, 97, 270–277, 398–402
 - size distribution, 24–27, 29, 51, 305
 - spacing, 76
 - velocity, 85–107
- Personal protective equipment, 320–321
- Pitting, 340, 429–431, 438
- Plasma-sprayed coating, 384, 393, 487
- Ploughing, 201, 204, 236–237
- PMMA, 248, 269
- Polarization, 430
- Polymers, 210–211, 212–224
- Powder coating, 217, 222, 225, 239, 286, 275, 493
- Power
 - availability, 32–34
 - density, 489
- Preparation grade, 341–346
- Pressure drop, 123–124, 130–140, 144–154
- Process efficiency, 284–286
- Profile of substrates, 380–411
- Pull-off strength, 341, 345, 373, 389–390, 467, 494–472, 476, 479, 482–485
- Quartz, 1, 11, 35, 41, 43, 45, 52, 63, 149–151, 161, 186, 190, 215, 222, 247, 258, 307–308, 374, 416, 96, 433
- Radial crack, 196, 197–200, 205, 206, 233
- Recycling, 332–335
- Residual stress, 386, 417–419
- Reynolds number, 72–73, 132–136
- Roughness, 380–412
 - factor, 383, 402, 443
- Roundness, 18–21
- Rubber, 213–224, 217, 219–221, 248, 259–260, 269, 273, 275, 280–281, 285, 365–366, 460–461
- Rust, 258, 264, 282–283, 340–343, 346, 347–357
- Safety, 295–296
- Saltation velocity, 142–144
- Salt spray test, 389, 460, 461, 467
- Screw compressor, 111–113
- Settling velocity, 147
- Shot
 - blast cleaning, 298–299, 301
- Sieve analysis, 24–25
- Silicon carbide, 106, 495
- Slag, 3, 46, 122, 147, 149–151, 243–245, 247, 256–257, 266–267, 271, 283, 307, 325, 331, 334, 341–343, 345–347, 361, 368, 374, 483
- Slurry blast cleaning, 296, 331
- Sound velocity, 301
- Sphericity, 18–21
- Splat, 393–394, 496–497
- Spreading coefficient, 442
- Stand-off distance, 77–80, 101–103, 256, 258, 325, 396–397, 488–491
- Steel grit, 64, 100, 127, 256, 264, 271, 275, 305, 382, 398, 399–405, 408, 417, 421, 432, 475, 483, 485
- Strain energy density, 169, 226, 284
- Strain rate, 170–172, 177, 193
- Stream density, 90–92
- Stress corrosion cracking (SCC), 429–430
- Stress-strain curve, 169–170, 204
- Substrate
 - deflection, 423
 - hardness, 397, 400, 414–416
- Surface energy, 434–437
- Surface integrity, 413–433
- Threshold velocity, 41–45, 222–223, 245
- Titanium, 179, 189–190, 377–379, 400, 402, 414–416, 412, 425, 431
- Traverse rate, 90, 243, 262, 406
- Tungsten carbide, 155, 161, 393, 468, 490, 497
- Ultrasonic cleaning, 379
- Underwater application, 290–291
- Vibrations, 301, 318–320
- Viscosity, 56–58, 132, 392, 481, 496
- Visual standard, 338–340
- Waste disposal, 325–331
- Water jet, 288, 302, 316–319, 366
- Weibull distribution, 8
- Weibull modulus, 8
- Weld seam, 425
- Wet blast cleaning, 296–299, 301, 302, 316, 459
- Wettability, 362, 440–450

Working line, 111–112, 153–155, 159, 250
Work of adhesion, 434–439, 445

Yield strength, 170–172, 177, 394
Young equation, 435, 441

Young's modulus, 169, 174, 175, 176, 179,
181, 187, 215, 219, 392, 407

Zinc, 327, 331, 353, 365, 372, 384,
458–462, 469

Zisman plot, 435–437